IMPERIAL

Spores-on-a-Chip: Investigations on arbuscular mycorrhizal fungi using novel microfluidic technology

Felix Richter

Submitted for the Degree of Doctor of Philosophy

Supervised by Dr Claire Stanley

Imperial College London

Department of Bioengineering

London, 27 September 2024

Word count: 54,706

STATEMENT OF ORIGINALITY

I, Felix Richter, certify that all the material presented in this thesis is entirely my own work, except from published and unpublished sources which are clearly indicated and acknowledged accordingly. No material in this thesis has been previously submitted for another degree from any other institution.

This thesis contains material directly from first author publications. Where this is done, author contributions are clearly outlined. Copyright was obtained from each publisher where open access was not already granted.

COPYRIGHT DECLARATION

The copyright of this thesis rests with the author. Unless otherwise indicated, its contents are licenced under a Creative Commons Attribution-Non Commercial 4.0 International Licence (CC BY-NC). Under this licence, researchers may copy and redistribute the material in any medium or format. They may also create and distribute modified versions of the work. This is on the condition that: They credit the author and do not use it, or any derivative works, for a commercial purpose. When reusing or sharing this work, they must make the licence terms clear to others by naming the licence and linking to the licence text. Where a work has been adapted, they should indicate that the work has been changed and describe those changes. Please seek permission from the copyright holder for uses of this work that are not included in this licence or permitted under UK Copyright Law.

ABSTRACT

The arbuscular mycorrhizal fungi (AMF) form a symbiosis with most terrestrial plants on earth and provide them with soil nutrients and an increased general resilience against environmental stresses. AMF research, however, due to their soil-borne nature, is commonly hampered by soil's lack of transparency, rendering experiments "black-box" studies. To overcome these issues, this PhD-project set out to fill existing gaps in AMF research, such as morphogenesis and space navigation at the asymbiotic stage, exploiting novel microfluidic technologies.

The first part of the thesis describes and discusses the development of the *AMF-SporeChip*, a microfluidic device designed to trap and germinate AMF spores and confront asymbiotic hyphae with physical obstacles. After demonstrating the functionality of the final device design, new insights and observations uncovered are detailed. As such, the highly dynamic space navigation repertoire of AMF is analysed, revealing the never before described phenomenon of *reversible* cytoplasmic retraction. To round off the examination of the fungi's growth behaviour, a search was started for the Spitzenkörper in AMF. Therefore, tissue-specific fluorescent dyes were introduced into the devices but no Spitzenkörper could be detected.

The second part of the thesis concerns itself with a new device, coined the *AMF-AnastomosisChip*. This device was specifically developed to isolate and study hyphal fusions, called anastomoses, in AMF. The final device was successfully tested and characterised based on loading performance as well as the growth behaviour of the fungi including anastomosis types and frequency. Furthermore, the establishment of chemical gradients in the device was first modelled and then demonstrated.

The thesis concludes with a presentation of alternative uses of the *AMF-SporeChip*, involving oxygen sensing as well as cultivation of *Mucoromycotina* fine-root endophytes (MFRE). Finally, possible future avenues that could be followed with microfluidics-assisted research on AMF are discussed.

ACKNOWLEDGEMENTS

This thesis would not have been possible without the support and contribution of many people. Therefore, I would like to express my gratitude to everyone involved in the course of this project.

First and foremostly I would like to thank Dr Claire Stanley for creating and giving me the opportunity to work on this project and simply for being an amazing supervisor over the last 4 years.

Special thanks go to Prof Stéphane Declerck and Dr Maryline Calonne-Salmon for not only providing the biological material for this project, but also invaluable expertise all around AMF and AMF cultivation. In that sense I would also like to thank Prof Marcel van der Heijden, Prof Pilar Junier and Dr Saskia Bindschedler for their important input which made publishing our papers possible.

I would especially like to thank Prof Ian Sanders and Dr Erica McGale for the great and fruitful collaboration on the *AMF-AnastomosisChip*. Furthermore, I thank Dr Lukas Wick, Dr Bijing Xiong and Yiqing Zhang for collaborating with me on the sensor foil device. I would also like to thank Dr Silvia Pressel and Dr Victor Rodriguez-Morelos for assisting me with setting up the MFRE experiments at the Natural History Museum.

Many thanks also to all current and past Stanley Lab members for fantastic co-operation in organising the lab as well as mutual scientific support at all times. A special thank you I would like to extend to Kate Collins for all the fantastic COMSOL modelling.

Another thank you goes out to the departmental facility managers Dr Shahrzad Forouzanfar, Dr Florent Seichepine and Dr Miguel Hermida Ayala for helpful training and aid in troubleshooting microfabrication or confocal microscopy as well as to the SynBio technicians Nana Asamoah-Danso and Ellie Wareham.

And of course, thank you to my family for their unconditional support, even from afar.

Last but not least I thank soon-to-be Dr Gabriela Rebeca Velasquez Diaz for her image drawing skills, being so cute and all the love.

TABLE OF CONTENTS

STATEMENT OF ORIGINALITY **3**

COPYRIGHT DECLARATION **4**

ABSTRACT **5**

ACKNOWLEDGEMENTS **6**

TABLE OF CONTENTS **7**

LIST OF FIGURES **9**

LIST OF TABLES **11**

LIST OF SUPPLEMENTARY MOVIES **12**

LIST OF ABBREVIATIONS **14**

PUBLICATIONS **16**

CHAPTER 1: INTRODUCTION **17**

1.1 Introduction 17
1.2 Background 18
1.2.1 Fungi *18*
1.2.1.1 Mycorrhizal fungi 20
1.2.2 Microfluidics *28*
1.2.2.1 Microfluidics for fungi 31
1.3 Research Objective 39
1.4 Thesis outline 42

CHAPTER 2: MATERIALS AND METHODS **43**

2.1 PDMS device manufacturing 43
2.1.1 Master mould manufacturing *43*
2.1.2 PDMS device manufacturing *46*
2.2 AMF cultivation 47
2.2.1 Root organ and pot cultures *47*
2.2.2 Media preparation *48*
2.2.3 Chicory root culture *48*
2.2.3 AMF two-compartment culture *49*
2.3 Microscopy and image processing 51

CHAPTER 3: DEVELOPMENT OF THE *AMF-SPORECHIP* **53**

3.1 Chapter overview 53
3.2 Results and Discussion 54
3.2.1 Device Development *54*
3.2.1.1 Device Design 54
3.2.1.2 Optimisation of the photolithography protocol 61
3.2.1.3 Spore isolation and introduction into the device 65
3.2.2 Device characterisation *71*
3.2.2.1 Spore loading and trapping 71
3.2.2.2 Spore germination and hyphal growth behaviour in the confined environment 73
3.3 Chapter conclusion 89

CHAPTER 4: AMF SPACE SEARCHING 90

4.1 Chapter overview 90
4.2 Results and Discussion 92
4.2.1 Space searching in AMF 92
4.2.2 Reversible cytoplasmic retraction 98
4.2.3. Introduction of fluorescent dyes 103
4.2.4. Using fluorescent staining for studying sub-cellular structures 106
4.2.5. Anastomosis formation in the device 126
4.3 Chapter conclusion 132

CHAPTER 5: ANASTOMOSIS DEVICE 134

5.1 Chapter overview 134
5.2 Results and Discussion 135
5.2.1. Device development 135
5.2.2 Spore loading and growth performance in the AMF-AnastomosisChip 153
5.2.3 Application of the AMF-AnastomosisChip for establishment of diffusion gradients 163
5.3. Chapter conclusion 168

CHAPTER 6: FUTURE DIRECTIONS AND CONCLUSION 169

6.1 Chapter overview 169
6.2 Results and Discussion 170
6.2.1 Development of a sensor foil device 170
6.2.2 Proof-of-concept growth experiments of Mucoromycotina fine-root endophytes (MFRE) in the AMF-SporeChip 183
6.3 Concluding remarks and future directions for microfluidic AMF research 189

BIBLIOGRAPHY 194

APPENDIX 207

Appendix 1: Composition of the MSR medium 207
Appendix 2: Measurements of hyphal diameters 208
Appendix 3: Schematics of secondary devices used in the project 209
Appendix 4: Publications 211

LIST OF FIGURES

Figure 1: Schematic of the AMF life cycle illustrating the main stages. 25
Figure 2: Examples of microfluidic platforms for space searching studies in filamentous fungi. 33
Figure 3: Microfluidic platforms for the study of hyphal interactions. 37
Figure 4: Overview of the research objectives of the thesis. 41
Figure 5: Two-compartment co-culture of *Rhizophagus irregularis* MUCL 41833 and chicory roots. . 50
Figure 6: Schematic design of the first prototypes of the *AMF-SporeChip* highlighting the different parts of the device and channel heights. 55
Figure 7: Phase contrast images showing hyphae of *Rhizophagus irregularis* MUCL 41833 growing in the *AMF-SporeChip* prototype. 57
Figure 8: Schematic designs of the *AMF-SporeChip* highlighting the different parts of the device and channel heights for the obstacle-type designs. 58
Figure 9: Geometries of the open obstacle-type structures with internal angles and contact interfaces indicated in red. 59
Figure 10: Schematics showing the development of the lane-type designs of the *AMF-SporeChip*. ... 60
Figure 11: Photographs of the hot plate set-up for the lithography process in the clean room. 62
Figure 12: Images showing results of the master mould manufacturing. 65
Figure 13: Images of different spore dissection attempts. 68
Figure 14: Images of different needle assisted spore dissection attempts. 69
Figure 15: Spore introduction into the devices. 70
Figure 16: Spore trapping performance in the *AMF-SporeChip*. 72
Figure 17: Measured spore diameters of the arbuscular mycorrhizal fungi (AMF) strains used in the project. 74
Figure 18: Germination of 3 *Rhizophagus* strains in the *AMF-SporeChip*. 76
Figure 19: Fungal growth assays comparing on-chip and on-plate. 80
Figure 20: Germination rates of the three *Rhizophagus* strains in the *AMF-SporeChip*. 82
Figure 21: Fungal growth assays comparing two different media on-chip. 84
Figure 22: *Gigaspora margarita* growing in the *AMF-SporeChip*. 87
Figure 23: Comparison of nestling/tracking behaviour in hyphae of *Rhizophagus irregularis* and *Neurospora crassa*. 93
Figure 24: Comparison of hit-and-split behaviour in hyphae of *Rhizophagus irregularis* and *Neurospora crassa*. 94
Figure 25: Head-on collision of *Rhizophagus irregularis* hypha with channel wall. 96
Figure 26: Reversible cytoplasmic retraction in the *AMF-SporeChip*. 99
Figure 27: Quantitative analysis of reversible cytoplasmic retraction in the *AMF-SporeChip*. 102
Figure 28: Fluorescent end-point staining of vital and empty hyphae. 105
Figure 29: Comparison of FM4-64 concentration for fluorescent staining of *Rhizoctonia solani*. 107
Figure 30: Response of *Rhizoctonia solani* hypha to introduction of 10 µM FM4-64 with a flow rate of 120 µl/min. 109
Figure 31: Response of *Rhizoctonia solani* hypha to introduction of 10 µM FM4-64 with a flow rate of 20 µl/min. 110
Figure 32: Fluorescence images of *Rhizoctonia solani* hyphae. 112
Figure 33: Confocal fluorescent images of *Rhizoctonia solani* hyphae. 113
Figure 34: Fluorescence images of *Neurospora crassa* hyphae. 114
Figure 35: Response of *Neurospora crassa* hypha to light exposure during fluorescence microscopy. 116

Figure 36: Response of *Neurospora crassa* hypha to light exposure during fluorescence microscopy. 117
Figure 37: Response of *Neurospora crassa* hypha to light exposure during fluorescence microscopy. 118
Figure 38: Fungal growth assays comparing effects of different FM4-64 concentrations on-chip..... 121
Figure 39: Comparison of FM4-64 concentration for fluorescent staining of *Rhizophagus irregularis* MUCL 43194. 123
Figure 40: Confocal fluorescent images of *Rhizophagus irregularis* MUCL 43194 spore and hyphae. 124
Figure 41: Anastomosis events in *Rhizophagus irregularis* MUCL 43194 in the *AMF-SporeChip*..... 128
Figure 42: Anastomosis in *Rhizophagus irregularis* MUCL 43194 in the *AMF-SporeChip*. 130
Figure 43: Schematics of the first prototypes of the *AMF-AnastomosisChip*. 137
Figure 44: Spore loading performance of the first prototypes of the *AMF-AnastomosisChip*. 138
Figure 45: Schematics of the second prototypes of the *AMF-AnastomosisChip*. 141
Figure 46: Spore loading performance of the second prototypes of the *AMF-AnastomosisChip*. 142
Figure 47: Spore loading performance of the second prototypes of the *AMF-AnastomosisChip*. 144
Figure 48: Schematics of the third prototypes of the *AMF-AnastomosisChip*..... 145
Figure 49: COMSOL modelling of flow in prototypes of the *AMF-AnastomosisChip*..... 147
Figure 50: COMSOL modelling of flow in prototypes of the *AMF-AnastomosisChip*..... 148
Figure 51: Spore loading performance of the third prototypes of the *AMF-AnastomosisChip*..... 149
Figure 52: Spore loading performance of the third prototypes of the *AMF-AnastomosisChip* after optimisation of the loading protocol. 151
Figure 53: Final design and loading performance of the *AMF-AnastomosisChip*..... 153
Figure 54: Quantitative analysis of the spore loading performance in the *AMF-AnastomosisChip*. .. 155
Figure 55: Quantitative analysis of the growth performance in the *AMF-AnastomosisChip*. 158
Figure 56: Anastomosis event in the *AMF-AnastomosisChip*. 161
Figure 57: Example of anastomosis in the *AMF-AnastomosisChip*..... 162
Figure 58: COMSOL model of diffusion behaviour in the *AMF-AnastomosisChip*..... 164
Figure 59: Real-life diffusion in the *AMF-AnastomosisChip*. Fluorescence time series showing the diffusion of fluorescein into the device. 165
Figure 60: Spin coating of PDMS onto sensor foil..... 172
Figure 61: Oxygen measurements with the sensor foil. 174
Figure 62: Oxygen level measurements in sensor foil device. 176
Figure 63: Problems with visibility through sensor foil..... 177
Figure 64: Oxygen depletion within the sensor foil device over time. 179
Figure 65: Development of oxygen levels around fungal hyphae..... 180
Figure 66: Loading of two different microfluidic devices with a *Mucoromycotina* fine-root endophyte (MFRE)..... 185
Figure 67: Growth of *Mucoromycotina* fine-root endophytes (MFRE) in a microfluidic device..... 188
Figure 68: Overview of the research objectives and outcomes of the thesis..... 190

Figure A1: Hyphal diameters of arbuscular mycorrhizal fungi (AMF) strains used in this project. 208
Figure A2: Schematic representation of the *fluid exchange device.* 209
Figure A3: Schematic representation of the device used for sensor foil application. 209
Figure A4: Schematic representation of the *BFI device.* 210

LIST OF TABLES

Table 1: Summary of total anastomoses and related events counted. 160

Table A1: Composition of modified Strullu-Romand (MSR) medium (after Fortin *et al.* (2002)). 207

LIST OF SUPPLEMENTARY MOVIES

Movies 1-4, 6-8, 10-13, 16, 17 and 19 reproduced from Richter *et al.* (2024) with permission from the Creative Commons Attribution license (www.creativecommons.org/licenses/by/4.0/).

Movie 1: Germination of *Rhizophagus irregularis* MUCL 41833 in the *AMF-SporeChip*.

Movie 2: Germination of *Rhizophagus irregularis* MUCL 43194 in the *AMF-SporeChip*.

Movie 3: Germination of *Rhizophagus intraradices* MUCL 49410 in the *AMF-SporeChip*.

Movie 4: Hypha of *Gigaspora margarita BEG 34* growing into the *AMF-SporeChip*.

Movie 5: Hypha of *Rhizophagus irregularis* MUCL 43194 tracking a channel wall in the *AMF-SporeChip*.

Movie 6: “Hit and split” event of *Rhizophagus irregularis* MUCL 43194 in the *AMF-SporeChip*.

Movie 7: Dynamic hyphal behaviour of *Rhizophagus irregularis* MUCL 41833 in the *AMF-SporeChip* involving cytoplasmic retraction events.

Movie 8: Head-on collision of *Rhizophagus irregularis* MUCL 43194 hypha with channel wall in the *AMF-SporeChip* involving pushing itself backwards.

Movie 9: Head-on collision of *Rhizophagus irregularis* MUCL 43194 hypha with a Pac-Man-type obstacle in the *AMF-SporeChip* involving pushing itself backwards.

Movie 10: Growth arrest of *Rhizophagus irregularis* MUCL 43194 hypha in the *AMF-SporeChip*.

Movie 11: Spore forming in asymbiotic hypha of *Rhizophagus irregularis* MUCL 43194 in the *AMF-SporeChip*.

Movie 12: Spores of *Rhizophagus intraradices* MUCL 49410 internally collapsing in the *AMF-SporeChip*.

Movie 13: Reversible cytoplasmic retraction of *Rhizophagus irregularis* MUCL 41833 hypha in the *AMF-SporeChip*.

Movie 14: Fluorescent timelapse of *Neurospora crassa* hypha branching in the *AMF-SporeChip*.

Movie 15: Fluorescent timelapse of “Hit and split” event of *Neurospora crassa* in the *AMF-SporeChip*.

Movie 16: Tip-to-tip anastomosis between a hypha and a germination site of *Rhizophagus irregularis* MUCL 43194 in the *AMF-SporeChip*.

Movie 17: Tip-to-side anastomosis between two hyphae of *Rhizophagus irregularis* MUCL 43194 in the *AMF-SporeChip*.

Movie 18: Unsuccessful tip-to-side anastomosis between two hyphae of *Rhizophagus irregularis* MUCL 43194 in the *AMF-SporeChip*.

Movie 19: Tip-to-tip anastomosis between two hyphae of *Rhizophagus irregularis* MUCL 43194 in the *AMF-SporeChip*.

LIST OF ABBREVIATIONS

2-NBDG	2-Deoxy-2-[(7-nitro-2,1,3-benzoxadiazol-4-yl)amino]-D-glucose
3D	Three-dimensional
ABC	ATP-binding cassette (transporter)
AMF	Arbuscular mycorrhizal fungi
ANOVA	Analysis of variance
BAS	Branched adsorbing structures
BTB	Bromothymol blue
CFW	Calcofluor white
CMN	Common mycorrhizal networks
DAPI	4′,6-Diamidino-2-phenylindole
DNA	Deoxyribonucleic acid
dTom	dTomato
FITC	Fluorescein-5-Isothiocyanate
FM4-64	Fei-Mao 4-64 (dye)
GFP	Green fluorescent protein
GlcNAc	N-acetylglucosamine
GM	Gamborg B5 (medium)
HF	Hydrogen fluoride
IR	Infrared (light)
LED	Light-emitting diode
LTCC	Low temperature co-fired ceramics

MAPK	Mitogen-activated protein kinase
Max IP	Maximum intensity projection
MSC	Microbiological Safety Cabinet
MSR	Modified Strullu-Romand (medium)
Myc-LOC	Mycorrhiza-lipochitooligosaccharides
NopE1	Nodulation outer proteins E1
PC	Polycarbonate
PDA	Potato dextrose agar
PDB	Potato dextrose broth
PDMS	Poly(dimethylsiloxane)
PDR1	Pleiotropic drug resistance 1
PET	Polyethylene terephthalate
PMMA	Poly(methyl methacrylate)
PS	Polystyrene
PSB	Phosphate solubilising bacteria
PVC	Polyvinylchloride
RNA	Ribonucleic acid
ROS	Reactive oxygen species
TAL	Transcription activator-like (effector)
TPX	Trademark of Mitsui Chemicals for Polymethylpentene
TRITC	Tetramethylrhodamine-isothiocyanate
UV	Ultraviolet (light)

PUBLICATIONS

Richter F, Bindschedler S, Calonne-Salmon M, Declerck S, Junier P, Stanley CE. Fungi-on-a-Chip: microfluidic platforms for single-cell studies on fungi, *FEMS Microbiology Reviews*, Volume 46, Issue 6, November 2022, fuac039

Richter F, Calonne-Salmon M, van der Heijden MGA, Declerck S, Stanley CE. *AMF-SporeChip* provides new insights into arbuscular mycorrhizal fungal asymbiotic hyphal growth dynamics at the cellular level, *Lab on a Chip*, Volume 24, Issue 7, February 2024, 1930-1946

Richter F, McGale E, Calonne-Salmon M, Collins K, Declerck S, Sanders IR, Stanley CE. Spores-on-a-Chip: a new microfluidic platform for investigations on anastomosis in asymbiotic hyphae of arbuscular mycorrhizal fungi, 2024, *in preparation*.

CHAPTER 1: INTRODUCTION

1.1 Introduction

The mycorrhiza is one of the most important symbioses on earth. This interaction between plant roots and fungi forms the foundation for all soil-based ecosystems on the planet. Colonising ca. 70-80% of all terrestrial plants, the arbuscular mycorrhizal fungi (AMF), soil-dwelling fungi belonging to the phylum *Glomeromycota*, form the most abundant group (Bonfante and Genre, 2010; van der Heijden *et al.*, 2015; Cosme *et al.*, 2018). Within this mutually beneficial interaction, the plant host obtains soil nutrients, mainly phosphorous and nitrogen, but also zinc, copper and iron (Smith and Read, 2008a), from the fungus, while the obligate symbiont fungi receive essential photosynthesis products in return. Due to their enormous importance, AMF have been subject of many studies within the last decades, with implications for agriculture (Basu *et al.*, 2018), understanding ecosystem stability (Rillig, 2004) and co-evolution with plants (Corradi and Bonfante, 2012). Despite these efforts, much still remains unknown about, for example, the influence of environmental cues on spore germination, hyphal morphogenesis and space searching as well as hyphopodium formation in AMF, processes marking the first steps of the fungi's life cycle. This is mainly due to the solely soil-borne nature of these fungi, rendering experiments often to be a "black-box". In addition, inoculation with AMF spores in the field still often fails (Verbruggen *et al.*, 2013; Berruti *et al.*, 2016; Prado-Tarango *et al.*, 2021). Furthering the grasp on these aspects would benefit the overall understanding of the symbiosis establishment, which in turn could help advance harnessing AMF for biofertilisation and bioremediation. To overcome these issues and fill existing gaps in AMF knowledge, the development of different experimental platforms is needed and we set out to employ a new method – microfluidic technology – to AMF research. The field of microfluidics is relatively new, having been applied to tackle research questions in both chemistry and biology for a variety of applications, such as synthesis (Sun *et al.*, 2016), analysis (Ohno *et al.*, 2008; Berlanda *et al.*, 2021) as well as cultivation and screening (Warrick *et al.*, 2008; De Stefano *et al.*, 2022). These systems rely on microchannels filled with liquid or gas, which can be tailored with unique patterns, allowing for a strong controllability of the process and the on-chip environment, e.g., by implementing a specific

physical layout or chemical gradients made possible by the laminar flow profile intrinsic to the micro dimension. Microfluidic devices are often made from optically transparent materials, such as the elastomeric polymer poly(dimethylsiloxane) (PDMS), which, as another major advantage, allows for precise brightfield and fluorescence imaging that is further enhanced by Z-axis confinement to improve focus. Further to the confinement, the enclosed nature of the system entails an intrinsic sterility and containment of pathogens or hazardous substances. Making use of these benefits, we were seeking to gain deeper insight into AMF spore germination, anastomosis formation as well as hyphal space searching strategies upon confrontation with physical obstacles.

1.2 Background

1.2.1 Fungi

For a long time, fungi have impressed and puzzled biologists with their enormous diversity and assigning them to Aristotle's classic dual classification system of Plantae and Animalia has proven difficult if not impossible. Only recently (compared to the age of the old system), when Whittaker (1969) introduced his novel five-kingdom classification system supported by advances in molecular genetics (Kendrick, 2017), fungi received the status of an independent kingdom. Fungi possess traits from the other kingdoms, such as a heterotrophic lifestyle like animals, or cells surrounded by a cell wall and containing vacuoles, as well as co-existing sexual and asexual reproduction like plants. Furthermore, many fungi form vast hyphal networks in soil, called mycelium, just like the root networks of plants. These mycelia have been found to span areas of up to 10 km^2 (e.g., the mycelia of the Basidiomycete *Armillaria ostoyae* (Schmitt and Tatum, 2008)), which beats dimensions of root networks by far, and signifying up to 50% of soil dry weight (Ingham *et al.*, 1991). In spite of their vast dimensions, however, fungi count as microorganisms like bacteria. Besides these microscopic dimensions, especially in yeasts, which are mainly unicellular, fungi share certain metabolic pathways with bacteria, as for instance the specific isomerisation between homoaconitate and homoisocitrate (Fazius *et al.*, 2012). Apart from yeasts, the other two main types of fungi are filamentous moulds and mushrooms with their famous fruiting bodies (Webster and Weber, 2007). Some fungal species are dimorphic, which means they can switch from one morphology to another

(i.e., unicellular to filamentous). The opportunistic pathogen *Candida albicans*, for example, is capable of morphing from its single-cell yeast form to a filamentous configuration and vice versa (Kadosh, 2019), which, in fact, is crucial for the infection process (Mayer *et al.*, 2013). Besides this shape-shifting ability, some fungi show different morphologies depending on which current stage of their life cycle they are at, i.e., vegetative, asexual, or sexual phase. In the past, this has led to the same species accidentally being named more than once. To account for this phenomenon, unprecedented in nature, the terms teleomorph (the sexual form), anamorph (the asexual form), and holomorph (fungi for which both a sexual and asexual lifestyle is known) were coined. For some species, a dual nomenclature was kept until 2013, when, after much disagreement amongst mycologists, the principle of one fungus having one name ('one fungus, one name'; (Wingfield *et al.*, 2012)) was implemented.

Mycology, compared to the other fields of study in biology, is still considered a young discipline and niche. Out of the 2.2–3.8 million fungal species estimated to exist in nature, only around 148,000 have been described so far (Hawksworth and Lücking, 2017) and only in the last 20 years, mycology has dropped its popular image of being the sole study of mushrooms, i.e., the macroscopic structures that are found in forests or that can be bought in a supermarket to eat. Other types and aspects of fungi, e.g., symbionts or pathogens, have been studied in other fields but not as part of a wider, common research discipline. Fungi are not only mysterious and intriguing, they also hold an immense and extensive significance in medicine, biotechnology, agriculture as well as for nature as a whole. Historically, fungi have been harnessed in food or beverage processing for millennia. Nowadays, backed by extensive knowledge of fungal metabolic pathways, optimised biotechnological processes use fungi for the mass production of ethanol by, for example, the yeast *Saccharomyces cerevisiae* (estimated 110 billion litres produced annually, (U.S. Department of Energy, 2020)) or citric acid by the mould *Aspergillus niger* (Show *et al.*, 2015). In medicine, fungi can be both friend and foe. The famous antibiotic penicillin (Barrios-González *et al.*, 1988) or the immunosuppressant cyclosporin A (Ramana Murthy *et al.*, 1999), for example, are important medicaments, produced by fungi. On the other hand, however, certain fungi are the cause of severe diseases in humans (e.g., *Cryptococcus neoformans* or *Aspergillus fumigatus*) as well as other animals, but also in plants. Fungal infections of crops regularly lead to food shortages

or financial losses on the order of billion dollars. In the US, for instance, the fungal plant pathogen *Fusarium graminearum* causes annual losses in wheat and barley harvest ranging between 6% and 19% (McMullen *et al.*, 2012). In general, potent antifungal agents are lacking (Almeida *et al.*, 2019), but here again, fungi can be of assistance. As promising alternatives for chemical fungicides, mycoparasitic fungi such as *Clonostachys rosea* and *Trichoderma* spp. are being studied as biocontrol agents (M. Butt and G. Copping, 2000; Köhl *et al.*, 2019). In nature, as the main decomposer, fungi degrade dead organic matter and return it into the natural nutrient cycle, thus significantly affecting the availability of many elements. This ability can be utilised for artificial bioremediation or in biofertilisation (Carvajal-Muñoz and Carmona-Garcia, 2012). For the latter, mycorrhizal fungi in particular have been reported to increase yields in crops considerably (Hamel, 2007) due to their ability to form a symbiosis with the roots of plants.

1.2.1.1 Mycorrhizal fungi

The unique symbiosis between certain fungi and the roots of higher terrestrial plants was first termed “mycorrhiza” in 1885 by Albert Bernhard Frank (1885). This mutualism is considered to be as old as 450 million years (Redecker *et al.*, 2000) and co-evolved along with plants; indeed, only with the help of mycorrhizal fungi, were plants able to colonise the land (Smith and Read, 2008b). Mycorrhiza have established in every soil-based ecosystem on Earth and plants which are non-mycorrhizal are a clear minority (Bonfante and Genre, 2010; van der Heijden *et al.*, 2015; Cosme *et al.*, 2018). This renders the mycorrhiza the symbiosis with the most widespread importance in nature, compared to the similar interaction between *Rhizobia* and roots of legumes, which, however, is only common to one plant family, *Fabaceae* (or *Leguminosae*) (Peter *et al.*, 1996). The main aspect of the mycorrhizal symbiosis is the nutrient exchange between plant and fungus, with the fungus providing prospected soil nutrients, mainly phosphorous and nitrogen, but also zinc, copper and iron, and the plant delivering photosynthetic carbon in return (Smith and Read, 2008b). Furthermore, the symbiosis increases the resistance against soil pathogens, heavy metals or drought, reduces nutrient leaching and improves the environment for the establishment of fresh plant seedlings (van der Heijden *et al.*, 1998). The formation of the exchange interface can be invasive, with the fungus

penetrating the cell walls of host root cells, or not, as observed with ectomycorrhizal fungi. In this mycorrhizal type, fungal hyphae grow around the host root in a dense so-called “mantle”. From this sheath, several hyphae penetrate into the root, growing between and around epidermis, cortex and endodermis cells. The depth of this so-called “Hartig net” depends on the species (Blasius *et al.*, 1986; Smith and Read, 2008b). The ectomycorrhiza is mainly found in forest ecosystems (predominantly temperate) involving most tree families such as *Pinaceae*, *Salicaceae*, and *Tiliaceae*, as well as members of other plant families such as *Rosaceae*, *Leguminaceae* and *Myrtaceae* (Smith and Read, 2008b). In some instances, ectomycorrhizal colonisation has even been reported in lower plants like liverworts (Edwards *et al.*, 2000). On the fungal side, many mushrooms of the divisions *Basidiomycota* and *Ascomycota*, including the genera *Boletus*, *Suillus*, *Russula*, *Laccaria*, *Scleroderma* and *Pisolithus* (Basidiomycetes) or *Tuber* and *Cenococcum* (Ascomycetes) form ectomycorrhizae (Smith and Read, 2008b).

All other types of mycorrhiza are endomycorrhizal, i.e., the fungi penetrate the cell wall and form the interface for nutrient exchange within the host cell. The three types of endomycorrhiza are ericoid, orchid and arbuscular mycorrhiza. Ericoid mycorrhizae are found predominantly in heathland-type ecosystems including common heathlands in the northern hemisphere, tropical cloud forests, woodlands in the Mediterranean, as well as the dry and sandy plains of Australia, which all share very low nutrient availability, with, however, an abundance of metals, low pH, inefficient drainage and high or low temperatures (Cairney and Meharg, 2003). Here, the ericoid mycorrhizal fungi, which are mainly Ascomycetes of the *Leotiomycete* class and a few Basidiomycetes in the *Serendipitaceae* (Perotto *et al.*, 2018), play a crucial role in populating these harsh environments by assisting the pioneer plants. These plants are members of the *Ericaceae* family, eponymous for this mycorrhiza (Cairney and Meharg, 2003).

The orchid mycorrhiza equally received its name from the plant host, orchids. Here, intriguingly, the plant is the obligate symbiont, while in the other mycorrhizae, either the fungus depends on the plant (see *2.1.2. Arbuscular mycorrhizal fungi*) or the mutualism is beneficial but not essential for both partners. During the so-called protocorm stage, orchid seedlings are only able to develop into a grown plant if colonised by an orchid mycorrhizal fungus (Dearnaley *et al.*, 2016). Only Basidiomycetes have been reported to associate with orchids, so far,

including the genera *Thanatephorus*, *Sebacina*, *Tulasnella*, *Armillaria* and *Ceratobasidium* (Rasmussen, 2002). The latter genus contains *Rhizoctonia solani*, which is featured in several experiments in this thesis (see *4.2.4. Using fluorescent staining for studying sub-cellular structures*).

The most abundant type of mycorrhiza and thus one of the most important ones, is the arbuscular mycorrhiza. Because of its significance and central role in this thesis, it will be discussed in a separate, dedicated section.

Three other types of mycorrhiza, i.e., ectendo-, arbutoid- and monotropoid mycorrhiza have so far not qualified as separate groups and are rather currently counted as sub-groups of the ectomycorrhiza (Brundrett, 2004). While they form the typical mantle and Hartig net, ectendo- and arbutoid mycorrhizal fungi penetrate plant cell walls. While ectendomycorrhizae form with regular ectomycorrhizal hosts, like pine trees (Yu *et al.*, 2001), both arbutoid and monotropoid mycorrhizae are found in plants of the *Ericaceae* family (like the ericoid mycorrhiza), i.e., *Arbutoideae* and *Monotropideae*, respectively. Interestingly, it has been shown under controlled experimental conditions that arbutoid mycorrhizal fungi form an arbutoid mycorrhiza with one plant and a regular ectomycorrhiza with another (Horton *et al.*, 1999). The monotropoid mycorrhiza is described as parasitic, rather than symbiotic, with the plant host mycoheterotrophically exploiting the fungus for carbon (Dickie *et al.*, 2013). Recently, a new group of endophytic fungi has split away from the *Glomeromycotina*. These so-called *Mucoromycotina* fine root endophytes (MFRE), historically described along *Glomeromycotina* (AMF), are currently, backed with mounting evidence, emerging as a new and unique group of mycorrhizal fungi (Prout *et al.*, 2023). These fungi are further discussed in *6.2.2 Proof-of-concept growth experiments of Mucoromycotina fine-root endophytes (MFRE) in the AMF-SporeChip*.

The arbuscular mycorrhiza

Fungi able to form an arbuscular mycorrhiza are exclusively members of the *Glomeromycota* phylum. Unlike other mycorrhizal fungi, which also possess saprotrophic capabilities, AMF are obligate symbionts, i.e., incapable of completing their life cycle without a suitable host. AMF can be found in all soil-based ecosystems, with some species being cosmopolitan, i.e.,

globally distributed, while other species are limited to specific regions (Stürmer *et al.*, 2018). It is estimated that about 300-1600 AMF species form a symbiosis with ca. 200,000 plant species (van der Heijden *et al.*, 2015). Even though arbuscular mycorrhizae are predominantly formed with grassland or understorey plants, which extends to many important crops, including onion, carrot, lettuce, cucumber, bean, as well as tomato, some trees like maple (Moutoglis and Widden, 1996) and poplar (Hooker *et al.*, 1992) are also AMF hosts. The arbuscular mycorrhiza, as by far the oldest of the mycorrhizal symbioses, developed intricate interaction mechanisms and highly specialised structures, i.e., the eponymous arbuscules (see *Stages of arbuscular mycorrhiza development*). The intracellular architecture varies between two types according to Gallaud (1905). In the Arum-type, as the "classical" image of the arbuscule structure, hyphae grow in the intercellular spaces between the root cortical cells and penetrate single cortex cells to form terminal, intracellular arbuscules (one per cell). The Paris-type describes a layout of entirely intracellular hyphae, moving from cell to cell. Within the cell, the hyphae coil irregularly and form small, non-terminal arbuscules (not limited to one per host cell) (Dickson *et al.*, 2007). Quite often, however, a clear distinction proves difficult and intermediate forms are adopted. Moreover, the same fungus can display both morphologies depending on the plant host (Dickson, 2004). While the plant species tends to be the determining factor, especially the intercellular space availability between the cortex cells (Brundrett and Kendrick, 1988), co-ocurrence of the Paris and Arum types in the same root system has been shown (Kubota *et al.*, 2005). Besides the arbuscules, some AMF form vesicles for lipid storage inside of the host roots and AMF have therefore been called vesicular-arbuscular mycorrhizal (VAM) fungi until the late 1990s (name change first suggested by Daft and Nicolson (1974)). However, as only some AMF genera such as *Glomus, Entrophospora* and *Sclerocystis* form vesicles and *Gigaspora* and *Scutellospora* do not, the name was changed to arbuscular mycorrhiza, based on the key and connecting characteristic of the symbiosis, the arbuscules (Douds and Millner, 1999).

For the experiments detailed in this thesis, *Rhizophagus irregularis*, *Rhizophagus intraradices* and *Gigaspora margarita* were used. *R. irregularis*, a species in the *Glomus* genus, is the best studied AMF strain, acting as a model organism for most investigations on the symbiosis and whose genome has been fully sequenced. This species, however, has undergone several

name changes over the years, from *Glomus intraradices*, to *Glomus irregulare* and finally *Rhizophagus irregularis*. And yet another name, *Rhizoglomus irregulare*, as the latest change has been proposed but so far not adopted in the field (Young, 2015). *R. irregularis* can be either homokaryotic (i.e., containing only genetically similar nuclei) or dikaryotic (i.e., containing two distinct nuclei genotypes) (Serghi *et al.*, 2021) with spores ranging between 10 and 160 µm in diameter (measured, see *3.2.2.2 Spore germination and hyphal growth behaviour in the confined environment*). *Gi. margarita* sports very large spores of up to 580 µm in diameter (average 470 µm, measured, see *3.2.2.2 Spore germination and hyphal growth behaviour in the confined environment*) with an equally gigantic genome compared to other fungi. While the higher fungi, Ascomycetes and Basidiomycetes, possess an average genome size of 37 Mbp and 46 Mbp, respectively, *Mucoromycotina* 39 Mbp and *R. irregularis* 91 Mbp (Mohanta and Bae, 2015), *Gi. margarita* genomes have been found to carry as much as 773 Mbp (Venice *et al.*, 2020). Interestingly, like many other fungi, *Gi. margarita* harbours highly host-specific and unculturable endobacteria. While the partnership is essential for the bacteria, the fungus is able to grow in absence of the endosymbiont, however, does benefit from the bacteria with an overall higher bioenergetic and antioxidant capacity (Bonfante and Desirò, 2017).

Stages of arbuscular mycorrhiza development

While the precise mechanisms, e.g., of host recognition, remain unknown and subject to intensive research, the main stages of arbuscular mycorrhiza formation and development are mostly clear. In general, the process can be split into presymbiotic communication, contact and penetration, outer cortex invasion, arbuscule formation, as well as vesicle and spore formation (Choi *et al.*, 2018). A schematic of the developmental stages is shown in Figure 1.

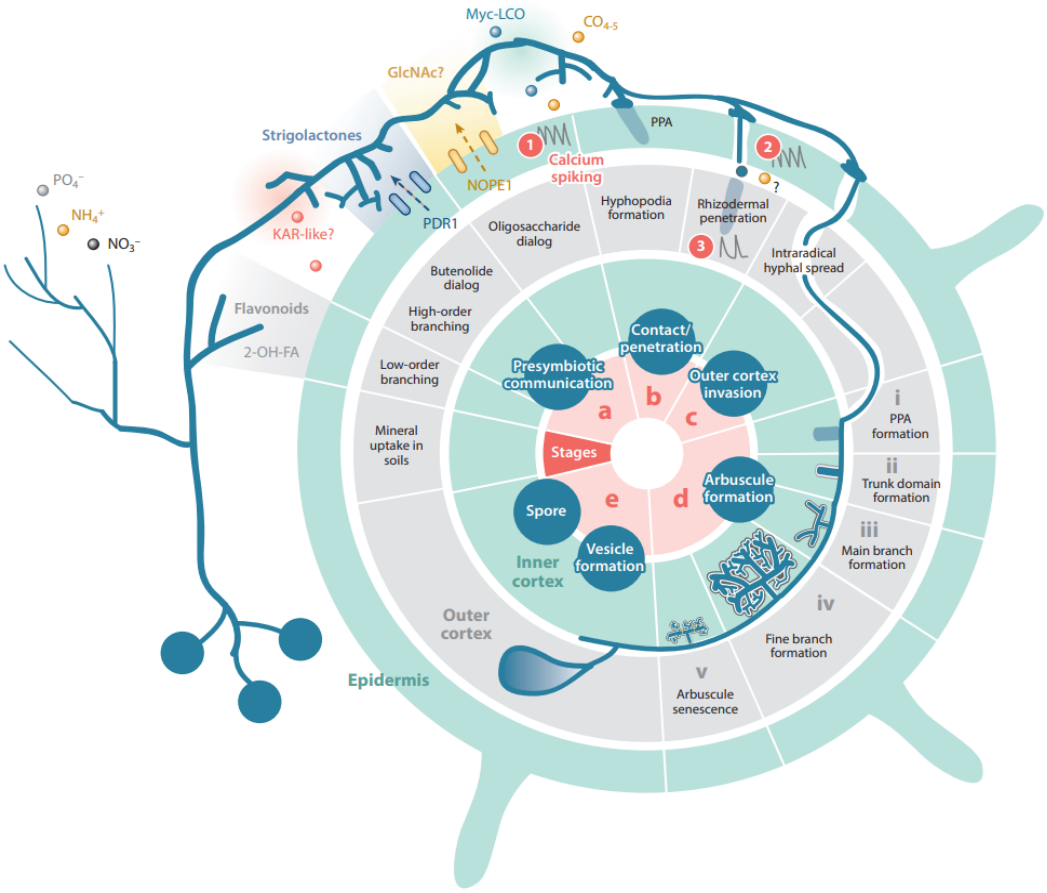


Figure 1: Schematic of the AMF life cycle illustrating the main stages. Presymbiotic communication, contact and penetration, outer cortex invasion, arbuscule formation, and vesicle & spore formation as well as sub-stages and involved signalling cues (a-e). Image reproduced from Choi *et al.* (2018) with permission from Annual Reviews (Licence Number: 1515015-1).

The arbuscular mycorrhiza commences with the germination of the AMF spores. Germination happens naturally without specific inducing cues but has been reported to be enhanced by certain substances, such as strigolactones and flavonoids (Tsai and Phillips, 1991; Buee *et al.*, 2000). Depending on the AMF strain, the fresh hypha or germ tube can emanate either directly from the spore wall (e.g., in *Gigaspora gigantean*, (Gerdemann and Trappe, 1974; Siqueira *et al.*, 1982) and own observations) or from an old hypha attached to the spore, also called the subtending hypha, as part of a cicatrisation process (e.g., in *R. irregularis*, (Gerdemann and Trappe, 1974) and own observations). Strigolactones, a group of recently discovered phytohormones, not only promote germination, as mentioned above, but also play a key role in presymbiotic signalling (Ruyter-Spira *et al.*, 2013). Released by an ATP-binding cassette transporter (ABC transporter) called Pleiotropic drug resistance 1 (PDR1), a strigolactone gradient is created, which leads the fungal hyphae towards the host root. Usually,

this cue is specific to a certain species to exclusively attract the beneficial symbiont. However, there are few parasitic plants, like *Striga* spp. or *Orobanche* spp., which hijack this strategy to attack the AMF host (Bouwmeester *et al.*, 2007). Further signalling molecules required for AM symbiosis initiation have been reported, such as N-acetylglucosamine (GlcNAc) with its respective plasma membrane transporter NOPE 1 (Nadal *et al.*, 2017), and more are likely to be discovered. Similar to GlcNAc, many other saccharide-based molecules, often associated with lipids and therefore called mycorrhiza-lipochitooligosaccharides (Myc-LOC), are exuded by the fungus. These signals prime the epidermal cells of the host plant and make it susceptible for the symbiotic association, coinciding with a calcium spiking in the root just before contact (Kosuta *et al.*, 2008). These calcium oscillations vary depending on plant or nutrient regime for instance (Li *et al.*, 2022). Once the actual contact has been established, the calcium response in the plant subsides, the fungus nestles against the root wall and displays isotropic growth resulting in a radial swelling, called the hyphopodium. The formation of this differentiated fungal body is suspected to be triggered by specific host markers, again with GlcNAc likely to be involved (Lefebvre, 2017). Another putative role is attributed to cutin monomers. While cutin itself, is a waxy polyester in the cuticle layer in plants and acts as a protective and water-repellent substance, its monomers were found to play a key role in signalling processes linked to host recognition (Murray *et al.*, 2013).

Following this initial fungal-plant interaction, the next step is the generation of a prepenetration apparatus or penetration peg, which emerges from the hyphopodium and pierces the epidermal cell wall. The formation of this secondary infection organ is triggered by specific cues, which are similar but different from those associated with hyphopodium formation. Moreover, Zhao *et al.* (2016) were able to demonstrate that knocking-out the VdNoxB or VdPls1 gene in *Verticillium dahlia* prevented penetration pegs from forming, while hyphopodia generation was unaffected, showing that different molecular mechanisms of cellular reorganisation for both steps in the infection process are involved. Prior to that, Giovannetti *et al.* (1993) proclaimed that for a successful hyphopodium and penetration peg formation both the right physical surface structure as well as chemical cues are necessary. The exact mechanisms underlying hyphopodium formation, however, remain unclear.

On the host side, a profound restructuring and softening of the cell wall is induced to embrace the fungal penetration peg (Parniske, 2000). The hypha then penetrates cell after cell, repeating the process again and again, until it finally reaches the cortical cells. For the invasion of these cells, a penetration peg is formed in an analogous manner, with the only difference being that it coincides with a division of the nucleus. This way, the fungus prepares for the arbuscule formation, entailing a high degree of differentiation and transcriptional work (Genre *et al.*, 2008). This highly complex fungal structure is produced in three steps. Following the invagination of the cortex cell with the prepenetration apparatus, firstly a single hyphal trunk grows into the plant cell which secondly starts to branch dichotomously into the cytoplasmic lumen. During the invasion, the cell wall of the cortical cell is not penetrated; it yields but stays wrapped around the hypha like a coat. Later in the arbuscule forming process, this plant-hyphal interface is remodelled into the so-called periarbuscular membrane, which involves glucanase and cellulose-synthase activity (Balestrini and Bonfante, 2014). Finally, many fine lateral branches are grown to enlarge the surface area, thus facilitating nutrient exchange between the symbionts. Further to the enzyme-assisted restructuring of the invaginated cell wall, the host cell undergoes profound transcriptional reprogramming (Heck *et al.*, 2016) and actively makes room for the arbuscule by shrinking the main vacuole and compressing cell organelles into a compact space saving unit (Pumplin and Harrison, 2009). These sophisticated structures, however, are highly transient and only after a few days, the arbuscule goes into senescence. Several septa are formed, gradually cutting off the arbuscule from the rest of the fungus. The final septum forms at the base of the trunk and the branches of the arbuscule degenerate while the main hypha remains vital (Alexander *et al.*, 1988).

Immediately after successful establishment of the symbiosis, the fungus produces vesicles. These lobular swellings at the end of hyphal branches, either situated within or in between the cortex cells, represent storage units for lipids. In a similar manner to the vesicles, the fungus generates asexual spores which also containing large amounts of lipids (Choi *et al.*, 2018). Same as most other fungi, AMF spores have been reported to be aerially dispersed (Chaudhary *et al.*, 2020). From there, the life cycle of the AMF starts anew.

1.2.2 Microfluidics

As the entire life cycle of AMF happens underground, concealed within the opaque soil, specific methods need to be applied for investigating these fungi. One such methodology, especially for phenotypical studies (e.g. of morphology or physiology), is microfluidics. While first developed for chemical synthesis and analysis (Terry *et al.*, 1979; Manz *et al.*, 1990), microfluidic (or Lab-on-a-Chip) technology quickly outgrew its origins. The underlying idea was inspired by the advances in the field of microelectronics, with its switch-like controllability of processes; not long after, the advantages were recognised in the field of biology as well (Azizipour *et al.*, 2020).

The field of microfluidics is dedicated to the design of microdevices and study of fluids, either gas or liquid, in miniature dimensions down to femtolitres, which are tailored to the task at hand for numerous applications. On the microscale, other effects are predominant than in the macroworld. Due to the small volumes, gravitational effects and inertial forces (except in inertial microfluidics) are usually negligible, whereas friction and capillary forces take over. Linked to that and representing one of the most characteristic aspects of microfluidics is the laminar and parabolic flow, described by the law of Hagen and Poiseuille (Zhang and Hoshino, 2014). Thus, in many microfluidic systems, mixing is dominated by diffusion. If, for instance, rapid mixing is required (e.g. during a chemical synthesis), special structures need to be implemented into the device to artificially create turbulences. The laminar or parabolic flow itself however can also be exploited for applications where creating and maintaining separate phases is desired (Stanley *et al.*, 2018), as well as in the field of inertial microfluidics (Di Carlo, 2009; Liu *et al.*, 2021). Besides the common continuous phase set-ups, multi-phase systems are used to create droplet sequences within the microchannels. This branch of microfluidics, the so-called droplet-based techniques, offers an unprecedented level of throughput for screening tasks (Payne *et al.*, 2020) or the ability to manipulate chemical reactions to an immensely enhanced product specificity (Skelton *et al.*, 2001; Carroll *et al.*, 2008). The intrinsic short pathlength in microfluidic systems for diffusion, heat transfer as well as photons, allows for a nearly undelayed “switching on” of reaction or incubation conditions (DeMello, 2006; Dittrich and Manz, 2006), just as envisioned in the original microelectronic-esque concept of microfluidics. This highly precise process control along with the enclosed nature of the

systems, further allows for a much safer handling of hazardous processes like, e.g., fluorination or the synthesis of hydrogen peroxide (Sun *et al.*, 2016) as well as an intrinsic sterility and containment of pathogens.

One drawback of this miniaturised approach is the low total output compared to conventional industrial batch processes, which however, can be compensated by “numbering-up” (Kriel *et al.*, 2016). Here, an aggregate of multiple identical microdevices is assembled to increase the overall synthesis output, which in turn circumvents the tedious scale-up process.

Microfluidic devices can be produced from many different materials and often feature a combination of several. Most commonly, polymers are used for manufacturing devices as the material is generally cheap and the processes require relatively little effort and machinery. Thermoplastics, such as poly(methyl methacrylate) (PMMA), polycarbonate (PC), polystyrene (PS), polyethylene terephthalate (PET), and polyvinylchloride (PVC), can be thermomoulded or milled into the desired shape, in an industrial setting at very high rate and low cost. Thermoplastic devices generally feature a good transparency and medium solvent compatibility, yet, very low gas permeability. In order to combine parts or close channels, the pieces need to be thermobonded or glued. Elastomers, and especially PDMS, can be easily bonded to PDMS or glass through a relatively simple plasma activation. PDMS has a good transparency, is elastic and is highly gas permeable, which made it the most popular material for biological microfluidics applications. The high porosity of the PDMS matrix, allowing for gas to permeate, causes on the flip side water evaporation through the material as well as a strong ad- and absorption of molecules, which makes it widely incompatible with solvents and has to be considered when working with large biomolecules (Ren *et al.*, 2013). PDMS devices are usually cast from moulds which can be made by SU-8 silicon phototlithography (McDonald and Whitesides, 2002) or 3D printed (or directly 3D printed) (Hinton *et al.*, 2016). For the project of the thesis, PDMS bonded onto a glass bottom, prepared from SU-8 silicon photolithographed master moulds was chosen for its biocompatibility, gas permeability and transparency, to provide a suitable growth and microscopy chamber for studying AMF. Furthermore, the manufacturing method and facilities were established and readily available in the department and tested regularly for applications with similar fungi and organisms.

Microfluidic devices for biological and medical applications can further be made from hydrogels based on agarose, alginate, collagen or hyaluronic acid, for instance. These devices are especially well-suited for 3D cell cultures in an Organ-on-a-Chip context (Ling *et al.*, 2007; Cosson and Lutolf, 2014; Nie *et al.*, 2018). Other popular materials for microfluidics are inorganic compounds, mainly glass and silicon. These materials are highly thermostable, compatible with solvents, withstand high pressure and are gas impermeable. Especially glass has become popular for microscale gas chromatography, capillary electrophoresis and general chemical reactions. These materials, however, are less common in an every-day lab setting as the production requires arduous and dangerous methods such as hydrogen fluoride (HF) etching. As one of the more exotic substrates for microfluidics, ceramics is currently gaining more and more attention. Ceramic-based microdevices provide similar, highly resilient properties as glass or silicon, are however easier to manufacture. Especially low temperature co-fired ceramics (LTCC) tapes can be laser-machined or milled and sintered into the desired device structure. This methodology has successfully been applied to several sensor set-ups (Achmann *et al.*, 2008; Bartsch de Torres *et al.*, 2010) or even PCR devices, as ceramics generally have a good biocompatibility (Bembnowicz *et al.*, 2011). Similarly emerging in recent years, paper has become a mainstream microdevice material. Here, the intrinsic capillary effect of the material is exploited and “channels” are created by patterning, e.g., printed or simply cut (Ma *et al.*, 2019). This cheap method is very useful to produce hand-held assays for point-of-care diagnostics (Gong and Sinton, 2017). Metals are used for microfluidic devices, however, mainly as components in combination with other base materials, to introduce electrodes into the microfluidic setup, for example. For this purpose, the metal can be implemented via physical vapour deposition (Scott and Ali, 2021), galvanically deposited (Schrott *et al.*, 2009) or even printed in the form of liquid metals, such as Galinstan (Khoshmanesh *et al.*, 2017).

The devices featured in this thesis, were all manufactured in house from PDMS cast from self-made SU-8 silicon master moulds. To close the channels and to improve the microscopy clarity, the PDMS was plasma bonded to glass (see *2.1 PDMS device manufacturing*).

1.2.2.1 Microfluidics for fungi

For biological applications, including fungi, microfluidic high-throughput platforms have proven their usefulness for studies in genetics (RNA/DNA) (Lee *et al.*, 2019; Wang *et al.*, 2019), proteomics (Kotz *et al.*, 2010; Balasubramanian *et al.*, 2021) as well as drug screening (Watterson *et al.*, 2020) and delivery (Zafar Razzacki *et al.*, 2004). Fungal-specific microfluidic research, however, has focussed mainly on yeast single cell trapping for studying mating (Moore *et al.*, 2008; Taylor *et al.*, 2009) or stress responses (Hersen *et al.*, 2008; Hao and O'Shea, 2011), as well as blood-cleansing (Yung *et al.*, 2009; Fuchs *et al.*, 2019) or organ-on-a-chip devices (Barkal *et al.*, 2017) for studying or treating fungal pathogens.

Space searching of filamentous fungi

For the study of filamentous fungi, microfluidic technology offers optical transparency for precise brightfield or fluorescence imaging and the ability to mimic aspects of the natural habitat, including physical shapes and obstacles as well as chemical gradients. Especially for soil-dwelling organisms like AMF, where events normally occur inside a “black-box” and are thus hidden by the opacity of soil, this is of the utmost importance. Microdevices, usually made from PDMS, are patterned with physical obstacles or mazes for the fungi to manoeuvre around or through. At the forefront of this line of studies, Nicolau, Held and colleagues conducted numerous experiments with the Ascomycete model-organism *Neurospora crassa*, as well as other fungal strains. The fungus was found to respond to the physical challenge by changing its branching behaviour (e.g., angle and frequency). This was depending on the type of obstacle they were facing and, interestingly, occurred immediately without any adjustment period (Held *et al.*, 2009b; Held *et al.*, 2009a; Held *et al.*, 2010; Held *et al.*, 2011a). These changes included increased hyphal branching levels after passing through bottlenecks, directed hyphal growth into openings employing the ability to sense and identify these patterns (i.e., thigmotropism (Brand and Gow, 2009)), so-called ‘hit-and-split’ (i.e., the division of the tip of a mother hypha into two daughter hyphae) when colliding head-on with an obstacle, as well as nestling (i.e., hyphae attach to structures and track them)(Held *et al.*, 2011a). The observations were further examined to determine whether the phenomena are purely mechanically induced or chemical interactions play a role. Therefore, micrometre-sized PS

beads with epoxy-functionalized surfaces were introduced into the medium and hyphae were subjected to different bead densities. From comparing the fungus' reaction in the bead environment with their bead-free microfluidic platforms, they inferred the interactions to be not only mechanically induced but rather dependent upon the chemical property of the surface as well, hypothesising an electrical attraction between the positively polarized apex of the hypha (due to a high concentration of calcium ions) and the negatively charged bead surface (Held *et al.*, 2011b). An important part of the fungus' space navigation strategy is directional memory, i.e., maintenance of growth direction after encounters with obstacles. In a later study, Held *et al.* (2019) found cellular microtubules and the so-called Spitzenkörper, an apical body present in many filamentous fungi and consisting of an agglomerate of vesicles, to be involved. The Spitzenkörper acts like a gyroscope, while being stabilised by the microtubule scaffold. In the apical region of the hyphae, these microtubules show a very strict alignment in growth direction, while further downstream, in sub-apical regions, this scaffold is rather loosely organised or lacks organisation altogether. The results obtained in these studies on fungal space searching were further translated into bioinspired computational algorithms, which proved to be able to solve problems in a more efficient manner, from which the programming and design of nanomachines and sensors could immensely benefit (Hanson *et al.*, 2006; Nicolau *et al.*, 2006; Asenova *et al.*, 2016).

Following these pioneering studies, other groups developed similar devices and devised new experiments with different fungal species, such as *Talaromyces helicus* (Baranger *et al.*, 2020) and *Cladosporium macrocarpum* (Podwin *et al.*, 2021), uncovering differences between the fungi, which could be systematically correlated to their lifestyle (including foraging and exploration strategies) and habitat. One such study, conducted by Fukuda *et al.* (2021) is focussed on the behaviour of different fungi when encountering bottlenecks (i.e., spatial confinements smaller than that of the hyphal diameter) (Figure 2b). They found hyphae of slower growing fungi, e.g., *Aspergillus nidulans* or *Fusarium oxysporum*, to pass the confinement without difficulty and remain polarized. Faster growing strains, such as *Rhizopus oryzae* or *N. crassa*, in contrast, either depolarize, (i.e., they bulge at the apex and loose directional growth) or find themselves unable to pass the confinement altogether. Fast growth along with extensive branching is aided by high turgor pressure and high numbers of vesicles.

When encountering a bottleneck obstacle, this however leads to complications. An excess of vesicles is pressured into the hyphal tip and leads to the observed bulging and loss of directional memory, in some cases this disruption causes growth arrest.

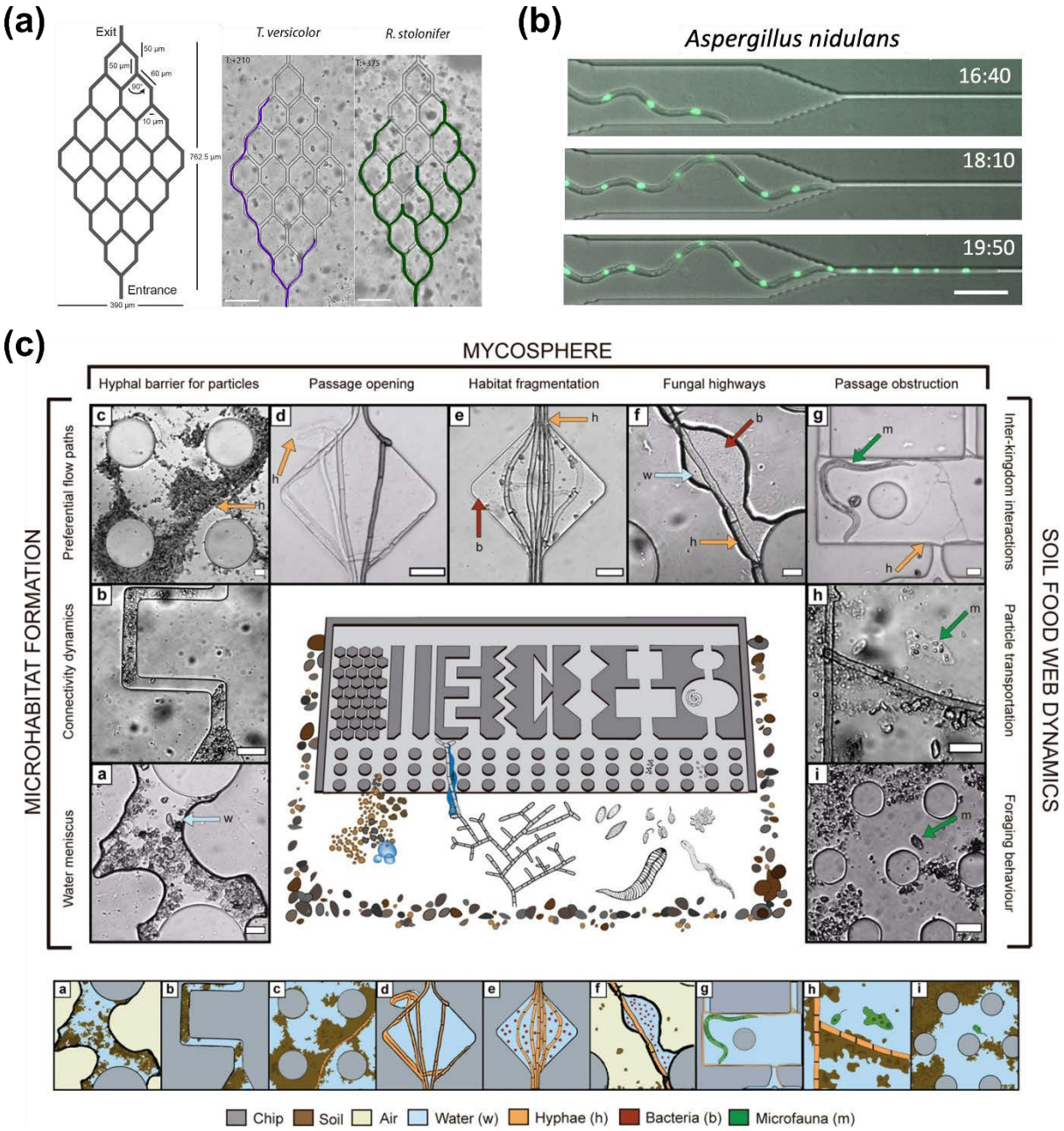


Figure 2: Examples of microfluidic platforms for space searching studies in filamentous fungi. (a) Device featuring honeycomb-like grid of channels to analyse exploration strategies in different fungal strains. Scale bars: 100 µm. (b) Microfluidic device for the study of hyphae squeezing through special confinements. Scale bar: 20 µm. (c) "*Soil chip*" mimicking a soil community, containing different soil particles, bacteria, microfauna, and filamentous fungi as well as complex microchannel geometries, either water saturated or filled with air. Scale bars: 20 µm. Images in (a), (b) and (c) reproduced with modifications from Hopke *et al.* (2021), Fukuda *et al.* (2021) and Mafla-Endara *et al.* (2021), respectively, with permission from the Creative Commons Attribution licence (www.creativecommons.org/licenses/by/4.0/). Image composition and legend obtained with

modifications from Richter *et al.* (2022) , with permission from the Creative Commons Attribution licence (www.creativecommons.org/licenses/by/4.0/).

A similar but broader approach was pursued by Aleklett *et al.* (2021). With their *Obstacle Chip*, featuring several different structural patterns, they monitored five behavioural traits in seven different filamentous fungi. Based on their growth velocity, branching behaviour, hyphal shape, mycelial density and foraging style, the fungi were originally grouped into guerilla (exploratory, far-reaching but short-lived, not competitive) or phalanx (slow progression as dense mat with united front, durable) strategists. However, as a result of their experimentation at the cellular level, they found the classic phalanx/guerilla categorisation to be insufficient, with the fungi's lifestyle traits more complexly tailored to their specific niche habitat. In a comparable study, (Hopke *et al.*, 2021) hosted the "Fungus Olympics". In this crowdsourced investigation, they confronted a broad range of filamentous fungi with different obstacle courses and found that, depending on the individual foraging style, each fungus found its strength in a different "discipline" (Figure 2a).

With microfluidic devices facilitating the simulation of soil physical properties, while maintaining microscopy accessibility, these studies have provided a lot of insight into the lifestyle of soil-dwelling fungi. To bring their system even closer to the natural habitat, Mafla-Endara *et al.* (2021) "buried" the chips in soil and thus introduced real soil particles, water/media and air, as well as fungi, bacteria, and protists as biotic factors into their device. Here, they observed closely how the fungi shape their environment through e.g., opening or obstruction of passages, water dispersal (along with nutrients), relocation or accumulation of soil particles, and thus connecting or fragmenting microhabitats, as well as through interaction directly with other soil organisms (Figure 2c). Bacteria, for instance, depend on or at least profit from fungal hyphae making nutrients accessible, either through the "fungal highway" (Kohlmeier *et al.*, 2005; Warmink *et al.*, 2011), where bacteria "ride" fungal hyphae to cross challenging structures, such as air gaps, or through assisting in the decomposition of nutritious substances. Interestingly, the latter was found to be working vice versa, too, with fungi relying on bacterial enzyme power for "unlocking" certain nutrients (Jiang *et al.*, 2021). Another microfluidic device for fungal foraging strategies was presented by Baranger *et al.* (2021). In their compartmentalised system, they created a niche containing benzo[α]pyrene (a polycyclic

aromatic pollutant) and found how the fungus *Talaromyces helices* actively sought after, reached, decomposed and took up the hydrophobic substance, which involved the excretion of biosurfactants. This knowledge could be used to further develop bioremediation strategies for polluted land.

Besides the optical transparency, biocompatibility and comparably easy device manufacturing with PDMS, the polymer possesses elastic properties, which can be used for force measurements on the cellular and hyphal level (Thomson *et al.*, 2015; Sun *et al.*, 2018; Puerner *et al.*, 2020).

Fungal interactions

Soil fungi engage in a variety of interactions, with abiotic factors as well as biotic partners. They reach from inter-kingdom down to interspecies as well as self-self interactions and can be both pathogenic or parasitic as well as beneficial. Here again, microfluidic technology has proven to be a powerful tool to allow to trigger and gain deeper insight into interactions on the level of single hyphae between fungi and bacteria (Stanley *et al.*, 2014; Uehling *et al.*, 2019), fungi and nematodes (Schmieder *et al.*, 2019), fungi and viruses (Ghanem *et al.*, 2019) as well as fungi and other fungi (Gimeno *et al.*, 2021).

Bacterial-fungal interactions

Making the first fungal interaction device, Stanley *et al.* (2014) designed the so-called *bacterial-fungal interaction (BFI) device*, which allowed for fungal hyphae to grow in and a subsequent co-inoculation with bacteria through a second inlet (Figure 3a). In their study, they confronted the fungus *Coprinopsis cinerea* with the bacterium *Bacillus subtilis* and found that when inoculated with the wild-type strain (*B. subtilis* NCIB 3610) the fungus arrested hyphal growth, however, seemed unaffected by the laboratory strain *B. subtilis* 168. The growth arrest coincided with the collapse of some hyphal compartments and the subsequent formation of blebs, i.e., exocytotic vesicles still containing the fluorescent marker, that lingered for up to several hours after the collapse (Figure 3c). Additionally, it was revealed how the bacteria attached to specific subsets of hyphae, suggesting hyphal differentiation within the mycelium (Figure 3b). With a second microfluidic device, named the *fluid exchange device*, hyphae were

perfused with lipophilic extracts and bacterial supernatant and a similar effect on the hyphae was observed, attributing the fungicidal activity to these exudates rather than active bacterial enzymes. Here, microfluidic technology allowed to expose isolated hyphae to bacterial stress and observe reactions on the single-cell level. The *BFI device* was further used to study the endosymbiotic relationship between the fungal plant pathogen *Rhizopus microsporus* and the bacterium *Burkholderia rhizoxinica*, revealing the release of transcription activator-like (TAL) effector by endobacteria as a crucial part of the symbiosis (Richter *et al.*, 2023). Another example of mutualism between *Burkholderia* spp. and fungi was investigated by Uehling *et al.* (2019) with results suggesting a complex exudate-based multistage bidirectional communication. In an attempt to make these microfluidic techniques more accessible, the group manufactured and distributed vacuum-sealed, ready-to-use microfluidic devices around the world and received reports about applications on BFIs, fungal highways, fungal biofilms, as well as some experiments involving plant seeds or even neurons (Millet *et al.*, 2019). Other groups designed similar microfluidic devices to study the antagonism between certain *Verticillia* spp. (fungal crop pathogen) and *Pseudomonas* spp., to gain insights into how the bacteria inhibit fungal growth and thus plant colonisation as well as the molecular and cellular processes involved (Harting *et al.*, 2021). For AMF, microfluidic platforms for studying fungal-bacterial interaction could prove highly beneficial, especially now with mounting evidence for essential collaboration between, for example, phosphate solubilising bacteria and AMF (further discussed in *6.3 Concluding remarks and future directions for microfluidic AMF research*). This could help address whether and how these bacteria directly interact with hyphae, how the bacteria benefit from the interaction or whether the bacteria use the hyphal network for distribution (á la fungal highway) and/or as a niche habitat.

The benefits of microfluidic technology were further employed to examine the distribution of bacteriophages along fungal hyphae and revealed, for instance, a strong retention of up to 93% of hydrophobic T4 phages on hydrophobic *C. cinerea* hyphae (Ghanem *et al.*, 2019). These findings facilitated by microfluidic technology provide important information for answering environmental as well as medical questions.

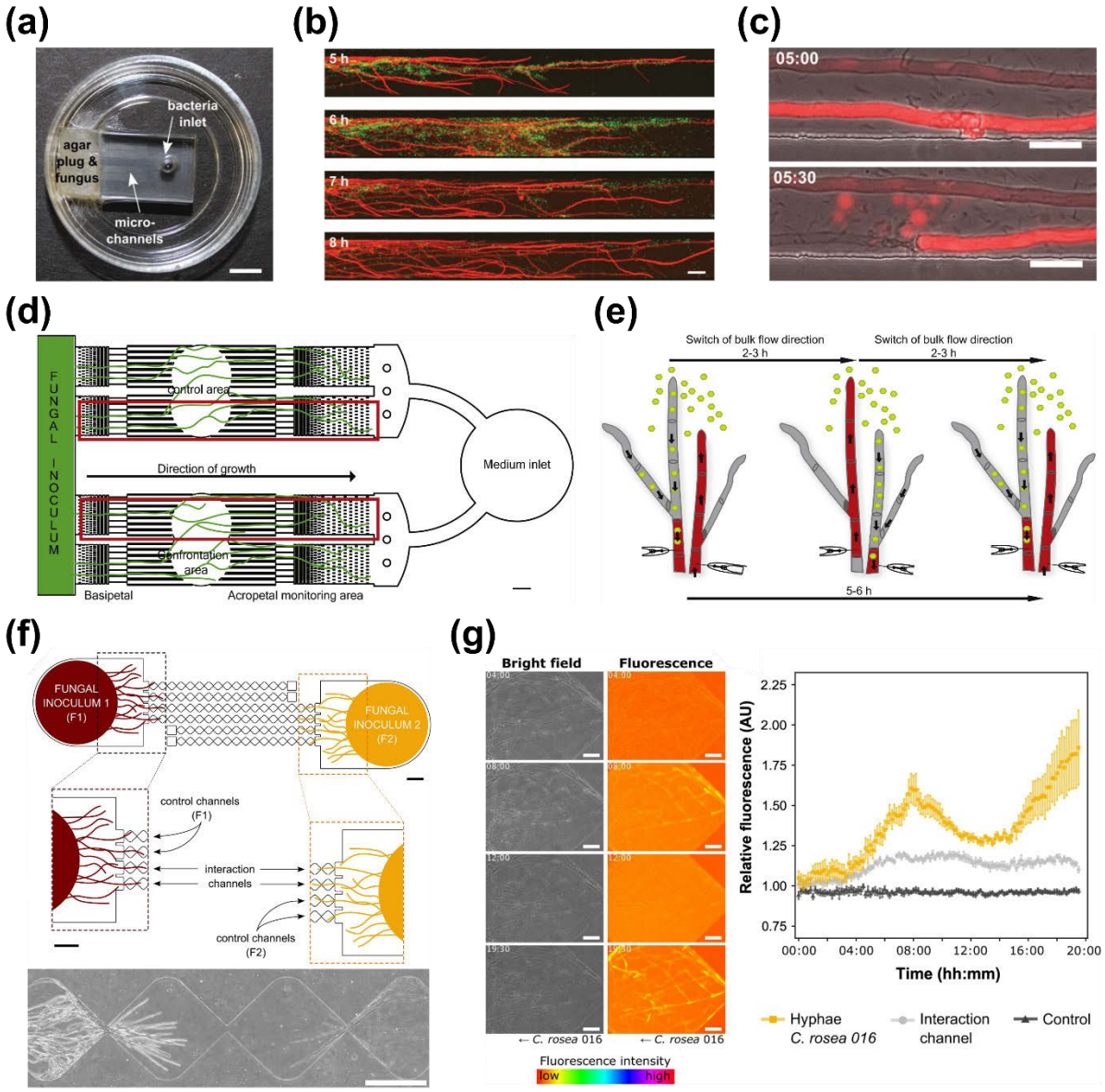


Figure 3: Microfluidic platforms for the study of hyphal interactions. (a) Photography of an inoculated *bacterial–fungal interaction (BFI) device*. Highlighted are the inoculum, i.e. agar plug containing fungal mycelium, the microchannels as well as the bacterial inlet. Scale bar: 5 mm. (b) Time series of *Coprinopsis cinerea* hyphae (red) surrounded by *Bacillus subtilis* (green) inside channels of the *BFI device*. Scale bar: 50 µm. (c) *C. cinerea* cell collapsing through the action of *B. subtilis* and subsequently losing its cellular contents. Scale bar: 25 µm. Images (a)–(c) reproduced with modifications from Stanley *et al.* (2014) with permission from Oxford University Press (Licence Number: 5846560852683). (d) Schematics showing a fungal-nematode interaction device. Scale bar: 500 µm. (e) Model of proposed fungal response upon nematode predation, involving bulk hyphae switching cytoplasmic bulk flow direction every 2–3 h and thus redistributing nutrients (e.g. 2-Deoxy-2-[(7-nitro-2,1,3-benzoxadiazol-4-yl)amino]-D-glucose (2-NBDG), green hexagons). The spatial distribution of the *C. cinerea* defence response when attacked by the nematode is indicated in red. Images (d) and (e) reproduced with modifications from Schmieder *et al.* (2019) with permission from Elsevier (Licence Number: 5846571165932). (f) (Top) Schematics of the *fungal–fungal interaction (FFI) device* (top). Scale bar: 1 mm. (Bottom) *Clonostachys rosea* and *Fusarium graminearum* approaching each other in the interaction zone of the *FFI device*. Phase contrast. Scale bar: 250 µm. (g) (Left) Fluorescent time lapse revealing GFP within the mycelium of *C. rosea*. Scale bars: 50 µm. (Right) Graph showing an increasing

and decreasing fluorescence signal within the hyphae in comparison to the control channel. Images (f) and (g) reproduced with modifications from Gimeno *et al.* (2021) with permission from the Creative Commons Attribution license (www.creativecommons.org/licenses/by/4.0/). Image composition and legend obtained with modifications from Richter *et al.* (2022), with permission from the Creative Commons Attribution licence (www.creativecommons.org/licenses/by/4.0/).

Fungal-fungivorous interactions

Soil, like all other ecosystems on the planet, constitutes a complex network of interplay with interchanging roles of prey or predator. Besides bacteria, fungi also are preyed upon by fungivores such as protists and microfauna.

With a microfluidic device derived from the *BFI device*, Schmieder *et al.* (2019) subjected *C. cinerea* to attacks by the nematode *Aphelenchus avenae* (Figure 3d). In line with earlier findings concerning bacterial confrontations, hyphae seem to be specialised to certain tasks and defence responses are only activated at the attack site, in direct contact with the nematode, which then, however, quickly propagated throughout the mycelium via specialised "trunk" hyphae (Figure 3e). In an extension to the study, fungal material from the attack site was extracted for PCR and poly(A)+ RNA sequencing to analyse the transcriptome directly linked to the defence mechanisms. Thus, 1229 differentially expressed genes were identified (so far, with conventional plate-based methods, only 37 genes had been discovered). Interestingly, antibacterial defence genes were found to be involved in the response, suggesting a tripartite interaction between the fungus, the nematode, as well as its microbiome (Tayyrov *et al.*, 2019).

Fungal-fungal interactions

To investigate the fungal–fungal interactions (FFIs) between the plant pathogen *Fusarium graminearum* and biocontrol agent *Clonostachys rosea*, Gimeno *et al.* (2021) developed a new microfluidic platform, termed the *fungal–fungal interaction (FFI) device* (Figure 3f). It was observed how *C. rosea* antagonises the GFP-tagged *F. graminearum* and forces it to arrest growth. Further, the single hyphae resolution revealed how not only GFP slowly disappears from the prey mycelium but later reappears in the predators' mycelium, indicating an active uptake of nutritious material from the prey (Figure 3g).

Microfluidics-assisted research on AMF, is virtually non-existent to date, but offers numerous possibilities for in-depth studies on these interesting and important organisms, in particular relating to key aspects of mycorrhiza development. Only recently, Srisom *et al.* (2020) developed a device for AMF spore sorting and Hammer *et al.* (2024) published an extensive study on extraradical AMF hyphae with a modification of their "*soil chip*" (further discussed in *4.2.1 Space searching in AMF*).

1.3 Research Objective

The aim of this thesis was to develop microfluidic devices for investigating AMF asymbiotic hyphae and their space navigation behaviour, for the first time. A big step towards this goal was done by the invention of the root organ culture, which allowed for spore production as well as studying hyphae on plate with much detail (Mosse and Hepper, 1975; Declerck *et al.*, 1998; de La Providencia *et al.*, 2007) and later by the introduction of the cellophane sandwich method, confining spores and hyphae in z direction for better microscopy results (Giovannetti *et al.*, 2001; Giovannetti *et al.*, 2003). Even confronting hyphae with physical obstacles in the form of micro threads of different materials (Giovannetti *et al.*, 1993) or combining spores of different strains for anastomosis studies (Croll *et al.*, 2009) was now possible. Establishing a microfluidics-based approach for these investigations was expected to provide even more insight. With microfluidic devices, the z confinement can be tuned precisely to the organisms used, which, together with the near perfect transparency of the device materials (glass and PDMS) significantly enhances the microscopy quality. Furthermore, these devices allow for a high degree of control over spore positioning, the physical environment (i.e., channel shapes or micro-obstacles) as well as control over introduction of nutrients, chemicals or dyes. This methodology was therefore anticipated to aid with elucidating the space searching strategies of AMF, similar to studies performed with other fungi (Held *et al.*, 2011a; Hopke *et al.*, 2021) (see also *1.2.2.1 Microfluidics for fungi*), as well as to systematically isolate and study anastomosis events with higher throughput. Space navigation is a crucial part of the first stage of the establishment of the mycorrhiza and thus the survival of the obligate symbionts AMF. How these fungi manage the challenging task of finding a suitable host with limited resources is intriguing and important to understanding the symbiosis as a whole. Due to their unique

lifestyle, hyphal growth and space searching strategies were expected to share similarities but also widely differ from other fungi. Anastomoses are an important element of a fungus' exploration strategy, involving nutritional networking (Fleißner *et al.*, 2008) but also genetic transfer (Friesen *et al.*, 2006); hence, establishing a method for studying anastomoses between different AMF genotypes in a systematic manner would be highly beneficial. Additionally, it was shown that the devices were further applicable to studying non-AMF fungi. In a side project the devices were equipped with an oxygen sensitive foil for monitoring peri-hyphal oxygen gradients.

An overview of the main research questions this thesis aimed to answer is detailed in Figure 4. All microfluidic devices used for the studies were entirely self-made, from conceptualisation and photomask design (using the software AutoCAD) to master mould fabrication and PDMS device-making. In order to address the aforementioned research questions, the devices were required to accommodate and sufficiently trap spores within the channel and then confront hyphae with micro-obstacles of different shapes to study the physical aspect of their natural environment and the fungus' reaction towards it. Later, the device was further developed and adapted to inoculate spores of two different strains at the same time in order to examine anastomosis events in more detail.

Key questions	Objectives	Chapter No.
1. How do asymbiotic hyphae of AMF interact with physical obstacles and what are ther space searching mechanisms?	Developing a microfluidic device to trap AMF spores and confront asymbiotic hyphae with physical obstacles, allowing for a high-resolution and real-time microscopy Characterise functionability of device with germination and growth experiments Perform timelapse studies of space searching events	3,4
Hypothesis: The microfluidic system provides a beneficial platform to reveal similarities and differences compared to other fungi, as well as novel space navigation mechanisms.		
2. Do AMF have Spitzenkörper?	Establish dye-supported imaging method for discovering Spitzenkörper	4
Hypothesis: Fluorescent staining alongside dynamic growth observations in the microfluidic device can help uncover the Spitzenkörper in AMF.		
3. Does the anastomosis phenotype of AMF depend on the genotype?	Develop microfluidic device to encourage, isolate and study anastomosis events in AMF Demonstrate functionability of device with device loading characterisation, anastomosis images and gradient experiments	5
Hypothesis: The microfluidic system will aid in uncovering strain-specific anastomosis patterns, which can be linked to the genetic set up.		
4. What are alternative and future applications of the *AMF-SporeChip*?	Implement and test sensor foils in the device for examining oxygen gradients in the hyphosphere Introduce and grow MFRE in the device	6
Hypothesis 1: Integrating an oxygen sensor into the device will allow to analyse oxygen depletion around single hyphae. Hypothesis 2: The *AMF-SporeChip* provides a system for studying growth behaviour in other fungi such as MFRE.		

Figure 4: Overview of the research hypotheses and objectives of the thesis.

1.4 Thesis outline

To tackle the objectives and research questions outlined previously, this thesis has been organised into 6 chapters. The first chapter sets the scene with an introduction into the thesis, including general background, methodology used and reasons for this research. The chapter then delves deeper into the biology of AMF, as well as working principles, advantages and applications of microfluidic technology. In the course of the literature background research for the project I produced and published the first review on the topic of Fungi-on-a-Chip (Richter *et al.*, 2022), summarising and discussing all published works on microfluidic applications involving fungi, thus far.

In chapter 2, all materials and devices used for this project as well as a thorough description of the methods employed is detailed.

Chapter 3 describes the development process and technical details of the *AMF-SporeChip*, which has been published in *Lab on a Chip* (Richter *et al.*, 2024).

Chapter 4 focusses on the main application and findings regarding AMF hyphal space searching (published in *Lab on a Chip* (Richter *et al.*, 2024)) and further describes steps to establish a fluorescent staining method for discovering the Spitzenkörper in AMF.

Chapter 5 details the development of the *AMF-AnastomosisChip*, which was designed to systematically study anastomosis events between different strains of AMF at the hyphal level.

Chapter 6 presents further applications of the *AMF-SporeChip*, including analysis of oxygen gradients around hyphae by inclusion of an oxygen sensitive foil into the device design, as well as the study of other mycorrhizal organisms, i.e., *Mucoromycotina* fine root endophytes (MFRE). This chapter concludes the thesis with a detailed outlook into future explorations and possible continuations of the experiments.

CHAPTER 2: MATERIALS AND METHODS

A substantial part of this thesis was the development of a new method and microfluidic device for studying AMF spores and asymbiotic hyphae. The development process of these specialised methods is detailed in separate chapters. In this chapter, all generic methods used repeatedly throughout the project, i.e., cultivation of the biological material, PDMS device production and imaging, are described.

2.1 PDMS device manufacturing

2.1.1 Master mould manufacturing

To conduct investigations on various aspects of AMF spore germination and hyphal exploring and morphogenesis at the level of single cells, PDMS-based, self-manufactured microfluidic devices were employed. The devices were poured from master moulds made from 100 mm silicon wafers in a photolithography process with SU-8 as photoresist material. The development of this protocol is described in *3.2.1.2 Optimisation of the photolithography protocol*.

The device designs (detailed in *3.2.1.1 Device Design* and *5.2.1. Device development*) were checked for correct structures using KLayout (Köfferlein, 2006) and then printed on a mylar® film to create the photolithography mask by Micro Lithography Services Ltd., UK.

All photolithography steps were done in a semi-clean-room environment, with several dust free laminar flow hoods. When moving the wafer between hoods, the wafer was put in a closed wafer box. The sash of the main hood is equipped with a blue light filter, to keep high energy light from entering and causing unspecific cross-linking of the photoresist. As substrate for the master mould, a fresh silicon wafer (Diameter: 4"; Orientation: <100>; Dopant: P(Boron); Resistivity: 0-100 ohm-cmCz; Centre Thickness: 425-550 µm; Surface: Single side polished, Si-Mat Silicon Materials, Germany) was used. The wafer was washed in acetone and isopropanol, dried with an airgun and subsequently plasma-cleaned for 5 min using a plasma cleaner (PDC-002-CE, Harrick Plasma, USA), which was briefly dusted off with an air gun beforehand. The blow drying is started from where the wafer is held by a pair of wafer tweezers.

Then, the liquid front is slowly blown off the wafer, moving the airgun carefully across the wafer to ensure that no residues are left behind. For the first layer, the wafer was placed onto the chuck of the spin coater, centred and vacuum-attached. As an extra measure, the wafer was briefly dusted off again with the air gun, as the following step is the most crucial, determining the quality of the layer. Then, avoiding producing bubbles, 5 ml of SU-8 2010 (Kayaku, USA) were slowly poured onto the wafer, performing spiral movements from the centre of the wafer outwards. The spin coater was then closed and run at 500 rpm for 10 s and 3700 rpm for 30 s (Spin Coater WS-650MZ Modular, Laurell, USA). The next step was soft baking at 65 °C for 30 s and 95 °C for 2.5 min ramping up with ~2 °C/min on a hot plate (Hot Plate EMS 1000-3, Ascon Tecnologic, Italy). In the meantime, the photomask was attached to a 10x10 cm glass plate with a thin film of water. For that purpose, a small droplet of water (without air bubbles) was put onto the centre of the glass. Then, the mask, bending both sides upwards, was carefully placed onto the water droplet and the held ends slowly lowered onto the glass. Now, a microscope slide wrapped in clean room tissue is used to streak gently from centre to the edges to squeeze out excess water and potential air pockets. The mask easily scratches, thus extra care has to be taken when streaking over it. Once the soft bake programme was finished, the wafer is lifted up from the hotplate surface with built in metal pins and left there for 5 min, before transferring onto a clean room tissue to cool down. Before placing the wafer into the mask aligner (UV KUB-3, Kloé SA, France), the resist has to be fully solidified and must not be sticky, otherwise the mask would stick to the wafer. Once, the wafer was transferred onto the vacuum holder of the mask aligner and the glass holding the mask placed on top of it, the wafer was loosely aligned with the marks on the mask, lowered into direct contact with the mask and exposed to ultraviolet (UV) light for 7.5 s. The wafer was then transferred back onto the hot plate and baked at 65 °C for 30s and 95 °C for 3.5 min, ramping up with 2 °C/min, subsequently cooling down as described above. This should be done immediately after the UV exposure as this activates the cross linking of the SU-8 and the baking concludes the reaction. Furthermore, any light from the environment hitting the wafer can cause unspecific cross-linking, leading to a reduced resolution of the structures. For the second layer, the wafer was again centred and vacuum-attached to the spin coater chuck and 5 ml of SU-8 2075 (Kayaku, USA) were spun onto the first layer at 500 rpm for 20 s and 2200 rpm for 30 s. The wafer is then transferred onto the hotplate and soft baked at 65 °C for 5 min and 95 °C for

15 min, ramping up with 2 °C/min and subsequently cooled down on the raised pins for 5 min. To better align the first and second layer, the SU-8 2010 was removed from the alignment marks using acetone and clean room sampling swabs (Berkshire, UK), performing wiping movements towards the edges to avoid building up of SU-8 walls. Care should be taken to not splash any acetone onto the wafer as it would dissolve the SU-8 and create holes in the layer. Before moving the wafer into the mask aligner, it has to be fully dried. The wafer was then aligned with the mask using the alignment marks and the cameras of the mask aligner. Once aligned, wafer and mask were brought into hard contact and the wafer exposed to UV for 11.5 s. Then, the wafer was immediately moved to the hotplate and baked at 65 °C for 3.5 min and 95 °C for 9 min ramping up with 2 °C/min and cooled down on the raised pins for 5 min. Now, for the development step, the wafer was transferred into a wide, flat beaker, fully immersed in SU-8 developer (2-(1-methoxy)propyl acetate, 99%, Thermo Scientific, USA) and agitated for 8 min. The wafer was then rinsed with isopropanol, placed in fresh developer and agitated again. After 1 min, the wafer was rinsed with isopropanol and dried off with an airgun, making sure that the liquid front is pushed uniformly off the wafer and no isopropanol remains in the corners of the structures. If the isopropanol washes off slightly opaque and in white lines, another 30 s of development should be added. In a final step, the master mould was hard baked at 150 °C for 2 min on a hot plate to seal cracks and increase durability of the structures.

The same protocol was used to produce the master mould with 5 µm channel height, apart from the following modifications. SU-8 TF 6005 was used for the first layer, which was spun onto the wafer at 500 rpm for 10 s and 2000 rpm for 30 s. Soft-baking was performed at 110 °C for 3 min, followed by UV exposure for 5.2 s and a post exposure baking at 110 °C for 2 min.

For the *Gigaspora* variant of the design, the first layer was prepared according to the above-described protocol for 10 µm channel height. For the second layer, 5 ml of SU-8 2150 were spun onto the first layer at 500 rpm for 20 s and 1300 rpm for 30 s. Soft baking was performed at 65 °C for 7 min and 95 °C for 60 min, ramping up with 2 °C/min and the wafer was subsequently cooled down on raised pins for 5 min. The wafer was UV exposed for 22.5 s followed by baking at 65 °C for 5 min and 95 °C for 35 min, ramping up with 2 °C/min, cooling down on raised pins for 5 min, after. Finally, the master mould was developed for 16 min and an additional 4 min with fresh SU-8 developer. Hard baking was performed at 150 °C for 5 min.

Before using a master mould for pouring PDMS, a silanisation step should be performed to facilitate peeling off the cure PDMS from the mould. For this purpose, the wafer was placed into a desiccator, leaning against the wall in an angle of approximately 45 °, structures facing upwards. An open glass vial is filled with 100 µl chlorotrimethylsilane (redistilled ≥99 %, Sigma Aldrich, UK) and put into the desiccator. As chlorotrimethylsilane is a highly reactive and hazardous substance, caution has to be taken and any other chemicals and especially water kept away when handling. The silanisation needs to be done in a chemical fume cupboard. To measure the 100 µl chlorotrimethylsilane, a Hamilton syringe (100µL 710N, cemented needle, 22S Gauge, 51mm, Point Style 2; Hamilton, USA) has to be used and immediately after use rinsed with isopropanol, as any remaining reagent would corrode the metal plunger of the syringe rapidly, leading to the plunger getting stuck and destroying the syringe. Once wafer and chlorotrimethylsilane had been placed into the desiccator, the desiccator was closed and vacuum applied for 1 min. All valves were then closed and the set-up left to react for 1 h. After this time, no liquid should be remaining in the vial and the silanisation of the master mould is concluded.

All photolithography steps were performed in the CRUK Microfabrication & Prototyping Facility of the Department of Bioengineering.

2.1.2 PDMS device manufacturing

To ensure a dust-free environment, all PDMS device manufacturing steps were executed in a laminar flow hood. Firstly, the silicone elastomer base was mixed with the curing agent in a ratio of 10:1, usually ca. 40 g was prepared in total per mould. The mixture was then degassed in a desiccator for about 45 min until no air bubbles remained, subsequently poured onto the master mould and baked at 70 °C for at least 4 h. After that, the cured PDMS was carefully peeled off from the mould using a spatula. Then, the devices were cut out and holes for the inlet(s) and outlet(s) were punched, using a 3 mm precision cutter. During the whole process, scotch tape was constantly kept and renewed on top of the channel side of the device, in order to further secure the absence of dust particles. Now, the devices were washed to remove remaining monomers and to increase sterility. Therefore, the chips were immersed in 0.5 M

NaOH and sonicated for 5 min. After rinsing with autoclaved MilliQ water, the step was repeated with 70% ethanol. Finally, the devices were rinsed again, dried with an air gun and put into the oven at 70 °C for about an hour. Later, the washed and dried devices were bonded to a glass-bottomed petri dish (Ø dish = 35 mm, Ø glass = 23.5 mm; Fluorodish, World Precision Instruments, Germany) to close the channels. Therefore, both the device and the petri dish were put into a plasma oven for 1 min, with the side to be bonded facing up. Directly afterwards, the device was placed into the petri dish and the edges gently tapped with tweezers to ensure bonding. Care must be taken to avoid applying excess pressure in the channel regions. Otherwise, this can result in collapse and undesirable bonding of the microchannels due to the small channel heights, thus obstructing them. Commonly, the devices are primed straight after the bonding process. Exploiting the hydrophilicity brought upon by the plasma treatment, the channels can be easily filled with water or the desired medium. This effect only lasts for a few minutes and then the device slowly loses the hydrophilicity.

2.2 AMF cultivation

2.2.1 Root organ and pot cultures

AMF are obligate biotrophs, meaning that they rely on direct feeding by a symbiotic host. Hence, a first major task was to set up root organ cultures to culture AMF and produce spores in house, using the procedures detailed in Declerck *et al.* (1998) and Cranenbrouck *et al.* (2005). To culture the three *Rhizophagus* strains, i.e., *Rhizophagus irregularis* MUCL 41833, *Rhizophagus irregularis* MUCL 43194 and *Rhizophagus intraradices* MUCL 49410, *in vitro*, root organ cultures of *Cichorium intybus* L. (Ri T-DNA-transformed chicory roots not able to develop shoots or leaves) were employed as the host. This task comprised of setting up and maintaining (i) chicory root cultures and (ii) two-compartment cultures. Initial inoculum, i.e., roots and spores, was provided by the *Glomeromycota in vitro* collection (GINCO, Belgium). Spores of *Gigaspora margarita* BEG 34 were not cultivated in house. Instead, they were obtained from GINCO. There, the spores are produced in pot culture in double-autoclaved (121 °C for 15 min) substrate composed of thin quartz (0.4-0.8 mm), larger quartz (1-2 mm) and calcinated clay (2/1/2; v/v/v) with *Plantago lanceolata*. After at least 9 months of cultivation,

spores were sampled and disinfected as described by Cranenbrouck *et al.* (2005) Briefly, spores were disinfected using a filtration apparatus connected to a vacuum outlet. First, they were cleaned twice in sterile water, then treated with chloramine T 2% solution (with 2 drops of Tween 20) for 10 min. Spores were then washed again 3 times with sterile water before treatment with a filtered (using a 0.22 µm Acrodisk filter) antibiotic solution composed of streptomycine sulfate 0.02% and gentamycine sulfate 0.01%, for 10 min. Spores were stored in sterile water at 4 °C and shipped. After shipping, the *Gigaspora* spores were used directly in the experiments.

2.2.2 Media preparation

For the AMF root organ cultures two media based on Modified Strullu-Romand (MSR) medium are required, i.e., MSR(-) and MSR(+). For the preparation of both media, 0.59 g Modified Strullu and Romand (MSR, Duchefa Biochemie, the Netherlands; see Table A1 for composition) powder was dissolved in 1 l sterile double distilled water. 10 ml of a 0.15 M calcium nitrate solution were added and the pH was adjusted to 5.5 using 0.1 M NaOH and HCl. Lastly, 3 g phytagel (Merck, Germany) was added. The difference between MSR(-) and MSR(+) is that MSR(+) contains an additional 10 g sucrose, which were added to the solution before adjusting the pH. After autoclaving, the media must be poured immediately or kept at 60 °C to prevent it from solidifying, as unlike agar media for instance, it cannot be melted again once it solidified. For on-chip experiments, a liquid version of MSR(-) was prepared, consisting of MSR(-) without phytagel and the pH adjusted to 7 using 0.1 M NaOH and HCl (as the phytagel was found to change the pH from 5.5 to approximately 7).

2.2.3 Chicory root culture

The chicory roots are grown on round Petri plates (Ø = 90 mm) containing MSR(+) medium. To maintain the root culture, subculturing is performed every 1-2 months. For this purpose, in a sterile Microbiological Safety Cabinet (MSC), the entire root-containing phytagel is detached from the plate with a scalpel and flipped over into the plate lid. The phytagel is then dissected with tweezers until the roots are exposed and young and healthy single roots, characterised by a bright hue of brown and branching nodules, can be selected. These are then placed onto

new MSR(+) culture plates. The inoculated plates are sealed with cling film and incubated in the dark at 27 °C.

2.2.3 AMF two-compartment culture

In order to produce spores of AMF and therefore ensure a constant supply of spore material for experiments, the two-compartment technique, as shown in Figure 5, is used (Declerck *et al.*, 1998; Cranenbrouck *et al.*, 2005). One compartment of the petri dish is filled with 10-15 ml MSR(+) (root compartment) and the other with 15-20 ml MSR(-) medium (hyphal compartment). The hyphal compartment is poured first, in a way that the liquid medium is held by the central wall and a curvature is formed due to surface tension. Once the medium has solidified, the chicory medium is carefully poured into the second compartment, while tilting the plate towards the hyphal compartment, to obtain a sigmoidal form and to ensure connectivity between the two compartments (Figure 5a). Then, a fresh and vital chicory root is selected from a chicory root plate (see *2.2.3 Chicory root culture*) and placed carefully into the root compartment. The two-compartment dishes are then sealed with cling film and incubated in the dark at 27 °C for 7 days.

One week later, the root is inoculated with the respective *Rhizophagus* spores. This is achieved by cutting a piece of phytagel containing a dense mycelium with a high number of spores from a hyphal compartment of an at least 3-month-old culture plate (first batch was inoculated with spores from GINCO), transferring it to an empty petri dish and mashing it up with a scalpel. This renders the phytagel a gooey, spreadable paste with a loosened up mycelial network, which is then distributed around the roots with tweezers. The plates are sealed with cling film and incubated in the dark at 27 °C. After about 1-2 weeks, the spores start to germinate and associate with the roots. Now, connected to the root network, the fungus gathers new energy and forms fast runner hyphae. First crossovers to the hyphal compartment can be observed from 3 weeks after inoculation. Usually, it takes between 3 and 6 months for cultures to be ready for harvesting.

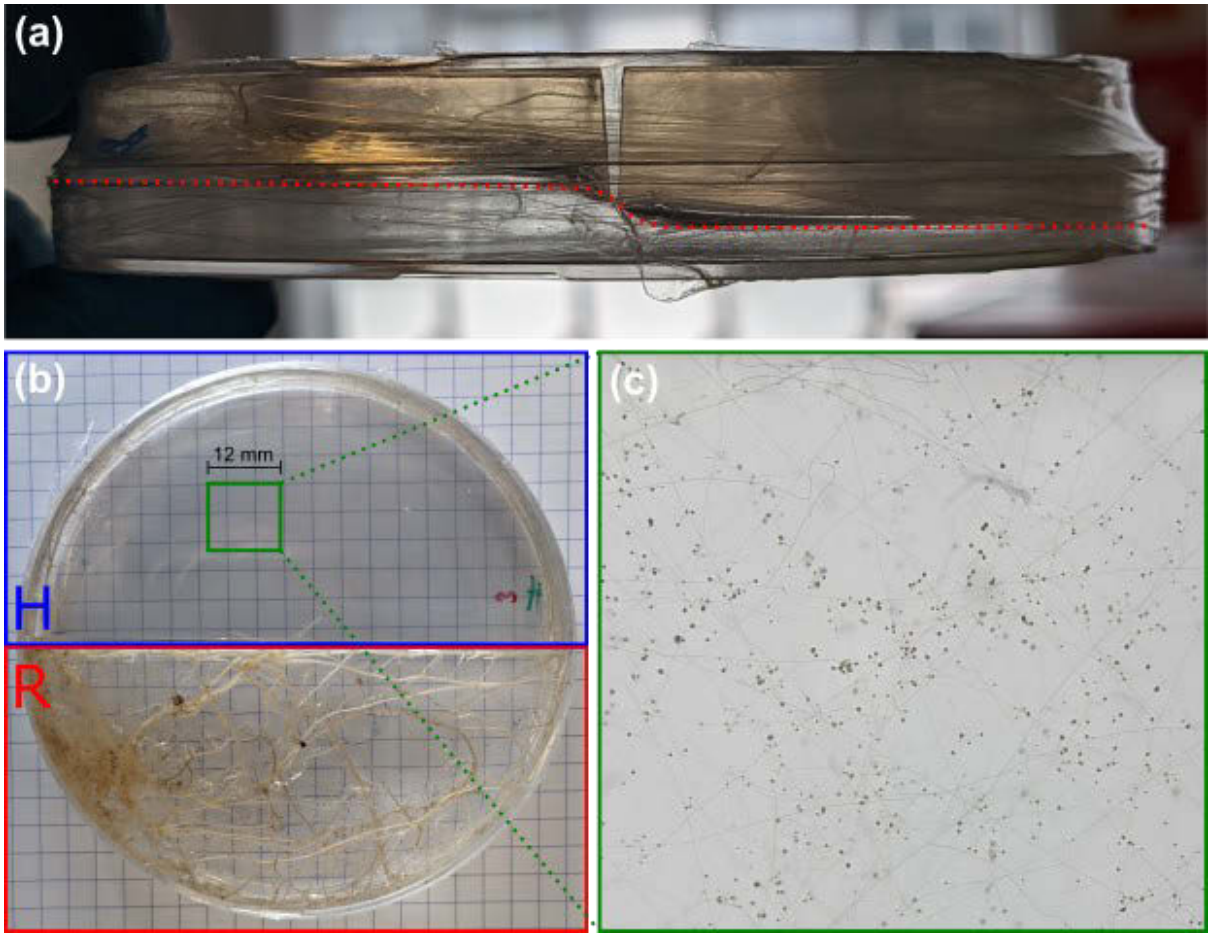


Figure 5: Two-compartment co-culture of *Rhizophagus irregularis* MUCL 41833 and chicory roots. (a) Side view with the characteristic sigmoidal shape highlighted with a red dotted line. (b) Top view with the hyphal compartment marked blue and the root compartment marked red. (c) Section of the hyphal compartment magnified with a stereoscope showing a dense hyphal network with spores after 4 months inoculation.

Both cultures are quite susceptible to contamination, as they are rich in nutrients contain plant inoculum naturally colonised by numerous microbes and dual cultures are occasionally kept for up to 1-2 years. Therefore, extra caution has to be taken. After each plate, the tools (tweezers and scalpel) are heated to 300 °C in a bead steriliser for ca. 2 min. Afterwards, plates are tightly wrapped in cling film and stored in plastic boxes. Cling film is faster in the handling and does not become brittle with time like, e.g., Parafilm. To back up the unlikely case of a severe mass-contamination, a second, independent set of roots is maintained in a separate plastic box with an offset of 2 weeks. Each set comprises generally between 30 and 60 plates with chicory roots.

2.3 Microscopy and image processing

For the imaging of the microfluidic devices, two inverted microscopes (Eclipse Ti-U, Nikon, Switzerland and Eclipse Ti-2, Nikon, UK) were used. Both microscopes are equipped with air immersed ×10/0.3 NA (numerical aperture) and x20/0.45 NA Plan Fluor objectives (Ti-2: aditional x40/0.6 NA and oil-immersed x100/1.3 NA objective), motorised stages and camera heads (Ti-U: Retiga R1 CCD camera (Qimaging, Canada); Ti-2: DS-Qi2 Mono Digital Microscope Camera (Nikon, UK)). The imaging software NIS-Elements Advanced Research (Nikon) provided a large image function, which stitches individual images together based on overlap, for obtaining time point images of entire devices or selected areas as well as time-lapse images. A temperature-controlled incubator (Okolab, Italy) mounted around the microscope stage, set to 27 °C, was used for long term microscopy. For fluorescence imaging the microscopes are equipped with a high-power light emitting diode (LED) light engine (LedHUB, Omicron-Laserage Laserprodukte GmbH, Germany). Two LEDs were used to excite AMF strains dyed with Calcofluor White (LED with peak wavelength of ca. 385 nm) and FM4-64 (LED with peak wavelengths of ca. 505-600 nm), respectively.

The following filters were used: (i) DAPI filter set (AHF Analysentechnik AG, Germany) with Excitation filter: 377/50 BrightLine HC (352-403 nm), Beamsplitter: 409 nm and Emission filter: 447/60 BrightLine HC (417-477 nm) and (ii) TRITC filter set with Bandpass filter: 495 nm (Omicron-Laserage Laserprodukte GmbH, Germany), Beamsplitter: 565 nm (AHF Analysentechnik AG, Germany) and Emission filter: 605/70 nm (570-640 nm) (AHF Analysentechnik AG, Germany). A third LED was used for imaging fluorescein in diffusion gradient experiments (LED with peak wavelength of ca. 470 nm). The following filters were used: FITC filter set with Bandpass filter: 465 nm (Omicron-Laserage Laserprodukte GmbH, Germany), Beamsplitter: 495 nm (AHF Analysentechnik AG, Germany) and Emission filter: 525/50 nm (500-550 nm) (AHF Analysentechnik AG, Germany).

The obtained microscopy images were exported as TIFF files with the microscope software (NIS elements viewer, version 5.21.00) and processed and analysed using ImageJ/Fiji (version 1.54f) (Schindelin *et al.*, 2012),. and timestamps as well as scale bars were added to videos and images. For measuring hyphal growth, the “segmented line” and “measurement” tool were used. For hyphal growth behaviour studies, lengths were measured and grouped into 5

intervals; 0.1-0.4 mm, 0.5-1.0 mm, 1.1-2.0 mm, 2.1-3.0 mm and >3 mm, represented as stacked column diagrams. To account for variation in number of spores per devices, the results were normalised by dividing the absolute number of counts by the number of germination sites. Here, sites where a germination within 14 days of inoculation occurred were defined as germination sites. The number of germination sites was used, instead of number of spores because spores were sometimes clustered in groups of 2-5 and could possess several cut ends of hyphal remnants (subtending hyphae), where germination usually occurs from. For calculation of the germination rates, we counted these hyphal ends as germination sites. Column diagrams, box charts and histograms for all chapters but CHAPTER 5: ANASTOMOSIS DEVICE were generated in Origin 2021-24 (OriginLab). Statistical tests (paired t-test and one-way ANOVA followed by Tukey test) were performed using the same programme. As p-value cut off for significance, 0.05 was chosen and every comparison generating p-values below 0.05 was considered significantly different. The significant differences were indicated as asterisks for p values <0.001 (***), <0.01(**) and <0.05 (*), as well as NS for no significant difference. For generating graphs shown in CHAPTER 5: ANASTOMOSIS DEVICE as well as for statistical analysis (paired t-test), RStudio (v.2024.04.2, Build 764) was used.

CHAPTER 3: DEVELOPMENT OF THE *AMF-SporeChip*

3.1 Chapter overview

This chapter details the development of a PDMS-based microfluidic device, which allows for introduction and subsequent immobilisation of AMF spores for microscopy-assisted germination and growth studies. The device design also enables the introduction of bespoke micro-obstacles to confront AMF hyphae with physical challenges to study space navigation mechanisms in these fungi. The introduction of the *Rhizophagus* spore material is no trivial task, as they come with hyphal remnants attached that vary in length and shape, or in small clusters connected through a common hypha. This inequality of the spore inoculant brings about differing flow properties and space needs, which have to be taken into consideration when designing the device. In this chapter, all developmental steps to overcome these challenges are discussed in detail. The main purpose of the microfluidic device is to study hyphal behaviour upon encountering physical obstacles. Therefore, once introduced and positioned within the device, growing hyphae needed to be confronted with a variety of different physical challenges, i.e., various angles, bottlenecks and dead-ends, offering higher or lower chances to escape or circumvent the obstacle. The main device was designed to accommodate spores of *Rhizophagus* spp., however, a modified device was also developed to study spores of *Gi. margarita*, highlighting the versatility of the design. Finally, the device was tested on technical aspects, i.e., spore loading and trapping performance as well as challenges posed by the obstacles, and biological aspects, i.e., spore germination and hyphal growth behaviour in the confined environment. It was hypothesised that the confinement and limited space availability within the devices would result in less extensive growth compared to on culture plates, without however, changing the overall growth behaviour of the fungi. The final device design was termed the *AMF-SporeChip* and was published in *Lab on a Chip* (Richter *et al.*, 2024).

3.2 Results and Discussion

3.2.1 Device Development

3.2.1.1 Device Design

The designs for the microfluidic device were drawn using AutoCAD 2021-24 (Autodesk). The first design was based on an older device developed by Dr Claire Stanley (Figure 6a). The main feature of this device is a channel height transition from 100 µm in the inlet region to 10 µm in the main channel. This step change in microchannel height allows trapping of *Rhizophagus* spores, which were measured to be between 10 and 160 µm in diameter (3.2.2.2 Spore germination and hyphal growth behaviour in the confined environment), as well as growth of asymbiotic hyphae (Ø = 2-12 µm; measured, see Figure A1) into the next part of the device. This section with a channel height of 10 µm, was named the “investigation zone”, and confines the hyphae in the z-direction for better imaging. Besides the channel height values, the general dimensions of the device are 14.0 mm total length and 3 mm diameter in- and outlets.

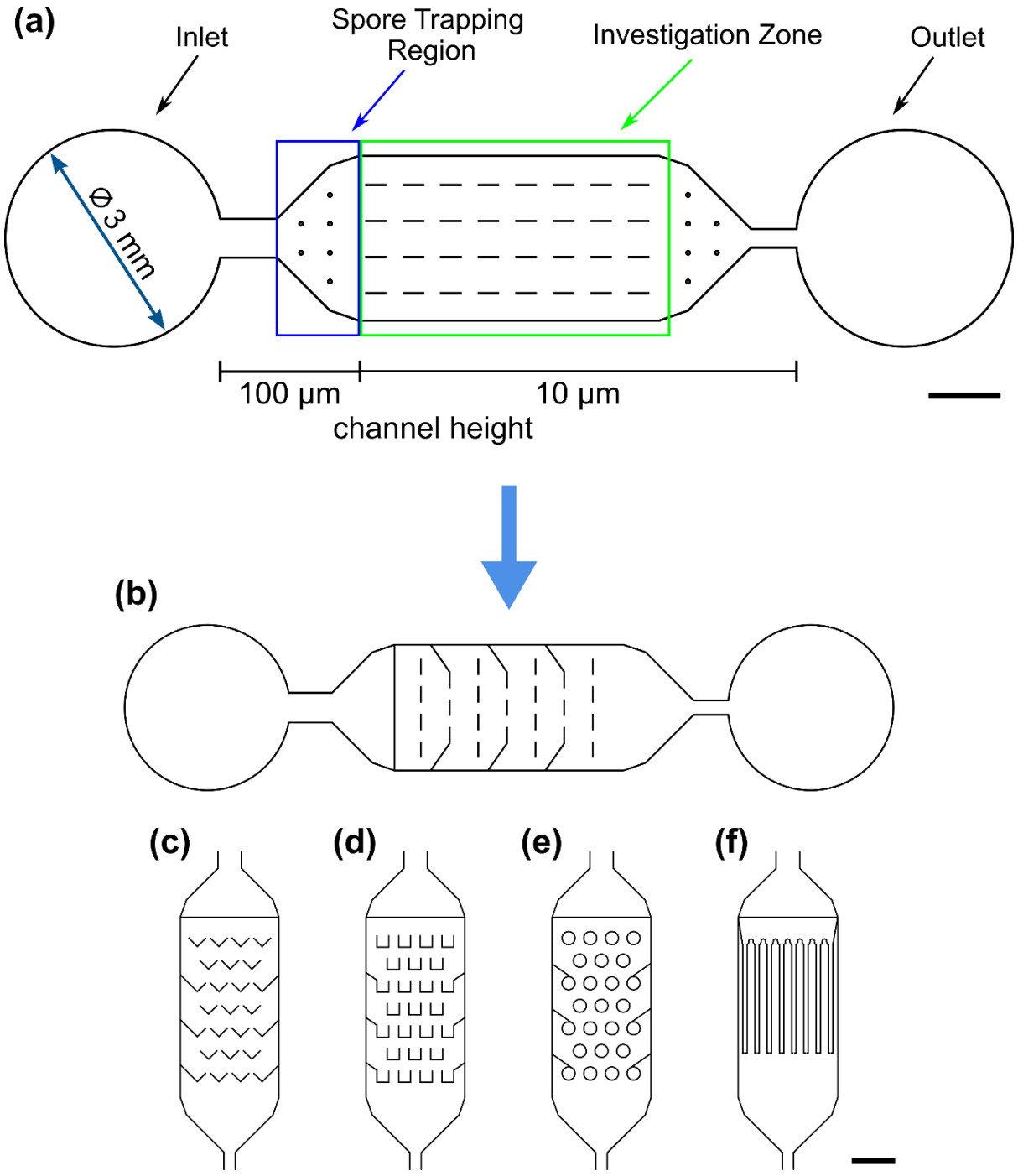


Figure 6: Schematic design of the first prototypes of the *AMF-SporeChip* highlighting the different parts of the device and channel heights. (a) Original prototype designed by Dr Claire Stanley. (b)-(f) First round of changes to the designs involving introduction of different obstacles, i.e. bars (b), open triangles (c), open squares (d) and closed circles (e), as well as lanes ending in a bottleneck (f). Scale bars: 1 mm.

The first changes made to the device design were removal of the small pillars before and after the investigation zone as well as implementation of several physical obstacles (Figure 6b-f). The pillars were designed to stabilise the channel and keep the wider areas from collapsing

due to unwanted bonding of the PDMS ceiling to the glass substrate; however, they partially obstructed the influx of spores and prevented an even distribution. As discussed in *3.2.1.3 Spore isolation and introduction into the device,* the spore inoculum is a mixture between true single spores and clusters of several spores still connected through a hypha, which makes them prone to getting stuck between the micropillars. When care was taken, no unwanted bonding occurred, and the channels retained their stability and thus the pillars were deemed dispensable. The addition of an assortment of different physical obstacles within the investigation zone aimed to challenge asymbiotic AMF hyphae in their space navigation. These structures can be grouped into single obstacle arrays, encompassing simple bars (Figure 6b), open triangular (Figure 6c), open square (Figure 6d) and closed circular shapes (Figure 6e), as well as lanes of 4 different lengths ending in a bottleneck (Figure 6f, only one length shown as an example). The bars, circles and squares are 300 µm wide and the triangles 400 µm. The lines connecting some of the outer obstacles with the chamber wall were meant to “collect” hyphae that track the edges of the microchannel, guiding them back towards the centre to increase the chances of obstacle confrontation. The lanes are all 100 µm wide and end in a 10 µm opening (bottleneck). Lengths of the lanes implemented and tested are 2500, 2000, 1500 and 1000 µm, respectively.

The loading of the lane devices (Figure 6f) with spores turned out to be problematic, as due to an enormous backpressure from the narrow bottlenecks, no sufficient flow could be generated to reliably flush spores into the trapping region. A very small number of hyphae, originating from spore in either the inlet or the entrance to the device chamber, managed to grow into the lanes. Generally, exceedingly high flow pressures cause the micro-obstacles to lift up and detach from the glass, which defeats their purpose and must therefore be avoided. With the devices containing arrays of single obstacles (Figure 6b-e), introduction of spores worked well. In terms of the physical challenge imparted by the obstacles, the bottleneck end did not seem to obstruct growth in any way and hyphae simply grew through the opening without problems (Figure 7a,b). The single obstacles proved to be more effective, occasionally halted growth and forced hyphae to withdraw cytoplasm, as mainly seen with the open square design (Figure 7c).

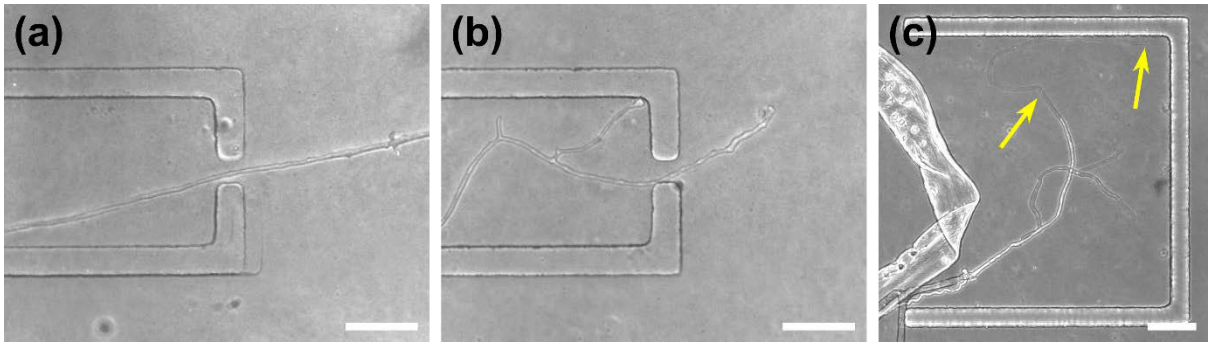


Figure 7: Phase contrast images showing hyphae of *Rhizophagus irregularis* MUCL 41833 growing in the *AMF-SporeChip* prototype. (a) and (b) Hyphae exiting the lane through the bottleneck. (c) Hypha grown into the open square obstacle, arresting growth and retracting cytoplasm, involving septa formation. Arrows indicate exemplary septa. Scale bars: 50 µm.

Still, as a conclusion from the observations, several changes in the device design were envisioned and are shown in Figure 8. Firstly, the total length of the device was shortened to 12.4 mm by reducing the size of the investigation zone (the in- and outlet channels remained the same). As most hyphae did not manage to grow past the first rows of obstacles, the last few rows were removed. The smaller device size also allowed us to fit two devices into the same glass-bottomed petri dish (Ø = 23 mm), which made the setup more economic but also benefited the imaging by enabling multi-ROI (region of interest) timelapses in two devices simultaneously. Additionally, the inlet channel was widened from 540 µm to 1540 µm to facilitate spore introduction and a more even distribution along the entire chamber width. Apart from the closed circle (Figure 8b), all single obstacles were reduced in size, to bring them closer to hyphal measurements, and changed in shape. A Pac-Man (Figure 8c), open-box (Figure 8d) and restricted open-box shape (Figure 8e) was implemented into the main chamber to confront hyphae with different numbers of contact interfaces and internal angles (Figure 9). The opening width of the Pac-Man, open-box and restricted open-box obstacle is 90 µm.

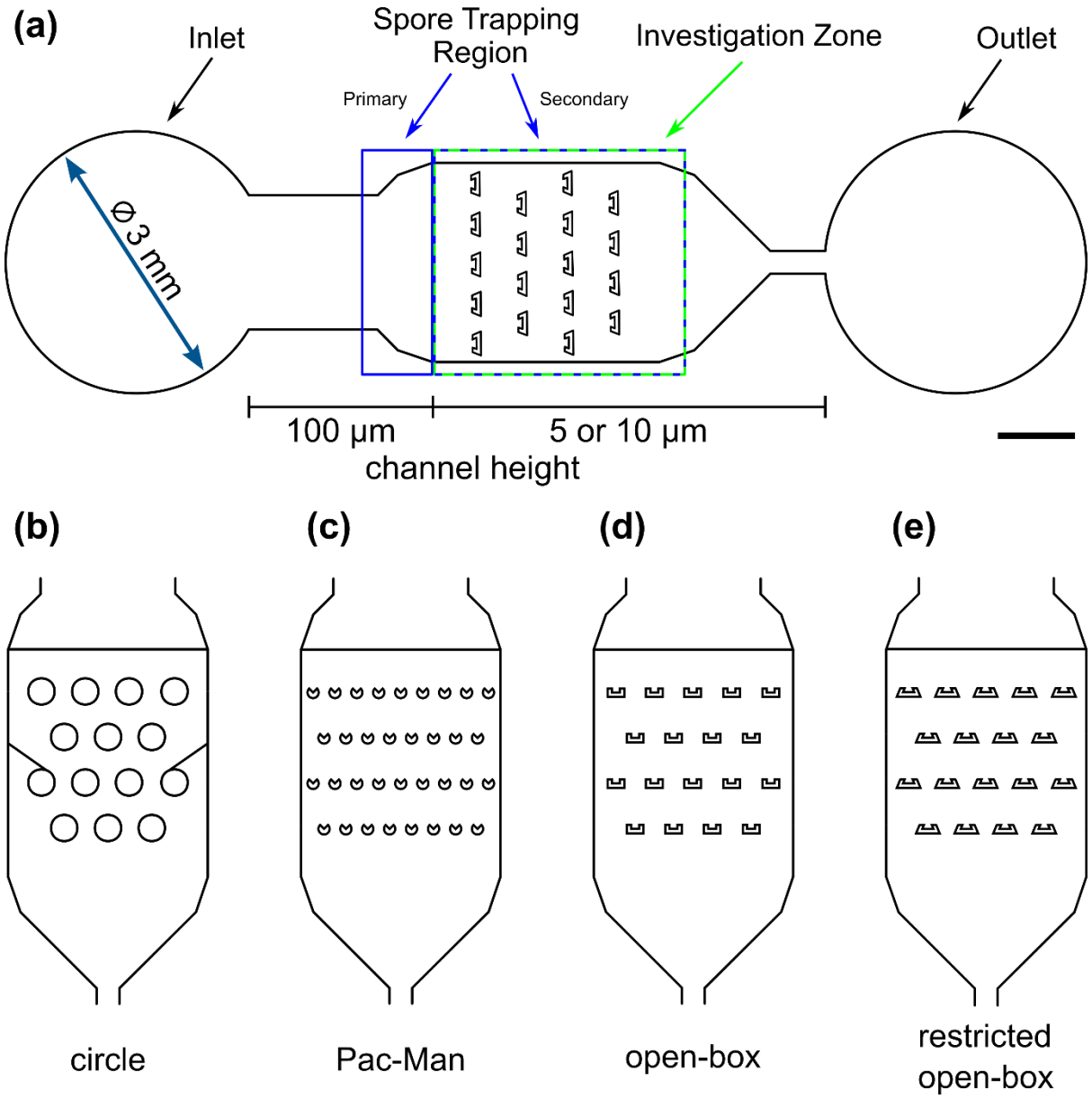


Figure 8: Schematic designs of the *AMF-SporeChip* highlighting the different parts of the device and channel heights for the obstacle-type designs. The designs differ in the obstacle shapes, (a) and (e) restricted open-box, (b) closed circle, (c) Pac-Man, (open-box). Scale bar: 1 mm.

This choice of obstacles granting reduced or increased opportunity for hyphae to “escape” from the obstacle, aimed to confront AMF hyphae with physical challenges that may be experienced within a soil environment. With soil being an extremely heterogenous environment, organic and inorganic particles of different shapes and angles can be found. The choice of obstacles for the microfluidic platform was aimed to represent a broad range of encounterable structures in a simplified and thus accessible manner. The interspaced array of the new and smaller obstacles provided an even inflow of medium and spores, further reducing

necessary pressure and facilitating a balanced distribution of spores within the device, while still giving plenty of chances for physical collisions.

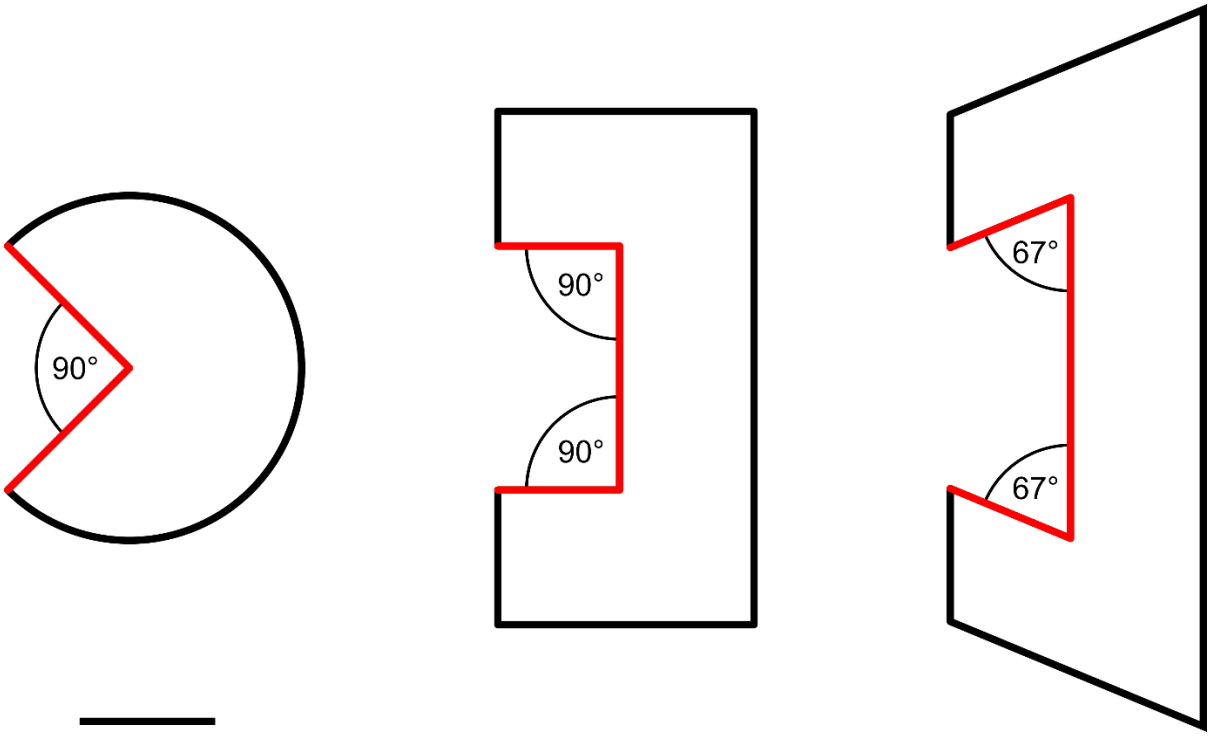


Figure 9: Geometries of the open obstacle-type structures with internal angles and contact interfaces indicated in red. Pac-Man: internal angle = 90°, number of contact interfaces = 2; open box: internal angles = 90°, number of contact interfaces = 3; restricted open-box: internal angles = 67°, number of contact interfaces = 3. Scale bar: 50µm.

For the lane designs, the width of the surrounding supporting walls was significantly increased, from 25 µm to 180 µm between the first half of the lane and 270 µm between the bottleneck part. The bottleneck was now not only an opening at the end of the lane but a very narrow lane itself (10 µm width, Figure 10a). The length of the lane measures 1000 µm in the first part and 1200 µm in the bottleneck part. This enhanced stability of the structure and precision of the bonding. In addition to the bottleneck design, a second lane device was introduced, featuring dead ends (Figure 10c). The former problem with sufficient inflow and thus spore introduction due to high backpressure from the narrow bottlenecks was hoped to be reduced by widening the inlet channel of the device. Even though the introduction was slightly improved, the pressure needed to introduce spores was still tremendously high. Therefore, the lane designs were slightly amended, entirely opening up to channels of 210 µm on both sides of the lane array (Figure 10b,d), to allow more flow through the device. In a third and last round

of modifications, the side channels of the dead-end lane design were further widened towards the outlet (210-450 µm), giving them a tapered shape (Figure 10e). These final versions of the lane designs allowed for a decent flow and introduction of spores into the device, however slightly biased towards the sides. As some hyphae nevertheless managed to grow into the lanes and results were obtained, the optimisation of the design was deemed sufficient.

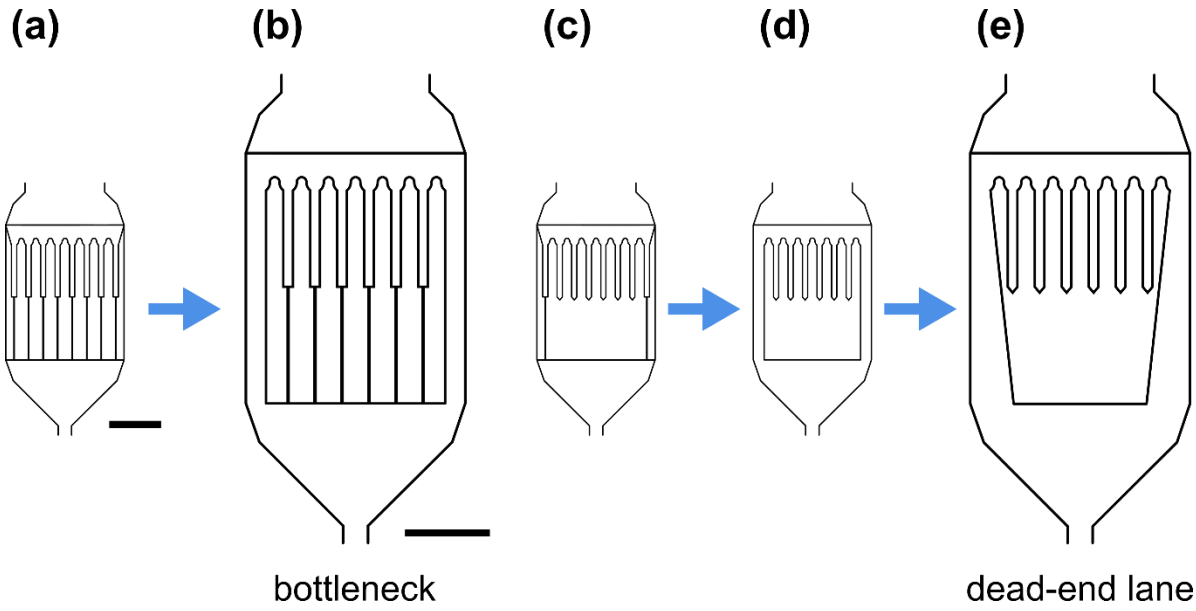


Figure 10: Schematics showing the development of the lane-type designs of the *AMF-SporeChip*. (a) and (b) for the bottleneck design, and (c)-(e) for the dead-end lane design. Scale bars: 1 mm.

Overall, the dead-end lane (Figure 10e) and the restricted open-box designs (Figure 8e) seemed to present hyphae with the biggest challenge to escape from. However, hyphal behaviours were found to vary widely, with several hyphae escaping from a restricted open-box obstacle for example, while others got stuck at the circular shapes. A clear pattern or obstacle dependence could not be determined. For measuring germination and growth dynamics, investigating how AMF hyphae respond to collisions with their environment (see *CHAPTER 4: AMF SPACE SEARCHING*), all device designs were used equally.

In an attempt to further improve the imaging quality, a device with 5 µm channel height (instead of 10 µm) in the investigation zone was manufactured (see *3.2.1.2 Optimisation of the photolithography protocol* for a description of the manufacturing). The desired effect, however, was not achieved and the lower channel height made the channel more prone to collapsing

and bonding to the glass bottom. Therefore, the experiments were conducted using the devices with a 10 µm channel height.

Later, an adaption of the final designs was developed in order to accommodate spores of *Gi. margarita*. This other species of AMF, belonging to a different order as *Rhizophagus*, possesses gigantic spores, as the name suggests, which are visible to the naked eye, of about 500 µm in diameter (measured, see *3.2.2.2 Spore germination and hyphal growth behaviour in the confined environment*). Therefore, the inlet channel height (primary trapping region) of 100 µm had to be increased, a feature adjustable through the photolithography process (see *3.2.1.2 Optimisation of the photolithography protocol*). All other dimensions of the designs remained unchanged.

3.2.1.2 Optimisation of the photolithography protocol

To realise the channel height transition in the trapping zone of the device, a 2-layer photolithography process had to be employed. Initially, a protocol based on the SU-8 photoresist datasheet and previous manufacturing session performed by Dr Claire Stanley was used. However, since the process is highly dependent on the clean room condition and the device design itself, many problems appeared in the first trials conducted in the new clean room environment and with the new designs, hence, many optimisation steps had to be conducted.

In general, thicker layers pose a bigger challenge compared to thinner layers, as the high viscosity needed to achieve layers of 100 µm and above are less forgiving. Any disturbances in the film, i.e., due to the presence of air bubbles or dust particles, is hardly rectifiable, whereas the less viscous photoresists used to create layers of 10 µm or below are usually able to “heal” and thus recover once the disturbance is removed. Air bubbles are readily created in the viscous resist and remain for a long time even in the stock bottle. The baking times similarly increase immensely with viscosity of the film. Longer baking times mean longer exposure to environmental conditions in its liquid, “vulnerable” state, thus making it more susceptible to any dust residues (which can never be 100% excluded) or micro slopes in the setup causing height gradients in the thickness of the structures. Further, it turned out that the adhesion of the thick resist to the silicon wafer is reduced. Thus, following the original protocol, the

photoresist started “contracting” in the soft baking step, creating an immensely uneven surface with wide craters (Figure 11a). To rectify this problem, an extra washing step for the wafer was added. Before the plasma treatment, the silicon wafer was washed first in acetone and subsequently in isopropanol and then thoroughly dried with an air gun. This improved the adhesion and reduced significantly the number of craters in the resist film, however, a few still remained. An increase in the plasma treatment time from 5 min to 10 min did not remove the issue and was therefore kept at 5 min. The critical change in the protocol, removing the crater problem entirely (Figure 11b,c), lay in the soft baking temperature. Originally, the baking was started at 35 °C and then ramped up first to 65 °C and then to 95 °C with a rate of 2 °C/min, to avoid shock cracking of the layer due to too rapid temperature changes. However, the initial 35 °C caused the resist to become more liquid and thus aggregate in patches, due to the imperfect adhesion to the substrate, before curing. When starting the baking directly at 65 °C and then ramping up to 95 °C, this effect was excluded and the resist was cured quicker to fix the layer in its current, confluent state, while still avoiding stress-induced cracks in the film.

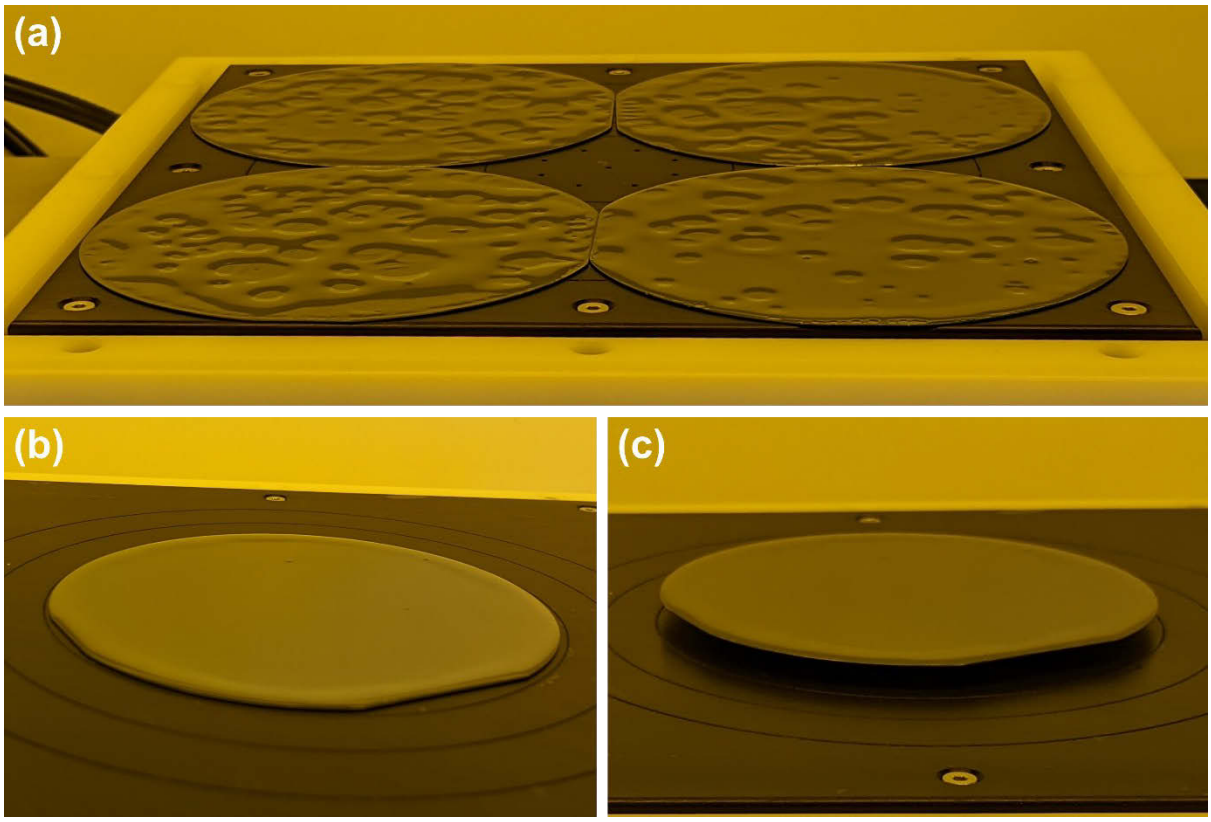


Figure 11: Photographs of the hot plate set-up for the lithography process in the clean room. (a) Issues with the adhesion of the photoresist to the silicon wafer and thus large craters developing during the soft baking. (b) A smooth and confluent layer of photoresist after optimising the lithography protocol. (c)

A wafer with a layer of photoresist hovering over the hot plate to cool down after the baking step, supported by raisable metal pins.

Another problem, which appears especially with very thin and long structures (<10 µm width, >400 µm), can be caused by cooling the wafer down too quickly directly from 95 °C to room temperature. Due to the temperature shock, some structures loose adhesion and stability and wash or break off during or after the development. Therefore, the wafer was left on the hotplate and the temperature ramped down to 65° C and then raised on the pins of the hotplate (~4 mm, Figure 11c). Since this extra step takes up much time (~30 min x 4 for soft baking and post exposure baking and two layers), the protocol was changed to only leave the wafer raised on the pins for 5 min, directly after finishing the baking programme at 95 °C, which proved sufficient for the structure aspects of the *AMF-SporeChip*. A similar effect of structures easily breaking off the substrate can be ascribed to an insufficient UV exposure and thus an incomplete cross-linking of the SU-8. The data sheet recommends an exposure dose of 130 mJ/cm^2 for a layer thickness of 10 µm. The UV mask aligner illuminates with an alleged UV intensity of 30 mW/cm^2, which would translate in an exposure time of 4.3 s, which proved to be insufficient to produce sturdy structures. Eventually, the time was optimised to 7.5 s, which represents an increase of ca. 80% compared to the recommendation. Similarly important is the development step at the end of the procedure. Here again, the recommended development time was not quite adequate, however was easily rectified by simply exchanging the developer after the recommended time and developing for another 30-60 s with fresh developer. A simple test to control whether the development was complete can be done when washing with isopropanol. When the development had been incomplete, white slime emerges from around the structures during the washing. Additionally, the structures of incompletely developed master moulds show poorly resolved, rounded corners when scrutinised under the microscope.

For spores of *Gi. margarita*, a height of about 500 µm in the inlet channel, i.e., the first height step, was envisioned. While the protocol for the first layer (10 µm) remained the same, for the second layer a different photoresist, SU-8 2150 (Kayaku, USA), was employed. This resin was even more viscous than the SU-8 2075, used for the regular *AMF-SporeChip* variant, and extreme caution and patience had to be practiced when pouring the resist onto the wafer.

However, with the experience gathered from working with SU-8 2075, this posed little problem. Based on the manufacturer's recommendation, a spin speed of 1300 rpm was supposed to yield a structure height of about 500 µm. A different issue arose later from a combination of multiple factors. As the much thicker layer of photoresist needed more time to cure, a small unevenness in the hot plate levelling might cause a layer height gradient on the wafer. Any variation in height then becomes more noticeable the thicker the total SU-8 layer is. Along with a noticeable deviation from the 500 µm reported in the manufacturer's protocol, which is often the case as environmental conditions as well as resist freshness play an important role, the resulting SU-8 layer thickness was spread over a range between 250 µm and 450 µm, averaging at 350 µm ± 100 µm. An improvement of the result could have been achieved by reducing the spin speed and levelling the hot plate with more accuracy, e.g., with a digital high precision levelling device. However, as the priority was lying on the *Rhizophagus* experiments, and the structure height gradient actually offered the means to test different inlet channel heights, it was refrained from attempting further rounds of manufacturing.

Lastly, after developing and drying the master mould, occasionally wide cracks in the larger structures (e.g., inlets) can be observed (Figure 12a). These can be reduced through hard baking (Figure 12b). This step further improves the longevity of the master mould. Fulfilling a similar purpose, the wafer is finally subjected to a silanisation treatment. In this process, the wafer is placed into an atmosphere of chlorotrimethylsilane, which reacts with nucleophilic functional groups, such as hydroxyl groups, on the surface of the wafer to create an even, more hydrophobic layer of methyl-groups on the surface. This reduces the adhesion of the PDMS to the wafer and thus assists in the peeling off of the cured PDMS slab. This protects both the PDMS devices as well as the SU-8 structures on the wafer from prematurely breaking. The silanisation protocol did not require optimisation and is described in full in *2.1.1 Master mould manufacturing*.

The real final heights of the layers of the *Rhizophagus AMF-SporeChip* variant were measured using an optical profilometer (Profilm3D, Filmetrics, USA) to be between 10.3 and 11.2 µm for the first layer and between 90.2 and 101.6 µm for the second layer. As the second layer was spun onto the first layer, the total height in the inlet region results in a height between 100.5 and 122.8 µm. Because both spore as well as hyphal diameters vary significantly (see *3.2.2.2*

Spore germination and hyphal growth behaviour in the confined environment), these deviations in channel height were deemed acceptable. For simplification, the channel heights are referred to as 10 and 100 µm, respectively, throughout the thesis.

A photography as well as a stereoscope (SMZ1270, Nikon, UK) image of the final master mould can be found in Figure 12c and d, respectively. The complete and optimised final protocol with all adjustments implemented is detailed in *2.1.1 Master mould manufacturing*.

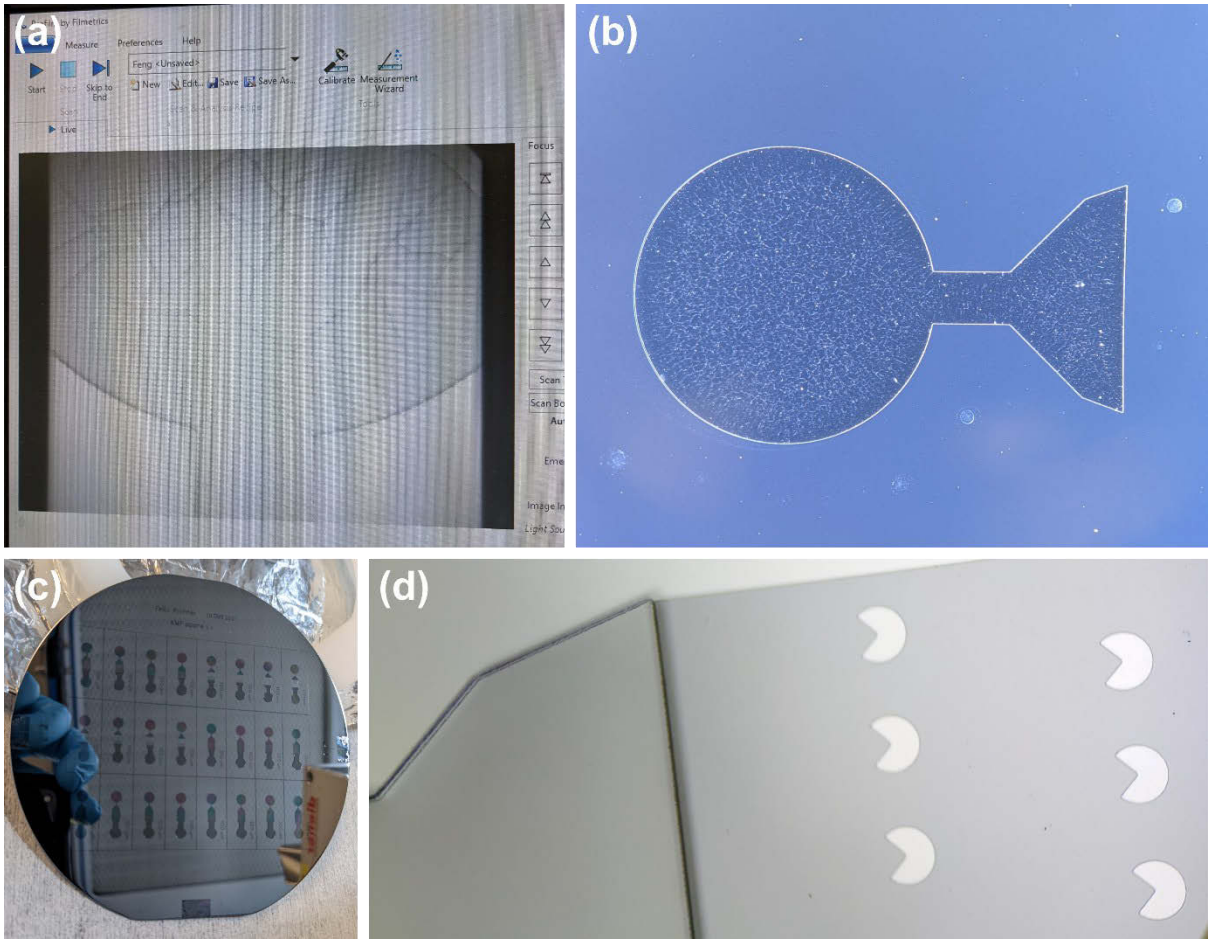


Figure 12: Images showing results of the master mould manufacturing. (a) Screenshot of the profilometer software revealing large cracks on the SU-8 structures. (b) Stereoscope image of an SU-8 structure with reduced cracks after hard baking. (c) Photograph of final master mould. (d) Image of an immaculate section of a Pac-Man design on the master mould, obtained with the profilometer camera.

3.2.1.3 Spore isolation and introduction into the device

Besides the development of the microfluidic device itself, another essential requirement to set up the entire method involved devising a robust means for isolating spores from the co-cultures and introducing them into the devices. *Rhizophagus* spores, unlike the propagules of many

Asco- or Basidiomycetes, e.g., conidia of *Trichoderma rossicum*, are not designed to easily and fully detach from the mycelium. Rather, germination and formation of new hyphae generally originate from the tips of hyphae attached to the spores, often referred to as subtending hyphae. This means that these hyphal remnants are necessary, however, separating the spores from each other and keeping the subtending hyphae as short as possible was desirable for the microfluidic experiments. Several approaches were considered and tested to isolate spores of *Rhizophagus* from the phytagel as well as the mycelium and are detailed herein.

Manual spore isolation with tweezers

The first attempt involved removing the spores from the phytagel by dissolving the medium. In brief, a piece of phytagel containing spores was cut out from the hyphal compartment, transferred into an empty petri dish and mashed up with a scalpel. Then, citrate buffer pH 6 was added so that the plate was about 50% filled (Recorbet *et al.*, 2020). Using a pipette, the mixture was stirred cautiously until all the phytagel had dissolved. The solution was then filtered through a nylon mesh (Hike Cold Brew Coffee, pore size 25 µm; Figure 13a) and subsequently washed 10 times with MilliQ water (simply adding the water onto the filter and letting it run through) before finally rinsing the spores from the filter into an empty petri dish. Usually, the spores were entangled in a large clump. Using two pairs of tweezers, it was possible to divide this into smaller clumps of about 30-100 spores with the naked eye (Figure 13b). For first orientational plate-based experiments on spore germination (not described herein) this was sufficient. However, in order to enable single spores to be incorporated into and germinate inside microfluidic channels, another method needed to be developed. Pulling apart the spores manually and separating them from the hyphae was found to be impossible with regular tweezers, even under a stereoscope, simply because the tweezers are not fine and precise enough. Moreover, new approaches were tested to explore the possibility of an automated (i.e., non-manual), reproducible and less time-consuming spore isolation technique.

Spore isolation with the sucrose gradient technique

Various “automated” mechanical means to remove the bulk mycelium and isolate single spores, without the need of manual one-by-one picking, were tested, beginning with the sucrose gradient technique. This method is commonly used for spores derived from soil samples, to remove dirt and debris (Fortin *et al.*, 2002; Xavier and Germida, 2003). For that, spores still attached to the mycelium were transferred into a 50 ml falcon tube, which was then filled with 25 ml MilliQ water. Next, 15 ml of 2 M sucrose solution were carefully injected into the bottom of the tube, so that two separate layers formed. The tube was then centrifuged at 1200 g for 5 minutes. Thus, spores were expected to detach from the mycelium, with the bigger hyphal debris being pushed down into the sucrose layer by centrifugal force, and the smaller and lighter spores floating on the sucrose solution and accumulating in the boundary layer. Unfortunately, the spores remained attached to the mycelium and even turning up the rotation speed did not have a positive impact. In the same way, both ultra-sonic treatment as well as vortexing were not able to break up the surprisingly strong connection between the spore and mycelium.

Spore isolation by deep freezing

For the next attempt, harsher conditions were considered. The idea was to freeze the spores, thus breaking up the hyphal connections between the spores as the intra-cellular water expands, while hoping for the more resilient spores to withstand the treatment. Therefore, spores were removed from the phytagel medium, using the citrate buffer method, as described above. Then, the mycelial spore clump was placed into MilliQ water and frozen at -80 °C overnight. After the treatment, the hyphae were clearly affected, showing signs of disruption (i.e., being surrounded by clouds of debris; Figure 13c). The sample was then sonicated to completely break up the hyphae, which resulted in mostly single spores with only small remains of hyphae attached (Figure 13d). The process was not reproducible, however, as upon repeating the procedure, most of the time the spores did not detach, even after multiple rounds (up to 5 repetitions) of freezing and sonicating. Furthermore, when the procedure did work and yield single spores, detached from one another, the spores were found to be critically damaged in the process. While still maintaining their shape after the treatment, they appeared empty (Figure 13d) and tests of their ability to germinate turned out to be entirely unsuccessful.

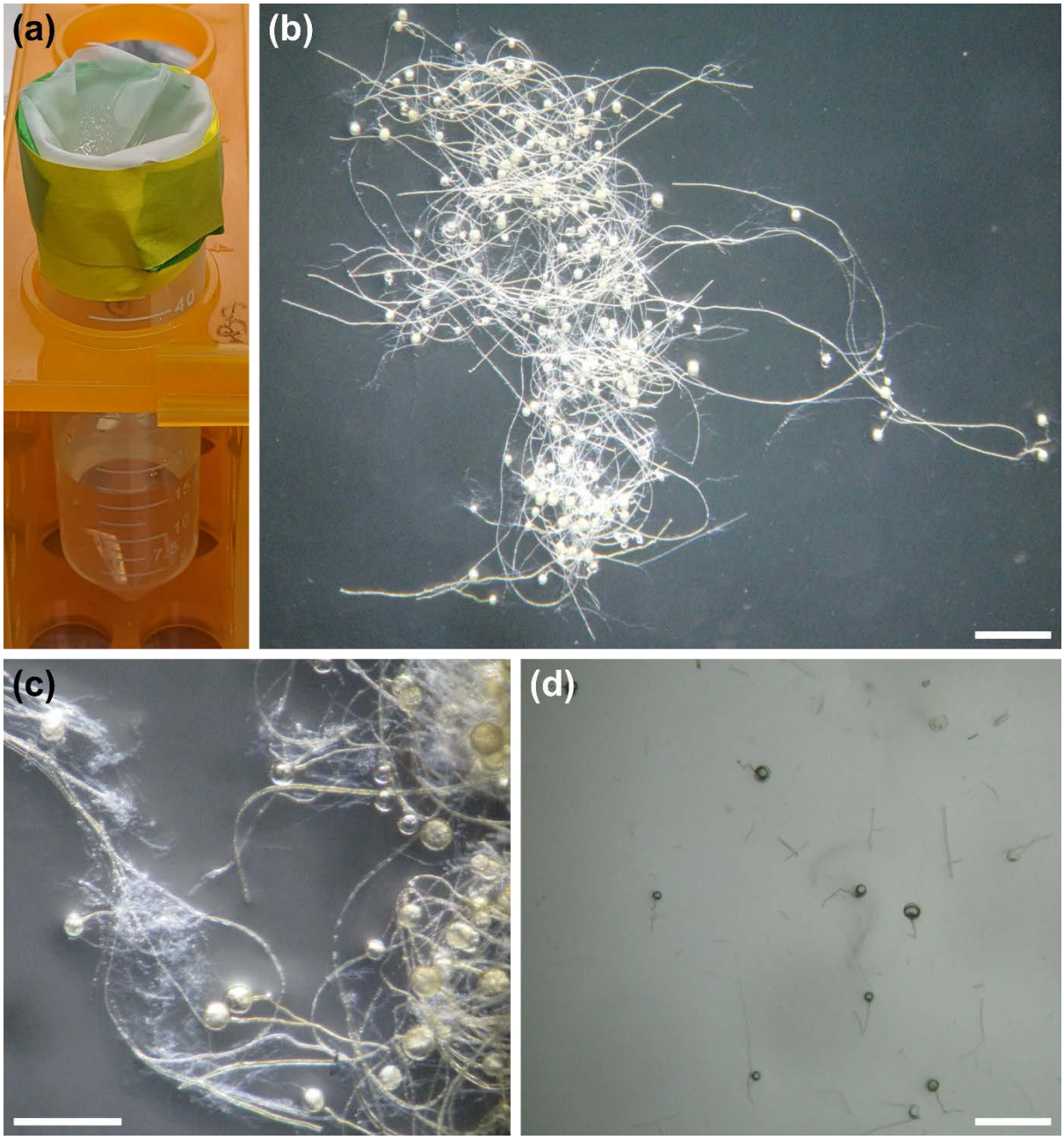


Figure 13: Images of different spore dissection attempts. (a) Filtering set-up with a nylon mesh to filter and rinse spore clumps from phytagel and citrate buffer remnants. (b) Stereoscope image of a clump of spores and hyphae obtained after tweezer dissection and filtering. (c) Stereoscope image of spores after deep freezing. Note the white clouds of cellular debris around the hyphae and spores, indicating major damage. (d) Stereoscope image of single spores after deep freezing and sonication. Spores appear empty. Scale bars: (b) and (d) 500 µm; (c) 250 µm.

Manual spore isolation with dissection needles

Based on the results from the non-manual methods and the fact that the spores are considerably sensitive, it was decided to move back to a manual handling using fine dissection needles (Figure 14c) and a stereoscope, small enough to fit into a laminar flow hood for (semi)

sterility, to retrieve spores. For this method, there is no need to dissolve the phytagel with the citrate buffer first. Chains of spores can easily be cut out with the needles, pulled out of the phytagel and transferred into a plate filled with liquid MSR(-) medium, as they cling to the needle. It was possible to dissect the clumps of mycelium into groups of 1-5 spores with short hyphae still attached (Figure 14a). Although the method is rather fiddly, time-consuming, and if not done with caution, may result in the spores being crushed (Figure 14b), it yields well-suited inocula for experiments in the microfluidic devices. Later, the dissection needles were replaced by tattoo needles (03 tight liner, pre-soldered, sterile, Barber DTS, UK), with much finer tips (3-pointed) for a more precise dissection (Figure 14d,e). By using the tattoo needles and performing a combination of careful cutting, twisting and ripping movements, the spore isolation process was further improved, allowing for an increase in the number of actual single spores in the mix as well as a decrease in the damage dealt to the spores.

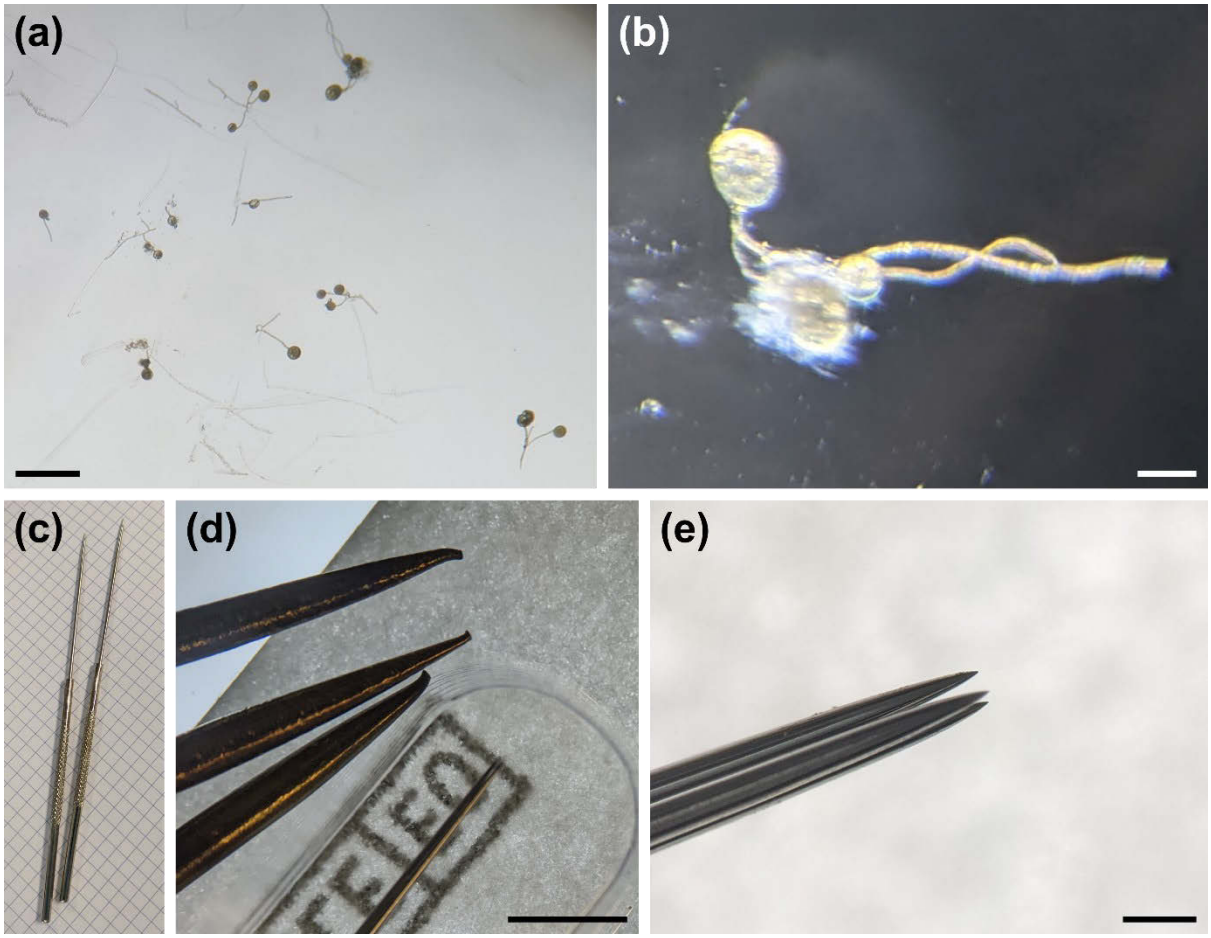


Figure 14: Images of different needle assisted spore dissection attempts. (a) Stereoscope image of single spores after manual dissection with dissection needles. The spores appear filled and healthy. (b) Stereoscope image of a spores crushed by the needle. (c) Photograph of the used dissection needles. (d) Comparative photograph of the tips of the dissection needles (top left) and tattoo needles. (e)

Stereoscope image of the tip of the tattoo needle. Note the 3-pointed tip. Scale bars: (a) and (e) 500 µm; (b) 50 µm; (d) 5 mm.

Introduction of spores into the microfluidic devices

In order to inoculate the devices with the spore material, a pipette (Pipetman G, 200 µl, Gilson, USA) set to 21 µl (to avoid overfilling of the inlets) was used to pick up isolated spores, aiming for a spore number between 10-15 per device. Then a syringe (Henke-Ject, Luer Lock, 5 ml, HenkeSassWolf, Germany) equipped with AlteSil High Strength Tubing (Bore: 1.00 mm, Wall: 1.00 mm, total diameter: 3 mm; Altec Extrusions Limited, UK) with a blunt tip syringe needle (1.28 mm, Shintop, China) and filled with liquid MSR(-) medium was slowly plugged into the inlet and spores were flushed into the device until all spores were inside of the channel and/or no more spores were coming from the inlet. The syringe was handled manually, without a syringe pump, and alternating the pressure in a pulsating manner was found to aid the spore introduction and dispersal within the device. Spores of *Gi. margarita*, 1-2 spores per device, were introduced in the same manner into the Gigaspora variant of the *AMF-SporeChip*. Figure **15** shows the set-up for the spore loading (a,b) as well as spores trapped in the *AMF-SporeChip* after loading (c).

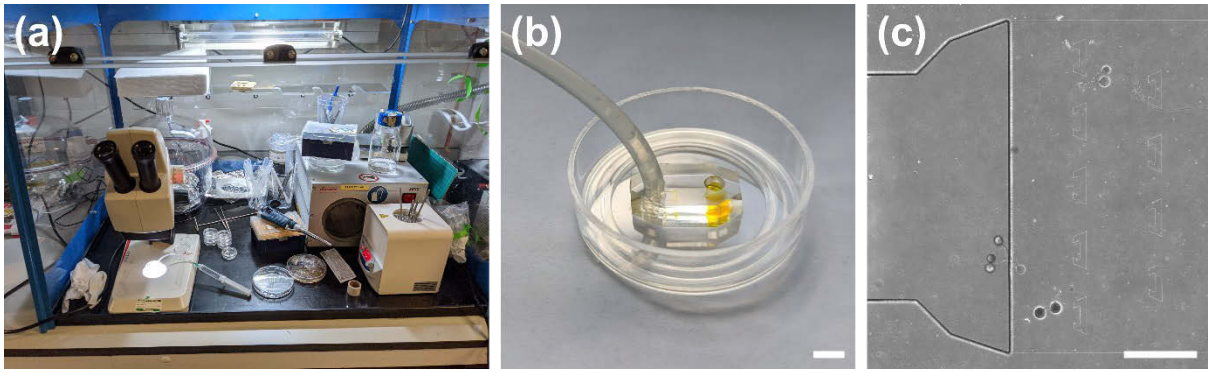


Figure 15: Spore introduction into the devices. (a) Experimental set-up within a semi-sterile laminar flow hood, involving stereoscope, dissection needles and syringes equipped with tubing. (b) Tubing inserted into the inlet of an *AMF-SporeChip* to flush in spores. Here, for demonstrative purposes to highlight channels, a fluorescein solution was injected. (c) Phase contrast image of a channel section with trapped spores. Scale bar: (b) 5 mm; (c) 500 µm.

3.2.2 Device characterisation

3.2.2.1 Spore loading and trapping

For introducing spores into the device, the inoculum was first dissected, to obtain single spores or small spore clusters, and subsequently flushed into the device as described in *3.2.1.3 Spore isolation and introduction into the device*.

The original device design (Figure 6a) envisaged the spores to be trapped at the height transition line, representing a clear separation between trapping region and investigation zone. By modifying the device design and especially by moving the first row of obstacles further away from the transition line (250 µm for the lane devices, 330 µm for the circle design and 450 µm for all other designs) a secondary trapping region and mechanism was introduced. The material of the devices, PDMS, is an elastomer and hence flexible, which allows the microchannels to widen slightly upon applying pressure when pumping in spores into the devices with the syringe. That way, spores can be pushed into the investigation zone and trapped there upon removing the applied pressure, as the microchannel reverts back to its original height. With the original design this was not possible as the first row of obstacle was nearly directly adjacent to the transition line. The mechanism of the secondary trapping was speculated and not further validated or characterised, also because the pressure was applied manually and not measured. Even though it can be assumed that the widening of the channels is involved, other effects, such as friction or varying hydrodynamic resistance, might play a role as well. The trait of flexible expansion in PDMS is actively utilised for cell trapping in microfluidics, mainly with yeast cells (Groisman *et al.*, 2005; Lee *et al.*, 2008; Zhang *et al.*, 2012).

To characterise the distribution of spores within the different trapping regions, the number of spores per device and per trapping region was counted and the percentages visualised in box-plots (Figure 16). Here, for a more precise representation of the observations, the secondary trapping region was grouped into “2° trapping region – first half” and “2° trapping region – second half”. A significant difference in the trapping behaviour was found between the obstacle-type devices and the lane-type devices. Because of the larger contact area between PDMS and glass bottom and the proximity of the lanes the height transition line, similar to the

original device design (discussed above), the expandability of the PDMS channels was reduced and spores were able to enter the investigation zone. Here, ca. 75% of the spores were trapped at the channel height transition and about 25% spores reached the secondary trapping region, only in one instance, spores reached the second half. In the obstacle-type devices, about 35% of the spores remained trapped in the primary trapping region and ca. 50% reached the first half of the secondary trapping region, however, no statistical difference could be determined. Approximately 15% of the spores were flushed into the second half of the secondary trapping region. This results in a distribution of spores in all devices combined of approximately 50% trapped in the primary trapping region, 40% in the first half of the secondary trapping region (no statistical difference determined) and ca. 10%, of spores in the second half of the secondary trapping region (Figure 16, note that the number of obstacle and lane devices is not equal). The individual spore distribution per device is dependent on numerous factors, such as spore size, size of the spore-cluster, length of hyphal remnants/subtending hyphae as well as the applied pressure for spore introduction (due to manual loading) etc.

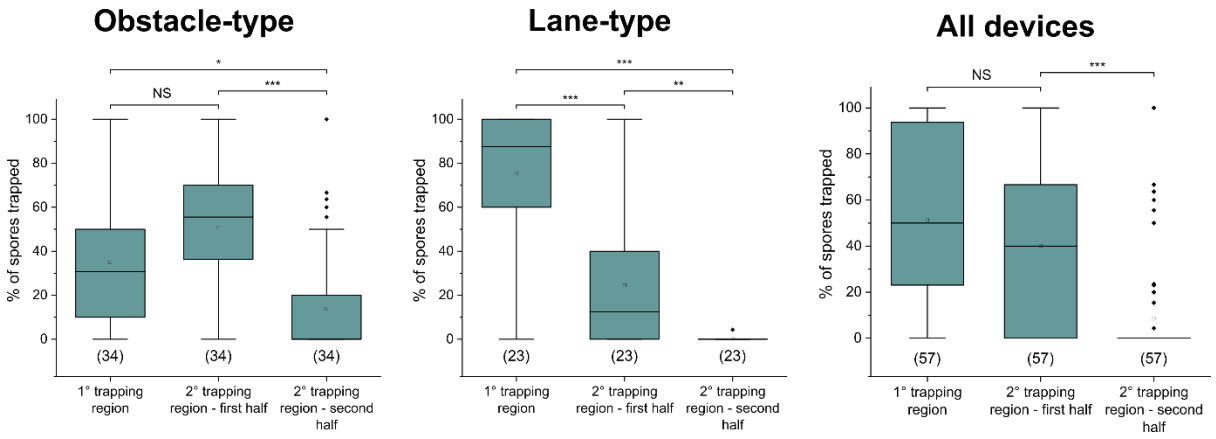


Figure 16: Spore trapping performance in the *AMF-SporeChip*. The box-plots show the percentage of spores trapped in each of the different trapping regions for lane-type and obstacle-type devices as well as all design types. Upper and lower whiskers represent the largest observation smaller or equal to the upper and lower percentile plus 1.5 × interquartile range, respectively. Squares indicate the means and the line the median. Data points beyond the whisker range (outliers) are plotted as diamonds. Significant differences according to one-way ANOVA followed by Tukey test are indicated with asterisks for p values <0.001 (***), <0.01(**) and <0.05 (*), as well as NS for no significant difference. The values in parentheses indicate the number of sample-points, i.e., the number of microfluidic devices analysed. The total number of spores analysed was 260 for the lane-type devices and 473 for the obstacle-type devices. For the secondary trapping region – second half, the medians are 0 for lane-type devices as well as for "All devices", hence the number of values above 0 was insufficient to draw a box and were therefore categorised as outliers. Images and figure legend reproduced with modifications from Richter

et al. (2024) with permission from the Creative Commons Attribution license (www.creativecommons.org/licenses/by/4.0/).

The rather serendipitous addition of the secondary trapping region proved to be beneficial for the experimental setup. Firstly, it helped dispersal of the spores within the device, spacing out spores to avoid spore clumps obstructing a clear imaging of individual hyphae. Secondly, when both spore and attached hyphae are trapped in the secondary region, the confinement allows for a high resolution imaging of the entire organism in the same focal plane, whereas when trapped at the transition line, often only the hyphae growing from the spore is clearly visible, while the spore is either out of focus or masked by the transition line. Even though this might suggest that the primary trapping region is inferior and could be dispensable, this is not the case. Only with an inlet channel higher than the 10 µm of the main chamber, a lifting of the PDMS is achievable and the introduction of spores into a device of only 10 µm would not be possible (tested with a similar device, not shown).

For the introduction of *Gi. margarita* spores into the *Gigaspora* variant of the device, several combinations of spore diameter and height of the inlet channel were tested. It was possible to flush most spores into the devices. Only very large spores with diameters of 500 µm did not fit into devices with inlet channels below 300 µm (the channel height in the Gigaspora variant devices varied between 250 µm and 450 µm, see *3.2.1.2 Optimisation of the photolithography protocol*). Occasionally, pulsating flow and high pressure (within the limits that the channels can withstand) had to be applied for spore introduction. As expected, no spores of *Gi. margarita* were able to traverse past the primary trapping region and into the investigation zone (secondary trapping region), which contrasts starkly to spores of *Rhizophagus*.

3.2.2.2 Spore germination and hyphal growth behaviour in the confined environment

To characterise the biological effect of the confinement of the *AMF-SporeChip* on germination and growth on the AMF strains, a series of experiments with (i) *R. irregularis* MUCL 41833, (ii) *R. irregularis* MUCL 43194 and (iii) *R. intraradices* MUCL 49410 to gather both qualitative and quantitative data was conducted. Within soil, the fungi regularly encounter confined spaces, where they might find themselves pressed between firm structures. These initial tests, however, were mainly conducted to rule out any possible detrimental effects of the microfluidic

system on the fungi's growth and general vitality. The results were obtained from studying about 600 spores with approximately 200 germination sites, in 6 devices per strain and 1 phytagel plate per strain with about 10 germination sites each. Spores were dissected and introduced into the devices as described in *3.2.1.3 Spore isolation and introduction into the device*. For the on-plate experiment, spores were picked up with a pipette (Pipetman G, 200 µl, Gilson, USA) and evenly distributed on a glass-bottomed Petri dish (Ø dish = 50 mm, Ø glass = 40 mm; Fluorodish, World Precision Instruments, Germany) containing a thin layer of MSR(-) (ca. 1-2 mm). The plates were then sealed with cling film and incubated at 27 °C. Spore germination and hyphal growth were imaged and measured alongside the microdevices in the same manner.

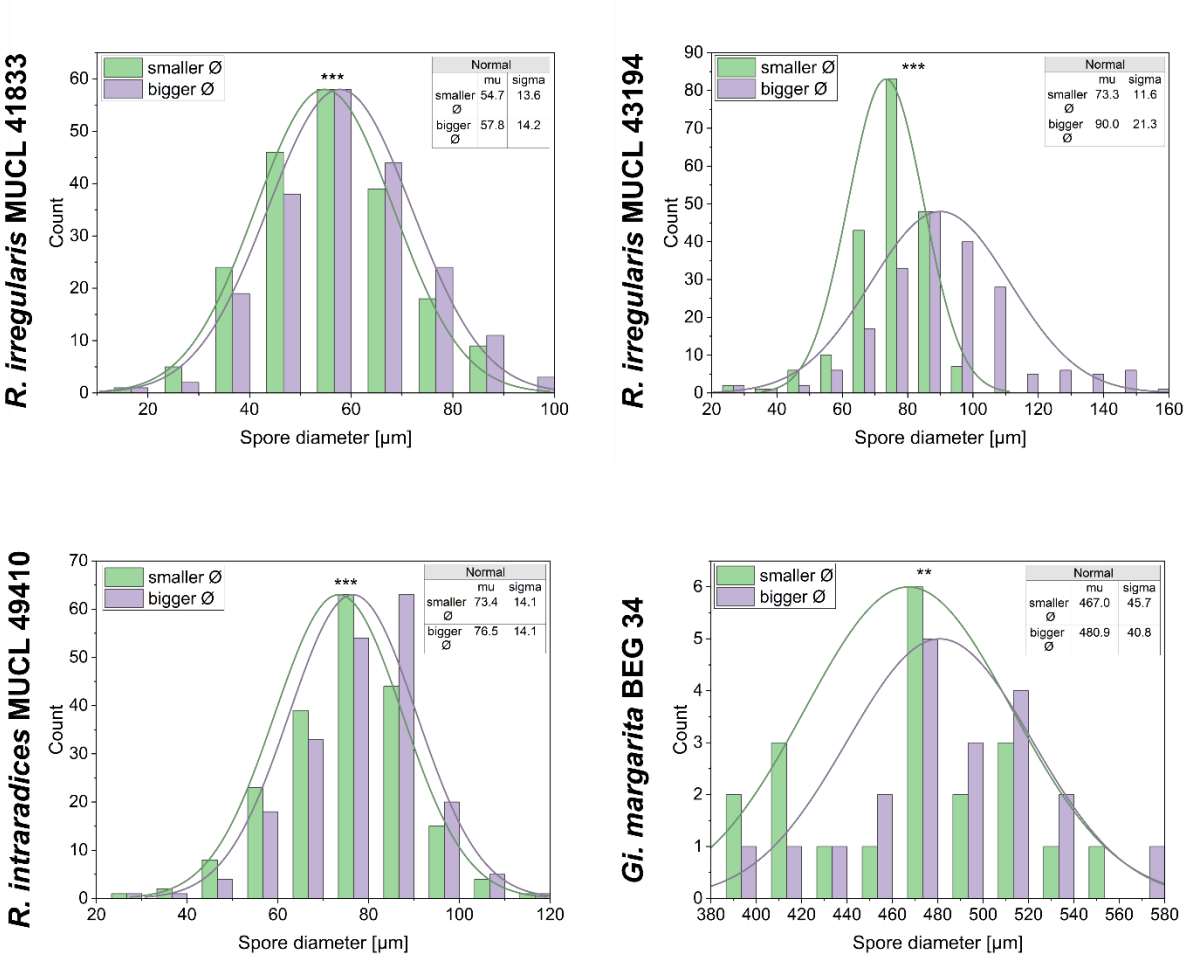


Figure 17: Measured spore diameters of the arbuscular mycorrhizal fungi (AMF) strains used in the project. The largest and smallest diameters of a total of 200 spores per strain (20 spores for Gigaspora margarita BEG 34) were measured using the "straight line" tool in ImageJ/Fiji and the size distribution plotted with Origin. For *Rhizopagus irregularis MUCL 41833* and *Rhizophagus intraradices MUCL 49410* the difference was very small; *Rhizopagus irregularis* MUCL 43194, however, showed a strong difference between the largest and smallest diameter, suggesting uneven shapes. Since the total spore

number for *Gi. margarita* BEG 34 was very limited, the distribution is quite irregular. For each diameter, the median value “mu (μ)” with a standard deviation “sigma (σ)” is given. Significant differences according to paired t-test are indicated with asterisks for p values <0.001 (***), <0.01(**) and <0.05 (*).

Images and figure legend reproduced with modifications from Richter *et al.* (2024) with permission from the Creative Commons Attribution license (www.creativecommons.org/licenses/by/4.0/).

Despite being the same strain or at least closely related, germination behaviour differed distinctly. This could be explained by their origin, which varies significantly in location, climate, human influence and seasonality, just to name a few. Furthermore, many organisms adapt a “lab-strain” behaviour after years in *in vitro* culture. While *R. irregularis* MUCL 41833 was isolated in the Canary Islands in 1999 (Cárdenas-Flores *et al.*, 2010), *R. irregularis* MUCL 43194 was taken from a white ash tree plantation in Canada in 1992 (Chabot *et al.*, 1992) and *R. intraradices* MUCL 49410 originated from a citrus plantation in Florida, USA (BCCM, 2024).

Exemplary, qualitative timelapse series images of the germination style of each strain can be observed in Figure 18 and Movies 1-3. Firstly, the strains were found to vary in spore size and shape. For *R. irregularis* MUCL 41833, a diameter on the order of 10-100 μm, for *R. irregularis* MUCL 43194 20-160 μm and for *R. intraradices* MUCL 49410 20-120 μm was measured (Figure 17). To show the irregularity in shape, both the smaller and the bigger diameter of a spore were measured and represented as a histogram. The smaller and bigger diameter of a spore were measured perpendicular to one another. This resulted in nearly congruent curves for *R. irregularis* MUCL 41833 and *R. intraradices* MUCL 49410 with a smaller diameter of 55 μm and a bigger diameter of 58 μm as well as a smaller diameter of 73 μm and 77 μm, respectively (Figure 17). This is contrasted by a clear shift between smaller and bigger diameter of the spores for *R. irregularis* MUCL 43194, with a mean of 73 μm and 90 μm, respectively. Spores of *Gi. margarita* BEG 34 came in diameters from 390 μm to 580 μm averaging around 470 μm. For all 4 strains, a statistical difference between the means of smaller and bigger diameter was found.

Visually, this meant a nearly perfect circular shape for *R. irregularis* MUCL 41833 and *R. intraradices* MUCL 49410 (Figure 18a,c), while *R. irregularis* MUCL 43194 spores were observed with a variety of elongated shapes in our study (Figure 18b). Secondly, distinct germination patterns were observed between the different strains. On one hand, *R. irregularis*

MUCL 41833 was generally found to germinate with a single hyphal branch, occasionally up to 4. Subsequent hyphal growth was found to be relatively linear and straight (Figure 18a). As shown in Figure 18b, *R. irregularis* MUCL 43194 spores contrast this observation by germinating typically with more hyphae emerging from the germination site (i.e., with usually 3-8 hyphae) or branching off with several ramifications very shortly after the initial site of germination. Overall, these hyphae grow in a rather curly and highly branched manner, not only during and the first hours succeeding germination, but also throughout their exploration. On plate, after about a month, a highly dense, curly network of hyphae formed around the spore with occasional runner hyphae growing out, exploring far into the plate, can be found. A very similar germination style was observed with *R. intraradices* MUCL 49410, germinating with 3-6 hyphal branches on average (Figure 18c). Interestingly, in several instances, an active discharge of phase bright cellular material could be observed to precede germination (Figure 18 and Movie 2).

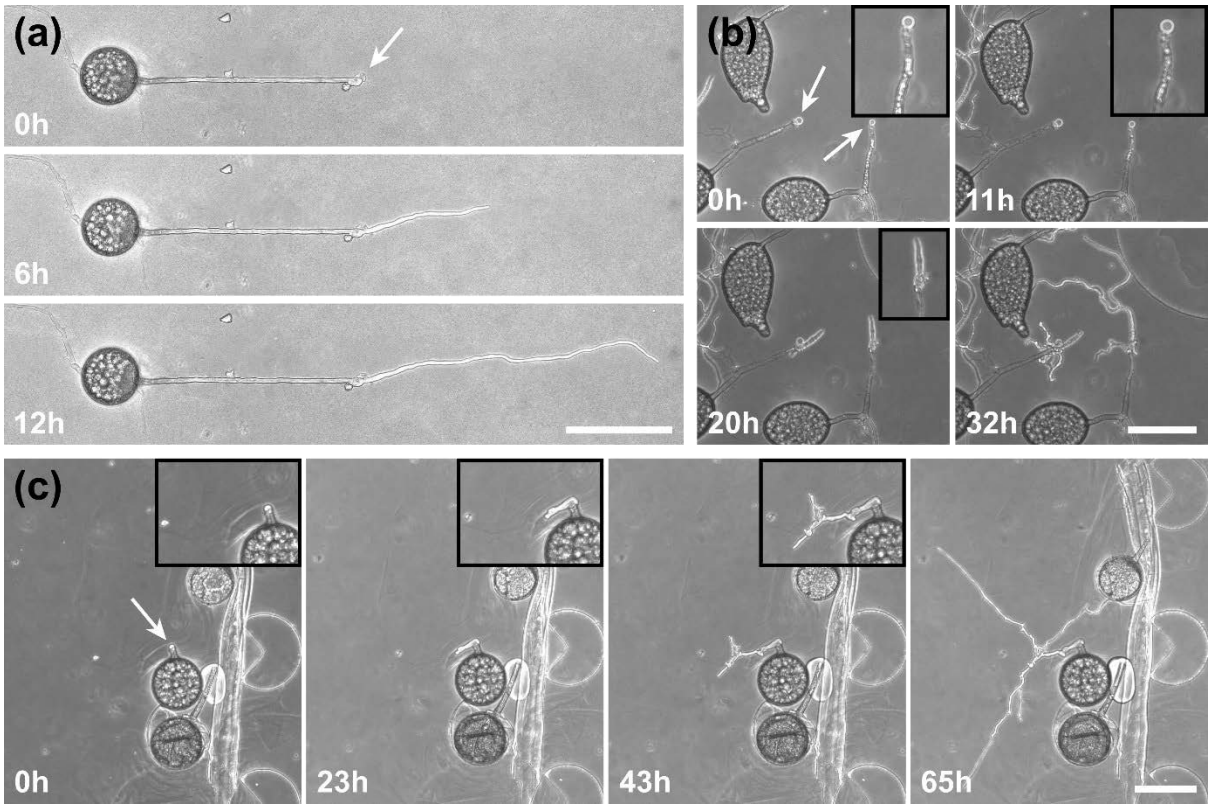
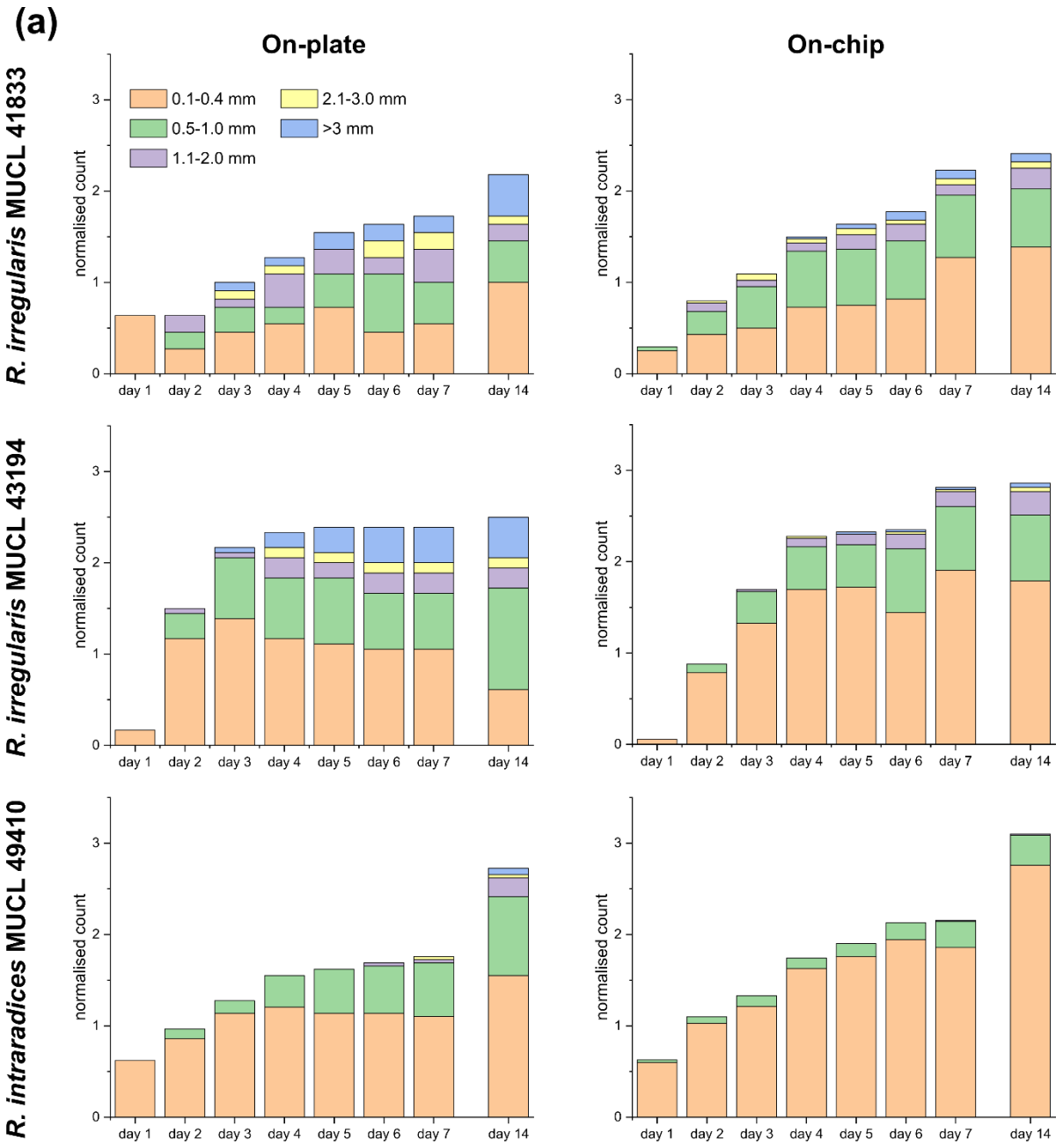


Figure 18: Germination of 3 *Rhizophagus* strains in the *AMF-SporeChip*. The images show the germination process of (a) *Rhizophagus irregularis* MUCL 41833, (b) *Rhizophagus irregularis* MUCL 43194 and (c) *Rhizophagus intraradices* MUCL 49410 in time series. In (c), remains from the root organ culture can be spotted. White arrows highlight the germination site. Inset boxes in (b) and (c) show an enlarged region of the germination event. Note the discharge of cellular contents in (b) preceding

germination. Scale bars: 100 µm. Images reproduced from Richter *et al.* (2024) with permission from the Creative Commons Attribution license (www.creativecommons.org/licenses/by/4.0/).

For the quantitative analysis of germination and growth behaviour and to compare on-chip with off-chip (on-plate), timepoint images of the three *Rhizophagus* strains were taken and hyphal length measured as described in *2.3 Microscopy and image processing*. The results, represented as stacked column charts, can be observed in Figure 19a. For *R. irregularis* MUCL 41833 on-chip, the column chart shows a constant increase of the orange-coloured bar segments, representing freshly grown hyphae with a length of 0.1-0.4 mm. Along with a considerably constant increase in the green segment (0.5-1.0 mm) over the first couple of days, this corroborates the qualitative findings in the timelapse studies described above (Figure 18), where only one or few germination branches formed, followed by considerably constant and linear hyphal growth. It further tells that the different germination sites or spores have very different pre-germination lag phases and fresh germinations appear constantly over the entire experimental period up to 14 days post inoculation. Few hyphae transition through 0.5-1.0 mm (blue) into the purple and yellow length category (1.1-3.0 mm) or grow even longer to a length of 3 mm or more (blue). For *R. irregularis* MUCL 43194 again the different germination and growth behaviour is salient. Over the first few days a rapid increase of the orange segments and total column height can be observed, indicating the emergence of many new hyphae from germination sites, without much growth beyond 0.4 mm. This surge plateaus on day 4 and an increased hyphal growth beyond 0.5 mm and occasionally up to more than 3 mm begins, reaching similar levels as *R. irregularis* MUCL 41833 towards the end of the experiment. Interestingly, in both *R. irregularis* MUCL 41833 *R. irregularis* MUCL 43194, a sudden rise in new germinations occurred on day 7 of the experiment. With *R. intraradices* MUCL 49410, a constant strong increase in the number of hyphae can be observed. The overall column height seems to plateau after 7 days, however, the immense number of hyphae after 14 days indicates that germination was continued, nearly matching a hypothetical extrapolation conducted from the slope of the first few days. Only few hyphae grew further than 0.4 mm, only one instance of a hyphal length in the purple segment (1.1-2.0 mm) and none longer than 2 mm was observed. This result is in line with the timelapse recordings, showing high levels of germination branches and thus a high total number of hyphae relative to germination sites. For

a more detailed view on the two aspects represented in the graphs, the development of the number of hyphae as well as the average hyphal length were extracted for days 2, 5 and 14 and plotted separately in Figure 19b. To account for the uneven number of spores/germination sites for the different strains, the total number of hyphae was again normalised by dividing by the number of germination sites. The analysis of the average hyphal length highlights the strong variability, especially for the two *R. irregularis* strains and on-plate. This variability was mostly expected and represent the inherent asymmetry of the growth of these fungi, known to form both small, branched hyphae as well as long runner hyphae. This also explains why only few comparisons showed a significant difference. Significant differences were only tested for between results with 2 common parameters, e.g., same strain and same day but different experimental platform, same platform and strain but different day or same platform and day but different strain. The *R. intraradices* showed hardly any hyphal elongation of their comparably numerous hyphae.


(a)
On-plate
On-chip
0.1-0.4 mm
0.5-1.0 mm
1.1-2.0 mm
2.1-3.0 mm
>3 mm
normalised count
day 1
day 2
day 3
day 4
day 5
day 6
day 7
day 14
R. irregularis MUCL 41833
R. irregularis MUCL 43194
R. intraradices MUCL 49410

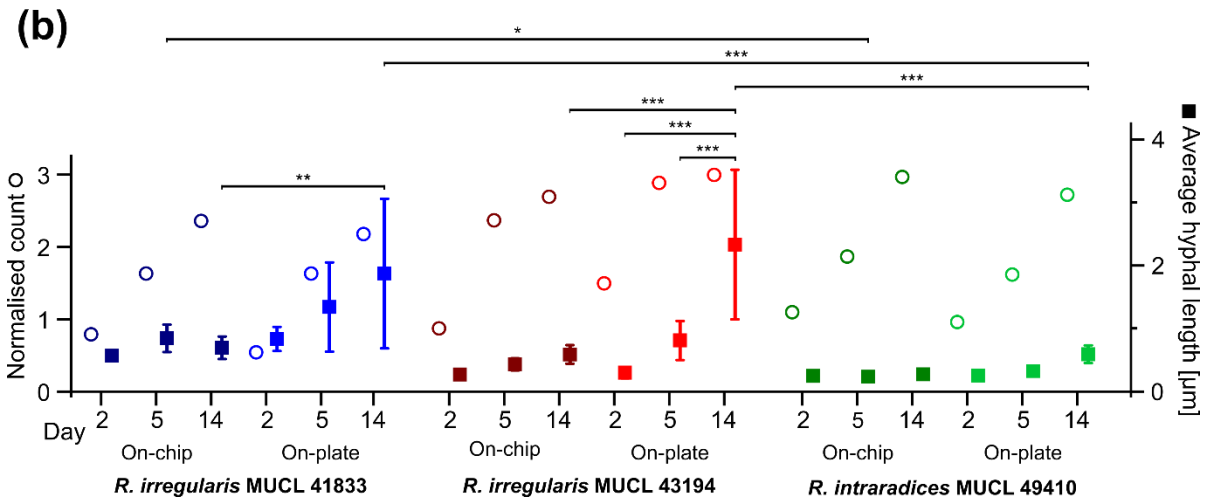

(b)
Normalised count
Average hyphal length [µm]
Day
On-chip
On-plate
R. irregularis MUCL 41833
R. irregularis MUCL 43194
R. intraradices MUCL 49410

Figure 19: Fungal growth assays comparing on-chip and on-plate. (a) The growth behaviour of *Rhizophagus irregularis* MUCL 41833, *Rhizophagus irregularis* MUCL 43194 and *Rhizophagus intraradices* MUCL 49410 in the *AMF-SporeChip* on plates containing MSR(-) medium is represented as stacked column graphs. The hyphal lengths were measured using Fiji/ImageJ, normalised (number of germination sites was determined, and the absolute value of counts divided by the number of germination sites) and categorised in 5 length sections (different colours). (b) Focussed analysis of hyphae number (left Y-axis; circle) and average hyphal length (right Y-axis; square) for day 2, 5 and 14. Normalised count represents the total number of hyphae divided by the number of germination sites. Average hyphal length is presented as the mean with confidence interval (95 %). Significant differences according to one-way ANOVA followed by Tukey test are indicated with asterisks for p values <0.001 (***), <0.01(**) and <0.05 (*). Significant differences were only tested for between results with 2 common parameters, e.g., same strain and same day but different experimental platform, same platform and strain but different day or same platform and day but different strain. Only significant differences are shown, all other comparisons did not reveal any difference. As germination site, any site with an occurrence of a germination/fresh hypha within the 14 days of the experiment was counted. In total, 6 devices with 40–60 germination sites per strain and 10–20 germination sites were found per plate. Images and figure legend reproduced with modifications from Richter *et al.* (2024) with permission from the Creative Commons Attribution license (www.creativecommons.org/licenses/by/4.0/).

Besides these interesting observations made possible with the *AMF-SporeChip,* comparing the different germination and growth behaviour with the traditional on-plate experiment is of higher importance, as only generic conclusions can be drawn if the device does not alter the fungi's overall development. Even though the on-plate method generally resulted in fewer but much longer, faster growing hyphae (i.e. larger purple, yellow and blue column segments in the graphs, Figure 19), with lengths of up to 20 mm, the overall trends observed and described above particular to the different strains, reflecting the manner of germination and hyphal growth are very similar and comparable between on-plate and on-chip, especially with the observed trend of hyphal numbers (Figure 19b, circles), i.e., an almost linear increase for strain MUCL 41833, a steep increase between day 2 and 5 and then flattening out of the curve for strain MUCL 43194 as well as a firstly flat increase followed by a steep increase between day 5 and 14 for strain MUCL 49410. The much higher growth intensity on-plate could be explained with the different immediate environment hyphae encounter, i.e., full submersion in culture medium within the microchannels in contrast to a tripartite environment on plate with a solid phytagel base, liquid film on top and direct contact with air surrounding the fungi as well as more available space (confinement is generally suspected to reduce overall growth (Baranger *et al.*, 2020)). Filamentous fungi are known to be able to sense the confinement and adapt their growth accordingly due to mechanosensory properties (Kumamoto, 2008). This not only happens on a mechanical level, i.e., upon direct contact with the wall or the obstacle, but also

on a chemical level, where the surface functionalisation is recognised by the fungus (Held *et al.*, 2011b). Comparing the development between day 7 and day 14, only few hyphae elongating and germination events could be observed on-chip for *R. irregularis* MUCL 41833 (ratio of normalised count for day 14/7 = 1.082), while on-plate there was further growth and new germinations (ratio of normalised count for day 14/7 = 1.263). For *R. irregularis* MUCL 43194, there were hardly any further germination events nor hyphal elongation occurred, equally on-chip and on-plate (on-chip ratio of normalised count for day 14/7 = 1.017; on-plate ratio of normalised count for day 14/7 = 1.047). For *R. intraradices* MUCL 49410, the clear development towards significantly more fresh germination events observed after 7 days on-chip, was evenly matched by the on-plate experiments (on-chip ratio of normalised count for day 14/7 = 1.437; on-plate ratio of normalised count for day 14/7 = 1.549). Unlike on-chip, some hyphae were found to elongate further after 7 days on-plate, reaching the purple, yellow and blue length category (>3 mm).

As another important indicator of vitality, the germination rates for the three fungi were determined and are shown in Figure 20. Here, a different definition of germination rate was applied (as described in *2.3 Microscopy and image processing*), counting any site that a germination usually is to be expected from (i.e. cut ends of hyphal remnants). These can only be spotted with enough focus and resolution, which the microfluidic device provides through confinement. Ungerminated germination sites could not be detected with certainty on-plate, which highlights an advantage of the *AMF-SporeChip*. The calculated spore germination rates were high for all three strains (no statistical differences detected). The means resulted to be 91 % (*R. irregularis* MUCL 41833), 88 % (*R. irregularis* MUCL 43194) and 93 % (*R. intraradices* MUCL 49410). Overall, this indicates that despite no flow is applied to the devices, the fungi are supplied with sufficient nutrients through diffusion from the reservoirs in- and outlets, as well as no detrimental strain resulting from the spatial confinement and trapping between PDMS and glass was exerted.

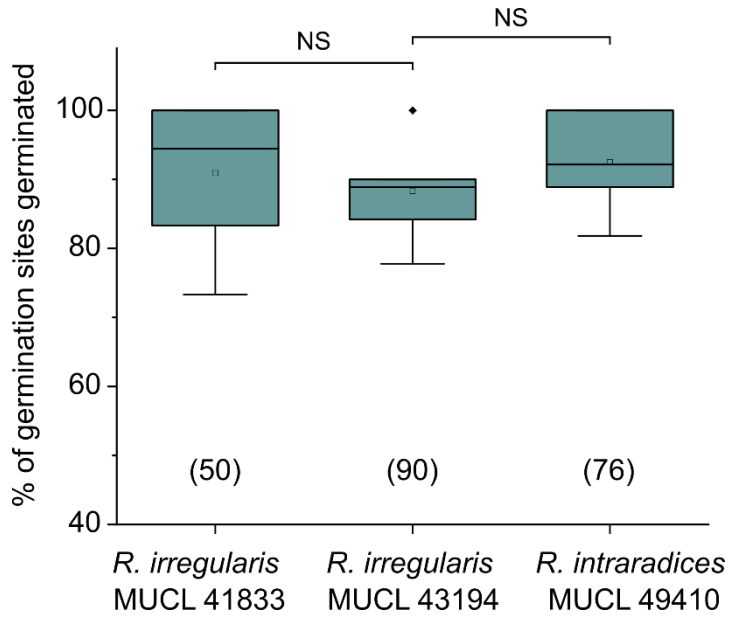


Figure 20: Germination rates of the three *Rhizophagus* strains in the *AMF-SporeChip*. The germination rates are represented as box-plots. To calculate the germination rates, again germination sites instead of spores were used (total number in parentheses below the boxes). Here, however, any site where normally a germination occurs from, i.e., cut ends of subtending hyphae, was counted as a germination site. The upper and lower whiskers in the box-plot represent the largest observation smaller or equal to the upper and lower percentile plus 1.5 × interquartile range, respectively. Squares indicate the means and the line the median. Data points beyond the whisker range (outliers) are plotted as diamonds. No significant differences between the results according to one-way ANOVA followed by Tukey test were found. Images and figure legend reproduced with modifications from Richter *et al.* (2024) with permission from the Creative Commons Attribution license (www.creativecommons.org/licenses/by/4.0/).

Along with this series of experiments, a side experiment was conducted, aiming to determine effects of a plant root exudate medium and to potentially accelerate and enhance spore germination and hyphal growth. In general, root exudates are commonly collected from hydroponic cultures, hybrid systems where a soil culture is transferred into a hydroponic culture for the exudate collection or small exudation traps directly attached to roots (Oburger and Jones, 2018). These setups always feature entire plants. Specifically for AMF, few attempts of obtaining root exudate medium directly from a root organ culture have been conducted. Bécard and Piché (1989), for example, grew carrot roots on agar medium covered with a membrane for 2 weeks, which later helped cleanly removing the roots from the medium without causing damage to the roots. Then, a spore of *Gi. margarita* was placed directly on the agar medium and germinated, however, no effect on the growth was observed. The composition of the exudate medium was not tested.

In order to obtain a simple “root exudate medium” for germination experiments in our microfluidic devices, roots where cautiously removed from a month-old chicory root culture (see *2.2.3 Chicory root culture*), so that only the phytagel medium remained behind. Care was taken so that the roots did not rip or harm in any way as damage on the roots might alter the exudate composition by either releasing other cellular contents or triggering a stress response in the root potentially leading to altering the signal conveyed by the exudates to “warn off” mycorrhizal fungi. The latter has never been demonstrated. It has been shown, however, that the composition of the root exudates is influenced by both biotic and abiotic factors. A phosphorus deficiency, for instance, triggers an increase in strigolactones exudation in clover in order to attract AMF (Yoneyama *et al.*, 2007). Similarly, the exudation was shown to change after successful establishment of the symbiosis (Ma *et al.*, 2022). The phytagel medium without the roots was then “liquified” by stirring with a magnetic stirrer and used to introduce *Rhizophagus* spores (MUCL 41833 and MUCL 43194) into the devices with a syringe as described in *3.2.1.3 Spore isolation and introduction into the device*. Although the exudate medium was still highly viscous and much resistance was met when flushing in the spores, the spores were introduced without problems. The devices were then incubated at 27 °C and monitored daily as described above along with the main germination experiment. The results are represented as stacked column charts in Figure 21. For a better comparison, the graphs from the above shown on-chip experiments (Figure 19) were put next to the exudate results.

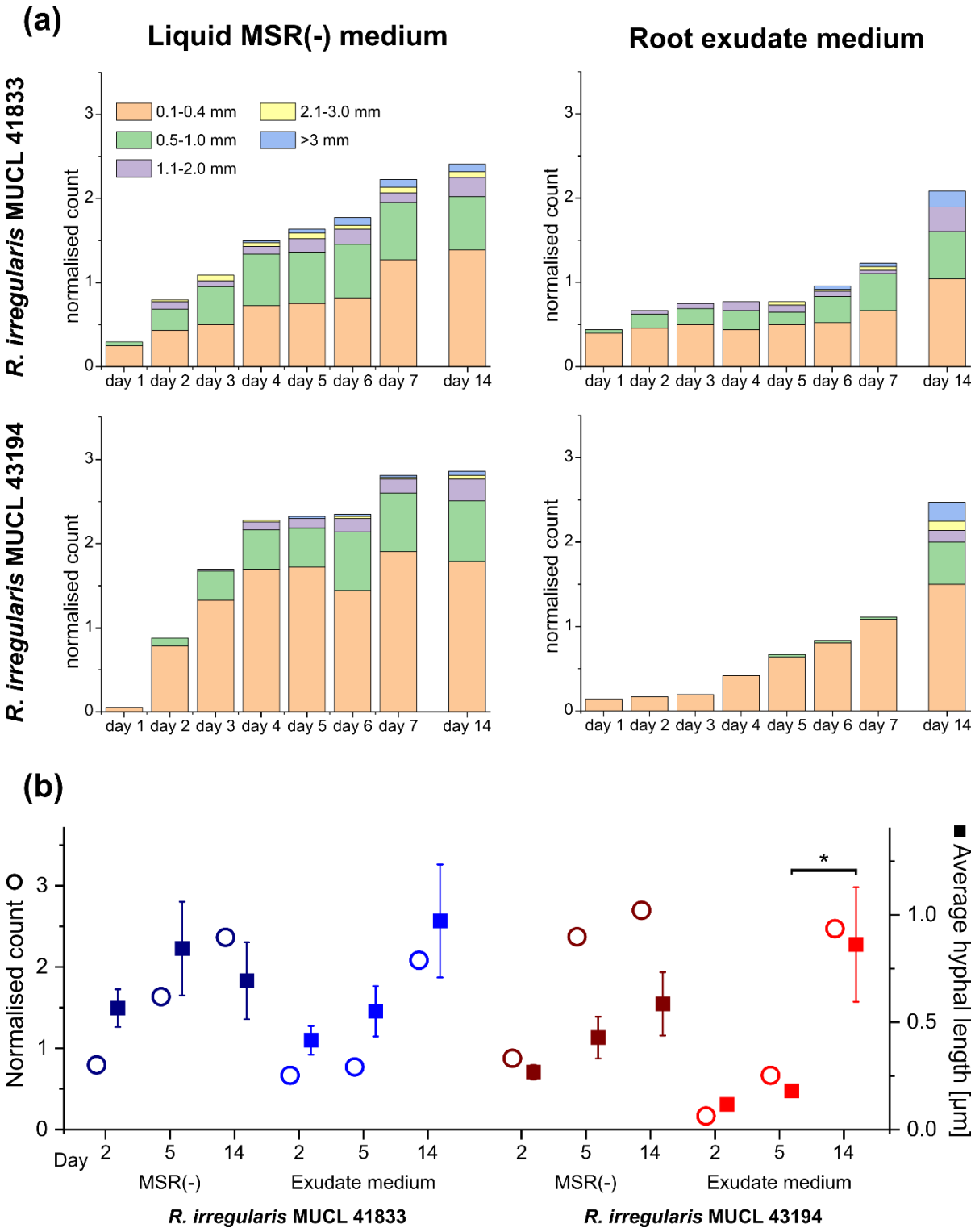


Figure 21: Fungal growth assays comparing two different media on-chip. (a) The growth behaviour of *Rhizophagus irregularis* MUCL 41833 and *Rhizophagus irregularis* MUCL 43194 in the *AMF-SporeChip* containing either liquid MSR(-) or root exudate medium is represented as stacked column graphs. The hyphal lengths were measured using Fiji/ImageJ, normalised (number of germination sites was determined, and the absolute value of counts divided by the number of germination sites) and categorised in 5 length sections (different colours). (b) Focussed analysis of hyphae number (left Y-axis; circle) and average hyphal length (right Y-axis; square) for day 2, 5 and 14. Normalised count represents the total number of hyphae divided by the number of germination sites. Average hyphal

length is presented as the mean with confidence interval (95 %). Significant differences according to one-way ANOVA followed by Tukey test are indicated with asterisks for p values <0.001 (***), <0.01(**) and <0.05 (*). Significant differences were only tested for between results with 2 common parameters, e.g., same strain and same day but different experimental platform, same platform and strain but different day or same platform and day but different strain. Only one significant difference is shown, all other comparisons did not reveal any difference. As germination site, any site with an occurrence of a germination/fresh hypha within the 14 days of the experiment was counted. In total, 6 devices with 40–60 germination sites per strain were analysed for the experiment. Parts of the images and figure legend reproduced with modifications from Richter *et al.* (2024) with permission from the Creative Commons Attribution license (www.creativecommons.org/licenses/by/4.0/).

The graphs (Figure 21) show a very different trend in the germination and growth behaviour observed between spores inoculate in the regular liquid MSR(-) medium and the root exudate medium with two *Rhizophagus* strains. The graphs representing the exudate medium show a much flatter increase in hyphal numbers (overall column height) as well as hyphal growth (green, purple, yellow and blue proportion of the column indicating long hyphae) over the first few days compared to the fungi inoculated in liquid MSR(-) medium. The column heights then start to significantly increase after day 5 for *R. irregularis* MUCL 41833 with some rise in numbers of long hyphae and after day 3 for *R. irregularis* MUCL 43194 with no increase in long hyphae. This tendency of a strong early germination and production of many initially short hyphae for *R. irregularis* MUCL 43194 and a relatively consistent increase in both hyphal number and length for *R. irregularis* MUCL 41833 correlates with the observations made with the liquid MSR(-) medium. Intriguingly, the germination and growth surge picking up after 3 or 5 days, respectively, ultimately lead to almost the same column height in the root exudate medium as with the liquid MSR(-) medium after 14 days. While the total number of hyphae (total column height) was slightly lower, more than double the amount of very long hyphae, measuring 2.1 mm or more, was obtained with the exudate medium. Again, for a more detailed view on the two aspects represented in the graphs, the development of the number of hyphae as well as the average hyphal length were extracted for days 2, 5 and 14 and plotted separately in Figure 21b. The graphs emphasise the initial lag-phase observed with the exudate medium for both strains and for both number of hyphae as well as average hyphal length. The plot further revealed a considerably higher average hyphal length after 14 days obtained with the exudate medium compared to regular liquid MSR(-) medium for both strains but especially for *R. irregularis* MUCL 43194. To account for the uneven number of spores/germination sites for

the different strains, the total number of hyphae was again normalised by dividing by the number of germination sites. The analysis of the average hyphal length highlights the strong variability of these fungi, observed before (e.g. Figure 19). This lead again to an overall low statistical difference, with only one comparison showing a significant difference. Significant differences were only tested for between results with 2 common parameters, e.g., same strain and same day but different experimental platform, same platform and strain but different day or same platform and day but different strain.

Even though the hoped for significant improvement in germination and hyphal growth was not achieved with the root exudate medium, the obtained results indicating some sort of initial lag-phase followed by a belated but relatively strong growth leading to a similar outcome of the experiment after 14 days, were quite interesting. Whether this strange behaviour was indeed caused by root exudates or not is hard to determine. Moreover, it remains unclear whether the medium obtained from the root organ cultures did contain AMF specific exudates and to which extent. Moreover, measuring the pH revealed a value of 5 instead of the 7 which the liquid MSR(-) is adjusted to, as well as a considerably strong variation from culture plate to culture plate with pH values of 5.4 or 6.3 measured. Similarly, the high viscosity of the exudate medium could have had an effect on the fungi. This could be tested simply by preparing solid MSR(-) medium and liquifying it in the same manner as the exudate medium. As this side experiment was only meant to search for a possible germination and growth improvement, it was refrained from setting up another experiment to follow up on this.

Introduction of *Gi. margarita* into the device

Later, experiments were extended beyond *Rhizophagus* and it was shown that spores of *Gi. margarita* are able to germinate inside of the devices. While germination in *Rhizophagus* was observed to originate from the hyphal remnants attached to the spore, Gigaspora germinates from the circular spore body directly, forming germ tubes (as discussed in *Stages of arbuscular mycorrhiza development*). Hyphae were found to grow into the investigation zone and encountered obstacles, like the dead-end lane shown in Figure 22 and Movie 4. The hypha grew into the lane and when hitting the dead-end it bent and tracked the channel wall back in

direction of the inlet. The hypha then branched off three times, ca. 350 µm, 720 µm and 1280 µm downstream from the hyphal tip. All hyphae, i.e., leading hyphae and branches, then arrested growth and started retracting the cytoplasm in a gradual manner, as described before with *Rhizophagus*, forming very noticeable septa.

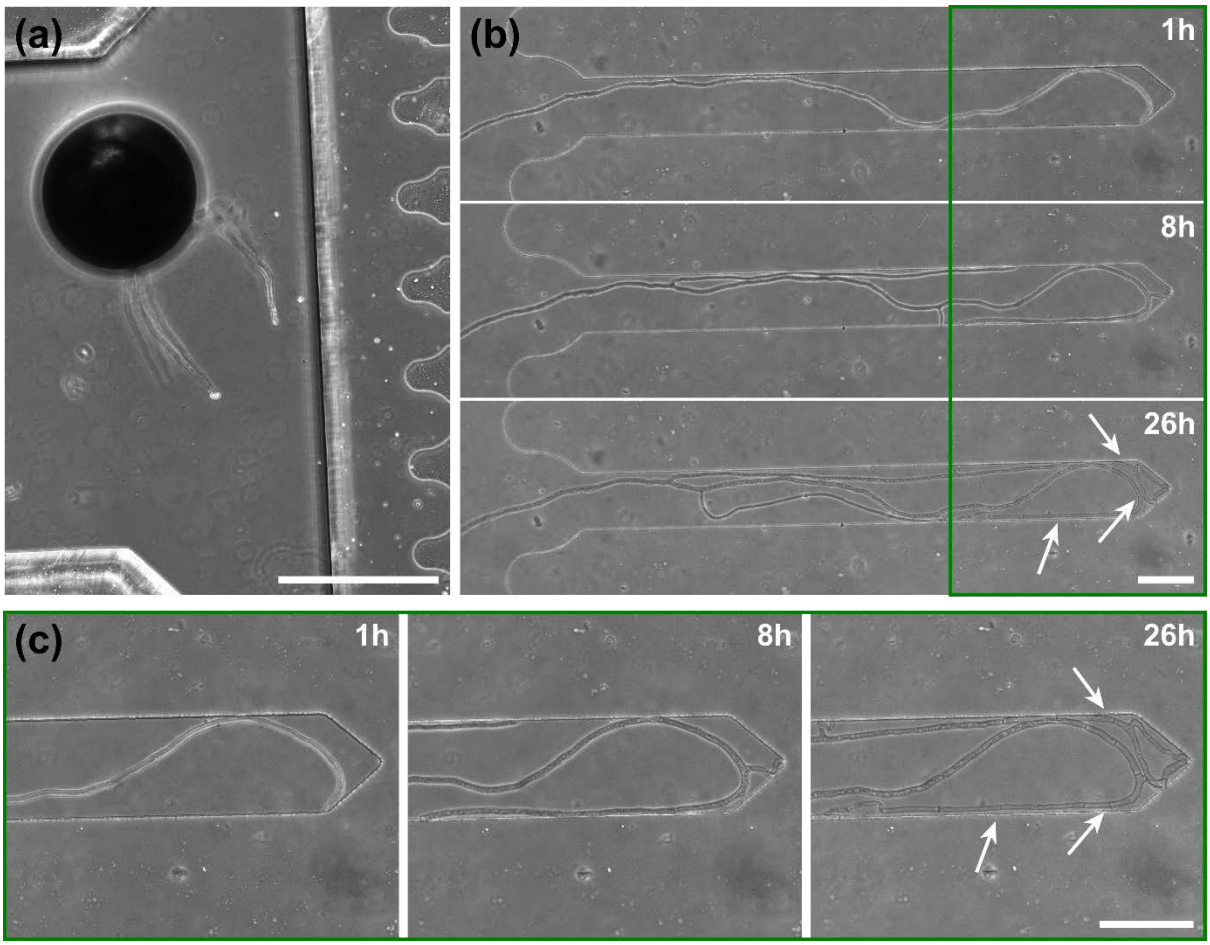


Figure 22: *Gigaspora margarita* growing in the *AMF-SporeChip*. Phase contrast images of (a) a spore of trapped in the inlet and (b) a time series of hypha growing into dead-end channels. Upon collision with the wall, the hypha bends and branches off in multiple positions, while gradually retracting cytoplasm involving septa formation. (c) Enlarged image sections of the dead-end of the microchannel. Image (a) was taken 2 days before the start of the timelapse series in (b). White arrows indicate examples of septa. Scale bars: (a) 500 µm, (b) and (c) 100 µm. Image and figure legend reproduced with modifications from Richter *et al.* (2024) with permission from the Creative Commons Attribution license (www.creativecommons.org/licenses/by/4.0/).

As the total number of *Gi. margarita* spores studied in the device was less than 10, no statistical analysis or comparison for patterns was possible. The low number of spores available for experiments was due to the origin of spores. These spores cannot yet be cultured *in vitro* and are grown in pot cultures at UC Louvain, Belgium (see *2.2.1 Root organ and pot cultures*). As

the conditions in these cultures are far from sterile, harvested spores had to be disinfected before shipping. This process could induce germination and, along with the shipping time, this caused the spores to arrive already germinated. Indeed, it was found that when removing the hyphae from the spore and inoculating the spore in a device, fresh germination occured from the spore body. In order to inoculate ungerminated spores, it was tested to ship spores without prior disinfection steps. As feared, about 90 % of the spores arrived highly contaminated, but ungerminated, leaving about 3-4 spores for experiments. After, experiments with Gigaspora were put on hold and the focus placed onto the *Rhizophagus* spp.

3.3 Chapter conclusion

In this chapter, the development of the *AMF-SporeChip* was described and discussed. This included design of the device to fulfil its requirements for spore inoculation, confronting hyphae with physical obstacles and high-resolution microscopy, optimising the lithography process for the device manufacturing as well as characterising the device for its loading performance and biocompatibility. The design was modified several times to improve loading flow through the device and efficiency and versatility of the challenge imposed by the obstacles. The lithography used for manufacturing the master moulds for the devices posed problematic and required multiple rounds of optimisation until a well-functioning and reliable protocol was established. These necessary modifications concerned almost every step of the manufacturing protocol, including UV exposure and development, however major problems had to be tackled in the wafer pre-treatment and baking, which led to immensely uneven layers. The final device was eventually inoculated with spores from 3 *Rhizophagus* strains and germination and hyphal growth were monitored, showing a high germination rate of about 90 % for all strains. Furthermore, a qualitative, high-resolution timelapse microscopy revealed distinctive spore shapes as well as germination and growth patterns, which corroborated quantitative measurements. A comparison with the on-plate germination assay showed, despite the expected overall stronger growth on-plate, the same germination and growth patterns as on-chip for all 3 strains. Later, a modification of the device for studying *Gigaspora* spp. was developed and inoculation, germination and growth of the spores successfully shown. The final *AMF-SporeChip* fulfilled all requirements for the device and thus paved the way for novel studies on hyphal space exploration, detailed in Chapter 4.

CHAPTER 4: AMF SPACE SEARCHING

4.1 Chapter overview

In this chapter, the *AMF-SporeChip* was utilised to study space searching of asymbiotic hyphae of AMF. The *AMF-SporeChip* was specifically tailored and optimised to accommodate and immobilise *Rhizophagus* spores, have them germinate and to confront hyphae with physical obstacles, while allowing for a high-resolution imaging. We hypothesised that the obstacles implemented in our devices, designed to trigger collision events, would provoke similar responses in AMF asymbiotic hyphae as reported for AMF extraradical hyphae (Hammer *et al.*, 2024) as well as for other filamentous fungi (Held *et al.*, 2019; Hopke *et al.*, 2021; Aleklett *et al.*, 2021). To test this hypothesis, spores of the 3 strains *R. irregularis* MUCL 41833, *R. irregularis* MUCL 43194 and *R. intraradices* MUCL 49410 were introduced into the *AMF-SporeChip*, phase contrast timelapse series taken and several intriguing observations obtained. Firstly, general space navigation mechanisms in comparison to AMF extraradical hyphae and a Basidiomycete are described herein. In the course of these experiments, a new and previously undescribed phenomenon was discovered; as opposed to the common cytoplasmic retraction in fungal hyphae, a reversibility of this process was found, which happened both as an incomplete or complete reversal of the process, both in the presence of an obstacle as well as in open space. To characterise this observation further, a combination of two fluorescent dyes was introduced to AMF and the system. Later, the staining method was employed in an attempt to search for and study the Spitzenkörper, an intracellular body found in the tip of most filamentous fungi, which, however, has so far not been officially discovered and described for AMF. We hypothesised that AMF have Spitzenkörper, as it is an integral part of fungal anatomy, differing, however, in their architecture. With a staining approach combined with dynamic observation of space navigation it was expected to unravel evidence of the Spitzenkörper. The chapter concludes with a discussion of anastomoses observed in the *AMF-SporeChip*, the results of which have led to the development of a new microfluidic device to aid systematic studies of these hyphal fusion events, which will be detailed in Chapter 5. The majority of the results detailed in this chapter have been published in *Lab on a Chip* (Richter *et al.*, 2024).

4.2 Results and Discussion

4.2.1 Space searching in AMF

In their natural habitat, soil fungi, like AMF, encounter many obstacles, such as mineral particles, roots or other fungi, both dead or alive. Moreover, a seemingly trivial endeavour as prospecting for nutrients, has to be planned thoroughly in this heterogenous and patchy environment when available resources are limited. Filamentous fungi have developed several different strategies and mechanisms to manage these challenges they are confronted with. The studies discussed herein were mainly inspired by and compared to previous microfluidics-assisted work done with *N. crassa* (Held *et al.*, 2009b; Held *et al.*, 2011a; Held *et al.*, 2019). They confronted the Ascomycete model organism with mazes in microfluidic devices and characterised the different space manoeuvring strategies. Phenotypes described in their publications and therefore considered potential observations with AMF as well, were apical and lateral branching, tracking or nestling, as well as hit-and-split events. Lateral branching, i.e., formation of a hyphal ramification happening downstream from the tip, as a rather generic mechanism, was often observed in my studies. Regardless of the current surroundings, i.e., when in contact with an obstacle or in open space, hyphae branched off frequently to extend the fungi's exploration network. Tracking of obstacle shapes or walls was observed several times, while nestling, where the fungus comes in contact with a wall and continues growing alongside this shape clinging and maintaining full contact until the wall ends, as described for *N. crassa* (Figure 23b), was only observed once with AMF (Figure 26). Here, tracking mainly happened when a hypha hit a wall in a flat angle and while attempting to continue its growth in the same direction, through or past the obstacle, they pushed themselves along the wall, thus tracking it down until the obstacle ended, the hyphae changed direction or arrested growth (Figure 23a and Movie 5).

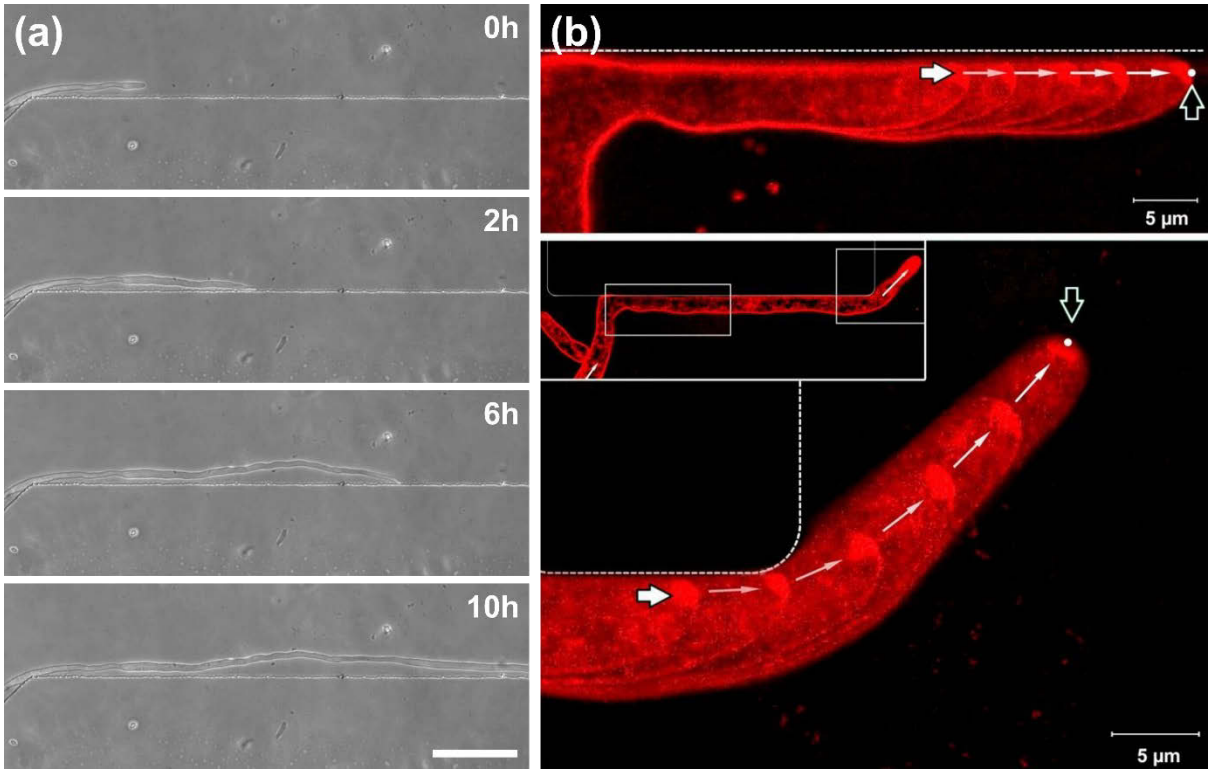


Figure 23: Comparison of nestling/tracking behaviour in hyphae of *Rhizophagus irregularis* and *Neurospora crassa*. (a) Time series of *R. irregularis* hypha tracking the wall of a microchannel over 10 h. (b) Fluorescent confocal image showing nestling of a hypha of *N. crassa* against a channel wall. Highlighted are the Spitzenkörper and the directional memory. Scale bar: (a) 50 µm. Images in (b) reproduced with modifications from Held *et al.* (2019) with permission from the Creative Commons Attribution licence (www.creativecommons.org/licenses/by/4.0/).

When hitting an obstacle head-on, *N. crassa* was described to respond frequently with a so-called hit-and-split. Upon impact, the hyphal tip gets compressed against the wall and bulges out into both directions along the wall before finally forming two new, independent daughter hyphae from these bulges (Figure 24b). This phenomenon was only observed one single time in my studies with AMF, in a hypha of *R. irregularis* MUCL 43194 (Figure 24a and Movie 6), and one could argue that the second daughter branch formed with a delay, meaning no true hit-and-split was observed.

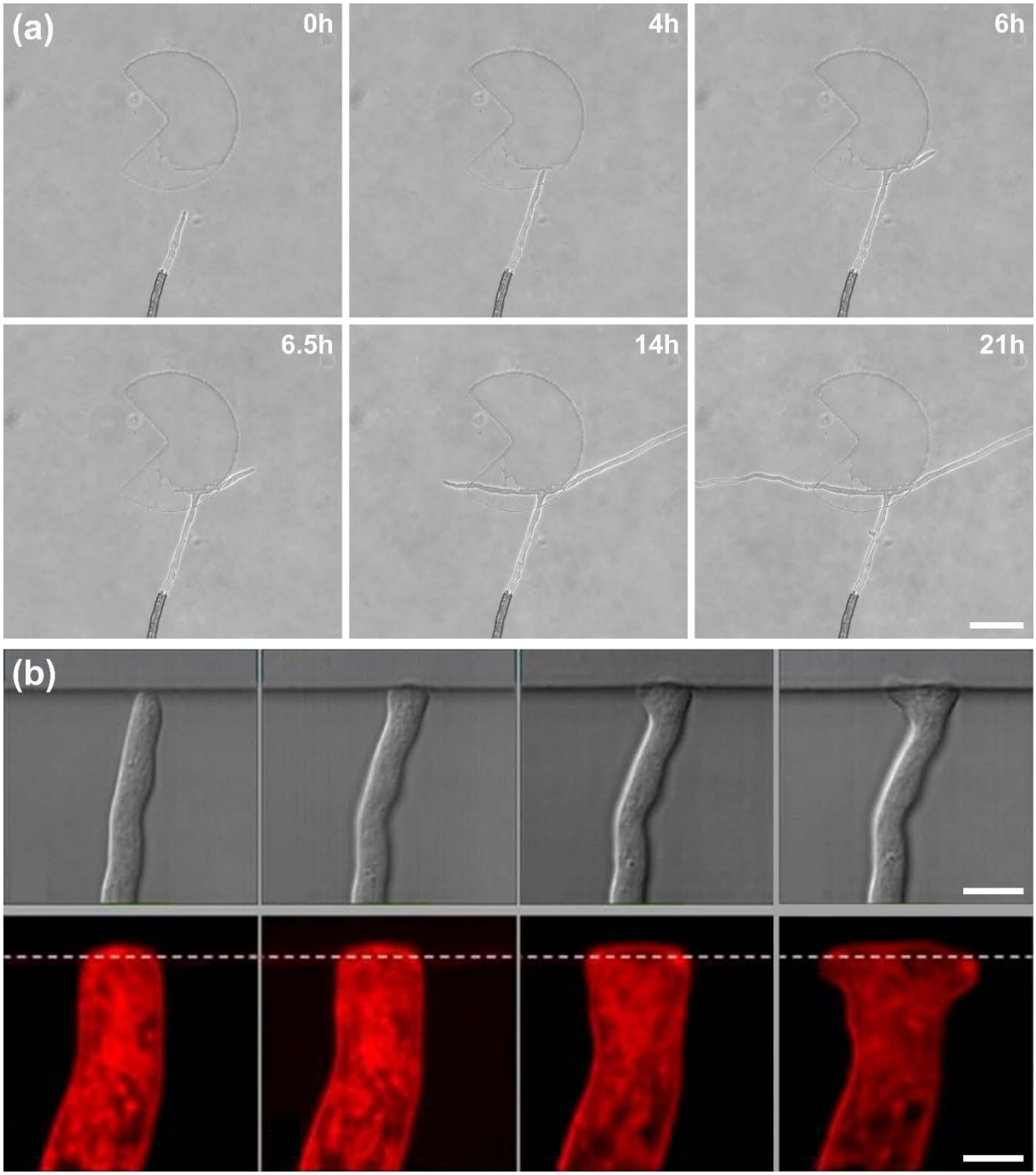


Figure 24: Comparison of hit-and-split behaviour in hyphae of *Rhizophagus irregularis* and *Neurospora crassa*. (a) Time series of *R. irregularis* hypha hitting an obstacle and branching semi-apically in response over the course of 21 h. (b) Bright field and fluorescent confocal image showing true hit and split of a hypha of *N. crassa* upon impact with a microchannel wall. The Spitzenkörper (bright red dot at tip) disappears and reappears in both daughter branches. Scale bars: (a) 50 µm; (b) 10 µm (top) and 5 µm (bottom). Images in (b) reproduced with modifications from Held *et al.* (2019) with permission from the Creative Commons Attribution licence (www.creativecommons.org/licenses/by/4.0/).

Apart from this one hit-and-split event, no true apical branching was observed in these studies on AMF. Apical branching, which can be observed regularly with *N. crassa*, both upon collision

or collision-free, involves a hyphal tip ramifying at the apex into two independent daughter hyphae. Instead, hyphae of the 3 *Rhizophagus* strains tested were predominantly found to stop growing when encountering impassable objects and retract cellular content from the apical parts of the hypha (e.g. Figure 25 and Figure 26 and Movie 7). This process of cytoplasmic retraction, which was also observed collision-free, occurs in a stepwise manner, each step marked by a formation of a septum, in these otherwise non-septate fungi, segregating emptied hyphal compartments from the rest of the hyphal network, which still contains cytoplasm and organelles. This phenomenon is very common and has often been described for filamentous fungi (Martínez-Camacho *et al.*, 2011) as well as AMF (Bago *et al.*, 1998; Kokkoris *et al.*, 2020). While no cytoplasmic retraction was reported for *N. crassa* and all the mechanisms described (Held *et al.*, 2019) point towards an overall strategy of attempting to outmanoeuvre the obstacles while maintaining growth direction, the observed results for AMF indicate the opposite, i.e., giving up on certain growth directions if found unfavourable and rather reusing and redistributing resources to new auspicious hyphae. Unlike *N. crassa*, which is a fast-growing saprophyte and thus equipped with virtually unlimited resources when grown on a rich medium, AMF are obligate symbionts. Requiring a suitable host root to complete their life cycle, AMF asymbiotic hyphae, feeding off of nutrients stored in the spore and only supplemented with minerals and vitamins from the medium, are crucially limited on resources. Finding a host as quickly as possible, while exhausting the least amount of reserves, is paramount for survival of these organisms. On a cellular level, differences between *N. crassa* and the *Rhizophagus* strains can be observed, too, providing an explanation for the different space navigating strategies and reactions to physical collisions. The underlying hypothesis for hyphal growth (Steinberg, 2007; Steinberg *et al.*, 2017), discusses three mechanisms: (i) the vesicle supply centre (where the Spitzenkörper regulates tip elongation and directional growth), (ii) steady-state (wall material, such as chitin is delivered to the apex in non-crystalline form, turgor extends the tip and crystallisation in the sub apex zone solidifies hypha) and (iii) the amoeboid model (Steinberg, 2007). It was observed that when a hit-and-split event occurs, both the Spitzenkörper and the microtubules disappear and only re-appear shortly after the branching is complete (Held *et al.*, 2019). In this stage, the growth mechanism seems to shift towards an amoeboid growth style until the hit-and-split branching is complete. In AMF, no Spitzenkörper has been reported, yet, suggesting a different mechanism of hyphal elongation. In the

experiments conducted for this thesis, AMF seemed to mostly maintain a rather rigid and sturdy hyphal texture. This sturdiness became obvious in the above-described tracking events (Figure 23) as well as when a hypha collided with a wall head-on but failed to retract its cytoplasm. In this case, hyphae kept growing as if not noticing the obstruction of its path or trying to break through and as no forward progress was possible, the hypha pushed itself away from the obstacle, while bending (Figure 25 and Movie 8 and 9).

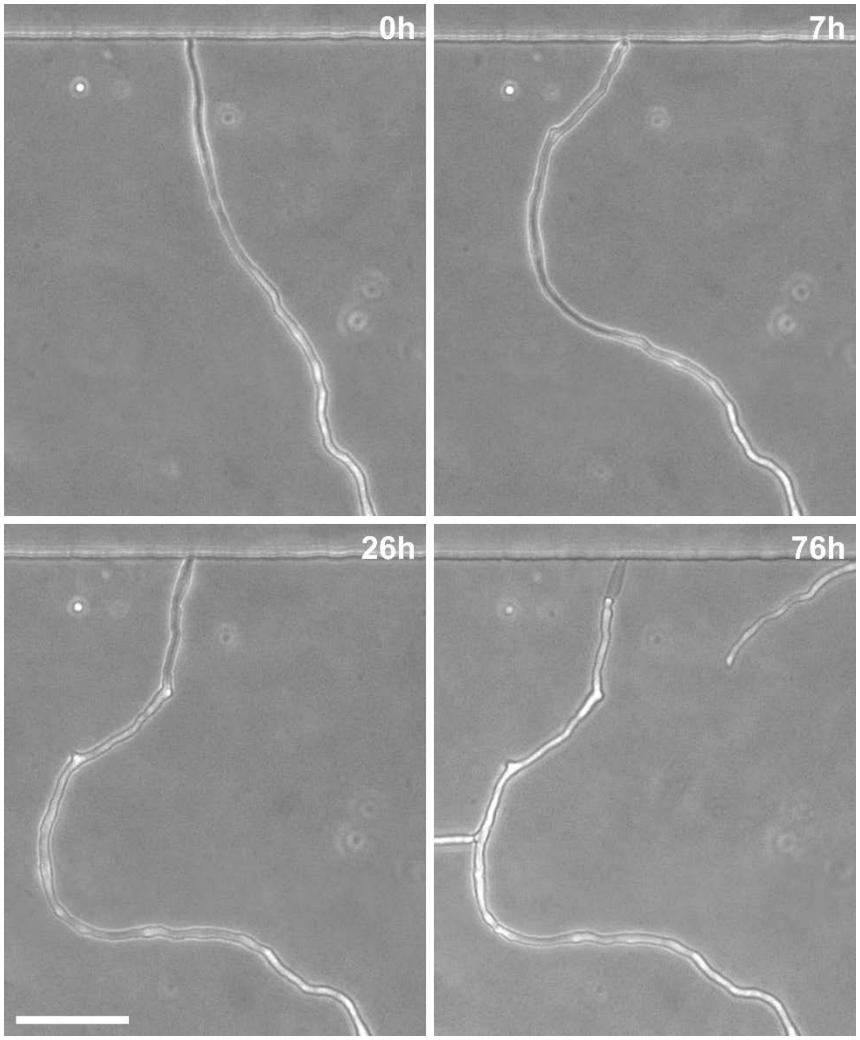


Figure 25: Head-on collision of *Rhizophagus irregularis* hypha with channel wall. Phase contrast time series over 76 h of a hypha of *R. irregularis* colliding perpendicularly with a microchannel wall. Note the cytoplasmic retraction seen after 76 h occurred in reality right after the image was taken after 26 h. Scale bar: 50 µm.

In a few odd instances, hyphae hit an obstacle or linger in the open space and virtually froze without bending nor withdrawing cytoplasm from the tip for 10s of hours until eventually retracting cytoplasm (Movie 10), while normally, growth arrest was followed by retraction within

a few hours. The retraction of cytoplasm was generally not only observed upon collision with obstacles but also frequently in open space. As the environment within the devices is expected to be homogenous regarding oxygen availability, which diffuses through the PDMS (McDonald and Whitesides, 2002) as well as nutrients, which are constantly replenished diffusively from the media reservoirs in inlet and outlet, the cytoplasmic retractions in open space are either caused by confinement within the microchannels of the device or some sort of randomised trial-and-error exploration strategy. Assuming the latter point to be the case, the AM fungus would send out hyphae in random directions and if no host root is found (or rather a gradient of signalling molecules that can then be actively followed to the root) or an impassable obstacle encountered, all cellular contents are withdrawn from this hypha and redistributed to a new hypha exploring another avenue.

On several occasions, spore formation in asymbiotic hyphae was observed (Movie 11). This phenomenon appears rather counterintuitive as spores are commonly formed in extraradical hyphae as a storage unit (mainly for lipids) and/or for reproductive purposes (see *Stages of mycorrhiza development*). As AMF at their asymbiotic stage solely feed off their original spore (and minerals from the medium or soil) and are hence strongly limited, both reasons seem implausible. Nevertheless, this has been reported before, vaguely attributing the observation to either a “survival process” or an aborted sporulation tentative (Dalpé *et al.*, 2005). Moreover, these spores have never been shown to germinate.

In a paper very recently published in *Fungal Ecology*, Hammer *et al.* (2024) present a similar study using a microfluidic device (called “*soil chip*”) for extraradical hyphae of *R. irregularis*. These hyphae’s task, growing directly from host roots, is to forage for nutrients and expand the network. An extraradical runner hypha has a diameter of 10-15 µm, which is about double the thickness of asymbiotic hyphae. These runner hyphae are in charge of exploration, while so-called branched adsorbing structures (BAS) (Bago *et al.*, 1998) are responsible for nutrient uptake. In their study, the group focussed on slightly different details of the fungi’s exploration behaviour, e.g. hyphae were forced to grow through tiny channels with different special orientations and bends, fitting only one hypha at a time. However, certain differences between asymbiotic and extraradical hyphae manifested in the results. The extraradical runner hyphae exploring the *soil chip*, were found to maintain a strong directionality, branching almost only

when forced to by an impassable obstacle, while the asymbiotic hyphae frequently changed growth direction and branched, both in open space and when encountering obstacles. As expected, the extraradical hyphae regularly formed spores, intriguingly even in the narrowest channels, leading to disfigured spore-esque organs.

Occasionally, towards the end of the experiments, an internal collapse and emptying of the spore can be witnessed appearing as if the storage vesicles are ejected suddenly in one final load of nutrients into the attached hyphae (Movie 12). A likely explanation for this is that the fungus slowly uses up the nutrients in the spore, mainly stored as lipids which also form the vesicles, to grow new hyphae to a point where the reduction of lipid content in the spore is threatening the stability and integrity of the vesicles, eventually leading to all of these vesicles collapsing in a chain reaction.

Moreover, adding to this versatile toolbox of exploration mechanisms and space navigating in AMF, a rather peculiar and previously undescribed phenomenon was found, which sees the cytoplasmic retraction process reversed.

4.2.2 Reversible cytoplasmic retraction

When analysing the timelapse images of the *Rhizophagus* hyphae interacting with the microenvironment, one observation in particular caught my attention. As shown in Figure 26 and Movie 13, a hypha of *R. irregularis* MUCL 41833 grew into a restricted open-box obstacle and hit the deep end corner, representing a dead end. As a result, the hypha halted growth and bent slightly. As observed and described before, the hypha responded by withdrawing cytoplasm from the trapped tip, forming a septum ca. 40 µm downstream from the hyphal tip to separate the empty segment from the rest of the vital hypha (that is filled), as if giving up on this growth direction. Then, however, the septum was breached and cytoplasm was reintroduced into the emptied segment, all the way up to the hyphal tip. Almost instantaneously, a new branch was formed, a few µm behind the tip, which then grew in direction of the opposite corner of the obstacle, tracking the obstacle wall closely.

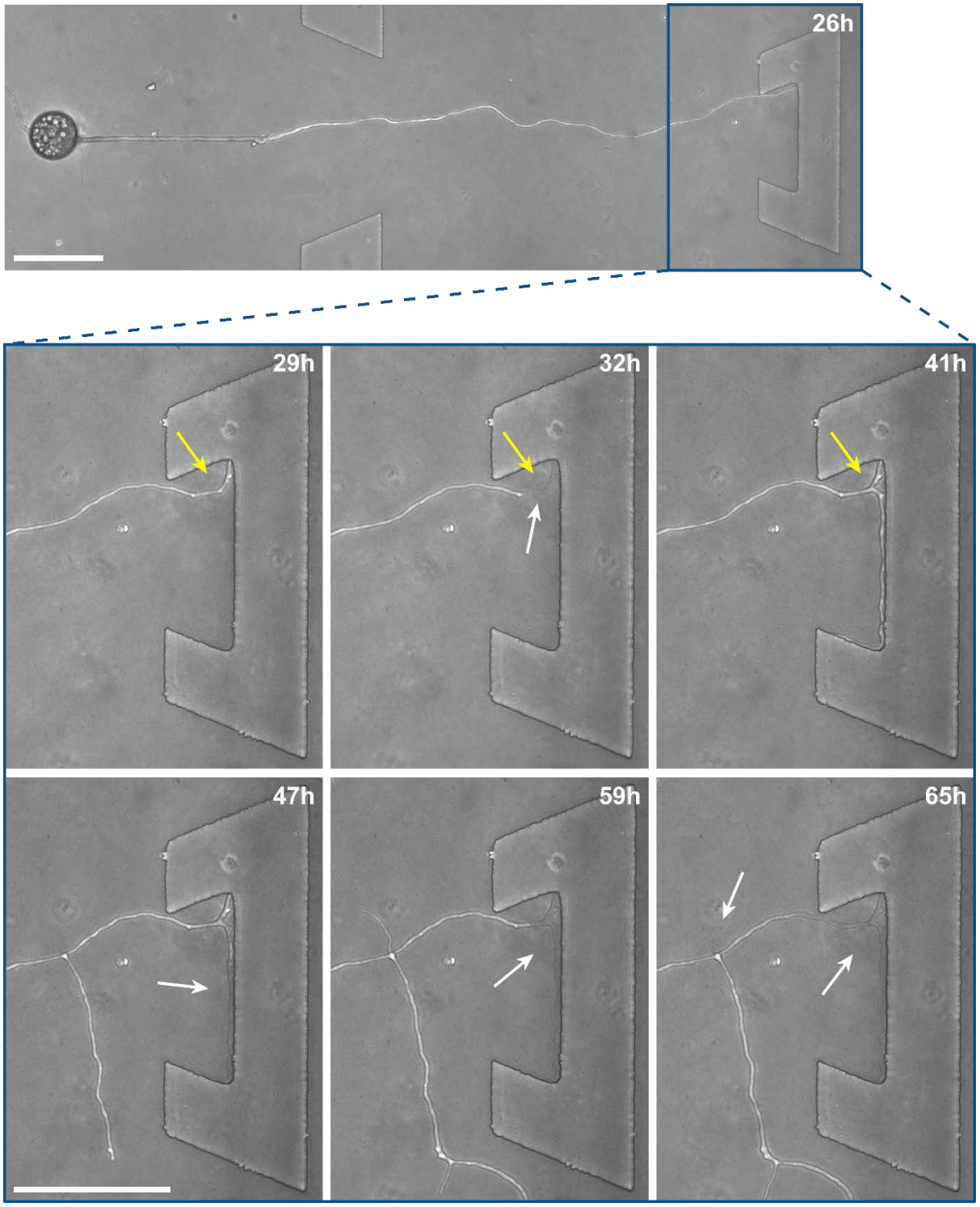


Figure 26: Reversible cytoplasmic retraction in the *AMF-SporeChip*. Phase contrast time series showing dynamic behaviour of a hypha of *Rhizophagus irregularis* MUCL 41833 upon impact with a micro-obstacle over 65 h. Timepoint 0 h marks the spore germination. The hypha enters the restricted open box obstacle and stops, followed by a series of dynamic, reversible cytoplasmic retraction and branching events. Yellow arrows highlight the “reversible” cytoplasmic retraction, white arrows indicate “empty” hyphae after cytoplasmic retraction. Scale bars: 100 µm. Image and figure legend reproduced with modifications from Richter *et al.* (2024) with permission from the Creative Commons Attribution license (www.creativecommons.org/licenses/by/4.0/).

Over the next few hours, the hypha kept following the wall even around the corner until it found itself facing its growth origin, the spore it germinated from. It stopped growing and retracted cytoplasm, forming two septa. This time the retraction was not reversed and the fungus formed a fresh branch well outside of the obstacle which then proceeded to grow past the obstacle over the following ca. 20 h. Having given up on fighting the obstacle, both hyphal branches inside the obstacle were being emptied entirely to reuse the resources to grow well around the obstacle. Similarly, another branch exactly opposite of the new hypha formed outside of the obstacle emerged but stopped soon after and cytoplasm was retracted. The vital hypha continued growing past the obstacle, forming a bifurcation after about 57 h after start of the timelapse series.

In a former study, a similar observation with extraradical mycelium on a root organ system was mentioned (Lee, 2011). This clear reversibility of the cytoplasmic retraction, however, has not been proven and described before. The mechanism could further aid these fungi to respond to the dynamic environment they are living in. Obstacles, which must be overcome, as well as suitable hosts AMF are attempting to find and associate with, are or can be living organisms that grow through soil and are hence subject to change. Therefore, the ability to re-explore avenues that have been explored before without success, can lead to success in a second attempt. Here, the already existing infrastructure, i.e., hyphal shell, can be easily harnessed and re-utilised and thus valuable resources and energy saved. While the opening and closing of septa in septate fungi such as Ascomycetes is a well-studied and common process, involving a so-called Woronin body functioning as a plug for septa pores that controls selective permeability through these septa (Bleichrodt *et al.*, 2015), septa opening in non-septate fungi like AMF, however, has not been thoroughly described to date. In AMF, septation is thought to be of a primarily defensive nature and not reversible. Lee (2011) suggested a complete removal of the septa when observing occasional migration of cytoplasm into emptied compartments of extraradical hyphae of *Rhizophagus*, however, mainly in a context of newly forming spores. It can be assumed that septa are broken down entirely, and when compartmentalisation is needed, newly formed.

Following this unexpected but intriguing finding, image material obtained in the space searching experiments, was closely re-analysed, in search of more instances of the reversible

retraction phenomenon. A total of 9 reversible retraction events were discovered (R1-R9), the majority occurring, other than in the initial finding, in open space (7 instances) rather than upon collision with an obstacle (2 instances). Reversible cytoplasmic retraction was found in both *R. irregularis* strains, i.e., *R. irregularis* MUCL 41833 (7 instances) and *R. irregularis* MUCL 43194 (2 instances) but not in *R. intraradices* MUCL 49410. Independent of whether the retraction occurred in open space or with an obstacle, the process varied significantly in all aspects, be it number of septa formed or breached, the ratio between septa formed and breached as well as temporal dynamics. Visual representations of the observations can be found in Figure 27. The maximum number of septa formed in a retraction process was 8, for the reversal either 1 or 2 septa were breached. In 5 instances, the observed number of septa formed/breached was the same, i.e., the retraction was reversed completely, in 4 instances, the number of formed septa was higher than breached septa, meaning that the reversal was incomplete and the cytoplasm was not pumped back all the way to the hyphal tip (Figure 27a). The retraction and reversal generally occured in a stepwise manner, septa formation marking the delimitation. Timings for the retraction steps, i.e., the time needed to fully retract the cytoplasm over the distance between tip and first septum or between septa, including complete formation of the septum, were ranging from as fast as 30 min to up to 10 h (Figure 27b). The reversal process was found to be less variable and ranged from 1 to 3 h per reversal step. Between retraction and initiating reversal, the fungi paused for at least 30 min. One instance of a 12 h pause between retraction and reversal was recorded. Generally, the hypha stops growing and then immediately initiates the cytoplasmic retraction. Occasionally, a lag-phase can be observed, where the fungus pauses for 1 to 3 h before finally retracting cytoplasm. To account for the variation in the distance between septa (or hyphal tip to first septum; average: 26.3 ± 11.8 µm) retraction and reversal rates, respectively, were calculated (Figure 27c). On average, the retraction rate was 0.4 ± 0.3 µm/min and the reversal rate 0.2 ± 0.1 µm/min. No statistically significant difference was found, also due to the low number of observations, however, a larger variation in the rate of retraction was observed.

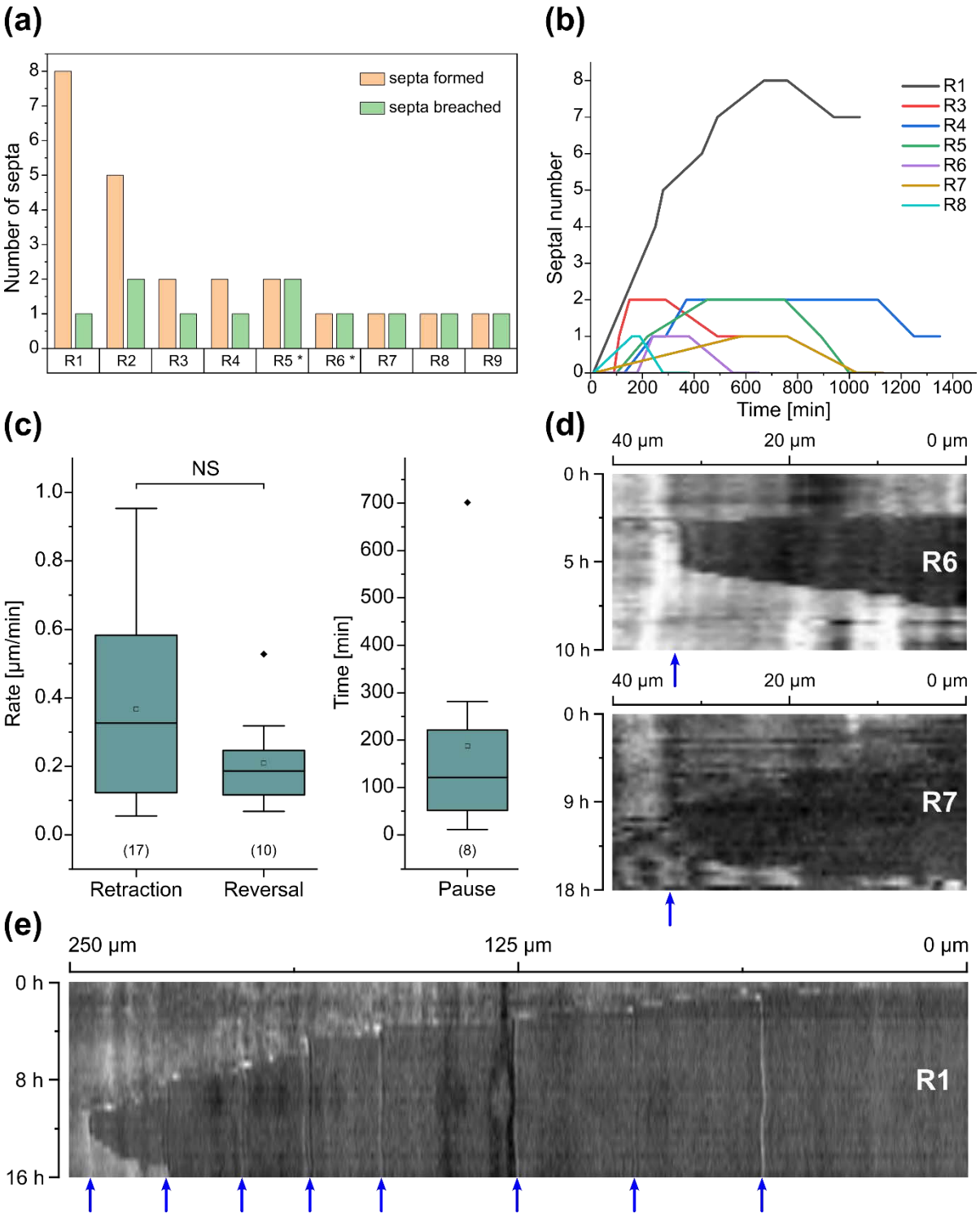


Figure 27: Quantitative analysis of reversible cytoplasmic retraction in the *AMF-SporeChip*. (a) Column graph displaying the number of septa formed and breached during complete and incomplete reversible cytoplasmic retraction (R). In two instances (marked with asterisks; R5 and R6) the retraction occurred upon collision with obstacles and in seven instances (R1–4 and R7–9) occurring in open space. (b) Line plot highlighting the temporal dynamics of the reversible retraction, including timings for cytoplasmic retraction, pausing and reversal of the retraction events shown in (a). For R2 and R9, no sufficient temporally resolved data could be extracted. (c) Box-plots extracting rates from (b) for cytoplasmic retraction and reversal as well as pause duration between retraction and reversal. Upper and lower whiskers represent the largest observation smaller or equal to the upper and lower percentile plus 1.5

× interquartile range, respectively. Squares indicate the means and the line the median. Data points beyond the whisker range (outliers) are plotted as diamonds. No significant difference between the rate of retraction and reversal according to one-way ANOVA was found, indicated as NS. The values in parentheses indicate the number of sample-points, i.e., the number of events analysed. (d) Kymograph illustrating retraction R6 and R7 and (e) kymograph of retraction R1. Blue arrows indicate septa. All retraction events were found with *Rhizophagus irregularis* MUCL 41833, except R3 and R9, which were found with *Rhizophagus irregularis* MUCL 43194. Images and figure legend reproduced with modifications from Richter *et al.* (2024) with permission from the Creative Commons Attribution license (www.creativecommons.org/licenses/by/4.0/).

For a more detailed visualisation of the process, kymographs for retraction events R1, R6 and R7 were constructed (Figure 27d,e), which were the only recordings suitable though representative of the different behaviours observed (one short retraction, two long retraction events in open space as well as with obstacle), demonstrating the variability observed between the reversible retractions studied. Creating a kymograph is only possible if the image series is completely still and the picture frame does not wander or shake. For R2 and R9, the imaging was started when the retraction had already happened and was thus missed. R6 and R7 show a clear asymmetry between retraction and reversal, however, while in R6 the retraction takes only 1 h and the reversal takes much longer, the contrary is the case for R7, with the reversal almost lasting 10 h. The kymograph for R1 shows a cascade of 8 retraction steps occurring first in a rapid succession, slowing down slightly towards the end, although the distance between the first couple of septa was much larger than the distance between the later forming ones. Similarly, a rather slow reversal was observed. Together with the fact that the retraction process was initiated immediately after growth arrest and that a very long overall distance was covered by the retraction (~250 µm), this suggests a very strong pull or negative pressure built up preceding the cytoplasmic retraction.

4.2.3. Introduction of fluorescent dyes

As all above discussed findings are purely based on phase contrast brightfield imaging, an additional readout using fluorescent staining was deemed useful to prove the retraction of cytoplasm and potentially further highlight sub-cellular structures. Therefore, a combination of the dyes FM4-64 and Calcofluor White M2R (CFW) was envisioned. As one of the Fei Mao (FM) dyes, FM4-64 associates with cell membranes and membranous organelles. Only this association with the sample brings out the fluorescence, otherwise, this dye is non-fluorescent

(Betz *et al.*, 1992; Betz *et al.*, 1996). FM4-64 has been frequently employed in studies on filamentous fungi (Fischer-Parton *et al.*, 2000; Dijksterhuis and Molenaar, 2013; Garduño-Rosales *et al.*, 2022) but never before for AMF. CFW, also known as Fluorescent Brightener 28, on the other hand, is a dye that intercalates into chitin and cellulose and is hence commonly used to specifically stain cell walls of bacteria (Postma and Altemüller, 1990), algae (Fiołka *et al.*, 2020), higher plants (Galbraith, 1981) and insects (Henriques *et al.*, 2020). For fungi, it is primarily known for staining in a medical diagnosis context (Hageage and Harrington, 1984; Zhang *et al.*, 2010; Chen *et al.*, 2021). Besides their complimentary tissue specificity, the combination of dyes for the experiments described herein was chosen for the good spectral separation, with CFW and FM4-64 exhibiting emission maxima of 432 nm and 670 nm (wide spectrum), respectively (Au - Lichius and Au - Zeilinger, 2019). FM4-64 is commonly used for live staining as it is considered relatively non-toxic; the dye frequently associates and dissociates in rapid succession, thus forming of localised membrane faults can be avoided (Wu *et al.*, 2009; Au - Lichius and Au - Zeilinger, 2019). CFW was reported to be more intrusive, associating with nascent chitin and thus disrupting a normal chitin assembly and cell wall formation (Herth, 1980). For a first analysis, the dyes were used solely for end-point staining to reveal the intra-hyphal situation after the proposed cytoplasmic retraction. Hence, any potential toxic effects could be neglected.

For the end-point staining experiments, CFW (to a final concentration of 0.5 µM) and FM4-64 (to a final concentration of 5 µM) were added to autoclaved liquid MSR(-) medium and sterile filtered. The dye medium was then carefully flushed into a device containing AMF spores and mycelium from an experiment detailed in *3.2.2.1 Spore loading and trapping*. When replacing the old medium, care was taken as to not agitate the fungal material inside of the device. The results are shown in Figure 28. In this example, all hyphae, independent of their age, can be seen in the phase contrast microscopy image (Figure 28a). Differences in the individual hyphal brightness can be observed, just as found after cytoplasmic retraction (see *4.2.1 Space searching in AMF*), where a phase-bright colour was considered to mark a “normal”, vital hypha and phase-dark an emptied hypha, following withdrawal of cellular contents. Imaging with the DAPI filter (wavelength ~395 nm, used for imaging CFW fluorescence) revealed that all hyphae that were observable in the phase contrast, were visible in a bright fluorescence,

too (Figure 28b). Using the TRITC filter set-up of the microscope (wavelength ~544 nm, used for imaging FM4-64 fluorescence), only certain hyphae are visible (Figure 28c). Here, the lookup table "spectrum" in Fiji/ImageJ had to be used as the overall fluorescence intensity was very low. As FM4-64 stains the lipid bilayers of membranes and organelles, only vital hyphae containing all these cellular contents can be made visible, while with CFW, which stains the cell wall, all hyphae (regardless of their vitality and cellular contents) are detectable. Moreover, CFW was found to highlight septa in the hyphae, which can also be seen in phase-dark hyphae in phase contrast images, but less pronounced. As discussed in *4.2.1 Space searching in AMF*, AMF are non-septate fungi and form septa only as a defensive measure, when withdrawing cellular material from abandoned parts of the hyphal network. These septa can therefore be taken as an additional indicator for cytoplasmic retraction, which was now proven with the results obtained from the fluorescence staining experiments. Due to the weak signal from the FM4-64 staining and a slight autofluorescence observed with the *Rhizophagus* strains studied, which overlaps with the FM4-64 spectrum, it cannot be proclaimed with certainty whether the cell membrane is removed along with the cytoplasmic retraction, decays shortly after or rather remains behind with the cell wall.

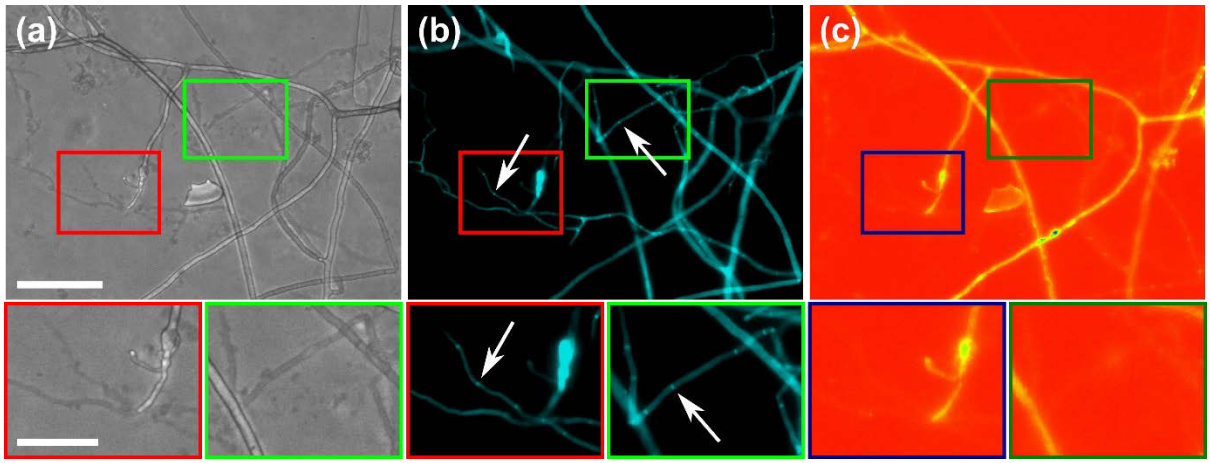


Figure 28: Fluorescent end-point staining of vital and empty hyphae. The images show the same region of interest of hyphae of *Rhizophagus irregularis* MUCL 41833 within the *AMF-SporeChip*, in the (a) phase contrast, (b) DAPI and (c) TRITC channel. The dyes used are calcofluor white (CFW), staining chitin in the cell walls and FM4-64, staining lipid bilayers. White arrows indicate two exemplary emptied hyphae, with pronounced septa as remnants of gradual cytoplasmic retraction. The lookup tables "cyan" (b) and "spectrum" (c) were applied in ImageJ/Fiji to improve the visibility of the fluorescence intensity. Scale bars: 100 µm and 50 µm in the magnification images. Images and figure legend reproduced with modifications from Richter *et al.* (2024) with permission from the Creative Commons Attribution license (www.creativecommons.org/licenses/by/4.0/).

4.2.4. Using fluorescent staining for studying sub-cellular structures

Next, the fluorescent dyes, especially FM4-64, were implemented for live-cell imaging of AMF hyphae. In combination with the microdevices presented herein, it was envisioned to characterise the dynamic retraction process in further detail on a sub-cellular level and in particular use the setup in search for the Spitzenkörper, which has not been described for AMF to date. Now, the toxicity effects of the dyes, as well as the influence of the excitation wavelengths of light, on the fungi had to be considered. As strong fluorescence signals are required to resolve sub-cellular structures, higher dye concentrations are often needed in the medium to increase the signal-to-noise ratio; however, toxicity increases with rising dye concentrations. The same holds true for the excitation light intensity and exposure times, with high levels improving the resolution of the imaging but causing cellular photodamage to the fungus (Maddison and Manners, 1973; Gao and Garcia-Pichel, 2011). Therefore, an optimal balance between these opposing effects had to be found. As no Spitzenkörper has been reported so far for AMF, the method for staining and imaging was first established using fungi that are well known for their pronounced Spitzenkörper. The primary choice was the Ascomycete *N. crassa*, which is often used for Spitzenkörper studies. Furthermore, a Basidiomycete and orchid mycorrhizal fungus already growing in the lab, *R. solani*, was used for first tests. In *R. solani* the Spitzenkörper is of a different type compared to *N. crassa* and less pronounced and was hence more difficult to visualise but a good test for the method.

As imaging *R. solani* was merely a pre-experiment and the AMF would likely differ in their response, dye toxicity and fluorescence intensity were only rudimentarily tested. Concentrations of the dye FM4-64 tested were 5 µM and 10 µM (e.g., Held *et al.* (2019) used 8 µM in their experiments). A fungal inoculum was taken from a 2-month-old potato dextrose agar (PDA) fridge stock culture of *R. solani*. The *AMF-SporeChip* was pre-filled with potato dextrose broth (PDB) containing the required concentration of FM4-64 by pipetting the media into the device inlet straight after the plasma bonding, utilising the temporary hydrophilicity inside the channels for a quick and even filling. A 3 mm circular plug was then punched out of the culture plate and the fungal sheet without the agar transferred into the device, pushing it gently down all the way into the inlet. Lastly, both inlet and outlet were topped up with dye-containing medium and the device incubated at 26 °C in the dark. Incubation for 3 days

resulted in complete overgrowth of the device, i.e., the fungus was densely covering the entire chamber area, in the negative control (no dye added) as well as with 5 µM FM4-64. A concentration of 10 µM yielded a significantly slower growth, with the fungus reaching the end of the investigation zone after 3 days. To test the fluorescence intensity obtained for each concentration, the devices were imaged using a 20x objective and the TRITC filter setup. With 5 µM, due to its complete overgrowing the device, no active growth front and only a very dense, mature mycelium could be imaged (Figure 29). A vital, sparser growth front as observed with 10 µM (Figure 29) undoubtedly improves the fluorescence quality, thus introducing a slight bias towards utilising a concentration of 10 µM FM4-64. As the brightness obtained with the latter, however, was much more intense compared to 5 µM, and considering that the higher concentration did only slightly slow down the growth but did not have detrimental effects, 10 µM was deemed dye concentration of choice for the *R. solani* experiments.

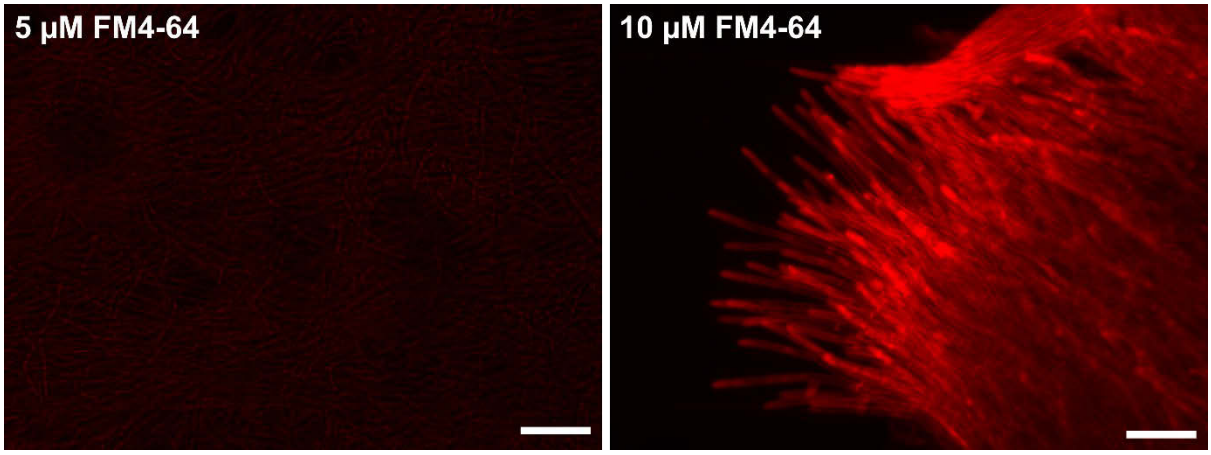


Figure 29: Comparison of FM4-64 concentration for fluorescent staining of *Rhizoctonia solani*. Hyphae were stained with 5 µM or 10 µM FM4-64 and microscoped using the TRITC channel and a 20x magnification. Scale bars: 100 µm.

Inspired by work conducted by Dijksterhuis and Molenaar (2013), a dynamic dye uptake approach was considered for imaging the Spitzenkörper. In their study, *R. solani* hyphae were transferred onto a microscope glass slide and medium containing 3.2 or 6.4 µM FM4-64 was added. Then, the stained fungus was immediately imaged using a confocal microscope to monitor uptake of the dye. This revealed a virtually instantaneous staining of the cell membrane, followed by staining of organelles after about 1 min. The Spitzenkörper was visible after approximately 2 min and became increasingly clearer over the following 4-5 min. During imaging, the hypha elongated, and grew further.

To reproduce this setup in a microfluidics setting, a different device was utilised. The *fluid exchange device*, developed by Dr Claire Stanley (Stanley *et al.*, 2014), features a 10 µm wide fungal inlet channel that feeds into a tapered main chamber, with two fluid delivery channels opening into the main chamber right next to the fungal inlet (Figure A2). With this device, the idea was to allow *R. solani* to grow in PDB through the fungal inlet and then introduce the media containing the dye via the fluid delivery channels using a syringe pump. Initially, a flow rate of 120 µl/min was used to introduce the dye. Microscopy was performed 2 days after inoculation as the fungus generally started growing into the main chamber after this time period, providing a good number of vital, spaced-out hyphae. Furthermore, hyphae growing backwards into the fluid delivery channels, which commonly happens after a dense colonisation of the growth chamber, is widely avoided. When subjected to a dye concentration of 10 µM FM4-64, introduced with a flow rate of 120 µl/min, the majority of hyphae were observed to collapse internally, rapidly expel cell material and pull back out of the field of observation, virtually exploding (Figure 30). This drastic response could have been produced by the shear stress exerted by the media flow or a sudden change in the composition of the surrounding liquid. In static growth conditions, where the fungus grows into the new conditions and has time to adapt, this detrimental reaction was not observed. Osmotic effects, however, due to the small dye concentrations, can be ruled out.

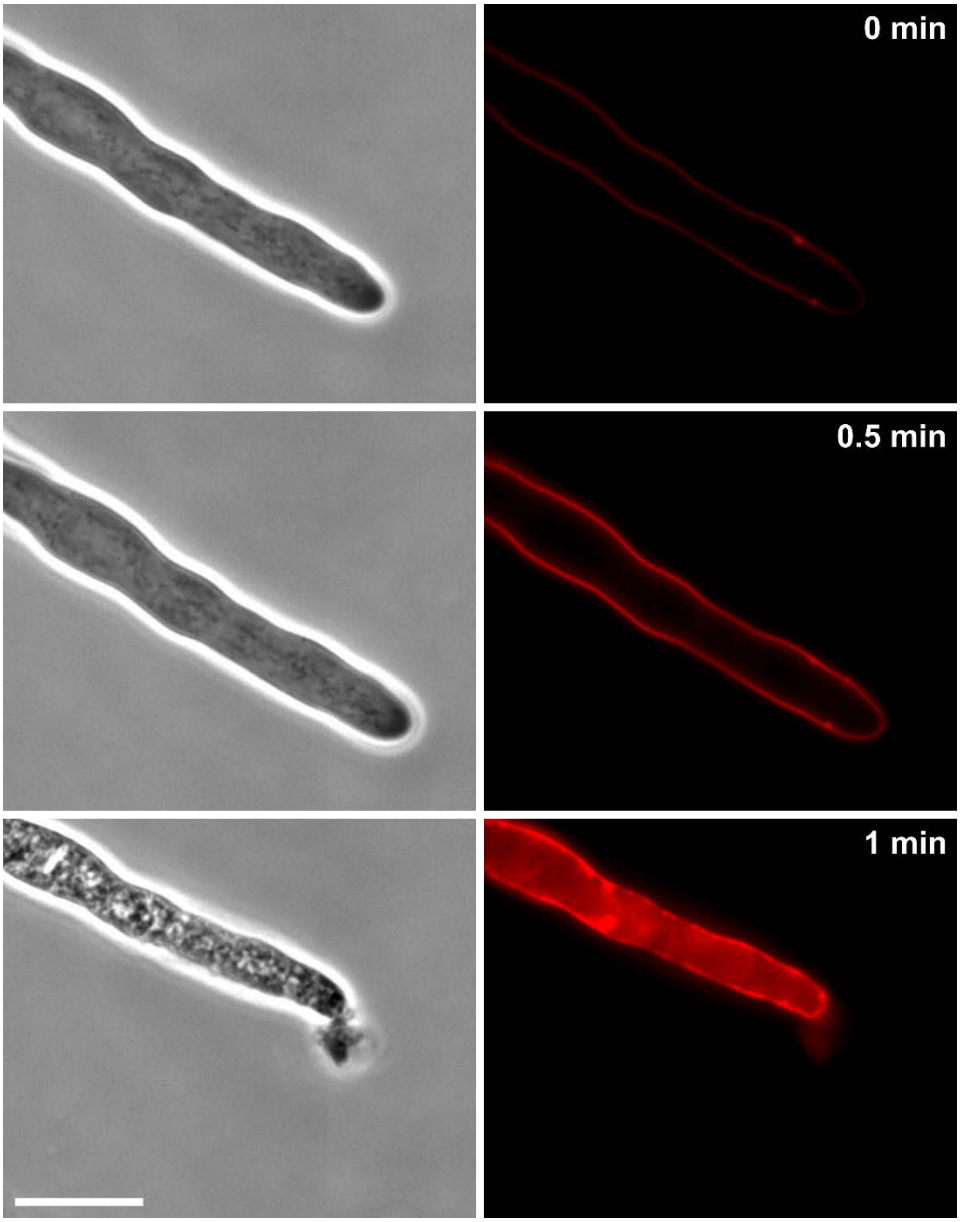


Figure 30: Response of *Rhizoctonia solani* hypha to introduction of 10 µM FM4-64 with a flow rate of 120 µl/min. Time series showing the disintegration of the hypha in the phase contrast channel (left) and the uptake of the dye in the TRITC channel (right) over 1 min. Scale bar 10 µm.

To mitigate this negative impact, the flow rate was reduced to 20 µl/min and later to 5 µl/min, which significantly reduced the disruption of the hyphae, but did not eliminate it entirely. As shown in Figure 31, the liquid exchange and thus introduction of the FM4-64 did work as envisioned and the periphery, i.e., the cell membrane, of the hypha started to fluoresce, increased brightness and covered the entire hypha, staining the cellular contents, after 1 min. This coincided with a less vigorous reaction of the fungus compared to experiments using higher flow rates. Nevertheless, the hypha still retreated, expelled material at the hyphal tip

and a complete disarrangement of the hyphal insides was clearly visible. No such effects were documented by Dijksterhuis and Molenaar (2013).

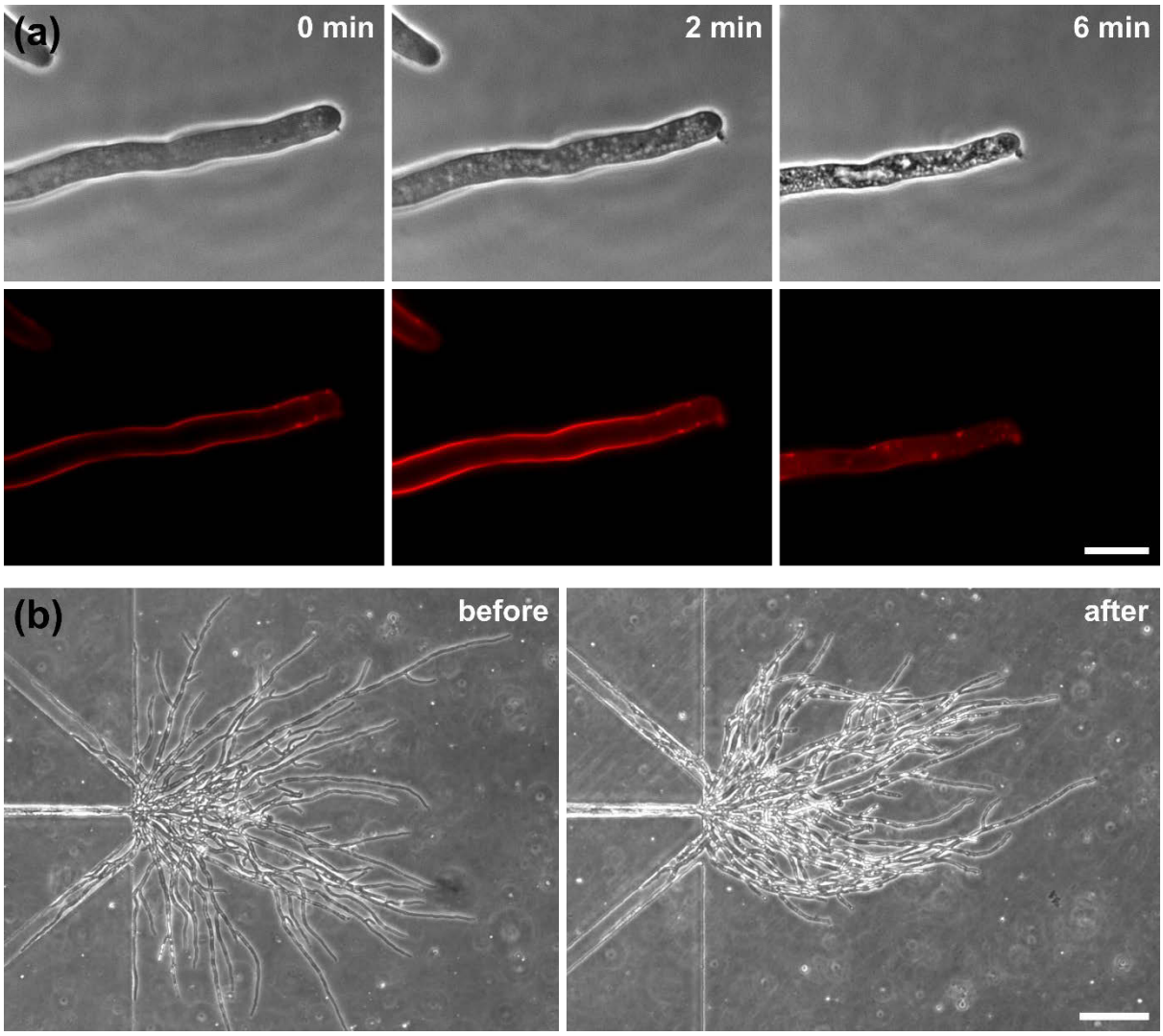


Figure 31: Response of *Rhizoctonia solani* hypha to introduction of 10 µM FM4-64 with a flow rate of 20 µl/min. (a) Time series showing the disintegration of the hypha in the phase contrast channel (top) and the uptake of the dye in the TRITC channel (bottom) over 6 min. (b) Phase contrast image of the hyphal network before and after introduction of the dye. Scale bars: (a) 10 µm and (b) 100 µm.

Another (additional) reason causing the hyphal disruption could most likely be photodamage. This was also observed and analysed in further detail with *N. crassa* (see below). Many filamentous fungi, mostly being soil dwellers, are known to be very sensitive towards light, often cultivated in the dark for that reason. Ultraviolet (UV) light can cause DNA damage, infrared (IR) can generate focussed heat spots and light excitation of dye molecules in the tissue can lead to generation of reactive oxygen species (ROS), which stress and damage the cell (Frigault *et al.*, 2009). For the excitation of the fluorophore, high intensity, focussed laser

beams are used, which are likely prone to causing disruption of cell integrity. This problem, however, was impossible to overcome with the dynamic uptake study set-up. In order to image the entire uptake process, the recording has to start immediately upon arrival of the dye at the hypha. However, there is no way of knowing when this happens without observing the hypha via the fluorescence channel throughout the entire duration of the experiment, until a fluorescence signal is observed in the hypha. In turn, the fungus is exposed to large doses of excitation light even before the actual imaging had begun. At the hyphal level, the cytoplasm turns from a homogeneous grey mass containing small regular organelles into a blotchy mix of phase-dark and phase-bright irregularly shaped objects. Again, an expulsion of cell material in the area of the apex can be observed. Similarly, at the mycelial level (Figure 31b), the fungus appears significantly changed after the exposure. Despite the local light exposure focussed only on one hypha, the entire fungal network in the device had retracted and crumpled up and the hyphae seem less homogeneous and patchy. This could hint towards either a systemic reaction of the fungus upon light stress or that indeed an additional damaging effect by shear stress of the inflowing dye medium was experienced. As the entire cellular integrity was severely disrupted, no evidence of a Spitzenkörper was found in these dynamic experiments.

As a consequence, the dynamic set-up was abandoned and future attempts re-focussed on simple, static staining and imaging, using the *AMF-SporeChip* again. Now, in a few instances, stained with 10 µM FM4-64, clear images of hyphae could be obtained and indeed Spitzenkörper were found. As shown in Figure 32c, the Spitzenkörper is a faint, half-circular, hollow-appearing entity, as described by López-Franco and Bracker (1996), rather than a bright filled circular shape as shown in Dijksterhuis and Molenaar (2013) or seen with *N. crassa* (Held *et al.*, 2019). Care had to be taken, as random, intensely bright spots occasionally appeared all over the hyphae, some misleadingly close to an expected Spitzenkörper position (Figure **32**a,b). Although their exact origin could not be determined, it was considered highly unlikely, that these bright spots were healthy cell organelles. Much rather, it was random lipid-dye aggregates formed as a potential stress response or stained debris adhering to the outside of the hyphae. Moreover, the referenced publications show only selected examples of hypha containing clear Spitzenkörper, with no appreciation for number or frequency of occurrence of the Spitzenkörper in hyphae.

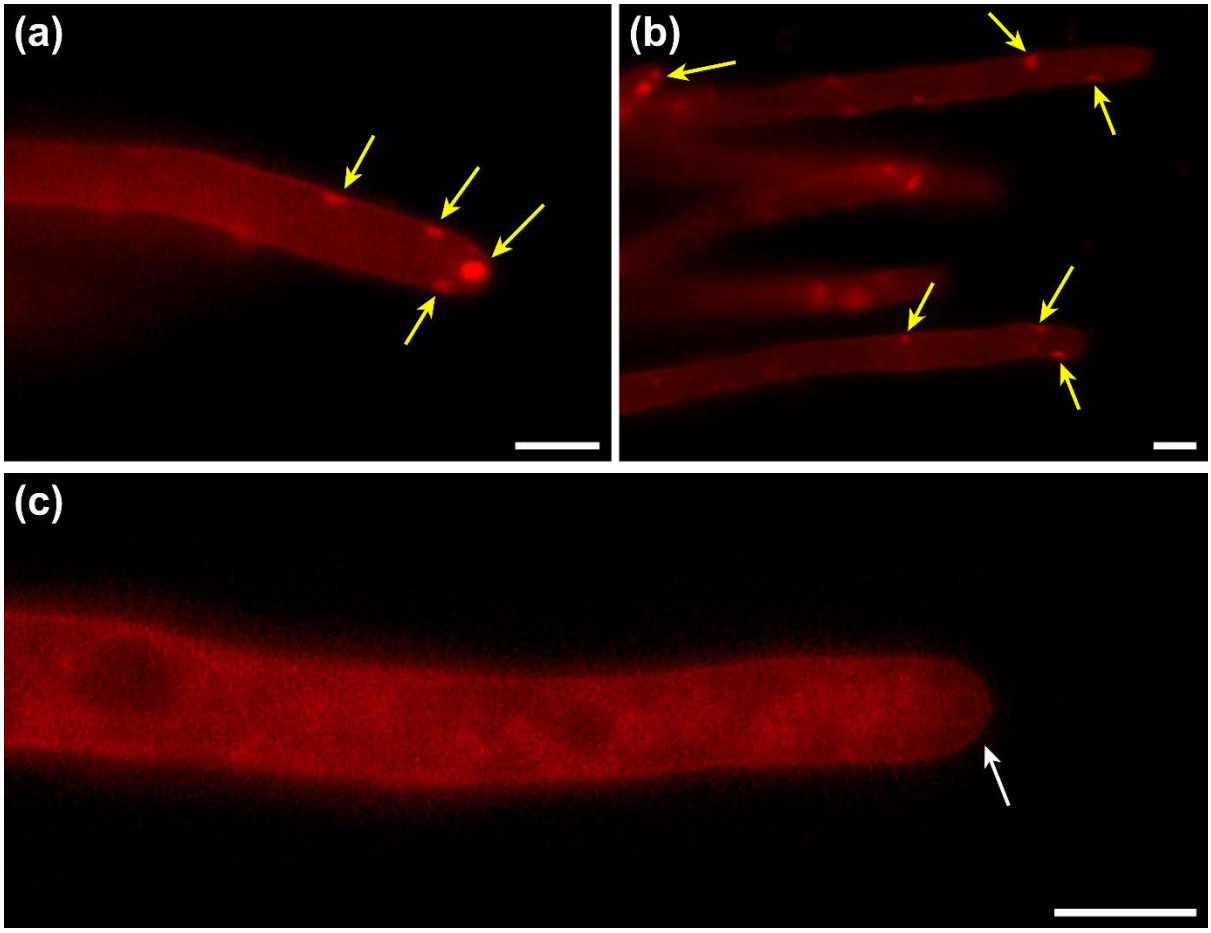


Figure 32: Fluorescence images of *Rhizoctonia solani* hyphae. Images showing hyphal tips and intracellular layout. Hyphae stained statically with 10 µM FM4-64 and microscoped using the TRITC channel and 100x magnification in (a), 40x in (b) and 150x in (c). Yellow arrows in (a) and (b) highlight bright spots in hyphae, white arrow in (c) highlights the Spitzenkörper. Scale bars: 5 µm.

Most of the studies concerning Spitzenkörper found in the literature use confocal microscopy for imaging, a technique that produces much higher image clarity than simple widefield fluorescence microscopes for instance. This is achieved by focussing the excitation laser more on the objects focal plane and excluding light that is not reflecting or radiating directly from the plane, which in normal microscopy setups is the main source for causing blurriness effects and reduced contrast (Semwogerere and Weeks, 2005). Therefore, in an attempt to obtain clearer images of the sub-hyphal composition and the Spitzenkörper, a confocal microscopy session was conducted, using a Leica SP8 Confocal Microscope (Leica Microsystems, UK). The fungus was stained as described above using 10 µM FM4-64 for a static imaging. Exemplary results obtained using a 40x oil immersion objective (plus automatic zoom) and a TRITC excitation/emission set-up are shown in Figure 33. The images were taken as a z-stack

and processed with the integrated “Maximum Intensity Projection” (Max IP) function of the microscope software.

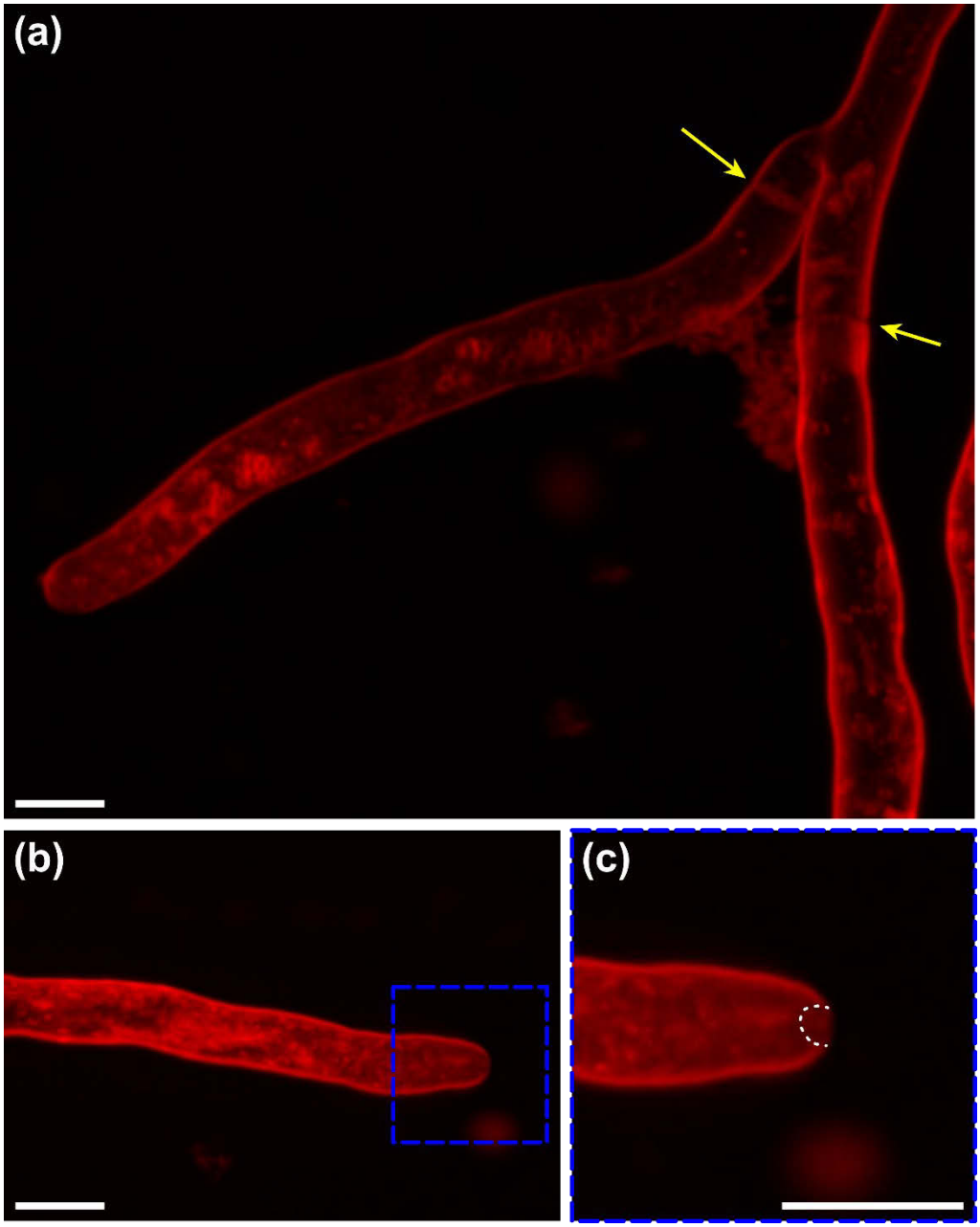


Figure 33: Confocal fluorescent images of *Rhizoctonia solani* hyphae. Images showing hyphal tips and intracellular layout. Hyphae stained statically with 10 µM FM4-64 and microscoped using the TRITC set-up on a confocal microscope. Yellow arrows in (a) indicate septa. (c) Magnification of hyphal tip in (b). White dotted line highlights the outline of the Spitzenkörper. Scale bars 5 µm.

The images acquired of stained *R. solani* hyphae were indeed of improved resolution, compared to the regular imaging on the Nikon Ti2 inverted microscope. Organelle visibility was much better and they could be discerned from one another. Similarly, septa were visualised

with high precision, even revealing a slight constriction in the tubular shape of the hyphae where the septa are, a detail formerly not resolvable with the standard microscopy. Once more, some brightly stained accumulations were found both in- and outside of hyphae. In one instance, a Spitzenkörper was observed, again as a cup-shaped, faint structure in the hyphal tip (Figure 33b,c). Although these results indicate that using confocal microscopy for the Spitzenkörper imaging is an option, the clearness of the Spitzenkörper itself was only marginally improved. Hence, as this is expensive and more laborious than standard microscopy, the regular inverted microscope was continuedly used as primary resource for the fluorescent imaging.

Shortly after obtaining these results, I received *N. crassa* to work with and transferred the imaging attempts onto *N. crassa*. Since *N. crassa* is an immensely fast-growing fungus, the window for imaging is much smaller. As with *R. solani*, the timing of the experiment has to be tuned such that there are plenty of freely growing hyphae with exposed tips in the investigation zone. Hence, the fungus needs to have grown well into the microfluidic channels, without however overgrowing and covering the entire channel. A time frame between 12 and 16 h post inoculation was found to be optimal. Both 5 µM and 10 µM in malt broth were tested. While the concentration of FM4-64 did not result in any growth differences, 5 µM was not enough to achieve a sufficiently bright staining to resolve internal hyphal structures. Therefore, malt broth containing 10 µM FM4-64 was introduced into the devices prior to fungal inoculation. Indeed, the first results instantly revealed very pronounced Spitzenkörper in the tips of *N. crassa* hyphae (Figure 34).

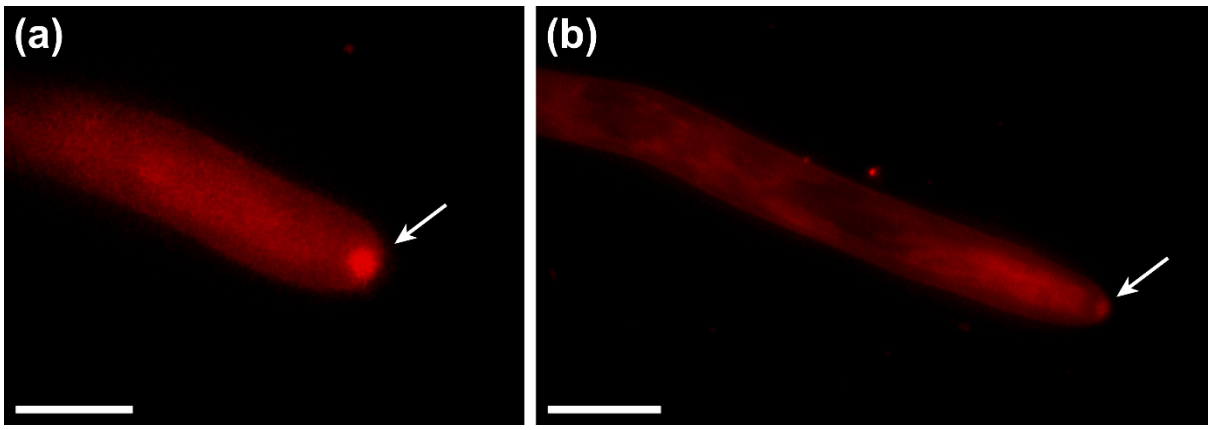


Figure 34: Fluorescence images of *Neurospora crassa* hyphae. Images showing hyphal tips and intracellular layout. Hyphae stained statically with 10 µM FM4-64 and microscoped using the TRITC

channel and 100x magnification. White arrows in (a) and (b) highlight the very pronounced Spitzenkörper. Scale bars: 5 µm and 10 µm.

In a next step, monitoring hyphal growth and Spitzenkörper dynamics over time and upon collision with obstacles was attempted. Again, an extremely high photosensitivity was encountered, which resulted in hyphae arresting their growth and loosing cellular integrity, including disappearance of the Spitzenkörper after only a few seconds of exposure. At the sub-hyphal level, changes of less than a µm in z-position can change the focus area and resolution entirely, even with the vertical confinement in the microfluidic devices. Therefore, timelapse imaging required the use of either autofocus or z-stack imaging. For both methods, multiple images of the same x-y-position and timepoint had to be taken, which increases the exposure dose significantly. Yet again, a balance has to be struck between image quality and disturbing the fungus, with only a small margin of seconds in this case. Here, using the z-stack function rather than autofocus and applying the Max IP of the Nikon software on the z-stack proved to yield the best and clearest images. The Max IP feature merges the different z-level images together, based on the fluorescence intensity, thus creating an image showing all aspects of the hypha as if lying perfectly in the same focal plane. Max IP does not always generate the best picture and commonly over-enhances brightness, resulting in loss of resolution. Here, however, it worked well. For the first round of imaging, a z-stack acquisition with 11 scanning steps in the z direction with 0.5 µm intervals was utilised, with images taken every 5 s (Figure 35).

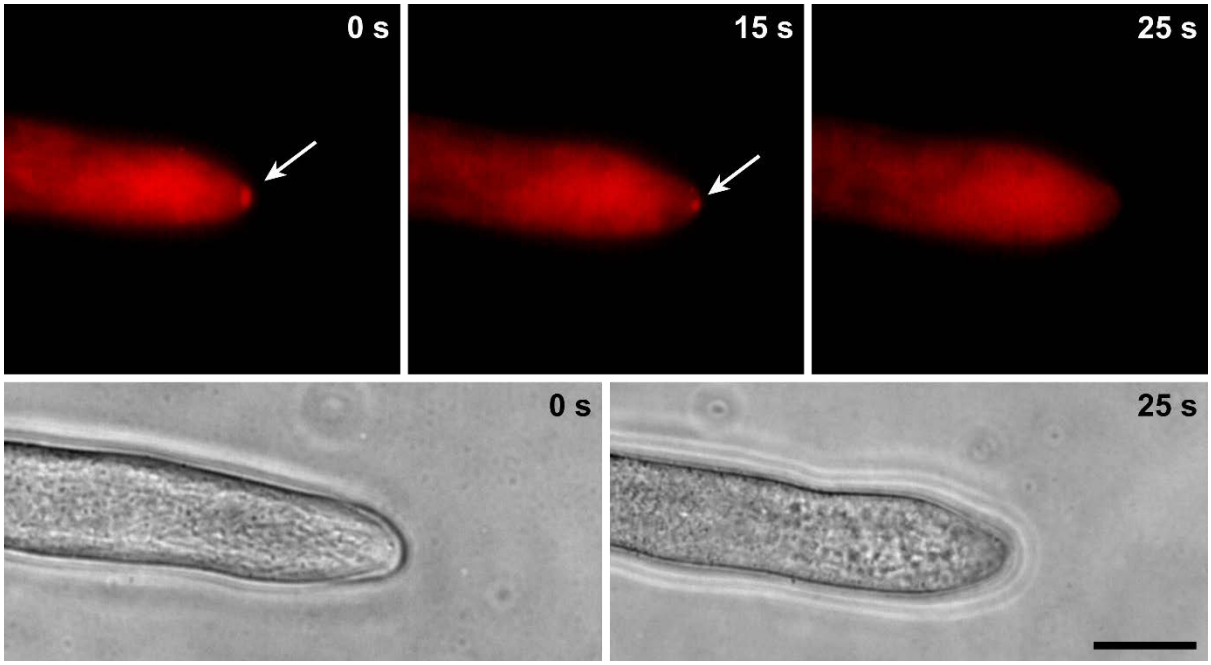


Figure 35: Response of *Neurospora crassa* hypha to light exposure during fluorescence microscopy. Time series showing the intracellular disruption of the hypha in the phase contrast channel (bottom) and the disappearance of the Spitzenkörper in the TRITC channel (top) over 25 s. Z-stack acquisition with 11 scanning steps in the z direction with 0.5 µm intervals followed by maximum intensity projection was performed, with images taken every 5 s and 100x magnification. White arrows indicate the Spitzenkörper. Scale bar 10 µm.

At the beginning of the experiment, a Spitzenkörper is clearly visible as a bright spot in the hyphal tip, which starts to disappear after 15 s and vanished entirely after only 25 s when the timelapse was terminated (Figure 35). The overall brightness decreases as well, hinting towards a possible photobleaching effect as a cause for the disappearance of the Spitzenkörper. Observation of the hypha under phase contrast showed growth arrest after the exposure, while the forward growth of the hypha before exposure can even be followed in real-time. Furthermore, cellular organelles seem to move in an organised fashion and cytoplasmic streaming can be observed before the timelapse imaging, while after exposure, these organelles vibrate uncoordinatedly on a fixed spot. In a next attempt, the time intervals for the recording were extended to 20 s (Figure 36) to reduce this phototoxicity effect.

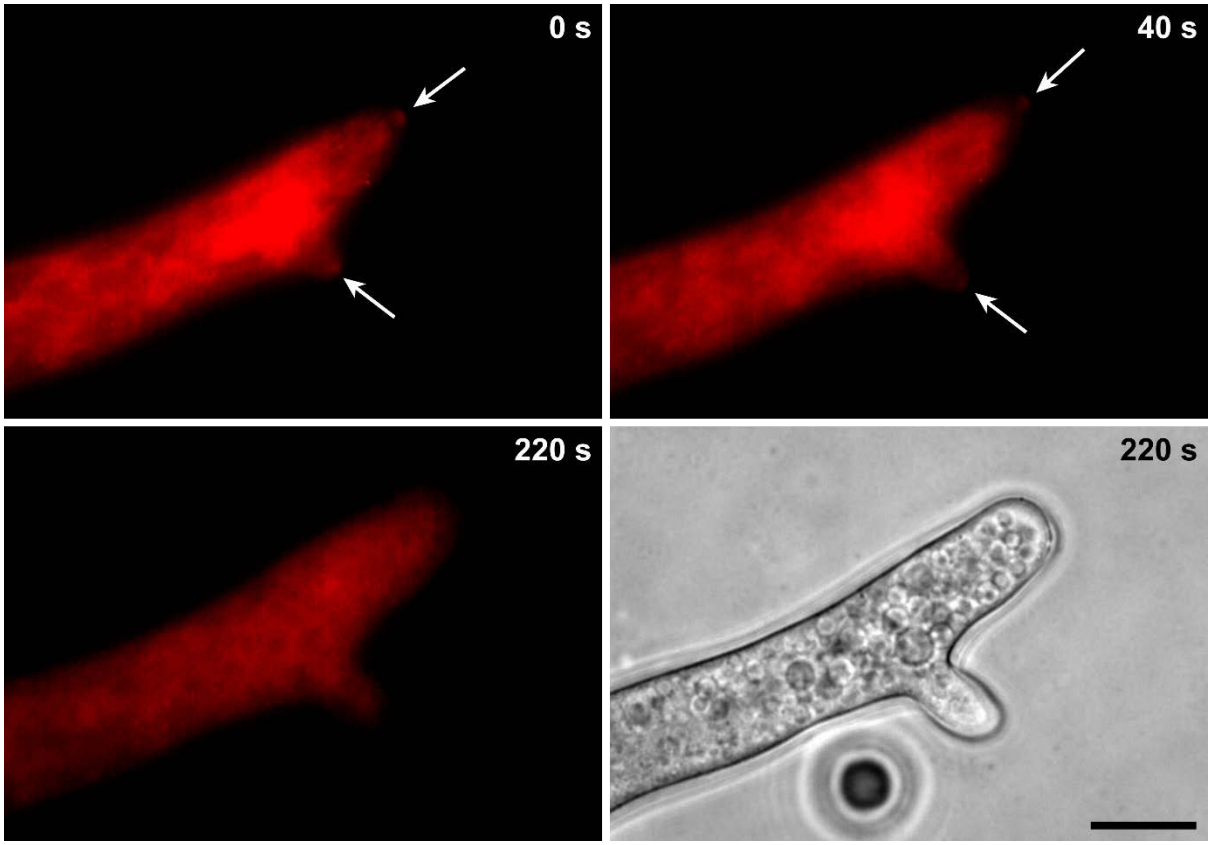


Figure 36: Response of *Neurospora crassa* hypha to light exposure during fluorescence microscopy. Time series showing the intracellular disruption of the hypha in the phase contrast channel (bottom right) and the disappearance of both Spitzenkörper in the TRITC channel over 220 s. Z-stack acquisition with 11 scanning steps in the z direction with 0.5 µm intervals followed by maximum intensity projection was performed, with images taken every 20 s and 100x magnification. White arrows indicate the Spitzenkörper. Scale bar 10 µm.

Still, after only 40 s, the two formerly bright spots in the branches vanish. The acquisition ended after 220 s, when the hypha stopped growing, the Spitzenkörper disappeared and the overall fluorescence intensity was significantly reduced. In the fluorescence image, but more clearly in the phase contrast image, clear signs of cellular disruption in the hypha are visible. Instead of the grainy, rather homogeneous cellular contents and faint traces of the cytoskeleton with its microtubules (Figure 36, top), the hyphal insides appear as an aggregate of irregularly sized, bubble-like shapes (Figure 36, bottom). These observations indicate that photobleaching does indeed happen, however, the loss of the Spitzenkörper is not only an imaging effect but a physiological change of the fungus coinciding with growth arrest and cellular disruption of the hypha. Next, to further reduce total exposure time, the number of z steps was reduced from 11 to 5, while keeping the time intervals and intervals between z steps equal. This extended the imaging time to about 500 s, i.e., until disappearance of the

Spitzenkörper. Then, the step interval was changed to 1 µm with 7 steps per timepoint to cover a wider z range. This did not recognisably change the maximum possible timelapse duration. While 5 steps of 0.5 µm, as the more precise scanning approach, was expected to generate a slightly better detail resolution, 7 steps of 1 µm, imaging more overall z layers of the sample, might ensure capturing the entire hypha even when it grows through different focal planes. A timelapse series captured using the latter setting with time intervals of 20 s are shown in Figure 37 and Movies 14 and 15.

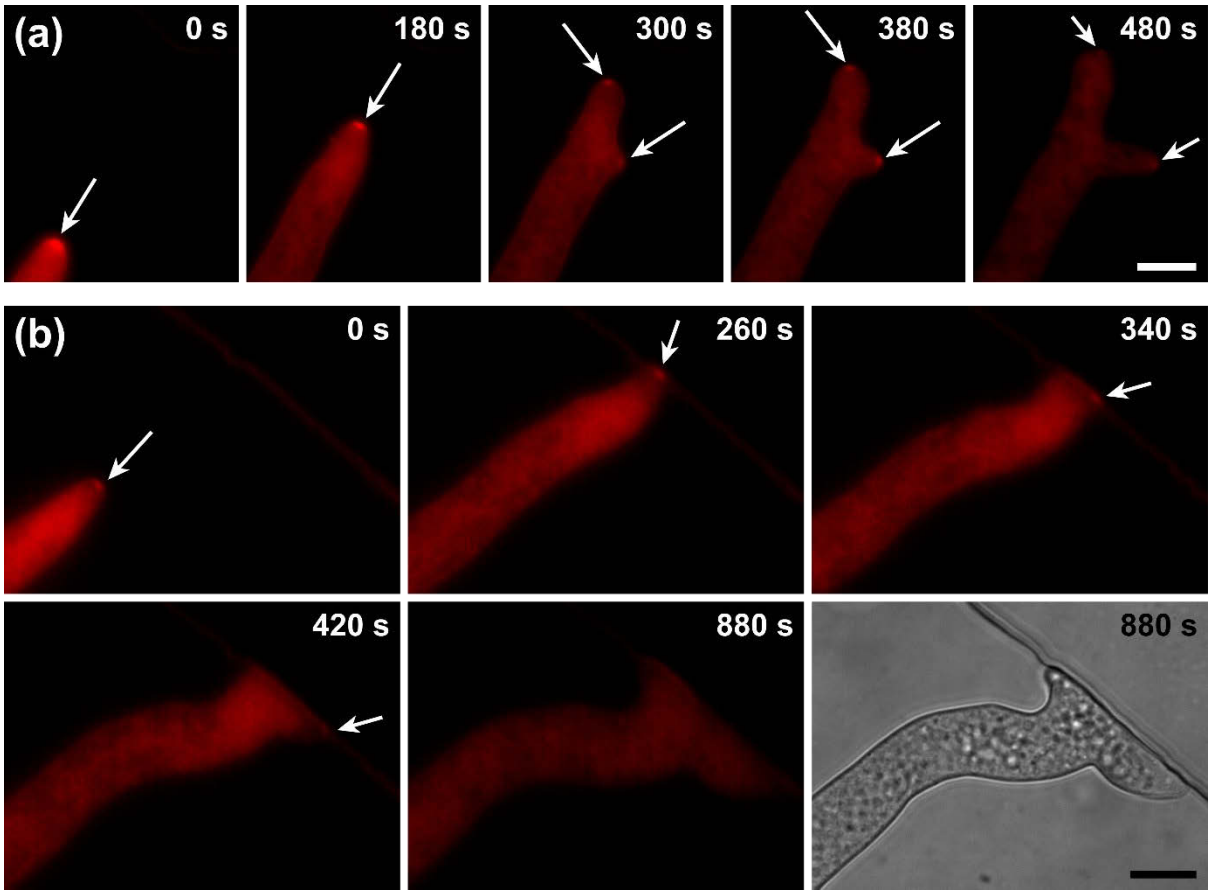


Figure 37: Response of *Neurospora crassa* hypha to light exposure during fluorescence microscopy. (a) Time series showing branching and formation of new Spitzenkörper, followed by disappearance of both Spitzenkörper in the TRITC channel over 480 s. (b) Hypha colliding with a channel wall and performing hit and split and disappearance of the Spitzenkörper in the TRITC channel over 880 s. The phase contrast image (bottom right) shows the intracellular disruption of the hypha after the experiment. All images were acquired with 7 scanning steps in the z direction with 1 µm intervals followed by Maximum Intensity Projection, with images taken every 20 s and 100x magnification. White arrows indicate the Spitzenkörper. Scale bars: 10 µm.

With the above-described microscopy settings, the hypha can be followed growing over a distance of 30-40 µm until the Spitzenkörper disappears and the fluorescence fades. In Figure

37b, a head-on collision with a channel wall can be observed. The hypha reacts in a hit-and-split manner, as discussed in *4.2.1 Space searching in AMF*, and forms 2 daughter branches growing off in opposite directions, which follow the wall closely. Unlike described by Held *et al.* (2019), no formation of a second Spitzenkörper in the left-hand daughter branch could be observed. The right-hand daughter hypha retained the Spitzenkörper from the original hypha throughout the entire collision process, until it disappears about 3 min after the impact. As the timing of the disappearance coincides with that observed in open space (Figure 37a), the loss of the Spitzenkörper was accredited to the phototoxicity rather than the collision event. Moreover, the phase contrast image of the hyphal condition after the fluorescence imaging shows once more clear signs of intracellular disruption (Figure 37b). To further improve the fluorescence imaging of the Spitzenkörper in fungal hyphae, as seen in Held *et al.* (2019), a confocal microscope could be employed again, as the effective exposure dose is reduced at a same or better imaging quality because of the higher precision focussing (see above). Additionally, the number of timepoints can be lowered; as a comparison, the Held group used time intervals between 45 and 80 s, to further reduce the overall exposure time. However, as the experiments described in this section were mere preparation for the main studies on AMF, and sufficient experience and knowledge of the methodology was acquired, the venture to further improve imaging of *R. solani* and *N. crassa* was terminated here.

To finally transfer the methodology onto sub-cellular studies in AMF hyphae, first, a thorough germination and growth experiment was set up in the *AMF-SporeChip*. To test the effect of the dye FM4-64 on *R. irregularis*, two different concentrations were added to the medium as well as the timepoint at which the dye was introduced was varied. Spores of *R. irregularis* MUCL 43194 were introduced into the devices as described in *3.2.1.3 Spore isolation and introduction into the device* using liquid MSR(-) medium. The medium was supplemented with 5 µM and 10 µM FM4-64, respectively, and directly used to flush the spores into the devices. This way, the spores were exposed to the dye from the very beginning and throughout the entire experiment, in an analogous manner to the experiments described above using *N. crassa* and *R. solani*. As an additional condition, the dye was added at a later timepoint. Here, the spores were introduced into the devices and pre-inoculated in regular liquid MSR(-) medium to germinate and grow hyphae. Then, after 4 days, the medium was exchanged by gently flushing

through dye-containing medium, again with 5 µM and 10 µM FM4-64, respectively. This way, the fungi were allowed to establish themselves in the device, germinating and growing hyphae, before coming into contact with the dye, ideally granting a window for fluorescent imaging of fully grown hyphae before a potential toxic effect of the dyes can manifest. The medium exchange had to be done with care and slowly, as to not disturb or even flush out the spores. Generally, the spores were found to be well-fixed in position and remained unaffected by a light flow. To ensure a complete exchange of the medium, any liquid from the in- and outlet was removed and the new medium pumped in until the outlet was completely re-filled. As the outlet holds more than 10-fold the volume of the microchannel, this was deemed a good and easy means to make sure that a complete medium exchange was performed. Due to the dense nature of their mycelium, this did not work with *N. crassa* and *R. solani* and a different device had to be used. With the AMF inoculum, fluid exchange was no problem as only single spores occupied the device that yield a small number of hyphae growing sparsely. Moreover, a direct detrimental effect observed with *N. crassa* and *R. solani* of hyphae disintegrating and retracting cytoplasm immediately during the medium exchange was not visible with the AMF. For a quantitative analysis of the effect of the dye on germination and growth, the devices were imaged and hyphae measured every day for 7 days and again on day 14, as described in *2.3 Microscopy and image processing*. A graphical representation of the growth behaviour of *R. irregularis* in the presence of the dye FM4-64 can be found in Figure 38.

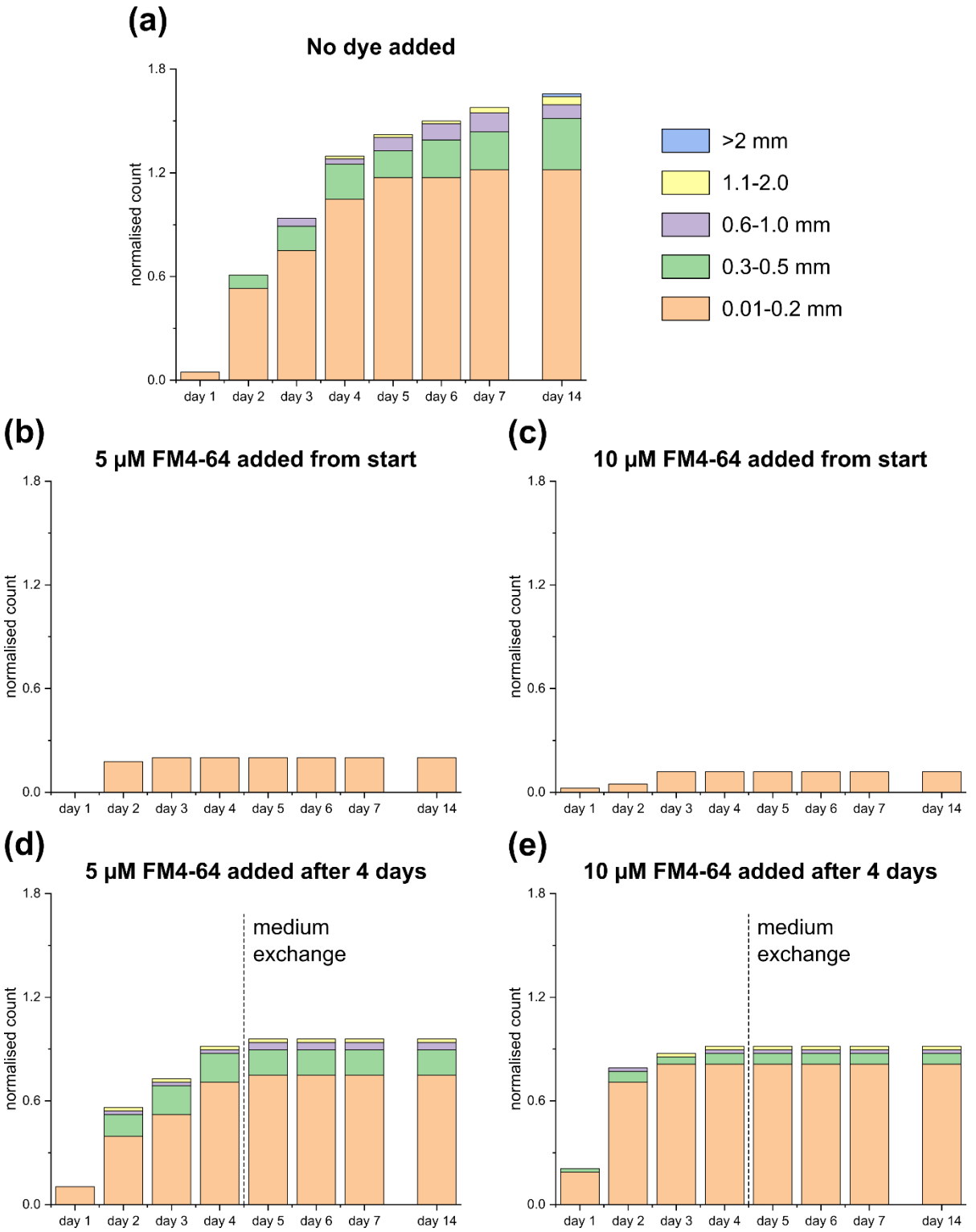


Figure 38: Fungal growth assays comparing effects of different FM4-64 concentrations on-chip. The growth behaviour *Rhizophagus irregularis* MUCL 43194 in the *AMF-SporeChip* containing 5 µM or 10 µM FM4-64, either added from the start of the experiment or after 4 days, is represented as stacked column charts. The hyphal lengths were measured using Fiji/ImageJ, normalised (number of germination sites was determined, and the absolute value of counts divided by the number of germination sites) and categorised in 5 length sections (different colours). As germination site, any site with an occurrence of a germination/fresh hypha within the 14 days of the experiment was counted. In

total, 6 devices with 40–65 germination sites per strain were analysed for the experiment. The dotted line in the bottom graphs indicates the time point of the medium exchange.

For the spores germinated and grown in the standard liquid MSR(-) medium without any dye added (Figure 38a), the column chart shows a constant increase in numbers of hyphae, which flattens after day 4 and 5. Hyphal elongation occurs up to the end of the experiment after 14 days, as seen from the increase in the green, purple, yellow and blue proportions of the columns. The only hypha reaching a length above 2 mm (blue segment) in the entire experiment was observed under this growth condition. With both concentrations of FM4-64, 5 µM and 10 µM introduced from the start of the experiment (Figure 38b,c), very little growth was observed, manifested in a handful of germinations emerging within the first 3 days of the experiment, however, no further germination beyond day 3 and no further hyphal growth beyond 0.2 mm length occurred. In the final 2 conditions (Figure 38d,e), with pre-inoculation in liquid MSR(-) medium for 4 days and subsequent medium exchange to dye-containing medium the same growth behaviour as in the topmost graph (Figure 38a) was expected for the first 4 days. In Figure 38d the same trend as in Figure 38a, can be observed with a constant increase in hyphae within the first 4 days, while in Figure 38e a steeper increase within the first 2 days and flattening of the trend thereafter was found. Moreover, in Figure 38a a considerably overall higher germination and stronger growth was observed. This variation despite equal growth conditions can be accredited to the variability inherent to the spore material as well as the spore dissection and selection method. The effect of adding the dye medium, however, becomes clearly apparent from the graphs, as any growth or germination beyond the addition of the dye (between day 4 and 5) was halted. These results indicate a strong sensitivity of *R. irregularis* towards FM4-64 concentrated 5 µM or above, much more than what was observed with *N. crassa* and *R. solani*. Virtually any contact with the dye-containing media resulted in growth arrest and prevented germination in nearly all cases. As this becomes very clear from the results, I refrained from producing additional graphs for statistical analysis (as I did for Figure 19 and Figure 21). While the growth studies shown in Figure 19 and Figure 21 were meant to compare the effect of different conditions on the growth behaviour of different strains in detail and a establishing a statistical grasp on these results was insightful, Figure 38 is only supposed to show how the addition of the dye, regardless of

time point or concentration makes any growth study impossible, which it sufficiently does without further statistical analysis. In conclusion, these suggest that a dynamic fluorescent growth imaging is not feasible and an end-point fluorescent imaging had to be resorted to.

Next, the staining properties of the different FM4-64 concentration with *R. irregularis* hyphae was tested. Therefore, hyphae were imaged with a 100x magnification on day 5 of the experiment, after adding the dyes. No microscopy was possible with devices inoculated with dye-containing medium from the start as hardly any germination was observed and the few hyphae that did emerge appeared rather stunted and barely vital. Adding the dye at a later point, after germination and some initial hyphal growth had been established, at least enabled some hyphal imaging. Representative microscopy images of *R. irregularis* hyphae stained with 5 µM and 10 µM FM4-64, respectively, are shown in Figure 39.

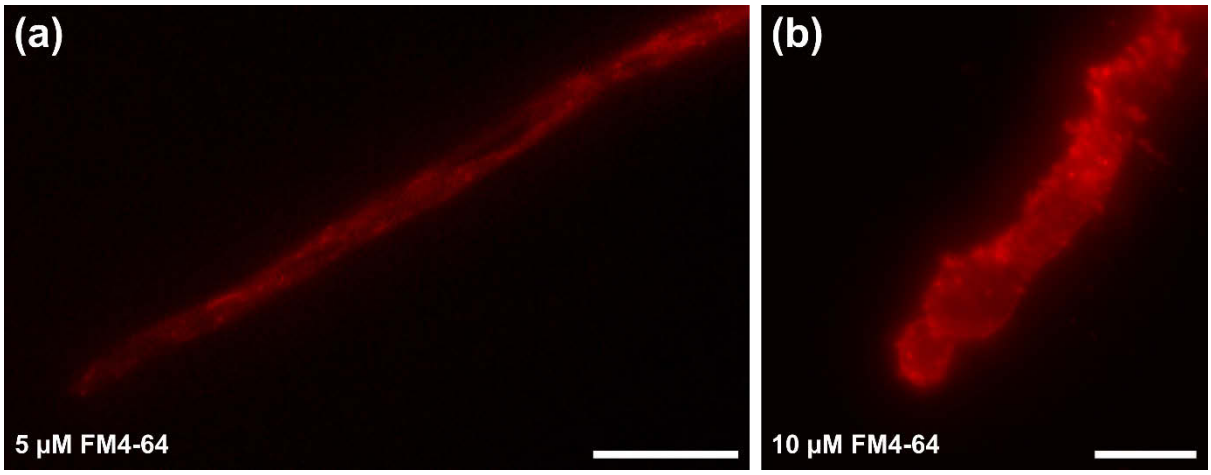


Figure 39: Comparison of FM4-64 concentration for fluorescent staining of *Rhizophagus irregularis* MUCL 43194. Hyphae were stained with 5 µM or 10 µM FM4-64 and microscoped using the TRITC channel and a 100x magnification. Scale bars: 10 µm.

Staining with 5 µM dye revealed the hypha with a certain level of sub-cellular detail (Figure 39a). However, as the general brightness of the fluorescence was comparably low, especially in the hyphal tip, no higher resolution was achievable. Adding 10 µM dye increased the brightness considerably. Nonetheless, obtaining high sub-cellular resolution and detail was foiled by the accumulation of bright clumpy debris alongside the hyphal wall (Figure 39b). This phenomenon has been observed before with *R. solani* (Figure 30 and Figure 31). Most likely the toxic effect of the high dye concentration causes the hyphae to collapse and exude cellular contents, which stain easily with the dye. In no hypha of *R. irregularis* imaged a bright structure

resembling a Spitzenkörper like in *N. crassa* (Figure 34, Figure 35, Figure 36 and Figure 37) nor a semi-circular, faint shape as in *R. solani* (Figure 32 and Figure 33) was observed. However, due to the low sub-cellular resolution and apparent toxicity of the dye on *R. irregularis*, still no definite statement against the existence of a Spitzenkörper in AMF could be made. Initially, it was hoped that a dynamic study involving following stained hyphae growing and interacting with physical obstacles, while monitoring coinciding sub-cellular behaviour, could shed some light onto the Spitzenkörper-question. However, this was made impossible by the nearly complete growth shut down caused by the dye.

As a final attempt, a confocal microscope was used once again. This method did improve the image quality slightly in the staining experiments with *R. solani* (see above) and revealed a Spitzenkörper. Therefore, a small experiment with *R. irregularis* MUCL 43194 inoculated in *AMF-SporeChips* with liquid MSR(-) medium without any dye to germinate and establish hyphal growth, was set up. As before, medium supplemented with 5 µM FM4-64 was added on day 4 of the experiment and the confocal imaging was performed the following day. Prior, a brief scrutiny of the growth performance using phase contrast microscopy revealed that once again several hyphae arrested growth and retracted cytoplasm after addition of the dye. Exemplary confocal microscopy results obtained using a 40x oil immersion objective (plus automatic zoom) and a TRITC excitation/emission set-up are shown in Figure 40. The images were taken as a z-stack and processed with the integrated Max IP function of the microscope software.

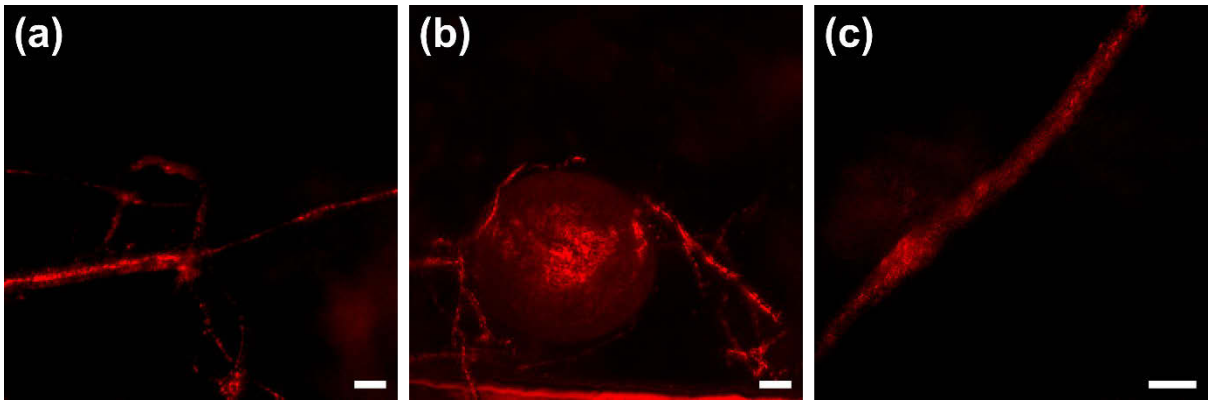


Figure 40: Confocal fluorescent images of *Rhizophagus irregularis* MUCL 43194 spore and hyphae. Hyphae were stained with 10 µM FM4-64 and microscoped using the TRITC channel and a 100x magnification. Scale bars: 5 µm.

The images chosen, show a germination with 3 branches (Figure 40a), a spore with several hyphae curled around (Figure 40b) and a large, single hypha (Figure 40c). As with the inverted microscope before, the staining with 5 µM FM4-64 reveals most hyphae and spores was however not sufficient to resolve intracellular details. Moreover, imaging fresh hyphal tips was entirely impossible and therefore the confocal microscopy was not capable of improving the imaging with AMF.

Within the scope of this thesis, attempts to elucidate the Spitzenkörper question for AMF was terminated at this point. The dye FM4-64, commonly used for fluorescent Spitzenkörper imaging in fungi was successfully applied to both *R. solani* and *N. crassa*, however, failed to facilitate such studies with the AMF *Rhizophagus*. In combination with the cell wall dye CFW, it was possible to show the cytoplasm retraction in static imaging on a hyphal level. Resolving details down to a sub-cellular level, however, was thwarted by the lower staining capacity and high toxicity of the FM4-64 with AMF compared to other filamentous fungi.

As a next step, other dyes could be tested. The lipophilic carbocyanine dye CellBrite™, a direct alternative to FM4-64, stains phospholipids and has been reported as a reliable non-toxic and stable membrane dye. It is available in 4 different spectral ranges (Lichius, 2022) and has been successfully used with plant microspores (Corral-Martínez *et al.*, 2020) as well as mammalian cells (Zhang and Yang, 2019; Bryan *et al.*, 2023), however, never before with fungi. As the Spitzenkörper mainly consists of macrovesicles, these internalising membrane dyes are generally a good choice for Spitzenkörper staining. Besides that, the only other major component are chitosomes, which contain chitin synthases, essential for cell wall synthesis in filamentous fungi (Riquelme and Sánchez-León, 2014). These organelles in turn are microvesicles and no organelle specific dye has been reported, yet (Bartnicki-Garcia, 2006). To describe the organelles, negative staining (i.e., staining of the sample background to increase contrast) was performed after previous extraction and isolation of the chitosomes from the organism (Bracker *et al.*, 1976), which is not applicable to the desired Spitzenkörper staining.

4.2.5. Anastomosis formation in the device

When studying the hyphae's space searching behaviour, another intriguing phenomenon was observed. Filamentous fungi, including AMF, are well-known to form fusions between hyphae, so called anastomoses, which help interconnect and expand their mycelial network. This is of major importance for exchange of nutrients (Fleißner *et al.*, 2008) and genetic material (Friesen *et al.*, 2006), as well as to heal damages in the hyphal network (de la Providencia *et al.*, 2005) and thus a crucial part of their exploration and foraging strategy. As discussed before, these fungi need to find a suitable host as quick as possible with the only available carbon source being the spore contents, which is only enough to cover distances in the mm and low cm range (see *3.2.2.2 Spore germination and hyphal growth behaviour in the confined environment*). With this short a reach, it appears that the only reasonable and reliable way to encounter a suitable root, if not by chance, is to "team up" with other spores to form a large hyphal network through anastomoses. Intriguingly, certain fungi have been found to form loops with their hyphae, constituting elaborate traps to capture nematodes for consumption (Haj Hammadeh *et al.*, 2022). Here, the fungus connects in a "self-self" manner, although anastomoses with another individuum are also possible (Glass *et al.*, 2000; Novais *et al.*, 2017). With our high-resolution imaging approach, we managed to monitor both types of connection, between different individuals of the same strain as well as self-self, which formed in a tip-to-tip or tip-to-side manner, tracking the events over relatively large, confined areas, yielding real-time videos of the entire anastomosis process. The images presented herein, show only *R. irregularis* MUCL 43194; however, anastomosis events were also observed in *R. irregularis* MUCL 41833 and *R. intraradices* MUCL 49410. Figure 41a and Movie 16, show a tip-to-tip anastomosis formation followed over a period of 100 h. Strikingly, the connection is made between an approaching hypha and a second hypha which is in the process of germination from an older hypha, rather than a fully developed hypha. The hypha approaching from the bottom side of the microscope image targets the germination site, hits it head on and fuses within the first about 30 h of the timelapse observation. The formation of a continuum becomes clear shortly after contact and even more so when phase-bright cellular contents are pushed into the newly attached hypha coming from the direction of the spore, transitioning through the fusion site (between timepoint 40 h and 80 h). Later, in conclusion of the unification process, multiple new

branches form, likely using the transferred cellular material. Figure 41b and Movie 17 show an example of a tip-to-side anastomosis. Here, a hypha approaches from the lower portion of the microscope image and connects laterally with the other hypha after only 4 h. In an instant, the hyphae fuse and a cytoplasmic continuum is established. Demonstrating that contact between hyphae not always leads to anastomosis formation, Figure 41c and Movie 18 show a hypha approaching and hitting another hypha laterally. Instead of opening the cell wall and merging, the approaching hypha starts retracting cytoplasm after about 6 h, forming two distinct septa. Moreover, the cytoplasmic retraction process seems to be disturbed, as the apical segment retains its cellular contents, while the second segment, between the two septa gets emptied. This indicates that a specific cross-talk is necessary between the hyphae in order to form a functional connection and mere contact does not suffice. In the case of insufficient signalling (or some sort of “anti-anastomosis” signal), hyphae simply cross-over and continue growing or as seen in Figure **41**c, interpret the other hypha as an insurmountable obstacle, arrest growth and retract cytoplasm (as described in *4.2.1 Space searching in AMF*). This observation of cytoplasmic retraction and septa formation is often used as a marker for unsuccessful anastomosis in fungi (Giovannetti *et al.*, 1999).

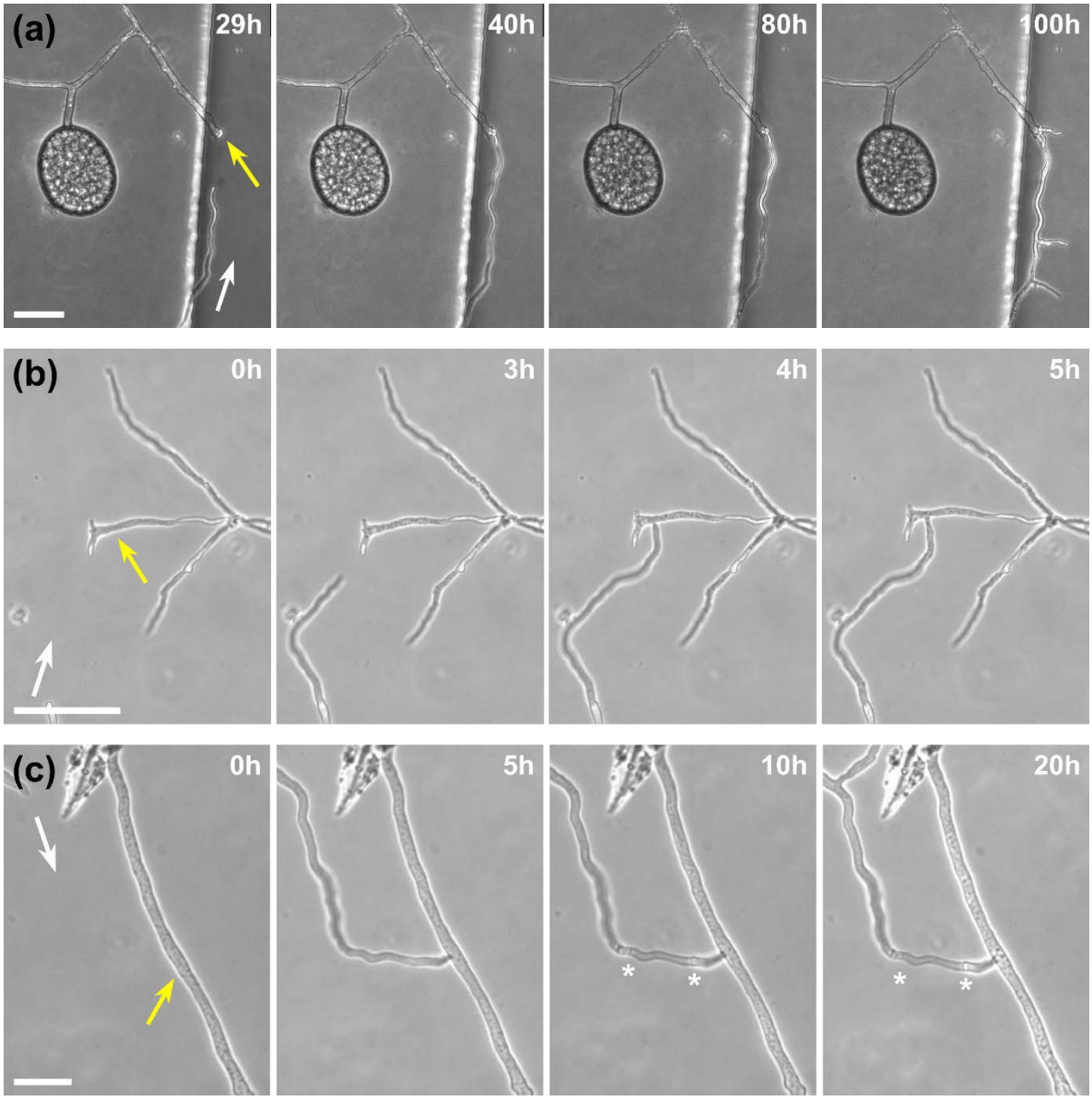


Figure 41: Anastomosis events in *Rhizophagus irregularis* MUCL 43194 in the *AMF-SporeChip*. (a) Phase contrast time series of tip-to-tip anastomosis forming between an approaching hypha and an older hypha about to germinate, over 100 h. Then, the formation of a continuum can be clearly observed, with cellular contents (phase-bright) being transferred from the spore into the newly attached hypha, followed by branching. (b) Phase contrast time series of tip-to-side anastomosis over 5 h. (c) Phase contrast time series of tip-to-side contact without anastomosis formation. Following the contact, the approaching hypha stops growing and retracts cytoplasm, forming an intermediate empty compartment. Yellow arrows indicate the contact site, white arrows show the growth direction of the approaching hypha. Asterisks in (c) highlight septa. Scale bars: (a) and (b) 50 µm; (c) 20 µm. Images and figure legend for (a) and (b) reproduced with modifications from Richter *et al.* (2024) with permission from the Creative Commons Attribution license (www.creativecommons.org/licenses/by/4.0/).

Clear indications of signalling involved prior to and during anastomosis formation between hyphae were further observed in Figure 42 and Movie 19. In this highly interesting observation, two hyphae approach each other from opposing sides at a distance of approximately 200 µm,

while occasionally arresting growth and readjusting growth direction in a peculiar stop-and-go manner, and finally anastomosing after about 21 h (Figure **42**a,b). A quantitative representation of this approaching phenomenon can be found in Figure 42c. The hypha on the left-hand side grows towards the other hypha in 4 main phases, interrupted by growth pauses. From beginning to end of the data recording, the covered distance as well as the duration of the growth phase decrease from a rate of about 0.3 µm/min for the first two and 0.1 µm/min for the latter two phases. In between, the hypha was found to pause growth, initially for ca. 3 h, then ca. 4 h and before the final growth phase <2 h. In contrast, the hypha on the right-hand side of the image barely grows at all and covers a total distance of only about 12 µm in the entire 21 h time period. It becomes evident from the observations how the left-hand side hypha, despite having an adequate amount of space to explore and avoid the other hypha, specifically directs its growth towards the hypha on the right-hand side, which would be impossible without signalling, decision-making and targeted searching prior to the anastomosis. The underlying mechanisms for these phenomena are widely unknown to date. For other filamentous fungi, the potential involvement of the signalling protein Soft and mitogen-activated protein kinases (MAPK), the latter also playing an important role in yeast mating signals, has been described (Fischer and Glass, 2019). The signalling cross-talk occurs in anti-phasic oscillations, to separate sending and receiving messages (Wernet *et al.*, 2023). The stop-and-go growth observed herein might be a symptom of such an intermittent dialogue, with similar proteins involved. Interestingly, for certain fungi, it has been reported that specialised hyphae are needed for anastomosis (Read *et al.*, 2009).

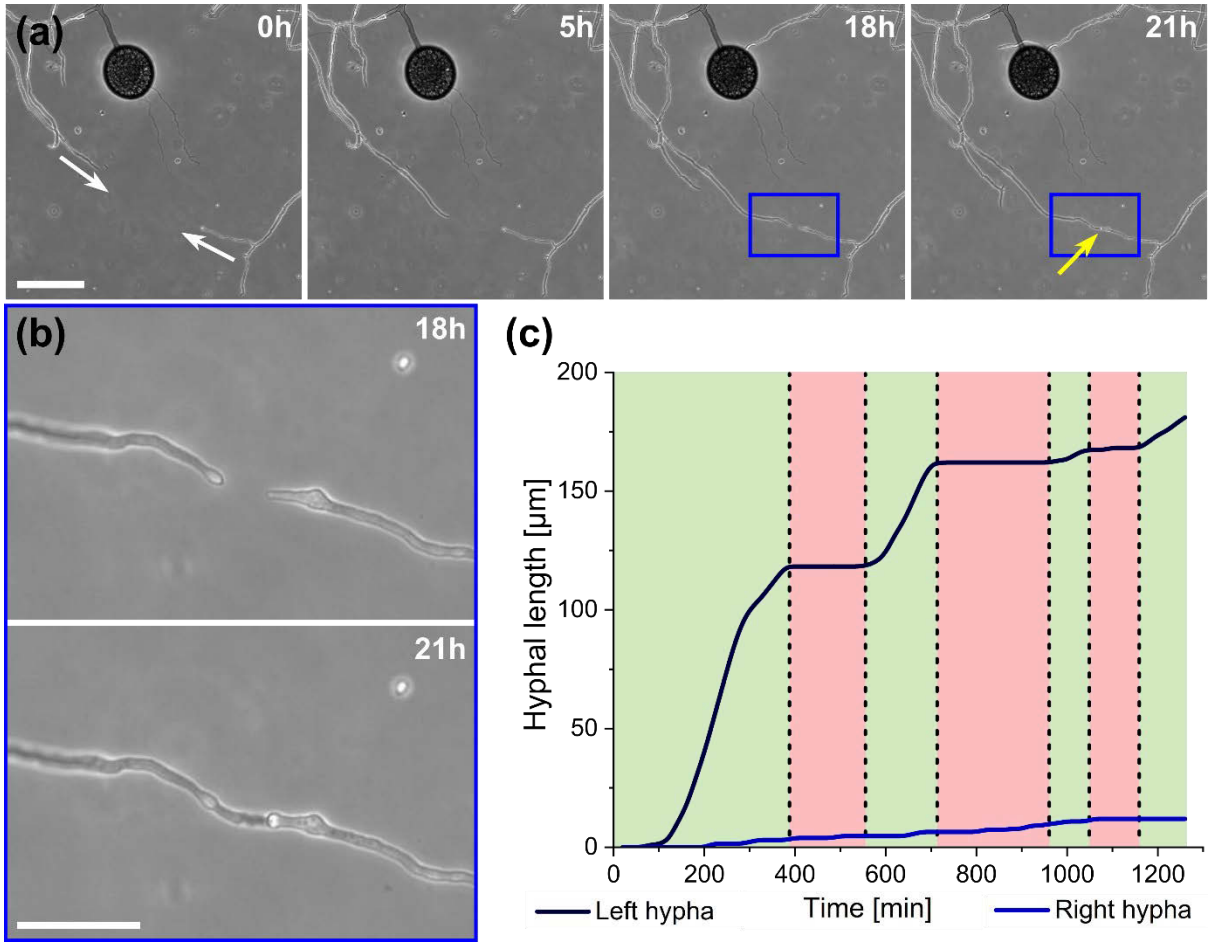


Figure 42: Anastomosis in *Rhizophagus irregularis* MUCL 43194 in the *AMF-SporeChip*. Phase contrast time series of tip-to-tip anastomosis. The left hypha approaches in a "stop-and-go" manner, while the right hypha hardly grows. Yellow arrows indicate the contact site, white arrows show the growth direction of the approaching hypha. (b) Focussed image of the time point just before and upon contact. (c) Graph showing the temporal growth pattern of the two hyphae. Scale bars: (a) 50 µm; (b) 25 µm. Images and figure legend reproduced with modifications from Richter *et al.* (2024) with permission from the Creative Commons Attribution license (www.creativecommons.org/licenses/by/4.0/).

To follow up on these findings, larger scale studies were envisioned. To this end, a new device, specifically tailored to accommodate two strains of *Rhizophagus* and encourage anastomosis formation, was developed. This forms the basis of the work detailed in Chapter 5.

The observed overall growth and space navigation behaviour of the AMF is of utmost peculiarity. Firstly, it has been shown that these fungi germinate reliably without a host or host exudates present, which sounds counterintuitive. As resources are significantly limited without a plant partner, it seems reckless to germinate without a host in close vicinity. However, the observations put this in context. Same as the extension reach of an AMF hypha, the range of plant signals is relatively short. If spore germination was only possible upon direct contact with

plant exudates, spores would need to be dispersed very close to the roots of a suitable host for successful establishment of a symbiosis, which would narrow the window considerably. Now, as spores are able to germinate without said exudates, germination occurs further away from the plant. The fungus then sparsely and dynamically starts exploring its surrounding, as described above, until it finds a root (unlikely in this scenario), or better, the hypha of another spore with which it can “partner up” through anastomosis, then the next one and so on and so forth. That way much larger distances can be covered and even the position of close-by plant could potentially be communicated through the network, thus raising the chances of encountering a host significantly. As spores can be generally expected to be dispersed in groups and anastomose frequently, such a scenario is very likely. The apparent randomness of the exploration in all directions increases the chances of finding a host or spore partner, trading off farther reach against higher spatial inclusiveness when no directional guidance (i.e. signal cue) present. Here, the cytoplasmic retraction, both reversible and irreversible, helps to repurpose and manage the limited resources available.

Even though the microfluidics approach made these intriguing observations possible and provided insight into AMF growth and space searching behaviour with an unprecedented clarity, it is not a perfect system and can only represent reality in a simplified manner. The confinement, enabling the high-resolution images presented, also eliminates the 3rd dimension, which of course is part of the real-life scenario, from the experimental set up. As the fungi are expected to navigate their habitat three-dimensionally, the hyphal reach is most likely much shorter than measured in the experiments, as more space is available to be explored. Furthermore, due to the spore loading process, all devices were saturated with medium, while the reality in soil is a patchy (temporally and spatially) mix of liquid- and air-filled pockets. With some modification of the method, this would be possible to replicate in the device, was however, not studied within the scope of the thesis.

4.3 Chapter conclusion

In this chapter, the main applications of the *AMF-SporeChip* were described and discussed. Firstly, the device was used to conduct a general examination of space searching behaviour in response to physical obstacles inside the devices with *Rhizophagus*. This was the first study of this kind on asymbiotic hyphae. The fungi displayed a range of strategies and growth behaviour varied strongly from hypha to hypha. The results were compared to observations reported for *N. crassa*, representative for higher filamentous fungi and were found to be somewhat similar. One observation, however, stood out as curious due to its novelty. Unlike the established mechanism of cytoplasmic retraction as part of a self-preservation response, an undescribed reversal of the process was found and analysed in this thesis. Details concerning speed and completeness of the process, as well as involvement of septa formation and breaching have been presented in this chapter. Thereafter, in order to prove that a retraction of the cytoplasm including all cellular contents had taken place, two fluorescent dyes, Calcofluor white and FM4-64, were utilised. This combination revealed the emptying of hyphae in static, endpoint microscopy images. Building upon these findings, FM4-64 was further intended to be used for a search for a Spitzenkörper in AMF. Therefore, the staining and imaging method was first established with two filamentous fungi, *R. solani* and *N. crassa*, and pictures of Spitzenkörper for both fungi were produced. Moreover, dynamic, live imaging was achieved for *N. crassa*. Eventually, the method was transferred to *Rhizophagus*. Here, however, it was found to be not applicable. Due to toxicity effects and low staining properties at smaller concentrations, no sufficient sub-cellular resolution was achieved and no sign of a Spitzenkörper detected. Any further advances on that front had to be ended at this point and other dyes were suggested. Besides the reversable cytoplasmic retraction, another important space navigation mechanism observed was anastomoses between hyphae. With the *AMF-SporeChip* it was possible to examine these fusion events in much detail and over a considerably wide area. Anastomosis types observed were both tip-to-tip and tip-to-side as well as “self-self“ and between hyphae originating from a different individuum (i.e., spore). Moreover, in one instance a peculiar “stop-and-go” approach prior to anastomosis formation was observed. Here, one hypha advanced towards the target partner hypha from afar with occasional stopping and readjustment of growth direction, indicating a signalling taking place.

These findings showed how effective the microfluidic approach is for detailed observations of these processes and the last observations further instigated the development of a new microfluidic device specifically tailored to the isolation and study of anastomosis events in AMF. The design and application of the anastomosis device are detailed in Chapter 5.

CHAPTER 5: ANASTOMOSIS DEVICE

5.1 Chapter overview

In this chapter, a new microfluidic device specifically for studying anastomosis events with AMF was developed. The requirements for the design were to allow for the introduction of spores of two AMF species at the same time and lanes that guide hyphae towards a central region where they would encounter each other and anastomose (or not). The device inoculation and spore immobilisation within the channels was based on the designs developed for the *AMF-SporeChip*. Flushing in the spores from opposing sides posed a major challenge, as the flow from the spore introduction of the second strain could cause the first strain to be flushed out of the device. A further requirement was to ensure isolation of single spores and therefore allow physically separation within the channels. In multiple iterative rounds of development, the interior channel layout, relative channel geometries and channel lengths were altered and tested. Each developmental round consisted of design conceptualisation, master mould fabrication, PDMS device manufacturing and spore introduction experiments. Coinciding with the general device development, the spore inoculation method had to be amended accordingly and optimised for spore dispersion, separation and, most importantly, how the flow affected any pre-introduced spores. Additionally, the possibility of multiplexing, with up to 4 devices combined in one, was trialled. After two initial test rounds of series of device models to get an idea about which design types were feasible, computational flow simulation using COMSOL was included in the examination. With this tool it was possible to fine-tune channel geometries and dimensions before manufacturing of a master mould. In turn, the *AMF-AnastomosisChip* was developed, sufficiently fulfilling all requirements, and anastomosis events were observed. It was hypothesised that the microfluidic device would allow for a precise positioning of spores in close proximity and thus significantly increase the anastomosis rate compared to plate-based methods. Later, as an additional feature to the device, the implementation of diffusion gradients for nutrients or effector substances was explored, using both COMSOL modelling and fluorescent microscopy on fluorescein gradients.

5.2 Results and Discussion

5.2.1. Device development

As discussed in the previous chapter, the ability of asymbiotic AMF hyphae to form networks via anastomoses is of the utmost importance for navigating soil and finding suitable hosts and thus their survival. A new microfluidic device specifically tailored for isolating and studying anastomoses was anticipated to allow for a more detailed examination of these fusion events and, moreover, different strains and species could be confronted with one another to evaluate whether and to which degree different AMF collaborate with each other.

The device designs were drawn, as before, on AutoCAD and based off the design of the *AMF-SporeChip* (see *CHAPTER 3: DEVELOPMENT OF THE AMF-SporeChip*). Generally, for the introduction of AMF into the device, spores were pipetted into the inlet and flushed into the main chamber of the device using a syringe equipped with tubing (as described in *3.2.1.3 Spore isolation and introduction into the device*). Spores then became trapped in the primary trapping region, i.e., loosely along the height transition interface between inlet channel and investigation zone, or clamped between PDMS and glass bottom in the secondary trapping region. Now, the new anastomosis device required a second group of spores (of the same or a different strain) to be introduced into the device, without removing the first spores from the device in the process. It was hypothesised that only spores firmly trapped in the secondary trapping region could possibly withstand a strong introduction flow from the opposing side, while spores loosely immobilised in the primary trapping region would be flushed out. Therefore, the new device would either need to rely fully on the secondary trapping region or on a diverted flow for the introduction of the second group of spores trapping was not efficient. To this end, in the first design round, a broad selection of device layouts, featuring different relative angles between the in- and outlet channels were made and assessed (Figure 43). Both lane-type and obstacle-type designs tested. The obstacles were limited to circular pillars (Ø = 140 µm), which were smaller than those accommodated in the *AMF-SporeChip*, with the main function of supporting the channel integrity to prevent collapse. Figure 43a,b show the first design type, which resembles the *AMF-SporeChip* but opened to both sides as inlets. Now, both ends feature an inlet channel of 100 µm height, transitioning into the 10 µm high

investigation zone. Here, the device was either equipped with an array of pillars (Figure 43b) or lanes that are 150 µm in width (Figure 43a). In Figure 43c,d, the same designs, both containing either lanes or pillars, were equipped with two outlets attached on both sides of the investigation zone in an attempt to guide flow away from the opposite inlet, thus relieving pressure. To theoretically allow a similar amount of flow through in- and outlet channels, the outlets were manufactured with a 100 µm channel height, as well. As the original, continuous lanes would obstruct the flow towards the outlets as well as create a bias towards the outermost lanes, an interruption of 300 µm in each of the lanes in the centre was implemented. For the designs shown in Figure 43e-g, only one outlet was added to the main channel, with varying relative angles between the inlet channels and the outlet, ranging from 90° (Figure 43e) to 135° (Figure 43g). In theory, the wider this angle, the better the flow gets deviated and the flow pressure onto the opposite inlet reduced. For the device with an angle of 105° (Figure 43f), the chamber wall connecting both inlets was pulled down slightly into the chamber to create a nose or invagination that could create a perpendicular stream towards the outlet which could function as a “blockade” against flow towards the opposite inlet.

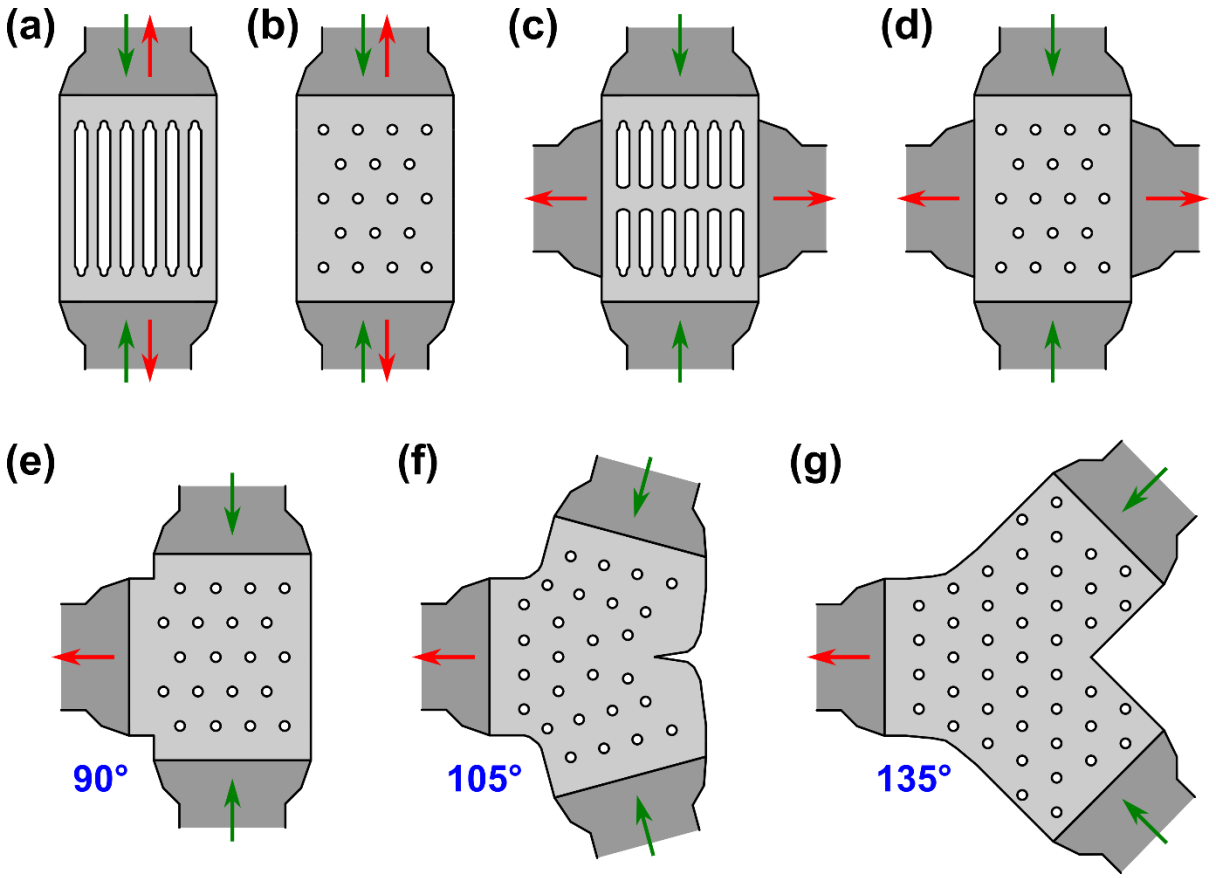


Figure 43: Schematics of the first prototypes of the *AMF-AnastomosisChip*. In blue, angles of the bent channels, measured between the outlet and an inlet, are shown. Dark grey indicates the inlet and outlet channels with channel heights of 100 µm and light grey a channel height of 10 µm. Green arrows point out the inlets, while red arrows highlight outlets.

The devices were manufactured using the protocols described in *2.1 PDMS device manufacturing*. Two *Rhizophagus* strains, *R. irregularis* MUCL 41833 and *R. irregularis* MUCL 43194 were used for the experiments. *R. irregularis* MUCL 41833 was flushed into the devices first, with a ratio of approximately 50:50 between the trapping in primary or secondary trapping region. This ratio is adjustable by varying the applied pressure, with high flow pressure resulting in more spores in the secondary trapping region and low pressure in spores positioning themselves along the height transition (primary trapping region). Then, the medium was pipetted out of the second inlet and the outlet(s), spores of *R. irregularis* MUCL 43194 transferred into the second inlet and flushed into the device. Spore loading, dispersion and the amount of spores flushed out were observed and examples of microscoped devices are shown in Figure 44.

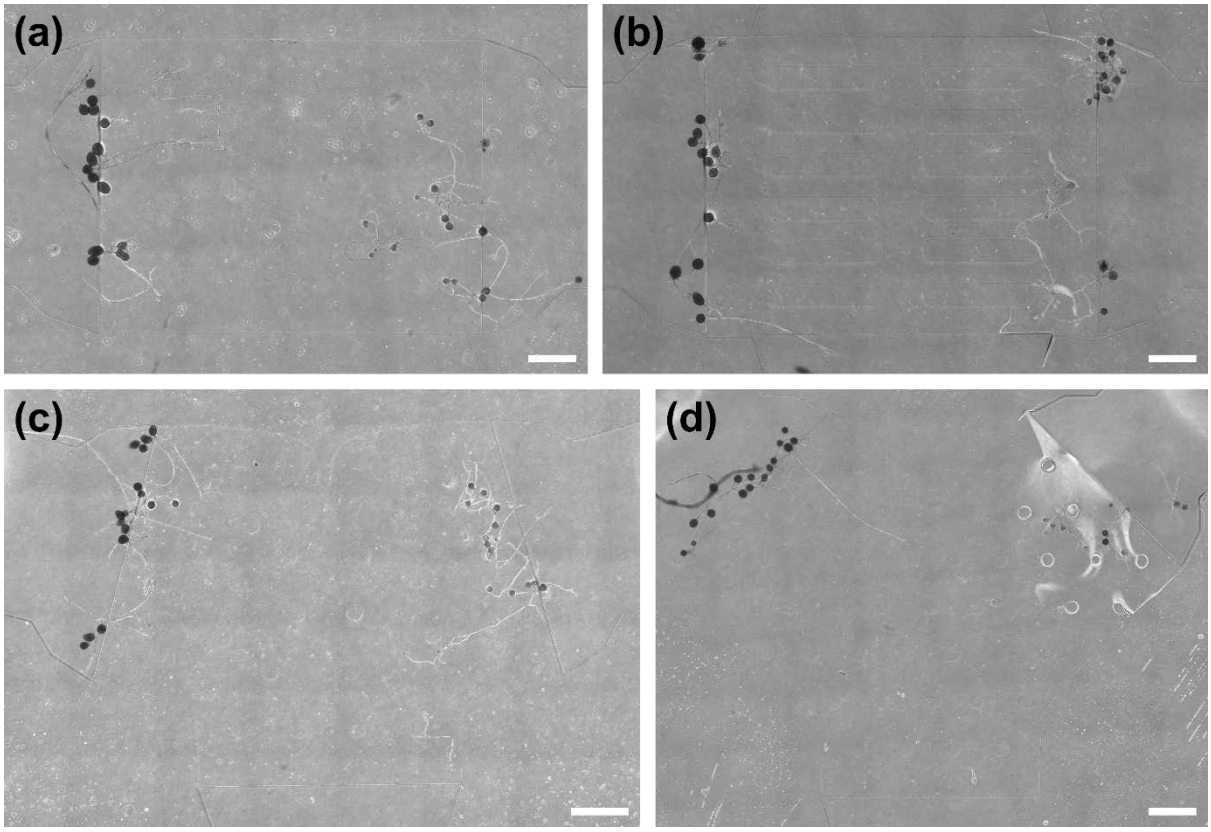


Figure 44: Spore loading performance of the first prototypes of the *AMF-AnastomosisChip*. Phase contrast images showing the spore distribution in a representative selection of devices of the first round of development after loading. Scale bars: 500 µm.

Spores of *R. irregularis* MUCL 41833 are smaller and of a less dark shade and can be found on the right-hand side inlet, while the spores of *R. irregularis* MUCL 43194 are larger and darker (left inlet). In general, the results with all designs were overall positive. After introducing the second strain into the device, spores of the first strain remained in position. This was mainly the case when spores were firmly trapped in the secondary trapping region. Most loosely trapped spores of the first strain in the primary trapping region were flushed out in nearly all designs, which was mainly expected with the basic design without any additional outlets (Figure 43a,b; Figure 44a) and with only one outlet attached in a 90° angle (Figure 43e). With two outlets (Figure 43c,d; Figure 44b), the flow towards the opposing inlet was indeed slightly relieved, allowing even loosely trapped spores to maintain their place. Due to the deviated flow, however, a slight loading bias towards the sides was introduced. The one-outlet design with an angle of 105° did not manage to re-direct the flow significantly, leading to the majority of loosely immobilised spores being flushed out (Figure 43f; Figure 44c) and only spores firmly trapped underneath the PDMS in the investigation zone remained. The invagination did not

produce the anticipated effect of a flow blockade, at least not sufficient enough to block flow from going towards the opposite inlet. With the wider angle of 135° (Figure 43g; Figure 44d), it was possible to re-direct a portion of the flow towards the outlet, away from the first inlet, leaving some loosely spores in the channels, suggesting that this layout could be a sensible base design moving forward, with room for improvement. Overall, utilising the secondary trapping method was a safe way to load both strains into the device. Furthermore, it was possible to re-direct flow away from the opposing inlet when using certain angles between the channels. While the loading worked well, the dispersion and especially separation of the spores was poor. As a requirement for the anastomosis device was to inoculate single spores in a physically separated manner from one another, the designs now had to be further modified.

In the second development round for the anastomosis device, solely lane-type designs were resorted to, as the obstacle-type channel layout was not able to produce sufficient separation of spores and hyphae. All designs developed in this round can be seen in Figure 45. The main idea behind the new designs was to create an array of lanes opening into pockets towards the respective inlet to capture single spores. Those spores would then germinate, forming hyphae that would grow and be guided by the lane that eventually opens into a central region (subsequently referred to as “hyphal interaction zone”) where contact with other hyphae of either the same strain (i.e., from the same device side) or the other strain from the opposite side of the device. To increase the chances of possible anastomoses by decreasing the distance between the two strains, the total length of the main interaction chamber was reduced (for the straight devices from 3000 µm to 2250 µm). The new designs were either a simple single channel system with directly opposing inlets and no additional outlets (Figure 45a-d) or a variation with two non-parallel inlets (with an enclosed angle of 90°) leading into a single outlet (Figure 45e-j). This Y-shape layout was meant to deviate the flow away from the inlets and was inspired by the device shown in Figure 43g, which produced the best results for spore loading in round 1. The width of the outlet was significantly reduced, to either 500 µm (Figure 45f,g,h,i) or 300 µm (Figure 45e,j). This reduction in size was meant to bring the terminal openings of the lanes closer together and thus hyphae within signalling range and recognition. As a smaller outlet size was expected to increase the fluid backpressure and thus have an adverse effect on the desired flow deviation away from the inlets, two widths were tested in

order to assess the magnitude of the effect. Similarly, two lane widths were tested with the wider being 150 µm and opening into a 230 µm broad half-circular pocket (Figure 45a-c,e,f,i,j), which in theory should allow one large spore to be captured comfortably, however, two or more smaller spores could also theoretically be trapped in the same pocket. The narrower variation featured a width of only 100 µm, opening into spike-shaped narrow pockets with a maximum space of 140 µm at the widest point (Figure 45d,g,h), which was expected to fit a single spore of the majority of the measured spore diameters. For both lane widths, besides the outlet size (see above), the position of the pockets was varied by extending the lanes all the way up to height transition or even beyond. While the designs shown in Figure 45a,i,j (lanes directly adjacent to the transition line) and Figure 45c (lanes end inside the investigation zone with ~140 µm to the transition line) were expected to retain the possibility of a more rigid spore trapping between channel ceiling and bottom, as described above, this would be entirely lost with the designs shown in Figure 45b,d-g. Here, the lanes extend beyond the transition line and thus the pocket portions of the lanes possess a channel height of 100 µm. This removed the secondary trapping mechanism entirely, only allowing for a loose capturing of the spores in the pockets, however, it was expected to improve the spore dispersion.

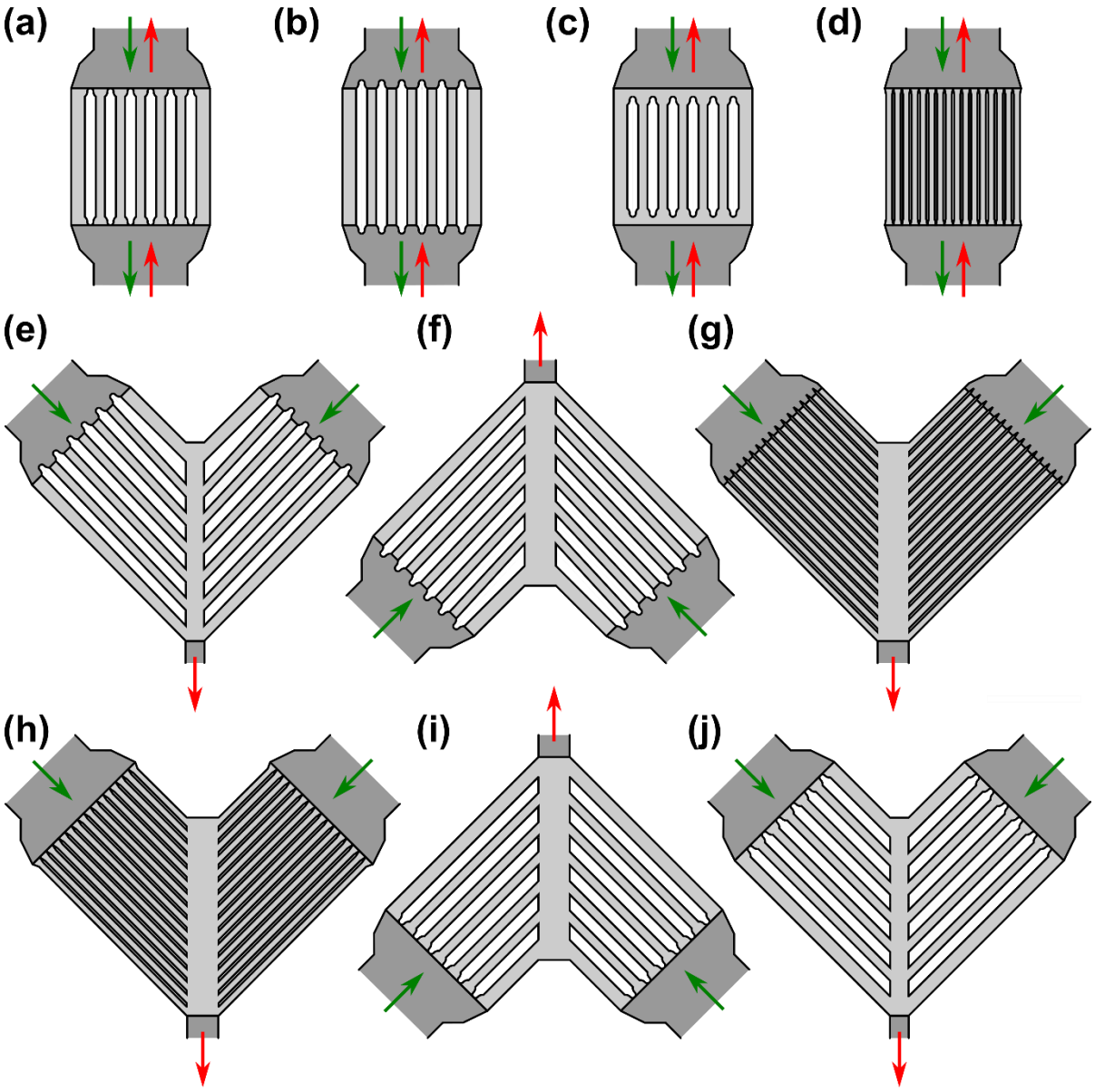


Figure 45: Schematics of the second prototypes of the *AMF-AnastomosisChip*. Dark grey indicates the inlet and outlet channels with channel heights of 100 µm and light grey a channel height of 10 µm. Green arrows point out the inlets, while red arrows highlight outlets.

The devices were then manufactured, loaded with both *Rhizophagus* strains, *R. irregularis* MUCL 41833 (on the right-hand side inlet) and *R. irregularis* MUCL 43194 (on the left-hand side inlet), as described above for development round 1, and assessed on spore loading and dispersion performance. Here, increased caution was taken in picking only single spores for the experiments. Exemplary microscopy images of the obtained outcomes are shown in Figure 46 and Figure 47. As expected, the designs without an extra outlet did not produce very positive results. With the lanes extended into the primary trapping region, and pockets with a height of 100 µm (Figure 45b), the introduction of the first strain was smooth and with a decent

control over the spore distribution, however, when flushing in the second strain, all initial spores got expulsed from the channel without exception. In the same way, the device variation with narrower lanes (Figure 45d), did not hold any spore of the first strain in place, as it proved virtually impossible for spores to enter the pockets. As formerly discussed, the hyphal remnants attached to the spores, render the effective diameter of the spores generally larger, moreover, along with its flow behaviour, unpredictable. A similar outcome was observed using the design with lanes extending to the height transition line (Figure 45a; Figure 46a). Generally, spores were not able to enter the pockets, as the rigid design significantly reduced the flexibility of the PDMS channel ceiling and as a consequence got flushed out of the channel. Only occasionally, smaller spores managed to enter the pockets and now tightly trapped, were able to resist the flow and remained in place. When the lanes ended before the transition line and the pockets were located well within the investigation zone (Figure 45c), high channel expandability was retained and spores got trapped regularly to withstand flow. This, however, prohibited achieving good homogeneous spore dispersion (Figure 46b). Spores of strain 2 (left-hand side) were not able to enter the pockets and/or the investigation zone. This is the result of caution taken with the introduction of strain 2 to prevent expulsion of the first strain. Even though these spores got trapped considerably tightly, a strong pressure - strong enough to force strain 2 into the pockets - would lift up the PDMS ceiling and flush out all spores of strain 1.

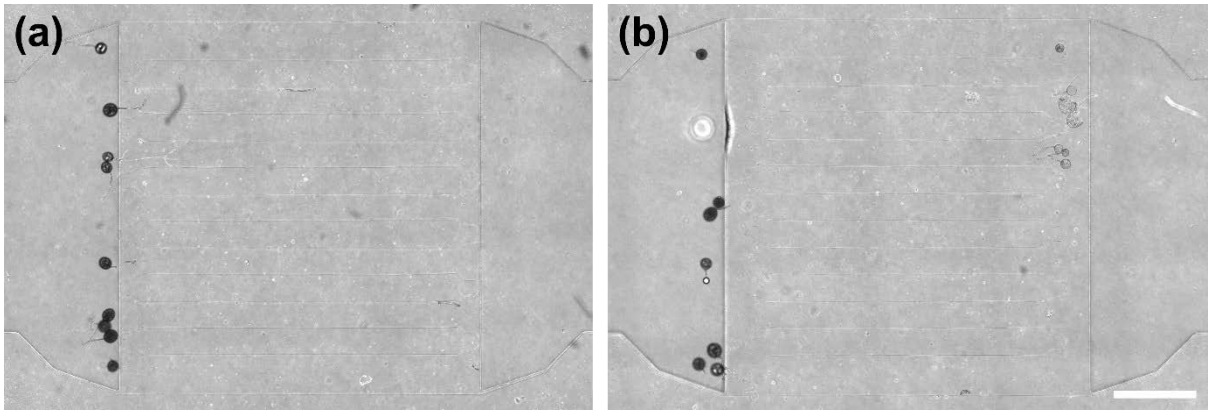


Figure 46: Spore loading performance of the second prototypes of the *AMF-AnastomosisChip*. Phase contrast images showing the spore distribution in straight-channel devices of the second round of development after loading. Scale bars: 500 µm.

In contrast, the Y-shaped designs were anticipated to allow for an improved spore loading, and while all showed improved flow profiles with a significant re-direction towards the outlet and thus reduced fluid pressure towards the opposing inlet, the success was found to be highly variable and dependent on details. The first observation made and confirming the findings from the straight devices described above was that the narrower lanes and pockets proved to be too narrow for most spores. The version with the pockets protruding out of the investigation zone allowed for the occasional small spore to get captured (Figure 45g; Figure 46; Figure 47a), while for the version with the lanes ending at the transition line (Figure 45h) the pockets were entirely inaccessible. Good spore loading was achieved with all designs containing wide lanes and pockets (Figure 45e,f,i,j), although, again, when the pockets were located inside of the investigation zone, spores were rarely able to enter and get captured. Figure 47b shows spores aligning along the height transition line, even positioning themselves in front of the pockets, however not managing to actually access the pockets. The most promising designs tested featured wide lanes with pockets protruding beyond the transition line into inlet region with a channel height of 100 µm (Figure 45e,f; Figure 47; Figure 45c). Here, spore loading and equal distribution over the pockets was well controllable and many single spores got and remained captured in separate pockets, as a considerable portion of the flow was deviated away from the opposing inlet with spores of the first strain towards the outlet. The last aspect tested here was the effect of the centre width, i.e., distance between the lane ends. It was found that the reduced width of 300 µm (Figure 45e,j) provoked a higher flow pressure towards the inlet compared to a width of 500 µm (Figure 45f,i; Figure 47c), thus causing more spores to get flushed out. As 500 µm was still deemed a reasonable distance for hyphae to cover and to initiate contact, this layout was used moving forward. Despite this progress and result, a considerable amount of flow was still going towards the inlet.

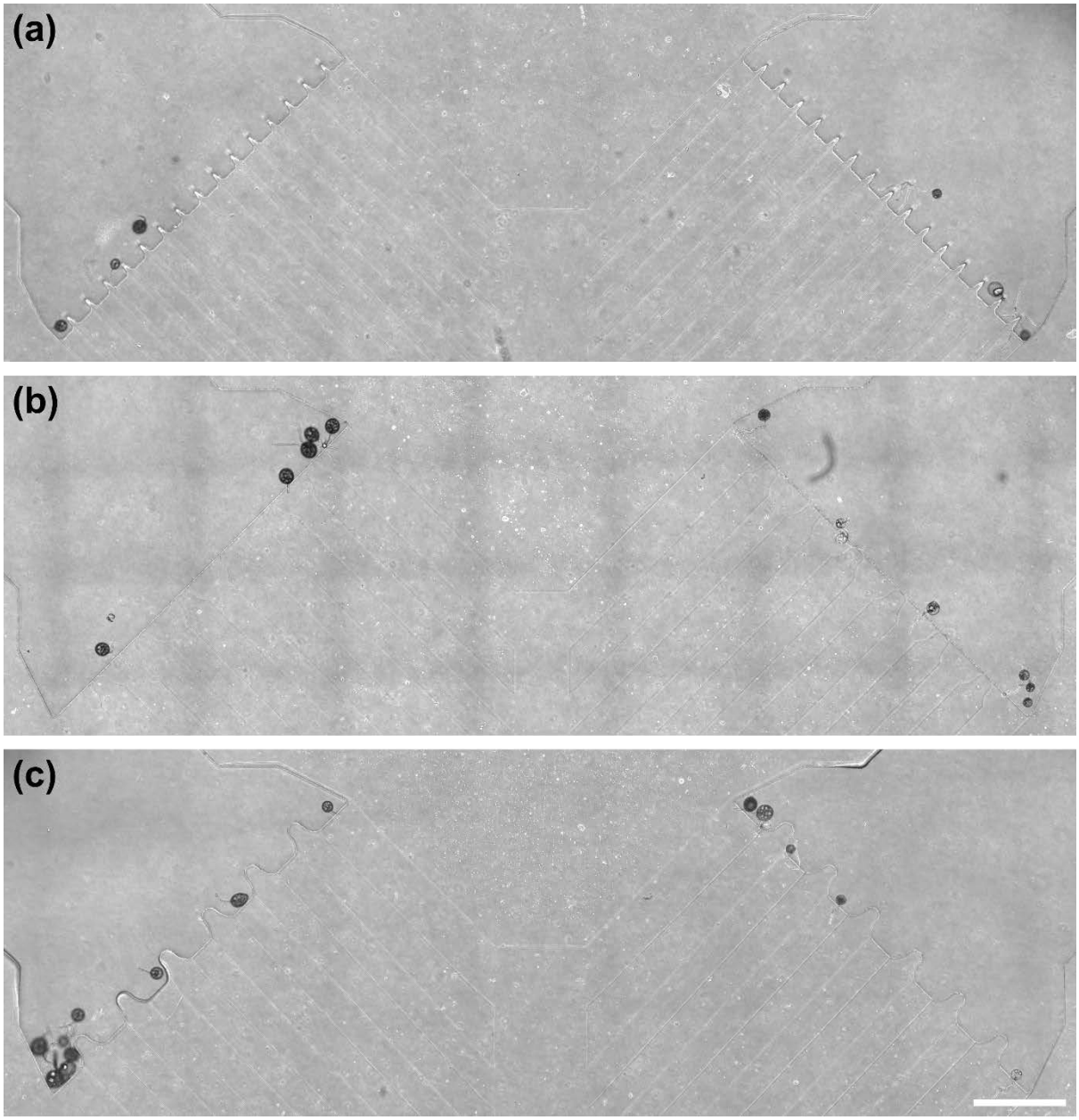


Figure 47: Spore loading performance of the second prototypes of the *AMF-AnastomosisChip*. Phase contrast images showing the spore distribution in Y-shaped devices of the second round of development after loading. Scale bars: 500 µm.

As it was found that in order to compel with the required single spore dispersion over the pockets only loose capturing rather than fixed clamping between PDMS and glass bottom was possible, and thus a small percentage of spores still got flushed out, a further reduction of flow towards the inlet was needed. Therefore, a third round of further development, based on the design shown in Figure 45f was performed. In this batch of new device designs, the inlets were bent down in a way that the inlets were facing each other in parallel, making the former Y-

shape of the device now resembled a bird in flight. An exemplary assortment of the designs is shown in Figure 48.

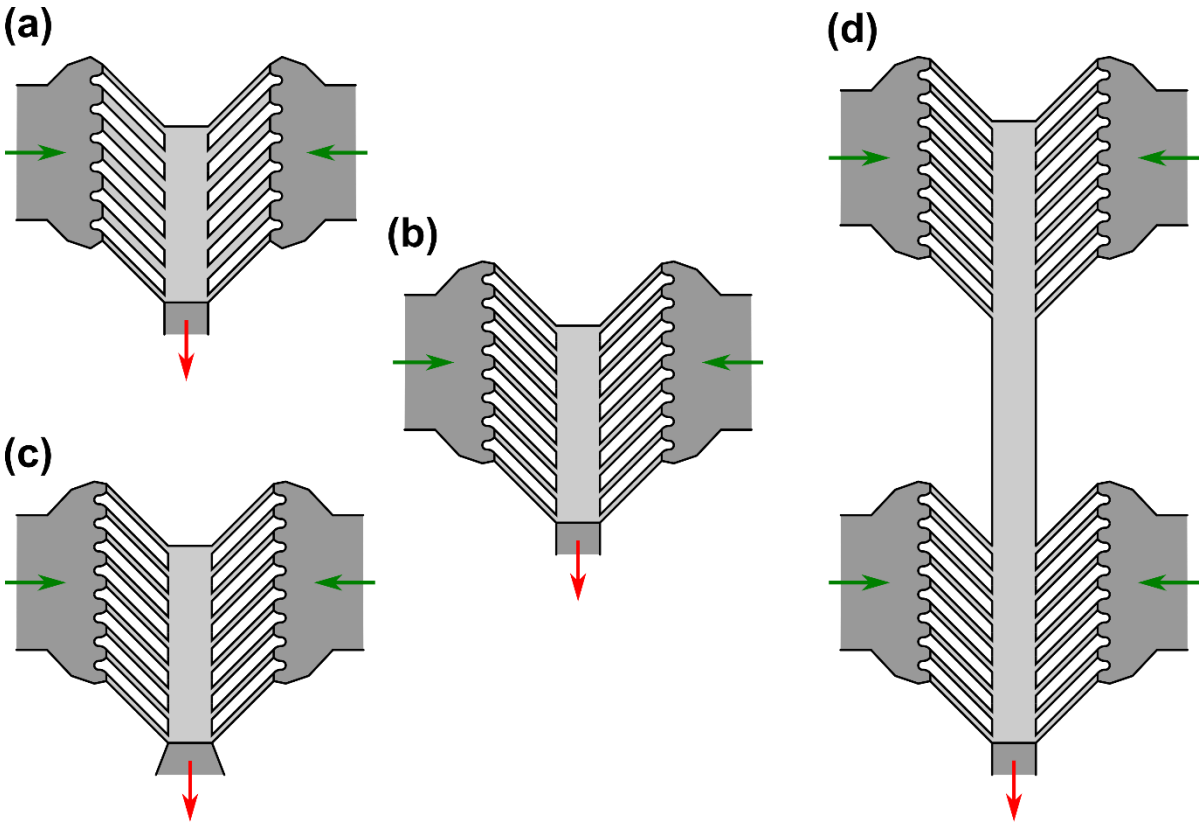


Figure 48: Schematics of the third prototypes of the *AMF-AnastomosisChip*. Dark grey indicates the inlet and outlet channels with channel heights of 100 µm and light grey a channel height of 10 µm. Green arrows point out the inlets, while red arrows highlight outlets.

Only the lane portion of the device was still bent in a 45° angle, guiding both flow and hyphae towards the centre and the outlet. This was not only expected to bring about a continued improvement of the flow profile, furthering the bias towards the outlet rather than the inlet, but also to equalise the lengths of the lanes to 1000 µm. With the former Y-shaped design, the lanes varied immensely in length, ranging from 1200 µm in the topmost lane to almost 3500 µm in the bottom lane, thus rendering conditions and changes for encounters highly inhomogeneous. Moreover, in the entirety of experiments conducted in the course of this project, only a very small minority of hyphae were observed to travel as far as 3000 µm or further inside of a microfluidic device (see *3.2.2.2 Spore germination and hyphal growth behaviour in the confined environment*). Besides these changes in overall device shape and relative inlet position, the dimensions of the design were kept the same. As the narrow lane

version of the device in round 2 was found to be inaccessible for most spores, however, pockets of the wider lane version were able to comfortably fit two or more spores at the same time, it was decided to further modify the lanes in an attempt to find a compromise between both extremes (Figure 45f,g). It was concluded that the main issue with the narrow lane design were the pocket size and shape. Therefore, the lane widths were reduced from 150 µm to 90 µm and the pocket maximum size from 230 µm to 170 µm. That way, the actual lane width, as seen in Figure 48b,c was even smaller than before in the narrow-lane devices (Figure 45d,g,h; 100 µm), while the pockets were larger (140 µm in the narrow-lane devices). This changed the number of lanes from 7 in the wide-lane designs to 9 on each side (16 in the narrow-lane device). Furthermore, the lane widths were equalised in the process. The design in Figure 48a still featured 7 lanes of the same width as before, with, however, narrower outermost lanes compared to the rest of the lanes, mainly impacting the flow behaviour in the device. Figure 48c shows a version of the design with an outlet widening in a tapered manner, which was expected to increase the flow bias further towards the outlet. In an addition to this round of development, multiplexing devices were introduced. Therefore, the device designs were connected to form double-channel (Figure 48d) as well as 4-channel devices. These devices comprised either of the designs shown in Figure 48a,b and were meant to improve imaging throughput and capacities. In the most space-economic way, this allowed for multi-ROI (region of interest) timelapse microscopy and thus significantly increasing the chances of observing anastomoses in real-time. These larger devices were bonded into FluoroDish glass-bottomed petri dishes with a glass diameter of 35 mm (50 mm outer diameter). The 4-channel device was very similar to the double-channel device and is not further discussed herein.

At this point, the possibility of computational modelling of the flow behaviour in the devices arose. With the help of a colleague (PhD student, Kate Collins), the designs were fed into a COMSOL model. To facilitate the processing, the device designs had to be simplified. Therefore, the pockets featuring round shapes were replaced by simple triangles. It was assumed that the flow profile would not be significantly impacted by the modification. As model scenario, a flow pulse with an amplitude of 0.2 ml/s from the left-hand inlet was chosen (representing the second spore loading). As the spore introduction is performed by hand (described above), this can only be a rough estimate. Additionally, the design shown in Figure

45f was modelled retroactively, to be able to compare the impact of the changes made in round 3 of the development on the flow profile. The results of the modelling can be found in Figure 49 and Figure 50.

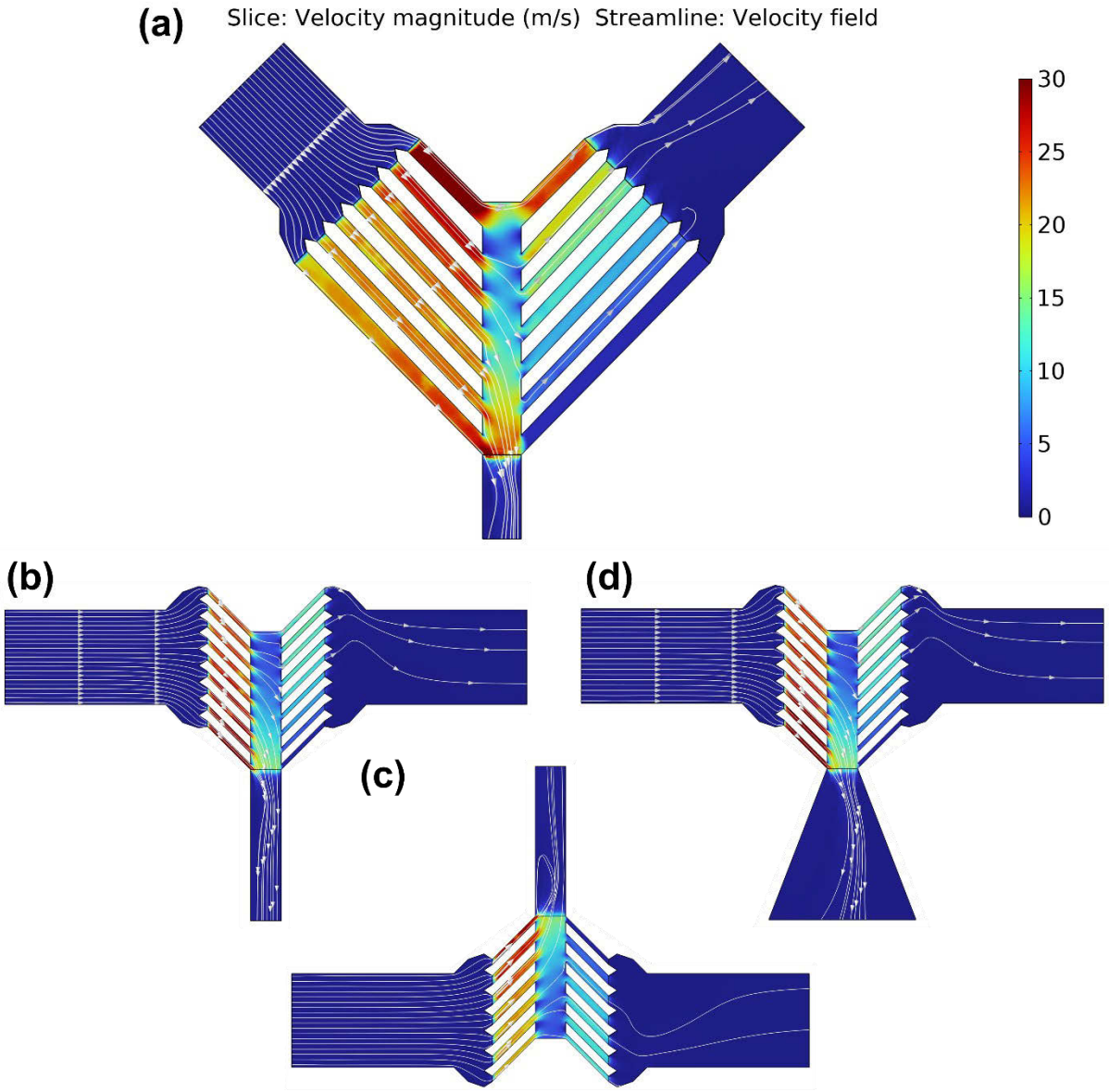


Figure 49: COMSOL modelling of flow in prototypes of the *AMF-AnastomosisChip*. Modelled were in (a) a Y-shape design of the second prototypes and in (c) the single channel designs of the third prototypes. In the model scenario, a flow of 0.2 ml/s is introduced from the left inlet into the devices. White lines with arrows represent the velocity field and the colour code indicates the velocity magnitude in m/s, with dark red equalling 30 m/s and dark blue 0 m/s.

The images represent the flow profile in the form of a heat map as well as with streamlines. A red colour and a high density of streamlines indicate high flow pressure, whereas blue and low-density streamlines symbolise low flow pressure. The modelling results suggest that the

modifications made in round 3 of the development improved the flow profile for the single devices by guiding the flow towards the outlet rather than the opposite inlet, as indicated by only 3 streamlines in all round 3 designs (Figure 49b-d) and a few more streamlines observed with the round 2 device (Figure 49a). Furthermore, the modelling for the round 2 device shows a very high flow velocity in the upper lanes (red colours). A comparison between the 3 individual designs of round 3 did not show any significant differences.

The flow behaviour in the double-channel device was modelled for each individual channel (Figure 50). Here, only in the lowest channel, directly opening into the outlet, the flow pressure in the opposite inlet was low, while high pressure (red colours) was suggested for the upper channel. This is most likely due to the higher backpressure from the narrow neighbouring channels while the lowest channel opens into the outlet with 100 µm channel height. Furthermore, the model revealed flow down into the adjacent channel.

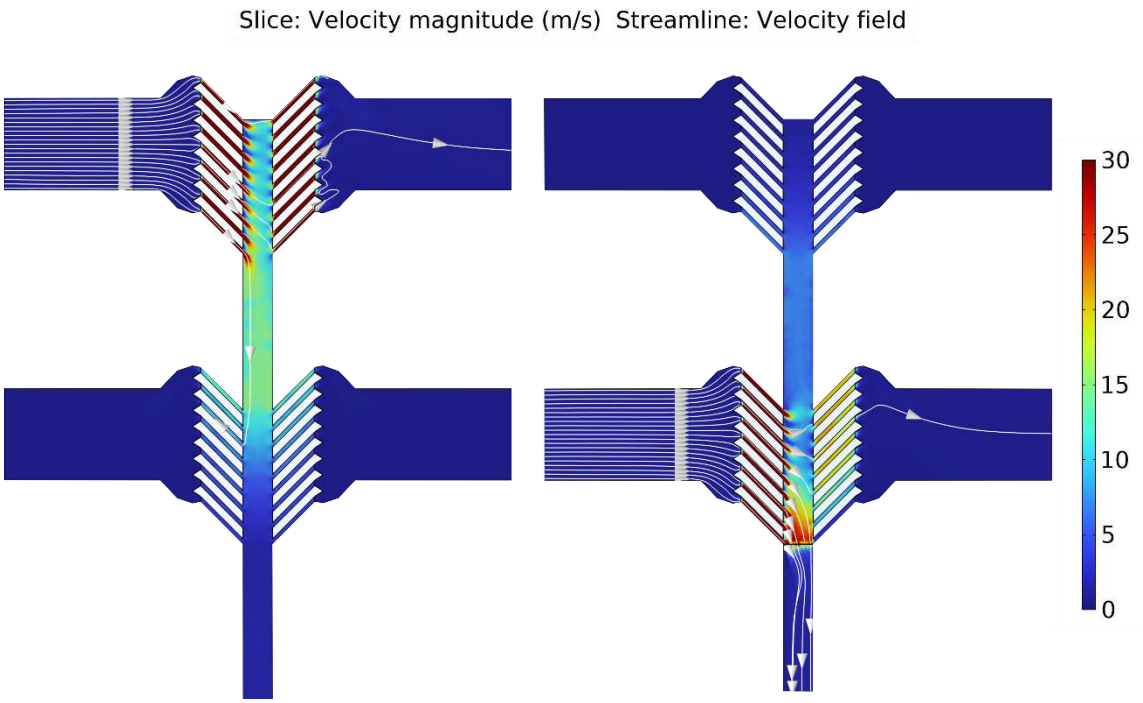


Figure 50: COMSOL modelling of flow in prototypes of the *AMF-AnastomosisChip*. Modelled were the double-channel designs of the third prototypes. In the model scenario, a flow of 0.2 ml/s is introduced from the top left inlet (left) and bottom left inlet (right) into the devices. White lines with arrows represent the velocity field and the colour code indicates the velocity magnitude in m/s, with dark red equalling 30 m/s and dark blue 0 m/s.

As most of the modelling, however, provided promising results and suggested an improvement of the designs, the devices were manufactured and assessed on real-life spore loading and

dispersion performance. Therefore, the devices were once more loaded with *R. irregularis* MUCL 41833 (on the right-hand side inlet) and *R. irregularis* MUCL 43194 (on the left-hand side inlet), as described for rounds 1 and 2. Indeed, the modelled prognosis could be corroborated and the spore loading was improved. With all single channel devices, only few spores of the first strain were flushed out when introducing the second strain from the left inlet, resulting in better spore numbers and dispersion (Figure 51). No significant differences were observed between the design featuring fewer and wider lanes (Figure 51) and the design with more and narrower lanes (Figure 51b), however, a slightly better separation of the spores can be achieved. Similarly, the tapered outlet channel did not show an improved flow re-direction compared to the regular straight outlet channel design. The double-channel device performed even worse than expected from the modelling. When introducing spores, all spores immobilised in any of the adjacent channels, on both left and right-hand sides, were flushed out. As a result, only one pocket array remained filled after finishing loading spores.

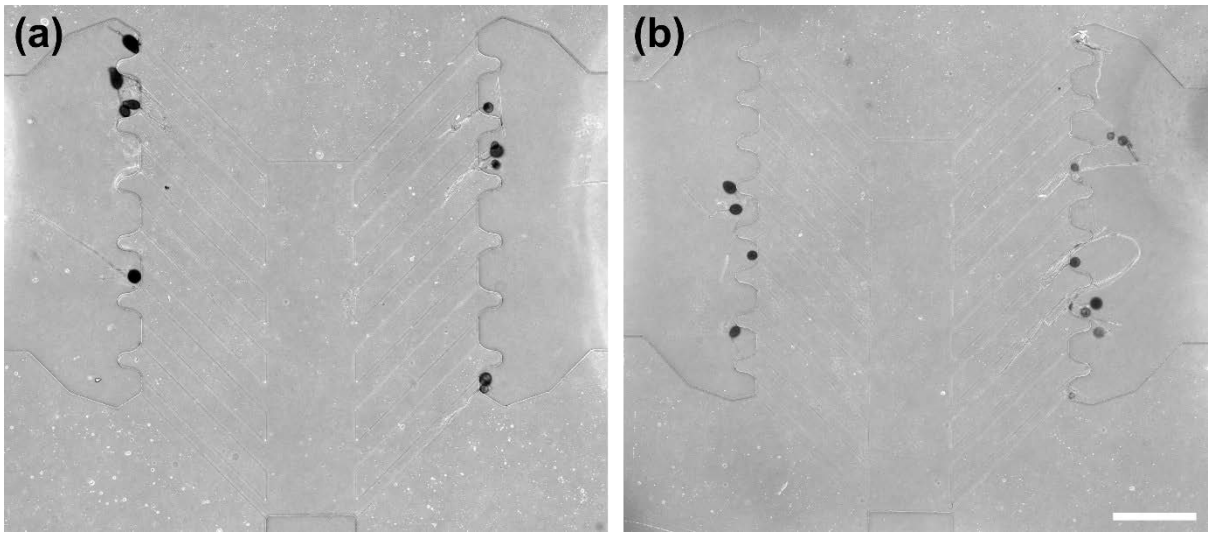


Figure 51: Spore loading performance of the third prototypes of the *AMF-AnastomosisChip*. Phase contrast images comparing the spore distribution in (a) the design with fewer and wider lanes and (b) the design with more and narrower lanes of the third round of development after loading. Scale bars: 500 µm.

Even though a significant improvement of the single channel designs was achieved in this round, still around 30-50% of the initially loaded spores of the first strain were removed from the channels when flushing in the second strain. To exploit the full potential of the devices, first, before once more changing the design, several tests concerning the loading method were conducted. In the previous experiments, the first strain was flushed in using a syringe equipped

with tubing, the syringe was unplugged from the inlet, liquid was pipetted out of the second inlet and outlet, spores of strain 2 were pipetted into the second inlet and flushed into the device using the syringe again, and no particular attention was paid to details. Besides spores getting pushed out of the pockets or the device altogether when flushing in the other strain, spores sometimes drifted out of the pockets and back into the inlet when pulling out the tubing. Therefore, as a first optimisation of the method, the syringe was left inside of the inlet for about 1 min after loading of the spores was finished to allow for the pressure to equilibrate, before carefully pulling it out. This improved both the loading of the first strain as well as the second strain.

Furthermore, the possibility of sealing off the first inlet before introducing the second strain was explored. Therefore, PDMS plugs, which were punched out from in- and outlets in the device manufacturing process, were kept and used to close off the inlet after finished introduction of strain 1. At first, huge air pockets were created when inserting the plug into the inlet. As air is compressible, other than the aqueous medium, this air bubble acted as a spring and made the spores bounce around and lose their position in the lane pockets when flushing in the second strain or pulling out the tubing. Removing the air bubble by sucking from the opposite side with the syringe proved to be impossible and some air always remained, continuously re-entering through tiny gaps between inlet wall and the PDMS plug or even through the PDMS itself. This issue could be eliminated by overfilling inlet 1 with medium before inserting the PDMS plug, and no air pocket was created. Due to the flexibility of the PDMS, however, spores were still found to bounce around occasionally when introducing strain 2.

Introducing both strains at the same time through two inputs simultaneously was not feasible for several reasons. As discussed before, flushing spores into a device was not feasible with a syringe pump as it would reduce throughput and more importantly control over the spore introduction and dispersal within the device. Furthermore, often an irregularly pulsating flow was necessary to introduce spores as they tend to get stuck or tangle up due to their irregular shapes and hyphal remnants. Now, in order to load both sides of the *AMF-AnastomosisChip*, handling two syringes at the same time would be less of a problem but applying the same pressure with both hands would be impossible. Moreover, with no hand free to hold down the

device onto the stereoscope stage, the device would need to be fixed to the stage, e.g., with tape, rendering the method more tedious and time-consuming.

Instead, introducing the spores by sucking from the outlet was tested. Therefore, after introducing strain 1, liquid was pipetted out of inlet 2, spores of strain 2 were pipetted in, liquid was pipetted out of the outlet, a syringe was plugged in and a negative pressure was built up with the syringe. The syringe should be slightly filled with medium and air should be avoided as it would act as a buffer and reduce the control over the suction. This approach proved to be highly promising and no spores of the first strain were removed. As a small drawback, the suction method introduces a bias towards the lower pockets when loading strain 2 (Figure 52), i.e., the topmost pockets often remained unfilled with spores, which is why strain 1 was continued to be pushed in rather than sucked in. Often, in order to get all spores into the pockets, the entire medium has to be sucked through, resulting in air-filled channels (spores tend to follow the liquid front at the air-liquid interface). Then, the syringe is left plugged in and fresh medium is pipetted into both inlets. Here, again, the system was left to equilibrate for about 1 min before unplugging the syringe, in order to avoid spores bouncing out of the pockets.

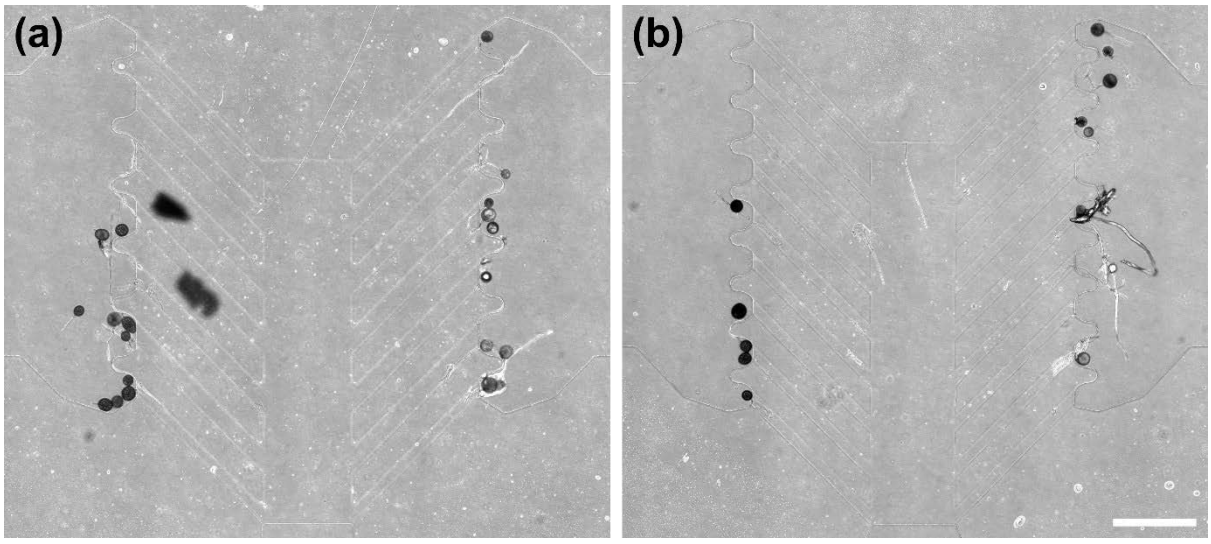


Figure 52: Spore loading performance of the third prototypes of the *AMF-AnastomosisChip* after optimisation of the loading protocol. Phase contrast images showing the spore distribution in the design with 9 narrow lanes of the third round of development after improved loading with the suction method. Scale bars: 500 µm.

This method, involving introduction of strain 1 in the classical pumping manner, followed by strain 2 introduced by suction, was deemed most effective. For further improvement of the spore loading and dispersion it was found that by tilting the device towards the top and tapping it against the surface while sucking helps usher spores into the top pockets, thus reducing the introduction bias towards the lower pockets. Furthermore, after concluded spore introduction, pulling out the tubing from the inlet while bending it down over the device edge, thus segregating the contents of the tip of the tubing from the syringe, keeps spores from bouncing around and the 1 min waiting time for pressure equilibration is not needed. From then on, the procedure was established as standard method for spore introduction into the *AMF-AnastomosisChip*. In general, the loading performance is furthermore greatly dependent on the spore material and best results can be achieved with truly single spores with short hyphal remnants (100-200 µm). Larger spore clusters, long hyphal remnants and hyphal debris interfere strongly with the loading by blocking pockets or acting as flow guides (very long hyphae) thus causing spores to aggregate instead of dispersing. Unfortunately, this cannot always be avoided, as some hyphae, be as hyphal remnant or debris, are invisible under the stereoscope and are only revealed after the final loading under the microscope.

For the final device design, the design shown in Figure 48b was slightly modified. To increase the chances of interaction between strain 1 and 2, the length of the lanes was reduced from 1000 µm to 500 µm, thus halving the distance to be covered by the hyphae. Even though several hyphae managed to reach lengths of 3 mm or more throughout the experiments, the majority of hyphae did not grow beyond 0.5 mm in the devices (see Figure 19 and Figure 38). With this final design of the *AMF-AnastomosisChip* and the improved spore loading technique, good results for introducing two AMF strains into the channels were achieved. The final design schematics and a representative microscopy image showing the spore distribution within the pockets can be found in Figure 53.

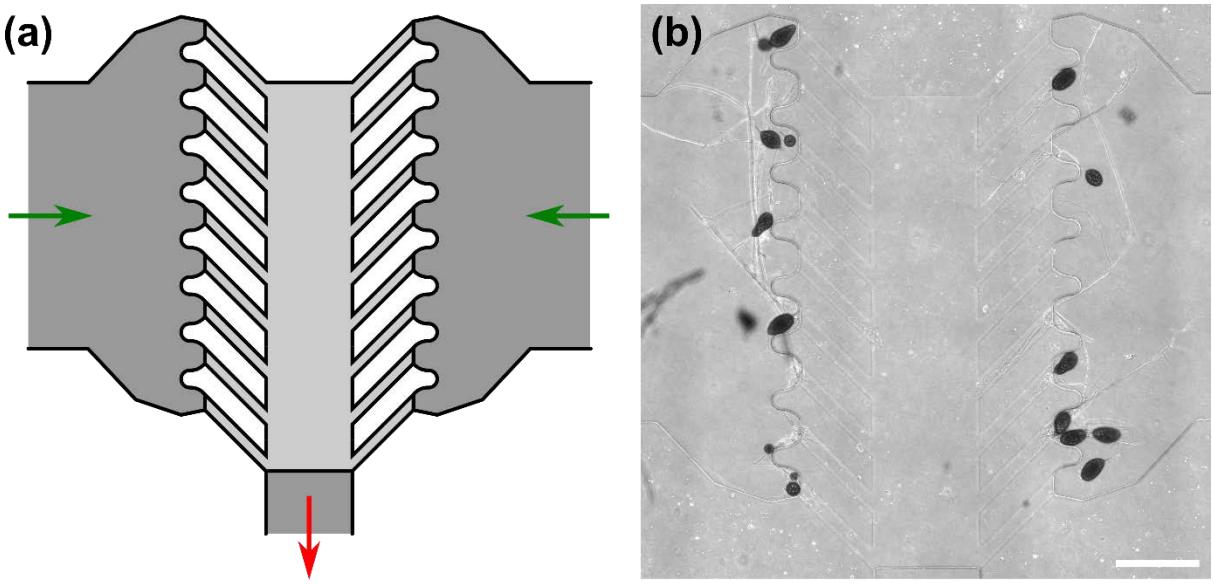


Figure 53: Final design and loading performance of the *AMF-AnastomosisChip*. (a) Schematics of the final design with lanes reduced to 500 µm length. Dark grey indicates the inlet and outlet channels with channel heights of 100 µm and light grey a channel height of 10 µm. Green arrows point out the inlets, while red arrows highlight the outlet. (b) Phase contrast image showing the spore distribution in the final design version. Scale bar: 400 µm.

5.2.2 Spore loading and growth performance in the *AMF-AnastomosisChip*

To examine the behaviour of the fungi within the *AMF-AnastomosisChip*, 20 devices were loaded as described in the above section with liquid MSR(-) medium and incubated at 27 °C (both sides loaded with *R. irregularis* MUCL 43194). The devices were observed (Eclipse Ti-U, Nikon, see *2.3 Microscopy and image processing*) daily until 13 days post inoculation (dpi), as well as at 27 and 36 dpi.

Firstly, to characterise the functionality of the microfluidic device, numbers of pockets holding spores were recorded (n = 18 per device, 9 left (L), 9 right (R), with increasing numeration from 1 to 9 towards the device outlet), represented as “Loaded pockets” per device in Figure 54a, as well as numbers of spores per respective pocket were counted, represented as “Average spores per loaded pocket” per device in Figure 54b. All spores sitting inside of the pocket, even if only slightly, were included. Spores situated outside the pocket, without direct contact to the other spores but possessing a subtending hypha in the respective pocket, were added as 0.5 towards the count. To reveal any loading bias for the pockets, the total instances of a respective pocket filled by pocket name (e.g., 1R or 7L) are shown in Figure 54c. A count of 20 would signify that this pocket had been filled each time in every single device. In Figure 54d, the total

instances per device side were summed up over all 20 devices, to account for any side-related loading bias. The maximum achievable count here is 180 (9 pockets per side * 20 devices). Figure 54e shows the same result but as an average over all devices. Furthermore, the orientation of the spores within the pocket was analysed, i.e., whether the subtending hypha was pointing into the pocket and lane or away from it (Figure 54f). The plotted y-values are derived from the difference between the IN and OUT count, e.g., if out of a total of 3 spores in a pocket 2 were pointing inwards and one spore outwards, this was recorded as 1, similarly, if 2 spores were pointing inwards and 3 outwards, this was recorded as -1. Again, these results were plotted as the average over all pockets of a device.

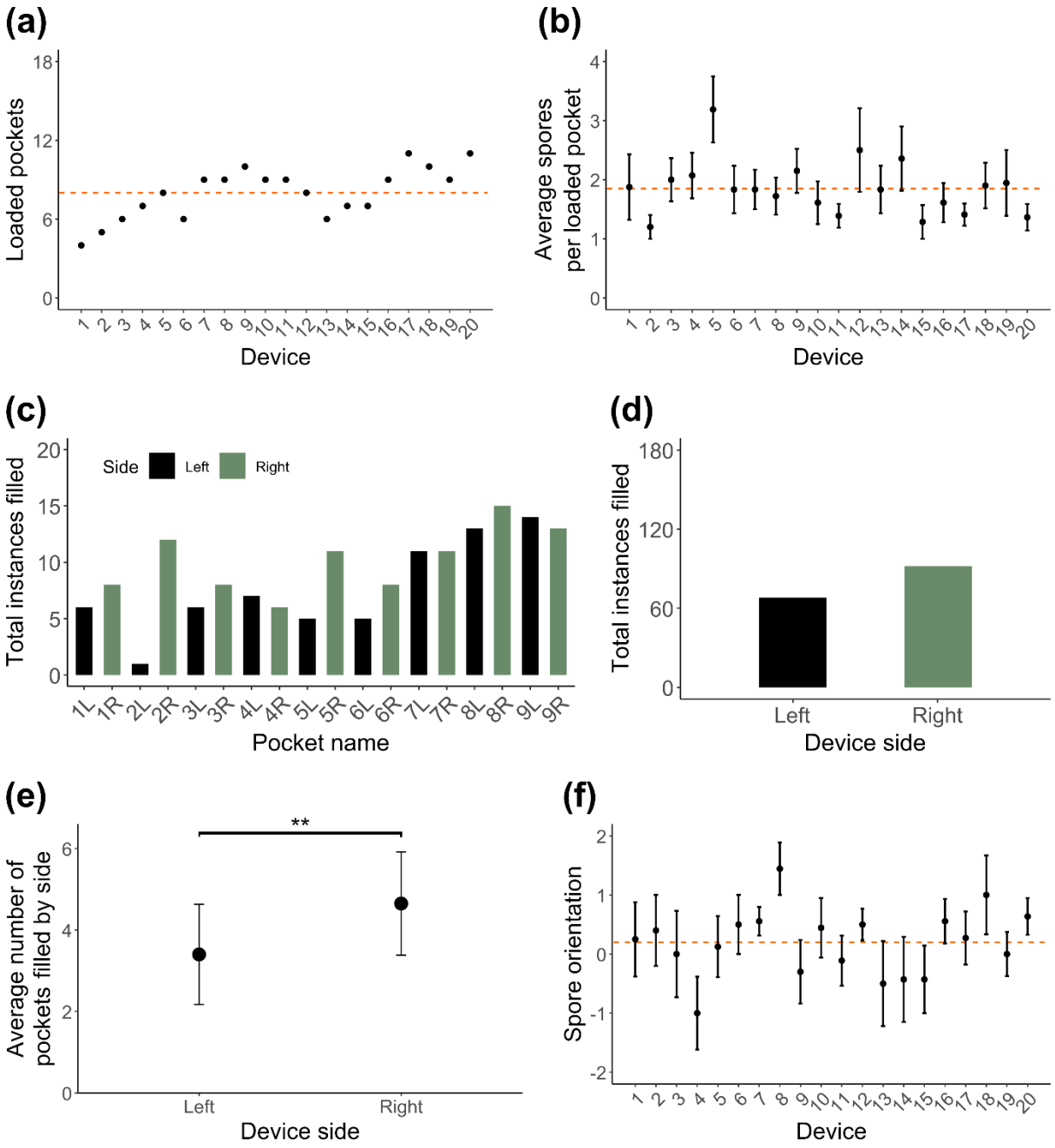


Figure 54: Quantitative analysis of the spore loading performance in the *AMF-AnastomosisChip*. The experiment comprised 20 devices inoculated with spores of *Rhizophagus irregularis* MUCL 43194, inoculated over 36 days. Orange dashed lines indicate mean values. (a) Point plot with standard errors, showing number of loaded pockets per device. Mean = 8.0 ± 2.0 (b) Point plot detailing the average number of spores per loaded pocket. Mean = 1.9 ± 0.5. (c) Column chart representing the total instances a specific pocket contained spores in all devices. Colours highlight the device side with black for left and green for right. (d) Column chart summing up the total instances pockets contained spores grouped by side in all devices, 68 counted left and 92 right. (e) Point plot with error bars showing the average number of pockets filled by side per device. Left: 3.40 ± 1.23; right: 4.65 ± 1.27. A significant difference between the results according to paired t-test was found and indicated with asterisks for p values <0.001 (***), <0.01(**) and <0.05 (*). (f) Point plot with error bars indicating the average spore orientation per device. A y-value of 0 means that the same number of spores in a pocket were facing in- and outwards of the lane, a positive value that more spores were facing into the lane. Mean = 0.2 ± 0.6.

The results in Figure 54 indicate an overall good loading of the *AMF-AnastomosisChip*, with an average of 8 pockets filled per device, i.e., nearly every second pocket was filled. On average, each of these filled pockets held 1.9 spores. Figure 54c-e reveal a loading bias towards the right-hand side of the device as well as towards the bottom pockets, closer to the device outlet. This was behaviour was expected, as mentioned in *5.2.1. Device development*. As the device was designed to guide any flow from the inlets towards the outlet, spores get preferentially drawn towards the lower pockets/lanes, closer to the outlet. This was countered by gently knocking the device against the stereoscope stage on the device top side while flushing in the spores (described in *5.2.1. Device development*), otherwise the recorded loading bias would have been stronger. This can be also seen in Figure 54c, where a clear tendency towards the lower pockets is shown for the left side, while this trend is less clear and pronounced on the right side. The bias towards the pockets on the right-hand device side can be explained by the difference in loading method between left and right. The spores on the right-hand side are flushed in, while the spores on the left are sucked in. Sucking in the spores allows for less force to be exerted and spores occasionally get stuck in the device inlet and do not make it into a pocket. Moreover, by sucking, the bias towards the bottom pockets cannot be countered as well as with flushing in (as described in *5.2.1. Device development*). Ideally, spores sitting in a pocket, would face into the lane with its subtending hypha (and thus its germination site), as this would be expected to increase the chance of any emerging hypha growing down the lane and into the hyphal interaction zone. Even though the subtending hypha occasionally acts as a “fin” and thus, following the stream, turning the spore towards the lane, this is in practice not consistent and depends on too many other factors, such as length of the subtending hypha, spore size and shape, number of spores per pocket or other obstructions like hyphal debris. Despite this uncertainty, Figure 54f reveals on average a nearly even distribution between spores facing in- or outwards (mean = 0.2 ± 0.6), which means that at least no bias away from the lane was created and spores have on average a fair chance to germinate into the lane. Originally, an even distribution of spores, i.e., every pocket filled with a single spore, and all spores facing down the lane was aimed and hoped for. While a higher number of loaded pockets per device as well as “perfect” spore orientation remain desirable although practically impossible, the irregularity in number of spores per pocket might actually be advantageous. The results included pockets filled with both only one spore as well as

multiple. That way, the effect of grouping on germination and growth behaviour could be studied, which is difficult on plate.

Following the characterisation of the device loading, the growth behaviour of fungi in the *AMF-AnastomosisChip* was analysed. Therefore, firstly, the germination rate of the spores was calculated for each device (Figure 55a). Next, the growth activity was evaluated. Therefore, any lane with growth, regardless of direction, was counted each day and averaged over all devices in order to highlight the growth phases of the fungus inside the device. To account for the discrepancy in number of loaded lanes, the active lane count was normalised by dividing by the number of loaded lanes for the device. The results are plotted in Figure 55b. In Figure 55c this was further split into hyphae growing down the lane (“Down”) or in opposite direction away from the lane (“Away”). Occasionally, when the germination site was lying already inside the lane, and the hypha was growing away from the hyphal interaction zone, this hypha was counted towards both “Down” and “Away”. While the activity in Figure 55b was recorded in an ON/OFF manner, i.e., any growth in the pocket/lane was counted as 1 and no growth as 0, for Figure 55c the exact instances of germinations was considered. Lastly, the number of hyphae reaching the hyphal interaction zone was recorded and plotted for all 20 devices in Figure 55d.

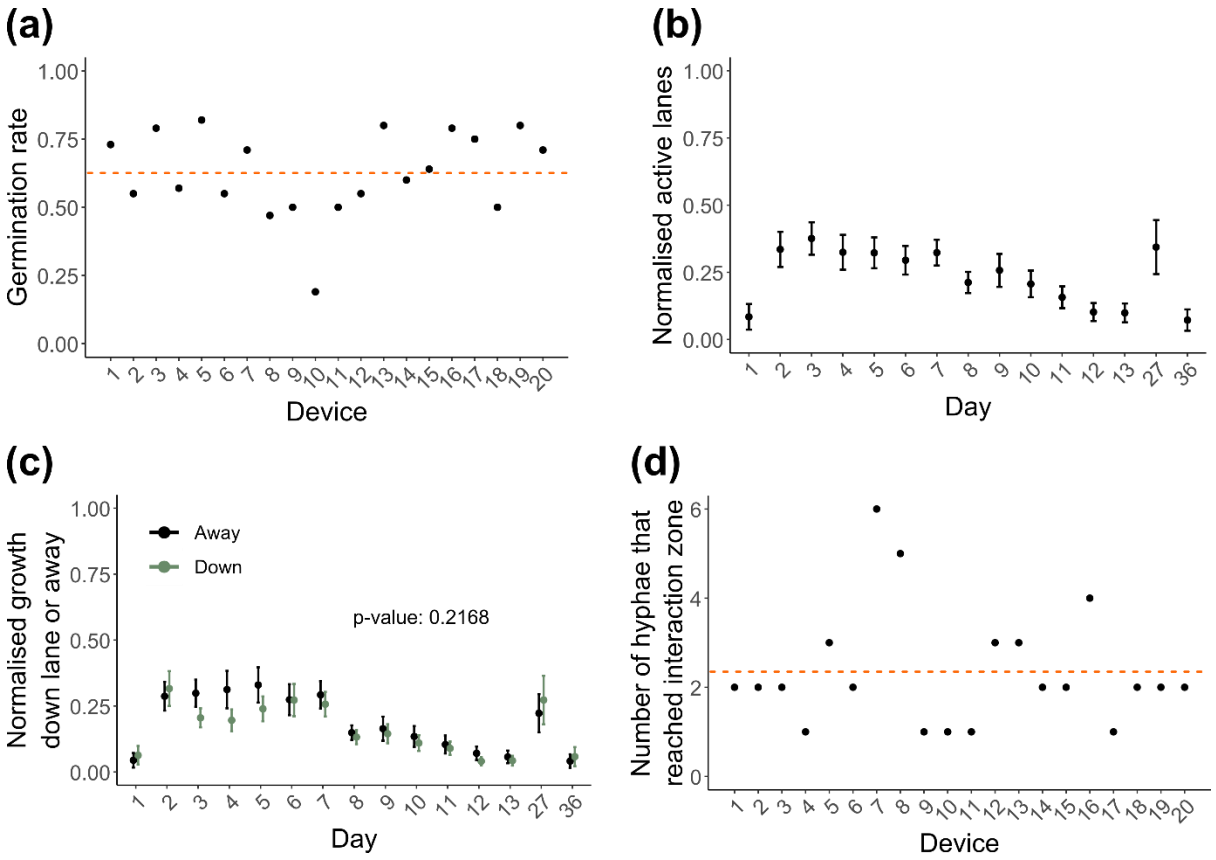


Figure 55: Quantitative analysis of the growth performance in the *AMF-AnastomosisChip*. The experiment comprised 20 devices inoculated with spores of *Rhizophagus irregularis* MUCL 43194, inoculated over 36 days. Orange dashed lines indicate mean values. (a) Point plot showing the germination rates per device. Mean = 0.63 ± 0.16. (b) Point plot representing the growth activity per day, averaged over all devices. A lane was counted as active if any growth regardless of the direction occurred. The number of active lanes was normalised by dividing by the number of loaded lanes per device. (c) Point plot detailing the growth activity considering the direction, i.e. away from the lane (black) or down the lane (green) towards the hyphal interaction zone, per day averaged over all devices. The number of active lanes was normalised by dividing by the number of loaded lanes per device. A t-test did not reveal a significant difference between "Away" and "Down" (p-value: 0.2168). (d) Point plot showing the number of hyphae that reached the hyphal interaction zone per device. Mean = 2.35 ± 1.35.

The germination rate of the spores, as shown in Figure 55a, reveals an average germination success of 62.6 %, which is lower than in previous experiments (see *3.2.2.2 Spore germination and hyphal growth behaviour in the confined environment*) and varies considerably from device to device (SD = 15.8%). These mediocre germination rates bleed into the lane activity by day (Figure 55b), with percentages well below 50 throughout. Moreover, the growth behaviour was observed to be immensely varied between individual spores, with widely asynchronous growth phases. While some spores started germinating from day 1, other spores only germinated after many days, even after 27 days, fresh germinations have been recorded. Similarly, while some growth was maintained over several days, some hyphae stopped growing the day following

emergence. Overall, the highest activity was recorded between day 2 and 5, followed by a continuous slow decrease up to day 13. Interestingly, an intermediate activity drop on day 8 was observed quite consistently for most devices. Surprisingly, an extreme growth spurt was recorded on day 27. This can most likely be explained by a medium refill after data acquisition on day 13, was, however, by no means anticipated. Quite consistently, devices which were topped-up with fresh medium because of medium loss through evaporation during the first 13 days of the experiment to avoid drying out of the device showed this sudden growth spurt, while devices that weren't filled up did not. Deviation from this could be explained by the different levels of medium added, i.e., for some devices the entire inlet had to be filled up (equivalent to ~21 µl per inlet), while other inlets received only a few µl. This was, however, not annotated and can therefore not be traced back. When looking at the growth activity by direction (Figure 55c), a similar trend can be observed for both away and down and no overall significant difference was found. Nevertheless, it seems that during the main growth phase (day 2-5), more growth occurs directed away from the pocket rather than down the lane. This could be caused by hyphae preferring to grow in the less confined environment, i.e., the inlet channels and pockets which have 100 µm channel height, compared to the more confined environment of the lanes and hyphal interaction zone (channel height 10 µm) and the effect becoming more apparent when overall more growth activity is taking place. As a next step, the number of hyphae reaching the hyphal interaction zone was analysed. Figure 55d shows numbers ranging from at least 1 to 6 and averaging around 2.35 (SD = 1.35) instances per device. This number theoretically translates into at least one anastomosis between two distinct spores for each device possible. Equally positive is the fact that in every device at least one hypha managed to grow into the hyphal interaction zone.

Next, total number of anastomoses observed during the experiment, along with cross-over events, non-anastomotic contact between hyphae, as well as approximation to 100 µm, 200 µm and 400 µm followed by growth arrest were recorded and can be found in Table 1. In total, 23 anastomoses were recorded, regardless of location within the device or anastomosis type. While some fusion events occurred in the hyphal interaction zone, some hyphae merged in the lane or pocket. Similarly, both self-self anastomoses between hyphae originating from the same spore or connections between hyphae from different spores were observed. The

majority of the recorded anastomoses were tip-to-side and only two instances of tip-to-tip anastomoses were observed. On 10 occasions, cross-over events were recorded, i.e., a hypha comes in contact with another hypha but instead of anastomosing, continues growing over the other hypha. Similarly, contact between hyphae sometimes leads to growth arrest (but no fusion). This was observed 4 times during the experiment. Furthermore, growth arrest just before contact establishment between two hyphae was observed multiple times. 5 times both hyphae got within 100 µm, 3 times within 200 µm and 4 times within 400 µm tip-to-tip or tip-to-side distance but then stopped growing. Moreover, these premature growth arrests thwarted all attempts of acquiring timelapse series of successful anastomoses during the experiment, as it happened in any timelapse imaging set up overnight. Photosensitivity causing this phenomenon is a possible but unlikely explanation, as the light exposure time of the hyphae was relatively low (few seconds every 20 minutes) and no such effect was observed in any of the previous timelapse experiments with AMF of this project.

Table 1: Summary of total anastomoses and related events counted.

Anastomosis	Cross-over	Contact but no anastomosis	Growth arrest within 100 µm hyphal distance	Growth arrest within 200 µm hyphal distance	Growth arrest within 400 µm hyphal distance
23	10	4	5	3	4

An example of an anastomosis event in the interaction zone can be found in Figure 56. Between day 12 and 13 of the experiment, a hypha grew into the field of view from the top and, interestingly, crossed over the other hypha without interacting. On day 27, however, it was found that the hypha then had branched and one of the branches was growing back upwards, back towards the crossed over hypha. Then it did yet another cross-over but within only a few µm, it turned around again and this time formed an anastomosis. This intriguing observation suggests that hyphae are not only potentially spatially specialised for anastomosis but also temporally, with the same hypha becoming susceptible for fusion with other hyphae over time.

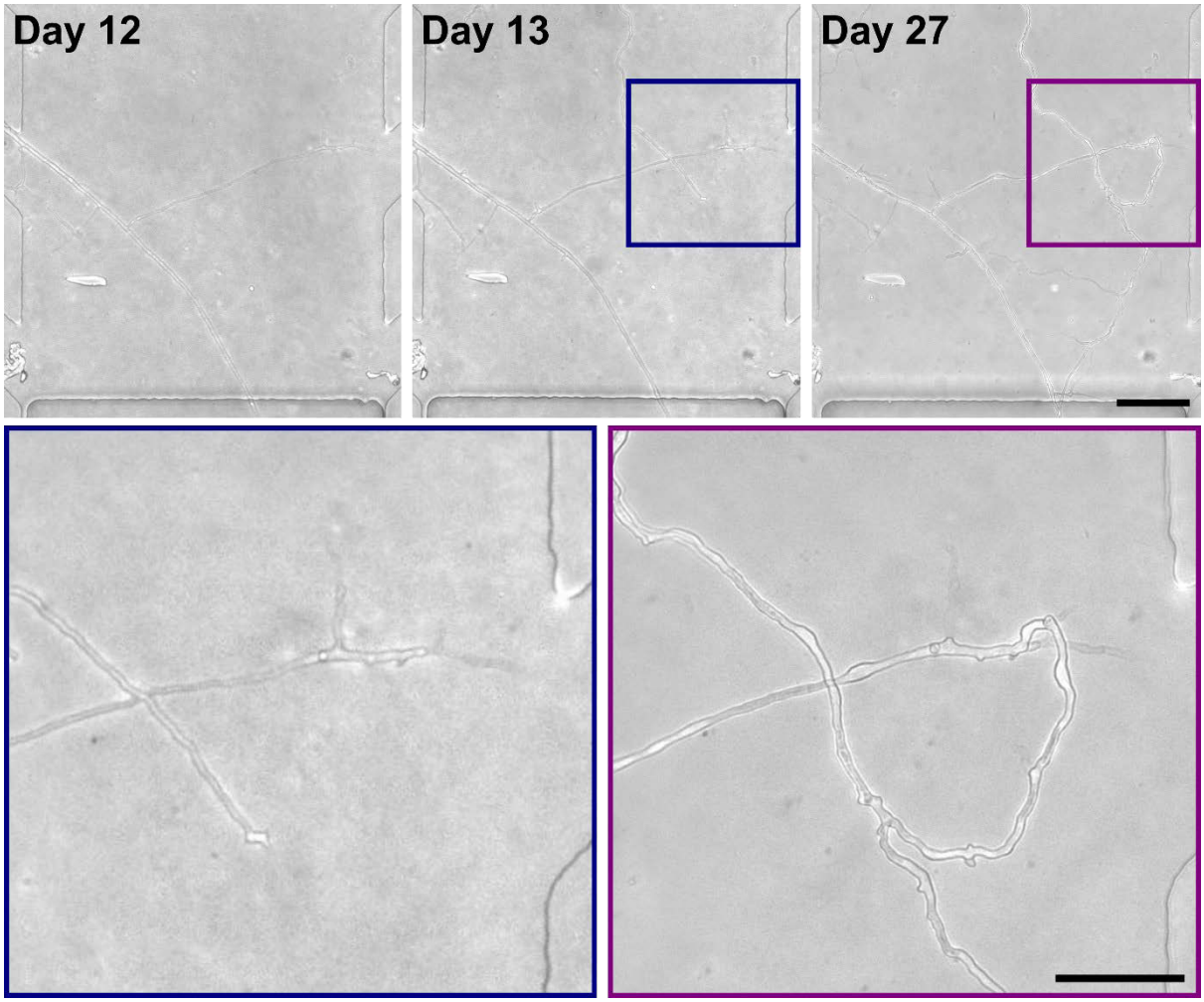


Figure 56: Anastomosis event in the *AMF-AnastomosisChip*. Phase contrast time series showing two cross-over events followed by a tip-to-side anastomosis on day 12, 13 and 27 of the experiment. (Bottom) Magnifications of the cross over and anastomosis on day 13 (blue) and 27 (purple). Scale bars: 100 µm.

Another fascinating observation involved a spore "hijacking" a hyphal fragment to extend its reach. Figure 57 shows a single spore germinating between day 8 and 9 and then, on day 10, fusing with a hyphal fragment in the lane on one end (Figure 57, white arrow) and re-emerging from the other end of the fragment (Figure 57, yellow arrow), further down the lane, with several strong hyphae. One of these hyphae eventually proceeded to grow through the investigation zone and formed an anastomosis with another hypha (not shown in figure). Normally, hyphal fragments without spores are regularly "germinating", forming hyphae, which, however, never extend beyond ~100 µm, as nutrients from a spore are missing. The described "hijacking" was observed several times and is strongly reminiscent of the hyphal healing process (de la Providencia *et al.*, 2005; de La Providencia *et al.*, 2007).

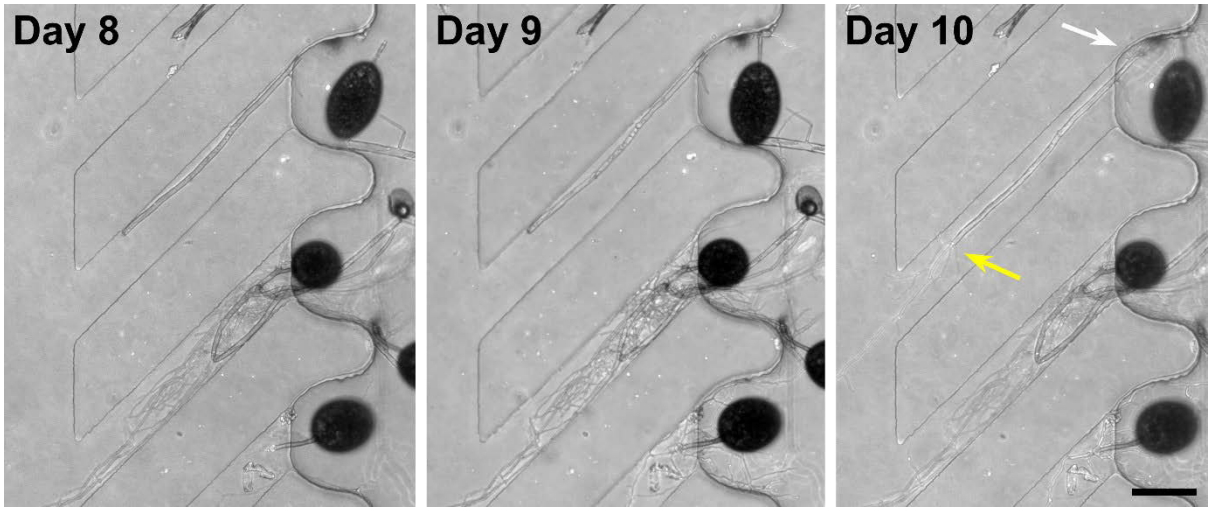


Figure 57: Example of anastomosis in the *AMF-AnastomosisChip*. Phase contrast time series showing a spore anastomosing with an old hyphal fragment to extend its reach, using the fragment as a bridge on day 8, 9 and 10 of the experiment. White arrow indicates the upper end of the hyphal fragment and anastomosis site, yellow arrow indicates the lower end of the hyphal fragment, where fresh hyphae emerge following successful anastomosis. Scale bars: 100 µm.

Overall, the proof-of-concept experiment demonstrated good functionality of the *AMF-AnastomosisChip*. It revealed great spore loading performance as well as growth into the hyphal interaction zone and hyphal contact. A significant improvement of the method could be achieved with improved spore material (also discussed in *5.2.1. Device development*). Truly single spores with short subtending hyphae (~100µm) are most beneficial for a more controlled device loading, as long and/or branched hyphae tend to get caught on either channel structures or other spore/spore clusters. Similarly, loose hyphal fragments or debris, derived from the spore dissection, are highly disruptive for both the loading as well as the imaging process, as they cover spores and germinated hyphae, making it difficult to track and analyse growing hyphae. Unfortunately, avoiding introduction of hyphal fragments is very difficult, as they are not easily spotted or filtered out. A less manual method involving a blender was tested by our collaborator but needs further optimisation. Here, the spore material is dissected in bulk using a blender and subsequently filtered with a sucrose-gradient centrifugation. This process allows for a relatively quick production of a high volume of single spores, however, still leaves a lot of hyphal debris behind. With some improvement this method could become the protocol of choice for future experiments. As another important factor of the spore material, the spore fitness could be better. With an average germination rate of only 60%, less hyphae emerged from the introduced spores and thus less chances of hyphal interaction were provided.

The device allows for positioning of single spores in very close proximity, while, however, being physically separated by channel walls. This precision is impossible in plate-based experiments with manual spore placing, which, to a considerable degree explains the immense improvement of anastomosis rate per spores inoculated, compared to previous plate-based experiments performed by the collaborator (unpublished observation by the collaborator).

5.2.3 Application of the *AMF-AnastomosisChip* for establishment of diffusion gradients

In an attempt to explore the possibility of coercing hyphae into growing preferentially down the lanes and into the device centre (i.e., hyphal interaction zone) using a chemical gradient/attractant, the diffusion behaviour in the device was studied. Therefore, the diffusion of the fluorescent molecule fluorescein was first modelled using COMSOL, with the help of a colleague (PhD student, Kate Collins), and subsequently tested in real life through fluorescence microscopy.

As parameters, the device geometries including the two different channel heights, $4.25E^{-10}m^2/s$ as the diffusion coefficient and a supply of fluorescein from the device outlet (bottom channel) with a concentration of 0.5 mM was fed into the model. The dimensions of in-and outlets were defined as 3 mm wide (diameter) and 5 mm high and the two inlets, just as the main channels, were filled with water. The modelled concentration gradients for the time points 1 h, 10 h, 50 h, 100 h, 200 h and 300 h after inoculation are presented in Figure 58. For more conciseness in the figure, the in- and outlets were cut out.

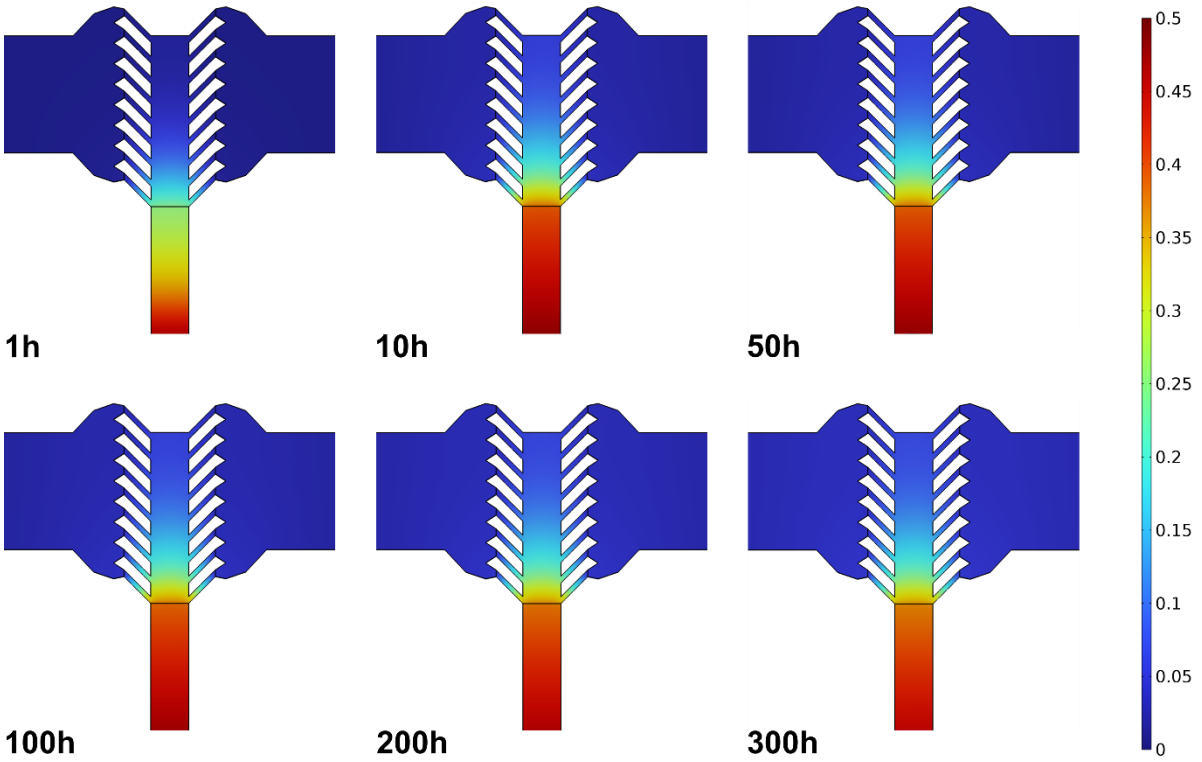


Figure 58: COMSOL model of diffusion behaviour in the *AMF-AnastomosisChip*. The model assumes filled in- and outlets with a diameter of 3 mm and a height of 5 mm. The outlet at the bottom is filled with a liquid containing a substance with a diffusion coefficient of $4.25E^{-10}$ m^2/s (fluorescein) and concentration of 0.5 mM, which diffuses into the device over 300 h. Scale shows the concentration levels in mM, with dark red equalling 0.5 mM and dark blue 0 mM.

The results show an unexpectedly slow diffusion through the device. A gradient is established between 1 and 10 h, which radiates out into the lanes. The gradient is maintained over the next couple of days, remaining almost unchanged, with the overall concentration levels very slowly rising and dropping in the outlet region (bottom of device).

These findings were sought to be replicated in real life, filling the outlet of the *AMF-AnastomosisChip* with a solution of 0.5 mM fluorescein. Therefore, the device was filled with liquid MSR(-) medium straight after the bonding. Then, the liquid in the outlet was pipetted out and immediately filled up with a solution of 0.5 mM fluorescein in liquid MSR(-), before transferring the device onto the microscope (see *2.3 Microscopy and image processing*). Here it was revealed, that even when pipetting in the fluorescent medium with utmost care, a flow was created that prematurely introduced fluorescence into the channels, thus offsetting the starting point for the experiment. Therefore, the fluorescein was added to medium containing 15 g/L bacto agar (VWR, UK), autoclaved and poured to solidify. Then, a device is prepared

as before but instead of the liquid MSR(-) a plug of about 2 mm diameter was punched out and carefully pushed into the outlet. This way, the liquid “extracts” the fluorescein from the plug and the dispersal within the channels is solely diffusion dependent. The device is then immediately placed under the microscope and a timelapse with 1 h intervals using the GFP filter of the microscope started. Representative microscope images after 1 h, 10 h, 50 h and 100 h are shown in Figure 59.

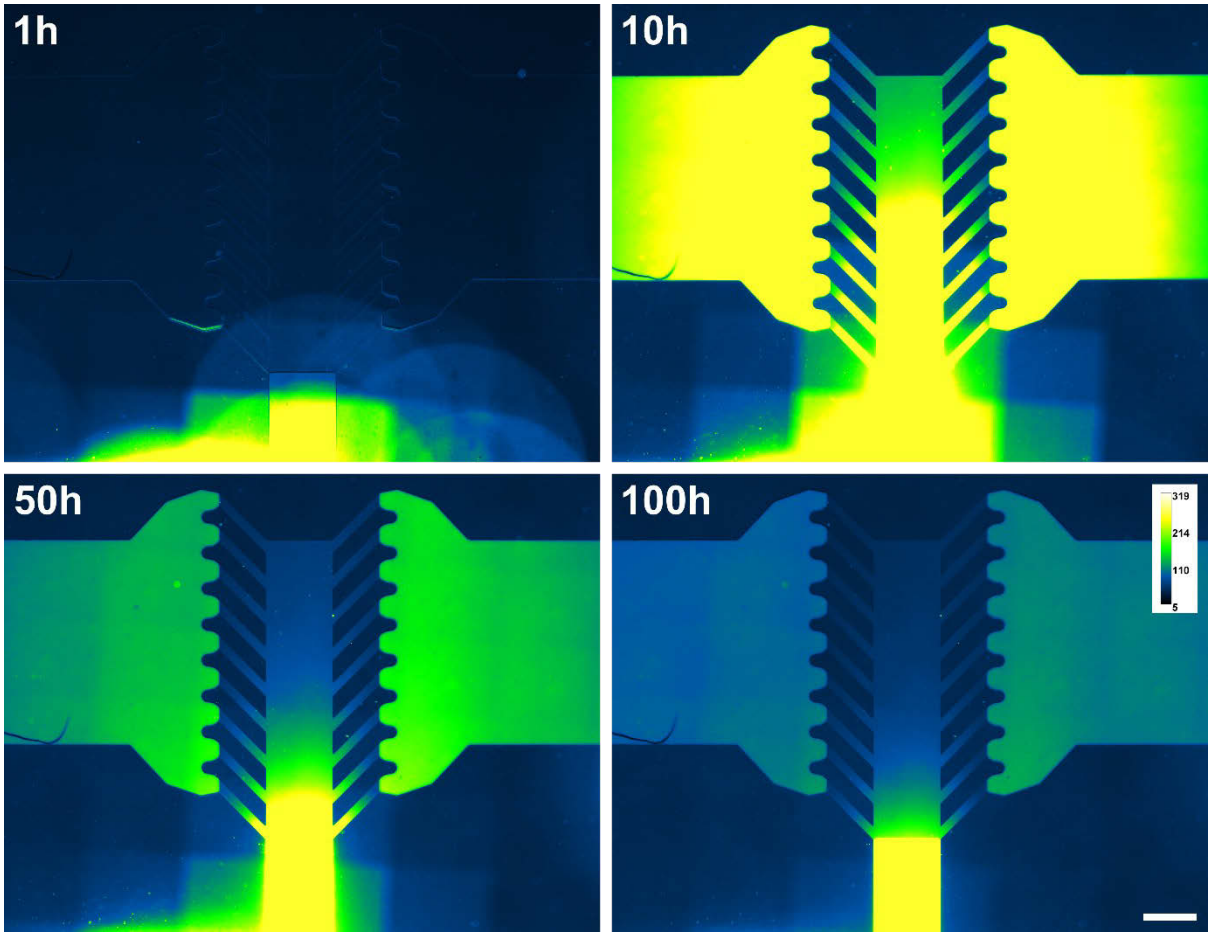


Figure 59: Real-life diffusion in the *AMF-AnastomosisChip*. Fluorescence time series showing the diffusion of fluorescein into the device. An agar plug containing 0.5 mM fluorescein was inserted into the outlet of an *AMF-AnastomosisChip*, pre-filled with liquid MSR(-). The fluorescence levels were recorded using the GFP channel of the microscope over 100 h. For better visibility, the look up table “greenfireblue” in ImageJ/Fiji was applied. The calibration bar shows the relative fluorescence intensity, with white being the brightest and dark blue the darkest. Scale bar: 200 µm.

At first glance, the microscope images (Figure 59) vary significantly from the diffusion model (Figure 58). The fluorescence intensity is taken as a proxy for the fluorescein concentration, with yellow being high and dark blue low intensity. Firstly, it has to be remarked that from 10 h onwards, the left and right channel with the pockets appear much brighter than the respective

adjacent lanes. This phenomenon can be explained by the different channel heights in the device (10 µm in the central area and 100 µm in in- and outlet channels, see also *5.2.1. Device development*). As the microscopy images show the fluorescence intensity, which besides the concentration also depends on the thickness of the liquid layer (Cherdantsev *et al.*, 2023), the 100 µm areas appear brighter than the 10 µm areas. The model, in contrast, presents concentration values, which are independent of the channel height. Same as predicted, a gradient is established in the central device area, radiating into the lanes. After only 10 h, very high brightness levels (yellow) can be seen penetrating far up the hyphal interaction zone (well into the second half), while this concentration level was not reached in the model. This could, however, be explained by the microscopy method not being able to resolve the different brightness levels as well as in the computer model. Then, surprisingly, while maintaining a gradient throughout, the brightness starts constantly subsiding after 10 h until at 100 h no yellow can be found outside of the outlet channel anymore, while in the prediction the concentrations remain mostly unchanged in the device channels. This regress of the fluorescence intensity could be due to photobleaching (Saylor, 1995), however, as the light source is not a laser and hence of relatively low intensity, and pictures were taken only once per hour, this effect should be small. Another likely reason could be explained by evaporation of water. This evaporation would “dry out” the agar plug in the outlet, which in turn would “restock” the lost moisture from the medium in the device channels due to the capillary-like effect of the agar matrix, thus creating a slow suction flow towards the outlet, working against the diffusion into the device. When repeating the experiment, the same overall behaviour was observed, only varying in the maximum forward progress of the yellow brightness level before the retraction. Complete elimination of the drying-out effect is nearly impossible, as measures such as pipetting liquid on top of the agar plug, adding water around the device and tightly sealing the device containing petri dish with multiple layers of cling film to maintain high moisture, had already been in place, without success. Sealing the device directly, through e.g. a glass cover and or a layer of film or varnish would interfere with the microscopy and prospectively exclude oxygen, which would be important for future experiments with living organisms (i.e., the AMF).

Despite the experimental results deviating from the predicted model, a concentration gradient is established and maintained for up to 3-5 days, which falls within the main growth period of the AMF. Even though a “neutral” environment is most desirable for the envisioned anastomosis experiments confronting different strains with each other, establishing some kind of (additional) drive towards the hyphal interaction zone of the device could be indeed interesting. The ability of the fungi to follow gradients of known signalling molecules, such as flavonoids and strigolactones (see *Stages of arbuscular mycorrhiza development*), or drivers of fungal-fungal signalling for, e.g., anastomosis, (as discussed in *4.2.5. Anastomosis formation in the device*) could be explored well with such a device set-up.

5.3. Chapter conclusion

In this chapter, the development of the *AMF-AnastomosisChip* was described and discussed. This encompassed designing of the device to meet its criteria for spore loading and foster and isolate hyphal contact for anastomosis studies. This involved several iterative rounds of designing, testing, computer-assisted modelling and repetition of the process. The main challenge was to introduce spores from opposing sides without flushing the previously loaded ones out as well as physical separation of single spores in pockets. To accomplish this task, along with optimising the device design, the spore loading method was improved, too. Eventually, the functionality of the final design was shown in a large proof-of-concept experiment, analysing several aspects of the loading performance as well as biological parameters, such as germination rates and growth activity with brightfield images taken daily. The experiment further resulted in multiple contact events between hyphae, in several instances leading to anastomosis formation. As an additional application of the device, the establishment of directional chemical gradients was demonstrated. This was first modelled computationally, subsequently tested in real-life with fluorescein and results compared. The final *AMF-AnastomosisChip* fulfilled all requirements for the device and thus paves the way for systematic inter- and intra-species anastomosis studies in AMF, to further examine collaboration in space searching beyond the strain level and eventually to unravel links between the anastomosis phenotype and genotype.

CHAPTER 6: FUTURE DIRECTIONS AND CONCLUSION

6.1 Chapter overview

This chapter is concerned with alternative and future applications of the developed devices. First, an oxygen-sensing foil was implemented into the *AMF-SporeChip* to monitor the oxygen depletion in the hyphosphere in real time. The successful integration of the foil as well as the many challenges faced with the method are discussed herein. We hypothesised that resolving oxygen levels around hyphae would reveal varying levels of oxygen depletion based on activity and vitality. Furthermore, the *AMF-SporeChip* was used for the cultivation of a different type of mycorrhizal fungi, the MFRE. In order to test the cultivability of MFRE in microfluidic devices, two strains of these fungi were inoculated using different methods, media and devices (*AMF-SporeChip* and the *BFI device*). In turn, this preliminary work laid the foundation for a new PhD project dedicated to these fungi. It was expected that establishing MFRE for studies in microfluidic devices would allow to study growth behaviour of MFRE in comparison to other fungi and would reveal a mixed behaviour due to their dual lifestyle between symbiosis and saprotrophy. The chapter concludes the thesis with a graphical overview of all project aims and achieved outcomes, as well as a paragraph dedicated to future outlook. Here, additional ways in which the microfluidics-based methodologies developed in this thesis could further benefit the field of AMF research are explored, such as examining fungal decision-making in response to chemical stimuli or biological partners (e.g., plants or bacteria) or their role in the “wood-wide web” including potential electrical signalling.

6.2 Results and Discussion

6.2.1 Development of a sensor foil device

In an attempt to add an additional readout parameter to the microfluidic system, the possibility of integrating a sensor foil into the *AMF-SporeChip* was explored. In a collaboration with Dr Lucas Wick from the Helmholtz Centre for Environmental Research in Leipzig, I aimed to implement pH and oxygen sensor foils (SF-HP5R and SF-RPSu4, respectively; PreSens, Germany) into microfluidic devices with the intention of resolving the establishment of pH and oxygen gradients in the hyphosphere of fungi. Especially resolving oxygen levels around single hyphae could be a good measure for activity, which would be an interesting additional insight into the space navigation dynamics, and prospectively, the change in activity when facing, for instance, starvation, plant exudates or whole roots in the vicinity. Furthermore, oxygen consumption and depletion in the hyphosphere could be compared to other fungi. As studied by our collaborators, the oxygen depletion creates niches for anaerobic bacteria (Xiong *et al.*, 2022). With an oxygen-sensor device it could be determined whether AMF are equally able to create these niches or not, especially now with mounting evidence of AMF collaborating with soil bacteria (Zhang *et al.*, 2018; Jiang *et al.*, 2021).

The sensor foils translate the chemical signal (i.e., oxygen level or pH) into a fluorescence output, to be read out by a specific detector (VisiSens TD, PreSens, Germany). The company does not disclose any further details regarding the working principle of the foil. However, such optical sensors are generally based on inert micro-beads coated with a layer of a fluorescent dye that shifts its emission spectrum or is quenched in the presence of oxygen (e.g., the coordination compound Ru(Ph2phen3)Cl2 (Wang *et al.*, 2013)). For pH sensing, indicators such as bromothymol blue (BTB) can be integrated into a bead-based system (Maruyama *et al.*, 2008).

As PDMS is generally considered permeable to gases, devising a method for the integration of the oxygen-sensitive foil was anticipated to be more straightforward and achievable. In order to make the sensor foil “bondable”, a thin film of PDMS was spin-coated (Ni-Lo 5XL Vacuum Digital Spin Coater, Ni-Lo Scientific, Canada) onto the foil and cured. According to Ochs *et al.* (2014) a PDMS thickness of up to 500 µm does not affect the gas permeability. Still, a thinner

film was expected to yield a more even and stable film as well as a better curing behaviour. Moreover, with a thinner PDMS layer the oxygen is expected to pass quicker and reach the sensor foil earlier. On the other hand, a thicker film could give more sturdiness to the foil, thus possibly improving the later stability of the device. In first trial runs, three different spinning conditions were tested, first with a dummy foil. For the spin coating process, the foil was taped onto a microscopy glass slide. The PDMS was prepared in a 1:10 ratio (see *2.1.2 PDMS device manufacturing*), degassed and a droplet of about 500 µl placed into the centre of the foil piece. The spinning programme was started immediately after. A rather slow spinning speed of 500 rpm for 90 s was used to obtain a film of ca. 100 µm (according to Mata *et al.* (2005)), a speed of 1000 rpm for 90 s, yielding a thickness of about 55 µm (according to Mata *et al.* (2005)) and 2500 rpm for 300 s yielding a thickness of about 10 µm as reported by Ochs *et al.* (2014). The slides were then cured over night at 70 °C. Curing at room temperature to avoid a negative effect of the heat exposure onto the foil sensitivity was attempted, however, even after days no solidification was observed. Moreover, a significant reduction of the sensor foil sensitivity caused by curing at 70 °C was later not observed. Measuring the thicknesses after the coating was not possible as the profilometer used for the characterisation of the SU-8/silicon master moulds (see *3.2.1.2 Optimisation of the photolithography protocol*) did not work for the foil/PDMS composite. Similarly, measuring with callipers did not yield reliable values, as the PDMS is highly flexible, making the results highly dependent on the pressure exerted with the callipers during the measurement. The lowest spinning speed (500 rpm) was not able to spread the rather viscous PDMS over the entire foil, not even with four times the spinning duration. With 1000 rpm and 2500 rpm the entire foil was covered with an apparently even layer of PDMS.

The microfluidic devices were then bonded onto the coated foil using the method described in *2.1.2 PDMS device manufacturing* and finally cut out and removed from the glass slide. It was found that bonding the devices onto the coated foil while still attached to the glass slide and subsequently carefully cutting the foil with the devices off the glass slide and finally into pieces was the most successful method. Scrutinising the devices under the stereoscope revealed that the bonding did not work properly for all devices, leaving some only loosely attached to the foil and some with caved-in and obstructed channels (Figure 60c,d). This was especially observed

for the foil coated at 1000 rpm, most likely due to an uneven distribution of the PDMS across the substrate when spinning at lower pace. Furthermore, issues with dust and particles on the PDMS surface were encountered, which significantly disturbed the bonding process (Figure **60**b in comparison to Figure 60a). This problem occurred, because the original set-up of the spin coating station was not in a dust free environment, e.g., laminar flow hood, but was later arranged accordingly. Spin-coating at 2500 rpm resulted in good bonding and a relatively even but very thin and delicate layer. To give the film more stability a spinning speed of 2000 rpm was tested and finally established as condition of choice for the method. Furthermore, the spinning duration was reduced from 300 s to 90 s as this time was found to be sufficient for consistently creating steady film layers on the sensor foil. The thickness of the entire device was between 4-5 mm.

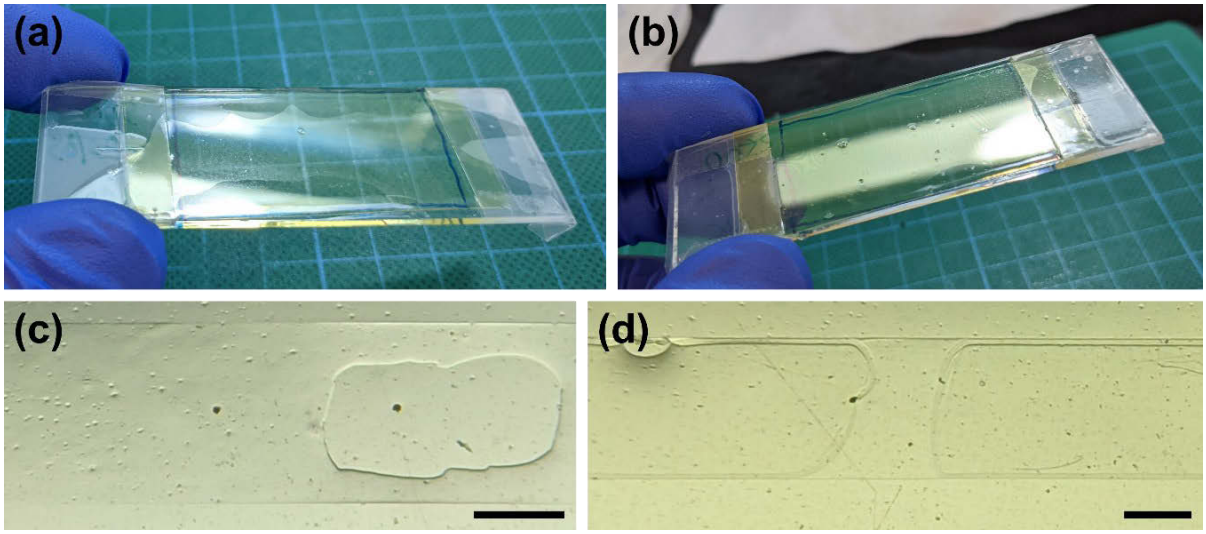


Figure 60: Spin coating of PDMS onto sensor foil. Photographs showing the surface of the PDMS layer after spin coating onto the sensor foil with (a) hardly any disturbances and (b) multiple disturbances. (c) and (d) are showing bonding problems due to surface disturbances on the PDMS layer. Scale bars: 500 µm.

As the sensor foil devices were meant to be tested with both filamentous fungi and AMF, the device published by Ghanem *et al.* (2019) for studying phage interactions (see Figure A3 for device layout), was used next to the *AMF-SporeChip*. The phage device possesses a fungal inlet, which consists of a wide opening on one side of the device and a channel leading into the main chamber of the microdevice. This channel guides the fungus ultimately through a constriction of 10 µm to allow only 1 or few hyphae to enter the observation chamber. For the inoculation of the phage device, a piece of mycelium is either cut or punched (using a cork

borer) from a culture plate and simply placed fungal side facing down in front of the fungal inlet of the device. The mycelium is left attached to the piece of agar to provide initial nutrients for crossing over into the device and keeps it moist. Furthermore, the agar helps establish close contact with the device wall, forming a kind of bridge for the fungus to cross. To this end, an overhang of the sensor foil was left in front of the fungal inlet, to hold the fungal inoculum on the same height as the inlet. To read out the sensor foil, the VisiSens TD sensor is needed, which was situated in the collaborator's lab in Leipzig. Therefore, sensor devices (both the phage device and *AMF-SporeChip* designs), along with pieces of the sensor foil coated with PDMS but without a device structure on top for negative controls were manufactured as described above and taken to Leipzig.

The available sensor had a field of view of 350 x 350 µm^2 and did not possess any means of automatically obtaining larger images (later, the manufacturer improved the sensor unit to a wider field of view of 2 x 2 mm^2, first, and very recently to 30 x 25 cm^2). Therefore, a construction was improvised utilising the stage of a microscope (Figure 61a). A mechanical arm was attached to the microscope stage and the sample attached to the other end of the arm, thus hovering over the sensor. Then, using the "large image" function of the microscope software, the sample was moved around the sensor, taking a series of images which was later manually stitched together to obtain a large image of the entire device or plate. This image can then be overlayed with a separately taken microscopy image of the sample. In previous experiments, the collaborator imaged oxygen gradients around mycelia of *Coprinopsis cinerea* on agar plates using this method (Figure 61b). Therefore, a piece of the mycelium was cut out from the agar plate and simply placed onto the sensor foil (with the agar still attached to the mycelium), with the fungal side in direct contact with the sensor foil. Here, a clear oxygen depletion (blue) in the centre of the fungal inoculum can be observed, which transitions into oxygen richer levels towards the growth front (from red to yellow). This was published by Xiong *et al.* (2022) and discussed in the context of dispersal of the anaerobic soil bacterium *Clostridium acetobutylicum* along hyphae.

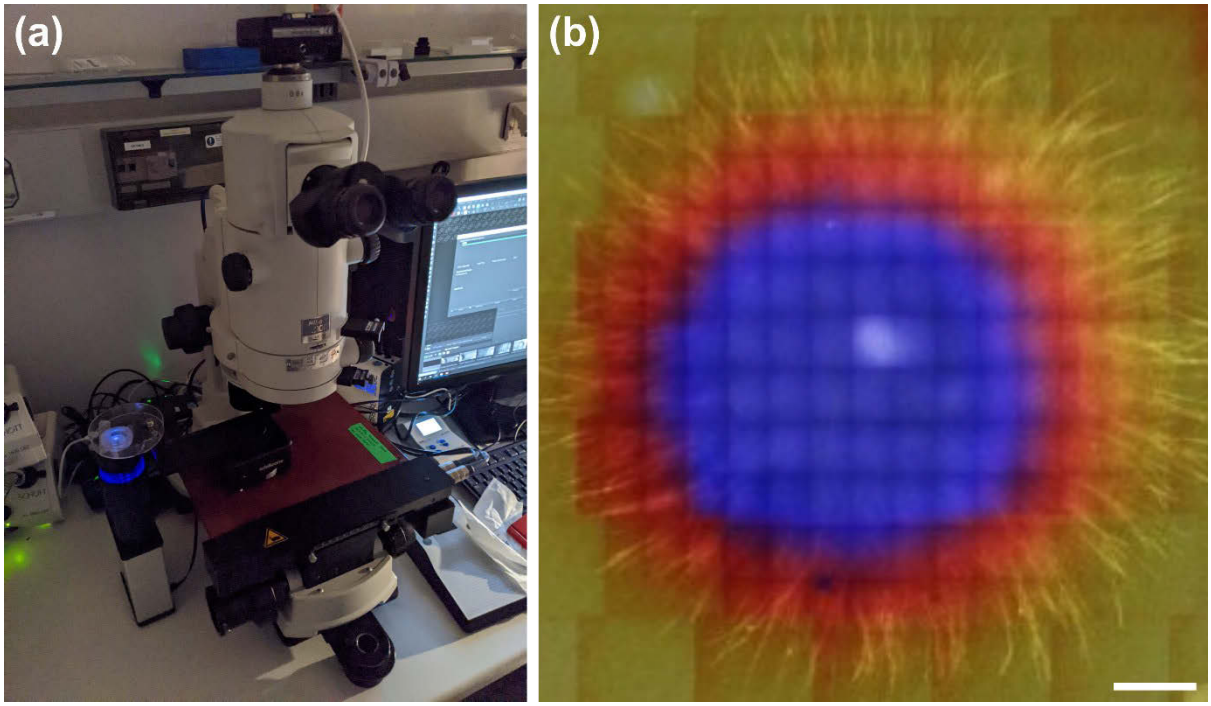


Figure 61: Oxygen measurements with the sensor foil. (a) Experimental set-up involving a microscope and the VisiSens TD sensor to measure oxygen levels in fungal mycelium. (b) Microscope image of *Coprinopsis cinerea* mycelium overlayed with the oxygen measurement on the naked sensor foil. Blue indicates low and yellow high oxygen levels. Scale bar: 250 µm.

Now, the task was to establish whether, using the sensor devices, a similar resolution of gradients could be achieved on a hyphal level, for filamentous fungi as well as AMF spores and hyphae.

Before each use, the measurement set-up, i.e., sensor foil and sensor, had to be calibrated. Therefore, a solution of sodium dithionite ($Na_2S_2O_4$) was prepared. The sodium dithionite reacts with oxygen and thus creates “oxygen-free water”. The foil was immersed in the solution for 3 min and an image was taken, marking calibration point 0 (0% relative oxygen saturation). In order to set calibration point 100 (100 % relative oxygen saturation), the sensor foil is simply exposed to ambient air and an image recorded. Furthermore, after calibrating the naked sensor foil, the oxygen-free water was used to test the effect of the PDMS coating as well as the device itself. Therefore, the PDMS-coated sensor foil was immersed in the oxygen-free water and it was found that the time needed to establish 0% oxygen saturation was within 3 min, same as with the naked sensor foil before. Next, the channels of a sensor device were flushed with oxygen-free water (using a syringe equipped with tubing) and the change in oxygen saturation monitored. Interestingly, the recorded change in oxygen saturation was considerably slower

and took about 4 h to reach a stable level. Moreover, this level was established around 70% oxygen saturation and never went lower, even after leaving overnight. This indicates that the PDMS acts as a buffer, constantly supplying the channels with oxygen from the environment, maintaining a stable oxygen level slightly below the ambient air level, after a lengthy equilibration period. To further establish the PDMS effect, the experimental conditions were reversed. The entire device was fully immersed in the oxygen-free water and left immersed until full oxygen depletion was established. The channels were flushed with a syringe again to ensure complete filling of the device. Then, the device was taken out of the solution, the channels flushed with water and the change in oxygen saturation monitored. Again, it required several hours for the system to revert back to the oxygen-saturated state, on a global level. Interestingly, when focussing on the inlet of the device, after filling the oxygen-depleted device with water, initially a blurry orange spot, indicating elevated oxygen levels was observed (Figure 62). This spot, however, fades away and disappears within 20 min, showing how the surrounding PDMS buffers even the relatively large volume of oxygen-rich water (compared to the microchannels; inlet diameter = 1 mm) in only a short time. As the orange spot is barely visible, the intensity profile across the image, centred over the spot, was measured in ImageJ/Fiji using the “straight line” tool and the “plot profile” function and plotted underneath the images. Here the above-described effect becomes more obvious through the flattening of the curves over time. The image series in Figure 62 suggests both a poor temporal as well as spatial resolution with the current system.

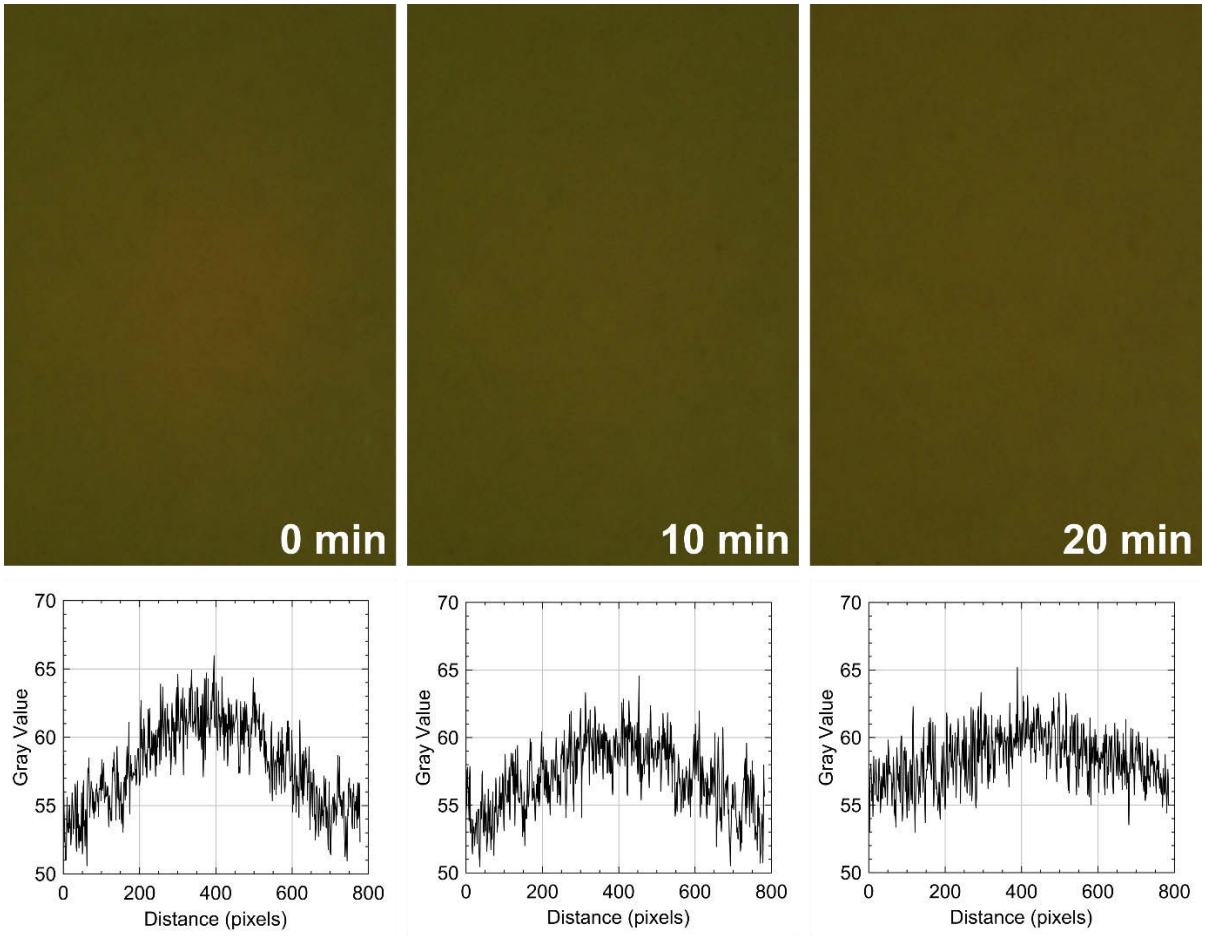


Figure 62: Oxygen level measurements in sensor foil device. (Top) Time series of the development of the oxygen level around a device inlet after filling an oxygen-depleted sensor device with water, acquired with the VisiSens TD sensor over 20 min. (Bottom) Intensity profile plot acquire with ImageJ/Fiji using the “straight line” tool, drawn across the centre of the orange spot, and “plot profile” function. Note how the initially orange spot fades away and the peak in the profile flattens, highlighting the PDMS buffer effect.

Another issue emerged with the microscopy. As described above, separate microscopy images can be taken and then overlayed with the oxygen-level images. Imaging through the opaque sensor foil, however, significantly reduces the quality of the picture, resulting in very poor resolution in brightfield on the hyphal and spore level (Figure 63a). Fluorescence microscopy with a dTomato tagged *C. cinerea* made hyphae at least visible, however, with a strong background and blur (Figure 63b).

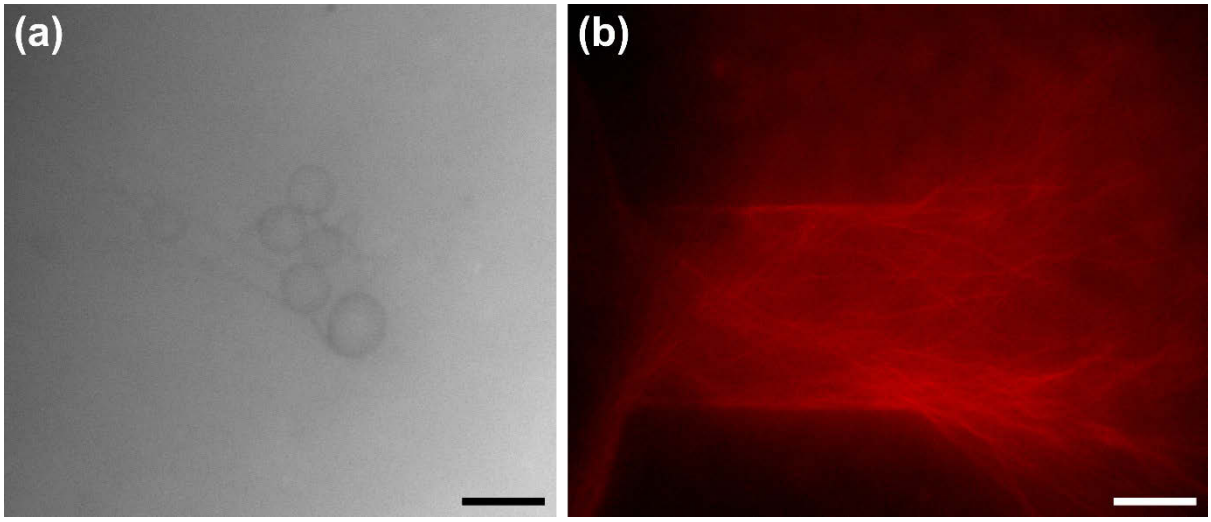


Figure 63: Problems with visibility through sensor foil. (a) Bright field image of spores in a sensor foil device. The spores are barely visible due to the effect of the foil. (b) Fluorescence image of dTom *Coprinopsis cinerea* in a sensor foil device using the TRITC channel. The clarity of the imaging is also reduced because of the foil. Scale bars: (a) 100 µm; (b) 200 µm.

The images were obtained using an inverted microscope. Flipping the devices so that the image would have been taken through the PDMS rather than the sensor foil could have worked, however due to the thickness of the device the channels were outside of the working distance of the objective lens when the device was inverted. Later, the sensor foil manufacturer supplied a new, transparent foil, which significantly improved the microscopy issue.

In order to be able to potentially invert the device on the microscope but moreover to examine the dependency of the PDMS oxygen buffer effect on the PDMS thickness, it was envisioned to manufacture thinner devices. This was achieved by simply reducing the amount of PDMS poured into the mould, yielding devices with total thicknesses between 1 and 3 mm, as opposed to the initial 4-5 mm, which is the standard thickness of my devices. Here, due to the high viscosity of the PDMS, even distribution across the mould was not always possible. In an attempt to reduce viscosity and thus improve spreading of the PDMS, different ratios of PDMS base to curing agent, 20:1 and 40:1 (instead of 10:1), were tested. Both mixtures, however, failed to cure. To reduce the thickness even further, spin coating had to be applied. Using the lowest spinning speed the spin coater is capable of (500 rpm), a PDMS layer of about 200 µm was spun directly onto the master mould. Handling these very thin PDMS slabs got increasingly difficult and several of the 200 µm devices, being themselves more of a foil rather than solid pieces, simply ripped apart in the process or did not bond properly to the sensor foil.

Eventually, however, it was possible to assemble a few functioning devices of 200 µm thickness. The devices were then sent to the collaborator for testing with dTom *C. cinerea*.

Unfortunately, due to issues with the inoculation of some of the thinner devices, no reliable comparison of the oxygen saturation behaviour in dependence of PDMS thickness could be performed. Especially with the 200 µm devices, no growth into the devices was observed. Moreover, flushing in fresh medium was impossible as the tiny inlets did not fit the tubing, which, was necessary as the devices had dried out during the shipping. Although, it was not possible to test the original idea and correlate PDMS thickness with equilibration speed for establishment of stable oxygen levels as well as the final oxygen level within the sensor foil devices, some of the thicker devices (ca. 2 mm) were put to use to test another idea.

In an attempt to block off the PDMS with a gas impermeable (or less permeable at least) layer to avoid oxygen replenishing continuously within the PDMS and the device channels, three different methods were devised. Firstly, after an initial inoculation period in which the fungus was allowed to grow into and establish a mycelium inside of the device, the entire device, including fungal inoculum at the fungal inlet, was immersed in water. This was supposed to shut out the gaseous atmospheric oxygen. A dilution effect of the growth medium inside the device by the added water was expected to be minimal, as due to the small diameter and capillary action of the inlets, turbulent mixing could be mostly ruled out and only diffusion had to be considered. As the direct contact interface area between water and medium was reduced to the opening of the inlets, which is small compared to the volume of medium underneath, diffusion effects were also deemed as negligible for the experiment. Secondly, a layer of mycelium on top of the device was tested for its oxygen-blocking properties. Therefore, the fungus is simply left to grow onto the device, which naturally happens in most of the cases. Normally, any fungus growing on top of the device is removed for better microscopy, here, however, a dense layer of mycelium was desired to both passively block off oxygen from the device as well as actively consume it. Two devices of the same thickness were set up accordingly, one with a thick mycelial layer on top and one with any fungus wiped off the top and immersed in water. The development of the oxygen levels inside the devices was recorded over the course of two days. The results obtained by the collaborator are displayed in Figure 64. The fungal mass inside the channels was similar in both devices, however, no replicates

were possible as the two devices were the last ones in this batch. The region of interest was a 2 x 2 mm^2 square at the beginning of the main investigation chamber (where the fungal inlet enters the chamber).

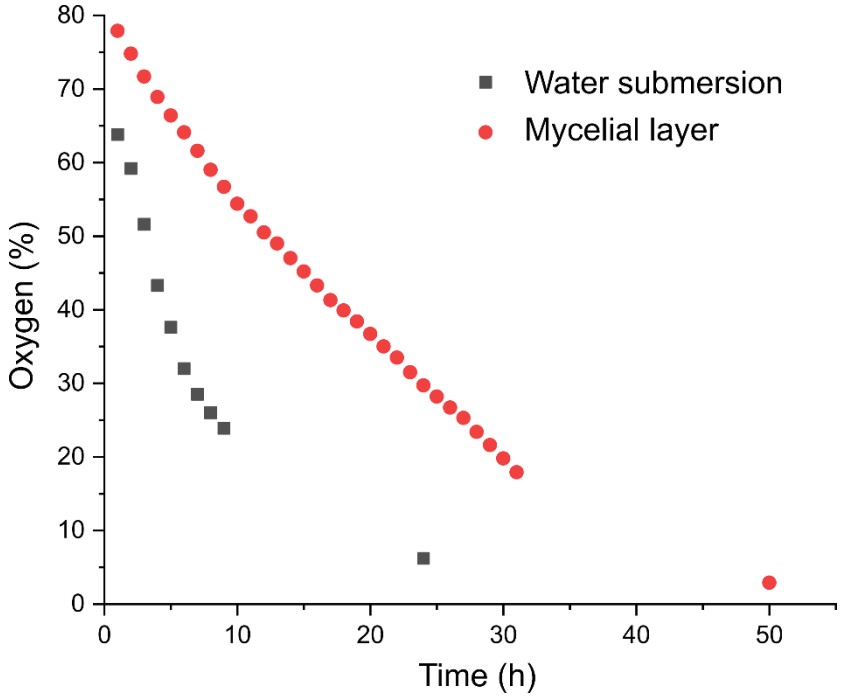


Figure 64: Oxygen depletion within the sensor foil device over time. Point plot showing the decrease in the oxygen levels over 50 h within a sensor foil device inoculated with *Coprinopsis cinerea*. The device was either (black) fully submersed in water or (red) covered under a mycelial layer to block environmental oxygen from replenishing the oxygen levels in the device.

The graph in Figure 64 shows the oxygen depletion within the devices over time. As the starting point the moment in which the entire channel area was covered in fungus was chosen. Therefore, the oxygen levels at the beginning of the measurements (t = 0h) were not the same, with about 80 % in the device with the mycelial cover layer compared to approximately 65 % in the submerged device. The experiment does not represent a statistically reliable analysis, however, does give an overall idea about the functionality of the two tested methods. Despite the absence of replicates, the strong dependence on total fungal biomass, which could not be controlled in this experiment, and the dynamicity of the mycelial cover layer, which in turn was also continuously growing during the experiment, a clear difference in the trend of the curves can be observed. The water submersion produced a much steeper decrease in oxygen compared to the mycelial cover layer, reaching an oxygen level below 10 % after about 24 h, in contrast to approximately double the time (48 h) for the mycelial layer. Moreover, it was

shown that both methods allowed to achieve and measure oxygen depletion caused by a fungus inside the sensor device. Between the two methods, submerging the device in water proved to be the more efficient one. During the experiments, however, it became equally clear that the resolution (both temporally and spatially) remained extremely low. Qualitative, spatially resolved results of the oxygen level development along with a microscopy image of the measured area are shown in Figure 65.

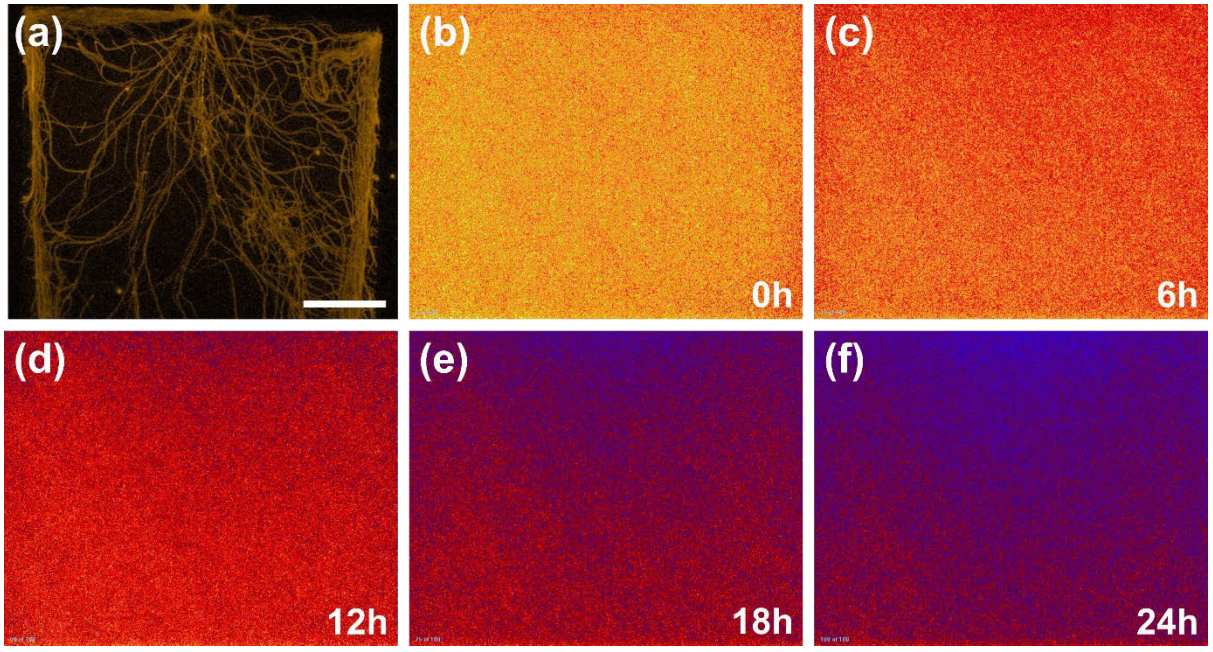


Figure 65: Development of oxygen levels around fungal hyphae. (b)-(f) Time series of the development of the oxygen level in a sensor foil device around hyphae of *Coprinopsis cinerea*, acquired with the VisiSens TD sensor over 24 h. Blue indicates low and yellow high oxygen levels (a) Fluorescence confocal image of the hyphal distribution in the measured field of view at timepoint 24 h. Scale bar: 250 µm.

According to the user manual released by the manufacturer, a maximal spatial resolution of about 25 µm can be achieved. In our devices, however, no fine resolution of that level could be observed and only a slight gradient with a stronger oxygen depletion (Figure 65, blue/purple areas) in areas with more fungal density was found. Here the PDMS most likely, as discussed above, creates a blur effect. But equally on plate no resolution of 25 µm was achieved (Figure **61**b). Here, a gradient in oxygen level was observed over a distance of a few hundred µm, however, no gradient around the hyphal tips was discernible. This suggests that a significant amount of fungal biomass is needed in order to reliably consume a measurable amount of oxygen. Consequently, as the original idea of growing fungi inside the devices, confined to a

layer of 10 µm height (single or few hyphal layers) and resolving oxygen gradients around single hyphae or groups of few hyphae, did not work out, we decided to pursue a rather indirect measurement method to infer the oxygen consumption of a single hypha. Therefore, a modification of the phage devices was envisioned, featuring stepwise changes in channel height of the investigation chamber, e.g., starting at 10 µm and then gradually going up to 100 µm in intervals of 10 µm. The fungus would then be supposed to fill the entire chamber volume with mycelium, thus providing a linear series of 10 different volumes of fungal biomass. The fungal volume would then be calculated using a confocal laser scanning microscope and correlated with the results obtained with the oxygen sensor. From this, the oxygen consumption of individual hyphae or hyphal segments could be inferred. With 10 different step heights, errors due to patchy fungal growth and uneven filling of the chamber with fungus could be averaged out; however, this constitutes a major challenge for the device manufacturing.

The SU-8/silicon soft lithography technique used for producing the master moulds for our devices (see *3.2.1.2 Optimisation of the photolithography protocol*) would demand the preparation of 10 stacked layers, each including all process steps, i.e., spin coating, baking and UV exposure, as well as requiring precise alignment of every single subsequent layer with the previous structures. This would render the device manufacturing a very expensive, time consuming and error-prone procedure. While at least the need for 10 separate expensive photomasks could be circumvented by using a maskless lithography system (e.g., Smart Print UV, France), which allows to “UV-print” the desired structures from a digital mask without the need of a physical, printed photomask, there is no substitute for the other lithography steps available. Therefore, to first test the overall feasibility of the idea, a device featuring only two different step heights, 10 µm and 80 µm, was manufactured. The devices were then shipped and put to use by inoculation with dTom *C. cinerea* and immersion in water for the oxygen measurements. For the measurements of the fungal biomass it was found that the density of the mycelium in the 80 µm chamber was too high to be quantified with the confocal microscope, however, it was suggested that an interference microscope (available at the collaborators institute) would be able to precisely measure the fungal biomass even at high density. Generally, as the microscopes had to image through the sensor foil, very high levels of laser intensity and exposure had to be used, which resulted in killing the fungi, rendering

this microscopy as the end point of each experiment. Furthermore, an important concern for the experiment was that in the course of the measurements, no significant further fungal growth should be taking place, while the fungus still needs to be vital. As the oxygen sensor system is not compatible with the microscopy set-up and therefore significant time passes between the oxygen measurements and determining the fungal biomass with the microscope, fungal growth would introduce a major systematic error into the results. Unfortunately, at this point all further proceedings in the project, including the important measurements of oxygen levels in the 10 µm compared to the 80 µm chamber compartment, had to be halted until further notice. Furthermore, even though progress was made with the filamentous fungus *C. cinerea*, the system remained unfeasible for AMF. This was mainly due to the lack of fluorescence and thus visibility in the microscopy images as well as no detectable oxygen depletion because of the sparse hyphal growth particular to these asymbiotic AMF spore cultures.

As potential future directions of the project, firstly, follow-up tests with the sensor device with different step heights were envisioned. Furthermore, another experiment inoculating the fungi with various media (suggested were 100 % YMG, 10 % YMG and PBS) was devised, in order to test whether a difference in oxygen consumption could be detected with the sensor devices. Secondly, the possibility of using single oxygen sensitive beads (rather than immobilised on a foil) directly introduced into the microfluidic channels could be investigated. Such beads come in diameters between 5-40 µm (similar to or slightly above common widths of hyphae) and have been reported to be non-toxic and sporting equilibration times of a few minutes with good reversibility (Acosta *et al.*, 2009). So far, this methodology has been successfully applied to studies in mammalian cells (Wang *et al.*, 2013; Gehre *et al.*, 2020), but never before with fungi. With the help of these beads, oxygen levels in the hyphosphere could be resolved, without the decrease in microscopy imaging quality caused by the sensor foil. That bead-like sensors can be a very promising methodology, was shown before by our collaborators (Xiong *et al.*, 2021). Here they used the cyanobacterium *Synechocystis* sp. PCC6803_peripHlu, immobilised in an agarose base, as a bioreporter for pH and created a pH map in the hyphosphere of *C. cinerea* resolved down to 3 x 3 μm^2. Implementing a pH sensor into our devices was initially refrained from, as mentioned above. This was due to the fact that while oxygen is able to easily permeate

through the PDMS layer on the sensor foil, necessary for bonding, pH levels cannot be sensed through the PDMS. Therefore, a different microfabrication approach would have had to be developed. One such work-around would require only coating areas to be bonded in PDMS while leaving areas that will become channels free from PDMS, which is difficult to achieve.

During the experiments, we eventually managed to minimise the issue with the PDMS "buffering" the oxygen levels. By immersing the entire device in water, we achieved to establish measurable oxygen depletion within hours. However, still, a considerably poor spatial and temporal resolution remained. Finally, to further improve this aspect, a change of the device material could be theoretically contemplated. Besides oxygen permeability of the material, other parameters such as diffusivity and solubility play a crucial role (Grist *et al.*, 2022). For PDMS, all 3 factors are very high, compared to other materials, which effectively translates into the PDMS device accumulating high amounts of oxygen and gradually releasing it into the chamber, thus distorting the results obtained for the oxygen saturation. Materials suggested to lower this adverse effect and aid controlling oxygen levels, were TPX™ (a polymethylpentene co-polymer) and Mylar® (biaxially-oriented polyethylene terephthalate). Both materials have been used for microfluidic applications before (Mylar® (Neils *et al.*, 2004; Irawan *et al.*, 2005); TPX™ (Qiaole *et al.*, 2009; Sønstevold *et al.*, 2023)), however, require manufacturing procedures entirely different to the PDMS method established in our lab.

6.2.2 Proof-of-concept growth experiments of *Mucoromycotina* fine-root endophytes (MFRE) in the *AMF-SporeChip*

As another type of mycorrhizal fungi, *Mucoromycotina* fine-root endophytes (MFRE) have recently (within the last 2 decades) emerged on the scene as members of their own separate sub-phylum, the *Mucoromycotina* (Orchard *et al.*, 2017). Previously, these fungi have been classified into the sub-phylum *Glomeromycotina*, along with AMF, due to them co-infecting the same plant host (Rimington *et al.*, 2015) and the close resemblance in their infection mechanism, both being endomycorrhizal fungi and hence forming the nutrient exchange interface inside of the root cell (epidermal and cortical), which can be "arbuscule-like" in MFRE (Yamamoto *et al.*, 2019). Despite their similarities, however, both groups of fungi have also very distinct characteristics. While AMF are known to be obligate symbionts and strictly rely

on the presence of a suitable plant host, MFRE possess both saprotrophic as well as symbiotic properties (Field *et al.*, 2015). Moreover, MFRE have been found to colonise roots of non-host *Arabidopsis thaliana* (Prout *et al.*, 2023). MFRE feature a dense network of overall very fine hyphae (<1.5 µm; hence the name "*fine* root endophyte"), whereas AMF grow thicker hyphae (>3 µm) in a much sparser network (Orchard *et al.*, 2017). AMF produce large spores (10-160 µm in *Rhizophagus*, measured, see *3.2.2.2 Spore germination and hyphal growth behaviour in the confined environment*, sub-mm in *Gigaspora*). MFRE on the other hand grow "fan-like" structures at hyphal ends, as well as swellings, with shapes ranging from amorphous to circular, closely resembling spores. So far, however, no clear function could be attributed to these swellings, although a storage function is likely.

Little else is known about the morphology and lifestyle of these MFRE, especially outside of the plant host. Therefore, due to their close relation to AMF, a follow up project to study MFRE in an asymbiotic as well as presymbiotic stage, on the hyphal level and real-time, using the *AMF-SporeChip* as a base device, was envisioned. In preparation of this venture, first the culturability of MFRE had to be demonstrated in microfluidic devices. This project was started in collaboration with Dr Silvia Pressel (Natural History Museum, London), who, along with her colleagues, recently managed to cultivate an MFRE strain in a monoxenic culture with clover and showed first evidence of nutritional mutualism of MFRE (Hoysted *et al.*, 2023). Currently, they maintain cultures of two different MFRE strains in the lab, provisionally named *Lyc 1* and *Lyc 2*, based on the plant they were isolated from, *Lycopodiella inundata* (L.), which were both supposed to be tested in microfluidic devices. For the experiments, six-week-old MFRE monoxenic cultures were subcultured in Magenta vessels containing 100 ml liquid MSR(+) medium or liquid Gamborg's B-5 (GM) basal medium with Minimal Organics (Sigma-Aldrich, Germany) containing 10 g/L sucrose, set to a pH of 4.5 (subsequently called GM(+)). Additionally, MFRE cultures were set-up in 90 mm Petri-dishes containing either MSR(+) medium solidified with 1 g/L phytagel or GM(+) medium with 3 g/L agar (Sigma-Aldrich, Germany) for a semi-solid substrate as well as 4 g/L phytagel or 12 g/L agar, respectively, added for a fully solidified substrate. The media were autoclaved at 121 °C for 15 min before use. The cultures were incubated in the dark at 26 °C for 6 weeks before using in experiments with the microfluidic devices. Thereafter, the MFRE can be subcultured from axenic plate to

axenic plate, like filamentous fungi. Other than AMF, which can only be propagated in the form of spores or along with a plant host as extraradical hyphae, MFRE can be treated like regular filamentous fungi and pieces of mycelium can be transferred as inoculum for the experiment. Therefore, besides the *AMF-SporeChip*, the *BFI device* (see *1.2.2.1 Microfluidics for fungi* and Figure A4 for device layout) was employed for experiments. The *BFI device* features two lateral openings on the side of the device that function as the fungal inlet. Here, just like with regular filamentous fungi, a plug punched from a solid agar or phytagel culture plate containing MFRE mycelium is simply placed fungal-side-down in front of the fungal inlet and expected to grow into the device. Due to the lack of spore-like propagules, the inoculation of the *AMF-SporeChip* had to be slightly adapted and the *Gigaspora* device variant was used. Taken from a liquid culture, a small piece of mycelium was dissected from the bulk using tweezers and placed into the inlet of the device. Then a syringe containing the respective medium, equipped with tubing, was plugged into the inlet and the piece of mycelium was flushed into the device, becoming trapped in the spore trapping region (and in parts entering the investigation zone, Figure 66a).

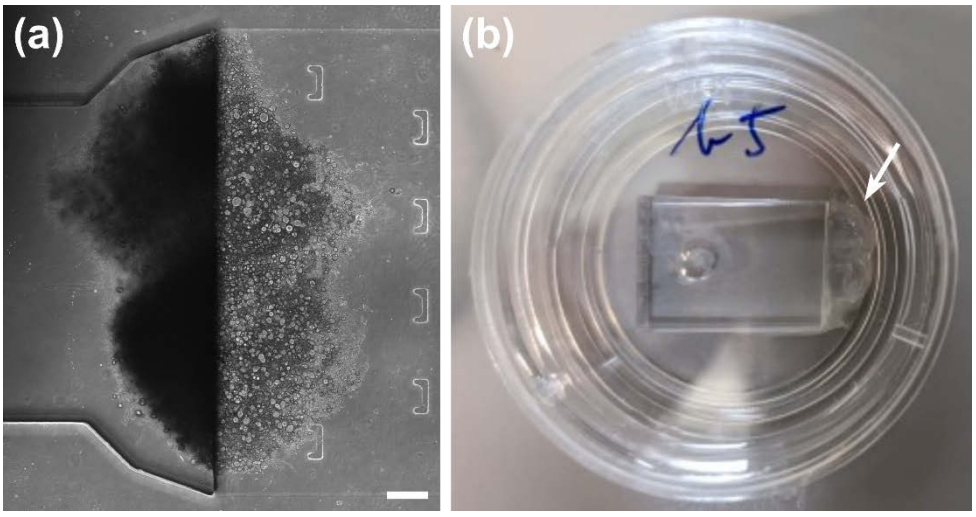


Figure 66: Loading of two different microfluidic devices with a *Mucoromycotina* fine-root endophyte (MFRE). (a) Mycelium of the MFRE *Lyc 1* obtained from a liquid culture loaded into the *AMF-SporeChip* (*Gigaspora* variant). (b) Phytagel plugs containing mycelium of *Lyc 1* (white arrow) placed in front of the fungal inlets of the *BFI device*. Scale bar: 200 µm.

Initial brief trials to grow the MFRE inside of the device failed due to unanticipated drying out as well as lack of vitality of the inoculum. Although the MFRE can be subcultured and maintained on axenic cultures for months, empirical observations suggest a gradual reduction of vitality from subculture to subculture and an occasional co-inoculation with a plant host is

needed in order to restore full vitality in the fungal culture. Therefore, for the next experiment, fresh inoculum from a monoxenic culture was used to prepare fresh axenic cultures for the device inoculation. Furthermore, a large variety of combinations of conditions was planned to be tested in an attempt to obtain a broad idea about the feasibility of potential experimental set-ups. This included both MFRE strains (*Lyc 1* and *Lyc 2*), both microfluidic devices (*AMF-SporeChip* and the *BFI device*) as well as both media (MSR(+) and GM(+)). For the media, all three consistencies, i.e., liquid, semi-solid and solid, were used for the pre-inoculation, meaning that fungal inoculum was taken from all three medium types (times two for the different base media MSR(+) and GM(+)). For pre-filling the devices only two consistencies, i.e., liquid and semi-solid, were used. The semi-solid media were kept at 70 °C after the autoclaving, stirred thoroughly on a hot plate and quickly pipetted into the devices, right after the bonding (see *2.1.2 PDMS device manufacturing*). Generally, agar is a much stronger solidifying agent than phytagel and therefore the semi-solid GM(+) medium with agar results in a considerably sturdy texture, while the semi-solid MSR(+) medium with phytagel turned out to be rather a viscous liquid. As inoculating the *AMF-SporeChip* requires a syringable medium in order to flush in the mycelium piece, no semi-solid GM(+) but only semi-solid MSR(+) could be used with these devices. The idea behind preparing the media with different viscosities was to test, firstly, whether a change of media, e.g., inoculating mycelium obtained from a solid culture (phytagel or agar) in a microfluidic device filled with liquid medium, impacts the growth performance. Secondly, pre-filling devices with semi-solid media was trialled to explore the possibility of a medium with higher viscosity and hence higher physical resistance in the microenvironment, just like it is found in the fungus' natural habitat, soil, playing a role in fungal development.

Overall, the experiment was very successful and good growth inside the devices was observed with nearly all tested conditions, after only a few days (3-4 days). Between the two MFRE strains, *Lyc 1* showed a slightly better growth compared to *Lyc 2*, however, good results were obtained with both strains. No apparent influence of the pre-filling media viscosity was observed and both liquid and semi-solid medium produced roughly the same amount of mycelium. Similarly, a change in medium texture from culture to device, did not have any salient impact on the fungi. A clear difference, however, was obtained between the two media

themselves, with overall much stronger growth in devices filled with GM(+) medium and weaker growth with the MSR(+) medium. The semi-solid pre-cultures were generally quite poorly developed at the start of the experiments and therefore also results observed inside the devices were no good. Moreover, *Lyc 1* did not grow at all in the semi-solid subcultures and could hence not even be used in the experiments.

More importantly, both device types worked for the experiment and no impediment or overall negative influence on the fungal growth could be observed, however, significant differences between the two devices with regards to handling and performance still have to be considered. The *AMF-SporeChip* for instance is notably more difficult to inoculate. As mentioned earlier, the *AMF-SporeChip* adapted for *Gigaspora* was used as it features a channel height of approximately 350 µm and thus offers more room for the MFRE mycelium to be introduced into. Still, it was found to be considerably challenging to dissect the mycelium into small enough pieces. As soon as the fungal mass was removed from the liquid, it collapses into a hardly visible clump, which is hard to dissect with tweezers. Therefore, often several attempts to obtain a suitable inoculum were needed or very high pressure had to be applied with the syringe to flush in the bulky pieces (relative to the microdimensions of the device) into the channel. In contrast, as described above, simply placing a plug carrying mycelium punched out from the culture and placed in front of the fungal inlet is required to inoculate the *BFI device* (Figure 66b). Once inoculated, however, the fungus is immediately observable in the *AMF-SporeChip* and any growth can be traced directly from the initial mycelium. In the *BFI device*, on the other hand, the fungus first has to enter the channels to be imageable. This, however, functions as clear evidence of fungal growth, while in the *AMF-SporeChip* “before and after” images have to be taken and compared to prove whether the mycelium is proliferating or not. Furthermore, the interior design of the *AMF-SporeChip* offers a much wider and more complex investigation zone where the hyphae can expand their network more freely while simultaneously being challenged by the physical obstacles. The *BFI device*, contrarily, features very long, straight narrow channels (110 µm wide) without obstacles, that restricts any major expansions of the mycelium. This led to a wide expansion in a sparse hyphal network of the MFRE in the *AMF-SporeChip* (Figure 67a) and hyphae being mainly compressed to a highly

dense mycelium, including a very dense and compact growth front down the lanes in the *BFI device* (Figure 67b).

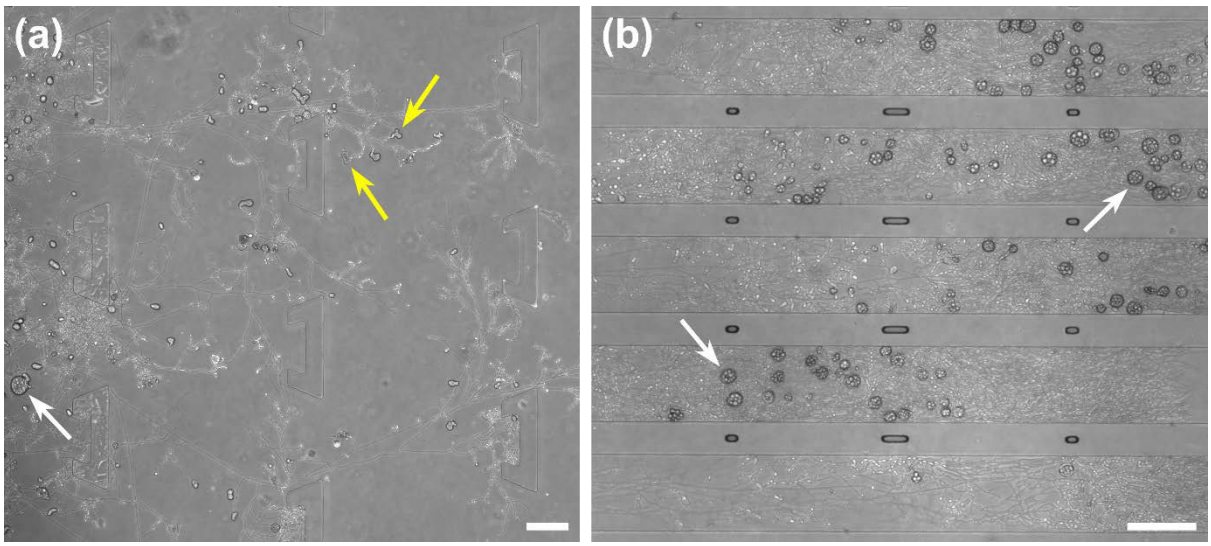


Figure 67: Growth of *Mucoromycotina* fine-root endophytes (MFRE) in a microfluidic device. Phase contrast images of the MFRE *Lyc 2* growing in (a) the *AMF-SporeChip* (*Gigaspora* variety) and (b) the *BFI device* after 7 days. Yellow arrows in (a) highlight fan-like structures and white arrows in (a) and (b) swellings. Scale bars: 100 µm.

The figure shows results obtained with *Lyc 2* grown in liquid GM(+) medium after 7 days in the two different microfluidic devices. Besides the growth pattern of the hyphal network, the previously reported hyphal swellings as well as fan-like structures (Hoysted *et al.*, 2023) were clearly observed. The development of the mycelia in the devices was monitored up to day 32 and in most conditions, hyphal extension, branching and extensive swelling formation was registered up to the last day of the experiment. Due to a relatively high variability in the phenotypes regarding network density and number, size, shape and density of swellings observed, however, no clear distinction between the two strains could be made. Generally, as mentioned above, this experiment was designed to act as a proof-of-concept initial trial to set the scene for a new PhD project. Therefore, the analyses performed were qualitative in manner. To evaluate and compare the different conditions, the number of devices with any fungal growth, the number of times the fungus managed to grow through the entire device (from inlet to outlet) after 7 days as well as whether further development occurred after, were chosen as assessment criteria.

In future studies, a reliable and consistent method for analysing the results needs to be devised, ideally involving some sort of computational automatic analysis tool. The results of

this pre-experiment show that MFRE are very-well culturable in the microfluidic devices and further suggest the use of GM(+) medium for the experiments; however, further examinations are advisable and should be extended to testing the effect of nutrient availability on the development of the hyphal network as well as starvation effects, e.g., by inoculating fungus from a nutrient-rich pre-culture in a nutrient-depleted environment and vice versa. With regards to the microfluidic system, advantages and disadvantages were found for both device types tested. Going forwards, a new device should be designed, featuring beneficial aspects from both devices, like for instance a BFI-type fungal inlet, to be inoculated from mycelial plugs, leading into a wide main-chamber with or without an array of physical obstacles, as featured in the *AMF-SporeChip*. With such microfluidic systems, the growth behaviour of MFRE could be further analysed in detail and compared to AMF and other fungi. As MFRE form a mycorrhiza similar to AMF, however, also have saprotrophic properties, their overall behaviour in soil is expected to be a mix between traits of the other fungi. Moreover, a potential switch between symbiotic and saprotrophic mode could be tested, by changing nutrient availability and/or applying symbiotic cues or roots. Prospectively, a device providing a platform for an encounter between the fungi and a plant root, e.g., building on the *dual-flow-RootChip* (Grossmann *et al.*, 2011; Stanley *et al.*, 2018), would be highly desirable to study the fungi's interaction with its host, not only for MFRE but also AMF. Even though much has been uncovered in recent years about the (pre-)symbiotic signalling between AMF and their hosts (see *Stages of arbuscular mycorrhizal development*), there is little appreciation for the dynamics and range of the processes. With a tailored device, it could be studied, for instance, at which distance approaching AMF hyphae start triggering a calcium spiking response in the root. For MFRE, this is all widely untrodden ground.

6.3 Concluding remarks and future directions for microfluidic AMF research

The herein presented project describing and discussing the study of AMF on a microfluidic platform is one of the first of its kind. Two well-functioning microfluidic devices have been developed to study the behaviour of asymbiotic AMF spores and hyphae in depth. Moreover, a foundation was laid for further extensive research in the field. A complete overview of the

research objectives and final outcomes of this thesis can be found in Figure 4 and Figure 68, respectively.

Outcomes	Chapter No.
Developed the *AMF-SporeChip*, a microfluidic device for trapping AMF spores and confronting asymbiotic hyphae with physical obstacles	3
Elucidated space searching behaviour including novel reversible cytoplasm retraction	4
Adapted *AMF-SporeChip* to allow studying of *Gigaspora margarita*	3,4
Established fluorescent staining method on-chip, however, without finding a Spitzenkörper in AMF	4
Developed the *AMF-AnastomosisChip*, a microfluidic device for trapping spores of different AMF strains and isolating anastomosis events	5
Demonstrated gradient formation in *AMF-AnastomosisChip*	5
Equipped *AMF-SporeChip* with oxygen-sensitive foil to study oxygen gradients in the hyphosphere	6
Used *AMF-SporeChip* to examine MFRE growth on the hyphal level	6

Figure 68: Overview of the research outcomes of the thesis.

Moving on from the asymbiotic to the pre-symbiotic stage of the AMF lifecycle, devices could be equipped to either simulate a host in proximity or introduce an actual host. One of the main challenges for designing such a device is the asymmetry in dimensions between plant roots (usually >100 µm wide) and hyphae (<10 µm wide), which makes it difficult to confine both partners in the same focal plane. As discussed for MFRE, a device holding both fungi and roots, thus providing an opportunity for direct interaction between both partners, could be highly useful for studying not only pre-symbiotic signalling but also important steps of the infection process, such as hyphopodium formation. Besides analysing the process of "successful" infections leading to a mutually beneficial interaction, it would be equally interesting to shed light on why certain plant species (an approximation of 29%) including the plant model *Arabidopsis thaliana* are not able to form a functional symbiosis with AMF. Moreover, some of these nonhost plants have been found to be colonised by AMF under certain conditions, however, with underdeveloped, rudimentary phenotypes of the symbiosis, i.e., arbuscules and vesicles (Cosme *et al.*, 2018). To more specifically focus on the pre-symbiotic signalling, microfluidic devices can be equipped with chemical gradients (Bernier *et*

al., 2024). When supply channels are attached to the main investigation zone, gradients or niches can be created due to the laminar flow behaviour intrinsic to microfluidic systems. These set-ups could then be used to study the reaction of the fungus towards gradients of signalling molecules, such as strigolactones, known to be involved in guiding hyphae towards a suitable host root (Ruyter-Spira *et al.*, 2013), as well as towards nutrient patches.

Besides hyphae in the asymbiotic or pre-symbiotic stage, AMF further form extraradical hyphae once the mycorrhiza has been successfully established. These hyphae then radiate out from the rhizome of the host into the soil, foraging for soil nutrients and forming spores to herald the beginning of a new potential AMF lifecycle. These hyphae are further involved in forming so-called “common mycorrhizal networks” (CMN) (Simard *et al.*, 2012). These networks connect plants underground and transfer nutrients as well as information such as warning signals to induce defence mechanisms in the plant (Babikova *et al.*, 2013). The specificity of the conveyed signals as well as the exact nature of the effectors, remains unclear, and even the involvement of RNA or virus genomes has been suggested, with importance for agriculture (Wang *et al.*, 2017). As extraradical hyphae are always directly connected to the plant, introducing them into microfluidic devices is quite challenging and requires the microfluidic system to be part of a larger, aseptic system including the plant host carrying the fungus. Such systems have been developed by Dr Claire Stanley (in preparation) and Hammer *et al.* (2024).

Another important aspect of AMF lifestyle are interactions with organisms other than the plant host or each other/themselves (see *4.2.5. Anastomosis formation in the device*). Bacterial-fungal interactions have been found to be immensely important in the context of soil ecology and are being thoroughly studied in microfluidic devices (Stanley *et al.*, 2014; Clark *et al.*, 2024). For AMF, a highly intriguing interaction with phosphate solubilising bacteria (PSB) was recently discovered, which suggests a tripartite interaction going beyond the well-known dual mycorrhiza (Zhang *et al.*, 2018; Jiang *et al.*, 2021). Here it was presented how AMF are able to selectively recruit PSB along their hyphae. These bacteria help the fungus prospect for organic phosphorus in soil, which the fungus alone would not be able to exploit, and in turn receive hyphal exudates as recompensation. These experiments were enabled by *in vitro* cultivation of AMF on whole plants or root organs (used in this project for spore production),

which provides large amounts of AMF hyphae free from both roots as well as unwanted bacterial contamination. Microfluidic technology could take these studies even further to a single-hypha level and provide real-time results on these interactions.

Filamentous fungi are known to contain multiple nuclei within the same hyphal compartment (Maheshwari, 2005), especially coenocytic fungi like *Mucoromycota*, i.e., AMF and MFRE. Often, these nuclei get redistributed between different individua through anastomoses leading to heterokaryosis, the coexistence of genetically different nuclei within the same hyphal compartment (Strom and Bushley, 2016; Scott *et al.*, 2019). The underlying rules of these processes are still widely elusive. Microfluidic devices such as the *AMF-AnastomosisChip* or a variation of it could aid in witnessing nuclei circulation and exchange within the mycelial network and in through anastomoses newly formed networks. This, in turn, are important pieces of the puzzle in elucidating elementary parts of the biology of fungi in general such as sexual compatibility (Nieuwenhuis *et al.*, 2013) or self/nonself recognition mechanisms (Kahmann and Bölker, 1996). Acquiring such knowledge would also have further relevance for biotechnological applications where suitable fungi could be selected on a nucleus level rather than the strain level.

Even though the romanticised concept of CMNs or popularly called “wood-wide web”, awarding mycorrhizal fungi the role of the “central computation unit” in soil-based ecosystems is controversial (Merckx *et al.*, 2024), it is factual that fungi span immense networks underground connecting organisms of same and different species as well as kingdoms in many ecosystems. Understanding about communication within the system is scarce, as discussed above, and besides chemical signals, electrical currents could be theoretically involved in connecting and coordinating such a complex network like soil, as precedented in the central nervous system of vertebrates. Electricity has been shown to be involved in coordinating cell behaviour in organisms ranging from mammals (Piccolino, 1997) over plants (Brenner *et al.*, 2006; Canales *et al.*, 2018) down to bacteria (Prindle *et al.*, 2015) and moreover in communication on an intracolony or interspecies level (Clarke *et al.*, 2013; Beagle and Lockless, 2015; Prindle *et al.*, 2015). Electrical measurements on fungi have been performed multiple times before (Olsson and Hansson, 1995; Adamatzky, 2018) and electrical oscillations were attempted to be deciphered as a fungal language (Adamatzky, 2022), however, mainly

on a rather macroscopic level, i.e., mycelium or entire organisms including fruiting bodies. Integrating electronics into microfluidic devices could take these studies further down to the hyphal level. This emerging field widely remains untrodden territory, however, Duarte *et al.* (2022) have shown the feasibility and potential with their PDMS microfluidic chip containing an array of nanoelectrodes for dielectrophoretic trapping and subsequent detection and identification of spores from the phytopathogenic fungus *Sclerotinia sclerotiorum*.

BIBLIOGRAPHY

Achmann S, Hämmerle M, Kita J, Moos R. 2008. Miniaturized low temperature co-fired ceramics (LTCC) biosensor for amperometric gas sensing. *Sensor Actuat B-Chem* **135**: 89-95.

Acosta MA, Ymele-Leki P, Kostov YV, Leach JB. 2009. Fluorescent microparticles for sensing cell microenvironment oxygen levels within 3D scaffolds. *Biomaterials* **30**: 3068-3074.

Adamatzky A. 2018. On spiking behaviour of oyster fungi *Pleurotus djamor*. *Sci Rep* **8**: 7873.

Adamatzky A. 2022. Language of fungi derived from their electrical spiking activity. *Roy Soc Open Sci* **9**: 211926.

Aleklett K, Ohlsson P, Bengtsson M, Hammer EC. 2021. Fungal foraging behaviour and hyphal space exploration in micro-structured Soil Chips. *ISME J* **15**: 1782-1793.

Alexander T, Meier R, Toth R, Weber HC. 1988. Dynamics of arbuscule development and degeneration in mycorrhizas of *Triticum aestivum* L. and *Avena sativa* L. with reference to *Zea mays* L. *New Phytol* **110**: 363-370.

Almeida F, Rodrigues ML, Coelho C. 2019. The still underestimated problem of fungal diseases worldwide. *Front Microbiol* **10**: 214-214.

Asenova E, Lin HY, Fu E, Nicolau DV, Nicolau DV. 2016. Optimal fungal space searching algorithms. *IEEE T Nanobiosci* **15**: 613-618.

Au - Lichius A, Au - Zeilinger S. 2019. Application of membrane and cell wall selective fluorescent dyes for live-cell imaging of filamentous fungi. *JoVE*: e60613.

Azizipour N, Avazpour R, Rosenzweig DH, Sawan M, Ajji A. 2020. Evolution of biochip technology: a review from Lab-on-a-Chip to Organ-on-a-Chip. *Micromachines* **11**: 599.

Babikova Z, Gilbert L, Bruce TJ, Birkett M, Caulfield JC, Woodcock C, Pickett JA, Johnson D. 2013. Underground signals carried through common mycelial networks warn neighbouring plants of aphid attack. *Ecol Lett* **16**: 835-43.

Bago B, Azcón-Aguilar C, Goulet A, Piché Y. 1998. Branched absorbing structures (BAS): a feature of the extraradical mycelium of symbiotic arbuscular mycorrhizal fungi. *New Phytol* **139**: 375-388.

Balasubramanian S, Chen J, Wigneswaran V, Bang-Berthelsen CH, Jensen PR. 2021. Droplet-based microfluidic high throughput screening of *Corynebacterium glutamicum* for efficient heterologous protein production and secretion. *Front Bioeng Biotechnol* **9**: 668513.

Balestrini R, Bonfante P. 2014. Cell wall remodeling in mycorrhizal symbiosis: a way towards biotrophism. *Front Plant Sci* **5**: 237.

Baranger C, Fayeulle A, Le Goff A. 2020. Microfluidic monitoring of the growth of individual hyphae in confined environments. *Roy Soc Open Sci* **7**: 191535.

Baranger C, Pezron I, Lins L, Deleu M, Le Goff A, Fayeulle A. 2021. A compartmentalized microsystem helps understanding the uptake of benzo[α]pyrene by fungi during soil bioremediation processes. *Sci Total Environ* **784**: 147151.

Barkal LJ, Procknow CL, Alvarez-Garcia YR, Niu M, Jimenez-Torres JA, Brockman-Schneider RA, Gern JE, Denlinger LC, Theberge AB, Keller NP, Berthier E, Beebe DJ. 2017. Microbial volatile communication in human organotypic lung models. *Nat Commun* **8**: 1770.

Barrios-González J, Tomasini A, Viniegra-González G, López L. 1988. Penicillin production by solid state fermentation. *Biotechnol Lett* **10**: 793-798.

Bartnicki-Garcia S. 2006. Chitosomes: past, present and future. *FEMS Yeast Res* **6**: 957-965.

Bartsch de Torres H, Rensch C, Fischer M, Schober A, Hoffmann M, Müller J. 2010. Thick film flow sensor for biological microsystems. *Sensor Actuat A-Phys* **160**: 109-115.

Basu S, Rabara RC, Negi S. 2018. AMF: The future prospect for sustainable agriculture. *Physiol Mol Plant P* **102**: 36-45.

BCCM. 2024. *BCCM/MUCL environmental & agro-food fungi & yeasts catalogue* [Online]. Available: https://bccm.belspo.be/MUCL-catalogue-search [Accessed 26/11 2024].

Beagle SD, Lockless SW. 2015. Electrical signalling goes bacterial. *Nature* **527**: 44-45.
Bécard G, Piché Y. 1989. Fungal growth stimulation by CO2 and root exudates in vesicular-arbuscular mycorrhizal symbiosis. *Appl Environ Microb* **55**: 2320-2325.
Bembnowicz P, Herbut P, Malodobra M, Karpiewska A, Golonka L, Jonkisz A, Dobosz T. 2011. The low temperature co-fired ceramics (LTCC) chip for polymerase chain reaction (PCR) application. *Opt Appl* **41**: 10.
Berlanda SF, Breitfeld M, Dietsche CL, Dittrich PS. 2021. Recent advances in microfluidic technology for bioanalysis and diagnostics. *Anal Chem* **93**: 311-331.
Bernier LS, Estoppey A, Bindschedler S, Stan G-B, Junier P, Stanley CE. 2024. Microfluidic platform for microbial spore germination studies in multiple growth conditions. *bioRxiv*: 2024.05.13.593863.
Berruti A, Lumini E, Bianciotto V. 2016. AMF components from a microbial inoculum fail to colonize roots and lack soil persistence in an arable maize field. *Symbiosis* **72**: 73-80.
Betz WJ, Mao F, Bewick GS. 1992. Activity-dependent fluorescent staining and destaining of living vertebrate motor nerve terminals. *J Neurosci* **12**: 363.
Betz WJ, Mao F, Smith CB. 1996. Imaging exocytosis and endocytosis. *Curr Opin Neurobiol* **6**: 365-371.
Blasius D, Feil W, Kottke I, Oberwinkler F. 1986. Hartig net structure and formation in fully ensheathed ectomycorrhizas. *Nord J Bot* **6**: 837-842.
Bleichrodt R-J, Hulsman M, Wösten HAB, Reinders MJT. 2015. Switching from a unicellular to multicellular organization in an *Aspergillus niger* hypha. *mBio* **6**: e00111-15.
Bonfante P, Desirò A. 2017. Who lives in a fungus? The diversity, origins and functions of fungal endobacteria living in *Mucoromycota*. *ISME J* **11**: 1727-1735.
Bonfante P, Genre A. 2010. Mechanisms underlying beneficial plant-fungus interactions in mycorrhizal symbiosis. *Nat Commun* **1**: 48.
Bouwmeester HJ, Roux C, Lopez-Raez JA, Becard G. 2007. Rhizosphere communication of plants, parasitic plants and AM fungi. *Trends Plant Sci* **12**: 224-30.
Bracker CE, Ruiz-Herrera J, Bartnicki-Garcia S. 1976. Structure and transformation of chitin synthetase particles (chitosomes) during microfibril synthesis *in vitro*. *PNAS* **73**: 4570-4574.
Brand A, Gow NA. 2009. Mechanisms of hypha orientation of fungi. *Curr Opin Microbiol* **12**: 350-7.
Brenner ED, Stahlberg R, Mancuso S, Vivanco J, Baluška F, Van Volkenburgh E. 2006. Plant neurobiology: an integrated view of plant signaling. *Trends Plant Sci* **11**: 413-419.
Brundrett M. 2004. Diversity and classification of mycorrhizal associations. *Biol Rev* **79**: 473-495.
Brundrett MC, Kendrick B. 1988. The mycorrhizal status, root anatomy, and phenology of plants in a sugar maple forest. *Can J Botany* **66**: 1153-1173.
Bryan A, Pingali P, Joslyn M, Li H, Bernas T, Koblinski J, Landry J, Lee WS, Patel B, Neuwelt A. 2023. High-dose acetaminophen with N-acetylcysteine rescue inhibits M2 polarization of tumor-associated macrophages. *Cancers* **15**: 4770.
Buee M, Rossignol M, Jauneau A, Ranjeva R, Bécard G. 2000. The pre-symbiotic growth of arbuscular mycorrhizal fungi is induced by a branching factor partially purified from plant root exudates. *Mol Plant Microbe In* **13**: 693-698.
Cairney JWG, Meharg AA. 2003. Ericoid mycorrhiza: a partnership that exploits harsh edaphic conditions. *Eur J Soil Sci* **54**: 735-740.
Canales J, Henriquez-Valencia C, Brauchi S. 2018. The integration of electrical signals originating in the root of vascular plants. *Front Plant Sci* **8**: 2173.
Cárdenas-Flores A, Draye X, Bivort C, Cranenbrouck S, Declerck S. 2010. Impact of multispores in vitro subcultivation of *Glomus* sp. MUCL 43194 (DAOM 197198) on vegetative compatibility and genetic diversity detected by AFLP. *Mycorrhiza* **20**: 415-425.
Carroll NJ, Rathod SB, Derbins E, Mendez S, Weitz DA, Petsev DN. 2008. Droplet-based microfluidics for emulsion and solvent evaporation synthesis of monodisperse mesoporous silica microspheres. *Langmuir* **24**: 658-661.

Carvajal-Muñoz J, Carmona-Garcia C. 2012. Benefits and limitations of biofertilization in agricultural practices. *Livest Res Rural Dev* **24**: 1-8.
Chabot S, Bécard G, Piché Y. 1992. Life cycle of *Glomus intraradix* in root organ culture. *Mycologia* **84**: 315-321.
Chaudhary VB, Nolimal S, Sosa-Hernández MA, Egan C, Kastens J. 2020. Trait-based aerial dispersal of arbuscular mycorrhizal fungi. *New Phytol* **228**: 238-252.
Chen B, Li W, Pang Y, Zhang N, Bian S, Liu C, Yang Z, Jiang Y, Li R, Xie Y. 2021. Rapid detection of fungi from blood samples of patients with candidemia using modified calcofluor white stain. *J Microbiol Meth* **184**: 106202.
Cherdantsev A, Bobylev A, Guzanov V, Kvon A, Kharlamov S. 2023. Measuring liquid film thickness based on the brightness level of the fluorescence: methodical overview. *Int J Multiphas Flow* **168**: 104570.
Choi J, Summers W, Paszkowski U. 2018. Mechanisms underlying establishment of arbuscular mycorrhizal symbioses. *Annu Rev Phytopathol* **56**: 135-160.
Clark AJ, Masters-Clark E, Moratto E, Junier P, Stanley CE. 2024. Visualizing liquid distribution across hyphal networks with cellular resolution. *bioRxiv*: 2024.08.01.606151.
Clarke D, Whitney H, Sutton G, Robert D. 2013. Detection and learning of floral electric fields by bumblebees. *Science* **340**: 66-69.
Corradi N, Bonfante P. 2012. The arbuscular mycorrhizal symbiosis: origin and evolution of a beneficial plant infection. *PLOS Pathog* **8**: e1002600.
Corral-Martínez P, Siemons C, Horstman A, Angenent GC, de Ruijter N, Boutilier K. 2020. Live Imaging of embryogenic structures in *Brassica napus* microspore embryo cultures highlights the developmental plasticity of induced totipotent cells. *Plant Reprod* **33**: 143-158.
Cosme M, Fernandez I, van der Heijden MGA, Pieterse CMJ. 2018. Non-mycorrhizal plants: the exceptions that prove the rule. *Trends Plant Sci* **23**: 577-587.
Cosson S, Lutolf MP. 2014. Hydrogel microfluidics for the patterning of pluripotent stem cells. *Sci Rep* **4**: 4462.
Cranenbrouck S, Voets L, Bivort C, Renard L, Strullu D-G, Declerck S. 2005. Methodologies for *in vitro* cultivation of arbuscular mycorrhizal fungi with Root Organs. *In:* Declerck S, Fortin JA, Strullu D-G, eds. *In Vitro Culture of Mycorrhizas.* Berlin Heidelberg, Germany: Springer Berlin Heidelberg, 341-375.
Croll D, Giovannetti M, Koch AM, Sbrana C, Ehinger M, Lammers PJ, Sanders IR. 2009. Nonself vegetative fusion and genetic exchange in the arbuscular mycorrhizal fungus *Glomus intraradices*. *New Phytol* **181**: 924-937.
Daft MJ, Nicolson TH. 1974. Arbuscular mycorrhizas in plants colonizing coal castes in scotland. *New Phytol* **73**: 1129-1138.
Dalpé Y, de Souza FA, Declerck S. 2005. Life cycle of *Glomus* species in monoxenic culture. *In:* Declerck S, Fortin JA, Strullu D-G, eds. *In Vitro Culture of Mycorrhizas.* Berlin, Heidelberg: Springer Berlin Heidelberg, 49-71.
de la Providencia IE, de Souza FA, Fernandez F, Delmas NS, Declerck S. 2005. Arbuscular mycorrhizal fungi reveal distinct patterns of anastomosis formation and hyphal healing mechanisms between different phylogenic groups. *New Phytol* **165**: 261-71.
de La Providencia IE, Fernández F, Declerck S. 2007. Hyphal healing mechanism in the arbuscular mycorrhizal fungi *Scutellospora reticulata* and *Glomus clarum* differs in response to severe physical stress. *FEMS Microbiol Lett* **268**: 120-125.
De Stefano P, Bianchi E, Dubini G. 2022. The impact of microfluidics in high-throughput drug-screening applications. *Biomicrofluidics* **16**.
Dearnaley J, Perotto S, Selosse M-A. 2016. Structure and development of orchid mycorrhizas. *In:* Martin F (ed.) eds. *Molecular Mycorrhizal Symbiosis.* Hoboken, New Jersey: John Wiley & Sons, inc., 63-86.

Declerck S, Strullu D, Plenchette C. 1998. Monoxenic culture of the intraradical forms of *Glomus* sp. isolated from a tropical ecosystem: a proposed methodology for germplasm collection. *Mycologia* **90**: 579-585.

DeMello AJ. 2006. Control and detection of chemical reactions in microfluidic systems. *Nature* **442**: 394-402.

Di Carlo D. 2009. Inertial microfluidics. *Lab Chip* **9**: 3038-3046.

Dickie IA, Martínez-García LB, Koele N, Grelet GA, Tylianakis JM, Peltzer DA, Richardson SJ. 2013. Mycorrhizas and mycorrhizal fungal communities throughout ecosystem development. *Plant Soil* **367**: 11-39.

Dickson S. 2004. The Arum-Paris continuum of mycorrhizal symbioses. *New Phytol* **163**: 187-200.

Dickson S, Smith FA, Smith SE. 2007. Structural differences in arbuscular mycorrhizal symbioses: more than 100 years after Gallaud, where next? *Mycorrhiza* **17**: 375-393.

Dijksterhuis J, Molenaar D. 2013. Vesicle trafficking via the Spitzenkörper during hyphal tip growth in *Rhizoctonia solani*. *A Van Leeuw J Microb* **103**: 921-931.

Dittrich PS, Manz A. 2006. Lab-on-a-chip: microfluidics in drug discovery. *Nat Rev Drug Discov* **5**: 210-218.

Douds DD, Millner PD. 1999. Biodiversity of arbuscular mycorrhizal fungi in agroecosystems. *Agr Ecosyst Environ* **74**: 77-93.

Duarte PA, Menze L, Shoute L, Zeng J, Savchenko O, Lyu J, Chen J. 2022. Highly efficient capture and quantification of the airborne fungal pathogen *Sclerotinia sclerotiorum* employing a nanoelectrode-activated microwell array. *ACS Omega* **7**: 459-468.

Edwards D, Read DJ, Duckett JG, Read DJ, Duckett JG, Francis R, Ligrone R, Russell A. 2000. Symbiotic fungal associations in 'lower' land plants. *Philos T Roy Soc B* **355**: 815-831.

Fazius F, Shelest E, Gebhardt P, Brock M. 2012. The fungal alpha-aminoadipate pathway for lysine biosynthesis requires two enzymes of the aconitase family for the isomerization of homocitrate to homoisocitrate. *Mol Microbiol* **86**: 1508-30.

Field KJ, Rimington WR, Bidartondo MI, Allinson KE, Beerling DJ, Cameron DD, Duckett JG, Leake JR, Pressel S. 2015. Functional analysis of liverworts in dual symbiosis with *Glomeromycota* and *Mucoromycotina* fungi under a simulated Palaeozoic CO2 decline. *ISME J* **10**: 1514-1526.

Fiołka MJ, Takeuchi N, Sofińska-Chmiel W, Mieszawska S, Treska I. 2020. Morphological and physicochemical diversity of snow algae from Alaska. *Sci Rep* **10**: 19167.

Fischer-Parton S, Parton R, Hickey P, Dijksterhuis J, Atkinson H, Read N. 2000. Confocal microscopy of FM4-64 as a tool for analysing endocytosis and vesicle trafficking in living fungal hyphae. *J Microsc* **198**: 246-259.

Fischer MS, Glass NL. 2019. Communicate and fuse: how filamentous fungi establish and maintain an interconnected mycelial network. *Front Microbiol* **10**.

Fleißner A, Simonin AR, Glass NL. 2008. Cell fusion in the filamentous fungus *Neurospora crassa*. *In:* Chen EH (ed.) eds. *Cell Fusion: Overviews and Methods.* Totowa, NJ: Humana Press, 21-38.

Fortin JA, Bécard G, Declerck S, Dalpé Y, St-Arnaud M, Coughlan AP, Piché Y. 2002. Arbuscular mycorrhiza on root-organ cultures. *Can J Botany* **80**: 1-20.

Frank AB. 1885. Über die auf Wurzelsymbiose beruhende Ernährung gewisser Bäume durch unterirdische Pilze. *Ber Deut Bot Ges* **3**: 128–145.

Friesen TL, Stukenbrock EH, Liu Z, Meinhardt S, Ling H, Faris JD, Rasmussen JB, Solomon PS, McDonald BA, Oliver RP. 2006. Emergence of a new disease as a result of interspecific virulence gene transfer. *Nat Genet* **38**: 953-956.

Frigault MM, Lacoste J, Swift JL, Brown CM. 2009. Live-cell microscopy – tips and tools. *J Cell Sci* **122**: 753-767.

Fuchs BB, Eatemadpour S, Martel-Foley JM, Stott S, Toner M, Mylonakis E. 2019. Rapid isolation and concentration of pathogenic fungi using inertial focusing on a chip-based platform. *Front Cell Infect Mi* **9**: 1-9.

Fukuda S, Yamamoto R, Yanagisawa N, Takaya N, Sato Y, Riquelme M, Takeshita N. 2021. Trade-off between plasticity and velocity in mycelial growth. *mBio* **12**: e03196-20.
Galbraith DW. 1981. Microfluorimetric quantitation of cellulose biosynthesis by plant protoplasts using Calcofluor White. *Physiol Plantarum* **53**: 111-116.
Gallaud I. 1905. Études sur les mycorrhizes endophytes. *Rev Gen Bot*.
Gao Q, Garcia-Pichel F. 2011. Microbial ultraviolet sunscreens. *Nat Rev Microbiol* **9**: 791-802.
Garduño-Rosales M, Callejas-Negrete OA, Medina-Castellanos E, Bartnicki-García S, Herrera-Estrella A, Mouriño-Pérez RR. 2022. F-actin dynamics following mechanical injury of *Trichoderma atroviride* and *Neurospora crassa* hyphae. *Fungal Genet Biol* **159**: 103672.
Gehre C, Flechner M, Kammerer S, Küpper J-H, Coleman CD, Püschel GP, Uhlig K, Duschl C. 2020. Real time monitoring of oxygen uptake of hepatocytes in a microreactor using optical microsensors. *Sci Rep* **10**: 13700.
Genre A, Chabaud M, Faccio A, Barker DG, Bonfante P. 2008. Prepenetration apparatus assembly precedes and predicts the colonization patterns of arbuscular mycorrhizal fungi within the root cortex of both *Medicago truncatula* and *Daucus carota*. *Plant Cell* **20**: 1407-20.
Gerdemann JW, Trappe JM. 1974. The endogonaceae in the Pacific Northwest. *Mycologia* **5**: 1-75.
Ghanem N, Stanley CE, Harms H, Chatzinotas A, Wick LY. 2019. Mycelial effects on phage retention during transport in a microfluidic platform. *Environ Sci Technol* **53**: 11755-11763.
Gimeno A, Stanley CE, Ngamenie Z, Hsung MH, Walder F, Schmieder SS, Bindschedler S, Junier P, Keller B, Vogelgsang S. 2021. A versatile microfluidic platform measures hyphal interactions between *Fusarium graminearum* and *Clonostachys rosea* in real-time. *Commun Biol* **4**: 262.
Giovannetti M, Ayio L, Sbrana C, Silvia Citernesi A. 1993. Factors affecting appressorium development in the vesicular–arbuscular mycorrhizal fungus *Glomus mosseae* (Nicol. & Gerd.) Gerd. & Trappe. *New Phytol* **123**: 115-122.
Giovannetti M, Azzolini D, Citernesi AS. 1999. Anastomosis formation and nuclear and protoplasmic exchange in arbuscular mycorrhizal fungi. *Appl Environ Microb* **65**: 5571-5575.
Giovannetti M, Fortuna P, Citernesi AS, Morini S, Nuti MP. 2001. The occurrence of anastomosis formation and nuclear exchange in intact arbuscular mycorrhizal networks. *New Phytol* **151**: 717-724.
Giovannetti M, Sbrana C, Strani P, Agnolucci M, Rinaudo V, Avio L. 2003. Genetic diversity of isolates of *Glomus mosseae* from different geographic areas detected by vegetative compatibility testing and biochemical and molecular analysis. *Appl Environ Microb* **69**: 616-624.
Glass NL, Jacobson DJ, Shiu PKT. 2000. The genetics of hyphal fusion and vegetative incompatibility in filamentous ascomycete fungi. *Annu Rev Genet* **34**: 165-186.
Gong MM, Sinton D. 2017. Turning the page: advancing paper-based microfluidics for broad diagnostic application. *Chem Rev* **117**: 8447-8480.
Grist SM, Bennewith KL, Cheung KC. 2022. Oxygen measurement in microdevices. *Annu Rev Anal Chem* **15**: 221-246.
Groisman A, Lobo C, Cho H, Campbell JK, Dufour YS, Stevens AM, Levchenko A. 2005. A microfluidic chemostat for experiments with bacterial and yeast cells. *Nat Methods* **2**: 685-9.
Grossmann G, Guo W-J, Ehrhardt DW, Frommer WB, Sit RV, Quake SR, Meier M. 2011. The RootChip: an integrated microfluidic chip for plant science. *Plant Cell* **23**: 4234-4240.
Hageage GJ, Harrington BJ. 1984. Use of calcofluor white in clinical mycology. *Lab Med* **15**: 109-112.
Haj Hammadeh H, Serrano A, Wernet V, Stomberg N, Hellmeier D, Weichert M, Brandt U, Sieg B, Kanofsky K, Hehl R, Fischer R, Fleißner A. 2022. A dialogue-like cell communication mechanism is conserved in filamentous ascomycete fungi and mediates interspecies interactions. *PNAS* **119**: e2112518119.
Hamel C. 2007. *Mycorrhizae in crop production.* Boca Raton: CRC Press.
Hammer EC, Arellano-Caicedo C, Mafla-Endara PM, Kiers ET, Shimizu T, Ohlsson P, Aleklett K. 2024. Hyphal exploration strategies and habitat modification of an arbuscular mycorrhizal fungus in microengineered soil chips. *Fungal Ecol* **67**: 101302.

Hanson KL, Nicolau DV, Jr., Filipponi L, Wang L, Lee AP, Nicolau DV. 2006. Fungi use efficient algorithms for the exploration of microfluidic networks. *Small* **2**: 1212-20.

Hao N, O'Shea EK. 2011. Signal-dependent dynamics of transcription factor translocation controls gene expression. *Nat Struct Mol Biol* **19**: 31-9.

Harting R, Nagel A, Nesemann K, Hofer AM, Bastakis E, Kusch H, Stanley CE, Stockli M, Kaever A, Hoff KJ, Stanke M, deMello AJ, Kunzler M, Haney CH, Braus-Stromeyer SA, Braus GH. 2021. *Pseudomonas* strains induce transcriptional and morphological changes and reduce root colonization of *Verticillium* spp. *Front Microbiol* **12**: 652468.

Hawksworth DL, Lücking R. 2017. Fungal diversity revisited: 2.2 to 3.8 million species. *Microbiol Spectr* **5**: 10.

Heck C, Kuhn H, Heidt S, Walter S, Rieger N, Requena N. 2016. Symbiotic fungi control plant root cortex development through the novel GRAS transcription factor MIG1. *Curr Biol* **26**: 2770-2778.

Held M, Edwards C, Nicolau DV. 2009a. Fungal intelligence; Or on the behaviour of microorganisms in confined micro-environments. *J Phys Conf Ser* **178**: 012005.

Held M, Edwards C, Nicolau DV. 2011a. Probing the growth dynamics of *Neurospora crassa* with microfluidic structures. *Fungal Biol* **115**: 493-505.

Held M, Farkas DL, Edwards C, Nicolau DV, Leif RC, Nicolau DV. 2011b. Hyphal responses of *Neurospora crassa* to micron-sized beads with functional chemical surface groups. *Proc SPIE* **7902**.

Held M, Kaspar O, Edwards C, Nicolau DV. 2019. Intracellular mechanisms of fungal space searching in microenvironments. *PNAS* **116**: 13543-13552.

Held M, Komaromy A, Fulga F, Edwards C, Boysen RI, Hearn MTW, Nicolau DV. 2009b. Dynamic behaviour of microorganisms on microstructures. *Microelectron Eng* **86**: 1455-1458.

Held M, Lee AP, Edwards C, Nicolau DV. 2010. Microfluidics structures for probing the dynamic behaviour of filamentous fungi. *Microelectron Eng* **87**: 786-789.

Henriques BS, Garcia ES, Azambuja P, Genta FA. 2020. Determination of chitin content in insects: an alternate method based on Calcofluor staining. *Front Physiol* **11**.

Hersen P, McClean MN, Mahadevan L, Ramanathan S. 2008. Signal processing by the HOG MAP kinase pathway. *PNAS* **105**: 7165.

Herth W. 1980. Calcofluor white and Congo red inhibit chitin microfibril assembly of *Poterioochromonas*: evidence for a gap between polymerization and microfibril formation. *J Cell Biol* **87**: 442-450.

Hinton TJ, Hudson A, Pusch K, Lee A, Feinberg AW. 2016. 3D printing PDMS elastomer in a hydrophilic support bath via freeform reversible embedding. *ACS Biomater Sci Eng* **2**: 1781-1786.

Hooker JE, Munro M, Atkinson D. 1992. Vesicular-arbuscular mycorrhizal fungi induced alteration in poplar root system morphology. *Plant Soil* **145**: 207-214.

Hopke A, Mela A, Ellett F, Carter-House D, Pena JF, Stajich JE, Altamirano S, Lovett B, Egan M, Kale S, Kronholm I, Guerette P, Szewczyk E, McCluskey K, Breslauer D, Shah H, Coad BR, Momany M, Irimia D. 2021. Crowdsourced analysis of fungal growth and branching on microfluidic platforms. *PLoS One* **16**: e0257823.

Horton TR, Bruns TD, Parker VT. 1999. Ectomycorrhizal fungi associated with *Arctostaphylos* contribute to *Pseudotsuga menziesii* establishment. *Can J Botany* **77**: 93-102.

Hoysted GA, Field KJ, Sinanaj B, Bell CA, Bidartondo MI, Pressel S. 2023. Direct nitrogen, phosphorus and carbon exchanges between *Mucoromycotina* 'fine root endophyte' fungi and a flowering plant in novel monoxenic cultures. *New Phytol* **238**: 70-79.

Ingham ER, Griffiths RP, Cromack K. 1991. Comparison of direct vs fumigation incubation microbial biomass estimates from ectomycorrhizal mat and non-mat soils. *Soil Biol Biochem* **23**: 465-471.

Irawan R, Tjin SC, Yager P, Zhang D. 2005. Cross-talk problem on a fluorescence multi-channel microfluidic chip system. *Biomed Microdevices* **7**: 205-211.
Jiang F, Zhang L, Zhou J, George TS, Feng G. 2021. Arbuscular mycorrhizal fungi enhance mineralisation of organic phosphorus by carrying bacteria along their extraradical hyphae. *New Phytol* **230**: 304-315.
Kadosh D. 2019. Regulatory mechanisms controlling morphology and pathogenesis in *Candida albicans*. *Curr Opin Microbiol* **52**: 27-34.
Kahmann R, Bölker M. 1996. Self/nonself recognition in fungi: old mysteries and simple solutions. *Cell* **85**: 145-148.
Kendrick B. 2017. *The Fifth Kingdom.* Indianapolis: Hackett Publishing.
Khoshmanesh K, Tang S-Y, Zhu JY, Schaefer S, Mitchell A, Kalantar-zadeh K, Dickey MD. 2017. Liquid metal enabled microfluidics. *Lab Chip* **17**: 974-993.
Köfferlein M. 2006. *KLayout—high performance layout viewer and editor, v.0.27.5*. Munich, Germany: URL https://www.klayout.de/.
Köhl J, Kolnaar R, Ravensberg WJ. 2019. Mode of action of microbial biological control agents against plant diseases: relevance beyond efficacy. *Front Plant Sci* **10**.
Kohlmeier S, Smits THM, Ford RM, Keel C, Harms H, Wick LY. 2005. Taking the fungal highway: mobilization of pollutant-degrading bacteria by fungi. *Environ Sci Technol* **39**: 4640-4646.
Kokkoris V, Stefani F, Dalpé Y, Dettman J, Corradi N. 2020. Nuclear dynamics in the arbuscular mycorrhizal fungi. *Trends Plant Sci* **25**: 765-778.
Kosuta S, Hazledine S, Sun J, Miwa H, Morris RJ, Downie JA, Oldroyd GED. 2008. Differential and chaotic calcium signatures in the symbiosis signaling pathway of legumes. *PNAS* **105**: 9823.
Kotz KT, Xiao W, Miller-Graziano C, Qian W-J, Russom A, Warner EA, Moldawer LL, De A, Bankey PE, Petritis BO, Camp DG, Rosenbach AE, Goverman J, Fagan SP, Brownstein BH, Irimia D, Xu W, Wilhelmy J, Mindrinos MN, Smith RD, Davis RW, Tompkins RG, Toner M, Baker HV, Balis UGJ, Billiar TR, Calvano SE, Cobb JP, Cuschieri J, Finnerty CC, Gamelli RL, Gibran NS, Harbrecht BG, Hayden DL, Hennessy L, Herndon DN, Jeschke MG, Johnson JL, Klein MB, Lowry SF, Maier RV, Mason PH, McDonald-Smith GP, Minei JP, Moore EE, Nathens AB, O´ Keefe GE, Rahme LG, Remick DG, Schoenfeld DA, Shapiro MB, Sperry J, Storey JD, Tibshirani R, Warren HS, West MA, Wispelwey B, Wong WH, the I, the Host Response to Injury Collaborative Research P. 2010. Clinical microfluidics for neutrophil genomics and proteomics. *Nat Med* **16**: 1042-1047.
Kriel FH, Woollam S, Gordon RJ, Grant RA, Priest C. 2016. Numbering-up Y–Y microfluidic chips for higher-throughput solvent extraction of platinum(IV) chloride. *Microfluid Nanofluid* **20**.
Kubota M, McGonigle TP, Hyakumachi M. 2005. Co-occurrence of Arum- and Paris-type morphologies of arbuscular mycorrhizae in cucumber and tomato. *Mycorrhiza* **15**: 73-77.
Kumamoto CA. 2008. Molecular mechanisms of mechanosensing and their roles in fungal contact sensing. *Nat Rev Microbiol* **6**: 667-673.
Lee J. 2011. The distribution of cytoplasm and nuclei within the extra-radical mycelia in *Glomus intraradices*, a species of arbuscular mycorrhizal fungi. *Mycobiology* **39**: 79-84.
Lee PJ, Helman NC, Lim WA, Hung PJ. 2008. A microfluidic system for dynamic yeast cell imaging. *Biotechniques* **44**: 91-5.
Lee SH, Song J, Cho B, Hong S, Hoxha O, Kang T, Kim D, Lee LP. 2019. Bubble-free rapid microfluidic PCR. *Biosens Bioelectron* **126**: 725-733.
Lefebvre B. 2017. Arbuscular mycorrhiza: a new role for N-acetylglucosamine. *Nat Plants* **3**: 17085.
Li X-R, Sun J, Albinsky D, Zarrabian D, Hull R, Lee T, Jarratt-Barnham E, Chiu CH, Jacobsen A, Soumpourou E, Albanese A, Kohlen W, Luginbuehl LH, Guillotin B, Lawrensen T, Lin H, Murray J, Wallington E, Harwood W, Choi J, Paszkowski U, Oldroyd GED. 2022. Nutrient regulation of lipochitooligosaccharide recognition in plants via NSP1 and NSP2. *Nat Commun* **13**: 6421.

Lichius A. 2022. Concentration, cellular exposure and specificity of organelle selective fluorescent dyes in fungal cell biology. *Fungal Biol Rev* **41**: 45-51.
Ling Y, Rubin J, Deng Y, Huang C, Demirci U, Karp JM, Khademhosseini A. 2007. A cell-laden microfluidic hydrogel. *Lab Chip* **7**: 756-762.
Liu P, Liu H, Yuan D, Jang D, Yan S, Li M. 2021. Separation and enrichment of yeast *Saccharomyces cerevisiae* by shape using viscoelastic microfluidics. *Anal Chem* **93**: 1586-1595.
López-Franco R, Bracker CE. 1996. Diversity and dynamics of the Spitzenkörper in growing hyphal tips of higher fungi. *Protoplasma* **195**: 90-111.
M. Butt T, G. Copping L. 2000. Fungal biological control agents. *Pestic Outlook* **11**: 186-191.
Ma J, Wang W, Yang J, Qin S, Yang Y, Sun C, Pei G, Zeeshan M, Liao H, Liu L, Huang J. 2022. Mycorrhizal symbiosis promotes the nutrient content accumulation and affects the root exudates in maize. *BMC Plant Biol* **22**: 64.
Ma J, Yan S, Miao C, Li L, Shi W, Liu X, Luo Y, Liu T, Lin B, Wu W, Lu Y. 2019. Paper microfluidics for cell analysis. *Adv Healthc Mater* **8**: 1801084.
Maddison AC, Manners JG. 1973. Lethal effects of artificial ultraviolet radiation on cereal rust uredospores. *T Brit Mycol Soc* **60**: 471-494.
Mafla-Endara PM, Arellano-Caicedo C, Aleklett K, Pucetaite M, Ohlsson P, Hammer EC. 2021. Microfluidic chips provide visual access to *in situ* soil ecology. *Commun Biol* **4**: 889.
Maheshwari R. 2005. Nuclear behavior in fungal hyphae. *FEMS Microbiol Lett* **249**: 7-14.
Manz A, Graber N, Widmer HM. 1990. Miniaturized total chemical analysis systems: a novel concept for chemical sensing. *Sensor Actuat B-Chem* **1**: 244-248.
Martínez-Camacho AP, Cortez-Rocha MO, Castillo-Ortega MM, Burgos-Hernández A, Ezquerra-Brauer JM, Plascencia-Jatomea M. 2011. Antimicrobial activity of chitosan nanofibers obtained by electrospinning. *Polym Int* **60**: 1663-1669.
Maruyama H, Arai F, Fukuda T. 2008. On-chip pH measurement using functionalized gel-microbeads positioned by optical tweezers. *Lab Chip* **8**: 346-351.
Mata A, Fleischman AJ, Roy S. 2005. Characterization of polydimethylsiloxane (PDMS) properties for biomedical micro/nanosystems. *Biomed Microdevices* **7**: 281-293.
Mayer FL, Wilson D, Hube B. 2013. *Candida albicans* pathogenicity mechanisms. *Virulence* **4**: 119-128.
McDonald JC, Whitesides GM. 2002. Poly(dimethylsiloxane) as a material for fabricating microfluidic devices. *Accounts Chem Res* **35**: 491-499.
McMullen M, Bergstrom G, De Wolf E, Dill-Macky R, Hershman D, Shaner G, Van Sanford D. 2012. A unified effort to fight an enemy of wheat and barley: *Fusarium* head blight. *Plant Dis* **96**: 1712-1728.
Merckx VSFT, Gomes SIF, Wang D, Verbeek C, Jacquemyn H, Zahn FE, Gebauer G, Bidartondo MI. 2024. Mycoheterotrophy in the wood-wide web. *Nat Plants* **10**: 710-718.
Millet LJ, Aufrecht J, Labbe J, Uehling J, Vilgalys R, Estes ML, Miquel Guennoc C, Deveau A, Olsson S, Bonito G, Doktycz MJ, Retterer ST. 2019. Increasing access to microfluidics for studying fungi and other branched biological structures. *Fungal Biol Biotechnol* **6**: 1.
Mohanta TK, Bae H. 2015. The diversity of fungal genome. *Biol Proced Online* **17**: 8.
Moore TI, Chou CS, Nie Q, Jeon NL, Yi TM. 2008. Robust spatial sensing of mating pheromone gradients by yeast cells. *PLoS One* **3**: e3865.
Mosse B, Hepper C. 1975. Vesicular-arbuscular mycorrhizal infections in root organ cultures. *Physiol Plant Pathol* **5**: 215-223.
Moutoglis P, Widden P. 1996. Vesicular-arbuscular mycorrhizal spore populations in sugar maple (*Acer saccharum* Marsh.) forests. *Mycorrhiza* **6**: 91-97.
Murray JD, Cousins DR, Jackson KJ, Liu C. 2013. Signaling at the root surface: the role of cutin monomers in mycorrhization. *Mol Plant* **6**: 1381-3.
Nadal M, Sawers R, Naseem S, Bassin B, Kulicke C, Sharman A, An G, An K, Ahern KR, Romag A, Brutnell TP, Gutjahr C, Geldner N, Roux C, Martinoia E, Konopka JB, Paszkowski U. 2017. An

N-acetylglucosamine transporter required for arbuscular mycorrhizal symbioses in rice and maize. *Nat Plants* **3**: 17073-17073.

Neils C, Tyree Z, Finlayson B, Folch A. 2004. Combinatorial mixing of microfluidic streams. *Lab Chip* **4**: 342-350.

Nicolau DV, Nicolau DV, Solana G, Hanson KL, Filipponi L, Wang L, Lee AP. 2006. Molecular motors-based micro- and nano-biocomputation devices. *Microelectron Eng* **83**: 1582-1588.

Nie J, Gao Q, Wang Y, Zeng J, Zhao H, Sun Y, Shen J, Ramezani H, Fu Z, Liu Z, Xiang M, Fu J, Zhao P, Chen W, He Y. 2018. Vessel-on-a-chip with hydrogel-based microfluidics. *Small* **14**: 1802368.

Nieuwenhuis BPS, Billiard S, Vuilleumier S, Petit E, Hood ME, Giraud T. 2013. Evolution of uni- and bifactorial sexual compatibility systems in fungi. *Heredity* **111**: 445-455.

Novais CBd, Pepe A, Siqueira JO, Giovannetti M, Sbrana C. 2017. Compatibility and incompatibility in hyphal anastomosis of arbuscular mycorrhizal fungi. *Sci Agr* **74**: 411-416.

Oburger E, Jones DL. 2018. Sampling root exudates – Mission impossible? *Rhizosphere* **6**: 116-133.

Ochs CJ, Kasuya J, Pavesi A, Kamm RD. 2014. Oxygen levels in thermoplastic microfluidic devices during cell culture. *Lab Chip* **14**: 459-62.

Ohno K-i, Tachikawa K, Manz A. 2008. Microfluidics: Applications for analytical purposes in chemistry and biochemistry. *Electrophoresis* **29**: 4443-4453.

Olsson S, Hansson BS. 1995. Action potential-like activity found in fungal mycelia is sensitive to stimulation. *Naturwissenschaften* **82**: 30-31.

Orchard S, Hilton S, Bending G, D., Dickie I, A., Standish R, J., Gleeson D, B., Jeffery R, P., Powell J, R., Walker C, Bass D, Monk J, Simonin A, Ryan M, H. 2017. Fine endophytes (*Glomus tenue*) are related to *Mucoromycotina*, not *Glomeromycota*. *New Phytol* **213**: 481-486.

Parniske M. 2000. Intracellular accommodation of microbes by plants: a common developmental program for symbiosis and disease? *Curr Opin Plant Biol* **3**: 320-328.

Payne EM, Holland-Moritz DA, Sun S, Kennedy RT. 2020. High-throughput screening by droplet microfluidics: perspective into key challenges and future prospects. *Lab Chip* **20**: 2247-2262.

Perotto S, Daghino S, Martino E. 2018. Ericoid mycorrhizal fungi and their genomes: another side to the mycorrhizal symbiosis? *New Phytol* **220**: 1141-1147.

Peter J, Young W, Haukka KE. 1996. Diversity and phylogeny of rhizobia. *New Phytol* **133**: 87-94.

Piccolino M. 1997. Luigi Galvani and animal electricity: two centuries after the foundation of electrophysiology. *Trends Neurosci* **20**: 443-448.

Podwin A, Janisz T, Patejuk K, Szyszka P, Walczak R, Dziuban J. 2021. Towards microfluidics for mycology–material and technological studies on LOCs as new tools ensuring investigation of microscopic fungi and soil organisms. *B Pol Acad Sci-Tech* **69**: e136212.

Postma J, Altemüller HJ. 1990. Bacteria in thin soil sections stained with the fluorescent brightener calcofluor white M2R. *Soil Biol Biochem* **22**: 89-96.

Prado-Tarango DE, Mata-González R, Hovland M, Schreiner RP. 2021. Assessing commercial and early-seral arbuscular mycorrhizal fungi inoculation to aid in restoring sagebrush steppe shrubs. *Rangeland Ecol Manag* **79**: 87-90.

Prindle A, Liu J, Asally M, Ly S, Garcia-Ojalvo J, Süel GM. 2015. Ion channels enable electrical communication in bacterial communities. *Nature* **527**: 59-63.

Prout JN, Williams A, Wanke A, Schornack S, Ton J, Field KJ. 2023. *Mucoromycotina* 'fine root endophytes': a new molecular model for plant–fungal mutualisms? *Trends Plant Sci*.

Puerner C, Kukhaleishvili N, Thomson D, Schaub S, Noblin X, Seminara A, Bassilana M, Arkowitz RA. 2020. Mechanical force-induced morphology changes in a human fungal pathogen. *BMC Biol* **18**: 122.

Pumplin N, Harrison MJ. 2009. Live-cell imaging reveals periarbuscular membrane domains and organelle location in *Medicago truncatula* roots during arbuscular mycorrhizal symbiosis. *Plant Physiol* **151**: 809-19.

Qiaole Z, Qing-An H, Yu-Cheng L. 2009. Design and numerical analysis of a joule-heating-induced continuous-flow polymerase chain reaction microchip. *J Micro-Nanolith MEM* **8**: 021102.

Ramana Murthy MV, Mohan EVS, Sadhukhan AK. 1999. Cyclosporin-A production by *Tolypocladium inflatum* using solid state fermentation. *Process Biochem* **34**: 269-280.
Rasmussen HN. 2002. Recent developments in the study of orchid mycorrhiza. *Plant Soil* **244**: 149-163.
Read ND, Lichius A, Shoji J-y, Goryachev AB. 2009. Self-signalling and self-fusion in filamentous fungi. *Curr Opin Microbiol* **12**: 608-615.
Recorbet G, Courty P-E, Wipf D. 2020. Recovery of extra-radical fungal peptides amenable for shotgun protein profiling in arbuscular mycorrhizae. *In:* Ferrol N, Lanfranco L, eds. *Arbuscular Mycorrhizal Fungi: Methods and Protocols.* New York, NY: Springer US, 223-238.
Redecker D, Kodner R, Graham LE. 2000. Glomalean fungi from the ordovician. *Science* **289**: 1920-1921.
Ren K, Zhou J, Wu H. 2013. Materials for microfluidic chip fabrication. *Accounts Chem Res* **46**: 2396-2406.
Richter F, Bindschedler S, Calonne-Salmon M, Declerck S, Junier P, Stanley CE. 2022. Fungi-on-a-Chip: microfluidic platforms for single-cell studies on fungi. *FEMS Microbiol Rev*: fuac039.
Richter F, Calonne-Salmon M, van der Heijden MGA, Declerck S, Stanley CE. 2024. AMF-SporeChip provides new insights into arbuscular mycorrhizal fungal asymbiotic hyphal growth dynamics at the cellular level. *Lab Chip*.
Richter I, Wein P, Uzum Z, Stanley CE, Krabbe J, Molloy EM, Moebius N, Ferling I, Hillmann F, Hertweck C. 2023. Transcription activator-like effector protects bacterial endosymbionts from entrapment within fungal hyphae. *Curr Biol* **33**: 2646-2656.e4.
Rillig MC. 2004. Arbuscular mycorrhizae and terrestrial ecosystem processes. *Ecol Lett* **7**: 740-754.
Rimington WR, Pressel S, Duckett JG, Bidartondo MI. 2015. Fungal associations of basal vascular plants: reopening a closed book? *New Phytol* **205**: 1394-1398.
Riquelme M, Sánchez-León E. 2014. The Spitzenkörper: a choreographer of fungal growth and morphogenesis. *Curr Opin Microbiol* **20**: 27-33.
Ruyter-Spira C, Al-Babili S, van der Krol S, Bouwmeester H. 2013. The biology of strigolactones. *Trends Plant Sci* **18**: 72-83.
Saylor JR. 1995. Photobleaching of disodium fluorescein in water. *Exp Fluids* **18**: 445-447.
Schindelin J, Arganda-Carreras I, Frise E, Kaynig V, Longair M, Pietzsch T, Preibisch S, Rueden C, Saalfeld S, Schmid B. 2012. Fiji: an open-source platform for biological-image analysis. *Nat Methods* **9**: 676-682.
Schmieder SS, Stanley CE, Rzepiela A, van Swaay D, Sabotic J, Norrelykke SF, deMello AJ, Aebi M, Kunzler M. 2019. Bidirectional propagation of signals and nutrients in fungal networks via specialized hyphae. *Curr Biol* **29**: 217-228 e4.
Schmitt CL, Tatum ML. 2008. *The Malheur National Forest location of the world's largest living organism* [Online]. Forest Service, US Department of Agriculture. Available: https://upload.wikimedia.org/wikipedia/commons/1/1a/The_Malheur_National_Forest_Location_of_the_World%27s_Largest_Living_Organism_%28The_Humongous_Fungus%29_-_fsbdev3_033146.pdf (28 April 2022, date last accessed) [Accessed].
Schrott W, Svoboda M, Slouka Z, Šnita D. 2009. Metal electrodes in plastic microfluidic systems. *Microelectron Eng* **86**: 1340-1342.
Scott SM, Ali Z. 2021. Fabrication methods for microfluidic devices: an overview. *Micromachines* **12**: 319.
Scott TW, Kiers ET, Cooper GA, dos Santos M, West SA. 2019. Evolutionary maintenance of genomic diversity within arbuscular mycorrhizal fungi. *Ecol Evol* **9**: 2425-2435.
Semwogerere D, Weeks ER. 2005. Confocal microscopy. *In:* Wnek G, Bowlin G, eds. *Encyclopedia of biomaterials and biomedical engineering.* 2nd ed. Boca Raton: CRC Press, 10.
Serghi EU, Kokkoris V, Cornell C, Dettman J, Stefani F, Corradi N. 2021. Homo- and dikaryons of the arbuscular mycorrhizal fungus *Rhizophagus irregularis* differ in life history strategy. *Front Plant Sci* **12**: 15.

Show PL, Oladele KO, Siew QY, Aziz Zakry FA, Lan JC-W, Ling TC. 2015. Overview of citric acid production from *Aspergillus niger*. *Front Life Sci* **8**: 271-283.

Simard SW, Beiler KJ, Bingham MA, Deslippe JR, Philip LJ, Teste FP. 2012. Mycorrhizal networks: mechanisms, ecology and modelling. *Fungal Biol Rev* **26**: 39-60.

Siqueira JO, Hubbell DH, Schenck NC. 1982. Spore germination and germ tube growth of a vesicular-arbuscular mycorrhizal fungus *in vitro*. *Mycologia* **74**: 952-959.

Skelton V, Greenway GM, Haswell SJ, Styring P, Morgan DO, Warrington BH, Wong SYF. 2001. The generation of concentration gradients using electroosmotic flow in micro reactors allowing stereoselective chemical synthesis. *Analyst* **126**: 11-13.

Smith SE, Read D. 2008a. 5 - Mineral nutrition, toxic element accumulation and water relations of arbuscular mycorrhizal plants. *In:* Smith SE, Read D, eds. *Mycorrhizal Symbiosis (Third Edition).* London, UK: Academic Press, 145-VI.

Smith SE, Read DJ. 2008b. *Mycorrhizal symbiosis.* London, UK: Academic press.

Sønstevold L, Czerkies M, Escobedo-Cousin E, Blonski S, Vereshchagina E. 2023. Application of polymethylpentene, an oxygen permeable thermoplastic, for long-term on-a-chip cell culture and Organ-on-a-Chip devices. *Micromachines* **14**: 532.

Srisom K, Tittabutr P, Teaumroong N, Lapwong Y, Phatthanakun R, Sirivisoot S, Kuntanawat P. 2020. New method for arbuscular mycorrhizal fungus spore separation using a microfluidic device based on manual temporary flow diversion. *Mycorrhiza* **30**: 789-796.

Stanley CE, Shrivastava J, Brugman R, Heinzelmann E, van Swaay D, Grossmann G. 2018. Dual-flow-RootChip reveals local adaptations of roots towards environmental asymmetry at the physiological and genetic levels. *New Phytol* **217**: 1357-1369.

Stanley CE, Stockli M, van Swaay D, Sabotic J, Kallio PT, Kunzler M, deMello AJ, Aebi M. 2014. Probing bacterial-fungal interactions at the single cell level. *Integr Biol* **6**: 935-45.

Steinberg G. 2007. Hyphal growth: a tale of motors, lipids, and the Spitzenkorper. *Eukaryot Cell* **6**: 351-60.

Steinberg G, Peñalva MA, Riquelme M, Wösten HA, Harris SD. 2017. Cell biology of hyphal growth. *Microbiol Spectrum* **5**: 5.2.30.

Strom NB, Bushley KE. 2016. Two genomes are better than one: history, genetics, and biotechnological applications of fungal heterokaryons. *Fungal Biol Biotechnol* **3**: 4.

Stürmer SL, Bever JD, Morton JB. 2018. Biogeography of arbuscular mycorrhizal fungi (Glomeromycota): a phylogenetic perspective on species distribution patterns. *Mycorrhiza* **28**: 587-603.

Sun B, Jiang J, Shi N, Xu W. 2016. Application of microfluidics technology in chemical engineering for enhanced safety. *Process Saf Prog* **35**: 365-373.

Sun Y, Tayagui A, Garrill A, Nock V. 2018. Fabrication of in-channel high-aspect ratio sensing pillars for protrusive force measurements on fungi and oomycetes. *J Microelectromech S* **27**: 827-835.

Taylor RJ, Falconnet D, Niemistö A, Ramsey SA, Prinz S, Shmulevich I, Galitski T, Hansen CL. 2009. Dynamic analysis of MAPK signaling using a high-throughput microfluidic single-cell imaging platform. *PNAS* **106**: 3758.

Tayyrov A, Stanley CE, Azevedo S, Kunzler M. 2019. Combining microfluidics and RNA-sequencing to assess the inducible defensome of a mushroom against nematodes. *BMC Genomics* **20**: 243.

Terry SC, Herman JH, Angell JB. 1979. A gas chromatographic air analyzer fabricated on a silicon wafer. *IEEE T Electron Dev* **26**: 1880-1886.

Thomson DD, Wehmeier S, Byfield FJ, Janmey PA, Caballero-Lima D, Crossley A, Brand AC. 2015. Contact-induced apical asymmetry drives the thigmotropic responses of *Candida albicans* hyphae. *Cell Microbiol* **17**: 342-354.

Tsai SM, Phillips DA. 1991. Flavonoids released naturally from alfalfa promote development of symbiotic glomus spores *in vitro*. *Appl Environ Microb* **57**: 1485-1488.

U.S. Department of Energy. 2020. *Global annual ethanol production by country or region* [Online]. Available: https://afdc.energy.gov/data/10331 (28 April 2022, date last accessed) [Accessed].

Uehling JK, Entler MR, Meredith HR, Millet LJ, Timm CM, Aufrecht JA, Bonito GM, Engle NL, Labbe JL, Doktycz MJ, Retterer ST, Spatafora JW, Stajich JE, Tschaplinski TJ, Vilgalys RJ. 2019. Microfluidics and metabolomics reveal symbiotic bacterial-fungal interactions between *Mortierella elongata* and *Burkholderia* include metabolite exchange. *Front Microbiol* **10**: 2163.

van der Heijden MGA, Klironomos JN, Ursic M, Moutoglis P, Streitwolf-Engel R, Boller T, Wiemken A, Sanders IR. 1998. Mycorrhizal fungal diversity determines plant biodiversity, ecosystem variability and productivity. *Nature* **396**: 69-72.

van der Heijden MGA, Martin FM, Selosse MA, Sanders IR. 2015. Mycorrhizal ecology and evolution: the past, the present, and the future. *New Phytol* **205**: 1406-1423.

Venice F, Ghignone S, Salvioli di Fossalunga A, Amselem J, Novero M, Xianan X, Sędzielewska Toro K, Morin E, Lipzen A, Grigoriev IV, Henrissat B, Martin FM, Bonfante P. 2020. At the nexus of three kingdoms: the genome of the mycorrhizal fungus *Gigaspora margarita* provides insights into plant, endobacterial and fungal interactions. *Environ Microbiol* **22**: 122-141.

Verbruggen E, van der Heijden MG, Rillig MC, Kiers ET. 2013. Mycorrhizal fungal establishment in agricultural soils: factors determining inoculation success. *New Phytol* **197**: 1104-9.

Wang G, Bjork SM, Huang M, Liu Q, Campbell K, Nielsen J, Joensson HN, Petranovic D. 2019. RNAi expression tuning, microfluidic screening, and genome recombineering for improved protein production in *Saccharomyces cerevisiae*. *PNAS* **116**: 9324-9332.

Wang L, Acosta MA, Leach JB, Carrier RL. 2013. Spatially monitoring oxygen level in 3D microfabricated cell culture systems using optical oxygen sensing beads. *Lab Chip* **13**: 1586-1592.

Wang M, Thomas N, Jin H. 2017. Cross-kingdom RNA trafficking and environmental RNAi for powerful innovative pre- and post-harvest plant protection. *Curr Opin Plant Biol* **38**: 133-141.

Warmink JA, Nazir R, Corten B, van Elsas JD. 2011. Hitchhikers on the fungal highway: the helper effect for bacterial migration via fungal hyphae. *Soil Biol Biochem* **43**: 760-765.

Warrick JW, Murphy WL, Beebe DJ. 2008. Screening the cellular microenvironment: a role for microfluidics. *IEEE Rev Biomed Eng* **1**: 75-93.

Watterson WJ, Tanyeri M, Watson AR, Cham CM, Shan Y, Chang EB, Eren AM, Tay S. 2020. Droplet-based high-throughput cultivation for accurate screening of antibiotic resistant gut microbes. *eLife* **9**: e56998.

Webster J, Weber R. 2007. *Introduction to Fungi.* New York: Cambridge University Press.

Wernet V, Kriegler M, Kumpost V, Mikut R, Hilbert L, Fischer R. 2023. Synchronization of oscillatory growth prepares fungal hyphae for fusion. *eLife* **12**: e83310.

Whittaker RH. 1969. New concepts of kingdoms of organisms. *Science* **163**: 150-160.

Wingfield MJ, De Beer ZW, Slippers B, Wingfield BD, Groenewald JZ, Lombard L, Crous PW. 2012. One fungus, one name promotes progressive plant pathology. *Mol Plant Pathol* **13**: 604-613.

Wu Y, Yeh FL, Mao F, Chapman ER. 2009. Biophysical characterization of styryl dye-membrane interactions. *Biophys J* **97**: 101-109.

Xavier LJC, Germida JJ. 2003. Bacteria associated with *Glomus clarum* spores influence mycorrhizal activity. *Soil Biol Biochem* **35**: 471-478.

Xiong B-J, Dusny C, Wang L, Appel J, Lindstaedt K, Schlosser D, Harms H, Wick LY. 2021. Illuminate the hidden: in vivo mapping of microscale pH in the mycosphere using a novel whole-cell biosensor. *ISME Commun* **1**: 75.

Xiong B-J, Kleinsteuber S, Sträuber H, Dusny C, Harms H, Wick Lukas Y. 2022. Impact of fungal hyphae on growth and dispersal of obligate anaerobic bacteria in aerated habitats. *mBio* **13**: e00769-22.

Yamamoto K, Shimamura M, Degawa Y, Yamada A. 2019. Dual colonization of *Mucoromycotina* and *Glomeromycotina* fungi in the basal liverwort, *Haplomitrium mnioides* (*Haplomitriopsida*). *J Plant Res* **132**: 777-788.

Yoneyama K, Yoneyama K, Takeuchi Y, Sekimoto H. 2007. Phosphorus deficiency in red clover promotes exudation of orobanchol, the signal for mycorrhizal symbionts and germination stimulant for root parasites. *Planta* **225**: 1031-1038.

Young JPW. 2015. Genome diversity in arbuscular mycorrhizal fungi. *Curr Opin Plant Biol* **26**: 113-119.

Yu TE, Egger KN, Peterson LR. 2001. Ectendomycorrhizal associations – characteristics and functions. *Mycorrhiza* **11**: 167-177.

Yung CW, Fiering J, Mueller AJ, Ingber DE. 2009. Micromagnetic-microfluidic blood cleansing device. *Lab Chip* **9**: 1171-7.

Zafar Razzacki S, Thwar PK, Yang M, Ugaz VM, Burns MA. 2004. Integrated microsystems for controlled drug delivery. *Adv Drug Deliver Rev* **56**: 185-198.

Zhang JXJ, Hoshino K. 2014. Chapter 3 - Microfluidics and micro total analytical systems. *In:* Zhang JXJ, Hoshino K, eds. *Molecular Sensors and Nanodevices.* Oxford: William Andrew Publishing, 103-168.

Zhang L, Feng G, Declerck S. 2018. Signal beyond nutrient, fructose, exuded by an arbuscular mycorrhizal fungus triggers phytate mineralization by a phosphate solubilizing bacterium. *ISME J* **12**: 2339-2351.

Zhang W, Yang H, Jiang L, Han L, Wang L. 2010. Use of potassium hydroxide, Giemsa and calcofluor white staining techniques in the microscopic evaluation of corneal scrapings for diagnosis of fungal keratitis. *J Int Med Res* **38**: 1961-1967.

Zhang Y, Luo C, Zou K, Xie Z, Brandman O, Ouyang Q, Li H. 2012. Single cell analysis of yeast replicative aging using a new generation of microfluidic device. *PLoS One* **7**: e48275.

Zhang Y, Yang H. 2019. A simple and robust fluorescent labeling method to quantify trophoblast fusion. *Placenta* **77**: 16-18.

Zhao YL, Zhou TT, Guo HS. 2016. Hyphopodium-specific VdNoxB/VdPls1-dependent ROS-Ca2+ signaling is required for plant infection by *Verticillium dahliae*. *PLoS Pathog* **12**: e1005793.

APPENDIX

Appendix 1: Composition of the MSR medium

Table A1: Composition of modified Strullu-Romand (MSR) medium (after Fortin *et al.* (2002)).

Component	Concentration [µM]
$N(NO_3^-)$	3800
$N(NH_4^+)$	180
P	30
K	1650
Ca	1520
Mg	3000
S	3013
Cl	870
Na	20
Fe	20
Mn	11
Zn	1
B	30
Mo	0.22
Cu	0.96
Panthotenate Ca	1.88
Biotin	0.004
Pyridoxine	4.38
Thiamine	2.96
Cyanocabalamine	0.29
Nicotinic acid	8.10

Appendix 2: Measurements of hyphal diameters

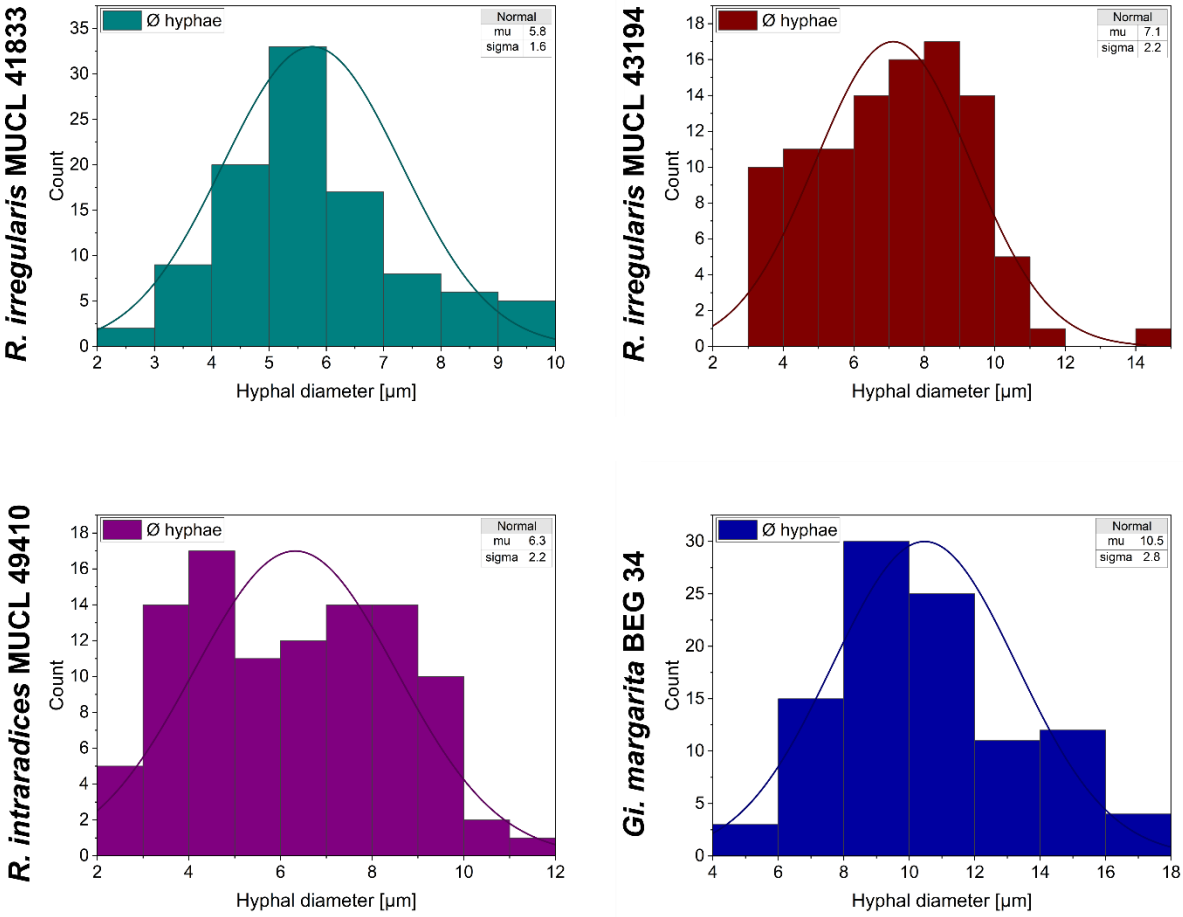


Figure A1: Hyphal diameters of arbuscular mycorrhizal fungi (AMF) strains used in this project. The diameters of a total of 100 hyphae per strain were measured in random spots on the hypha using the "straight line" tool in ImageJ/Fiji and the size distribution plotted with Origin. For each diameter, the median value "mu (µ)" with a standard deviation "sigma (σ)" is given. Images and figure legend reproduced from Richter *et al.* (2024) with permission from the Creative Commons Attribution license (www.creativecommons.org/licenses/by/4.0/).

Appendix 3: Schematics of secondary devices used in the project

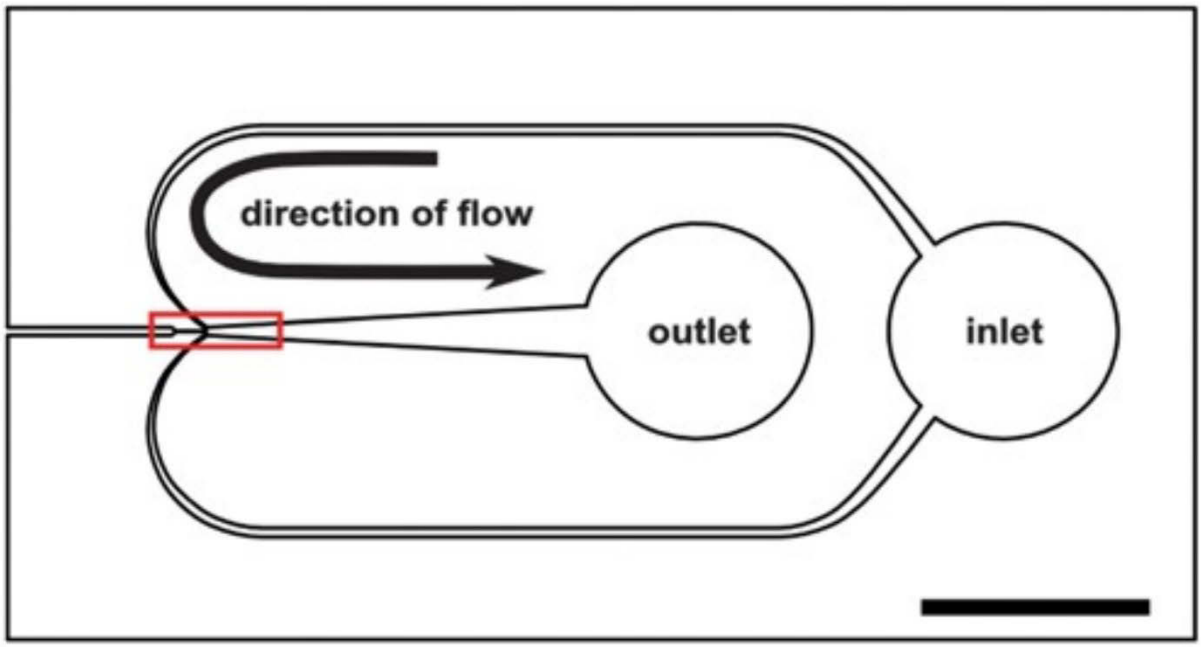


Figure A2: Schematic representation of the *fluid exchange device.* The figure shows the channel layout of the *fluid exchange device* as presented in Stanley *et al.* (2014), highlighting in- and outlet as well as the flow direction. Image reproduced with modifications with permission from Oxford University Press (Licence Number: 5874681051038). Scale bar: 3 mm.

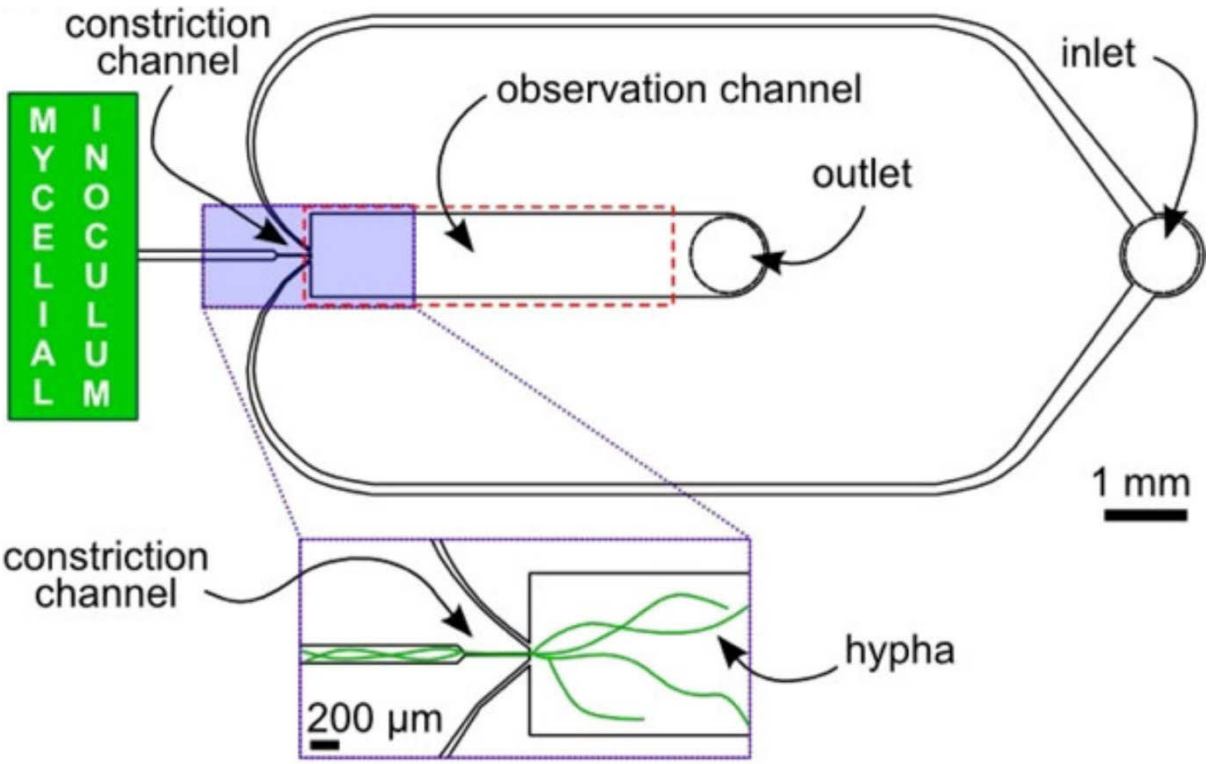


Figure A3: Schematic representation of the device used for sensor foil application. The figure shows the channel layout of the device published Ghanem *et al.* (2019), highlighting in- and outlet, the

observation chamber, constriction channel as well as the inoculation. Reprinted with permission from Ghanem *et al.* (2019). Copyright 2019 American Chemical Society.

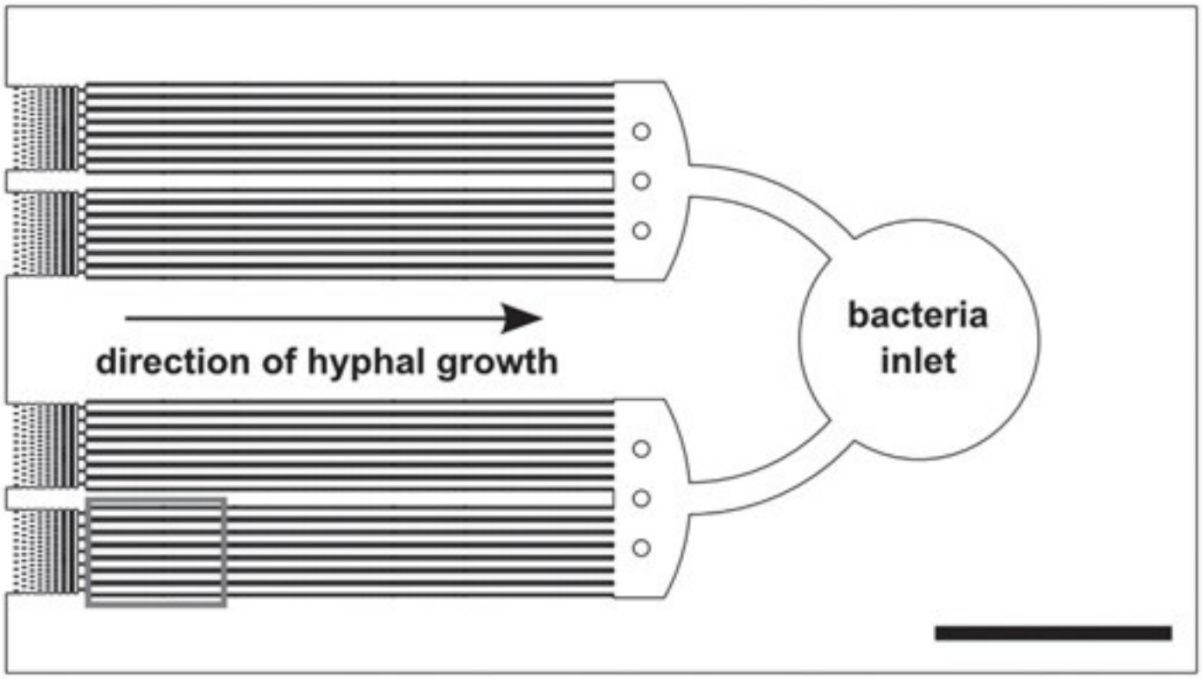


Figure A4: Schematic representation of the *BFI device.* The figure shows the channel layout of the *BFI device* as presented in Stanley *et al.* (2014), highlighting the bacteria inlet as well as the flow direction. Image reproduced with modifications with permission from Oxford University Press (Licence Number: 5846560852683). Scale bar: 3 mm.

Appendix 4: Publications

Richter F, Bindschedler S, Calonne-Salmon M, Declerck S, Junier P, Stanley CE. Fungi-on-a-Chip: microfluidic platforms for single-cell studies on fungi, *FEMS Microbiology Reviews*, Volume 46, Issue 6, November 2022, fuac039

Richter F, Calonne-Salmon M, van der Heijden MGA, Declerck S, Stanley CE. *AMF-SporeChip* provides new insights into arbuscular mycorrhizal fungal asymbiotic hyphal growth dynamics at the cellular level, *Lab on a Chip*, Volume 24, Issue 7, February 2024, 1930-1946

FEMS Microbiology Reviews, 1–29
DOI: 10.1093/femsre/fuac039
Advance access publication date: 24 August 2022
Review Article

Fungi-on-a-Chip: microfluidic platforms for single-cell studies on fungi

Felix Richter[1], Saskia Bindschedler[2], Maryline Calonne-Salmon[3], Stéphane Declerck[3], Pilar Junier[2], Claire E. Stanley[1]

[1]Department of Bioengineering, Imperial College London, South Kensington Campus, Exhibition Road, London SW7 2AZ, United Kingdom
[2]Laboratory of Microbiology, University of Neuchâtel, Rue Emile-Argand 11, CH-2000 Neuchâtel, Switzerland
[3]Laboratory of Mycology, Université catholique de Louvain, Place Croix du Sud 2, B-1348 Louvain-la-Neuve, Belgium
***Corresponding author:** Department of Bioengineering, Imperial College London, South Kensington Campus, Exhibition Road, London, SW7 2AZ, United Kingdom. E-mail: claire.stanley@imperial.ac.uk
Editor: Gerhard Braus

Abstract

This review highlights new advances in the emerging field of 'Fungi-on-a-Chip' microfluidics for single-cell studies on fungi and discusses several future frontiers, where we envisage microfluidic technology development to be instrumental in aiding our understanding of fungal biology. Fungi, with their enormous diversity, bear essential roles both in nature and our everyday lives. They inhabit a range of ecosystems, such as soil, where they are involved in organic matter degradation and bioremediation processes. More recently, fungi have been recognized as key components of the microbiome in other eukaryotes, such as humans, where they play a fundamental role not only in human pathogenesis, but also likely as commensals. In the food sector, fungi are used either directly or as fermenting agents and are often key players in the biotechnological industry, where they are responsible for the production of both bulk chemicals and antibiotics. Although the macroscopic fruiting bodies are immediately recognizable by most observers, the structure, function, and interactions of fungi with other microbes at the microscopic scale still remain largely hidden. Herein, we shed light on new advances in the emerging field of Fungi-on-a-Chip microfluidic technologies for single-cell studies on fungi. We discuss the development and application of microfluidic tools in the fields of medicine and biotechnology, as well as in-depth biological studies having significance for ecology and general natural processes. Finally, a future perspective is provided, highlighting new frontiers in which microfluidic technology can benefit this field.

Keywords: fungal biology, yeast, Fungi-on-a-Chip microfluidic technology, single-cell microscopy, arbuscular mycorrhizal fungi, fungal highways

Introduction

The kingdom Fungi is a most intriguing one. For centuries, mycologists have been baffled by the vast diversity of fungi and struggled to assign them to Aristotle's dual classification system of Plantae and Animalia. Only when Whittaker (Whittaker 1969) proposed the novel five-kingdom classification system in 1969, and advances in molecular genetics supported the classification (Kendrick 2017), did fungi obtain their status as an independent kingdom. Combining traits from each of the other kingdoms while having unique features, fungi share a heterotrophic lifestyle with animals, yet possess cells comprised of a cell wall, as well as vacuoles, and procreate via sexual and asexual reproduction just like plants. Moreover, the vast mycelium that many fungi form in the soil is reminiscent of the root system of plants, but with otherwise different dimensions. In fact, fungal mycelia have been found to span areas of up to 10 km^2, such as mycelia of the basidiomycete *Armillaria ostoyae* (Schmitt and Tatum 2008), and can represent up to 50% of soil dry weight (Ingham et al. 1991). However, despite these somewhat macroscopic dimensions, fungi are considered as microorganisms, just like bacteria. Common features shared with bacteria include unique metabolic pathways, such as the very specific isomerization between homoaconitate and homoisocitrate (Fazius et al. 2012), as well as the microscopic dimensions of most fungi, especially yeasts, which are commonly unicellular. Filamentous moulds and mushrooms, however, are comprised of microscopic features, termed hyphae, which form extensive mycelia and prominent fruiting bodies on the macroscale (Webster and Weber 2007). Other species are dimorphic, meaning they can switch from one morphology to another (i.e. unicellular to filamentous). *Candida albicans* for instance, has several forms, including single-cell yeast as well as filamentous forms (Kadosh 2019). Along with this shape-shifting at the microscopic scale, some fungal species also express different morphologies whether they are in a vegetative, asexual, or sexual phase. Historically, this has led to the accidental naming of the same species more than once. This is particularly common in filamentous fungi. For some species, a dual nomenclature was kept, with different names given for the sexual and asexual stage or part of the fungus. Unprecedented in nature, this phenomenon led to the coining of the terms teleomorph (the sexual form), anamorph (the asexual form), and holomorph (fungi for which both a sexual and asexual lifestyle is known). However, due to much disagreement among mycologists and confusion regarding the dual nomenclature system, it was abandoned as of 1 January 2013 and replaced by the principle of one fungus having one name ('one fungus, one name'; Wingfield et al. 2012). Of all the suspected 2.2–3.8 million fungal species in nature, it is estimated that only about 148 000 have been described so far (Hawksworth and Lück-

Received: April 29, 2022. **Revised:** August 11, 2022. **Accepted:** August 22, 2022
© The Author(s) 2022. Published by Oxford University Press on behalf of FEMS. This is an Open Access article distributed under the terms of the Creative Commons Attribution License (https://creativecommons.org/licenses/by/4.0/), which permits unrestricted reuse, distribution, and reproduction in any medium, provided the original work is properly cited.

Downloaded from https://academic.oup.com/femsre/advance-article/doi/10.1093/femsre/fuac039/6674677 by guest on 05 October 2022

ing 2017). Compared to the other fields of study in biology, mycology is a relatively young discipline and still considered a niche.

Until the last decade, mycology has regularly been considered as the study of mushrooms, i.e. the macroscopic structures that are found in forests or that we buy in a supermarket to eat. Other fungi, such as pathogens or symbionts (e.g. mycorrhizal fungi) have been handled in other fields, but not as integral parts of a larger and common area of research. As a result of this dispersion, their importance as a microbial clade has somewhat been underrepresented for many years. However, their significance is far reaching, and the relatively new fungal kingdom includes a vast number of species that are of the utmost importance for nature as a whole. Hence, not only are fungi fascinating and elusive, they also constitute an enormous significance for nature and humanity. Fungi act as the main decomposers in natural recycling processes and are responsible for degrading dead organic matter. Besides that, fungi are very potent biogeochemical engines, affecting the availability of numerous elements. This ability can be exploited artificially for bioremediation or in biofertilization (Carvajal-Muñoz and Carmona-Garcia 2012). In particular, the symbiotic association between a certain type of fungi and roots of plants—known as a mycorrhiza—is capable of significantly increasing yield in crops (Hamel 2007). Furthermore, fungal metabolic pathways can be harnessed for the biotechnological production of many important substances. Famous examples include the mass production of ethanol by the yeast *Saccharomyces cerevisiae*, with almost 110 billion litres produced annually, as estimated by the U.S. Department of Energy (2020), or the production of citric acid by the mould *Aspergillus niger* (Show et al. 2015). Medically relevant examples include the antibiotic penicillin (Barrios-González et al. 1988) and the immunosuppressant cyclosporin A (Ramana Murthy et al. 1999). On the other hand, however, some fungi are responsible for causing severe diseases in humans (e.g. *Cryptococcus neoformans* or *Aspergillus fumigatus*) and other animals, but also in plants. The pathogen *Fusarium graminearum*, for example, is responsible for annual losses in wheat and barley production ranging between 6% and 19% in the USA, which translates to a loss on the order of billions of dollars (McMullen et al. 2012). Due to a lack of effective antifungal agents (Almeida et al. 2019), promising alternatives to the use of chemical fungicides are being developed, including biocontrol agents such as the mycoparasitic fungi *Clonostachys rosea and Trichoderma* spp. However, more basic research into their infection mechanisms at the cellular and intracellular levels is needed to eventually harness their antifungal potential in a widespread, commercial way.

So-called microfluidic—or 'Fungi-on-a-Chip'—technologies are emerging as a new tool to aid such studies in mycology, as well as high-throughput applications in fungal biotechnology. The field of microfluidics involves the manipulation of small amounts of liquids in a controlled manner within artificial micron-sized fluidic networks of channels. It was established as a useful tool for different kinds of studies, including nanoparticle synthesis (Karnik et al. 2008), general chemical synthesis (Liu and Jiang 2017), and chromatography (Xie et al. 2005). The original concept stemmed from a need to implement different automated operations (e.g. sorting capabilities) into chemical processes, in an analogous manner to that of electrical networks, whilst increasing experimental throughput concomitantly. Due to the significantly smaller dimensions of micron-sized fluidic networks, other effects dominate when compared to the macroworld. Hence, a transition to miniaturized systems yields new experimental opportunities. Above all, the flow behaviour within microchannels is mostly laminar, having a parabolic streaming profile described by the law of Hagen and Poiseuille (Sutera and Skalak 1993). While gravity is widely negligible, capillary forces and surface tension dominate, allowing new possibilities to be exploited such as droplet trapping or inertial microfluidics. Generally, miniaturization enables the generation of high-throughput experimental systems that possess enhanced analytical accuracy and sensitivity, which is closely interlinked with the ability to control processes in an outstandingly precise manner, especially in terms of temperature, illumination, or flow dynamics. Moreover, this entails a safer handling, as well as intrinsic sterility, because of the enclosed nature of the microsystem. While the requirements for chemical or biological material, both in terms of quantity and cost, are usually significantly lower than those associated with conventional methods (e.g. batch processes), it is still possible to achieve high output of both results or products by following a modular approach and parallelization, also called numbering-up (Kriel et al. 2016).

In recent years, microfluidic technologies have been adopted for applications in the biological sciences and in particular for studies on whole (living) organisms. This trend is evidenced by the many advantages that microfluidic platforms offer, such as the optical transparency of most devices for brightfield and fluorescence-based imaging as well as the ability to mimic microenvironments both structurally and with well-defined chemical gradients. Material choice is key for the desired application, with the elastomeric polymer, poly(dimethylsiloxane) (PDMS) featuring as one of the most prominent materials used in microfluidic technology development (Box 1). In combination with high-throughput and automated approaches, microfluidic technologies are becoming increasingly recognized by biologists as experimental platforms that can afford precise analyses on a cellular, subcellular, and even molecular level, in genetics, proteomics, and cellular assays (Tian and Finehout 2009). The latter is especially well-represented in the literature, with numerous examples of studies with bacteria (Cao et al. 2013) and human cells (mainly blood, sperm, or stem cells; Zhang et al. 2018a). In particular, microfluidic technology has been extended to the study of small multicellular organisms, e.g. nematodes (Lockery et al. 2008, Tayyrov et al. 2019), as well as mammalian tissue (Zheng and Jiang 2018), plants (Stanley et al. 2018), and animals (Funfak et al. 2007). Microfluidic studies involving fungi, however, are rare. Indeed, the application of microfluidics to mycology is a very recent development with the first studies published only in the last 15 years. Indicative of this, Tian and Finehout's book 'Microfluidics for Biological Applications' published in 2009 (Tian and Finehout 2009) gives a very detailed overview about biological investigations using microfluidic methods, without, however, a single mention of fungi.

Box 1. Materials used in microfluidic technologies

As the field of microfluidics originated from microelectronics, silicon was one of the first materials to be used in microfluidic device development. Although having well-defined material characteristics and well-established manufacturing processes, silicon was soon replaced by glass. Glass possesses important properties, such as chemical inertness, mechanical resilience, and optical transparency, as well as the opportunity to etch micron-sized channel architectures. This, coupled with the overall good biocompatibility of glass, makes it a suitable material for the use in microscopy investigations of microorganisms and biological processes. With similar properties, but generally much easier, safer, and quicker to fabricate using lithography methods, polymers have mostly succeeded glass in microfluidic technology development. Especially the thermoplastics such as polycarbonate (PC; Ogończyk et al. 2010), poly(methyl

Downloaded from https://academic.oup.com/femsre/advance-article/doi/10.1093/femsre/fuac039/6674677 by guest on 05 October 2022

methacrylate) (PMMA; Hong et al. 2010), cyclic olefin copolymer (COC; Ochs et al. 2014), as well as polystyrene (PS; Young et al. 2011) are widely used. The microchannel layout is commonly engraved via hot embossing, precision milling, or laser ablation. Even though all of these materials have their benefits and applications, the elastomeric polymer poly(dimethylsiloxane) (PDMS) has emerged as one of the main materials of choice in microfluidic device fabrication. The majority of the studies discussed herein feature PDMS as the basis for their microfluidic devices. PDMS can be cast easily from master moulds using soft lithography, with little apparative requirements. Besides the uncomplicated device manufacturing, PDMS offers optical transparency, low autofluorescence, gas permeability, adjustable tensile strength, and exceptional biocompatibility (Raj and Chakraborty 2020). The elasticity of PDMS allows to form valve and pump structures (Nielsen et al. 2020) or to measure forces exerted by a microorganism, however, this also renders PDMS devices unsuitable for high-pressure tasks.

Besides these established methods, other materials have emerged for specialist applications. This includes smart materials, such as pressure-controlled adhesives (Nielsen et al. 2020) and certain hydrogels (Kang et al. 2013), the latter of which combines structural with functional properties. Similarly, ceramics are being used for microfluidic devices, contributing excellent thermostability and thermal insulation as well as chemical stability to the system (Vasudev et al. 2012).

Herein, we review the major studies conducted within the emerging field of Fungi-on-a-Chip microfluidic technology development for single-cell studies on fungal biology. First, we highlight the application of microfluidics for investigations on yeast cells, the first type of fungi to be featured in microfluidic systems. The collected publications are mainly dedicated to investigations on cellular life cycle and ageing, as well as the design of trapping facilities for single-cell capture. Through these single-cell studies, it was found that cellular responses and expression levels vary immensely from cell-to-cell, far more than previously expected and independent from the cell cycle stage. These findings will be important for improving the effectiveness of biotechnological processes and yield new hypotheses related to cell ageing studies, moving away from investigations at the population level to individuals. In the second major section, we discuss a range of medical applications, mainly blood cleansing devices for fungal pathogens, as well as Lung-on-a-Chip models for fungal disease studies. Highlights of this section include a microfluidic device that revealed an altered immune response in bronchiole models when coinfected with fungi and bacteria, compared to infection with both monocultures alone, an insight key to understanding dangerous diseases like cystic fibrosis. The third section is dedicated to investigations concerned with filamentous fungi and their interactions with other organisms within artificial microfluidic devices at the cellular level, which has formed a significant trend of late, especially in the emerging field of Soil-on-a-Chip microfluidics (Stanley et al. 2016). Using a microfluidics-based approach, microenvironments can be designed to allow environmental cues of a chemical, physical, and biotic nature to be studied in depth, while retaining transparency for detailed analyses, e.g. using high resolution microscopy techniques. For instance, the pioneering work by Held et al. (2009a, 2011a) unravelled the space searching strategies of the filamentous fungus *Neurospora crassa*, which is directed by the Spitzenkörper, an intracellular body that acts as a gyroscope for directional memory and manoeuvring coordination. Lastly, we provide a future perspective detailing a number of new frontiers in which microfluidic technology is expected to aid future research in this field of study, with a focus on arbuscular mycorrhizal fungi (AMF), nuclei behaviour in filamentous fungi, multispecies interactions, and electrical measurements for cell-to-cell communication.

Single-cell studies on yeast

The first type of fungi to be featured in a microfluidics-assisted investigation were yeasts. Because of their single-cell character, the transition from microfluidic studies on bacteria and mammalian cells was a smooth one, often starting with simply extending the application of established devices to the yeasts. Wu et al. (2004) designed the first microelectromechanical systems (MEMS)-based device involving yeast cells, which allowed single cells to be aligned in a row and subsequent fluorescence-based imaging and counting of individual cells. Due to a channel width of 7 μm and sheath flow-assisted focussing, only one cell at a time was able to pass through the channel network and be admitted into the image identification unit. Their simple glass-based microdevice comprised of an inlet for the cells, specifically *S. cerevisiae* and prostate cancer cells of the PC3 line, two channels to generate the sheath flow and three outlets with vacuum suction. In the study, the general functionality of the device was proven and further applications such as cell separation were proposed, marking the starting point of fungal microfluidics. Moreover, the authors proclaimed that the set up and entailing shear stress, as well as pressure, did not pose a negative impact on the cells, an issue debated in later studies.

Imaging microcolonies

Yeasts, especially the model organisms *S. cerevisiae* and *Schizosaccharomyces pombe*, are of the utmost importance to researchers. These unicellular fungi are eukaryotic entities with close resemblance to mammalian cells, making them perfect subjects for detailed studies concerning unravelling the function of every gene in the genome, as well as investigations on gene expression, intra- and intercellular signalling and replicative cell ageing (Dolinski and Botstein 2005, Pardo et al. 2016, Piper 2006). These processes occur across various microscopic scales, ranging from the microcolony level, to the level of single cells, and down to the subcellular level, for which microfluidic technologies are ideally suited. It is unsurprising, therefore, that numerous groups have integrated microfluidic techniques into their studies with yeast. Microfluidic devices allow cells to be aligned within one focal plane for precise imaging, as well as providing a means to separate them into different chambers (i.e. to conduct experiments in parallel) and afford highly controlled perfusion with effector solutions. The exact device designs can be then tailored to the task at hand. Several methods for the trapping of yeast cells within microfluidic devices have been employed to date, since yeasts—unlike many mammalian cells—generally do not adhere tightly to surfaces and, therefore, need to be fixed. Figure 1 highlights the major methods employed to immobilize yeast cells, which includes *in situ* polymerization, affinity binding, passive trapping in microchambers, and pressure-based active trapping. Some of these methods/techniques used for cell ageing-related studies have been reviewed by Chen et al. (2017) and Jo and Qin (2016).

In situ polymerization

A suitable means to accommodate yeast cells within a microfluidic channel is to immobilize them within a hydrogel, e.g. alginate

Downloaded from https://academic.oup.com/femsre/advance-article/doi/10.1093/femsre/fuac039/6674677 by guest on 05 October 2022

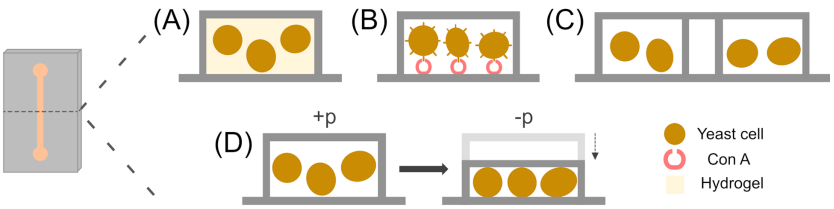


Figure 1. Schematic illustrating yeast cell immobilization strategies. The illustration shows cross-sections through a microchannel to describe different methods of immobilizing yeast cells in a microfluidic device. (A) Cells fixed by *in situ* polymerization of a hydrogel. (B) Yeast cells fixed by affinity binding using Concanavalin A. (C) Spatial segmentation of cells into microcolonies via passive trapping. (D) Pressure-based trapping of cells between the channel ceiling and bottom. When flow pressure is high (+p), the channel widens and cells enter into the microchamber. Upon release of pressure (-p), the channel shrinks to a size comparable to that of the cell diameter, thus immobilizing the cells.

(Vo et al. 2020) or agarose, which is a nontrivial task. The most used method, termed *in situ* polymerization (Falconnet et al. 2011), utilizes a low melting temperature liquid agarose gel, i.e. prepared and premixed with the cell suspension at 30°C. Once pumped into the designated chambers, the gel–cell mix is polymerized at 4°C for 3 min and the cells are robustly fixed. The sophisticated channel design and computer-assisted chemical control allows 128 parallel experiments to be conducted in a single run, whereby eight different *S. cerevisiae* genotypes and 16 different conditions can be probed simultaneously to investigate lineage-dependent pheromone signalling responses. While the results obtained reveal response dynamics on the single-cell level, the data is still statistically relevant. To demonstrate the potential of their device, the group conducted experiments of the mitogen-activated protein kinase (MAPK) involving mating responses towards different concentrations of the pheromone α-factor in different strains. As a read-out, they tagged the membrane receptor Ste2 with green fluorescent protein (GFP). Ste2 is up-regulated in the sexual tip extension of a yeast cell, called shmoo, and thus correlates with an enhanced mating activity, triggered by the pheromone gradient. The pheromone response found was highly variable from cell to cell. As an explanation, they suggested nongenetic inheritance of the behaviour since the yeast colonies were genetically identical.

The same experimental set up (with slight modifications) was used in further investigations probing the nongenetic heritability aspect of these pheromone response phenomena. The microfluidic design allowed to precisely track budding and thus create lineage maps within the microcolonies; the mother–daughter correlations in response to the α-factor pheromone differing from strain to strain could then be measured. Using a sophisticated tripartite fluorescent tagging strategy and targeted cell-cycle synchronization with hydroxyurea, the authors were able to reveal cell-to-cell variations in the cellular response, which would otherwise have been concealed within the colony. Moreover, it was found that the kinase Fus3 not only supresses the transition from the G1 to the S phase upon pheromone stimulation, but also modulates the cell cycle into the other direction, resulting in growth arrest preferably at the S phase and generally longer cell cycle phase duration in the Fus3 knockout mutant (*fus3*Δ), even without the pheromone stimulus. These findings suggest a stronger influence of cell cycle and the interplay between signalling pathways onto colony heterogeneities than formerly expected (Ricicova et al. 2013). Figure 2(A) shows a schematic experimental design utilizing hydrogel cell immobilization.

Affinity binding

Another method employed to immobilize yeast cells within the vicinity of the microchannel surface involves coating the channel with biomolecules, such as concanavalin A (Con A) or avidin (Xie et al. 2012). Con A, a lectin well-known for its application in affinity chromatography (Hage 1999), can bind specifically to several carbohydrate structures. In an analogous manner, Con A can bind to certain sugars presented on the surface of yeast cells, thus acting as an immobilizing agent. In comparison to agar, agarose and other hydrogel immobilization techniques, the use of Con A is claimed to cause minimal (or no) background fluorescence in microscopy (Pemberton 2014). Moore et al. (2008) demonstrated that a very simple chamber design could be employed, when Con A was used to prevent yeast cells from being flushed out. With their Y-shaped device design and using a relatively low volumetric flow rate, they generated a concentration gradient comprised of α-factor mating pheromone, which, under a laminar flow regime, relies on diffusion only. As a result, the gradient was the least steep closest to the outlet (Fig. 2B). The yeast cells then responded to the different concentrations of α-factor within the gradient, exhibiting different development of their mating projections (shmoo; i.e. involving directional growth strategies and error correction). Owing to the successful immobilization of single yeast cells, it was also possible to reveal the subcellular mechanisms underlying these behaviours.

A similar channel design was employed by Hersen et al. (2008), equipped with an electrovalve to create effector gradients more precisely and allow for oscillations of up to a few hertz (Hz). With this device, the cellular response of *S. cerevisiae* to environmental stresses was studied. To investigate the hyperosmolar glycerol (HOG) pathway, which involves MAPKs, a sorbitol solution was introduced to create osmotic stress. An increase in the osmotic pressure was followed by translocation of the MAP-Kinase Hog1 to the nucleus preceded by phosphorylation. If the stimulus frequency applied was lower than 4.6×10^{-3} Hz, the cellular response was found to follow the input oscillation instantaneously. Their findings suggested that the factor limiting the processing speed was the time required for the biochemical cascades to occur (e.g. phosphorylation) rather than physico-chemical mechanisms, which occur on much faster time scales (Hersen et al. 2008). The same device was later used by Hao and O'Shea (2011). In this study that used various stressors, such as potassium chloride, hydrogen peroxide, and high glucose concentrations, a deeper insight into the different kinetics of transcription factor-dependent cell responses was gained. It was shown that the transcription factors Msn2 (a general stress-responsive transcription factor in *S. cerevisiae*) and Crz1 (a zinc finger protein) are activated differently by these stimulants and that these patterns again trigger a specific promoter, thus encoding the input signal and translating it into

Downloaded from https://academic.oup.com/femsre/advance-article/doi/10.1093/femsre/fuac039/6674677 by guest on 05 October 2022

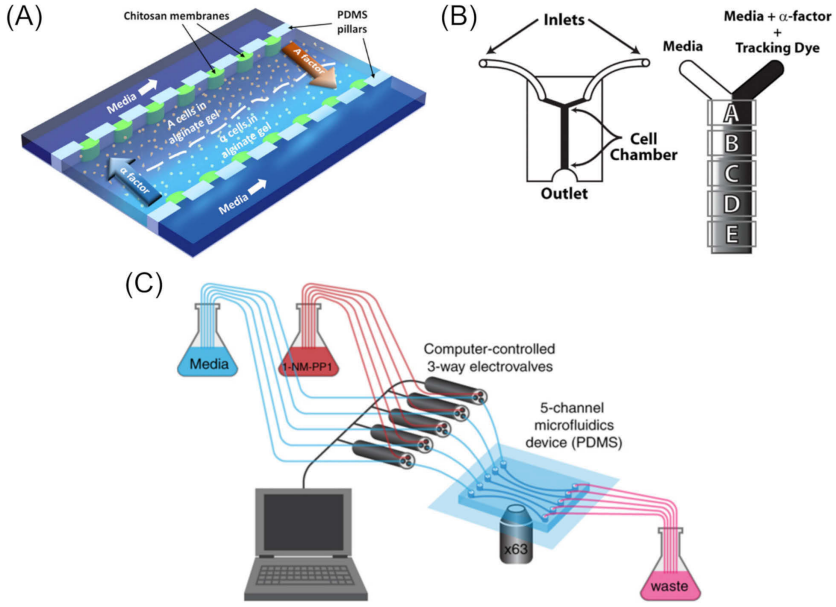


Figure 2. Examples of applications of microfluidic immobilization of yeast cells by *in situ* immobilization and affinity binding. (A) Device for studying pheromone chemotropism in α- and A-yeast cells. Cells are trapped in alginate gel and subjected to asymmetric pheromone conditions. Image reproduced with modifications from Vo et al. (2020) with permission from AIP Publishing (Licence Number: 5271490260805). (B) Y-device, coated with concanavalin A (Con A) to help α-cells adhere to the channel. A gradient of α-factor was created, followed with the aid of Dextran-3000-TRITC as a tracking dye. Cells in five different areas, A–E, were imaged. Image reproduced with modifications from Moore et al. (2008) with permission from the Creative Commons Attribution license (www.creativecommons.org/licenses/by/4.0/). (C) Example of five-channel device with computer-controlled 3-way valves to subject Con A-immobilized yeast cells to pulsed treatments with the protein kinase A (PKA) inhibitor 1-NM-PP1. A 63X microscope objective was used to monitor Msn2-mCherry translocation dynamics and gene expression in single cells. Image reproduced with modifications from Hansen and O'Shea (2013) with permission from John Wiley and Sons (Licence Number: 5271490732299).

an adequate stress response of the cell. More specifically, it was found that with slow promotors and high frequency input signals a temporal summation or 'head-start' effect can be caused, leading to a nonlinear relationship, while genes with rapid promotor kinetics are able to follow the input proportionally. At the molecular level, this can mainly be attributed to promotor structure, number, and position of binding sites and, thus the binding affinity. The idea of encoding or integration of environmental stresses into single molecule actuators (i.e. transcription factors) was further elaborated in a subsequent study conducted by the group (Hao et al. 2013). To elucidate the mechanism of the promotor activation and intrinsic amplitude thresholds, the group upgraded their microfluidic device from a single-channel to a five-channel architecture (Fig. 2C). With the additional throughput, they found trade-offs between the level of control regarding gene expression and expression noise. Thus, this work reiterates how different promotors can be seen as modules of signal-processing, with simple integrators, high-pass filters, and duration filters (Hansen and O'Shea 2013, Hansen et al. 2015). These collective studies suggest that the response can be specifically tuned to environmental factors through evolution of the promoters, for instance, a strategy that could be similarly applied to biotechnology.

Passive trapping in microchambers

The aforementioned techniques involved fixing yeast cells in gels (e.g. agarose) or with attachment agents (e.g. Con A) to provide immobilization. However, these approaches are claimed to affect the imaging quality of the yeast cells in a negative manner, e.g. by blurring the image or by introduction of crystals in case of incomplete polymerization, cells lose attachment after only a few hours (Ryley and Pereira-Smith 2006, Crane et al. 2014) and the cells themselves may also potentially be influenced with regard to their growth and development. Therefore, many groups set out to develop microfluidic devices to 'cage' cells, with microchambers able to hold the cells due to a specific channel design only, deciding to accept the trade-off between a less robust fixing of the cells with the added benefit of unaffected imaging and cell development. An example of a microfluidic device featuring an array of microchambers can be found in Fig. 3(A). Cookson et al. (2005) designed a simple, accessible microfluidic device loosely inspired by Nikola Tesla's diode loop (Tesla 1920) to trap microcolonies of budding yeast. Using their channel design, they were able to assemble the cells in a single focal plane to produce high-resolution images. Time-lapse fluorescence microscopy was employed to track single cell cycles as far as 10 divisions in a dynamic manner, gaining statistical data for predictive modelling (Cookson et al. 2005).

Paliwal et al. (2007) devised a more complex device design, which utilized small chambers for perfusing microcolonies of *S. cerevisiae* cells with effector-media solutions on two sides. After loading the cells into the device there was no active flow inside of the cell chambers and the effector gradient reached the cells by diffusion only, preventing the cells from being flushed out. Here, and continued by Hao et al. (2008), morphological changes in yeast cells as a mating response to the pheromone gradients were investigated, similar to Moore et al. (2008), but more emphasis was put on the regulatory pathways involved, including the signalling components Fus3, Ste5, and Kss1. The ability to subject cells to different concentration gradients of pheromones more closely simulates reality, as compared to uniform concentrations commonly applied in standard, plate-based assays. Thus, the authors revealed the function of Ste5 in the stimulation and control of Fus3 as the main mechanism for gradient sensing and directional growth of the mating projection, as part of a complex interplay of all the signalling components. Interestingly, as a result

Downloaded from https://academic.oup.com/femsre/advance-article/doi/10.1093/femsre/fuac039/6674677 by guest on 05 October 2022

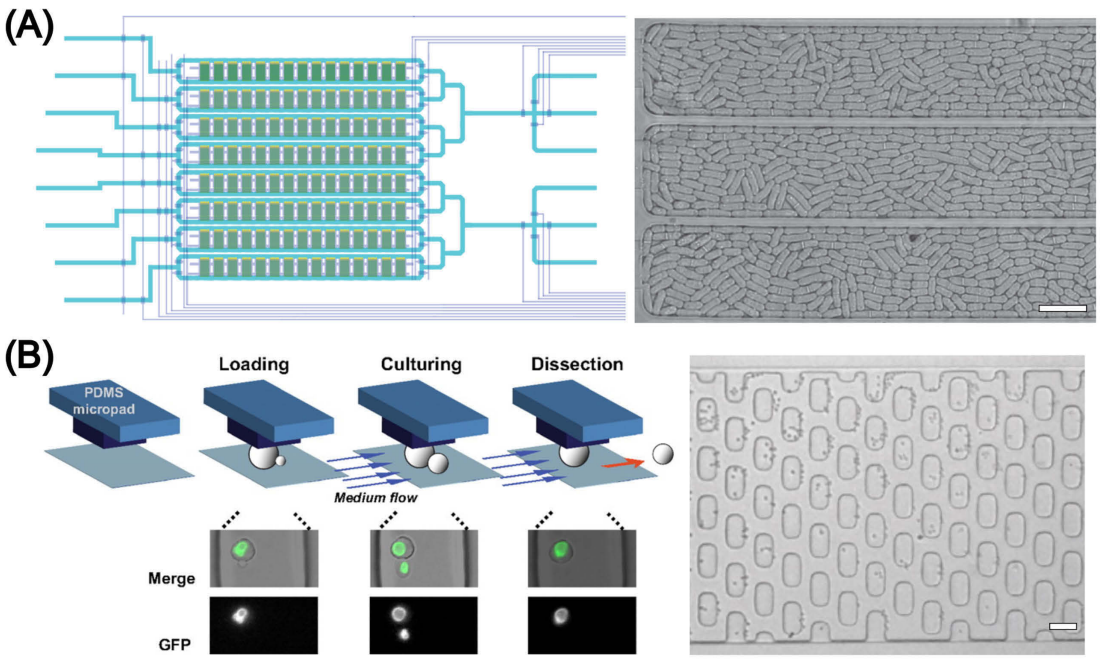


Figure 3. Exemplar applications of microfluidic immobilization of yeast cells by compartmentalization into microcolonies and active, pressure-based trapping. (A) Schematic illustration of a device having eight independently addressable rows each containing 15 microchemostats, highlighting the high degree of parallelization. Yeast microcolonies (here *S. pombe*) can be imaged and studied in parallel as well as subjected to different media conditions. The bright-field image shows three microchambers filled to confluence with yeast cells. Image reproduced with modifications from Nobs and Maerkl (2014) with permission from the Creative Commons Attribution license (www.creativecommons.org/licenses/by/4.0/). (B) Microfluidic platform for trapping single yeast cells (here *S. cerevisiae*) under pressure-based expandable micropads (30 × 15 μm), used to study cell ageing. During cell loading, the micropads are slightly lifted due to the hydrodynamic pressure created by the flow. Upon release of pressure, the micropads resume their original height, thus trapping cells. Smaller daughter cells budding off from the mother cells are automatically washed away during dynamic cultivation with a slow constant flow. Microscope image showing some yeast cells (mother cells) trapped underneath the micropads and some smaller cells (daughter cells) being flushed out. Image reproduced with modifications from Lee et al. (2012) with permission from National Academy of Sciences. Scale bars represent 20 μm.

of imaging with single-cell resolution, it was further discovered that a differentiated response occurs upon exposure of the microcolony to low pheromone levels, where some cells induce shmoo formation whereas others actively suppress this expression programme. Thus, they are effectively saving energy while waiting for the signal to become either stronger or subside (Hao et al. 2008, Paliwal et al. 2007). In an analogous manner, Taylor et al. (2009) studied pheromone mating responses in *S. cerevisiae*. Using their microfluidic device they achieved an immensely high analytical throughput, allowing them to take over 49 000 images of parallel experiments in just one run (~12 h). Besides Fus3 and Kss1, they further extended pheromone response studies onto the signalling proteins Ptp2 and Msg5.between the different signalling

Denervaud et al. (2013) built a microfluidic device able to accommodate more than 10 000 separate experiments, observing 1152 GFP-expressing yeast strains in one run. This set up allowed dynamic investigations on changing yeast proteomes to be conducted in response to stressors such as ultraviolet (UV) radiation, methyl methanosulfonate, hydroxyurea, and osmotic stress, in a pulsed and continuous manner, helping to unravel the full dynamics of changes, which are often transient. It was elucidated that the P-body components Scd6 and Pat1 are predominantly involved in the formation of the mRNA processing body (P-body). Moreover, it was found that four main proteins (Tsa1, Rtt101, Rai1, and Nam7) are involved in nuclear localization of the ribonucleotide-diphosphate reductase Rnr4. The advantage of the presented method is that it facilitates the analysis of cellular signalling and expression mechanisms in combination with real-time phenotypical changes, a read-out that conventional methods such as spot assays are lacking. A slightly modified microfluidic device was later used by Nobs and Maerkl (2014) to study *S. pombe*. They followed over 100 000 cell division events in up to 10 generations under normal conditions as well as heat stress.

Luo et al. (2008) designed a device with triangular- and later rectangular-shaped (Luo et al. 2009) cell chambers emanating from the main channel. The yeast cells can, thus be perfused with medium without being flushed away. As a proof-of-concept, they observed changing expression levels of the pCUP1 promotor in response to different Cu^{2+} concentrations. Other possibilities to isolate the cells in the cell chambers also exist, i.e. by manually closing the chambers after loading with valves (Park et al. 2013) or membranes (Charvin et al. 2008).

By implementing silicon oxide instead of PDMS as the material of choice in device manufacture, Huang et al. (2009) employed a roll-up technique to produce microchannels with a perfect circular cross-section and adjustable dimensions. The multistep manufacturing process involved forming a multilayered substrate using spin-coating, chemical vapour deposition, and chemical etching techniques, which creates an intrinsically strained SiO/SiO_2 bilayer system that automatically rolls up upon release. Interestingly, yeast cells growing within the microchannel were observed to form a peculiar elongation in proof-of-principle experiments, an adaption to the constriction that was not, however, lethal to the cells.

Pressure-based active trapping

In contrast, some groups followed a different approach to obtain arrays of locally fixed cells. They devised a cell trapping method

Downloaded from https://academic.oup.com/femsre/advance-article/doi/10.1093/femsre/fuac039/6674677 by guest on 05 October 2022

based on the flexibility of the elastomeric polymer, PDMS. Upon subjection to pressure the PDMS channels can be widened, allowing cells to enter, and upon relieving the pressure the PDMS returns back to its prior state, thus trapping cells within the channel. The schematic trapping principle along with a microscopic image of yeast cells trapped under elastic micropads is shown in Fig. 3(B).

Being the first to try this method, Groisman et al. (2005) probed the dynamics of large numbers of yeast cells at the microcolony level. Using a microfabricated chemostat, they were able to align bacteria, as well as yeast cells, in a biofilm-like manner using microchambers interspaced by hanging channel walls, leaving gaps of ∼0.6 μm between the wall and device bottom in the absence of pressure. These gaps permit exchange of substances, such as nutrients and waste, yet are impassable, however, to the cells. When a high gauge pressure (8 psi) is applied, cells can pass freely between the chambers. Thus, the cells can initially be distributed equally within the device, after which they can be isolated from one another. With this chemostat, colony growth behaviour and gene expression linked to quorum sensing were investigated; as such, dynamic response experiments were conducted and colonies subjected to temporarily changing exogenous stimuli. By addition of 10 nM of the autoinducer N-3-oxohexanoyl homoserine lactone to an *Escherichia coli* mutant with GFP(LVA) (tagged at C-terminal with amino acid sequence RPAANDENYALVA for faster degradation; Andersen et al. 1998) fused to the *luxR* gene, which is involved in quorum sensing, a rapid response (i.e. < 1 h) with an exponential increase in the fluorescence level of about 3–4 orders of magnitude was triggered. Upon removal of the autoinducer, this was followed by an equally fast decline in the fluorescence intensity, due to a rapid degradation of the GFP(LVA). While the main part of the investigations was conducted with bacterial cells, the group emphasized the potential of this or similar platforms for use with the yeast cells. They further highlighted the potential applicability of their device design for other studies, e.g. regarding aspects of gene expression and mutation, but also cell ageing, population dynamics, and sporulation (Groisman et al. 2005).

Lee et al. (2008) designed a device where whole channels are expanded and retracted upon the application and removal of applied pressure, respectively. In doing so, the yeast cells become trapped and are clamped between the channel ceiling and bottom. This was coupled with a sophisticated microfluidic circuit including different fluidic resistances, which facilitates a precise fluid and pressure control. Thus, flow velocity and pressure are decoupled, allowing key processes (i.e. flushing out nontrapped cells and nutrition) to be achieved without releasing trapped cells. This work was mainly concerned with creating an easy-to-use and easy-to-set-up system for widespread applications in cell biology. As a proof-of-concept, they monitored the expression of enhanced GFP (EGFP) from a Fus1 promoter region, which was activated by pulses of the α-factor pheromone intermitted by a washing step. The fluorescence signals, and hence cellular response was found to vary significantly from cell to cell, which was attributed, besides stochastic noise, to differences in the transcription and translation apparatuses of each cell. Possible effects deriving from different stages in the cell cycle were ruled out because all cells were pretreated with 200 mM hydroxyurea, arresting all cells in the S-phase. Similar set ups were later applied to investigations on stress response involving the high-osmolarity glycerol (HOG) pathway and crosstalk between the different signalling components (Lee et al. 2020, Uhlendorf et al. 2012).

Besides these studies, another big area of interest in yeast research is concerned with cell ageing and replicative lifespan. Therefore, obtaining isolated mother cells is desirable to study them in an unobstructed manner. Conventional methods involve manually removing budding daughter cells with a needle, a time-consuming and tedious task, which is also stressful for the cells because of the sheer size of the needle compared to the cell, making a precise dissection extremely difficult. Using microfluidic technologies, mother yeast cells can be trapped underneath micropads or pensile columns, while daughter cells that bud off are flushed away by a constant flow of medium. As an estimate, the dissection task that four to five trained people would achieve in 3–4 weeks, can be conducted with one microfluidic device in only 2–3 days (Zhang et al. 2012, Zou et al. 2017). As an additional benefit, nutrient medium is constantly refreshing in the microfluidic device. Furthermore, no agar, which lowers the resolution for microscopy, is needed. With such a device, Lee et al. (2012) discovered age-related morphological changes in cells of *S. cerevisiae*, with a so far unseen heterogeneity. By tagging VPH1, encoding a subunit of the vacuolar ATPase, with GFP, they focussed on the development and morphological changes in the vacuole. They found two cellular shapes at death, an ellipsoidal and a spherical shape. The shape correlated with the age of death, being 12 budding cycles for the spherical type and almost double the age for the ellipsoidal shape. The vacuole shape, herby, is either fragmented, fused, or tubular, the latter only occurring in ellipsoidal cells. Later, the group used the same device to investigate whether calorie restriction diets are indeed a reliable method to extend the live span of organisms (Huberts et al. 2014).

Differing from the other studies, Ohnuki et al. (2009) used a two-layered device design with a secondary air-filled channel through which pressure can be applied, trapping yeast cells in the main channel. Thus, they were able to trap the cells at will and on demand. Together with the semiautomatic image processing programme CalMorph (Ohtani et al. 2004), they were able to monitor cell cycle progression in *S. cerevisiae*. Another approach to trap yeast microcolonies was conducted by Frey et al. (2015), who manually pressed yeast cells down against PDMS clamping pads by bonding a glass cover slip onto the PDMS chamber after preloading with the cells using a pipette.

Single-cell trapping

As described previously, a common challenge that most studies in the field of yeast research are concerned with is the trapping of single, individual yeast cells in a sustained manner, ensuring daughter cells that bud off are automatically removed from the mother cell. To meet this need, a suitable method concerns the design of physical flow traps; the trap dimensions should be the size of one mother yeast cell so as to accommodate only one single cell. Different shapes were used to design trapping structures within a microfluidic device. An overview is illustrated in Fig. 4.

Ryley and Pereira-Smith (2006) proposed three different trapping structures, dubbed 'yeast jails'. A total of two of those, featuring groups of three micropillars per trap, were successfully used to capture yeast mother cells (Fig. 4A and B), while the third (a 'horseshoe'-shaped trap) was disregarded on the grounds of less space efficiency compared to the other designs. One minor drawback of these early designs was that in order to effectively remove the daughter cells, constant reversal of the flow direction was necessary. A constant flow provokes pseudohyphal growth, which in turn leads to daughter cells remaining attached to the mother yeast cell.

Downloaded from https://academic.oup.com/femsre/advance-article/doi/10.1093/femsre/fuac039/6674677 by guest on 05 October 2022

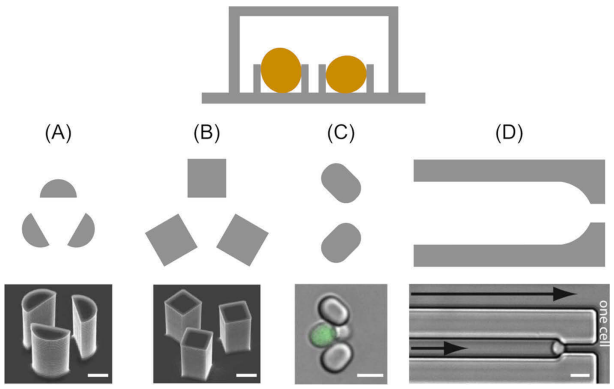


Figure 4. Overview of channel features used to trap single yeast cells. The above schematic depicts a cross-section taken through a microfluidic channel containing yeast traps, as well as top-down views of four different trap designs (A)–(D). Electron micrographs of semicircular (A) and square (B) three-pillar trap designs reproduced with modifications from Ryley and Pereira-Smith (2006) with permission from John Wiley and Sons (Licence Number: 5271491246941). (C) Microscopy image of an oval two-pillar trap design reproduced with modifications from Crane et al. (2014) with permission from the Creative Commons Attribution license (www.creativecommons.org/licenses/by/4.0/). (D) Microscopy image showing a channel-based trap design reproduced with modifications from Rowat et al. (2009) with permission from National Academy of Sciences. Scale bars represent 5 μm.

With the two three-pillar systems, the authors then investigated RAS2 and HSP104 expression, genes known to affect survival rates and life span. It was found that the expression levels vary significantly from cell to cell, with differences in fluorescence signals ranging from up to 2-fold for RAS2 and up to 9.6-fold in the case of HSP104. These findings, impossible to detect with conventional nonmicrofluidic methods, suggest that the expression of RAS2 is a key factor in varying life spans in otherwise identical yeast cells. As for HSP104, which is known to play a major role in survival strategies against external stressors, it was shown that the ability to track single cells over time allowed factors influencing survival, e.g. duration, type of stress or HSP104 basal levels, to be thoroughly investigated.

As their system was simple and effective, it was later adapted in similar studies (Ryley and Pereira-Smith 2006). Liu et al. (2015) used the same three-pillar system to trap cells and implemented their device in an automated high-throughput platform for investigations on cellular lifespan and gene expression. It was dubbed HYAA (High-throughput Yeast Aging Analysis) and later developed further into the HYAAC (for Cryptococcus) to accommodate another yeast, *C. neoformans* (Orner et al. 2019). The virulence and antifungal resistance of these pathogenic fungi is dependent on ageing and age-related phenotypes. Studies on their lifecycle as well as ageing are, therefore, highly needed and important for effective treatment (see also the 'Fungi-on-a-Chip technologies for medical applications' section).

Crane et al. (2014) developed '*A Long-term Culturing And TRApping System*', in short ALCATRAS, which diverged from the complex structures detailed in previous studies and exploited a very simple, yet efficient, array of cell traps. The two-pillar based system, as illustrated in Fig. 4(C), is able to catch flowing yeast mother cells, where a constant stream of fluid is required to keep them inside the traps and also flush away budding daughter cells. This straightforward approach offers a trapping efficiency of almost 100% and is easy and inexpensive to use and manufacture. Furthermore, the design allows for a high density of traps, and thus raises the level of data acquisition by an order of magnitude compared to similar devices. Moreover, the platform enables fast switching of media, as shown in a glucose limitation experiment. Upon monitoring the transcription factor Msn2p, which is involved in cellular stress response in *S. cerevisiae*, it was found that switching the medium to low glucose levels entailed an immediate relocalization of Msn2p-GFP to the nucleus, thus triggering the cellular stress response. This was followed by repeatedly switching between high (2%) and low (0.1%) glucose levels in intervals of a few hours. Interestingly, it was observed that after each cycle, fewer cells responded with nuclear localization of the Msn2p-GFP, indicating a learning behaviour. Since the stress was not persistent and a complete stress response became unnecessary, the cells might have reduced their stress response to save energy. Alternatively, they suggested that this observation could be caused by cell ageing. In a second experiment, Whi5p, a transcriptional repressor, expressed specifically in the transition from M to G1 phase, was used to gain new insights into the cell cycle of yeast cells. A periodic signal, representing cell division times, was measured, which was found to be strongly dependent on age and varied from individuum to individuum. These results were only made possible by the ability to precisely trap and track individual mother cells, while instantly and automatically removing budding daughter cells, demonstrating the usefulness of this type of microfluidic device. A very similar, two-pillar based design was later used by Jo et al. (2015) and for cell ageing studies and investigations on age-related disease (Jo et al. 2015, Jo and Qin 2016, Yu et al. 2020). Another group used similar arrays for studying the expression and inclusion of the Parkinson's disease associated protein, α-synuclein (Fernandes et al. 2014, Rosa et al. 2012).

Differing slightly to the aforementioned studies, Rowat et al. (2009) developed trapping channels, termed lineage chambers, instead of single traps, as illustrated in Fig. 4(D). They mainly trapped single cells at the channel ends following a Poisson distribution. As a result, all of the daughter cells that budded off remained within the channel, aligned in single file behind the mother yeast cell. Thus, using a GFP-tagged heat-shock protein Hsp12, they showed how such nonessential elements fluctuated randomly, but synchronized between mothers and daughters, while on the other hand essential proteins such as RPS8b-GFP expression is comparably constant throughout the colony and over time. A similar design, having shorter, dead-end channels, was designed by Fehrmann et al. (2013). They monitored shorter lineages for tracking mitochondrial dynamics involved in rejuvenation and cell ageing.

Stratz et al. (2018) designed a multifunctional microdevice, which combines both single-cell studies and studies on cell culture level under defined conditions. Their sophisticated two-valve system facilitates the isolation of cells, featuring a trapping system based on two triangular pillars that point towards one another. By switching the valves, it is possible to define two states around the trapped cells, as illustrated in Fig. 5(A). When the outer valve is closed, the yeast cells remain in contact with the surrounding medium, allowing for diffusion-controlled nutrient supply, removal of cell excretes and protection from shear stress induced by flowing medium. Upon closing the inner valve, the cells are entirely cut off from the surrounding environment. As a proof-of-concept, the authors investigated intracellular NAD(P)H levels in *S. cerevisiae* single cells and its dependency on stress factors. Therefore, the enzyme diaphorase and the substrate resazurin were added to the buffer and the trapped single cells were lysed. The released NAD(P)H then

Downloaded from https://academic.oup.com/femsre/advance-article/doi/10.1093/femsre/fuac039/6674677 by guest on 05 October 2022

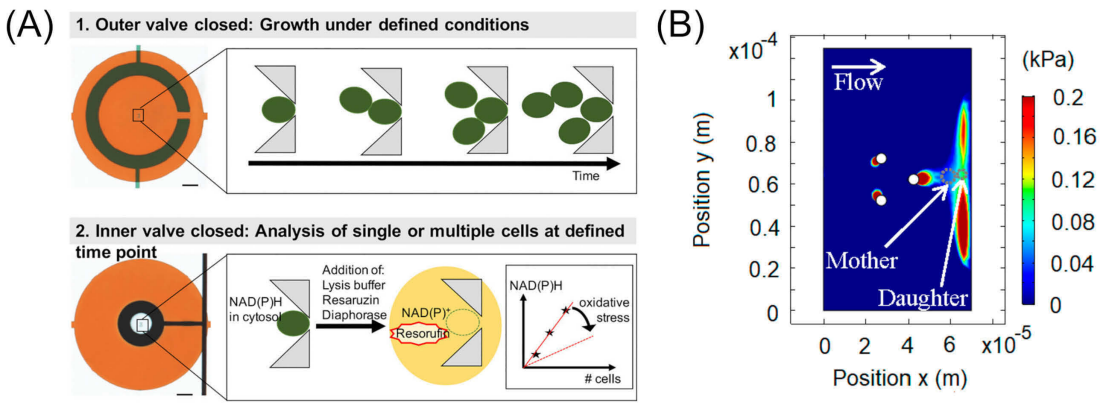


Figure 5. Single-cell trapping of yeast cells using on-chip valve and slipstream techniques. (A) The microfluidic trapping device allows a valve-controlled two mode operation, a dynamic growth study, as well as end point/time point analysis of lysed cells. Image reproduced with modifications from Stratz et al. (2018) with permission from John Wiley and Sons (Licence Number: 5271500367493). (B) A microdevice for contactless trapping utilizing the slipstream effect. Image reproduced with modifications from Duran et al. (2020) with permission from the Creative Commons Attribution license (www.creativecommons.org/licenses/by/4.0/).

functions to reduce resazurin to the pink-coloured and highly fluorescent resorufin. Due to the small analysis volume in the secluded cell chambers, dilution effects are strongly minimized, which enables very precise measurements of metabolites ranging down to attomoles. It was found that the NAD(P)H levels in yeast mother cells are mostly unaffected by a stress treatment with hydrogen peroxide, although this varied strongly from cell to cell. With these precise investigations, it was shown that this platform is well-suited for further bioanalyte studies on-chip.

The main aspect concerning each of the previously explained trapping systems relates to the physical nature of the method. It was commonly assumed that the mechanical contact with the traps had no or negligible impact on the cells (Wu et al. 2004). Duran et al. (2020), however, reinvestigated the matter and found a pressure dependent deformation of the cells in the range of a few submicrons, as well as a slight decrease in expression levels of a representative constitutive gene at the usual pressures exerted on the cells in physical traps. This suggests that trapping systems that involve physically 'grabbing' the cells may have an impact on the yeast cells, possibly altering outcomes of the investigations. Hence, the 'Mother Machine' device developed by the group omits any physical wall contact with the individually trapped yeast cells by exploiting the so-called slipstream effect (Fig. 5B). This sophisticated, yet simple, design is based on an array consisting of groups of three micropillars, which creates a disturbance in the flow, i.e. by inducing a pressure hole behind the pillars equivalent to the size of a yeast mother cell. While these are tightly entrapped, budding daughter cells are simply washed away. Importantly, the exerted pressure on the yeast mother cells in this wall-free environment is on the order of a few hundred pascals, as opposed to hundreds of kilopascals in the conventional devices, yet maintains a sufficiently firm grip around the cells.

Most of the above-described methods are immensely beneficial and impactful, however, tend to be quite elaborate and technically challenging, often requiring both specific expertise as well as very specific and often expensive equipment. In order to make these techniques accessible for a broader range of scientists and institutes, Cabrera et al. (2017) set out to create an easy-to-use device, which combines a simple, commercially available microfluidic device with a genetic tool to repress the formation of daughter cells. Chen et al. (2019) identified imaging as the most problematic and inaccessible aspect of these studies. Therefore, they designed simplistic and affordable hard- and software add-ons for automated microscopy of microfluidic single-cell study devices, by modifying existing imaging equipment.

Cell separation techniques

As yeast cultures commonly consist of not just single cells, but also budded doublets and clusters, trapping of single mother cells for the described studies is not a trivial task. Hence, automated or even integrated microfluidic devices to facilitate separation procedures are highly desirable. Cell collection and separation is a common and important task in many biological applications, e.g. for the removal of pathogens (see also the 'Fungi-on-a-Chip technologies for medical applications' section), as an experimental preparation step or to select certain high-performing entities from low-performing ones. Harnessing the benefits of microfluidics, numerous methods have been developed and applied with fungal spores (Park et al. 2019, Wang et al. 2020) as well as other nonfungal cell types, such as cancer cells or bacteria (Lee et al. 2013, Tang et al. 2019, Xiang et al. 2019, Yan et al. 2017). The yeast-focussed platform by Liu et al. (2021), which uses the viscoelastic liquid polyethylene oxide (PEO) as a sheath fluid to separate different shapes of *S. cerevisiae*, is another example of such a technique. By injecting a stream of PEO into the cell suspension and pumping through a rectangular microchannel, both elastic and inertial lift forces are exerted onto the yeast cells. This enables a separation into singlets, budded doublets, and clusters, based on shape and size. While doublets were still found in all of the outlets, it was possible to remove all clusters from the singlet fraction, as well as enrich the proportion of clusters through a different outlet by a factor of two. In this study, which was purely focussed on developing a separation device for *S. cerevisiae*, the effects of channel dimensions, polymer concentration, and flow rates of both sample flow and sheath flow on the separation success were analyzed. By conducting the SYTO 9 and EthD-III cell viability tests, harmful stress on the cells caused by the separation could be ruled out. The final, optimized microdevice opens new avenues for research or practical applications in industry or medicine, where only one or two of the different shape-types of *S. cerevisiae* is the desired subject.

Downloaded from https://academic.oup.com/femsre/advance-article/doi/10.1093/femsre/fuac039/6674677 by guest on 05 October 2022

Droplet-based microfluidics for applications in yeast biotechnology

Another very important trait of the universal model organism and working horse, *S. cerevisiae*, as well as other yeasts, is their capability to be easily recombinantly modified, either for fundamental research or for biotechnological applications. Already a yeast's natural capacity to produce bulk chemicals, like ethanol (Basso et al. 2011), isopropanol (Nandy and Srivastava 2018), or citric acid (Cavallo et al. 2017) as well as enzymes (Bussamara et al. 2010, Zaky et al. 2014) and pharmaceuticals (Walsh 2014) is huge. Facing the ongoing irreversible global deprivation of fossil resources, mainly oil and coal, as a source for basic chemicals, the responsibility of the biotechnology industry to provide these resources in the future will continue to grow. With similar severity, medicine has been confronted with a constant increase in antibiotic resistance. In the last decades, this process was further accelerated by industrial livestock farming with its mass use of antibiotics. Therefore, high through-put screening (HTS) for new yeast strains producing new substances, with higher yield is essential. Microfluidic platforms have proven to be an ideal tool for this, especially droplet-based methods (Box 2, Fig. 6), where thousands of parallel reaction vessels can be generated. So far, while being an extremely young field for yeasts, it has already been successfully applied to other organisms, such as mammalian cells, bacteria, or whole microbiota (Balasubramanian et al. 2021, Brouzes et al. 2009, Trivedi et al. 2010, Tu et al. 2021, Watterson et al. 2020).

Box 2. Droplet-based microfluidics

Droplet-based (or segmented flow-based) microfluidic technologies form a major subdiscipline within the field of microfluidics (Griffiths and Tawfik 2003, Tawfik and Griffiths 1998). Typically, two immiscible fluids are dispensed into a microchannel employing either the T-junction or flow focussing technique, resulting in the formation of microdroplets contained within the carrier liquid, as illustrated in Fig. 6(A) and (B). Commonly used carrier fluids include perfluorinated alkanes, such as perfluoromethyldecaline. The secondary phase is usually an aqueous solution or suspension, which can also be a solidified hydrogel. Aqueous droplets dispersed in an oil carrier fluid are known as 'water-in-oil' microdroplets; conversely, oil droplets dispersed in an aqueous carrier fluid are known as 'oil-in-water' microdroplets. If generating 'water-in-oil' microdroplets, for example, a hydrophobic channel material will aid droplet formation. Indeed, hundreds to thousands of separate reaction or incubation vessels can be created per second, depending on the degree of parallelization within the device (Baret 2012). With a static incubation, mixing within the droplet only occurs through diffusion. An improved mixing can be achieved through chaotic advection, instigated by incorporating meandering microchannels with narrow loops into the device design. The oscillating shear stress invokes a turbulent flow within the droplets, leading to thorough mixing within milliseconds (Bringer et al. 2004).

The carrier liquid, into which the microdroplets are dispersed, prevents cross-contamination. It also typically contains a surfactant that sits at the oil–water interface to stabilize droplet formation. This is especially important if the droplets are kept in a loose and random array, without physical interspacing, after initial droplet generation (emulsion-based microfluidics; Bauer et al. 2010, Bremond and Bibette 2012). Such amphiphilic additives, however, might intervene with the chemical reaction studied or can be toxic to some organisms, though biocompatible surfactants are being developed (Baret 2012, Wagner et al. 2016). The microfluidic droplet 'toolbox' allows various microdroplet unit operations to be performed, including droplet merging, splitting, and synchronization, as well as targeted injection of material into existing droplets (dosing; Berry et al. 2019, Köhler and Cahill 2013, Pekin et al. 2011) and integrated fluorescence-activated droplet sorting (FADS; Fig. 6C; Baret et al. 2009). Overall, droplet-based microfluidics afford significantly increased experimental throughputs and reduced reagent consumption compared to conventional methods, as well as automated pipetting robots. Moreover, high throughput experimentation leads to increased precision of the measurement with more datapoints collected (Miller et al. 2012).

A droplet-based microfluidic approach was employed by Hosokawa et al. (2015) for screening a metagenomic library for microbial enzymes. They extracted a fosmid library (Kim et al. 1992) from a soil microbe population and transfected the F-plasmids into *E. coli* and *S. cerevisiae*. With their microfluidic droplet generator, they encapsulated the transfected cells plus fluorescein dicaprylate as a fluorogenic lipolysis reporter into ~100 pl droplets. The droplets were stabilized with a surfactant and subsequently solidified with agarose to further improve droplet stability and thus segregation of the microenvironments. When a lipolytic enzyme is expressed within the capsule, the hydrolysis of fluorescein dicaprylate is catalysed and thus triggers the generation of a fluorescence signal. Fluorescent gel microdroplets were then sorted using fluorescence-activated cell sorting (FACS), isolated on plate and eventually characterized as well as sequenced. Using this method, they were able to screen 67 000 clones in 24 h with an overall reagent consumption of less than 10 μl. As a result, the esterase EstT1 was discovered and isolated. Later, the group used the platform to screen for ligands against G-protein coupled receptors (GPCRs), which are involved in many pathogenic signalling pathways of various diseases, for drug discovery. Resulting from their screening cycle, they discovered new functional ligands, occasionally with even higher activity than exendin-4 (Ex4), a well-known ligand. As a future improvement for the screening system, they proposed running several subsequential cycles to enhance overall resolution, e.g. by excluding nonspecific yeast cells from droplets with more than one cell (Yaginuma et al. 2019).

A further addition to the enormous portfolio of applications for this immensely beneficial high-throughput screening technology was made by Wang et al. (2019), with their droplet-based study on RNA interference processes. The improvement of protein secretion of an organism with RNA interference is, despite appearing counterintuitive or even paradoxical at first, a feasible technique. However, it has been impossible to employ this method in a targeted and planned manner to date, due to a deep lack of understanding regarding the intracellular mechanisms taking place at all stages of the process, i.e. synthesis, post-translational modifications, and secretion of the protein, involving transcriptional factors, promoters or inhibitors, protein transporters, and beyond. Therefore, an immensely high-throughput method is needed to screen randomized libraries for expression-enhancing RNAi candidates, which in turn would further accelerate the elucidation of functional mechanisms underlying this phenomenon. The group used a similar set up as featured in the above discussed studies, with an integrated FADS for sorting (Fig. 6C). In their proof-of-concept model system, they used α-amylase expressed in *S. cerevisiae*, combined with boron–dipyrromethene–starch as a fluorogenic substrate. Using this set up, they managed to narrow down the initial 1 million cells to a sample of 340 cells with potentially enhanced amylase production, in only three subsequential cycles, with ~7 h for each

Downloaded from https://academic.oup.com/femsre/advance-article/doi/10.1093/femsre/fuac039/6674677 by guest on 05 October 2022

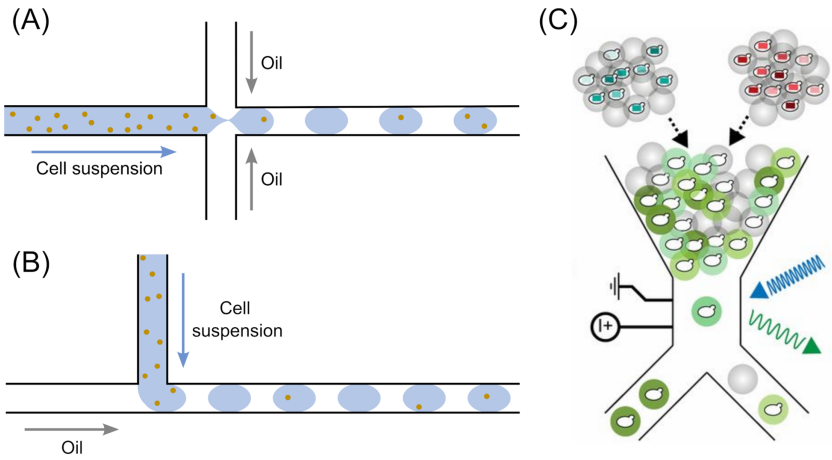


Figure 6. Droplet-based microfluidic methods. Schematics illustrating droplet generation using (A) flow focussing or (B) T-junction techniques. (C) Image showing the principle of fluorescence-activated droplet sorting as described in Wang et al. (2019), which was used to sort yeast genotypes with high amylase activity from a randomized library. Image reproduced with modifications from Wang et al. (2019) with permission from the National Academy of Sciences.

in-droplet assay cycle. Thus, the number of potential candidates was reduced to a sensible degree for further, more detailed and elaborate analyses. As a result, several novel amylases with a maximal improvement of 2.2-fold were recombined. Furthermore, it was found that genes associated with various cellular processes, such as metabolism, protein modification, or degradation and cell cycle, are involved in the modification of protein production. Moreover, they proved the applicability of their system to further studies on RNAi protein secretion modifications and mechanisms.

Another technique that immensely benefits from the droplet-based microfluidics approach is the so-called isogenic colony sequencing (ICO-seq). The problem with using mRNA for sequencing, is that mRNA concentrations are inherently very low. By encapsulating single cells from a randomized library into hydrogel droplets, the cells grow into isogenic colonies, thus automatically amplifying the mRNA for subsequent deep screening. Because the RNA stems from only one initial cell, a direct correlation between genotype and phenotype can be drawn. Liu et al. (2019) applied this technique to perform a heterogeneity analysis of a *S. cerevisiae* ARO4 mutagenesis library, as well as to analyze the underlying mechanisms for switching between white and opaque cells in *C. albicans*.

Besides these two yeasts, droplet-based microfluidics has also been employed with *Yarrowia lipolytica* (Beneyton and Rossignol 2021). This dimorphic yeast has enormous potential for the production of heterologous proteins combined with a high secretion power and has very recently become subject of further microfluidic investigation with an interest for biotechnological applications in the fields of biofuels and bioremediation (Lesage et al. 2021).

Not only yeasts, but fungi in general, due to their role as decomposers in nature, have an enormous repertoire of exudates and metabolites, including numerous enzymes and small molecules, useful for biotechnological applications. Thus, extending microfluidic high-throughput screening onto a wider range of fungi, in particular filamentous fungi, is highly desirable. So far, filamentous fungi featured in microfluidic HTS studies have been *Aspergillus nidulans* (Beneyton et al. 2016) and *Trichoderma reesei* (He et al. 2019), leaving much potential yet for applications in the future.

Fungi-on-a-Chip technologies for medical applications

Another important aspect of many fungi is their pathogenicity. One of the most common causes of nosocomial disease is the fungus *C. albicans*. In its yeast form, dimorphic *C. albicans* becomes quickly disseminated. Once in the body, however, it switches to its filamentous form and is, thus, able to penetrate host tissue and cells. Alongside other *Candida* species, the opportunistic pathogen is known for causing candidiasis in immunocompromised patients, an illness, which once acquired, proves fatal in about 40%–60% of the cases (Uppuluri et al. 2017). Even though the severity of this fungal threat has been known for decades, the frequency of cases is not expected to diminish in the future (Pfaller and Castanheira 2016). With all of these fungal diseases, the most crucial aspect is the time to diagnosis (and treatment), often a key factor determining the life or death of the patient. It has been approximated that antifungal intervention should be started no later than 6 h after the onset of symptoms for an effective treatment with the highest chances of a full recovery and fewest complications (Fuchs et al. 2019).

Conventional methods for diagnostics are slow and usually comprise initial blood and plate culture, followed by polymerase chain reaction (PCR) analyses. Therefore, new and much faster techniques for detecting, and possibly even removing, bloodborne pathogens from the patient's blood need to be developed. Faster identification of the prevalent pathogen would further prevent inappropriate initial antifungal treatment, which in turn again harms the patient and facilitates the development of drug-resistance (Morrell et al. 2005, Zhang et al. 2020). Besides this direct clinical relevance, *C. albicans* is also a well-known model organism for studies of fungal biology. Microfluidic technology allows for rapid and precise processing and detection on the microscale. Furthermore, laminar flow profiles can be exploited to allow membrane-free dialysis systems to be designed. These attributes are desirable for the development of diagnostic and therapeutic devices for those diseases involving microbes.

Downloaded from https://academic.oup.com/femsre/advance-article/doi/10.1093/femsre/fuac039/6674677 by guest on 05 October 2022

Microfluidic techniques for filtering pathogens from blood

In an attempt to develop a clinical blood filtration device to tackle candidiasis, Yung et al. (2009) employed a microfabricated high-gradient magnetic field concentrator (HGMC) for *E. coli* (Xia et al. 2006) as a prototype for redevelopment as a microfluidic platform for *C. albicans*. The basic idea involved coating superparamagnetic microbeads with pathogen specific antibodies. The bead suspension was then pumped parallel to the blood sample through a microfluidic separation channel, similar to a dialysis machine, but without the need for a physical membrane (i.e. as the device operates under a laminar flow regime). At the interface, the magnetic opsonins then pair with the pathogen and can be extracted from the blood, as illustrated in Fig. 7(A). By optimizing the channel design and arrangement, as well as using a tuneable electromagnet, they were able to optimize the device's efficiency to achieve a cleansing rate of 80% in human whole blood using a volumetric flow rate of 20 ml/h. While both rates would not be sufficient to treat a patient, therapeutically relevant standards can be achieved by combining several devices in multiplexed arrays, thus enhancing the total throughput and final cleansing rate.

To further develop a label free alternative, Hou et al. (2012) utilized the naturally occurring microcirculatory phenomenon of blood cell margination, thus avoiding the need for magnetic beads. In microtubes (e.g. blood vessels), red blood cells tend to migrate towards the centre of the channel due to their shape and deformability, while other particles (e.g. white blood cells, platelets, and bacteria) tend to be pushed towards the channel walls. A sudden expansion of the channel then allows bacteria, as well as inflammatory cellular components (e.g. platelets and leukocytes), to be extracted through side outlets, as illustrated in Fig. 7(B). In a two-stage design, this step is repeated, resulting in a cleansing rate in whole blood of 90% for *S. cerevisiae* (model organisms simulating pathogenic fungal cells such as *C. albicans*) and > 80% for sepsis-related blood components. Using this filtering principle, a simple and continuous dialysis setup was manufactured, which does not require any sample preparation and enables the return of the filtered blood back to the patient. The only drawback is the relatively low throughput of 1 ml/h, compared to the microbead-based methods, which again could possibly be enhanced by numbering-up.

Again, utilizing the magnetic particle principle, Kang et al. (2014) put emphasis on improving the used opsonin-bead entity. By engineering a mannose-binding lectin (MBL) complex bound to the human immunoglobin IgG1 Fc, which functions as a linker to the superparamagnetic nanobeads, they were able to significantly broaden the range of targeted pathogens. As part of the innate immune system, MBL detects and binds certain carbohydrate structures exhibited on the surface of human pathogens, i.e. fungi, bacteria, viruses, as well as protozoa (Tomaiuolo et al. 2012). Harnessing this ability is highly beneficial to tackle unspecific sepsis without needing to identify the pathogen first, thus saving time crucial for the survival of the patient. Further, this allows to fight infections with common nosocomial pathogens, such as MRSA, which are unresponsive to conventional treatments. In terms of channel design, the authors mimicked the vascular channel design of the venous sinusoids of a human spleen, hence the device's name 'biospleen'. A total of two microchannels, interspaced by rectangular slits, allow filtration with different flow velocities in the channels, even with stop-flow regimes, meaning that one fluid rests while another one is streaming past it. Another important aspect they improved concerns the extraction of the opsonin particles from the blood sample. Due to the bead diameter of 128 nm, their magnetic moment is relatively small, resulting in a removal efficiency of only 80%. By adding larger, uncoated 1 μm diameter beads, the local magnetic fields were enhanced, resulting in the smaller opsonin beads being dragged along and, therefore, enhancing the removal rate to > 99%.

While these devices are very well-suited to the removal of unspecific pathogens from blood, it is unfit for microscopical detection and diagnosis of the pathogen. Therefore, the design was refined by Cooper et al. (2014) to incorporate an array of microwells in the channel ceiling, having a diameter of 50 μm and a height of 20 μm, together with a ferromagnetic flux concentrator between the magnet and the channel to create a uniform magnetic gradient along the channel. Thus, they were able to capture pathogen-bead conjugates in an evenly distributed manner to facilitate imaging, without the beads obstructing one another. Using this set-up, approximately 70% of the initially seeded, fluorescently labelled *C. albicans* were detected, both in saline and whole blood (operated using a volumetric flow rate of 10 ml/h). That translates to a sensitivity of one fungal cell per ml in less than 3 h. The ability to concentrate diluted pathogens from blood samples and subsequently remove them from the channel is predicted to accelerate culture-based antibiotic susceptibility tests by a further 24 h, again crucial for a successful treatment of sepsis.

This represents a clear improvement compared to the device developed by Javanmard et al. (2012), where only 6.7% of the introduced *C. albicans* could be detected. Their channels are coated with anti-*C. albicans* antibodies, where the capturing mechanism is purely coincidental and relies solely on diffusion. The previously described set-ups utilize magnetic nanobeads to actively 'forage' for the pathogens. A similar microfluidic immunoassay was later developed by Asghar et al. (2019) to detect *C. albicans* from whole and lysed blood. In comparison, they achieved capture efficiencies of between 60% and 80% in run-times of less than 2 h.

Another attempt to circumvent the use of magnetic beads was conducted by Fuchs et al. (2019). Since the opsonin beads needed to be applied with a 1000-fold excess, eliminating these from the filtration principle would reduce costs significantly. Moreover, they designed a device, i.e. fully independent from any kind of labelling, called the Inertial Fungal Focuser (IFF; Fig. 7C). Their separation method relies on the phenomenon of inertial focussing. Due to the channel dimensions and parabolic flow profile, a wall force, directed away from the channel wall, and a shear force, directed towards the channel wall, are exerted on particles carried within the streaming fluid. The opposing effects result in an equilibrium position of the particle, which is strongly dependent on size and shape of the entity. A third force, called the Dean force, was introduced by incorporating a curved section into the channel design to improve the equilibration and specificity of the particle separation. With a recovery rate of 8.4% for different *Candida* spp. from lysed blood, they were able to trump the rate achieved by Javanmard et al. (2012) slightly, although still lagging significantly behind the aforementioned bead-based principles. Since the inertial flow effects are strongly dependent upon the viscosity of the liquid, these methods struggle in their handling of full blood samples, resulting in a relatively low filtration fidelity, even with lysed blood. Hence, the IFF device is not fit for blood cleansing tasks, however, it is applicable to concentrate and isolate fungal pathogens from blood, without the need for elaborate preparation steps. Thus, enough fungal material can be acquired within only 125 min using a volumetric flow rate of 24 ml/h to perform subsequent analyses downstream, such as PCR. Conventional

Downloaded from https://academic.oup.com/femsre/advance-article/doi/10.1093/femsre/fuac039/6674677 by guest on 05 October 2022

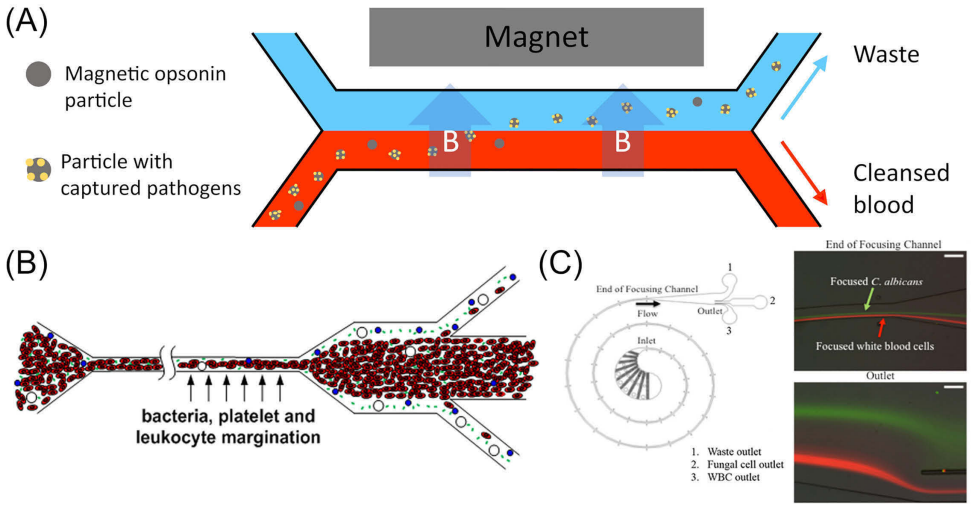


Figure 7. Microfluidic devices for blood cleansing tasks. (A) A dialysis-like microfluidic device employed to filter fungal pathogens from blood via magnetic opsonins beads specific to the targeted pathogen. The particles with the attached pathogen are then extracted from the blood into an aqueous parallel waste collection stream using a magnet. The illustration is based on Yung et al. (2009). (B) Microdevice used to filter pathogens from blood relying on margination. As observed in blood vessels, red blood cells tend to migrate to the channel centre resulting in other blood components such as platelets or microbes being pushed towards the channel walls. Subsequently, they can be removed by a sudden widening of the microchannel. Image reproduced with modifications from Hou et al. (2012) with permission from AIP Publishing (Licence Number: 5271501114499). (C) A device, termed the Inertial Fungal Focuser (IFF), used to remove fungal pathogens from blood via inertial focussing. Image reproduced with modifications from Fuchs et al. (2019) with permission from the Creative Commons Attribution license (www.creativecommons.org/licenses/by/4.0/). Scale bars represent ca. 100 μm.

methods, in contrast, take up to 5 days (plate-based) or 12–48 h (automated method), respectively. As well as enhancing the detection speed, the IFF significantly decreased the lower concentration limit for detection, with only 1600 cells/ml used in the experiment.

Besides these methods, another technique applied to sort cells using microfluidic set ups involves the use of electrodes. Such an approach was used by Cheng et al. (2007) to remove *C. albicans* from mixed cell cultures.

Very recently, many of the hitherto featured microfluidic disciplines and techniques were finally integrated into an automated diagnostics system, which was already launched in the field of medicine. The ePlex digital microfluidics platform by GenMark Dx combines on-chip PCR and DNA-hybridization-based probing with electrowetting (Choi et al. 2012) as the means to control the sample transportation and processing to detect fungal pathogens from whole blood samples (GenMark Dx 2021). Zhang et al. (2020) conducted a large-scale clinical evaluation of the system with real-live samples from several clinics as well as contrived samples containing clinically relevant fungal pathogens like *Candida* spp., *Cryptococcus* spp., *Fusarium* spp., as well as *Rhodotorula* spp. and compared the sensitivity, specificity, and overall performance with conventional and established methods such as bidirectional PCR, peptide nucleic acid fluorescence *in situ* hybridization (PNA-FISH), and matrix-assisted laser desorption ionization-time of flight mass spectrometry (MALDI-TOF MS). Strikingly, they found that neither the sensitivity nor specificity ever fell below 96% for any of the 15 species tested. In some samples, the automated platform was even able to detect pathogens, which were missed with the standard procedure. The time needed for a single run, which can be conducted with several samples in parallel, is approximately 100 min and, thus much faster than the above-mentioned conventional methods.

Microfluidic drug-screening methods

After diagnosis and identification of the pathogen, targeted drug-treatment needs to be deployed. Here too, microfluidic technologies can be highly beneficial for the development of antifungal drugs. With an enormous throughput and significantly reduced reagent consumption, microfluidic approaches, such as droplet-based microdroplet technologies (as discussed previously in the 'Droplet-based microfluidics for applications in yeast biotechnology' section) can also be used for testing the efficiency of drugs against fungi. In a first proof-of-concept study using this approach, Zheng et al. (2017) screened four antifungal drugs (5-fluorocytosine, amphotericin B, terbinafine, and caspofungin) against *C. albicans*. Their examination, performed using the microfluidic device and Alma blue as fluorescent dye, took only 2 h and was found to be in good agreement with the microwell plate-based result. Using a similar, but microscopy-assisted approach, Qiang et al. (2019) developed a platform that combined rapid throughput techniques with precise imaging. Thus, they reported an 18-fold reduction in the time needed to screen drug libraries, compared to conventional well-plate methods, with 50 520 drugs screened in only 1 week. Moreover, their analysis technique was even more precise; as the fungal cells are aligned one after another in their respective microchannels, the fluorescently labelled cells can be counted and checked for vitality directly, while conventional methods rely on indirect photometric analysis. Additionally, the volumina of the tested substances required are 100 times lower using the microfluidic chip, thus saving money and resources.

Microfluidic approaches for the development of antifungal strategies

Another way to fight these types of diseases is to prevent infection altogether. Understanding infection mechanisms and pathways aids the development of novel antifungal strategies. Again,

Downloaded from https://academic.oup.com/femsre/advance-article/doi/10.1093/femsre/fuac039/6674677 by guest on 05 October 2022

microfluidic platforms offer a great potential for studies on these processes mainly taking place on the microscale.

Exemplary to that, Richter et al. (2007) set out to investigate *C. albicans* and *Pichia pastoris* biofilms, a key factor in the spread of nosocomial fungemia. Therefore, they developed a microfluidic platform with integrated dielectric microsensors. This set up allows for a contact-less measurement of biofilms and morphological changes triggered by external stimuli in real-time. Both the effects of mechanical shear stress as well as the drug response against the antifungal agent Amphotericin B was, thus monitored and revealed significant changes in growth dynamics. The fungicide caused a stress-induced arrest of replication, while on the other hand repair mechanisms were up-regulated.

Similarly, Reinmets et al. (2019) used microchannels fabricated from either PDMS (usually hydrophobic) or glass (hydrophilic) substrates to investigate cell-surface as well as cell–cell adhesion in yeasts, key elements in biofilm formation (see Fig. 8A). Using the model organism *S. cerevisiae* it was found that the adhesive strength is highly dependent upon the genetic background of the fungi and differs significantly between strains. Beyond the medical implications, they further propose that this technology is able to aid studies in protein engineering, where adhesive forces of engineered yeast cells displaying surface proteins can be translated into affinity measurements. From a more practical angle, exploitation of this phenomenon also offers the opportunity to develop novel tools for cell separation based on different adhesive forces.

The dispersion of fungi from established biofilms marks the next step in the infection pathway. Li et al. (2020) approached this topic, introducing and utilizing a very new methodology in the field of microfluidics. Opposed to the traditional closed-channel microfluidics, the new open-channel designs only feature three solid enclosing sides, while one side is either open entirely or covered with a fluid, e.g. oil. This brings several advantages, such as free physical access to the microchannel, with the oil phase reducing evaporation and contamination. A schematic of their open-channel device design is displayed in Fig. 8(B).

Another important aspect of the infection pathway is the germination of fungal spores. Suppressing this would stop the infection at the very first instance, thus clearing the pathogen before it has the chance to start any metabolic activity at the expense of its host, thereby minimizing harm to the patient. A full understanding of the mechanisms underlying spore germination would, therefore, significantly benefit antifungal medication. To precisely study these cellular processes, Barkal et al. (2016) designed a microfluidic device for high resolution germination assays with *C. neoformans*. Amongst others, they were able to demonstrate that common clinical fungicides do not inhibit spore germination, showing that in order to intervene at the germination stage, new methods need to be developed and established (reviewed in Bernier et al. (2022)).

Lung-on-a-Chip

Some fungal pathogens target a specific organ rather than causing systemic infections. Especially for delicate organs like the lung, *ex vivo* models are useful to study the processes involved in the disease. Organ-on-a-Chip microfluidic technologies (Box 3), a subdiscipline within the field of microfluidics, have emerged in the last decades as a platform to replace animal and cell culture models in preclinical trials, thus making these trials more reliable and ethical (Beißner et al. 2016). Lung-on-a-Chip platforms have been used to investigate lung-related diseases and injuries over the last 15 years (reviewed in Shrestha et al. (2020) and Bennet et al. (2021)). With such microfluidic set-ups, it is possible to reconstruct the 3D architecture of the lung on a cellular level as well as simulate flow conditions and breathing motion (Huh et al. 2007, Huh 2015). Furthermore, pathogen–tissue interactions can be mimicked and precisely analyzed (Huh et al. 2010).

Box 3. Organ-on-a-Chip

The emergence of Organ-on-a-Chip technology, which stemmed from a fusion of the fields of tissue engineering and microfluidics, has been anticipated animatedly by the wider community of biological and medical scientists. This promising new approach aims to reconstruct parts of organs or tissues *in vitro* to obtain functional model systems, mimicking reality as closely as possible. Organ-on-a-Chip platforms combine 3D-cell cultures, grown with the aid of scaffolds, with fluid channel networks, e.g. simulating vascularization. Important for such a task is to understand the key physiological aspects, namely the parenchymal tissue function, tissue barrier properties, and interactions, e.g. endothelial-blood stream, epithelial-lumen, as well as the interplay with other organs (Zhang et al. 2018b). Organ models are of the utmost significance for drug discovery, both from an ethical and economical viewpoint, as they reduce the need for animal tests. From a medical standpoint, it is desirable to use human organ models for drug testing since results obtained with conventional 2D human cell cultures or animal models have a limited transferability onto the human anatomy and physiology. So far, this highly interdisciplinary methodology has been applied to model nearly all existing organs or tissues of the human body, such as the liver (Yoon No et al. 2015), kidney (Ashammakhi et al. 2018), and brain (Bang et al. 2019).

Recently, this methodology has been applied to the study of fungal respiratory diseases, using the human fungal pathogen *A. fumigatus* as a model organism (Paolicelli et al. 2019). Barkal et al. (2017) developed a microfluidic model of the human bronchiole, including the vascular and airway compartments as well as the extracellular matrix (Fig. 9). They then studied the inflammatory response caused by *A. fumigatus* infection and later a tripartite interaction, including a volatile contact with *Pseudomonas aeruginosa*. In the tripartite system, the inflammation-related cytokine secretion was significantly elevated, compared to both the dual interactions, however, showed significant variations with regards to cytokine type. Further, it was possible to monitor leukocyte distribution in response to the infection. The detection of this complex multikingdom aspect of the infection was only made possible due to the development of a sophisticated and accessible platform, such as the presented device. Bacteria and fungi were physically separated, hence communication could only occur through volatiles diffusing through a collagen–fibrinogen gel matrix, just like in the real bronchiole. As a future improvement and extension of their platform, they suggest implementing an appliance to introduce airborne pathogens into the system, to better mimic the main real-life infection pathway, which would facilitate studies concerning the early stages of the disease.

Investigations on filamentous fungi at the cellular level

In fungal infections with *C. albicans*, for instance, another stage in the infection cycle concerns the dissemination of the pathogen within the body. In the case of several *Candida* spp. this takes place in the filamentous form, with hyphae searching for susceptible cells and actively penetrating their membrane. To understand

Downloaded from https://academic.oup.com/femsre/advance-article/doi/10.1093/femsre/fuac039/6674677 by guest on 05 October 2022

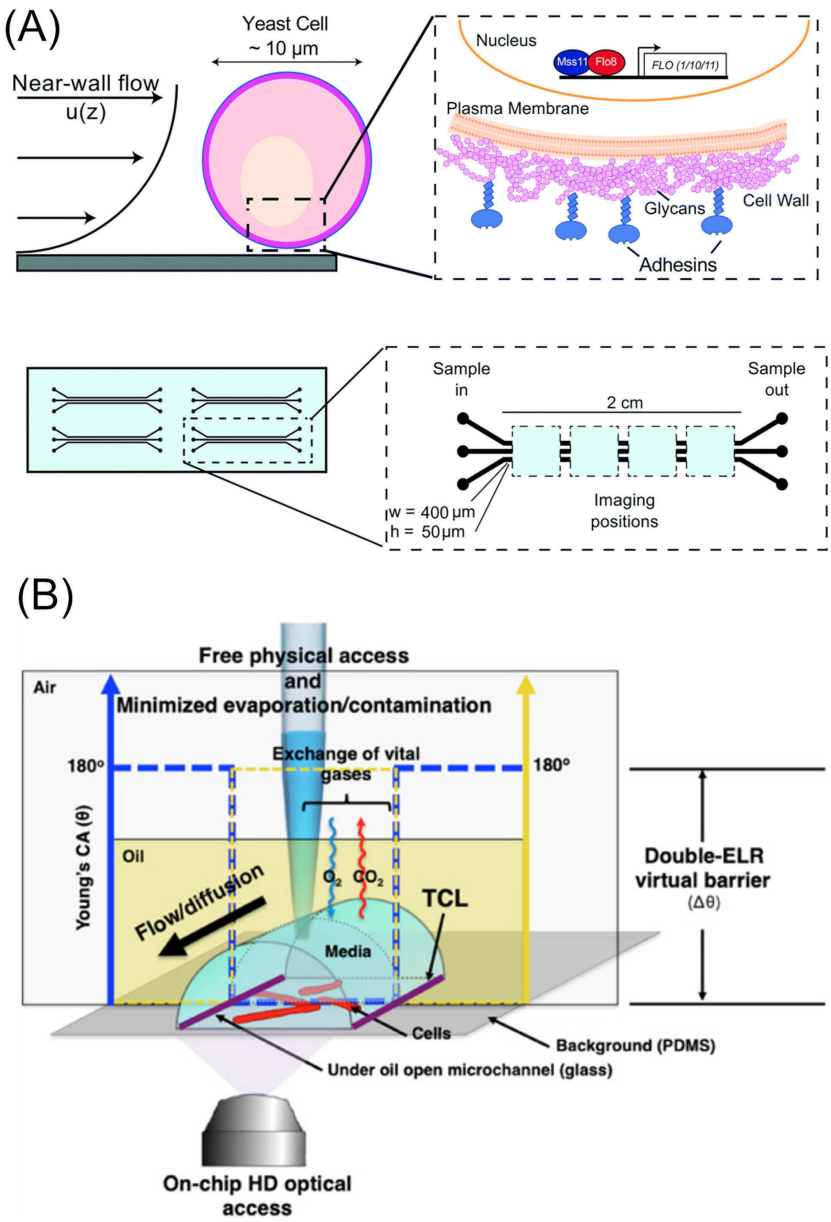


Figure 8. Microfluidic devices to study preinfection aspects of fungal pathogens. (A) Microdevice used to analyze surface adhesion of pathogenic yeasts under different shear-stress conditions. Shown are the principles of cell adhesion in yeasts, involving adhesin proteins under sheer stress (top) and the device design featuring arrays of parallel microchambers (bottom). (B) Under-oil microfluidic device for studying pathogenic fungal biofilm dynamics. The three-phase system consists of the PDMS substrate with micropatterned glass channels, an oil layer covering the channels and the aqueous medium or cell suspension, which is commonly injected into the oil phase. Images reproduced with modifications from Li et al. (2020) and Reinmets et al. (2019), respectively, with permission from the Creative Commons Attribution license (www.creativecommons.org/licenses/by/4.0/).

various aspects regarding the filamentous form of fungi, microfluidic techniques again provide a useful tool, where the possibility to design precise microstructures using established lithography techniques can be exploited to mimic naturally occurring habitats, not only for pathogenic fungi, but also soil or other filamentous fungi. This facilitates studies, which would otherwise simply not be possible. Creating artificial microenvironments to study fungal behaviour at different scales, from the hyphal to the cellular and even subcellular level should bring insights into biological processes and interactions that would otherwise take place within a 'black-box', i.e. within masked soil or organic tissue environments. As well as the physical elasticity of materials like PDMS, which can be exploited for force measurements, microfluidic device design can be specifically adapted to improve imaging, e.g. by guiding hyphal growth in a spiral, thus keeping the fungus in the focus area (Lee et al. 2016). A broad overview concerning microfabricated formats and their beneficial use for fungal research, with a focus on hyphal responses to microfabricated structures, can be found in a short review by Bedekovic and Brand (2021).

Space searching and foraging strategies

Nicolau and colleagues have dedicated intensive research efforts to uncover hyphal behaviours of different filamentous fungi. Specifically, they created microchips containing different obstacles and maze structures to mimic certain aspects of the fungus' natural environment at both the cellular (Held et al. 2009a,b,c,

Downloaded from https://academic.oup.com/femsre/advance-article/doi/10.1093/femsre/fuac039/6674677 by guest on 05 October 2022

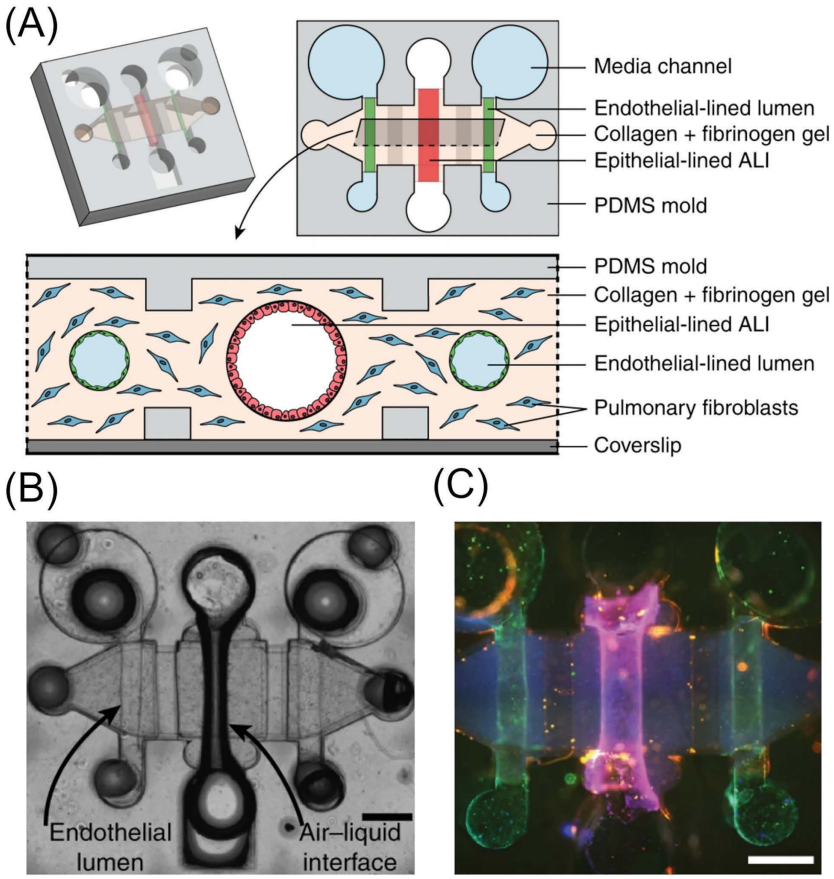


Figure 9. Lung-on-a-Chip device for studying fungal lung infections. (A) Schematic illustrating a microfluidic device used to mimic the human bronchiole. (B) Microscopy image of the experimental set up. (C) Channels coated with cells stained with Hoechst (blue, nuclear stain), anti-CD31 antibody (green, endothelial tight junction marker), and anti-EpCAM antibody (red, epithelial cell–cell adhesion maker). Scale bars are 500 μm. Images reproduced with modifications from Barkal et al. (2017) with permission from the Creative Commons Attribution license (www.creativecommons.org/licenses/by/4.0/).

2010a, 2011b) and subcellular level (Held et al. 2010b, 2019). These pioneering studies in the area have delivered new and important insights into both fungal life cycles and lifestyle.

When investigating the filamentous model fungus *N. crassa*, the authors found significant changes in its hyphal branching behaviour (e.g. frequency and angle). They observed an immediate onset and a lack of an adjustment period upon navigating through microfluidic network architectures (Held et al. 2010a). Interestingly, the hyphae were found to employ several strategies, depending on the type of obstacle they encountered. In general, *N. crassa* exhibited a directional memory, which was usually upheld after experiencing mechanically induced reformation events. Such events included 'hit and split' (i.e. the division of a mother hypha into two daughter hyphae) upon head-on collision with an obstacle, increased hyphal branching after passing through bottlenecks or active hyphal growth into openings through the ability to sense and identify these patterns (i.e. thigmotropism; Brand and Gow 2009, Held et al. 2011a). Occasionally, nestling was observed, meaning that the hyphae attached to the physical structure and were able to track it. This phenomenon was further studied by introducing micrometre-sized PS beads with epoxy-functionalized surfaces into the medium (Held et al. 2011b). By subjecting hyphae to different densities of the coated beads and comparing the results to the behaviour of the hyphae observed in their bead-free microfluidic systems, they found the attraction to be dependent upon the chemical property of the surface rather than being purely mechanically induced. They hypothesized an electrical attraction between the negatively charged bead surface and the positively polarized apex of the hypha, the latter due to a high concentration of calcium ions. With the generally less negatively charged and hydrophilic PDMS walls, this was not observed. This set up has great potential for further exploitation with other chemical moieties attached to the beads, or a direct functionalization of the microdevice channels, opening new avenues for the creation of more complex microenvironments. The involvement of cellular microtubules and the Spitzenkörper, the apical body present in many filamentous fungi, in hyphal space navigation and thigmotropism were later studied in more detail. According to their findings, the Spitzenkörper acts in a manner analogous to that of a gyroscope, which is stabilized by the microtubule scaffold; indeed, both structures are understood to be major players in directional memory. The microtubules are strictly aligned along the growth axis in the apical region, while less strict and rather randomly directed and distributed in the subapical regions. Furthermore, they discovered two distinct mechanisms related to hyphal space searching, specifically directional memory and obstacle-induced branching, with the former found to be the most effective and the latter implemented as a back-up strategy in *N. crassa* (Held et al. 2010b, 2019). Additionally, the acquired data on fungal space searching strategies was used to develop bioinspired computational algorithms to solve certain problems more efficiently. This could be beneficial for the design and programming of

Downloaded from https://academic.oup.com/femsre/advance-article/doi/10.1093/femsre/fuac039/6674677 by guest on 05 October 2022

nanosensors or nanomachines (Hanson et al. 2006, Nicolau et al. 2006, Asenova et al. 2016).

Inspired by these pioneering studies, several other researchers followed this path and designed new microfluidic chips for comparative studies with other fungi, such as *Armillaria mellea* (Held et al. 2009b), *Talaromyces helicus* (Baranger et al. 2020), and *Cladosporium macrocarpum* (Podwin et al. 2021), which revealed strong differences between species. These observed variations were then systematically correlated with their habitat, preferred foraging style, and overall growth behaviour. Fukuda et al. (2021) especially focussed on the effect of bottleneck-like structures (i.e. spatial confinements smaller than that of the hyphal diameter) upon hyphal growth (Fig. 10A). They found mainly two outcomes, based on which they grouped different fungal species. While fast growing fungi, such as *Rhizopus oryzae* or *N. crassa*, are forced to stop by the confinement or depolarize, meaning they bulge at the apex of the hypha and loose directional growth altogether, the hyphae of slower growing fungi, e.g. *A. nidulans* or *Fusarium oxysporum*, remain polarized and continue growing undisturbed after exiting the confinement. To explain this phenomenon, a correlation was drawn between the number of vesicles present in the hyphal cytoplasm, turgor pressure, and the ability to adapt to confined growth. A high number of vesicles and high intracellular pressure aids a fast growth with extensive branching; however, when entering a confinement, these attributes lead to an excess of vesicles and pressure, which eventually disrupts the directional memory (usually sustained by the Spitzenkörper) or results in complete growth arrest. On the other hand, slow growing fungi are well-equipped to manoeuvre through confined spaces. Which of these modes the fungi use, correlates with their overall growth and survival strategy.

A similar, but broader, categorization of filamentous fungi and their space searching capability was conducted by Aleklett et al. (2021), who took additional aspects into account. With their Obstacle Chip, which features a vast array of different parallel obstacle channels, they studied seven filamentous soil fungi based on their branching behaviour, growth velocity, foraging style, hyphal shape, and mycelial density. It was found that the fungi analyzed in their study can be categorized into two main groups: (i) the guerrilla strategists, developing few and short-lived, but long-reaching, fast growing hyphae and (ii) the phalanx strategists, forming dense, strong hyphal mats. This interspecies variation in growth pattern is, from an evolutionary and ecological standpoint, important for the exploration of all available niches within a biosphere/ecosystem. Similar findings were obtained by Hopke et al. (2021) in their crowdsourced study, aptly named the 'Fungus Olympics' (Fig. 10B). Here, some fungi were found to navigate faster through certain structures, while others trumped them in other 'disciplines', depending on their branching strategy. These studies have demonstrated how microfluidic technologies can help to unravel and investigate the behavioural patterns that these fungi exhibit in their natural environment, which are otherwise barely detectable. The most recent study in this field, conducted by Mafla-Endara et al. (2021), attempted to move even closer to the natural habitat by introducing abiotic and biotic factors into their microfluidic device. Besides physical obstacles, possessing different sizes and shapes, the Soil Chip contains real soil particles, water, and air, as well as fungi, bacteria, and protists. Thus, they projected the ecosystem soil environment, with numerous different niches, onto a small, imageable microfluidic platform (Fig. 10D). Amongst others, they were able to observe common events like soil particle relocation or accumulation, passage opening or obstruction, and thus habitat fragmentation, which are all processes that fungal hyphae are frequently involved in. Furthermore, they observed interactions between hyphae and other organisms, mainly bacteria. In line with previous discoveries and the novel concept of 'fungal highways' (Kohlmeier et al. 2005, Warmink et al. 2011), it was observed that bacteria strongly benefit from, or even rely upon, fungal hyphae to access and acquire nutrients, either by navigating through demanding soil structures, e.g. crossing air gaps, or assisting in the decomposition of organic or inorganic substances. The latter, however, also works *vice versa*, with fungi relying on bacterial enzyme activity for nutrient uptake (Jiang et al. 2021). Another important trait of filamentous fungi relates to their ability to transport and disperse water, together with soluble compounds, along their hyphae, an important aspect not only for bacteria, but the soil community as a whole (Mafla-Endara et al. 2021). The hyphal interactions discussed thus far have further been subject to more focussed studies of specific aspects of this complex ecological interplay. Specifically, compartmentalized microdevices can be used to investigate how fungi explore niches containing isolated substances. Baranger et al. (2021) studied how the soil fungus *T. helicus* forages for spatially isolated benzo[α]pyrene, an example of a polycyclic aromatic pollutant (Fig. 10C). Interestingly, they discovered that the fungus employed active mechanisms, involving the excretion of biosurfactants, to reach, decompose, and uptake this hydrophobic substance. These abilities could be exploited further as part of a bioremediation strategy, where the fungus would help to degrade lipophilic environmental toxins.

Hyphal tip force measurements

Hyphal tips can penetrate a range of host tissues, ranging from plant cells for symbiosis establishment (Parniske 2000), to insect cuticles (Gabriel 1968) and human cells in infectious disease (Fernandes et al. 2018). Even more impressive, hyphal tips can penetrate mineral substrata by digging into mineral grains or at the interface between grains (Landeweert et al. 2001). Microfluidic experimental systems enabling hyphal tip force measurements at the single-cell level are, therefore, evolving, with PDMS being the material of choice for these types of studies. Not only is PDMS permeable to gases, widely inert, biocompatible, transparent, and easily patterned using simple photolithography methods (Box 1), other exploitable aspects concern its elasticity (see also the 'Pressure-based active trapping in single-cell studies on yeasts' section) and ability to adjust the tensile strength of the polymer, simply by changing the ratio of PDMS base and curing agent. This, therefore, presents the opportunity to conduct tip force measurements without the need for expensive sensors. Just by imaging the deformation of a PDMS structure by a hyphal tip in a microfluidic device, the force can be calculated using the known Young's modulus for a mechanical deflection model (Ghanbari et al. 2012).

To further investigate infection mechanisms and pathogenicity in *C. albicans*, Thomson et al. (2015) utilized PDMS soft lithography to manufacture microdevices with several obstacles. The fungal hyphae had to navigate around these structures and were found to exhibit different behaviours. Furthermore, because of the known and adjustable tensile strength of PDMS, the force exerted by the hyphal tips could be calculated and analyzed. The measured forces of around 9 μN fall within the range of tensile strengths found in common cell walls and membranes. In agreement with studies from other groups, they hypothesized that the fungus executes two different modes of cell wall and membrane penetration. Depending on the toughness of the tissue, *C. albicans*

Downloaded from https://academic.oup.com/femsre/advance-article/doi/10.1093/femsre/fuac039/6674677 by guest on 05 October 2022

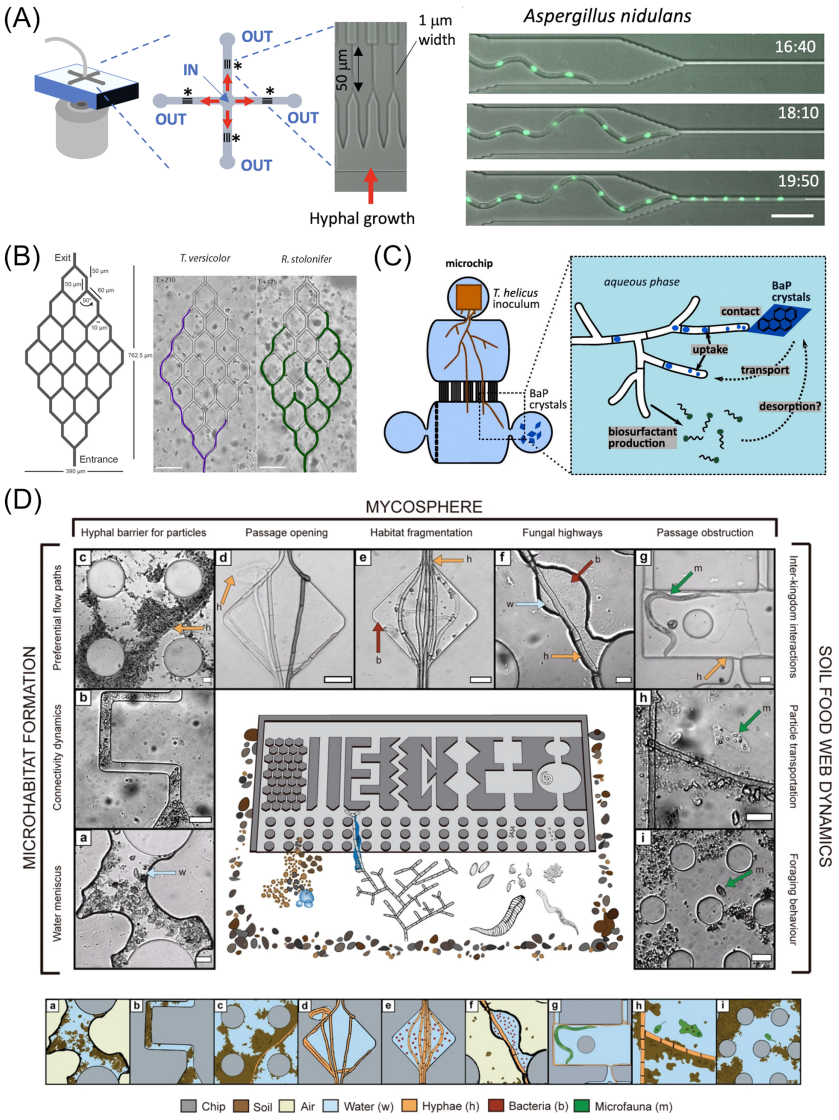


Figure 10. Microfluidic platforms for the study of fungal behaviour in artificial microenvironments mimicking aspects of the natural habitat. (A) Device used to study the behaviour of filamentous fungi upon facing special confinement on a subcellular level. Scale bar represents 20 µm. (B) Microdevice for studying space searching strategies in different fungal species. Scale bars represent 100 µm. (C) Microchip used to investigate chemotropism and uptake of lipophilic molecules (e.g. benzo[a]pyrene, BaP) by filamentous fungi. Image reproduced with modifications from Baranger et al. (2021) with permission from Elsevier (Licence Number: 5271511231788). (D) Microfluidic platform simulating several aspects of soil communities, featuring different channel designs filled with soil particles, soil bacteria, microfauna, and filamentous fungi, as well as being saturated with water or with air. Scale bars represent 20 µm. Images in (A), (B), and (D) reproduced with modifications from Fukuda et al. (2021), Hopke et al. (2021), and Mafla-Endara et al. (2021), respectively, with permission from the Creative Commons Attribution licence (www.creativecommons.org/licenses/by/4.0/).

is able to penetrate the barrier with pure mechanical force, while for others, an additional loosening of the wall with enzymes is necessary, involving complex cellular and morphological reorganization (Puerner et al. 2020). Alternatively, the fungus is able to navigate around impenetrable barriers (Thomson et al. 2015).

Similarly, Sun et al. (2018) designed a microdevice with force sensing pillars to measure protrusive forces exerted by *N. crassa* as well as the oomycete *Achlya bisexualis* (Fig. 11A). Oomycetes are fungus-like eukaryotes and are comparable to fungi in many ways, in particular for some species, their filamentous form and exploratory nature. Furthermore, many strains of the phylum Oomycota are pathogenic to fungi and plants (Beakes et al. 2012). Therefore, mycology and oomycete research are closely related. With their micropillar arrays, they measured protrusive forces of maximal 11 µN and 7 µN for *N. crassa* and *A. bisexualis*, respectively. When deflected by the pillar, the oomycete hypha was able to exert a bending force of up to 19 µN (Sun et al. 2018). Using another platform, they optimized the trapping of single zoospores of *A. bisexualis* with a sophisticated valve system to study forces exerted by germ tubes upon germination. The measured forces ranged between 0.73 and 1.66 µN, which is slightly less compared to the forces of adult hyphae (Sun et al. 2020).

Minc et al. (2009) exploited the elastic characteristics of PDMS for a slightly different application, i.e. to measure forces developed by growing cells of the fission yeast *S. pombe*. They trapped the rod-shaped cells in microwells having a diameter of between 10 and 50 µm and calculated the forces from the deformation of the wells upon stretching and buckling of the cells (Fig. 11B and C). Interestingly, the calculated forces exerted by the yeast cells were around 11 µN, which is within the range of the previously

Downloaded from https://academic.oup.com/femsre/advance-article/doi/10.1093/femsre/fuac039/6674677 by guest on 05 October 2022

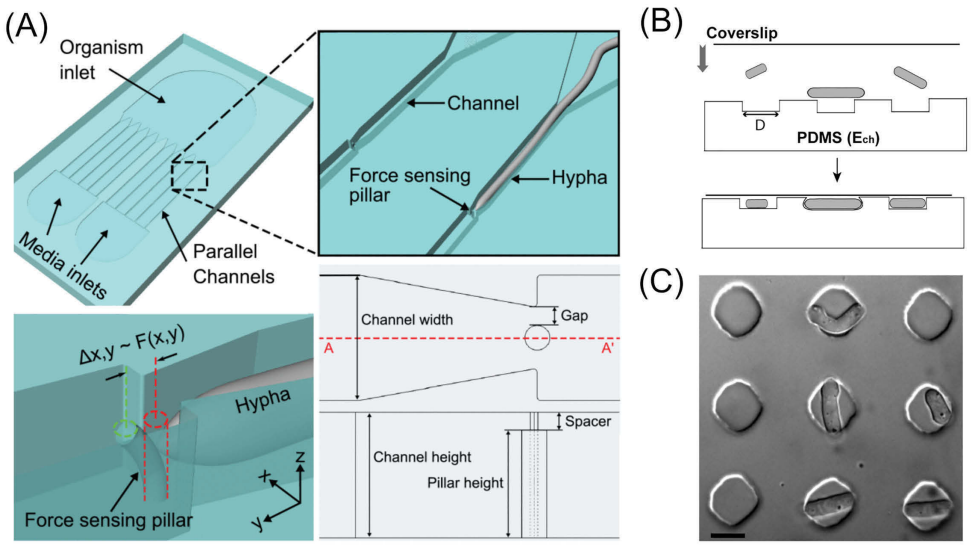


Figure 11. Microfluidic devices for measuring hyphal and cellular tip force. (A) A channel design containing a dead-end channel with a force sensing pillar. Upon deflection of the pillar, values for the force exerted by the hyphal tip can be calculated. Image reproduced with modifications from Sun et al. (2018) with permission from the Creative Commons Attribution license (www.creativecommons.org/licenses/by/4.0/). (B) Microwells precisely fitting single cells of *S. pombe*. Upon cell fission and growth, the elastic PDMS wells are deformed and forces exerted can be deduced. (C) Microscopic image of trapped yeast cells with clearly visible deformation of the wells upon cell growth. Scale bar represents 10 μm. Images (B) and (C) reproduced with modifications from Minc et al. (2009) with permission from Elsevier (Licence Number: 5271520737780).

discussed forces by *N. crassa* and *A. bisexualis*. Further, they studied the underlying intracellular mechanisms of the force generation and found that mainly turgor pressure was involved, which was actively regulated with enzymes such as glycerol-3-phosphate dehydrogenase. This enzyme catalyses the synthesis of glycerol, the main component determining turgor pressure. However, they assumed that the growth force is independent of actin cable organization, which is generally important for polarized cell growth, after comparing their findings with the behaviour of a mutant strain lacking actin cables, *for3*Δ.

Hyphal interactions

Besides the mechanical aspects influencing filamentous fungal growth and behaviour, another avenue that the microfluidic approach allows is the investigation of biotic factors, i.e. inter- or intraspecies interactions. By designing special microfluidic devices with channels, chambers, and perfusion facilities, this provides a means to precisely trigger and analyze interactions between bacteria and fungi (Stanley et al. 2014, Uehling et al. 2019), as well as fungal–nematode (Schmieder et al. 2019), fungal–virus (Ghanem et al. 2019), and fungal–fungal (Stockli et al. 2019) interactions.

Bacterial–fungal interactions

The first investigations involving the interaction of fungi with other microbial species at the single-cell level were dedicated to the study of bacterial–fungal interactions (BFIs). Stanley et al. (2014) developed a microfluidic device, termed the BFI device (Fig. 12A), specifically designed to accommodate fungal hyphae and facilitate coinoculation with bacteria through a separate inlet. The interaction between the fungus *Coprinopsis cinerea* and the bacterium *Bacillus subtilis* was investigated in this study, where it was observed that inoculation with the wild-strain (*B. subtilis* NCIB 3610) was followed by hyphal growth arrest, while the domesticated *B. subtilis* 168 laboratory strain did not exhibit this activity. Using the BFI microfluidic device, it was then possible to gain a deeper understanding of BFIs in real-time and at the cellular level. In turn, it was revealed that bacteria attached to specific subsets of hyphae, regardless of whether they were wild- or laboratory strain, or even dead bacterial cells (Fig. 12B). Additionally, this suggested the existence of hyphal differentiation within the mycelium. The hyphal growth arrest was found to coincide with the collapse of some hyphal compartments and the subsequent formation of blebs, exocytotic vesicles still containing the fluorescent marker for up to several hours after the collapse (Fig. 12C). In a further experiment using a second microfluidic device, termed the fluid exchange device, they perfused the hyphae with bacterial supernatant and lipophilic extracts. Since the effect on the hyphae was analogous to that observed with the bacteria, it was postulated that the fungicidal activity derived from lipophilic exudates rather than active bacterial enzymes.

To protect themselves against such bacterial attacks, fungi have developed antibacterial strategies. With microfluidic technology it is possible to single out hyphae and subject them to bacterial supernatant and extracts with subsequent precise imaging of the resultant effect, yielding important information for basic research as well as for practical applications, like pest control methods (Stockli et al. 2019). Harting et al. (2021) investigated the antagonistic relationship between certain *Verticillia* spp., pathogenic fungal species of important crops, and *Pseudomonas* spp. With the help of a microfluidic platform, they analyzed the fungal–bacterial interaction on a cellular level, granting insight into the cellular and molecular processes involved and how the bacteria inhibit fungal growth and plant colonization.

Similarly, mutually beneficial interactions can be investigated in microfluidic devices. The above featured BFI device was further employed to study the endosymbiosis between the fungal plant pathogen *Rhizopus microsporus* and the bacterium *Burkholderia rhizoxinica*, detailed in a preprint by Richter et al. (2020). Uehling et al. (2019) investigated the (pre-) symbiotic signalling between the fungus *Mortierella elongata* and the bacterial *Burkholderia* strain BT03. Their studies revealed a multistage bidirectional communication involving exudates. The first stage is marked by exudation

Downloaded from https://academic.oup.com/femsre/advance-article/doi/10.1093/femsre/fuac039/6674677 by guest on 05 October 2022

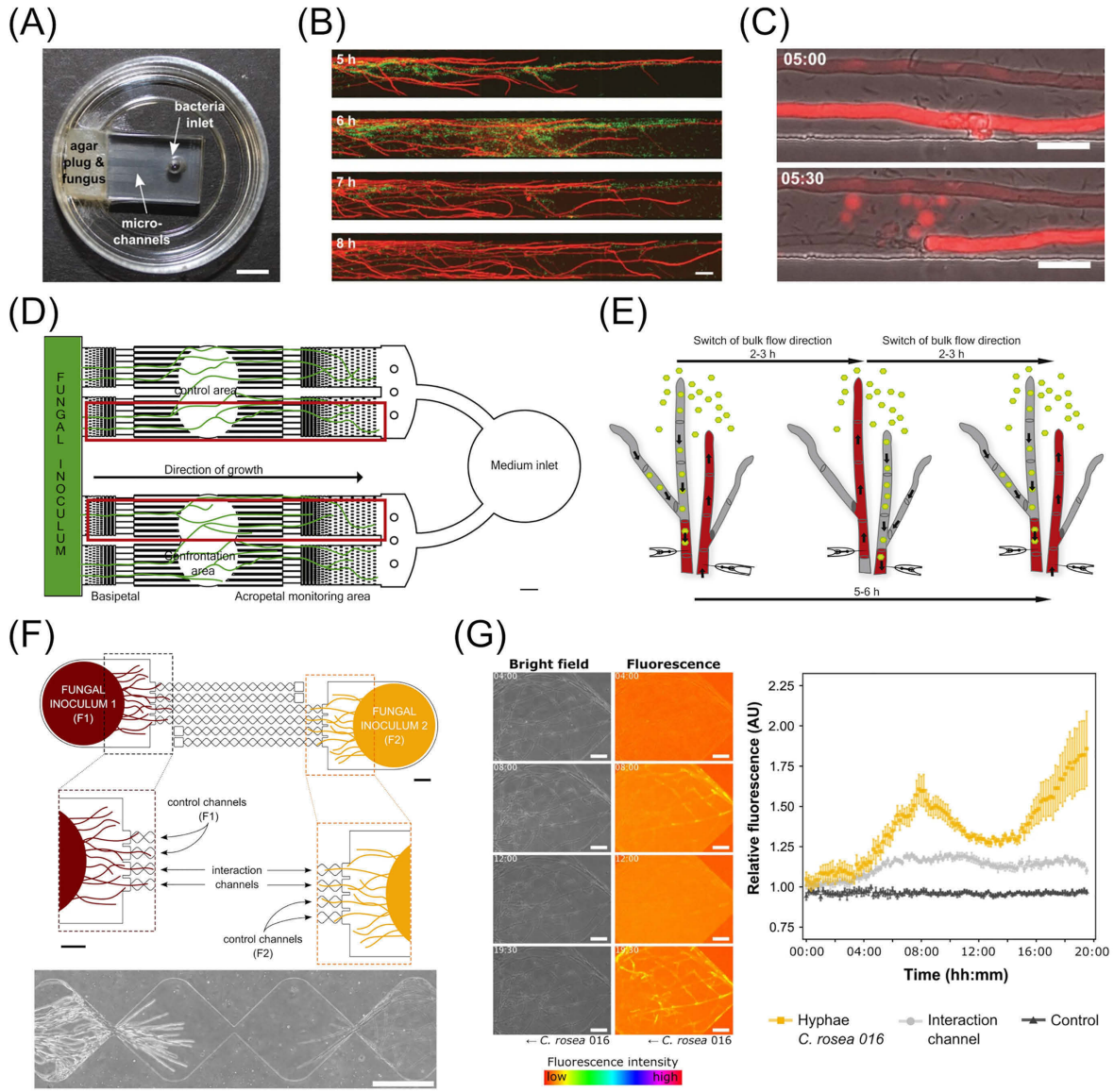


Figure 12. Microfluidic devices for investigating hyphal interactions. (A) Image of the bacterial–fungal interaction (BFI) device, inoculated with an agar plug containing fungal mycelium. Scale bar represents 5 mm. (B) *Bacillus subtilis* (green) attaching to *Coprinopsis cinerea* hyphae (red), coinoculated in the BFI device. Scale bar representing 50 μm. (C) Time series showing the collapse of a *C. cinerea* cell and subsequent loss of its cellular contents, caused by *B. subtilis*. Scale bar representing 25 μm. Images (A)–(C) reproduced with modifications from Stanley et al. (2014) with permission from Oxford University Press (Licence Number: 5297210130322). (D) Schematic design of a device for studying fungal–nematode interactions. Scale bar represents 500 μm. (E) Proposed model for fungal response upon nematode predation. Bulk hyphae switch cytoplasmic bulk flow direction every 2–3 h in order to redistribute nutrients (e.g. 2-Deoxy-2-[(7-nitro-2,1,3-benzoxadiazol-4-yl)amino]-D-glucose (2-NBDG), green hexagons). Red indicates the spatial distribution of the *C. cinerea* defence response upon predation. Images (D) and (E) reproduced with modifications from Schmieder et al. (2019) with permission from Elsevier (Licence Number: 5297260732132). (F) Schematic design of the fungal–fungal interaction (FFI) device (top). Scale bar represents 1 mm. (Bottom) Phase contrast image of hyphae of *C. rosea* and *F. graminearum* approaching each other in the interaction zone. Scale bar represents 250 μm. (G) Time series showing the detection of GFP within the mycelium of *C. rosea* (left). The fluorescence signal within these hyphae was found to increase and decrease compared to control channel (right). Images (F) and (G) reproduced with modifications from Gimeno et al. (2021) with permission from the Creative Commons Attribution license (www.creativecommons.org/licenses/by/4.0/).

of organic acids, such as erythronic acid, by the fungus, which are then recognized and used by the bacteria. The second stage involves a response signal (yet to be determined) sent out by the bacteria, which enhances hyphal growth of the fungus. The specificity of the signals is assumed to increase from stage to stage, though subsequent stages are so far not fully discovered. The group further set out to develop an easy-to-use microfluidic device in an attempt to democratize the microfluidic tools available for the bacterial–fungal research field. Their devices come premade, sterile, and vacuum packaged. Besides the obvious benefit for protection and conservation of the device during transport, with the help of the vacuum, channels fill automatically with the desired medium or solution within minutes after opening the sealing, thus avoiding problems with priming. To test the device's performance in the field, the group sent out samples to labs all over the world. In general, reports came back demonstrating successful application of the system to studies on fungal biofilms, fungal highways, BFIs, as well as a few investigations involving plant seeds or even neurons (Millet et al. 2019). This highlights the importance of designing microfluidic platforms that are amenable

Downloaded from https://academic.oup.com/femsre/advance-article/doi/10.1093/femsre/fuac039/6674677 by guest on 05 October 2022

for use by nonexperts, thus encouraging adoption and use of the technique by mycologists.

Another study demonstrating the flexibility of microfluidic devices was conducted by Ghanem et al. (2019). They investigated and quantified the retention and distribution of bacteriophages along fungal hyphae. This aspect of soil ecology has so far received little attention, although partly due to the fact that investigations in this area are far from trivial. The retention of phages by hyphae was found to be up to 93%, in the case of the hydrophobic T4 phage and hydrophobic *C. cinerea* hyphae. Complemented with calculated surface interaction energy values, their findings have significant implications for environmental as well as medical questions.

Fungal–fungivorous interactions

Besides the world of microbes, soil fungi also regularly encounter slightly bigger, fungivorous organisms, such as protists and microfaunal organisms, which they must defend themselves from. In a two-part study, using a device based on the BFI device, Schmieder et al. (2019) investigated the distribution of locally administered nutrients throughout the hyphal network of *C. cinerea* as well as response mechanisms upon attack by the nematode *Aphelenchus avenae* (Fig. 12D). The group followed up on and confirmed previous findings on specialized hyphae and dynamic responses within the mycelial network. With the aid of a fluorescent glucose analog, 2-NBDG, and high-resolution fluorescence microscopy they monitored bidirectional transport of cytoplasmic nutrients and found periodical switching of the direction every 2–3 h in certain specialized hyphae (trunk hyphae) (Fig. 12E). Further, it was hypothesized that the flow dynamics are mainly controlled by septa, which can open and close their pores reversibly. While nutrient distribution is rather global, intending to supply all parts of the mycelium equally, even if nutrient sources are locally restricted, defence mechanisms tend to be only activated at the immediate site of attack. The defence response against the nematode is very specific to the fungivore, with two effector promotors, cgl2p and cctx2p, mainly involved. The defence programme was only activated in areas in direct contact with *A. avenae*, but was, however, quickly propagated in the trunk hyphae. In a continuation of the study, the group focussed further on the genes involved in the defence response, using a slightly modified microfluidic platform. From a channel opening in the confrontation zone, it was possible to extract fungal mycelium for downstream analyses (i.e. PCR and poly(A)+ RNA sequencing), thus directly analyzing the transcriptome linked to the interaction with the nematode. They were able to identify 1229 differentially expressed genes; until this point, only 37 genes had been discovered using conventional plate-based techniques. Their results further show an involvement of antibacterial defence genes, suggesting the interaction to be a tripartite (fungus, nematode, and nematodal microbiome) instead of a bipartite one, which is true for many interactions in nature (Tayyrov et al. 2019).

Fungal–fungal interactions

Very recently, Gimeno et al. (2021) developed a microfluidic platform to investigate antagonistic fungal–fungal interactions (FFI) between the plant pathogen *F. graminearum* and biocontrol agent *C. rosea* (Fig. 12F). In the course of these investigations, further and more detailed insights into their antagonistic interaction was gathered. In particular, a loss of fluorescence in GFP-tagged *F. graminearum* was observed to coincide with the detection of GFP in the mycelial network of the predator, allowing to postulate an uptake and redistribution of material from the attacked fungus to the attacking fungus (Fig. 12G). In the future, the presented FFI device is anticipated to contribute further to revealing deeper insights into the mechanistic details of FFIs at the single-hyphal level, information needed for the development of novel and much needed strategies to control fungal pathogens in agriculture.

Future perspectives and concluding remarks

Lastly, we provide a future perspective and concluding remarks detailing a number of new frontiers in which microfluidic technology is expected to aid future research in this field of study, with a focus on AMF, nuclei behaviour in filamentous fungi, multispecies interactions, and electrical measurements for cell-to-cell communication.

AMF

When considering the study of soil microbes and interspecies interactions with fungi using microfluidic methods, mycorrhizal fungi, such as the obligate symbiotic AMF, call for inclusion. Forming one of the most important fungal–plant symbioses in nature, AMF interact with plant roots, providing mineral nutrients and water in exchange for carbon and lipids. Specifically, a key element of this mutualistic liaison is the plant's contribution of photosynthesis products in exchange for soil nutrients, mainly P (up to 90%) and N, but also Zn, Cu, and Fe (Smith and Read 2010). Furthermore, the mycorrhizal association contributes to an improved resilience against biotic and abiotic stresses in the plant, such as increased resistance against below and above-ground pathogens, and tolerance to trace elements and hydrocarbon pollutants or drought and salinity, as well as a reduction of nutrient leaching and an improved environment for the establishment of fresh seedlings (van der Heijden 2004). During the last decades, therefore, AMF have been subject to intensive research, with the main drive towards agricultural exploitation of the advantages. Here again, the soil-borne and obligate nature of these fungi and their symbiosis renders most studies 'black-box' experiments, with microfluidics representing a promising tool to lift this veil. Indeed, so far only a single publication has surfaced in this area, which focusses on AMF spore sorting (Srisom et al. 2020).

Besides giving insight into their hyphal thigmotropism and space searching strategies, the development of novel microfluidic technologies could help solve prominent questions that have been baffling researchers for decades. Much is still unknown about AMF hyphae morphogenesis and polarized growth of the extraradical mycelium. AMF develop an intricate network of hyphae that consists of runner hyphae, that ramify into secondary and tertiary hyphae, for example, and ultimately form the branched absorbing structures involved in the uptake of nutrients (Bago et al. 1998). A mathematical model used to simulate nutrient uptake was described in Schnepf et al. (2011), which provides a foundation for studies involving single hyphae at the cellular level within microfluidic systems. AMF hyphae also interconnect individual plants of the same or different species to form 'common mycorrhizal networks' (CMNs; Simard et al. 2012). CMNs can transfer nutrients between plants or warning signals in response to attacks by fungal pathogens and insect pests, thereby acting as below-ground interplant defence communication tools (Babikova et al. 2013). Crucial questions about the specificity of the signals regarding the species of plants or pests, and the nature of the signal(s) transferred, need to be resolved. In addition, other molecules, such as small RNAs, and virus genomes might be

Downloaded from https://academic.oup.com/femsre/advance-article/doi/10.1093/femsre/fuac039/6674677 by guest on 05 October 2022

transported through CMNs, with important implications for plant health and crop protection (Wang et al. 2017). The development of new microfluidic tools can help to understand the multitude of functions of hyphae and CMNs, taking the science well beyond the current state-of-the-art and, thus addressing global challenges such as food security and ecosystems management. One major challenge yet to address is the still-to-be-firmly demonstrated presence of the Spitzenkörper, a structure found at the hyphal tip that mediates hyphal growth direction and hyphal tip morphology by the delivery of secretory vesicles. These apical vesicular clusters have been suggested in AMF, although not firmly demonstrated (de la Providencia et al. 2005). These structures are associated with actively growing hyphal tips and, thus in the 3D architecture of extraradical mycelium, presumably being involved in the process of anastomosis formation and the hyphal healing mechanism (HHM), two important mechanisms of hyphal fusions between compatible mycelia evolved by AMF to increase their chances of survival. Curiously, anastomoses and HHM differ markedly between species belonging to the Gigasporaceae and Glomeraceae, two of the globally most predominant AMF families, suggesting divergent strategies for the colonies to explore and exploit their environments and create large networks (Voets et al. 2006). Recently, a negative impact of azoxystrobin and fenpropimorph, two active ingredients widely used in agriculture to protect crops from fungal diseases, was noticed on the HHM. In the presence of these compounds, contact and hyphal fusion are disturbed (Rodriguez-Morelos et al. 2021). One hypothesis is the possible perturbation of the Spitzenkörper, or sterol content and lipid rafts. Microfluidic platforms could thus help in the real-time observation of anastomoses and HHM (e.g. time series describing hyphal–hyphal fusion), but also in understanding the mechanisms involved in the polarized growth of hyphae and development of 'Wood Wide Webs' (Rhodes 2017) and CMNs, how changes in the environment disturb this essential mechanism involved in mycelium integrity and functioning, as well as AMF ecology, genetics, and evolution.

Another major avenue that can be approached with microfluidic technology development is the exploration of the wide variety of social interactions, including cooperation (e.g. mutualism, altruism, selfishness, and spite), that microorganisms have developed to survive and prosper in nature. In particular, the role of AMF hyphae in recruiting microbes into their hyphosphere, the so-called second genome of AMF, has become the center of attention of numerous studies (Zhang et al. 2022). Until the recent decade, the AMF hyphosphere has been overlooked mainly due to the difficulty of studying AMF–bacteria interactions on the surface of hyphae in a context free of any microorganisms other than those targeted (Duan et al. 2022). Fortunately, *in vitro* cultivation of AMF on root organs or whole plants has enabled the production of root-free compartments containing large amounts of hyphae devoid of any undesirable contaminants to study the interaction between AMF and phosphate solubilizing bacteria (PSB) or communities of bacteria growing on the surface of hyphae (Jiang et al. 2021, Zhang et al. 2018b). Using these systems, it has been shown that hyphae of AMF can selectively recruit PSB in the hyphosphere and reward them with hyphal exudates (Zhang et al. 2018b), which is a tangible sign of mutually beneficial cooperation between both partners, the so-called 'direct reciprocity' ['*individuals will tend to help those who help them*'—Roberts (2008)]. Microfluidic technology could help to explore the intimate relationship/interactions occurring at the hyphal surface using, amongst others, brightfield and fluorescence microscopy techniques. Interaction studies on the hyphal surface can also concern pathogenic bacteria or even tripartite scenarios involving hyphae/beneficial bacteria/pathogenic bacteria. For instance, the yet unexplored indirect reciprocity ['*I help you and somebody else helps me or does not harm me*'—Nowak and Sigmund (2005)] in the cooperation between AMF and bacteria can be explored using microfluidics.

A third important challenge related to the study of AMF regards understanding the reason as to why a restricted number of plant species (an approximation of 29%) including the plant model *Arabidopsis thaliana* are considered nonhost for AMF. Intriguingly, under some conditions, nonhost plants can become colonized by AMF and develop rudimentary AM phenotypes (Cosme et al. 2018). Microfluidic technologies could assist in elucidating the underlying reasons for these incompatibilities, e.g. by exploiting the capabilities of RootChips (Grossmann et al. 2011, Stanley et al. 2018).

Nuclei behaviour in filamentous fungi

One particular trait of filamentous fungi regards the presence of multiple nuclei within a single cell compartment (Maheshwari 2005). This is particularly true for coenocytic fungi such as Mucoromycota, but Dikarya fungi also experience this state, either after sexual cell fusion or in a parasexual cycle. In addition to this, many fungi form anastomoses between individual hyphae to reorganize their network (Chagnon 2014, Croll et al. 2009, Read et al. 2009), which eventually leads to a redistribution of nuclei between different parts of a fungal colony, but also between distinct 'individuals' (though what exactly a fungal individual may relate to is debatable, given that fungi are considered modular organisms; Andrews 1995). These peculiarities come with the coexistence of genetically different nuclei in a single cell compartment, a state called heterokaryosis (Scott et al. 2019, Strom and Bushley 2016). The rules that govern nuclei exchanges, how genetically divergent nuclei coexist and compete in a cell space, and how this impacts the biology of filamentous fungi are all open questions within the field. Following nuclei circulation and exchange within the mycelial network of one fungus or witnessing nuclei exchange between different networks could be investigated using microfluidic technologies. This in turn would open new avenues for the understanding of fundamental aspects of fungal biology such as self/nonself recognition mechanisms (Kahmann and Bölker 1996) or sexual compatibility (Nieuwenhuis et al. 2013). Such knowledge would also be highly relevant for selecting fungi for biotechnological purposes not at the strain level, but rather at the nucleus level.

Multispecies interactions involving fungi

Tailored microfluidic devices have started to reveal the complexity of interactions established by filamentous fungi with other soil dwellers, as detailed previously. As a result, given the diversity of organisms in the environment, still a myriad of additional relevant interactions could be investigated in detail using microfluidic platforms. Many of these interactions result from the exploratory behaviour of filamentous fungi (Aleklett and Boddy 2021) and their ability to construct an ever-changing network of hyphae that connects soil habitats throughout water unsaturated soil patches. This has led, for instance, to the observation of bacteria exploiting this network for their dispersal using the so-called fungal highways (Kohlmeier et al. 2005). Such dispersal paths in soils have been shown to be important for soil biogeochemical processes (Martin et al. 2012, Sun et al. 2019), but also for the promotion of genetic exchange (Berthold et al. 2016) and the encounter of bacterial viruses (bacteriophages) with their host populations (You et al. 2022). Interestingly, fungal highways also promote water redistribution in unsaturated systems, leading for instance to the

Downloaded from https://academic.oup.com/femsre/advance-article/doi/10.1093/femsre/fuac039/6674677 by guest on 05 October 2022

germination of dormant bacterial cells (Worrich et al. 2017). However, so far, none of these processes has been witnessed with the cell-to-cell resolution that microfluidic technologies can offer. Although the use of fluid-filled devices could be counterintuitive for investigating interactions that depend on the level of water saturation within an environment, fungal colonization of dry and nutrient deficient microfluidic devices leads to water redistribution in the channels, which can be combined with cocultures of interacting organisms (Gimeno et al. 2021). In this way, the rules governing the transport of bacteria along fungal highways (directionality, growth, and motility trade-offs or impact of fungal cell wall remodelling), the mechanics of displacement (speed, effect of chemoattractants, or chemorepellents) or even the characterization of the liquid layer on the surface of fungal hyphae (composition, thickness, and viscosity) can be investigated. A better understanding of these processes can contribute to improving the design of biotechnological approaches in which fungal highways can be relevant, such as in soil bioremediation (Wick et al. 2007) or the biocontrol of soil-borne pathogens.

Fungi also participate in beneficial associations with algae or cyanobacteria, or even both together, to form lichens (Grimm et al. 2021). As microfluidic technology development allows researchers to design tailored microarchitectures to accommodate and guide interspecies interactions precisely, artificial reconstruction of lichens could contribute immensely to further understanding this composite organism. Á la Organ-on-a-Chip technologies, reconstructing lichen architecture within multilayered systems with controlled perfusion could allow investigations regarding symbiosis establishment and underlying mechanisms associated with the partnership. Moreover, the ability to procure these pioneering organisms on demand could be used to repopulate destroyed ecosystems.

Electrical measurements in fungi

Furthermore, fungal mycelia are known to span vast networks in soil, connecting plants, and thus potentially acting as a 'central connecting system' within soil ecosystems. The communication mechanisms within the system are still poorly understood, but the possibility of having electrical currents as a means of fast information transfer would provide a system akin to a central neuronal system that could result in a coordinated behaviour required in such a complex system as a soil. Electrical currents have been shown not only to be important for the coordination of cell behaviour at all biological levels, i.e. from bacteria to humans (Brenner et al. 2006, Canales et al. 2018, Piccolino 1997, Prindle et al. 2015), but also for intracolony or interspecies communication (Beagle and Lockless 2015, Clarke et al. 2013, Prindle et al. 2015). The cell morphology and growth mode of filamentous fungi provides, in theory, an ideal system for electrical signalling, but the use of traditional electrophysiological methods for measuring these signals is extremely challenging (Adamatzky 2022). With integrated electronics, microfluidic chips are envisaged to be beneficial to further investigate these phenomena at the hyphal level.

While most microfluidic devices are made from mainly PDMS, other polymers or glass, the versatility of design possibilities goes far beyond these materials. Some groups set out to integrate metals into their polymer-based devices. Singh et al. (2017), for instance, coated microchannels with a thin layer of gold. Thus, they designed a microfluidic platform to capture bacteria and fungi efficiently, based on the affinity of gold towards thiol and amine groups, which are present in the microbes' cell walls. The applications of such a device range from immobilization for imaging to concentration of target microbes from mixed and real-life samples for further analyses or diagnostics. The primary property of metals, however, relates to their electrical conductivity. Duarte et al. (2022) built an array of nanoelectrodes into a PDMS microfluidic device. These electrodes allowed for both dielectrophoretic trapping, as well as subsequent detection and identification of spores from the phytopathogenic fungus *Sclerotinia sclerotiorum*. The possibility to combine visual, imaging studies with electrical measurements opens entirely new avenues. With the integration of microfluidic technologies with electronic components, electrophysiological measurements on fungi and their partners could be performed and further insights into the fungi's role as the 'brain' of the soil gained.

Acknowledgements

We acknowledge financial support from the Department of Bioengineering at Imperial College, London. Thanks go to Danaé Bregnard, Aislinn Estoppey, and Matteo Buffi for the beautiful photograph of wild mushrooms used in the Featured Image.

Conflict of interest. None declared.

Funding

This work was supported by the Leverhulme Trust (RPG-2020–352 to C.E.S.), the U.S. Department of Energy (LANLF59T to P.J. and S.B.), the Gebert Rüf Stiftung (GRS-064/18 to P.J.), and the Swiss National Science Foundation (194701 to P.J.).

References

Adamatzky A. Language of fungi derived from their electrical spiking activity. *R Soc Open Sci* 2022;**9**:211926.

Aleklett K, Boddy L. Fungal behaviour: a new frontier in behavioural ecology. *Trends Ecol Evol* 2021;**36**:787–96.

Aleklett K, Ohlsson P, Bengtsson M. *et al.* Fungal foraging behaviour and hyphal space exploration in micro-structured Soil Chips. *ISME J* 2021;**15**:1782–93.

Almeida F, Rodrigues ML, Coelho C. The still underestimated problem of fungal diseases worldwide. *Front Microbiol* 2019;**10**:214.

Andersen JB, Sternberg C, Poulsen LK. *et al.* New unstable variants of green fluorescent protein for studies of transient gene expression in bacteria. *Appl Environ Microbiol* 1998;**64**:2240–6.

Andrews JH. Fungi and the evolution of growth form. *Can J Bot* 1995;**73**:1206–12.

Asenova E, Lin HY, Fu E. *et al.* Optimal fungal space searching algorithms. *IEEE T Nanobiosci* 2016;**15**:613–8.

Asghar W, Sher M, Khan NS. *et al.* Microfluidic chip for detection of fungal infections. *ACS Omega* 2019;**4**:7474–81.

Ashammakhi N, Wesseling-Perry K, Hasan A. *et al.* Kidney-on-a-chip: untapped opportunities. *Kidney Int* 2018;**94**:1073–86.

Babikova Z, Gilbert L, Bruce TJ. *et al.* Underground signals carried through common mycelial networks warn neighbouring plants of aphid attack. *Ecol Lett* 2013;**16**:835–43.

Bago B, Azcón-Aguilar C, Goulet A. *et al.* Branched absorbing structures (BAS): a feature of the extraradical mycelium of symbiotic arbuscular mycorrhizal fungi. *New Phytol* 1998;**139**:375–88.

Balasubramanian S, Chen J, Wigneswaran V. *et al.* Droplet-based microfluidic high throughput screening of *Corynebacterium glutamicum* for efficient heterologous protein production and secretion. *Front Bioeng Biotechnol* 2021;**9**:668513.

Downloaded from https://academic.oup.com/femsre/advance-article/doi/10.1093/femsre/fuac039/6674677 by guest on 05 October 2022

Bang S, Jeong S, Choi N. *et al.* Brain-on-a-chip: a history of development and future perspective. *Biomicrofluidics* 2019;**13**:051301.

Baranger C, Fayeulle A, Le Goff A. Microfluidic monitoring of the growth of individual hyphae in confined environments. *R Soc Open Sci* 2020;**7**:191535.

Baranger C, Pezron I, Lins L. *et al.* A compartmentalized microsystem helps understanding the uptake of benzo[a]pyrene by fungi during soil bioremediation processes. *Sci Total Environ* 2021;**784**:147151.

Baret J-C. Surfactants in droplet-based microfluidics. *Lab Chip* 2012;**12**:422–33.

Baret JC, Miller OJ, Taly V. *et al.* Fluorescence-activated droplet sorting (FADS): efficient microfluidic cell sorting based on enzymatic activity. *Lab Chip* 2009;**9**:1850–8.

Barkal LJ, Procknow CL, Alvarez-Garcia YR. *et al.* Microbial volatile communication in human organotypic lung models. *Nat Commun* 2017;**8**:1770.

Barkal LJ, Walsh NM, Botts MR. *et al.* Leveraging a high resolution microfluidic assay reveals insights into pathogenic fungal spore germination. *Integr Biol* 2016;**8**:603–15.

Barrios-González J, Tomasini A, Viniegra-González G. *et al.* Penicillin production by solid state fermentation. *Biotechnol Lett* 1988;**10**:793–8.

Basso LC, Basso TO, Rocha SN. Ethanol production in Brazil: the industrial process and its impact on yeast fermentation. In: Dos Santos Bernardes MA (ed.), *Biofuel Production: Recent Developments and Prospects*. Rijeka: InTech, 2011, 85–100.

Bauer W-AC, Fischlechner M, Abell C. *et al.* Hydrophilic PDMS microchannels for high-throughput formation of oil-in-water microdroplets and water-in-oil-in-water double emulsions. *Lab Chip* 2010;**10**:1814–9.

Beagle SD, Lockless SW. Electrical signalling goes bacterial. *Nature* 2015;**527**:44–45.

Beakes GW, Glockling SL, Sekimoto S. The evolutionary phylogeny of the oomycete "fungi". *Protoplasma* 2012;**249**:3–19.

Bedekovic T, Brand AC. Microfabrication and its use in investigating fungal biology. *Mol Microbiol* 2021;**117**:569–77.

Beißner N, Lorenz T, Reichl S. Organ on Chip. In: Dietzel A (ed.), *Microsystems for Pharmatechnology: Manipulation of Fluids, Particles, Droplets, and Cells*. Cham: Springer International Publishing, 2016, 299–339.

Beneyton T, Rossignol T. Droplet-based microfluidic high-throughput screening of enzyme mutant libraries secreted by *Yarrowia lipolytica*. In: Walker JM (ed.), *Methods in Molecular Biology*. New York: Springer, 2021,205–19.

Beneyton T, Wijaya IP, Postros P. *et al.* High-throughput screening of filamentous fungi using nanoliter-range droplet-based microfluidics. *Sci Rep* 2016;**6**:27223.

Bennet TJ, Randhawa A, Hua J. *et al.* Airway-On-A-Chip: designs and applications for lung repair and disease. *Cells* 2021;**10**:1602.

Bernier LS, Junier P, Stan GB. *et al.* Spores-on-a-chip: new frontiers for spore research. *Trends Microbiol* 2022;**30**:515–8.

Berry SB, Lee JJ, Berthier J. *et al.* Droplet incubation and splitting in open microfluidic channels. *Anal Methods* 2019;**11**:4528–36.

Berthold T, Centler F, Hübschmann T. *et al.* Mycelia as a focal point for horizontal gene transfer among soil bacteria. *Sci Rep* 2016;**6**:36390.

Brand A, Gow NA. Mechanisms of hypha orientation of fungi. *Curr Opin Microbiol* 2009;**12**:350–7.

Bremond N, Bibette J. Exploring emulsion science with microfluidics. *Soft Matter* 2012;**8**:10549–59.

Brenner ED, Stahlberg R, Mancuso S. *et al.* Plant neurobiology: an integrated view of plant signaling. *Trends Plant Sci* 2006;**11**:413–9.

Bringer MR, Gerdts CJ, Song H. *et al.* Microfluidic systems for chemical kinetics that rely on chaotic mixing in droplets. *Philos Trans R Soc A* 2004;**362**:1087–104.

Brouzes E, Medkova M, Savenelli N. *et al.* Droplet microfluidic technology for single-cell high-throughput screening. *Proc Natl Acad Sci USA* 2009;**106**:14195.

Bussamara R, Fuentefria AM, Oliveira ESd. *et al.* Isolation of a lipase-secreting yeast for enzyme production in a pilot-plant scale batch fermentation. *Bioresour Technol* 2010;**101**:268–75.

Cabrera M, Novarina D, Rempel IL. *et al.* A simple microfluidic platform to study age-dependent protein abundance and localization changes in *Saccharomyces cerevisiae*. *Microb Cell* 2017;**4**:169–74.

Canales J, Henriquez-Valencia C, Brauchi S. The integration of electrical signals originating in the root of vascular plants. *Front Plant Sci* 2018;**8**:2173.

Cao J, Kursten D, Krause K. *et al.* Application of micro-segmented flow for two-dimensional characterization of the combinatorial effect of zinc and copper ions on metal-tolerant *Streptomyces* strains. *Appl Microbiol Biotechnol* 2013;**97**:8923–30.

Carvajal-Muñoz J, Carmona-Garcia C. Benefits and limitations of biofertilization in agricultural practices. *Livest Res Rural Dev* 2012;**24**:1–8.

Cavallo E, Charreau H, Cerrutti P. *et al. Yarrowia lipolytica*: a model yeast for citric acid production. *FEMS Yeast Res* 2017;**17**:fox084.

Chagnon P-L. Ecological and evolutionary implications of hyphal anastomosis in arbuscular mycorrhizal fungi. *FEMS Microbiol Ecol* 2014;**88**:437–44.

Charvin G, Cross FR, Siggia ED. A microfluidic device for temporally controlled gene expression and long-term fluorescent imaging in unperturbed dividing yeast cells. *PLoS ONE* 2008;**3**:e1468.

Chen KL, Crane MM, Kaeberlein M. Microfluidic technologies for yeast replicative lifespan studies. *Mech Ageing Dev* 2017;**161**:262–9.

Chen KL, Ven TN, Crane MM. *et al.* An inexpensive microscopy system for microfluidic studies in budding yeast. *Transl Med Aging* 2019;**3**:52–56.

Cheng IF, Chang HC, Hou D. *et al.* An integrated dielectrophoretic chip for continuous bioparticle filtering, focusing, sorting, trapping, and detecting. *Biomicrofluidics* 2007;**1**:21503.

Choi K, Ng AH, Fobel R. *et al.* Digital microfluidics. *Annu Rev Anal Chem* 2012;**5**:413–40.

Clarke D, Whitney H, Sutton G. *et al.* Detection and learning of floral electric fields by bumblebees. *Science* 2013;**340**:66–69.

Cookson S, Ostroff N, Pang WL. *et al.* Monitoring dynamics of single-cell gene expression over multiple cell cycles. *Mol Syst Biol* 2005;**1**:2005 0024.

Cooper RM, Leslie DC, Domansky K. *et al.* A microdevice for rapid optical detection of magnetically captured rare blood pathogens. *Lab Chip* 2014;**14**:182–8.

Cosme M, Fernandez I, Van der Heijden MGA. *et al.* Non-mycorrhizal plants: the exceptions that prove the rule. *Trends Plant Sci* 2018;**23**:577–87.

Crane MM, Clark IB, Bakker E. *et al.* A microfluidic system for studying ageing and dynamic single-cell responses in budding yeast. *PLoS ONE* 2014;**9**:e100042.

Croll D, Giovannetti M, Koch AM. *et al.* Nonself vegetative fusion and genetic exchange in the arbuscular mycorrhizal fungus *Glomus intraradices*. *New Phytol* 2009;**181**:924–37.

de la Providencia IE, de Souza FA, Fernandez F. *et al.* Arbuscular mycorrhizal fungi reveal distinct patterns of anastomosis formation and hyphal healing mechanisms between different phylogenic groups. *New Phytol* 2005;**165**:261–71.

Downloaded from https://academic.oup.com/femsre/advance-article/doi/10.1093/femsre/fuac039/6674677 by guest on 05 October 2022

Denervaud N, Becker J, Delgado-Gonzalo R. *et al.* A chemostat array enables the spatio-temporal analysis of the yeast proteome. *Proc Natl Acad Sci USA* 2013;**110**:15842–7.

Dolinski K, Botstein D. Changing perspectives in yeast research nearly a decade after the genome sequence. *Genome Res* 2005;**15**:1611–9.

Duan S, Declerck S, Zhang L. *et al.* Two-component system in *Rahnella aquatilis* is impacted by the hyphosphere of the arbuscular mycorrhizal fungus *Rhizophagus irregularis*. *Environ Microbiol Rep* 2022;**14**:119–29.

Duarte PA, Menze L, Shoute L. *et al.* Highly efficient capture and quantification of the airborne fungal pathogen *Sclerotinia sclerotiorum* employing a nanoelectrode-activated microwell array. *ACS Omega* 2022;**7**:459–68.

Duran DC, Hernandez CA, Suesca E. *et al.* Slipstreaming mother machine: a microfluidic device for single-cell dynamic imaging of yeast. *Micromachines* 2020;**12**:4.

Falconnet D, Niemisto A, Taylor RJ. *et al.* High-throughput tracking of single yeast cells in a microfluidic imaging matrix. *Lab Chip* 2011;**11**:466–73.

Fazius F, Shelest E, Gebhardt P. *et al.* The fungal alpha-aminoadipate pathway for lysine biosynthesis requires two enzymes of the aconitase family for the isomerization of homocitrate to homoisocitrate. *Mol Microbiol* 2012;**86**:1508–30.

Fehrmann S, Paoletti C, Goulev Y. *et al.* Aging yeast cells undergo a sharp entry into senescence unrelated to the loss of mitochondrial membrane potential. *Cell Rep* 2013;**5**:1589–99.

Fernandes J, Hamidi F, Leborgne R. *et al.* Penetration of the human pulmonary epithelium by *Aspergillus fumigatus* hyphae. *J Infect Dis* 2018;**218**:1306–13.

Fernandes JT, Tenreiro S, Gameiro A. *et al.* Modulation of alpha-synuclein toxicity in yeast using a novel microfluidic-based gradient generator. *Lab Chip* 2014;**14**:3949–57.

Frey O, Rudolf F, Schmidt GW. *et al.* Versatile, simple-to-use microfluidic cell-culturing chip for long-term, high-resolution, time-lapse imaging. *Anal Chem* 2015;**87**:4144–51.

Fuchs BB, Eatemadpour S, Martel-Foley JM. *et al.* Rapid isolation and concentration of pathogenic fungi using inertial focusing on a chip-based platform. *Front Cell Infect Microbiol* 2019;**9**:30809512.

Fukuda S, Yamamoto R, Yanagisawa N. *et al.* Trade-off between plasticity and velocity in mycelial growth. *Mbio* 2021;**12**:e03196–03120.

Funfak A, Brosing A, Brand M. *et al.* Micro fluid segment technique for screening and development studies on *Danio rerio* embryos. *Lab Chip* 2007;**7**:1132–8.

Gabriel BP. Histochemical study of the insect cuticle infected by the fungus *Entomophthora coronata*. *J Invertebr Pathol* 1968;**11**: 82–89.

GenMark Dx. *ePlex-Brochure*. 2021. https://www.genmarkdx.com/wp-content/uploads/2021/12/ePlex-Brochure-Digital-Version-Higher-Res.pdf. (28 April 2022, date last accessed).

Ghanbari A, Nock V, Johari S. *et al.* A micropillar-based on-chip system for continuous force measurement of *C . elegans*. *J Micromech Microeng* 2012;**22**:095009.

Ghanem N, Stanley CE, Harms H. *et al.* Mycelial effects on phage retention during transport in a microfluidic platform. *Environ Sci Technol* 2019;**53**:11755–63.

Gimeno A, Stanley CE, Ngamenie Z. *et al.* A versatile microfluidic platform measures hyphal interactions between *Fusarium graminearum* and *Clonostachys rosea* in real-time. *Commun Biol* 2021;**4**:262.

Griffiths AD, Tawfik DS. Directed evolution of an extremely fast phosphotriesterase by *in vitro* compartmentalization. *EMBO J* 2003;**22**:24–35.

Grimm M, Grube M, Schiefelbein U. *et al.* The lichens' microbiota, still a mystery?. *Front Microbiol* 2021;**12**:623839.

Groisman A, Lobo C, Cho H. *et al.* A microfluidic chemostat for experiments with bacterial and yeast cells. *Nat Methods* 2005;**2**:685–9.

Grossmann G, Guo W-J, Ehrhardt DW. *et al.* The RootChip: an integrated microfluidic chip for plant science. *Plant Cell* 2011;**23**:4234–40.

Hage DS. Affinity chromatography: a review of clinical applications. *Clin Chem* 1999;**45**:593–615.

Hamel C. *Mycorrhizae in Crop Production*. Boca Raton: CRC Press, 2007.

Hansen AS, Hao N, O'Shea EK. High-throughput microfluidics to control and measure signaling dynamics in single yeast cells. *Nat Protoc* 2015;**10**:1181–97.

Hansen AS, O'Shea EK. Promoter decoding of transcription factor dynamics involves a trade-off between noise and control of gene expression. *Mol Syst Biol* 2013;**9**:704.

Hanson KL, Nicolau DV, Filipponi L. *et al.* Fungi use efficient algorithms for the exploration of microfluidic networks. *Small* 2006;**2**:1212–20.

Hao N, Budnik BA, Gunawardena J. *et al.* Tunable signal processing through modular control of transcription factor translocation. *Science* 2013;**339**:460–4.

Hao N, Nayak S, Behar M. *et al.* Regulation of cell signaling dynamics by the protein kinase-scaffold Ste5. *Mol Cell* 2008;**30**:649–56.

Hao N, O'Shea EK. Signal-dependent dynamics of transcription factor translocation controls gene expression. *Nat Struct Mol Biol* 2011;**19**:31–39.

Harting R, Nagel A, Nesemann K. *et al.* Pseudomonas strains induce transcriptional and morphological changes and reduce root colonization of *Verticillium* spp. *Front Microbiol* 2021;**12**:652468.

Hawksworth DL, Lücking R. Fungal diversity revisited: 2.2 to 3.8 million species. *Microbiol Spectr* 2017;**5**:10.

He R, Ding R, Heyman JA. *et al.* Ultra-high-throughput picoliter-droplet microfluidics screening of the industrial cellulase-producing filamentous fungus *Trichoderma reesei*. *J Ind Microbiol Biotechnol* 2019;**46**:1603–10.

Held M, Binz M, Edwards C. *et al.* Dynamic behaviour of fungi in microfluidics: a comparative study. In: *Proceedings of SPIE - The International Society for Optical Engineering*. 2009b. San Jose, CA: SpIE BiOS. https://doi.org/10.1117/12.822464

Held M, Edwards C, Nicolau DV. Fungal intelligence; or on the behaviour of microorganisms in confined micro-environments. *J Phys Conf Ser* 2009a;**178**:012005.

Held M, Edwards C, Nicolau DV. Probing the growth dynamics of *Neurospora crassa* with microfluidic structures. *Fung Biol* 2011a;**115**:493–505.

Held M, Edwards C, Nicolau DV. Temporal and spatial *in vivo* optical analysis of microtubules in *Neurospora crassa*. In: *Proceedings of SPIE - The International Society for Optical Engineering*. 2010a. San Francisco, CA: SPIE BiOS. https://doi.org/10.1117/12.841328

Held M, Farkas DL, Edwards C. *et al.* Hyphal responses of *Neurospora crassa* to micron-sized beads with functional chemical surface groups. In: *Proceedings of SPIE - The International Society for Optical Engineering*. 2011b. San Francisco, CA: SPIE BiOS. https://doi.org/10.1117/12.881721

Held M, Kaspar O, Edwards C. *et al.* Intracellular mechanisms of fungal space searching in microenvironments. *Proc Natl Acad Sci USA* 2019;**116**:13543–52.

Held M, Komaromy A, Fulga F. *et al.* Dynamic behaviour of microorganisms on microstructures. *Microelectron Eng* 2009c;**86**:1455–8.

Held M, Lee AP, Edwards C. *et al.* Microfluidics structures for probing the dynamic behaviour of filamentous fungi. *Microelectron Eng* 2010b;**87**:786–9.

Downloaded from https://academic.oup.com/femsre/advance-article/doi/10.1093/femsre/fuac039/6674677 by guest on 05 October 2022

Hersen P, McClean MN, Mahadevan L. *et al.* Signal processing by the HOG MAP kinase pathway. *Proc Natl Acad Sci USA* 2008;**105**:7165.

Hong T-F, Ju W-J, Wu M-C. *et al.* Rapid prototyping of PMMA microfluidic chips utilizing a CO2 laser. *Microfluid Nanofluid* 2010;**9**:1125–33.

Hopke A, Mela A, Ellett F. *et al.* Crowdsourced analysis of fungal growth and branching on microfluidic platforms. *PLoS ONE* 2021;**16**:e0257823.

Hosokawa M, Hoshino Y, Nishikawa Y. *et al.* Droplet-based microfluidics for high-throughput screening of a metagenomic library for isolation of microbial enzymes. *Biosens Bioelectron* 2015;**67**:379–85.

Hou HW, Gan HY, Bhagat AA. *et al.* A microfluidics approach towards high-throughput pathogen removal from blood using margination. *Biomicrofluidics* 2012;**6**:24115–2411513.

Huang G, Mei Y, Thurmer DJ. *et al.* Rolled-up transparent microtubes as two-dimensionally confined culture scaffolds of individual yeast cells. *Lab Chip* 2009;**9**:263–8.

Huberts DH, Gonzalez J, Lee SS. *et al.* Calorie restriction does not elicit a robust extension of replicative lifespan in *Saccharomyces cerevisiae*. *Proc Natl Acad Sci USA* 2014;**111**:11727–31.

Huh D, Fujioka H, Tung Y-C. *et al.* Acoustically detectable cellular-level lung injury induced by fluid mechanical stresses in microfluidic airway systems. *Proc Natl Acad Sci USA* 2007;**104**:18886–91.

Huh D, Matthews BD, Mammoto A. *et al.* Reconstituting organ-level lung functions on a chip. *Science* 2010;**328**:1662–8.

Huh DD. A human breathing lung-on-a-chip. *Ann Am Thorac Soc* 2015;**12**:S42–44.

Ingham ER, Griffiths RP, Cromack K. Comparison of direct vs fumigation incubation microbial biomass estimates from ectomycorrhizal mat and non-mat soils. *Soil Biol Biochem* 1991;**23**:465–71.

Javanmard M, Babrzadeh F, Nyren P. *et al.* Improvement in cell capture throughput using parallel bioactivated microfluidic channels. *Biomed Microdevices* 2012;**14**:625–9.

Jiang F, Zhang L, Zhou J. *et al.* Arbuscular mycorrhizal fungi enhance mineralisation of organic phosphorus by carrying bacteria along their extraradical hyphae. *New Phytol* 2021;**230**:304–15.

Jo MC, Liu W, Gu L. *et al.* High-throughput analysis of yeast replicative aging using a microfluidic system. *Proc Natl Acad Sci USA* 2015;**112**:9364–9.

Jo MC, Qin L. Microfluidic platforms for yeast-based aging studies. *Small* 2016;**12**:5787–801.

Kadosh D. Regulatory mechanisms controlling morphology and pathogenesis in *Candida albicans*. *Curr Opin Microbiol* 2019;**52**:27–34.

Kahmann R, Bölker M. Self/nonself recognition in fungi: old mysteries and simple solutions. *Cell* 1996;**85**:145–8.

Kang DH, Kim SM, Lee B. *et al.* Stimuli-responsive hydrogel patterns for smart microfluidics and microarrays. *Analyst* 2013;**138**:6230–42.

Kang JH, Super M, Yung CW. *et al.* An extracorporeal blood-cleansing device for sepsis therapy. *Nat Med* 2014;**20**:1211–6.

Karnik R, Gu F, Basto P. *et al.* Microfluidic platform for controlled synthesis of polymeric nanoparticles. *Nano Lett* 2008;**8**:2906–12.

Kendrick B. *The Fifth Kingdom*. Indianapolis: Hackett Publishing, 2017.

Kim U-J, Shizuya H, de Jong PJ. *et al.* Stable propagation of cosmid sized human DNA inserts in an F factor based vector. *Nucleic Acids Res* 1992;**20**:1083–5.

Köhler JM, Cahill BP. *Micro-Segmented Flow*. Berlin Heidelberg: Springer, 2013.

Kohlmeier S, Smits THM, Ford RM. *et al.* Taking the fungal highway: mobilization of pollutant-degrading bacteria by fungi. *Environ Sci Technol* 2005;**39**:4640–6.

Kriel FH, Woollam S, Gordon RJ. *et al.* Numbering-up Y–Y microfluidic chips for higher-throughput solvent extraction of platinum(IV) chloride. *Microfluid Nanofluid* 2016;**20**:138.

Landeweert R, Hoffland E, Finlay RD. *et al.* Linking plants to rocks: ectomycorrhizal fungi mobilize nutrients from minerals. *Trends Ecol Evol* 2001;**16**:248–54.

Lee B, Jeong SG, Jin SH. *et al.* Quantitative analysis of yeast MAPK signaling networks and crosstalk using a microfluidic device. *Lab Chip* 2020;**20**:2646–55.

Lee KK, Labiscsak L, Ahn CH. *et al.* Spiral-based microfluidic device for long-term time course imaging of *Neurospora crassa* with single nucleus resolution. *Fung Genet Biol* 2016;**94**:11–14.

Lee MG, Shin JH, Bae CY. *et al.* Label-free cancer cell separation from human whole blood using inertial microfluidics at low shear stress. *Anal Chem* 2013;**85**:6213–8.

Lee PJ, Helman NC, Lim WA. *et al.* A microfluidic system for dynamic yeast cell imaging. *BioTechniques* 2008;**44**:91–95.

Lee SS, Avalos Vizcarra I, Huberts DH. *et al.* Whole lifespan microscopic observation of budding yeast aging through a microfluidic dissection platform. *Proc Natl Acad Sci USA* 2012;**109**:4916–20.

Lesage J, Timoumi A, Cenard S. *et al.* Accelerostat study in conventional and microfluidic bioreactors to assess the key role of residual glucose in the dimorphic transition of *Yarrowia lipolytica* in response to environmental stimuli. *New Biotechnol* 2021;**64**:37–45.

Li C, Hite Z, Warrick JW. *et al.* Under oil open-channel microfluidics empowered by exclusive liquid repellency. *Sci Adv* 2020;**6**:5333–48.

Liu L, Dalal CK, Heineike BM. *et al.* High throughput gene expression profiling of yeast colonies with microgel-culture Drop-seq. *Lab Chip* 2019;**19**:1838–49.

Liu P, Liu H, Yuan D. *et al.* Separation and enrichment of yeast *Saccharomyces cerevisiae* by shape using viscoelastic microfluidics. *Anal Chem* 2021;**93**:1586–95.

Liu P, Young TZ, Acar M. Yeast replicator: a high-throughput multiplexed microfluidics platform for automated measurements of single-cell aging. *Cell Rep* 2015;**13**:634–44.

Liu Y, Jiang X. Why microfluidics? Merits and trends in chemical synthesis. *Lab Chip* 2017;**17**:3960–78.

Lockery SR, Lawton KJ, Doll JC. *et al.* Artificial dirt: microfluidic substrates for nematode neurobiology and behavior. *J Neurophysiol* 2008;**99**:3136–43.

Luo C, Jiang L, Liang S. *et al.* High-throughput microfluidic system for monitoring diffusion-based monolayer yeast cell culture over long time periods. *Biomed Microdevices* 2009;**11**:981–6.

Luo C, Zhu X, Yu T. *et al.* A fast cell loading and high-throughput microfluidic system for long-term cell culture in zero-flow environments. *Biotechnol Bioeng* 2008;**101**:190–5.

McMullen M, Bergstrom G, De Wolf E. *et al.* A unified effort to fight an enemy of wheat and barley: fusarium head blight. *Plant Dis* 2012;**96**:1712–28.

Mafla-Endara PM, Arellano-Caicedo C, Aleklett K. *et al.* Microfluidic chips provide visual access to in situ soil ecology. *Commun Biol* 2021;**4**:889.

Maheshwari R. Nuclear behavior in fungal hyphae. *FEMS Microbiol Lett* 2005;**249**:7–14.

Martin G, Guggiari M, Bravo D. *et al.* Fungi, bacteria and soil pH: the oxalate–carbonate pathway as a model for metabolic interaction. *Environ Microbiol* 2012;**14**:2960–70.

Miller OJ, Harrak AE, Mangeat T. *et al.* High-resolution dose–response screening using droplet-based microfluidics. *Proc Natl Acad Sci USA* 2012;**109**:378.

Downloaded from https://academic.oup.com/femsre/advance-article/doi/10.1093/femsre/fuac039/6674677 by guest on 05 October 2022

Millet LJ, Aufrecht J, Labbe J. *et al.* Increasing access to microfluidics for studying fungi and other branched biological structures. *Fung Biol Biotechnol* 2019;**6**:1.

Minc N, Boudaoud A, Chang F. Mechanical forces of fission yeast growth. *Curr Biol* 2009;**19**:1096–101.

Moore TI, Chou CS, Nie Q. *et al.* Robust spatial sensing of mating pheromone gradients by yeast cells. *PLoS ONE* 2008;**3**:e3865.

Morrell M, Fraser VJ, Kollef MH. Delaying the empiric treatment of *Candida* bloodstream infection until positive blood culture results are obtained: a potential risk factor for hospital mortality. *Antimicrob Agents Chemother* 2005;**49**:3640–5.

Nandy SK, Srivastava RK. A review on sustainable yeast biotechnological processes and applications. *Microbiol Res* 2018;**207**:83–90.

Nicolau DV, Nicolau DV, Solana G. *et al.* Molecular motors-based micro- and nano-biocomputation devices. *Microelectron Eng* 2006;**83**:1582–8.

Nielsen JB, Hanson RL, Almughamsi HM. *et al.* Microfluidics: innovations in materials and their fabrication and functionalization. *Anal Chem* 2020;**92**:150–68.

Nieuwenhuis BPS, Billiard S, Vuilleumier S. *et al.* Evolution of uni- and bifactorial sexual compatibility systems in fungi. *Heredity* 2013;**111**:445–55.

Nobs JB, Maerkl SJ. Long-term single cell analysis of *S . pombe* on a microfluidic microchemostat array. *PLoS ONE* 2014;**9**:e93466.

Nowak MA, Sigmund K. Evolution of indirect reciprocity. *Nature* 2005;**437**:1291–8.

Ochs CJ, Kasuya J, Pavesi A. *et al.* Oxygen levels in thermoplastic microfluidic devices during cell culture. *Lab Chip* 2014;**14**:459–62.

Ogończyk D, Węgrzyn J, Jankowski P. *et al.* Bonding of microfluidic devices fabricated in polycarbonate. *Lab Chip* 2010;**10**:1324–7.

Ohnuki S, Nogami S, Ohya Y. A microfluidic device to acquire high-magnification microphotographs of yeast cells. *Cell Div* 2009;**4**:5.

Ohtani M, Saka A, Sano F. *et al.* Development of image processing program for yeast cell morphology. *J Bioinform Comput Biol* 2004;**01**:695–709.

Orner EP, Zhang P, Jo MC. *et al.* High-throughput yeast aging analysis for Cryptococcus (HYAAC) microfluidic device streamlines aging studies in *Cryptococcus neoformans*. *Commun Biol* 2019;**2**:256.

Paliwal S, Iglesias PA, Campbell K. *et al.* MAPK-mediated bimodal gene expression and adaptive gradient sensing in yeast. *Nature* 2007;**446**:46–51.

Paolicelli G, Luca A, Jose SS. *et al.* Using lung organoids to investigate epithelial barrier complexity and IL-17 signaling during respiratory infection. *Front Immunol* 2019;**10**:323.

Pardo B, Crabbé L, Pasero P. Signaling pathways of replication stress in yeast. *FEMS Yeast Res* 2016;**17**:27915243.

Park BS, Kye HG, Kim TH. *et al.* Continuous separation of fungal spores in a microfluidic flow focusing device. *Analyst* 2019;**144**:4962–71.

Park J, Wu J, Polymenis M. *et al.* Microchemostat array with small-volume fraction replenishment for steady-state microbial culture. *Lab Chip* 2013;**13**:4217–24.

Parniske M. Intracellular accommodation of microbes by plants: a common developmental program for symbiosis and disease?. *Curr Opin Plant Biol* 2000;**3**:320–8.

Pekin D, Skhiri Y, Baret J-C. *et al.* Quantitative and sensitive detection of rare mutations using droplet-based microfluidics. *Lab Chip* 2011;**11**:2156–66.

Pemberton LF. Preparation of yeast cells for live-cell imaging and indirect immunofluorescence. In: Smith JS, Burke DJ (eds.), *Yeast Genetics: Methods and Protocols*. New York: Springer, 2014, 79–90.

Pfaller MA, Castanheira M. Nosocomial candidiasis: antifungal stewardship and the importance of rapid diagnosis. *Med Mycol* 2016;**54**:1–22.

Piccolino M. Luigi Galvani and animal electricity: two centuries after the foundation of electrophysiology. *Trends Neurosci* 1997;**20**:443–8.

Piper PW. Long-lived yeast as a model for ageing research. *Yeast* 2006;**23**:215–26.

Podwin A, Janisz T, Patejuk K. *et al.* Towards microfluidics for mycology–material and technological studies on LOCs as new tools ensuring investigation of microscopic fungi and soil organisms. *Bull Pol Acad Sci Tech* 2021;**69**:e136212.

Prindle A, Liu J, Asally M. *et al.* Ion channels enable electrical communication in bacterial communities. *Nature* 2015;**527**:59–63.

Puerner C, Kukhaleishvili N, Thomson D. *et al.* Mechanical force-induced morphology changes in a human fungal pathogen. *BMC Biol* 2020;**18**:122.

Qiang L, Guo J, Han Y. *et al.* A novel anti *Candida albicans* drug screening system based on high-throughput microfluidic chips. *Sci Rep* 2019;**9**:8087.

Raj K, Chakraborty S. PDMS microfluidics: a mini review. *J Appl Polym Sci* 2020;**137**:48958.

Ramana Murthy MV, Mohan EVS, Sadhukhan AK. Cyclosporin-A production by *Tolypocladium inflatum* using solid state fermentation. *Process Biochem* 1999;**34**:269–80.

Read ND, Lichius A, Shoji J-y. *et al.* Self-signalling and self-fusion in filamentous fungi. *Curr Opin Microbiol* 2009;**12**:608–15.

Reinmets K, Dehkharghani A, Guasto JS. *et al.* Microfluidic quantification and separation of yeast based on surface adhesion. *Lab Chip* 2019;**19**:3481–9.

Rhodes CJ. The whispering world of plants: 'The wood wide web'. *Sci Prog* 2017;**100**:331–7.

Richter I, Uzum Z, Stanley CE. *et al.* Secreted TAL effectors protect symbiotic bacteria from entrapment within fungal hyphae. *bioRxiv*. 2020. https://doi.org/10.1101/2020.03.28.013177.

Richter L, Stepper C, Mak A. *et al.* Development of a microfluidic biochip for online monitoring of fungal biofilm dynamics. *Lab Chip* 2007;**7**:1723–31.

Ricicova M, Hamidi M, Quiring A. *et al.* Dissecting genealogy and cell cycle as sources of cell-to-cell variability in MAPK signaling using high-throughput lineage tracking. *Proc Natl Acad Sci USA* 2013;**110**:11403–8.

Roberts G. Evolution of direct and indirect reciprocity. *Proc Biol Sci* 2008;**275**:173–9.

Rodriguez-Morelos VH, Calonne-Salmon M, Bremhorst V. *et al.* Fungicides with contrasting mode of action differentially affect hyphal healing mechanism in *Gigaspora* sp. and *Rhizophagus irregularis*. *Front Plant Sci* 2021;**12**:642094.

Rosa P, Tenreiro S, Chu V. *et al.* High-throughput study of alpha-synuclein expression in yeast using microfluidics for control of local cellular microenvironment. *Biomicrofluidics* 2012;**6**:14109–141099.

Rowat AC, Bird JC, Agresti JJ. *et al.* Tracking lineages of single cells in lines using a microfluidic device. *Proc Natl Acad Sci USA* 2009;**106**:18149–54.

Ryley J, Pereira-Smith OM. Microfluidics device for single cell gene expression analysis in *Saccharomyces cerevisiae*. *Yeast* 2006;**23**:1065–73.

Schmieder SS, Stanley CE, Rzepiela A. *et al.* Bidirectional propagation of signals and nutrients in fungal networks via specialized hyphae. *Curr Biol* 2019;**29**:217–28.e214.

Downloaded from https://academic.oup.com/femsre/advance-article/doi/10.1093/femsre/fuac039/6674677 by guest on 05 October 2022

Schmitt CL, Tatum ML. The Malheur National Forest location of the world's largest living organism. 2008. https://upload.wikimedia.org/wikipedia/commons/1/1a/The_Malheur_National_Forest_Location_of_the_World%27s_Largest_Living_Organism_%28The_Humongous_Fungus%29_-_fsbdev3_033146.pdf. (28 April 2022, date last accessed).

Schnepf A, Jones D, Roose T. Modelling nutrient uptake by individual hyphae of arbuscular mycorrhizal fungi: temporal and spatial scales for an experimental design. *Bull Math Biol* 2011;**73**:2175–200.

Scott TW, Kiers ET, Cooper GA. *et al.* Evolutionary maintenance of genomic diversity within arbuscular mycorrhizal fungi. *Ecol Evol* 2019;**9**:2425–35.

Show PL, Oladele KO, Siew QY. *et al.* Overview of citric acid production from *Aspergillus niger*. *Front Life Sci* 2015;**8**:271–83.

Shrestha J, Razavi Bazaz S, Aboulkheyr Es H. *et al.* Lung-on-a-chip: the future of respiratory disease models and pharmacological studies. *Crit Rev Biotechnol* 2020;**40**:213–30.

Simard SW, Beiler KJ, Bingham MA. *et al.* Mycorrhizal networks: mechanisms, ecology and modelling. *Fung Biol Rev* 2012;**26**:39–60.

Singh R, Brockgreitens J, Saiapina O. *et al.* Microbial separation from a complex matrix by a hand-held microfluidic device. *Chem Commun* 2017;**53**:10788–91.

Smith SE, Read DJ. *Mycorrhizal Symbiosis*. Amsterdam: Elsevier Science, 2010.

Srisom K, Tittabutr P, Teaumroong N. *et al.* New method for arbuscular mycorrhizal fungus spore separation using a microfluidic device based on manual temporary flow diversion. *Mycorrhiza* 2020;**30**:789–96.

Stanley CE, Grossmann G, Solvas XC. *et al.* Soil-on-a-Chip: microfluidic platforms for environmental organismal studies. *Lab Chip* 2016;**16**:228–41.

Stanley CE, Shrivastava J, Brugman R. *et al.* Dual-flow-RootChip reveals local adaptations of roots towards environmental asymmetry at the physiological and genetic levels. *New Phytol* 2018;**217**:1357–69.

Stanley CE, Stockli M, van Swaay D. *et al.* Probing bacterial-fungal interactions at the single cell level. *Integr Biol* 2014;**6**:935–45.

Stockli M, Morinaka BI, Lackner G. *et al.* Bacteria-induced production of the antibacterial sesquiterpene lagopodin B in *Coprinopsis cinerea*. *Mol Microbiol* 2019;**112**:605–19.

Stratz S, Verboket PE, Hasler K. *et al.* Cultivation and quantitative single-cell analysis of *Saccharomyces cerevisiae* on a multifunctional microfluidic device. *Electrophoresis* 2018;**39**:540–7.

Strom NB, Bushley KE. Two genomes are better than one: history, genetics, and biotechnological applications of fungal heterokaryons. *Fung Biol Biotechnol* 2016;**3**:4.

Sun Q, Li J, Finlay RD. *et al.* Oxalotrophic bacterial assemblages in the ectomycorrhizosphere of forest trees and their effects on oxalate degradation and carbon fixation potential. *Chem Geol* 2019;**514**:54–64.

Sun Y, Tayagui A, Garrill A. *et al.* Fabrication of in-channel high-aspect ratio sensing pillars for protrusive force measurements on fungi and oomycetes. *J Microelectromech S* 2018;**27**:827–35.

Sun Y, Tayagui A, Garrill A. *et al.* Microfluidic platform for integrated compartmentalization of single zoospores, germination and measurement of protrusive force generated by germ tubes. *Lab Chip* 2020;**20**:4141–51.

Sutera SP, Skalak R. The history of Poiseuille's Law. *Annu Rev Fluid Mech* 1993;**25**:1–20.

Tang W, Jiang D, Li Z. *et al.* Recent advances in microfluidic cell sorting techniques based on both physical and biochemical principles. *Electrophoresis* 2019;**40**:930–54.

Tawfik DS, Griffiths AD. Man-made cell-like compartments for molecular evolution. *Nat Biotechnol* 1998;**16**:652–6.

Taylor RJ, Falconnet D, Niemistö A. *et al.* Dynamic analysis of MAPK signaling using a high-throughput microfluidic single-cell imaging platform. *Proc Natl Acad Sci USA* 2009;**106**:3758.

Tayyrov A, Stanley CE, Azevedo S. *et al.* Combining microfluidics and RNA-sequencing to assess the inducible defensome of a mushroom against nematodes. *BMC Genomics* 2019;**20**:243.

Tesla N. Valvular conduit. Google Patents. 1920.

Thomson DD, Wehmeier S, Byfield FJ. *et al.* Contact-induced apical asymmetry drives the thigmotropic responses of *Candida albicans* hyphae. *Cell Microbiol* 2015;**17**:342–54.

Tian W-C, Finehout E. *Microfluidics for Biological Applications*. Boston: Springer, 2009.

Tomaiuolo R, Ruocco A, Salapete C. *et al.* Activity of mannose-binding lectin in centenarians. *Aging Cell* 2012;**11**:394–400.

Trivedi V, Doshi A, Kurup GK. *et al.* A modular approach for the generation, storage, mixing, and detection of droplet libraries for high throughput screening. *Lab Chip* 2010;**10**:2433–42.

Tu R, Zhang Y, Hua E. *et al.* Droplet-based microfluidic platform for high-throughput screening of Streptomyces. *Commun Biol* 2021;**4**:647.

U.S. Department of Energy. *Global annual ethanol production by country or region*. 2020. https://afdc.energy.gov/data/10331. (28 April 2022, date last accessed).

Uehling JK, Entler MR, Meredith HR. *et al.* Microfluidics and metabolomics reveal symbiotic bacterial-fungal interactions between *Mortierella elongata* and *Burkholderia* include metabolite exchange. *Front Microbiol* 2019;**10**:2163.

Uhlendorf J, Miermont A, Delaveau T. *et al.* Long-term model predictive control of gene expression at the population and single-cell levels. *Proc Natl Acad Sci USA* 2012;**109**:14271–6.

Uppuluri P, Khan A, Edwards JE. *Candida albicans*: cellular and molecular biology. In: Prasad R (ed.), *Current Trends in Candidiasis*. Berlin: Springer, 2017,5–23.

van der Heijden MGA. Arbuscular mycorrhizal fungi as support systems for seedling establishment in grassland. *Ecol Lett* 2004;**7**:293–303.

Vasudev A, Kaushik A, Jones K. *et al.* Prospects of low temperature co-fired ceramic (LTCC) based microfluidic systems for point-of-care biosensing and environmental sensing. *Microfluid Nanofluid* 2012;**14**:683–702.

Vo T, Shah SB, Choy JS. *et al.* Chemotropism among populations of yeast cells with spatiotemporal resolution in a biofabricated microfluidic platform. *Biomicrofluidics* 2020;**14**:014108.

Voets L, De La Providencia IE, Declerck S. Glomeraceae and Gigasporaceae differ in their ability to form hyphal networks. *New Phytol* 2006;**172**:185–8.

Wagner O, Thiele J, Weinhart M. *et al.* Biocompatible fluorinated polyglycerols for droplet microfluidics as an alternative to PEG-based copolymer surfactants. *Lab Chip* 2016;**16**:65–69.

Walsh G. Biopharmaceutical benchmarks 2014. *Nat Biotechnol* 2014;**32**:992–1000.

Wang G, Bjork SM, Huang M. *et al.* RNAi expression tuning, microfluidic screening, and genome recombineering for improved protein production in *Saccharomyces cerevisiae*. *Proc Natl Acad Sci USA* 2019;**116**:9324–32.

Wang M, Thomas N, Jin H. Cross-kingdom RNA trafficking and environmental RNAi for powerful innovative pre- and post-harvest plant protection. *Curr Opin Plant Biol* 2017;**38**:133–41.

Wang P, Yuan S, Yang N. *et al.* The collection method for crop fungal spores based on an efficient microfluidic device. *Aerosol Air Qual Res* 2020;**20**:72–79.

Downloaded from https://academic.oup.com/femsre/advance-article/doi/10.1093/femsre/fuac039/6674677 by guest on 05 October 2022

Warmink JA, Nazir R, Corten B. *et al.* Hitchhikers on the fungal highway: the helper effect for bacterial migration via fungal hyphae. *Soil Biol Biochem* 2011;**43**:760–5.

Watterson WJ, Tanyeri M, Watson AR. *et al.* Droplet-based high-throughput cultivation for accurate screening of antibiotic resistant gut microbes. *Elife* 2020;**9**:e56998.

Webster J, Weber R. *Introduction to Fungi*. New York: Cambridge University Press, 2007.

Whittaker RH. New concepts of kingdoms of organisms. *Science* 1969;**163**:150–60.

Wick LY, Remer R, Würz B. *et al.* Effect of fungal hyphae on the access of bacteria to phenanthrene in soil. *Environ Sci Technol* 2007;**41**:500–5.

Wingfield MJ, De Beer ZW, Slippers B. *et al.* One fungus, one name promotes progressive plant pathology. *Mol Plant Pathol* 2012;**13**:604–13.

Worrich A, Stryhanyuk H, Musat N. *et al.* Mycelium-mediated transfer of water and nutrients stimulates bacterial activity in dry and oligotrophic environments. *Nat Commun* 2017;**8**:15472.

Wu WK, Liang CK, Huang JZ. MEMS-based flow cytometry: microfluidics-based cell identification system by fluorescent imaging. In: *Proceedings of the 26th Annual International Conference of the IEEE Engineering in Medicine and Biology Society*. 2004. San Francisco, CA: IEEE. https://doi.org/10.1109/IEMBS.2004.1403741

Xia N, Hunt TP, Mayers BT. *et al.* Combined microfluidic-micromagnetic separation of living cells in continuous flow. *Biomed Microdevices* 2006;**8**:299–308.

Xiang N, Wang J, Li Q. *et al.* Precise size-based cell separation via the coupling of inertial microfluidics and deterministic lateral displacement. *Anal Chem* 2019;**91**:10328–34.

Xie J, Miao Y, Shih J. *et al.* Microfluidic platform for liquid chromatography– tandem mass spectrometry analyses of complex peptide mixtures. *Anal Chem* 2005;**77**:6947–53.

Xie Z, Zhang Y, Zou K. *et al.* Molecular phenotyping of aging in single yeast cells using a novel microfluidic device. *Aging Cell* 2012;**11**:599–606.

Yaginuma K, Aoki W, Miura N. *et al.* High-throughput identification of peptide agonists against GPCRs by co-culture of mammalian reporter cells and peptide-secreting yeast cells using droplet microfluidics. *Sci Rep* 2019;**9**:10920.

Yan S, Zhang J, Yuan D. *et al.* Hybrid microfluidics combined with active and passive approaches for continuous cell separation. *Electrophoresis* 2017;**38**:238–49.

Yoon No D, Lee KH, Lee J. *et al.* 3D liver models on a microplatform: well-defined culture, engineering of liver tissue and liver-on-a-chip. *Lab Chip* 2015;**15**:3822–37.

You X, Kallies R, Kühn I. *et al.* Phage co-transport with hyphal-riding bacteria fuels bacterial invasion in a water-unsaturated microbial model system. *ISME J* 2022;**16**:1275–83.

Young EW, Berthier E, Guckenberger DJ. *et al.* Rapid prototyping of arrayed microfluidic systems in polystyrene for cell-based assays. *Anal Chem* 2011;**83**:1408–17.

Yu R, Jo MC, Dang W. Measuring the replicative lifespan of *Saccharomyces cerevisiae* using the HYAA microfluidic platform. In: Curran SP (ed.), *Aging: Methods and Protocols*. New York: Springer, 2020, 1–6.

Yung CW, Fiering J, Mueller AJ. *et al.* Micromagnetic-microfluidic blood cleansing device. *Lab Chip* 2009;**9**:1171–7.

Zaky AS, Tucker GA, Daw ZY. *et al.* Marine yeast isolation and industrial application. *FEMS Yeast Res* 2014;**14**:813–25.

Zhang B, Korolj A, Lai BFL. *et al.* Advances in organ-on-a-chip engineering. *Nat Rev Mater* 2018a;**3**:257–78.

Zhang L, Feng G, Declerck S. Signal beyond nutrient, fructose, exuded by an arbuscular mycorrhizal fungus triggers phytate mineralization by a phosphate solubilizing bacterium. *ISME J* 2018b;**12**:2339–51.

Zhang L, Zhou J, George TS. *et al.* Arbuscular mycorrhizal fungi conducting the hyphosphere bacterial orchestra. *Trends Plant Sci* 2022;**27**:402–11.

Zhang SX, Carroll KC, Lewis S. *et al.* Multicenter evaluation of a PCR-based digital microfluidics and electrochemical detection system for the rapid identification of 15 fungal pathogens directly from positive blood cultures. *J Clin Microbiol* 2020;**58**:e02096–02019.

Zhang Y, Luo C, Zou K. *et al.* Single cell analysis of yeast replicative aging using a new generation of microfluidic device. *PLoS ONE* 2012;**7**:e48275.

Zheng W, Jiang X. Synthesizing living tissues with microfluidics. *Acc Chem Res* 2018;**51**:3166–73.

Zheng Z, Chen Y, Li WH. *et al.* Study on droplet microfluidic chips for drug screening against *Candida albicans*. *Acta Pharm Sinic* 2017;**52**:1884–9.

Zou K, Ren DS, Ou-Yang Q. *et al.* Using microfluidic devices to measure lifespan and cellular phenotypes in single budding yeast cells. *J Vis Exp* 2017;**121** 55412.

Downloaded from https://academic.oup.com/femsre/advance-article/doi/10.1093/femsre/fuac039/6674677 by guest on 05 October 2022

Lab on a Chip

PAPER

View Article Online
View Journal

Check for updates

Cite this: DOI: 10.1039/d3lc00859b

AMF-SporeChip provides new insights into arbuscular mycorrhizal fungal asymbiotic hyphal growth dynamics at the cellular level†

Felix Richter,[a] Maryline Calonne-Salmon,[b] Marcel G. A. van der Heijden,[cde] Stéphane Declerck[b] and Claire E. Stanley *[a]

Arbuscular mycorrhizal fungi (AMF) form symbiotic associations with the majority of land plants and deliver a wide range of soil-based ecosystem services. Due to their conspicuous belowground lifestyle in a dark environment surrounded by soil particles, much is still to be learned about the influence of environmental (*i.e.*, physical) cues on spore germination, hyphal morphogenesis and anastomosis/hyphal healing mechanisms. To fill existing gaps in AMF knowledge, we developed a new microfluidic platform – the *AMF-SporeChip* – to visualise the foraging behaviour of germinating *Rhizophagus* and *Gigaspora* spores and confront asymbiotic hyphae with physical obstacles. In combination with timelapse microscopy, the fungi could be examined at the cellular level and in real-time. The *AMF-SporeChip* allowed us to acquire movies with unprecedented visual clarity and therefore identify various exploration strategies of AMF asymbiotic hyphae. We witnessed tip-to-tip and tip-to-side hyphal anastomosis formation. Anastomosis involved directed hyphal growth in a "stop-and-go" manner, yielding visual evidence of pre-anastomosis signalling and decision-making. Remarkably, we also revealed a so-far undescribed reversible cytoplasmic retraction, including the formation of up to 8 septa upon retraction, as part of a highly dynamic space navigation, probably evolved to optimise foraging efficiency. Our findings demonstrated how AMF employ an intricate mechanism of space searching, involving reversible cytoplasmic retraction, branching and directional changes. In turn, the *AMF-SporeChip* is expected to open many future frontiers for AMF research.

Received 10th October 2023,
Accepted 15th February 2024

DOI: 10.1039/d3lc00859b

rsc.li/loc

Introduction

Arbuscular mycorrhizal fungi (AMF) are a group of soil fungi belonging to the phylum Glomeromycota, forming a symbiosis with *ca.* 70–80% of all terrestrial plants. Laying the foundation for every soil-based ecosystem on earth,[1–3] the fungus colonises root cells (*i.e.*, the intraradical mycelium – IRM) and vastly extends into the soil (from 82 to 111 m cm^{-3} in prairie and 52 to 81 m cm^{-3} in ungrazed pasture[4]) to constitute the extraradical mycelium (ERM). This network of hyphae supplies the host plant with essential nutrients such as P and N, but also Zn, Cu and Fe,[5] and receives between 4 and 20% of the total carbon synthesised by plants in return.[6,7] Furthermore, this immensely important mutualism increases the ecosystem's overall resilience and facilitates plant productivity and plant diversity.[8] Moreover, AMF are not host specific and can interconnect different plant species forming so-called common mycorrhizal networks (CMNs).[9]

Despite their importance, much is still unknown about the influence of environmental cues on spore germination, hyphal morphogenesis, anastomosis/hyphal healing mechanisms in AMF, for example, with inoculation of crops with AMF spores in the field often failing.[10–12] This is primarily due to the fact that the study of AMF and other soil-dwellers at the cellular and sub-cellular level proves to be challenging. The opacity of soil makes it impossible to observe these organisms in their natural habitat and in real-time, rendering classic microscopy-based approaches either black-box experiments (*e.g.*, end-point microscopy) or very simplified with limited resolution.[13] The emergence, in recent decades, of *in vitro* cultivation techniques on root organs or whole plants has permitted to increase our knowledge on, for example, hyphal growth dynamics, three-dimensional architecture, anastomosis formation and hyphal

[a] *Department of Bioengineering, Imperial College London, London, SW7 2AZ, UK. E-mail: claire.stanley@imperial.ac.uk; Web: https://www.imperial.ac.uk/people/claire.stanley; Tel: +44 (0)20 75942893*
[b] *Laboratory of Mycology, Earth and Life Institute, Université catholique de Louvain, B-1348 Louvain-la-Neuve, Belgium*
[c] *Agroecology and Environment Research Division, Agroscope, 8046 Zurich, Switzerland*
[d] *Department of Evolutionary Biology and Environmental Studies, University of Zurich, 8057 Zurich, Switzerland*
[e] *Institute of Environmental Biology, Utrecht University, 3584 CS Utrecht, The Netherlands*

† Electronic supplementary information (ESI) available. See DOI: https://doi.org/10.1039/d3lc00859b

healing mechanisms.[14–16] However, the lack of vertical confinement and background of a phytagel medium restricts the microscopy quality. The membrane methods introduced by Giovannetti *et al.*[17] which involve sandwiching extraradical mycelium between Millipore or cellophane membranes[17,18] provide a confined two-dimensional system that allows for the study of cytoplasmic streaming, anastomosis formation as well as nuclear behaviours at the hyphal level. This two-dimensional confinement of the mycelium widely eliminated background hyphae, which hampered former studies, and thus improved microscopy precision and resolution. For the imaging, pieces were cut out of the sandwich cultures and results obtained from time-point microscopy. The method was further employed for the study of single spores and asymbiotic hyphae[19] where timelapse images of cytoplasmic streaming through freshly formed anastomoses were acquired.[20] In order to obtain real-time growth videos of exploring hyphae and live interactions with the environment or other hyphae, however, a system confined vertically and limited laterally, having perfect transparency, the ability to hold nutritious medium and trap spores was deemed necessary. Moreover, a major aim of this study was to explore the space-searching behaviour of AMF asymbiotic hyphae, which requires the presence of physical obstacles within the experimental platform. Although Giovannetti *et al.*[17] introduced micro-threads of different materials and diameters (10 μm to 350 μm) into their experimental system to act as non-host roots, the ability to create an array of microstructures having a defined shape and size is needed, however, to simulate more generic obstacles and particles found in soil. Therefore, a new microfluidic tool was developed to study AMF spores and asymbiotic hyphae in a visual, spatially and temporally resolved manner.

Microfluidic technology development for fungal research is a considerably young field, especially for studying hyphal behaviour and dynamics (reviewed in Richter *et al.*[21]). Being the first to explore this path, Nicolau and colleagues set out to study hyphal exploration strategies in micro-mazes, particularly with the filamentous model fungus *Neurospora crassa*.[22–25] In recent years, this was developed further to accommodate more complex studies on filamentous fungi. Thomson *et al.* and Puerner *et al.*[26,27] for instance, utilised the deformability of poly(dimethylsiloxane) (PDMS) structures to measure forces exerted by growing hyphae and Couttenier *et al.*[28] designed a device to study the effect of shear flow on hyphal bending. Further, microfluidic platforms have been developed to investigate interactions with other biological agents, such as bacteria,[29–32] nematodes,[33] bacteriophages[34] as well as fungal–fungal interactions.[35] However, only two single studies involving AMF have been published, which focus on spore sorting and extraradical hyphae.[36]

The use of microfluidic technology also allows to design microenvironments that mimic certain aspects of the natural habitat. Mafla-Endara *et al.*,[37] for example, created a soil-like microcosm featuring different geometries, species from various kingdoms, as well as water, air and soil particles as a substrate. In the course of that study, they observed how fungal hyphae help other organisms populate air-filled pockets in soil, hypothesising a water film in the mycosphere to be responsible for the transport. Further, gradients or niches of chemicals can be implemented for hyphal chemotaxis studies.[38] Ranking from highest to lowest in terms of complexity, field experiments, pot cultures and *in vitro* systems are all important experimental platforms for AMF research. Crucially, however, the microfluidics approach fills a significant experimental "gap", providing a system with a high controllability of the experimental process and precise imaging, which allows for tailored patterning of the physical, as well as chemical, environment.

Herein, we introduce a new microfluidic device, termed the *AMF-SporeChip*, that was specifically designed to accommodate spores of *Rhizophagus* species for the study of spore germination events and exploration dynamics of asymbiotic hyphae for the first time. The devices were manufactured in-house using the elastomeric polymer PDMS, which allows AMF hyphae to be confined to a single monolayer. Different micro-structures were included within the device design to mimic natural obstacles in soil (*e.g.*, mineral particles, roots *etc.*), enabling hyphal dynamics to be explored upon confrontation with physical obstacles. Owing to the material's near-perfect optical transparency, precise live imaging microscopy could be performed in real-time. To validate the compatibility of the device with AMF, we compared the germination and hyphal growth dynamics of 3 different *Rhizophagus* strains, both on-chip and on-plate, as well as demonstrating different germination behaviours between these strains. The flexibility of the system was also highlighted by (i) presenting a slightly modified device that can accommodate another AMF species, namely *Gigaspora margarita*, (ii) introducing fluorescent dyes (FM4-64 and calcofluor white) into the microchannels for staining hyphae and (iii) demonstrating the suitability of the *AMF-SporeChip* for monitoring anastomosis formation in *Rhizophagus*. As a key result, we present an interesting and so far undescribed insight concerning reversible cytoplasmic retraction within asymbiotic hyphae, which amongst hyphal branching and directional changes, we consider part of their space searching strategy.

Experimental

Chicory root and AMF culture

Three AMF strains, *i.e.*, *Rhizophagus irregularis* MUCL 41833, *Rhizophagus irregularis* MUCL 43194 and *Rhizophagus intraradices* MUCL 49410, were provided by the Glomeromycota *in vitro* collection (GINCO, Belgium). The fungi were maintained in bi-compartmented Petri plates on Ri T-DNA transformed roots of chicory (*Cichorium intybus* L.). The roots were provided by the Glomeromycota *in vitro* collection (GINCO, Belgium) and cultivated on modified Strullu and Romand (MSR) medium,[39] stored at 27 °C in the dark in an inverted position and subcultured monthly. Spores of *Gigaspora margarita* BEG 34 were produced in pots with *Plantago lanceolate* as host.[39,40] For

This journal is © The Royal Society of Chemistry 2024

more information and media preparation see the ESI† (Methods).

Microfluidic device fabrication

The device designs were drawn in AutoCAD 2022 (Autodesk) and checked for correct structuring using KLayout.[41] The design was then printed to create a Mylar® film photolithography mask by Micro Lithography Services Ltd., UK. Using these photomasks, two-layered master moulds were manufactured in a clean room (detailed in ESI† Methods).

To facilitate removal of the PDMS layer from the master moulds when casting devices, the wafers were silanised, *i.e.*, made more hydrophobic. Therefore, the masters were carefully cleaned with an air gun and placed into a desiccator. In the centre of the desiccator, a glass vial containing 100 μl chlorotrimethylsilane (redistilled ≥99%, Sigma Aldrich, UK; hazardous substance, consult safety data sheet of supplier) was placed. Using a vacuum pump, the desiccator was evacuated for 1 min and then closed off. The master moulds were left to react with the chlorotrimethylsilane for 1 h.

Using the master moulds, microfluidic devices can be produced on demand. All of the following steps were conducted in a laminar flow hood. Firstly, PDMS is mixed in a 10 : 1 ratio of base to curing agent (Sylgard 184, Dow Corning, USA) and degassed for *ca.* 45 min under vacuum in a desiccator. The master mould was fitted into a frame, the PDMS poured onto it and cured overnight at 70 °C. The PDMS was then removed from the mould, cut into slabs consisting of 2 device designs and holes for the in- and outlets were punched using a cork borer (Ø = 3 mm; Syneo, USA). To remove monomer remnants and to disinfect, the PDMS slabs were washed in 0.5 M NaOH and then 70% ethanol, rinsing with sterile water between washing steps, and dried at 70 °C for 1 h. Next, the PDMS slabs as well as glass-bottomed Petri dishes (Ø dish = 35 mm, Ø glass = 23 mm; Fluorodish, World Precision Instruments, Germany) were plasma activated using a Zepto plasma cleaner (Diener Electronic, Germany; vacuum pressure 0.75 mbar, power 50%, 1 min) and bonded together, resulting in each Petri dish holding 2 devices. Exploiting the transient hydrophilicity of PDMS right after the plasma treatment, devices were filled with liquid hyphal medium (see ESI† Methods). Before use, devices were re-sterilised under UV light (254 nm) for 30 min.

Device inoculation

The spore material of *R. irregularis* MUCL 41833 and MUCL 43194, as well as *R. intraradices* MUCL 49410 was obtained directly from the above-described bi-compartmented cultures (see ESI† Methods, AMF culture). All subsequent steps were performed in a sterilised laminar flow hood, under a stereoscope (EZ4 D, Leica, Germany). Using sterilised dissection needles, spore-bearing hyphae were extracted from a culture plate that is at least 3 months old and transferred into a 90 mm Petri dish filled with liquid MSR medium lacking sucrose, termed MSR(−) (see ESI† Methods). Sterile tattoo needles (03 tight liner, pre-soldered, Barber DTS, UK) were used to cut the mycelium into smaller pieces containing 1–5 spores. Then, 5–6 of these spore pieces were transferred into each inlet of a device using a pipette (Pipetman G, 200 μl, Gilson, USA) that was set to 21 μl (to avoid overfilling of the inlets). A syringe (Henke-Ject, Luer Lock, 5 ml, HenkeSassWolf, Germany) connected to AlteSil High Strength Tubing (bore: 1.00 mm, wall: 1.00 mm, total diameter: 3 mm; Altec Extrusions Limited, UK) with a blunt tip syringe needle (1.28 mm, Shintop, China) and filled with liquid MSR(−) medium was carefully plugged into the inlet and spores were manually flushed into the device until all spores were inside of the channel and/or no more spores were coming from the inlet.

Spores of *Gi. margarita* were picked up using a pipette set to 20 μl and transferred into the inlet of the device. As the spores are detectable with the naked eye, it is easy to check visibly that only a single spore is in the pipette tip. The spores were then flushed into the device using the same method previously described for spores of *Rhizophagus*.

For staining experiments with fluorescent dyes, calcofluor white (to a final concentration of 0.5 μM) and FM4-64 (to a final concentration of 5 μM) were added to autoclaved liquid MSR(−) medium, sterile filtered and used to fill the microchannels as described above.

Image analysis and quantification

Time-lapse images (used to produce growth and germination videos) as well as time-point large images (used for measuring growth rates) were obtained with two inverted microscopes (Eclipse Ti-U and Eclipse Ti-2, Nikon; ESI† Methods). Microscopy images were processed and analysed with Image J (Fiji).[42] To measure hyphal growth, the segmented line and measurement tool were used. The measured lengths were grouped into 5 intervals; 0.1–0.4 mm, 0.5–1.0 mm, 1.1–2.0 mm, 2.1–3.0 mm and >3 mm, and represented as stacked column diagrams using Origin 2021 (OriginLab). To account for the variation in number of spores loaded into the devices, the results were normalised. Therefore, the number of germination sites (instead of the number of spores) was determined and the absolute value of counts divided by the number of germination sites. For the hyphal growth behaviour, we counted sites where a germination within 14 days of inoculation occurred as germination sites. For calculation of the germination rates, we defined any site where usually a germination occurs from, *i.e.*, cut ends of hyphal remnants, as a germination site. Germinations were counted at the last day, day 14, of the experiment. For determining significant differences in the data points for germination rates and spore distribution within devices, 1-way ANOVA was performed in Origin 2021 (OriginLab).

$$\text{Normalised count} = \frac{\text{Total count of hyphae}}{\text{Number of germination sites}}$$

Results

Design and operation of the *AMF-SporeChip*

The *AMF-SporeChip* was designed to accommodate spores of different *Rhizophagus* strains, to enable high resolution dynamic imaging of spore germination and hyphal morphogenesis events at the cellular level. A two-dimensional (2D) sketch of the microchannel architecture is displayed in Fig. 1a, which features an inlet (Ø = 3 mm) connected to a "primary spore trapping region" (microchannel height = 100 μm) that then transitions into an "investigation zone" (microchannel height = 10 μm), with a total device length of 12.4 mm. The "investigation zone" also constitutes a "secondary spore trapping region". Fig. 1b and c illustrate an overview of the *AMF-SporeChip*, where the change in microchannel height can be clearly evidenced *via* the addition of a fluorescein-containing solution, as well as how tubing is fitted into the device inlet for the introduction of AMF spores. The step change in microchannel height results in trapping of the AMF spores (Fig. 1d), which usually have a diameter on the order of 10–100 μm for *R. irregularis* MUCL 41833, 20–160 μm for *R. irregularis* MUCL 43194 and 20–120 μm for *R. intraradices* MUCL 49410 (measured, Fig. S1†), and importantly allows the much smaller, asymbiotic hyphae (Ø = 2–12 μm; measured, Fig. S2†) to access (*i.e.*, grow into) and be confined within the investigation zone in the *z*-direction.

As PDMS is an elastomeric polymer and therefore flexible in nature, the microchannel widens slightly upon applying positive pressure when using a syringe to introduce spores into the *AMF-SporeChip*.[43] Hence, some spores can be pushed into the investigation zone. Upon removing the applied pressure, the microchannel resumes its original state, thus trapping spores between top and bottom of the microchannel. Approximately 50% of introduced spores were trapped in the primary spore trapping region and 40% in the first half of the secondary spore trapping region, *i.e.*, just after the transition in channel height; a small number of spores (*ca.* 10%) got flushed into the second half of the secondary spore trapping region (Fig. 1f). The distribution in the individual device depends on many factors, such as spore size, size of the spore-cluster, length of hyphal remnants/subtending hyphae, applied pressure for device loading (due to manual loading) *etc.* A significant difference in the trapping behaviour could be observed between the obstacle-type devices and the lane-type devices (Fig. 1f). Due to the larger contact area between PDMS and glass bottom near the channel height transition, the expandability of the PDMS channels was reduced in the lane-type devices, thus making it more difficult for spores to enter the investigation zone. For spores of *Gi. margarita* (Ø = 380–580 μm; measured, Fig. S1†), the microchannel height of the inlet and spore trapping region was adjusted from 100 μm to *ca.* 350 μm. The aforementioned flexibility of the PDMS allows spores bigger than 350 μm to be accommodated within the trapping region of the microdevice, however not in the investigation zone.

The investigation zone contains an array of obstacles designed to provoke hyphal collision events (Fig. 1a). One advantage of the *AMF-SporeChip* is that the investigation zone can be modified in a bespoke manner to accommodate different types of physical obstacles that vary in their shape and size (*i.e.*, obstacle-type devices, Fig. 1e), or even possess lanes containing dead-ends or bottlenecks (*i.e.*, lane-type devices, Fig. 1e). With our choice of obstacles, we aimed to confront AMF with a variety of physical challenges that may be experienced within a soil environment. The obstacle-type devices varied in form, ranging from shapes that are either closed (circle) or open (Pac-Man, open-box, restricted open-box), therefore affording different internal angles and numbers of contact interfaces and thus offering increased or reduced chances for hyphae to "escape" from an obstacle (Fig. S3†). As expected, the restricted open-box and the dead-end lane designs seemed to be the most challenging to escape from, however, the hyphal behaviours varied widely, some hyphae managed to escape from a restricted open-box obstacle, while others failed to circumnavigate the circular shapes, and a clear pattern or obstacle dependence could not be determined. For measuring germination and growth dynamics, we utilised all designs equally to investigate how AMF hyphal tips react upon physical collision with their environment. The array of interspaced obstacles provided an even inflow of medium and spore suspension, allowing for a balanced distribution of spores within the device, while giving plenty of opportunity for physical collisions.

Monitoring spore germination and asymbiotic hyphal growth

To demonstrate the functionality of the *AMF-SporeChip*, a germination assay was conducted with (i) *R. irregularis* MUCL 41833, (ii) *R. irregularis* MUCL 43194 and (iii) *R. intraradices* MUCL 49410. Since visual representation and a detailed description of spore germination within these species are scarce, illustrative timelapse images of the germination process have been provided herein (Fig. 2, Movies S1–S3†), acquired from the examination of a total of 600 spores. When comparing the different strains, we observed quite distinct differences in germination and hyphal growth patterns as well as spore shape, despite being closely related. While *R. irregularis* MUCL 41833 and *R. intraradices* MUCL 49410 have a nearly perfect circular spore shape in our study, *R. irregularis* MUCL 43194 spores came in various, elongated shapes (Fig. 2 and S1†). Generally, it was observed that *R. irregularis* MUCL 41833 germinated with a single hyphal branch, as observed in Fig. 2a, with occasionally up to 4 branches emerging from the germination site. Subsequent hyphal growth was found to be relatively linear and straight. In contrast, *R. irregularis* MUCL 43194 spores tended to branch more frequently at or shortly after the site of germination (*i.e.*, with typically 3–8 hyphae) as illustrated in Fig. 2b. Moreover, these asymbiotic hyphae possessed a curly and highly branched morphology. *R. intraradices* MUCL 49410 behaves similarly to *R. irregularis* MUCL 43194, with 3–6 hyphal branches emerging on average at or shortly after the germination site (Fig. 2c). Another interesting observation included an active discharge of phase-bright cellular contents

This journal is © The Royal Society of Chemistry 2024

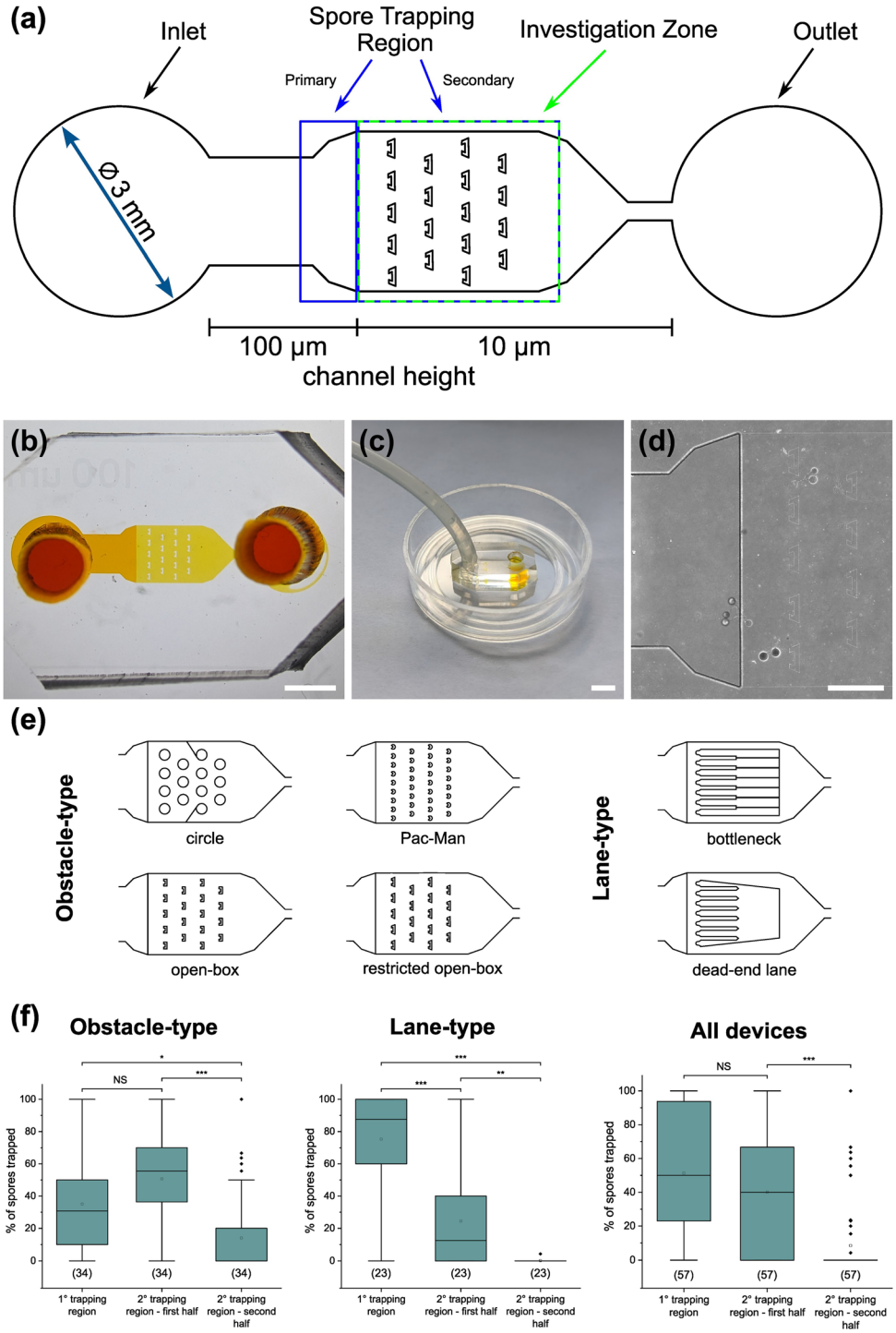


Fig. 1 Design of the *AMF-SporeChip*. (a) Two-dimensional schematic of the microfluidic device showing the dimensions and structure of the spore trapping region and investigation zone containing micron-sized obstacles. (b) Real life image of the device filled with 66 mM fluorescein solution to highlight the channels and the change in channel height. (c) The *AMF-SporeChip* fitted with tubing at the device inlet for the introduction of spores. The outer diameter of the Petri dish is 35 mm. (d) Brightfield image of the transition zone (microchannel height step-change) with trapped spores of *Rhizophagus irregularis* MUCL 41833. (e) Different geometries of the investigation zone of the *AMF-SporeChip*, including obstacle-type and lane-type structures. (f) Box-plots showing the percentage of spores trapped in each of the different trapping regions for lane-type and obstacle-type devices as well as all design types. Upper and lower whiskers represent the largest observation smaller or equal to the upper and lower percentile plus 1.5 × interquartile range, respectively. Squares indicate the means and the line the median. Data points beyond the whisker range (outliers) are plotted as diamonds. Significant differences according to one-way ANOVA are indicated with asterisks for p values <0.001 (***), <0.01(**) and <0.05 (*), as well as NS for no significant difference. The values in parentheses indicate the number of sample-points, *i.e.*, the number of microfluidic devices analysed. The total number of spores analysed was 260 for the lane-type devices and 473 for the obstacle-type devices. For the secondary trapping region – second half, the medians are 0 for lane-type devices as well as for "All devices", hence the number of values above 0 was insufficient to draw a box and were therefore categorised as outliers. Scale bars: (b) 2 mm; (c) 5 mm and (d) 500 µm.

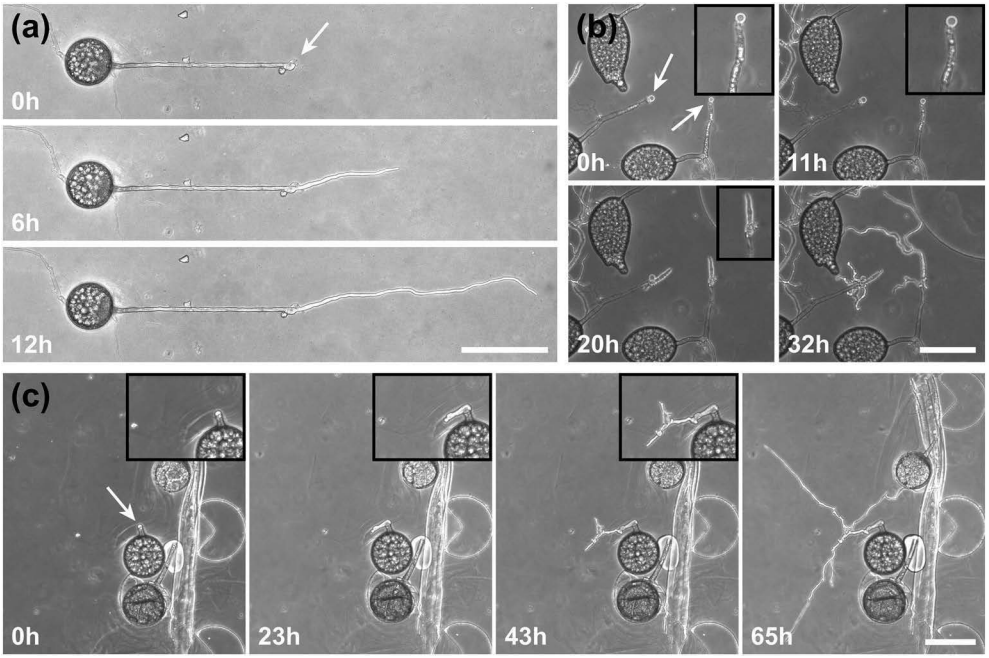


Fig. 2 AMF germination on chip. Time-series illustrating the germination process of (a) *Rhizophagus irregularis* MUCL 41833, (b) *Rhizophagus irregularis* MUCL 43194 and (c) *Rhizophagus intraradices* MUCL 49410. In (c), debris from the root-organ culture can be observed. White arrows indicate the germination site, with inset boxes in (b) and (c) illustrating an enlarged region of the germination event. Scale bars: 100 μm.

preceding germination (see Fig. 2b and Movie S2†). Occasionally, an internal collapse and emptying of the spore can be witnessed after a few days, after which the storage vesicles are ejected suddenly in one final load of cellular contents and nutrients into the attached hyphae (see Movie S4†). On several occasions, spore formation in asymbiotic hyphae, as reported by Dalpé *et al.*,[44] was observed (see Movie S5†).

For a quantitative analysis of growth dynamics on-chip in comparison to on-plate, hyphae of all three species were imaged and measured as described in the Experimental section. The results are illustrated in Fig. 3. For *R. irregularis* MUCL 41833, the on-chip measurements indicated a constant increase in spore germination. This is illustrated by the orange-coloured bar segments, which represent freshly germinated and short hyphae with a length of 0.1–0.4 mm, as well as a similarly constant growth of hyphae to lengths of 0.5–1.0 mm (green) and few hyphae to lengths of 1.1–3.0 mm (purple and yellow) and longer (>3 mm, blue). For *R. irregularis* MUCL 43194, a greater increase in the number of hyphae was observed over time on-chip, reaching a plateau after day 4, with few hyphae then growing longer. *R. intraradices* MUCL 49410 showed a constant increase in the number of hyphae over 7 days, similar to *R. irregularis* MUCL 43194, however with barely any hyphae growing further than 1.0 mm and only a few having lengths between 0.5–1.0 mm.

Growth on-plate generally yielded longer, fast-growing hyphae, reaching lengths of up to 20 mm, with slightly smaller total numbers of germination events, compared to on-chip. The trends illustrated by the stacked column charts within the first 7 days, which constitutes the main experimental phase used for all subsequent studies, however, are very much comparable and similar between on-chip and on-plate assay. Between day 7 and day 14, there was little growth and few germination events observed on-chip for *R. irregularis* MUCL 41833 (ratio of normalised count for day 14/7 = 1.082), while on-plate showed both elongating hyphae and new germinations (ratio of normalised count for day 14/7 = 1.263). For *R. irregularis* MUCL 43194, there were barely any further germination events observed, both on-chip and on-plate (on-chip ratio of normalised count for day 14/7 = 1.017; on-plate ratio of normalised count for day 14/7 = 1.047), with no further hyphal growth on-chip but further elongation on-plate. With *R. intraradices* MUCL 49410, there were numerous fresh germination events observed after 7 days, for both on-chip and on-plate experiments (on-chip ratio of normalised count for day 14/7 = 1.437; on-plate ratio of normalised count for day 14/7 = 1.549). Few hyphae were found to elongate further after 7 days on-plate, but not on-chip. The spore germination rates on-chip were found to be equally high between the three strains (no statistically significant differences), with means of 90.9% (*R. irregularis* MUCL 41833), 88.3% (*R. irregularis* MUCL 43194) and 92.5% (*R. intraradices* MUCL 49410). Germination rates on-plate could not be determined with this method. Due to the lack of confinement and thus focus, ungerminated germination sites could not be detected with certainty, highlighting the advantage of the *AMF-SporeChip*.

To highlight the versatility of the device, we modified the *AMF-SporeChip* to accommodate spores of *Gi. margarita*. Compared to the model organism *Rhizophagus* sp., as well as other AMF, *Gi. margarita* differs mainly in its macroscopic spore size. Further, a different anastomosis behaviour has

This journal is © The Royal Society of Chemistry 2024

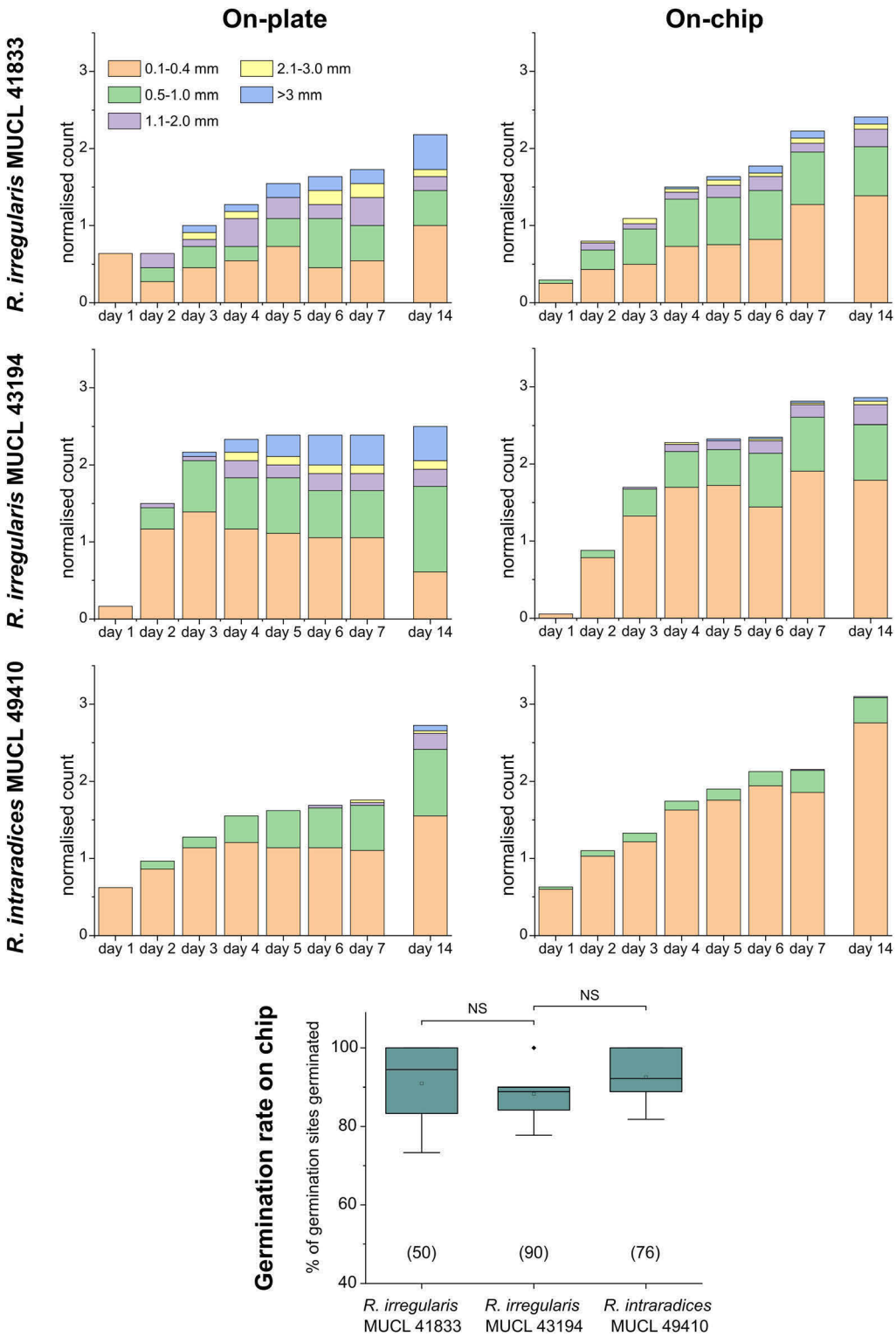


Fig. 3 Hyphal growth assay on-chip and on-plate. Stacked column charts showing the growth behaviour of *Rhizophagus irregularis* MUCL 41833, *Rhizophagus irregularis* MUCL 43194 and *Rhizophagus intraradices* MUCL 49410 in the *AMF-SporeChip* and on MSR(–) culture plates for comparison. Hyphal lengths were measured using ImageJ, normalised (number of germination sites was determined, and the absolute value of counts divided by the number of germination sites) and categorised in 5 length sections. For the hyphal growth behaviour, we counted sites where a germination within 14 days of inoculation occurred as germination sites. 6 devices with 40–60 germination sites in total per strain were used and 10–20 germination sites were found per plate. For calculation of the germination rates, we defined any site where usually a germination occurs from, *i.e.*, cut ends of hyphal remnants, as a germination site, which are indicated in parentheses below the boxes. Box-plot shows germination rates for all three AMF strains on-chip. Upper and lower whiskers represent the largest observation smaller or equal to the upper and lower percentile plus 1.5 × interquartile range, respectively. Squares indicate the means and the line the median. Data points beyond the whisker range (outliers) are plotted as diamonds. No significant differences between the results according to one-way ANOVA were found.

been documented.[15] By increasing the height of the microchannel in the spore trapping region from 100 to 350 μm, *Gi. margarita* spores were trapped successfully with subsequent germination and asymbiotic hyphal growth observed within the microchannels (Fig. 4). Upon encountering dead-end channels, the leading hypha bent and tracked the channel wall back in direction of the inlet, then branched in three different sites, *ca.* 350 μm, 720 μm and 1280 μm downstream from the hyphal tip. The hyphae then arrested growth and finally retracted the cytoplasm in a gradual manner, forming very pronounced septa (see Fig. 4 and Movie S6†).

"Stop-and-go" growth strategy prior to anastomosis formation

A highlight of the *AMF-SporeChip* involves the ability to observe fusion of hyphae to form a new cellular continuum, namely anastomosis. We witnessed both "tip-to-tip" and "tip-to-side" connections between hyphae originating from distinct spores, as well as from the same individuum. A representative depiction of anastomosis events observed within the *AMF-SporeChip* is shown in Fig. 5. The timelapse series presented show *R. irregularis* MUCL 43194 only; however, anastomosis events were also observed in *R. irregularis* MUCL 41833 and *R. intraradices* MUCL 49410. In Fig. 5a and b (and Movie S6†), a tip-to-tip anastomosis event can be observed. The hyphae approach each other from opposing directions with occasional arrestation of growth and readjustment of the growth direction. Fig. 5c quantifies the growth of both hyphae over a 21 h period. The left hypha approached the other hypha in 4 main growth phases. Both duration, as well as distance covered, decreased from the beginning to the end of data recording, with a growth rate of *ca.* 0.3 μm min^{-1} for the first two growth phases and 0.1 μm min^{-1} for the latter two. The growth phases were interrupted by arrestation of growth for *ca.* 3 h, then *ca.* 4 h and before the final growth phase <2 h. Meanwhile, the right hypha barely grows at all, covering a total distance of *ca.* 12 μm in the 21 h time period. In spite of having plenty of space to explore, and thus avoid one other, they specifically target the other hypha, indicating a clear signalling and searching prior to anastomosing (Fig. 5c and Movie S7†).

In Fig. 5d (and Movie S8†), a tip-to-tip anastomosis occurs in this instance, however, between a germination that is in progress and a hypha, rather than between two fully developed hyphae. The hypha approaching from the lower portion of the microscope image targets the end of an older hypha, which is just germinating, and fuses with the germination site. Following fusion, it can be clearly observed how a continuum is formed. Between timepoint 40 h and 80 h, cellular contents (phase-bright) are being pushed from the direction of the spore into the attached hypha. From this material, new branches are formed, concluding the process of unification. In Fig. 5e (and Movie S9†), a tip-to-side anastomosis can be observed. A hypha approaches from the bottom left corner of the image and after 4 h attaches laterally to the other hypha. Almost immediately, the

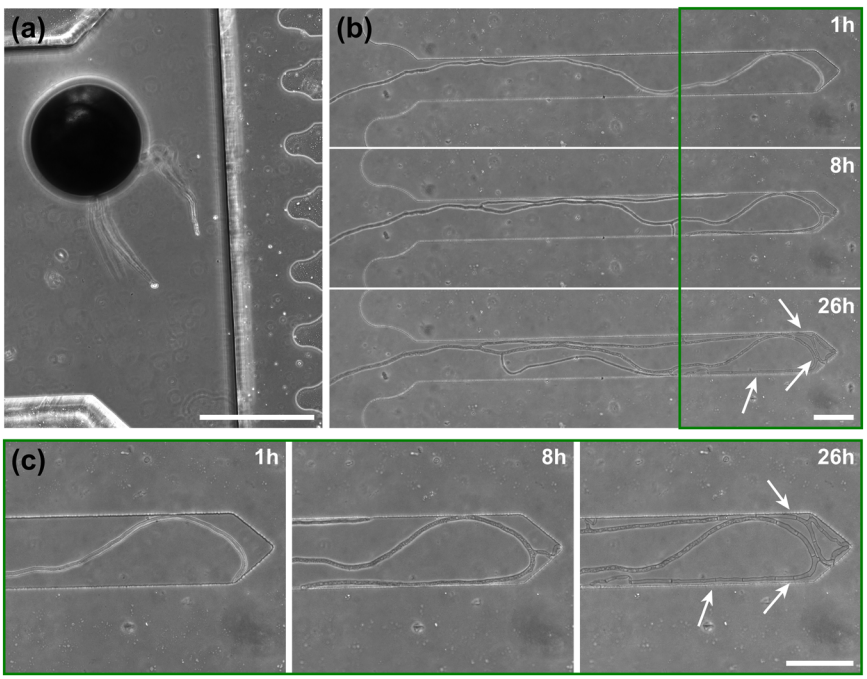


Fig. 4 *Gigaspora margarita* growing in a microfluidic device. Shown are (a) a spore of *Gi. margarita* trapped in the inlet and (b) a timelapse series of a *Gi. margarita* hypha growing into dead-end channels. When the hypha hits the wall, it bends, branches off in several positions and starts retracting cytoplasm from trapped tips. White arrows show examples of very pronounced septa formed in the retraction process. (c) Magnifications of the dead-end of the microchannel. White arrows indicate examples of septa. Image (a) was taken 2 days before the start of the timelapse series in (b). Scale bars: (a) 500 μm, (b and c) 100 μm.

This journal is © The Royal Society of Chemistry 2024

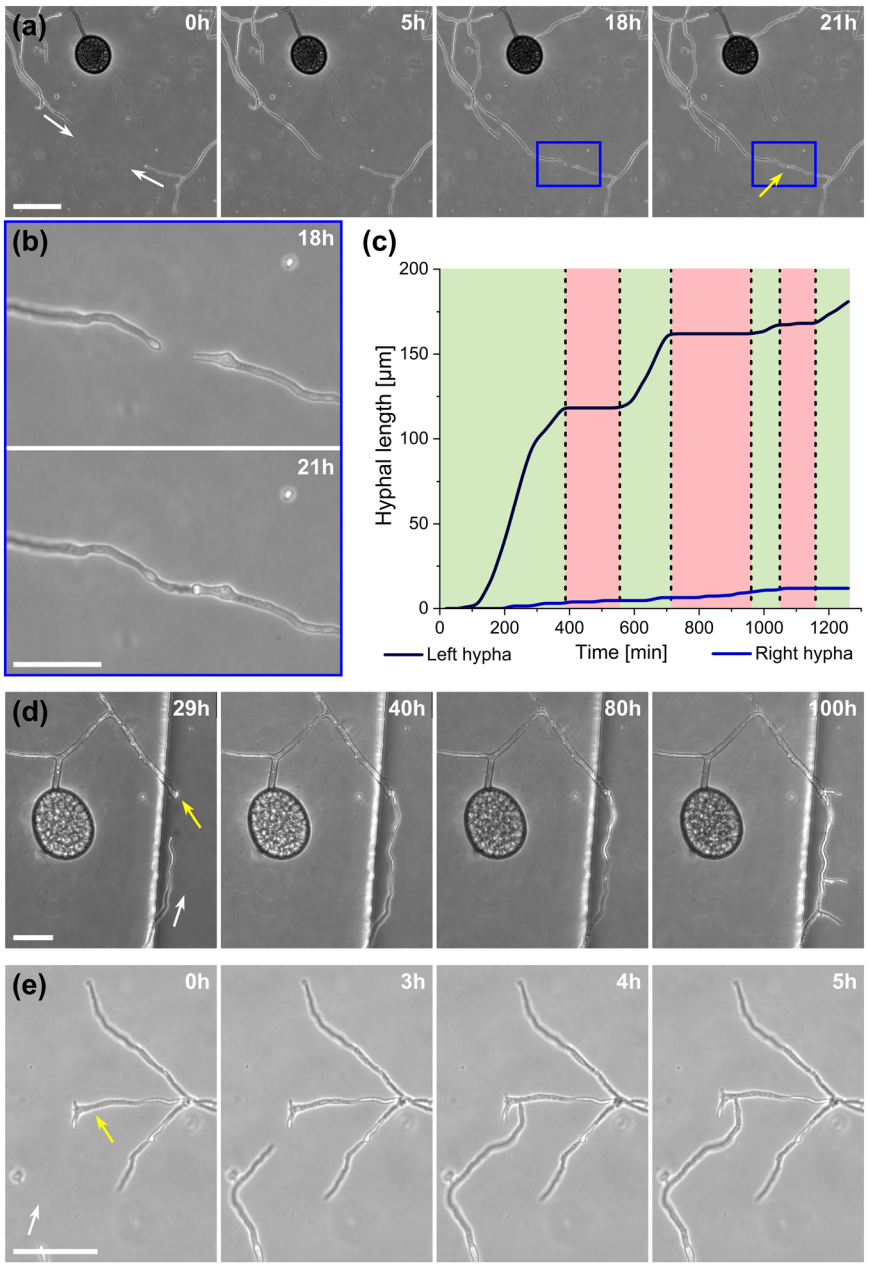


Fig. 5 Anastomosis formation of *Rhizophagus irregularis* MUCL 43194 in microfluidic device. (a) Two hyphae approaching one other and forming a tip-to-tip anastomosis. (b) An enlarged image of the moment just before contact and upon contact in (a). (c) Graph highlighting the growth of both hyphae before fusing, which illustrates the "stop-and-go" growth strategy of the left hypha, with the hypha on the right-hand side barely growing at all. (d) Another example of a tip-to-tip anastomosis event where, however, the hypha coming from the bottom of the image attaches to an older hypha, which is just about to germinate. Further, it can be observed how they from a continuum, with cellular contents (phase-bright) being pushed into the bottom hypha from the direction of the spore, with subsequent branching. (e) A tip-to-side anastomosis. Yellow arrows indicate the anastomosis site, white arrows indicate the growth direction of anastomosing hyphae. Scale bars: (a), (d) and (e) 50 µm; (b) 25 µm.

hyphae fuse and a cytoplasmic continuum is visible in the site of contact.

Hyphal behaviour upon encountering physical obstacles on the microscale

Inclusion of an array of obstacles within the investigation zone of the *AMF-SporeChip* afforded new insights into AMF spore hyphal growth dynamics. Specifically, the following was observed upon collision of *R. irregularis* MUCL 41833 hyphae with the restricted open-box obstacle (see Fig. 6 and Movie S10†). A hypha grew into the corner of the obstacle, *i.e.*, a dead-end, resulting in the hypha bending slightly and arresting growth. It then retracted the cytoplasm from the trapped tip and subsequently formed a septum *ca.* 40 µm downstream from the hyphal tip. The septa was then breached, and cytoplasm

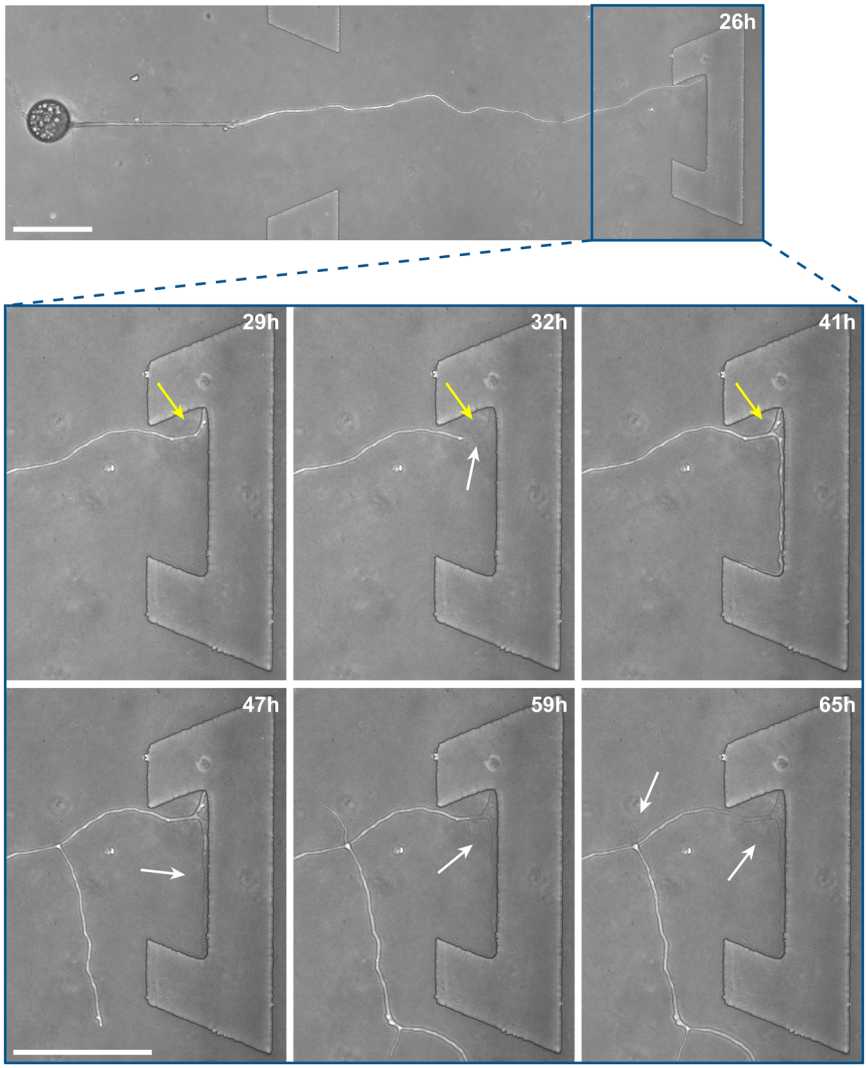


Fig. 6 Hyphal collision event in the *AMF-SporeChip*. Here, a time-series of images illustrates the dynamic behaviour of a *Rhizophagus irregularis* MUCL 41833 hypha upon interaction with an obstacle in the microfluidic device. Timepoint 0 h was defined as the point of spore germination. The hypha grows into the obstacle and becomes trapped, after which a series of dynamic, reversible cytoplasmic retraction and branching events occur in several positions at varying time points. Yellow arrows indicate the "reversible" cytoplasmic retraction, white arrows indicate "empty" hyphae following cytoplasmic retraction. Scale bars: 100 μm.

pumped back into the trapped hyphal tip followed by a new branch emerging shortly behind the tip. This new branch then grew towards the opposite corner of the obstacle and proceeded to track the edge of the obstacle for a few hours, with its tip now pointed towards the spore it originated from. It then stopped growing and retracted its cytoplasm with at least 2 visible septa formed downstream. A new hyphal branch emerged from a position outside the obstacle, followed by a second branch growing from the same branching point but into the opposite direction a few hours later. Eventually the fungus stopped growing to the left-hand side (with respect to initial growth direction) soon after and retracted further cytoplasm from this and the original, trapped branch and continued growing towards the right-hand side (with respect to initial growth direction), forming a bifurcation around hour 57 after the start of the experiment.

Interestingly, we observed several instances of reversible cytoplasmic retraction in both *R. irregularis* strains, not only with obstacles but also in open space. The number of septa formed upon retraction and septa breached upon reversal of the retraction varied (see Fig. 7a and Movie S11†), with up to 8 septa formed in a single retraction process and between 1 and 2 septa breached in the reversal phase. When the number of septa formed was higher than the number of septa breached, the retraction was not reversed all the way back to the hyphal tip and was hence incomplete. The retraction process varies not only in the number of septa formed/breached but also in the temporal dynamics (see Fig. 7b and c). Single retraction steps, *i.e.*, distance between tip and first septum or between septa, were found to be as fast as 30 min, however, can take up to 10 h. Similarly, some hyphae were observed to pause for up to 12 h between

This journal is © The Royal Society of Chemistry 2024

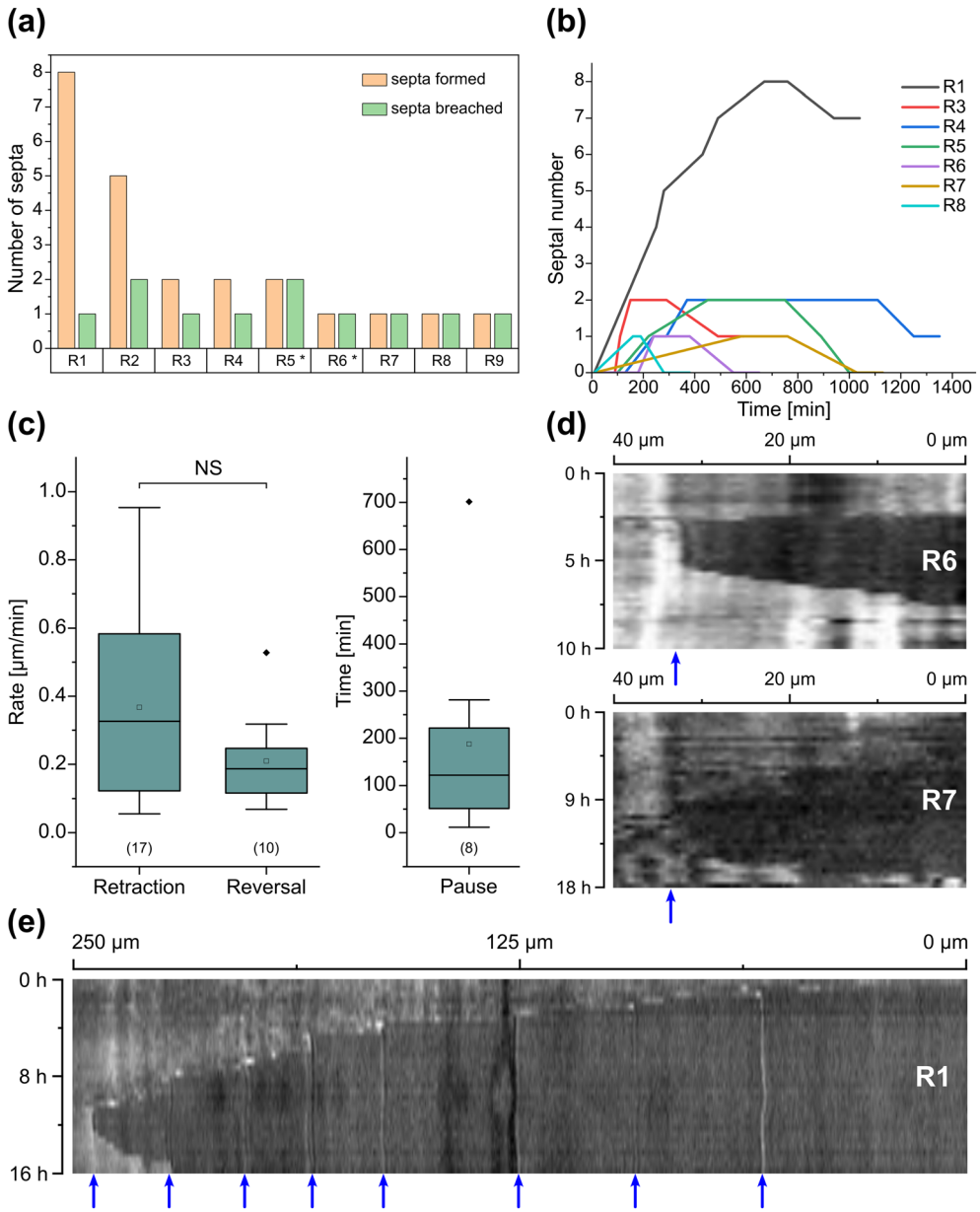


Fig. 7 Reversible cytoplasmic retraction in the *AMF-SporeChip*. (a) Column chart illustrating the number of septa formed and breached in the process of complete, as well as incomplete, reversible cytoplasmic retraction (R) upon interaction with obstacles (two instances, marked with asterisks; R5 and R6) as well as in open space (seven instances; R1–4 and R7–9). (b) Line graph showing temporal dynamics of the reversible retraction, highlighting timings for cytoplasmic retraction, pausing and reversal for the retraction events detailed in (a); for retraction R2 and R9, no sufficient temporally resolved data could be extracted. (c) Box-plots showing rates extracted from (b) for cytoplasmic retraction and reversal of the retraction as well as duration of pauses between retraction and reversal. Upper and lower whiskers represent the largest observation smaller or equal to the upper and lower percentile plus 1.5 × interquartile range, respectively. Squares indicate the means and the line the median. Data points beyond the whisker range (outliers) are plotted as diamonds. No significant difference between the rate of retraction and reversal according to one-way ANOVA was found, indicated as NS. The values in parentheses indicate the number of sample-points, *i.e.*, the number of events analysed. (d) Kymograph analysis of retraction R6 and R7 and (e) kymograph analysis of retraction R1. Blue arrows indicate septa. All retraction events were found with *Rhizophagus irregularis* MUCL 41833, except R3 and R9, which were found with *Rhizophagus irregularis* MUCL 43194.

retraction and reversal, while some reverse the process within minutes. The reversal was slightly less variable, with timings between 1 and 3 h. Retraction and reversal rates were calculated using the distance between two septa or tip and first septum, which was on average 26.3 ± 11.8 µm. The retraction (mean = 0.4 ± 0.3 µm min^{-1}) and reversal rates (mean = 0.2 ± 0.1 µm min^{-1}) were not found to be significantly different, however, a stronger variation in the rate of retraction can be observed. The kymographs in Fig. 7d and e visualise the entire retraction process in further detail for retractions R1, R6 and R7. It shows a strong asymmetry between retraction and reversal rate with a much

faster retraction and a slower reversal in R6, contrasted by a very slow retraction and relatively fast reversal for R7. In the kymograph for R1, it can be observed how the first retraction steps occur within a very short time frame, despite covering relatively long distances, while the last steps of the retraction with only little distance to cover take much longer (which is the case for the reversal in the last septum).

Besides this novel observation, further observations were made, described before in studies with other fungi, such as "hit-and-split" (see Movie S12†), tracking (*e.g.*, in Fig. 6 and Movie S10†) as well as numerous instances of irreversible cytoplasmic retraction in both obstacle and open space (*e.g.*, in Fig. 6 and Movie S11†). Growth arrest in hyphae was often found to coincide with cytoplasmic retraction within a few hours. However, in a few cases we found hyphae to freeze for long periods of time (tens of hours) before finally retracting their cytoplasm (see Movie S13†) or hitting an obstacle or a wall but continuing to grow and thus bending and gradually pushing itself away from the obstacle as if not recognising it (see Movie S14†).

To further highlight certain sub-cellular structures and characterise the nature of the hyphae observed in the cytoplasmic retraction, we employed two different fluorescent dyes, namely calcofluor white (CFW) and FM4-64 for end point staining. In Fig. 8a, all hyphae are visible in the phase contrast microscopy image, regardless of their developmental stage, however with differences observable, *i.e.*, "normal" phase-bright hyphae and "empty" phase-dark hyphae, the latter of which is akin to what is observed after cytoplasmic retraction. Staining with the chitin specific dye, calcofluor white, reveals all hyphae observed in the phase contrast image (Fig. 8b). In Fig. 8c only some hyphae are visible; here, the dye FM4-64 is employed, which stains lipid bilayers, *i.e.*, membranes and organelles. Thus, only viable hyphae that contain all cellular contents remain detectable. Cytoplasmic retraction is followed by sequential formation of septa, which separate the cytoplasm-filled portion of a hypha from the empty portion. These septa are visible in phase-dark hyphae in the phase contrast image and are particularly pronounced in the CFW staining.

Discussion

The *AMF-SporeChip* provides high-resolution dynamic imaging of AMF in defined environments

Here, we present the first microfluidic device of its kind, namely the *AMF-SporeChip*, designed to accommodate AMF spores for studying germination and the dynamic behaviour of asymbiotic hyphal growth at the cellular level. The device was specifically designed to trap spores of *Rhizophagus* and later adapted for *Gi. margarita*. The trapping relied on two main aspects, the first being simply a difference in channel height, which kept about 50% of *Rhizophagus* spores out of the investigation zone, while allowing the much smaller hyphae to grow in. Secondly, the high flexibility of PDMS allowed *ca.* 40% of the *Rhizophagus* spore population to be trapped in the first half of the secondary trapping region. This trait of PDMS is actively utilised for cell trapping in microfluidics, mainly with yeast cells,[44–46] but has also been used to measure force exerted by fungal-like Oomycete hyphal tips.[47] Here, the two trapping mechanisms facilitate a reliable introduction of spores into and even distribution within the devices. The application of microfluidic technologies for the study of yeast has received plenty of attention in the last two decades,[21] yet for other types of fungi, this technique is still very new. Indeed, its utility has been demonstrated only in a handful of studies,[24,48,49] which focussed mainly on examining the space-searching behaviour of filamentous fungi or interactions between fungi and other microorganisms,[29,33,35] but has never before considered AMF spore germination or asymbiotic hyphal growth.

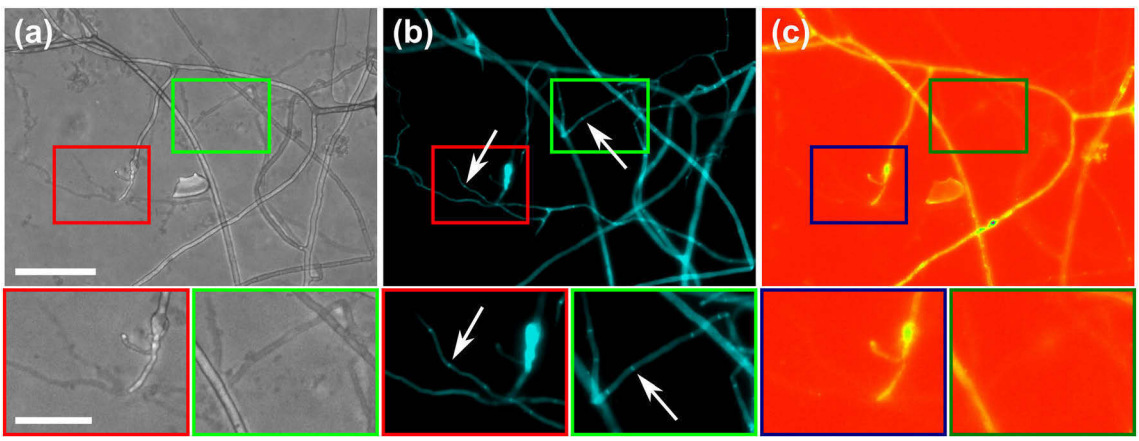


Fig. 8 Differential staining of vital and empty hyphae. The images displayed refer to the same region of interest within the *AMF-SporeChip* and represent: (a) phase contrast, (b) DAPI and (c) TRITC channels. The fluorescent dyes used in this study include calcofluor white (CFW), which stains chitin in the cell walls and FM4-64, staining lipid bilayers. White arrows indicate two exemplary hyphae which were emptied, with pronounced septa as artefacts of gradual retraction of cytoplasm. The images were edited using ImageJ/Fiji. The lookup tables "cyan" (b) and "spectrum" (c) were applied to improve the visibility of fluorescence intensity. Scale bar: 100 μm, 50 μm in zoomed-in images.

This journal is © The Royal Society of Chemistry 2024

Importantly, our devices featured obstacles within the investigation zone to mimic (micro) structures (*i.e.*, soil microaggregates) in their natural habitat by blocking their growth path and provoking physical collisions. The various designs provided hyphae with differing opportunities to interact with or escape from an obstacle; the "restricted open-box" or the "dead-end lane" designs forced hyphae to arrest growth or change direction entirely, for instance. For AMF asymbiotic hyphae, this behaviour has never been studied before. Investigating how the fungal mycelium adapts to the physical conditions in soil is important for understanding a fungus' lifestyle and eventually utilising this knowledge for potential applications in agriculture and horticulture/restoration as well as for the preservation of natural ecosystems.

Microfluidics-assisted imaging yields detailed visuals of spore germination in real-time

Germination of AMF spores has been described in the literature,[51] however, high-resolution visual material is scarcely available. To demonstrate the strength of the microfluidic approach and as proof-of-concept, we captured high resolution timelapse videos of spores of the three *Rhizophagus* strains studied, as well as with *Gi. margarita*.

Interestingly, distinct germination and branching patterns were observed between *R. irregularis* MUCL 41833 and MUCL 43194 (despite being two strains of the same species, and besides differences in shape and size), which suggest different exploration strategies. While *R. irregularis* MUCL 41833 germinated with 1–4 rather straight hyphae from the germination site, *R. irregularis* MUCL 43194 germinated with between 3–8 curly hyphae, which readily branched again shortly after the germination. Measuring hyphal elongation every 24 h for a week further revealed that *R. irregularis* MUCL 41833 has a growth pattern which is relatively balanced between new germination and hyphal elongation, whereas *R. irregularis* MUCL 43194 tended to germinate a lot more over the first 3 days and then resulted in elongation of some of these hyphae, corroborating the visually observed growth behaviour in both strains. It appears this strain first establishes a base around the spore and then starts exploring with single runner hyphae, while *R. irregularis* MUCL 41833 does not hesitate and starts exploring straight away with runner hyphae shooting randomly from the spore. The physiological stage (*i.e.*, spore age) was not taken into consideration. For both strains, hyphal elongation proceeded after day 7 but rarely were any new germinations observed. *R. intraradices* MUCL 49410 behaves in a similar manner to *R. irregularis* MUCL 43194, with typically 3–6 curly and branched hyphae emerging from one germination site, which, however, barely ever extended beyond 1 mm. Fresh germination events on the other hand continued to occur numerously even beyond day 7 until the end of the experiment.

For all three strains studied, the on-plate results followed closely the findings from the on-chip experiments, with the exception of increased hyphal elongation on-plate. This difference in growth is a pre-described observation, which occurs in microfluidic devices and could be explained by two observations: (i) the microchannels are saturated with culture medium, *i.e.*, the fungi are submersed in liquid, while on-plate they grow in an environment that has a solid phytagel base, with a liquid film on top as well as direct contact with air; (ii) the hyphae are physically confined inside microchannels, which has been suspected to influence hyphal growth.[52] Filamentous fungi are known to possess mechanosensory properties[53] allowing them to sense the confinement and adapt their growth accordingly. This sensing happens both on a mechanical level, upon direct contact with the wall or the obstacle, as well as chemical level, where the fungus recognises the surface functionalisation.[54] Overall, we can conclude from our results, however, that the germination and growth behaviour in the *Rhizophagus* strains is very much comparable between on-chip and on-plate and hence our microdevices are suitable to study these fungi. Further, the devices were modified to accommodate the much bigger spores of *Gi. margarita* and it was demonstrated that they, too, can germinate in the microdevice, illustrating the flexibility of our platform.

Anastomosis formation involves directed growth with readjustments in a "stop-and-go" manner

Another phenomenon implicating hyphal space searching strategies is anastomosis formation. Filamentous fungi are able to connect their hyphae with another individuum of the same strain or in a "self–self" manner (*i.e.*, hyphae from the same individuum).[55,56] Even interspecies anastomoses have been reported.[57] Fungi anastomose to interconnect and expand their mycelial network for exploring and foraging, to exchange nutrients[58] and genetic material,[59] to heal damages in the hyphal network[15] or even to form traps to capture nematodes.[60] Here, anastomoses were observed between different individuals of the same strain as well as self–self, and formed in a tip-to-tip or tip-to-side manner. Our high-resolution imaging approach, which affords a relatively large confined observation area, provided real-time videos of the entire anastomosis process in asymbiotic hyphae. This allowed us to image hyphal approach from a wide angle through to complete fusion, extending experimental opportunities detailed by de la Providencia *et al.*[15] and Voets *et al.*[61] for intraradical hyphae. As such, the *AMF-SporeChip* revealed how two hyphae hesitantly approached one other from opposing directions in a stop-and-go manner, occasionally halting to readjust growth direction. It is clear that these hyphae actively target each other since there is plenty of space for avoidance, which suggests an underlying signalling and decision-making that leads to tropism for one other. This was further corroborated by the occasional observation of hyphal contact that did not lead to successful anastomosis, indicated by cytoplasmic retraction and septation as earlier described by Giovannetti *et al.*[62] In certain filamentous fungi, it has been reported that there are

even specialised hyphae for fusion.[63,64] Large scale follow-up studies are now needed to explore this further.

Dynamic hyphal reactions involving reversible cytoplasmic retraction in obstacle-containing environments

The obstacles featured in our devices were designed to trigger collision events, which we hypothesised would provoke a response in AMF asymbiotic hyphae akin to that described for AMF extraradical hyphae[65] as well as for other filamentous fungi.[50,65,66] Expected phenotypes involved apical and lateral branching, tracking or nestling, as well as hit-and-split events.[67] Several instances of lateral branching were observed, occasional tracking of obstacle shapes, as well as one case of hit-and-split, though no true apical branching was found. Both irreversible and reversible cytoplasmic retraction were found with obstacles as well as in open space. Furthermore, collisions with obstacles did not always result in cytoplasmic retraction, at least not immediately, and instead hyphal growth ensued and resulted in hyphae gradually pushing themselves away from an obstacle as if they did not recognise, or tried to force their way through, the obstacle. Occasionally, hyphae froze mid-growth and remain unchanged for days without cytoplasmic retraction, highlighting a high overall versatility and breadth of their growth mechanisms.

As a new finding in this study, we identified a reversible cytoplasmic retraction, which involved withdrawal of cytoplasm, septa formation, breaching of septa and reintroduction of cytoplasm into previously emptied hyphae. Generally, it was observed that hyphae try to grow around an obstacle upon encountering it, tracking its edge to "escape" the obstacle. If the obstacle proves to be impassable, such as in dead-end corners, the fungus responds by branching off into another direction. As AMF are obligate symbionts (*i.e.*, do not possess saprotrophic capabilities) and their sole focus is to find a suitable host as fast as possible,[68] hyphae and spores have to be highly economical with their resources in the explorative asymbiotic state. Therefore, when the original growth path is blocked or appears unfavourable, they retract cytoplasm containing all cellular contents from the hyphal tip in order to redistribute it to another branch of the hyphal network; this retraction is a common observation in filamentous fungi in general,[69] as well as in AMF,[70,71] usually as a defence mechanism to keep the mycelial network from global compromisation.[72] The novelty of our finding, however, is that this process can be reversible in *R. irregularis* MUCL 41833 and MUCL 43194. The septa, which are formed to segregate empty compartments within a hypha from those that are filled, can be breached and cellular contents reintroduced into the emptied segments. Opening and closing of septa in septate fungi is a well-studied and common process. In Ascomycetes, for example, a so-called Woronin body functions as a plug for septa pores allowing for a controlled, selective permeability through these septa.[73] In non-septate fungi like AMF, where septation is of a primarily defensive nature, septal opening and closing has not been thoroughly described to date. Lee[74] proposed the removal of septa to control the expansion of cytoplasmic contents into new hyphal area in *Rhizophagus*. It can be assumed that septa are broken down entirely, as well as being newly formed, when compartmentalisation is needed. The observed reversible cytoplasmic retraction with septation, together with branching, makes hyphal exploration a highly dynamic process.

The repopulation of emptied hyphae might be an attempt to re-explore avenues to adapt to a changing environment, again with minimised resource requirements. Which signal or stimulus induces the retraction/repopulation here is unknown. Interestingly, we found that the number of formed septa was not always matched with the same number of septa breached, *i.e.*, the reversal of the retraction did not always occur all the way back to the hyphal tip, meaning the retraction can be reversed completely (*i.e.*, number of septa formed = number of septa breached) or incompletely (*i.e.*, number of septa formed > number of septa breached). The temporal dynamics of the retraction process were found to be most variable, with timings for retraction, reversal and pauses between retraction and reversal events fluctuating within a range of hours. No significant difference could be found for the retraction and reversal rates, which, however, does not mean retraction and reversal rates within a particular retraction event are always symmetrical. Furthermore, there was found to be less variation in reversal rates *cf.* retraction rates. To consolidate these observations and also to explore the influence of obstacles on the frequency, rates as well as symmetry of the retraction process, future focussed studies need to be conducted to obtain a higher sample size by, for example, implementing higher obstacle or spore densities in the devices as well as attempting to increase microscopy throughput for parallelised timelapse imaging. New preliminary insights into the dynamic behaviour of AMF at the cellular level, including identification of a reversible cytoplasmic retraction, were made possible using our high-resolution, real-time microfluidic approach.

To further characterise the reversible retraction of cytoplasm observed during hyphal space searching, we introduced the fluorescent dyes FM4-64[75–77] and calcofluor white[78–80] into the *AMF-SporeChip* to stain hyphae. Both dyes stained the fungal hyphae successfully and confirmed the identity of emptied hyphae. As expected, the chitin-specific calcofluor white stained every hypha, while the lipid bilayer-specific FM4-64 only stained certain hyphae, which usually appeared phase-dark under phase contrast, corroborating the finding that hyphae were emptied of their cytoplasmic content. In these empty hyphal "shells", only a very faint signal at 544 nm was visible; however, due to a slight autofluorescence of the studied strains it cannot be known with certainty whether the cell membrane remains behind after retraction of the cytoplasm, or rather is removed completely or decays shortly after the event. Implementation of fluorescent dyes such as these, especially FM4-64, for live-cell imaging of AMF hyphae in combination with our microdevices will help to characterise the dynamic retraction process in further detail, as well as aid examination of AMF hyphae for a potential Spitzenkörper.

This journal is © The Royal Society of Chemistry 2024

Conclusions

We have presented the first microfluidic device for studying AMF germination, asymbiotic hyphal development, anastomosis formation and space searching at the cellular level, which has provided new insights into AMF hyphal growth dynamics and revealed an intricate mechanism of space searching involving reversible cytoplasmic retraction, branching and directional changes. In the future, it is envisaged that the *AMF-SporeChip* could be modified easily to investigate several new frontiers in AMF research. One example includes modifying the design to accommodate two different strains of AMF simultaneously for the study of anastomosis phenotypes in a systematic manner. Further, our device could equally be used as a suitable platform to gain a deeper understanding of septa, as well as whether asymbiotic AMF hyphae possess a Spitzenkörper. To study metabolites involved in signalling, microfluidics could offer the opportunity to collect the fluidic volume for downstream metabolomics analyses, following visual examinations of these events. Our design is not only limited to AMF, as other fungal spores can be introduced into the *AMF-SporeChip* in a similar manner. Moreover, gradients of chemicals or nutrients can be implemented for studying foraging and signalling in soil exploration. The further development of our device could be also utilised for experiments on AMF interactions with bacteria, *e.g.*, phosphate solubilising bacteria, which have been reported to be important for phosphate uptake in AMF,[81] suggesting a tripartite symbiosis between plant, fungus and bacteria. To study the AMF symbiosis with their host roots in more detail, a device built from a combination of the *AMF-SporeChip* and the *RootChip*[82] could be of assistance.

Data availability

All relevant data are available from the corresponding author upon request.

Author contributions

The idea for the *AMF-SporeChip* and study was conceived by C. E. S., F. R. designed and fabricated the microfluidic device, and performed the experiments, the microscopy imaging and the data analysis. M. C. prepared the spore samples, as well as advice and training with regard to setting up AMF *in vitro* cultures. C. E. S. supervised this study, whereas S. D. and M. H. provided valuable feedback to the experimental work. F. R. and C. E. S. took the lead in writing the manuscript with contributions from all other authors. All authors read and approved the final version of the manuscript.

Conflicts of interest

The are no conflicts of interest to declare.

Acknowledgements

We acknowledge financial support from the Department of Bioengineering at Imperial College London, as well as the Swiss National Science Foundation in the form of an Ambizione Career Grant (PZ00P2_168005) to C. E. S. We thank Dr Emily Masters-Clark for informative scientific discussions.

References

1 P. Bonfante and A. Genre, *Nat. Commun.*, 2010, **1**, 48.
2 M. Cosme, I. Fernandez, M. G. A. van der Heijden and C. M. J. Pieterse, *Trends Plant Sci.*, 2018, **23**, 577–587.
3 M. G. A. van der Heijden, F. M. Martin, M. A. Selosse and I. R. Sanders, *New Phytol.*, 2015, **205**, 1406–1423.
4 R. M. Miller, J. D. Jastrow and D. R. Reinhardt, *Oecologia*, 1995, **103**, 17–23.
5 S. E. Smith and D. Read, in *Mycorrhizal Symbiosis (Third Edition)*, ed. S. E. Smith and D. Read, Academic Press, London, UK, 2008, pp. 145–188, DOI: **10.1016/B978-012370526-6.50007-6**.
6 I. Jakobsen and L. Rosendahl, *New Phytol.*, 1990, **115**, 77–83.
7 J. Shi, X. Wang and E. Wang, *Annu. Rev. Plant Biol.*, 2023, **74**, 569–607.
8 M. G. A. van der Heijden, R. D. Bardgett and N. M. van Straalen, *Ecol. Lett.*, 2008, **11**, 296–310.
9 S. W. Simard, K. J. Beiler, M. A. Bingham, J. R. Deslippe, L. J. Philip and F. P. Teste, *Fungal Biol. Rev.*, 2012, **26**, 39–60.
10 D. E. Prado-Tarango, R. Mata-González, M. Hovland and R. P. Schreiner, *Rangel. Ecol. Manag.*, 2021, **79**, 87–90.
11 A. Berruti, E. Lumini and V. Bianciotto, *Symbiosis*, 2016, **72**, 73–80.
12 E. Verbruggen, M. G. van der Heijden, M. C. Rillig and E. T. Kiers, *New Phytol.*, 2013, **197**, 1104–1109.
13 X. Zhu, K. Wang, H. Yan, C. Liu, X. Zhu and B. Chen, *Environ. Sci. Technol.*, 2022, **56**, 711–731.
14 M. Ijdo, S. Cranenbrouck and S. Declerck, *Mycorrhiza*, 2011, **21**, 1–16.
15 I. E. de la Providencia, F. A. de Souza, F. Fernandez, N. S. Delmas and S. Declerck, *New Phytol.*, 2005, **165**, 261–271.
16 I. E. De La Providencia, F. Fernández and S. Declerck, *FEMS Microbiol. Lett.*, 2007, **268**, 120–125.
17 M. Giovannetti, L. Ayio, C. Sbrana and A. Silvia Citernesi, *New Phytol.*, 1993, **123**, 115–122.
18 M. Giovannetti, P. Fortuna, A. S. Citernesi, S. Morini and M. P. Nuti, *New Phytol.*, 2001, **151**, 717–724.
19 M. Giovannetti, C. Sbrana, P. Strani, M. Agnolucci, V. Rinaudo and L. Avio, *Appl. Environ. Microbiol.*, 2003, **69**, 616–624.
20 D. Croll, M. Giovannetti, A. M. Koch, C. Sbrana, M. Ehinger, P. J. Lammers and I. R. Sanders, *New Phytol.*, 2009, **181**, 924–937.
21 F. Richter, S. Bindschedler, M. Calonne-Salmon, S. Declerck, P. Junier and C. E. Stanley, *FEMS Microbiol. Rev.*, 2022, fuac039, DOI: **10.1093/femsre/fuac039**.

CC BY

22 M. Held, C. Edwards and D. V. Nicolau, *J. Phys.: Conf. Ser.*, 2009, **178**, 012005.
23 M. Held, A. P. Lee, C. Edwards and D. V. Nicolau, *Microelectron. Eng.*, 2010, **87**, 786–789.
24 M. Held, C. Edwards and D. V. Nicolau, *Fungal Biol.*, 2011, **115**, 493–505.
25 M. Held, M. Binz, C. Edwards and D. Nicolau, *Proc. SPIE*, 2009, 7182.
26 D. D. Thomson, S. Wehmeier, F. J. Byfield, P. A. Janmey, D. Caballero-Lima, A. Crossley and A. C. Brand, *Cell. Microbiol.*, 2015, **17**, 342–354.
27 C. Puerner, N. Kukhaleishvili, D. Thomson, S. Schaub, X. Noblin, A. Seminara, M. Bassilana and R. A. Arkowitz, *BMC Biol.*, 2020, **18**, 122.
28 E. Couttenier, S. Bachellier-Bassi, C. d'Enfert and C. Villard, *Lab Chip*, 2022, **22**, 3898–3909.
29 C. E. Stanley, M. Stockli, D. van Swaay, J. Sabotic, P. T. Kallio, M. Kunzler, A. J. deMello and M. Aebi, *Integr. Biol.*, 2014, **6**, 935–945.
30 M. Stockli, B. I. Morinaka, G. Lackner, A. Kombrink, R. Sieber, C. Margot, C. E. Stanley, A. J. deMello, J. Piel and M. Kunzler, *Mol. Microbiol.*, 2019, **112**, 605–619.
31 L. J. Millet, J. Aufrecht, J. Labbe, J. Uehling, R. Vilgalys, M. L. Estes, C. Miquel Guennoc, A. Deveau, S. Olsson, G. Bonito, M. J. Doktycz and S. T. Retterer, *Fungal Biol. Biotechnol.*, 2019, **6**, 1.
32 J. K. Uehling, M. R. Entler, H. R. Meredith, L. J. Millet, C. M. Timm, J. A. Aufrecht, G. M. Bonito, N. L. Engle, J. L. Labbe, M. J. Doktycz, S. T. Retterer, J. W. Spatafora, J. E. Stajich, T. J. Tschaplinski and R. J. Vilgalys, *Front. Microbiol.*, 2019, **10**, 2163.
33 S. S. Schmieder, C. E. Stanley, A. Rzepiela, D. van Swaay, J. Sabotic, S. F. Norrelykke, A. J. deMello, M. Aebi and M. Kunzler, *Curr. Biol.*, 2019, **29**, 217–228.e4.
34 N. Ghanem, C. E. Stanley, H. Harms, A. Chatzinotas and L. Y. Wick, *Environ. Sci. Technol.*, 2019, **53**, 11755–11763.
35 A. Gimeno, C. E. Stanley, Z. Ngamenie, M. H. Hsung, F. Walder, S. S. Schmieder, S. Bindschedler, P. Junier, B. Keller and S. Vogelgsang, *Commun. Biol.*, 2021, **4**, 262.
36 K. Srisom, P. Tittabutr, N. Teaumroong, Y. Lapwong, R. Phatthanakun, S. Sirivisoot and P. Kuntanawat, *Mycorrhiza*, 2020, **30**, 789–796.
37 P. M. Mafla-Endara, C. Arellano-Caicedo, K. Aleklett, M. Pucetaite, P. Ohlsson and E. C. Hammer, *Commun. Biol.*, 2021, **4**, 889.
38 C. Baranger, I. Pezron, L. Lins, M. Deleu, A. Le Goff and A. Fayeulle, *Sci. Total Environ.*, 2021, **784**, 147151.
39 S. Declerck, D. Strullu and C. Plenchette, *Mycologia*, 1998, **90**, 579–585.
40 S. Cranenbrouck, L. Voets, C. Bivort, L. Renard, D.-G. Strullu and S. Declerck, in *In Vitro Culture of Mycorrhizas*, ed. S. Declerck, J. A. Fortin and D.-G. Strullu, Springer Berlin Heidelberg, Berlin Heidelberg, Germany, 2005, pp. 341–375, DOI: 10.1007/3-540-27331-X_18.
41 M. Köfferlein, *KLayout—high performance layout viewer and editor, v.0.27.25*, Munich, Germany, 2006, https://www.klayout.de/.
42 J. Schindelin, I. Arganda-Carreras, E. Frise, V. Kaynig, M. Longair, T. Pietzsch, S. Preibisch, C. Rueden, S. Saalfeld and B. Schmid, *Nat. Methods*, 2012, **9**, 676–682.
43 S. S. Lee, I. Avalos Vizcarra, D. H. Huberts, L. P. Lee and M. Heinemann, *Proc. Natl. Acad. Sci. U. S. A.*, 2012, **109**, 4916–4920.
44 Y. Dalpé, F. A. de Souza and S. Declerck, in *In Vitro Culture of Mycorrhizas*, ed. S. Declerck, J. A. Fortin and D.-G. Strullu, Springer Berlin Heidelberg, Berlin, Heidelberg, 2005, pp. 49–71, DOI: 10.1007/3-540-27331-X_4.
45 A. Groisman, C. Lobo, H. Cho, J. K. Campbell, Y. S. Dufour, A. M. Stevens and A. Levchenko, *Nat. Methods*, 2005, **2**, 685–689.
46 P. J. Lee, N. C. Helman, W. A. Lim and P. J. Hung, *BioTechniques*, 2008, **44**, 91–95.
47 Y. Zhang, C. Luo, K. Zou, Z. Xie, O. Brandman, Q. Ouyang and H. Li, *PLoS One*, 2012, **7**, e48275.
48 Y. Sun, A. Tayagui, A. Garrill and V. Nock, *Lab Chip*, 2020, **20**, 4141–4151.
49 S. Fukuda, R. Yamamoto, N. Yanagisawa, N. Takaya, Y. Sato, M. Riquelme and N. Takeshita, *mBio*, 2021, **12**, e03196-20.
50 A. Hopke, A. Mela, F. Ellett, D. Carter-House, J. F. Pena, J. E. Stajich, S. Altamirano, B. Lovett, M. Egan, S. Kale, I. Kronholm, P. Guerette, E. Szewczyk, K. McCluskey, D. Breslauer, H. Shah, B. R. Coad, M. Momany and D. Irimia, *PLoS One*, 2021, **16**, e0257823.
51 T. Souza, *Handbook of arbuscular mycorrhizal fungi*, Springer, Cham, Switzerland, 2015.
52 C. Baranger, A. Fayeulle and A. Le Goff, *R. Soc. Open Sci.*, 2020, **7**, 191535.
53 C. A. Kumamoto, *Nat. Rev. Microbiol.*, 2008, **6**, 667–673.
54 M. Held, D. L. Farkas, C. Edwards, D. V. Nicolau, R. C. Leif and D. V. Nicolau, *Proc. SPIE*, 2011, **7902**, 79020S-1.
55 C. B. D. Novais, A. Pepe, J. O. Siqueira, M. Giovannetti and C. Sbrana, *Sci. Agric.*, 2017, **74**, 411–416.
56 N. L. Glass, D. J. Jacobson and P. K. T. Shiu, *Annu. Rev. Genet.*, 2000, **34**, 165–186.
57 M. G. Roca, L. C. Davide, L. M. C. Davide, M. C. Mendes-Costa, R. F. Schwan and A. E. Wheals, *Mycol. Res.*, 2004, **108**, 1320–1326.
58 A. Fleißner, A. R. Simonin and N. L. Glass, in *Cell Fusion: Overviews and Methods*, ed. E. H. Chen, Humana Press, Totowa, NJ, 2008, pp. 21–38, DOI: 10.1007/978-1-59745-250-2_2.
59 T. L. Friesen, E. H. Stukenbrock, Z. Liu, S. Meinhardt, H. Ling, J. D. Faris, J. B. Rasmussen, P. S. Solomon, B. A. McDonald and R. P. Oliver, *Nat. Genet.*, 2006, **38**, 953–956.
60 H. Haj Hammadeh, A. Serrano, V. Wernet, N. Stomberg, D. Hellmeier, M. Weichert, U. Brandt, B. Sieg, K. Kanofsky, R. Hehl, R. Fischer and A. Fleißner, *Proc. Natl. Acad. Sci. U. S. A.*, 2022, **119**, e2112518119.
61 L. Voets, I. E. De La Providencia and S. Declerck, *New Phytol.*, 2006, **172**, 185–188.
62 M. Giovannetti, D. Azzolini and A. S. Citernesi, *Appl. Environ. Microbiol.*, 1999, **65**, 5571–5575.
63 P. M. McCabe, M. P. Gallagher and J. W. Deacon, *Mycol. Res.*, 1999, **103**, 487–490.

This journal is © The Royal Society of Chemistry 2024

64 N. D. Read, A. Lichius, J.-Y. Shoji and A. B. Goryachev, *Curr. Opin. Microbiol.*, 2009, **12**, 608–615.
65 E. C. Hammer, C. Arellano-Caicedo, P. M. Mafla-Endara, E. T. Kiers, T. Shimizu, P. Ohlsson and K. Aleklett, *Fungal Ecol.*, 2024, **67**, 101302.
66 K. Aleklett, P. Ohlsson, M. Bengtsson and E. C. Hammer, *ISME J.*, 2021, **15**, 1782–1793.
67 M. Held, O. Kaspar, C. Edwards and D. V. Nicolau, *Proc. Natl. Acad. Sci. U. S. A.*, 2019, **116**, 13543–13552.
68 S. E. Smith and D. J. Read, *Mycorrhizal Symbiosis*, Elsevier Science, Amsterdam, Netherlands, 2010.
69 A. P. Martínez-Camacho, M. O. Cortez-Rocha, M. M. Castillo-Ortega, A. Burgos-Hernández, J. M. Ezquerra-Brauer and M. Plascencia-Jatomea, *Polym. Int.*, 2011, **60**, 1663–1669.
70 V. Kokkoris, F. Stefani, Y. Dalpé, J. Dettman and N. Corradi, *Trends Plant Sci.*, 2020, **25**, 765–778.
71 B. Bago, C. Azcón-Aguilar, A. Goulet and Y. Piché, *New Phytol.*, 1998, **139**, 375–388.
72 C. Logi, C. Sbrana and M. Giovannetti, *Appl. Environ. Microbiol.*, 1998, **64**, 3473–3479.
73 R.-J. Bleichrodt, M. Hulsman, H. A. B. Wösten and M. J. T. Reinders, *mBio*, 2015, **6**, e00111–e00115.
74 J. Lee, *Mycobiology*, 2011, **39**, 79–84.
75 S. Fischer-Parton, R. Parton, P. Hickey, J. Dijksterhuis, H. Atkinson and N. Read, *J. Microsc.*, 2000, **198**, 246–259.
76 J. Dijksterhuis and D. Molenaar, *Antonie van Leeuwenhoek*, 2013, **103**, 921–931.
77 M. Garduño-Rosales, O. A. Callejas-Negrete, E. Medina-Castellanos, S. Bartnicki-García, A. Herrera-Estrella and R. R. Mouriño-Pérez, *Fungal Genet. Biol.*, 2022, **159**, 103672.
78 G. J. Hageage and B. J. Harrington, *Lab. Med.*, 1984, **15**, 109–112.
79 W. Zhang, H. Yang, L. Jiang, L. Han and L. Wang, *J. Int. Med. Res.*, 2010, **38**, 1961–1967.
80 B. Chen, W. Li, Y. Pang, N. Zhang, S. Bian, C. Liu, Z. Yang, Y. Jiang, R. Li and Y. Xie, *J. Microbiol. Methods*, 2021, **184**, 106202.
81 F. Jiang, L. Zhang, J. Zhou, T. S. George and G. Feng, *New Phytol.*, 2021, **230**, 304–315.
82 C. E. Stanley, J. Shrivastava, R. Brugman, E. Heinzelmann, D. van Swaay and G. Grossmann, *New Phytol.*, 2018, **217**, 1357–1369.

(cc) BY